

Numerical characterization of complex materials and vibro-acoustic systems

Author: Laura Río-Martín

PhD thesis, University of A Coruña / 2020

Supervisor: Andrés Prieto Aneiros

PhD program in Mathematical Modelling and Numerical Simulation in Engineering and Applied Science



UNIVERSIDADE DA CORUÑA



UNIVERSIDADE DA CORUÑA

Tese de doutoramento

Numerical characterization of complex materials and vibro-acoustic systems

Autora: Laura del Río Martín
Director: Andrés Prieto Aneiros

Tese presentada para a obtención do título de Doutor con Mención Internacional na Universidade da Coruña
Departamento de Matemáticas
Facultade de Informática, A Coruña (Spain)
Febreiro, 2020

Don Andrés Prieto Aneiros, profesor titular do Departamento de Matemáticas da Universidade da Coruña, informa que a memoria titulada:

**NUMERICAL CHARACTERIZATION OF COMPLEX MATERIALS AND
VIBRO-ACOUSTIC SYSTEMS**

foi realizada baixo a súa dirección por Dona Laura del Río Martín, estimando que a interesada atópase en condicións de optar ao grao de Doutora en Matemáticas, polo que solicitan que sexa admitida a trámite para a súa lectura e defensa pública.

En A Coruña, a 21 de febreiro de 2020.

O director:

Prof. Dr. Andrés Prieto Aneiros

A doutoranda:

Laura del Río Martín

*A mis padres, Agapito y María,
por su apoyo incondicional.*

*A mis sobrinos, Raquel y Alejandro,
para que luchen por sus sueños.*

*Life is not easy for any
of us. But what of that?
We must have perseverance
and above all confidence in
ourselves. We must believe
that we are gifted for
something and that this
thing must be attained.*

Marie Curie

Agradecimientos

Muchas personas me han acompañado a lo largo de este camino, y no me gustaría cerrar esta etapa sin dar las gracias a todos ellos.

A mi director de tesis, Andrés Prieto. Gracias por haber aceptado ser el director de mi trabajo fin de máster y por animarme a hacer el doctorado, por darme la oportunidad de realizar esta tesis bajo tu tutela, por tus palabras de ánimo (siempre has sido la parte optimista de este tandem), por abrirme todas las puertas que estaban en tu mano y por confiar en mí cuando ni siquiera yo lo hacía. Gracias por tu paciencia, por cuidar hasta el último detalle de la tesis y por permitirme aprender de ti, al mismo tiempo que me ayudabas a crear mi propio pensamiento crítico. Trabajar todos estos años contigo ha sido un privilegio. No podría haber llegado hasta aquí sin ti.

Gracias a Oscar P. Bruno por aceptar nuestra propuesta para hacer la estancia bajo tu supervisión, por darme parte de tu tiempo, por compartir tus conocimientos conmigo y por estar dispuesto a ayudarme siempre, tanto durante los meses que estuve en Caltech como al regresar. A Alfredo Bermúdez, por todo lo que aprendí de ti durante los casi dos años que colaboramos. Todo el mundo debería tener la oportunidad de trabajar con alguien como tú en algún momento de su carrera. A Jesús Carbajo y Jaime Ramis, por darme un punto de vista diferente de la acústica y por ayudarnos a entender mejor la parte física de los materiales. Siempre habéis sido muy generosos con nosotros, haciendo medidas y proponiendo nuevos problemas. Ha sido un placer trabajar con vosotros. También quiero agradecer a Elena Vázquez su inestimable ayuda y apoyo tanto durante el máster como después.

Gracias a todas las personas que han compartido momentos conmigo en todos estos años. A Bea, por acompañarme durante los años de máster y de doctorado. A Florian, por hacerme perder el miedo a contar mi trabajo en público y por seguir ahí después de tanto tiempo. A Patrick por escuchar cada una de mis presentaciones y ayudarme con todas ellas.

Mención especial se merecen Ana y Laura, que han sido mis grandes apoyos en estos duros años, en el laboratorio y sobre todo, fuera de él. Sois de lo mejor que me llevo de esta etapa.

Gracias a mis compañeros de mates de Valladolid (Eugis, Edu, Ana, Lidia, Laura), a mis amigas de Medina (Cris, Lara, Paula, Marta), por haberme apoyado en la distancia y por haber aguantado con paciencia mis ausencias durante estos años, y a Susana, por haber sido mi otra mitad desde siempre.

Y por último, pero no menos importante, gracias a mi familia y, en especial, a mis padres,

por apoyarme de forma incondicional en todas mis locuras. Nunca os podré agradecer lo suficiente todo lo que me habéis dado durante todos estos años y la paciencia que habéis tenido conmigo. Papá, me has inculcado el amor por aprender desde muy pequeña. Mi curiosidad es tu culpa (y bendita culpa). Mamá, si lUCHO cada día lo hago porque tú me has enseñado a no rendirme nunca. Espero poder devolveros algún día al menos una parte de todo lo que me habéis dado y enseñado. Gracias por todo. Espero que os sintáis orgullosos de mi.

Gracias a todos por confiar en mi, apoyarme y acompañarme en este camino.

Abstract

The acoustic characterization of materials plays an important role in a wide range of industrial applications. To get a proper acoustic characterization of a material, the knowledge of its intrinsic parameters is fundamental. However, this task is becoming increasingly difficult due to the continuous development of new materials. A classical parametric approach can be used to perform the acoustic characterization of a material. Once a model and its constitutive law are chosen, their unknown parameters are estimated by fitting the experimental data with the mechanical response of the model. The main drawback of this methodology is that the wrong choice of the parametric model can lead to get a response far from the experimental data.

The main purpose of this dissertation is to present a non-parametric methodology to characterize acoustically different materials. This data-driven methodology allows to avoid the epistemic uncertainty of an unsuitable model selection since the mathematical modeling of the materials is based only on the available experimental measurements. The proposed methodology requires the numerical solution of an inverse problem at each frequency of interest. To illustrate the efficiency of the methodology, numerical simulations are performed by using real-world measurements of porous, viscoelastic, and poroelastic materials.

Resumen

La caracterización acústica de materiales desempeña un papel importante en un gran número de aplicaciones industriales. Para lograr una caracterización adecuada del material es fundamental conocer sus parámetros intrínsecos. Sin embargo, la aparición y desarrollo de nuevos materiales hace esa tarea cada vez más difícil. Para caracterizar un material, es posible utilizar un enfoque paramétrico clásico: una vez elegido un modelo y su ley constitutiva, se estiman sus parámetros desconocidos ajustando los datos experimentales a la respuesta mecánica del modelo considerado. El inconveniente más relevante de esta metodología es que una elección errónea del modelo paramétrico puede llevar a obtener una respuesta muy alejada de los datos experimentales.

El principal objetivo de esta tesis es presentar una metodología no paramétrica para caracterizar materiales acústicamente. Es una metodología basada en datos y evita la incertidumbre epistémica de una selección de modelo inadecuada, ya que la modelización matemática de los materiales se basa únicamente en las medidas experimentales disponibles. La metodología propuesta requiere la resolución numérica de un problema inverso para cada frecuencia de interés. Para ilustrar la eficiencia de la metodología, se realizan simulaciones numéricas utilizando datos reales de materiales porosos, viscoelásticos y poroelásticos.

Resumo

A caracterización acústica de materiais xoga un papel importante nun gran número de aplicacións industriais. Co fin de obter una axeitada caracterización do material, é esencial coñecer os seus parámetros intrínsecos. Non obstante, a aparición e desenvolvemento de novos materiais fai que esta tarefa sexa cada vez máis difícil. Para caracterizar un material, é posible empregar un enfoque paramétrico clásico: unha vez escollido un modelo e a súa lei constitutiva, estímanse os seus parámetros descoñecidos axustando os datos experimentais á resposta mecánica do modelo elixido. A desvantaxe máis relevante desta metodoloxía é que unha elección errónea do modelo paramétrico pode levar a obter unha resposta moi afastada dos datos experimentais.

O principal obxectivo desta tese é expoñer unha metodoloxía non paramétrica para caracterizar materiais acusticamente. É unha metodoloxía baseada en datos e evita a incerteza epistémica dunha selección de modelo inadecuada, xa que a modelización matemática dos materiais baséase únicamente nas medidas experimentais dispoñibles. A metodoloxía proposta require a resolución numérica dun problema inverso para cada frecuencia de interese. Para ilustrar a efectividade da metodoloxía, realizanse simulacións numéricas empregando datos reais de materiais porosos, viscoelásticos e poroelásticos.

Contents

Preface	xiii
I Characterization of porous materials in a Kundt's tube	1
1 Parametric characterization of multilayer porous materials	3
1.1 Introduction	5
1.2 Mathematical models	6
1.2.1 Compressible fluid	6
1.2.2 Classical rigid-frame porous models	7
1.3 Coupling conditions	17
1.3.1 Contact interface	17
1.3.2 Rigid wall	17
1.3.3 Radiation conditions	18
1.3.4 Thin media models	18
1.4 Plane wave analysis	19
1.4.1 Absorption problem: multilayer medium backed by a rigid surface . .	20
1.4.2 Transmission problem: multilayer medium surrounded by a fluid . .	21
1.5 Acoustic quantities	22
1.6 Numerical procedure to solve the inverse problems	23
1.6.1 Absorbing materials	23
1.6.2 Films	24
1.7 Numerical results	25
1.7.1 Porous materials	25
1.7.2 Films	29
1.7.3 Foam	31
1.8 Conclusions	32
2 A non-parametric fluid-equivalent approach for the acoustic characterization of rigid porous materials	35
2.1 Introduction	37
2.2 Harmonic response of a rigid porous material	39
2.2.1 Macroscopic description	39

2.2.2	Experimental characterization	40
2.3	Acoustic characterization of a single porous layer using a fixed-frequency inverse problem	42
2.3.1	Statement of the direct propagation problem	42
2.3.2	Characterization with absorption datasets	46
2.3.3	Characterization with surface impedance datasets	48
2.4	Acoustic characterization of a double porous layer using a fixed-frequency inverse problem	50
2.4.1	Statement of the direct propagation problem	50
2.4.2	Characterization with four surface admittance datasets	52
2.5	Numerical procedure to solve the inverse problems	54
2.5.1	Non-parametric approach	54
2.5.2	Parametric JCAL approach	57
2.6	Characterization results	57
2.6.1	Spurious oscillations	58
2.6.2	Single layer case	60
2.6.3	Double layer case	62
2.7	Conclusions	66

II Characterization of viscoelastic materials in underwater environments

69

3 Non-parametric characterization of viscoelastic materials	71	
3.1	Introduction	73
3.2	Mathematical modeling	75
3.2.1	Mathematical models	75
3.2.2	Coupled problem	76
3.2.3	Acoustic quantities of interest	77
3.3	Statement of the direct problem: wave propagation in a multilayer medium .	78
3.3.1	Integral representation of pressure fields	79
3.3.2	Computation of reflection and transmission coefficients by using a plane-wave framework	83
3.4	Acoustic characterization of a viscoelastic solid using an inverse problem .	86
3.4.1	Constitutive laws for the primal unknowns	86
3.4.2	Adjoint problem	92
3.5	Numerical results	93
3.5.1	Code validation	94
3.5.2	Experimental data	104
3.5.3	Numerical simulation considering a parametric model	105
3.5.4	Numerical simulation considering a non-parametric approach	106
3.6	Conclusions	118
Appendices	123

3.A	Integral approximation	123
3.B	Derivatives	126
4	Numerical simulation of layered materials with non-planar geometries	129
4.1	Introduction	131
4.2	Sound-soft periodic surface with a single-layer representation	132
4.2.1	Statement of the problem	132
4.2.2	Classical quasi-periodic Green function	134
4.2.3	Slow-rise windowing Green function	134
4.2.4	Shifted quasi-periodic Green function	136
4.2.5	Integral formulation	138
4.3	Sound-soft periodic surface with a double-layer representation	142
4.3.1	Integral formulation	142
4.4	Transmission problem	146
4.4.1	Statement of the problem	146
4.4.2	Shifted quasi-periodic Green function	149
4.4.3	Integral formulation	149
4.5	Discretization	161
4.5.1	MKN quadrature rules	161
4.5.2	Efficiency computation	162
4.5.3	Discrete problems	166
4.6	Numerical results	171
4.6.1	Numerical results for the scattering problem by a sound-soft boundary with a single-layer formulation	172
4.6.2	Numerical results for the scattering problem by a sound-soft boundary with a double-layer formulation	175
4.6.3	Numerical results for the transmission problem	178
4.7	Conclusions	186
	Appendices	191
4.A	Bessel functions	191
4.B	Kernel decomposition in a periodic setting	193
4.B.1	Single-layer potential	193
4.B.2	Double-layer potential	195
4.B.3	Adjoint double-layer potential	198
4.B.4	Hypersingular formulation	201
4.C	Perfectly Matched Layers	211
4.C.1	Statement of the quasi-periodic problem	211
4.C.2	Variational formulation	214
4.C.3	Finite element discretization	215

III Characterization of complex systems using time-dependent problems	217
5 Characterization of porous materials using alpha cabins	219
5.1 Introduction	221
5.2 Methodology based on modal computations	222
5.2.1 Displacement formulation with rigid walls	222
5.2.2 Displacement formulation with absorbing boundaries	226
5.2.3 Displacement formulation with absorbing boundaries and porous sample	230
5.2.4 Finite element discretization	233
5.3 Methodology based on a full time-dependent discretization	237
5.3.1 Finite element discretization	239
5.4 Computation of the absorption values in an alpha cabin	241
5.4.1 Computation of the reverberation time	241
5.4.2 Computation of the absorption value	243
5.4.3 Computation of decay rates	244
5.5 Numerical results	245
5.5.1 Two-dimensional simulations	245
5.5.2 Three-dimensional simulation	251
5.6 Conclusions	254
6 Characterization of viscoelastic materials using impact excitations	257
6.1 Introduction	259
6.2 Experimental determination of the dynamic stiffness using the standard ISO 9052-1	259
6.3 Design of the hierarchy of models	261
6.4 Modal decomposition of compressional solutions of a viscoelastic model	261
6.5 Full time-dependent one- and three-dimensional viscoelastic model	263
6.5.1 Strong formulation	264
6.5.2 Variational formulation	265
6.5.3 Finite element discretization	266
6.6 Full time-dependent three-dimensional poroelastic model	268
6.6.1 Strong formulation	269
6.6.2 Variational formulation	270
6.7 Inverse problem to determine the elastic coefficients	274
6.8 Numerical results	275
6.8.1 Code validation	275
6.8.2 Viscoelastic sample	281
6.9 Conclusions	283
Further research	285

Contents

xi

Resumen en castellano	287
Fundings	295
Bibliography	297

Preface

The acoustic characterization of materials plays an important role in a wide range of industrial applications. For example, concern for acoustic comfort in means of transport is increasing over the years: the reduction of noise emitted from jet engines in aircrafts, or the control of vibrations in a vehicle are currently highly studied problems, and to use the best combination of materials to improve the acoustic comfort is a great challenge in automotive, and aerospace industries. Similarly, the use of new materials, such as natural or recycled fibers, which have a lower environmental impact, has become more and more popular in the industry.

Being aware of the acoustic behavior of a material and knowing its intrinsic properties can be a great advantage, especially at the design stage of noise control systems, because it allows us to be described precisely the acoustic behavior of the material. This means better use of existing materials, or even the use of new ones, during the design stage, leading to a reduction in both costs and production time.

The knowledge of the acoustic properties of a material is an increasingly difficult task. On the one hand, the constant development of new materials, some of them formed by a mixture of recycling materials with different properties, makes it difficult to find the intrinsic properties of the resulting material. On the other hand, there are materials with unknown properties, which are part of noise control devices, and which, due to their characteristics or nature, cannot be studied when the material is considered individually, and it is necessary to study its properties when such a material is part of a more complex system.

The main goal of this thesis is to give some novel tools that allow us to characterize acoustically both single and multilayer materials. In the literature, there exist a variety of parametric models to characterize, in a precise way, a layer of a significant part of the existing materials. In order to achieve an adequate characterization, the correct choice of the parametric model is fundamental because the more appropriate the model is, the more precise its mechanical response will be, compared to the experimental data. Usually, with these parametric models, it is necessary to set the frequency-dependent constitutive law, and then the available experimental measurements are fitted with the mechanical response of the chosen model to estimate its unknown parameters. This modeling methodology suffers potentially from the epistemic uncertainty of an unsuitable model selection. In this thesis, a data-driven approach is considered, avoiding the need to choose a constitutive law for fitting. The fitting problem consists of minimizing the distance between a set of available experimental data and the values obtained from the mechanical response of the model.

Therefore, the mathematical modeling of the materials and the choice of their frequency-dependent constitutive models are based only on the available experimental measurements, and not on imposing any functional dependence of the intrinsic parameters in terms of frequency. This data-driven methodology requires the numerical solution of an inverse problem at each frequency of interest.

In the present dissertation thesis, there are three different parts, with a common thread: the acoustic characterization of mono or multilayer materials that are used in the industry, considering a novel non-parametric approach. It is important to highlight that all the numerical simulations are performed by using real scenarios and in collaboration with different research groups. The first part of this thesis is devoted to characterizing porous and fibrous materials, and the available experimental data are absorption values at normal incident come from the Kundt's tube. In the second part, the material under study is a viscoelastic solid, and the available experimental data are the echo reduction, the insertion loss, and the fractional power dissipation, given at ultrasonic frequencies. Finally, the last part of the thesis shows the characterization of complex systems, which involve porous materials and viscoelastic solids, in time-dependent frameworks. The available experimental data for porous materials are absorption values at diffuse field, measured in an alpha cabin, and for viscoelastic materials, values of the dynamic stiffness measured using an excitation method. A summary of each part and each chapter is featured below.

Part I: Characterization of porous materials in a Kundt's tube. This part is focused on the characterization of porous and fibrous materials, which are used in the automotive industry, in the frequency domain. To predict the acoustic properties of these materials is of great interest for a wide range of industrial applications. However, the constant development of these materials makes it necessary to use new techniques to describe their acoustic behavior. From a classical point of view, porous materials are modeled by using fluid-equivalent models. But, in some cases, the chosen parametric model could not be suitable for a particular material. For this reason, a novel non-parametric approach is proposed. The main goal of this part is to compare the parametric approach and the non-parametric methodology, remarking the differences between both of them. This first part is organized as follows:

- **Chapter 1: Parametric characterization of multilayer porous materials.** Porous materials may be modeled as an equivalent fluid, from a macroscopic point of view. For this reason, a detailed review of the parametric fluid-equivalent models is given, attending to their intrinsic physical parameters. Since the available experimental data are the absorption values, measured in the Kundt's tube, for different configurations of single and multilayer materials, a study of several sound propagation problems in multilayer media with different configurations has been carried out, specifying the different coupling conditions used between media, such as contact, rigid wall, or radiation conditions, and the most relevant acoustic quantities, such as the absorption coefficient or the surface impedance of a medium. Finally, numerical results are shown to illustrate in which situations a parametric approach could be useful, and the weaknesses of this parametric methodology, where a non-parametric approach

can lead us to obtain better results in the fitting and can avoid the difficulties that appear with the parametric modelling.

- **Chapter 2: A non-parametric fluid-equivalent approach for the acoustic characterization of rigid porous materials.** Instead of this, a data-driven approach is considered, avoiding the choice of a frequency-dependent constitutive law for fitting. To avoid epistemic uncertainty when the parametric model chosen to characterize a rigid porous material is not appropriate, this chapter considers a data-driven approach, avoiding the choice of a frequency-dependent constitutive law for fitting. Taking into account the available experimental data, without considering any functional parameter dependence, an inverse problem is solved numerically at each frequency of interest. In this chapter, the acoustic quantities used to characterize the porous materials are defined, and the setup used to measure the experimental data is described. This setup reproduces the methodology developed by Utsuno [171] to characterize single layer materials, and has therefore been used to validate the results obtained with the proposed methodology. The used inverse problem methodology is explained in detail, and four different strategies used to choose the primal unknowns in the inverse problem are discussed. Each one of them overcomes the limitations of the traditional fitting procedures used for the same purpose. The numerical results show that the proposed methodology is useful in a single porous layer configuration, comparing the results with those obtained with the Utsuno's method, and that it can be extended to a double porous layer configuration, in which other methodologies can not be applied, showing good agreement in comparison with the experimental data.

The work described in this chapter is a collaboration with Jesús Carbajo and Jaime Ramis from the Department of Physics, Systems Engineering and Signal Theory of the University of Alicante, and some of the results presented in this chapter are published in [54].

Part II: Characterization of viscoelastic materials in underwater environments
The second part is devoted to studying the acoustic behavior of a viscoelastic material at ultrasonic frequencies in underwater environments. The material under consideration is a polymer tile which has a viscoelastic mechanical behavior at ultrasonic frequencies. The available experimental data are the echo reduction (ER), the insertion loss (IL), and the fractional power dissipation (FPD), measured within a water tank. This second part has two main goals. The first one is to characterize the viscoelastic material considering a planar surface by using a data-driven approach. In this first case, a problem of propagation has been studied where two different acoustic sources have been taking into account: a plane wave impinging on the material with an oblique incidence angle, and an acoustic source with a general non-planar directivity pattern. The second goal is to characterize the viscoelastic material considering its periodic and non-planar surface. For this purpose, an integral equation method is used to solve the transmission problem by a periodic coupling interface. Then, this part is organized as follows:

- **Chapter 3: Non-parametric characterization of viscoelastic materials.** In this chapter, a polymer tile has been characterized in an underwater environment. Since the considered frequencies are ultrasonic frequencies, the polymer shows a viscoelastic behavior. Although the material has a non-planar surface, it is considered as a first simplification that its surface is plane. First, the mathematical models of the media involved in multilayer are described: dissipative compressible fluid and viscoelastic solid. Then the coupled problem under consideration is described, and the acoustic quantities of interest (reflection and transmission coefficients, ER, IL and FPD). Two different direct problems of wave propagation have been considered: when the source is a plane wave impinging on the material at oblique incidence, and when the acoustic source is a parametric array, that is, the source has a non-planar directivity pattern. Since the methodology used for the characterization is a data-driven approach, an inverse problem is solved numerically at each frequency of interest. Throughout the chapter, different constitutive laws over the primal unknowns of the inverse problem are shown (consider the Young modulus as a linear function of frequency, consider that it is governed by an arbitrary smooth frequency-dependent function, or consider some new variables that depend on the wave number of the material and its thickness), showing the difficulties derived from each of them and how they can be overcome. A validation of the proposed methodology has been carried out, using manufactured data. To illustrate the robustness of the methodology with respect to the initial guess chosen to solve the optimization problem, a variety of initial guess in a grid around the exact value has been considered. Fitting curves have been computed for the quantities of interest, ER, IL, and FPD, to show the variability of frequency responses as the initial guess varies. Finally, numerical results are shown with a real-world material to illustrate the effectiveness of the proposed method.
- **Chapter 4: Numerical simulation of layered materials with non-planar geometries.** The same viscoelastic solid than in the previous chapter is considered, but, in this case, its surface is periodic and non-planar. Since the transmission problem between two media, with a non-planar periodic surface, considering that the source has a non-planar directivity pattern, presents many difficulties, several simplifications have been considered, such as to consider a plane wave impinging with an oblique incidence angle as acoustic source, or to neglect possible shear effects, assuming that the material can be only deformed on tension/compression mechanical stresses. In this chapter, an integral equation method is proposed to solve this problem. The more challenging issue is that the method does not converge for all frequencies. To achieve a fast convergence, a shifted quasi-periodic Green function and a windowing technique are used. Throughout the chapter, and for the sake of completeness, two different problems have been described. The first problem is the scattering of sound waves over a sound-soft periodic boundary. To solve this problem, single- and double-layer representations have been used. In both cases the integral equation method has been detailed, explaining the convergence problem that appears in the kernels. Since these kernels involve Hankel and Bessel functions, logarithmic singularities appear that

must be treated separately, splitting these kernel into a smooth and a logarithmic part. In addition, quadrature rules are defined to approximate all the integrals that appear in the method. The second problem to study is the problem of transmission by a periodic coupling interface between two media. As in the previous case, single- and double-layer potentials have been used in the integral formulations. In this case, it is also necessary to deal with an hypersingular kernel which present logarithmic singularities that are overcome by splitting the integral into two integrals (one with a smooth kernel and the other involving the logarithmic part), which are approximate with the quadrature rules described above. Numerical results are shown at the end of the chapter. To validate the methodology, the results have been compared with those obtained using the finite element method with a coarse mesh, showing that the errors are several orders smaller. In addition, efficiencies are calculated to show the fast convergence of the method.

The work described in this chapter is a collaboration with Professor Oscar P. Bruno of the California Institute of Technology, carried out during a predoctoral visit of 14 weeks.

Part III: Characterization of complex systems using time-dependent problems

The last part of the thesis shows the characterization of complex systems involving different types of materials, such as rigid porous materials, viscoelastic solids, or poroelastic materials, in time-dependent frameworks. The available experimental data come from two different setups: absorption coefficients at diffuse field, measured in an alpha cabin, and dynamic stiffness, measured by using an excitation method. Firstly, a methodology to compute the absorption coefficient of a porous material at diffuse field in an alpha cabin is proposed. Secondly, a new method based on a hierarchical modeling approach to compute the dynamic stiffness of a viscoelastic or poroelastic solid is explained. This part is organized as follows:

- **Chapter 5: Characterization of porous materials using alpha cabins.** Although the absorption coefficient of a material at diffuse field can be calculated by using the measurement in the Kundt's tube, the most common technique to compute it is the reverberation room method. In the automotive industry the absorption coefficient of a material is usually measured in an alpha cabin which is a reverberant chamber where the frequency range and sample size is adapted to the requirements of automotive acoustics. Since there is no standard to measure the absorption coefficient in an alpha cabin, this chapter proposes a modification of the technique used in the reverberant room. The main goal is to adapt the available methodology to the dimensions of the alpha cabin in order to be able to measure the diffuse field. For this reason, different assumptions are made about the behavior of the sound inside the cabin. To measure the absorption coefficient, it is necessary to measure the reverberation time in the cabin with the sample and without the sample. Therefore, a full time-dependent discretization is considered for calculating the reverberation time in the cabin, and two different expressions are given to obtain the diffuse field

absorption coefficient from this reverberation time (Sabine and Millington formulas). Finally, numerical results are shown in two- and three-dimensional domains to illustrate the effectiveness of the proposed method.

- **Chapter 6: An efficient hierarchical modeling approach to determine the mechanical properties of an elastic material using dynamic stiffness data.**

The dynamic stiffness of an elastic material is very important to quantify the reduction of noise propagation. For this reason, this quantity can be used to determine the acoustic insulation of these materials. The purpose of this chapter consists in obtaining the elastic coefficients of the material, by using a numerical methodology based on a hierarchical modeling approach, and considering only the available experimental data. The definition of the model hierarchy is made considering from the simplest models to those where the most sophisticated details are taken into account and their levels of accuracy are based on the assumptions made at each level. In this approach, the differences between the mathematical models are based on the choice of a one- or three-dimensional model and on neglecting or not the shearing modes that are possibly contributing to the solution. Different models are proposed to describe the behavior of viscoelastic and poroelastic materials, and a time-dependent discretization is considered to solve the problem. Some numerical results with manufactured data are presented to validate the code, in addition to some preliminary results with a real material are shown.

The work described in this chapter is a collaboration with Jesús Carbajo, Pedro Poveda and Jaime Ramis from the Department of Physics, Systems Engineering and Signal Theory from the University of Alicante.

The last part of this document is devoted to proposing some future research lines, some of them are starting to develop, and other ones are open problems.

Part I

Characterization of porous materials in a Kundt's tube

Chapter 1

Parametric characterization of multilayer porous materials

Contents

1.1	Introduction	5
1.2	Mathematical models	6
1.2.1	Compressible fluid	6
1.2.2	Classical rigid-frame porous models	7
1.3	Coupling conditions	17
1.3.1	Contact interface	17
1.3.2	Rigid wall	17
1.3.3	Radiation conditions	18
1.3.4	Thin media models	18
1.4	Plane wave analysis	19
1.4.1	Absorption problem: multilayer medium backed by a rigid surface	20
1.4.2	Transmission problem: multilayer medium surrounded by a fluid	21
1.5	Acoustic quantities	22
1.6	Numerical procedure to solve the inverse problems	23
1.6.1	Absorbing materials	23
1.6.2	Films	24
1.7	Numerical results	25
1.7.1	Porous materials	25
1.7.2	Films	29
1.7.3	Foam	31
1.8	Conclusions	32

1.1 Introduction

The acoustic characterization of porous materials such as foams, materials made of fibers, textiles or films, is of great interest for a wide range of industrial applications. These materials are frequently used in building, automotive, and aeronautics industries [22, 56, 135, 164]. Concern for acoustic comfort is increasing over the years: the reduction of noise in a vehicle or the control of vibrations are currently highly studied problems [19, 51]. Being aware of the acoustic behavior of a material and knowing its intrinsic properties can lead us to a reduction of costs and time in the design of the acoustic insulation of a vehicle. However, this task is increasingly difficult due to the constant development of new materials in the field of acoustic comfort. The main objective of this chapter is the acoustic characterization of porous materials used in the automotive sector by using parametric models. The samples under study are both materials with one layer and multilayer materials.

Usually, porous materials are modeled on a macroscopic scale as an equivalent fluid having frequency-dependent complex acoustic properties, namely, characteristic impedance and wave number [7]. These effective acoustic coefficients can be obtained from using specific measurement procedures ([70, 78, 79, 161, 169, 171]) or determined using a parametric prediction model (e.g. [55, 69, 93, 100]). In general, these parametric models are based on the asymptotic behavior at low and high frequencies of rigid porous media [55, 100] or make use of empirical relations [69] to describe the sound propagation through the material. In any case, it is necessary to determine one or several of its intrinsic physical properties (e.g., flow resistivity, porosity) before deriving its relation with respect to the effective acoustic coefficients. Although a variety of laboratory methods and techniques [66] are available to determine these physical parameters, a common alternative to these procedures consists of using a derivative-free optimization procedure [131] to fit the values of these properties. In brief, an inverse methodology can be employed to minimize the difference between the measured effective quantities of interest and those calculated using a prediction model whose parameters need to be fitted. In most cases, and to simplify the fitting procedure, a wide-band frequency spectrum of the surface impedance or the sound absorption coefficient are used for this adjustment [33, 83, 173]. Both the surface impedance and the sound absorption coefficient can be obtained for a given material when it is used as a sound absorber (i.e., a layer of porous material backed by a rigid wall) by using the standardized impedance tube method [1].

The purpose of this chapter is to characterize single and multilayer porous materials. In Section 1.2, the mathematical models used in this chapter are described. Most of the rigid-frame porous materials can be modeled by using a fluid-equivalent model. Despite their mathematical simplicity, such models involve a variety of intrinsic physical parameters, which should be determined for each sample material. Hence, throughout Section 1.2.2, the porous models derived in the last decades are described, giving a detailed definition of their intrinsic parameters in terms of quantities computed in representative elementary volumes of porous and fibrous materials. In Section 1.3, the coupling conditions used to characterize porous materials are described (contact, rigid wall, radiation conditions,...).

Moreover, Section 1.4 describes two different multilayer problems used for the characterization: one for computing the absorption coefficient of a multilayer medium and another one for calculating the transmission coefficient of a multilayer medium. In Section 1.5, a study of the most relevant acoustic quantities, such as the absorption coefficient, the transmission coefficient, or the surface impedance of a medium, is carried out. Section 1.6 shows the inverse problems solved to characterize the materials under consideration acoustically. In Section 1.7, different numerical results are shown. Some experimental data are used to illustrate in which situations a parametric approach may be useful and in which it may not. Finally, in Section 1.8, some conclusions about the parametric methodology are given, explaining the advantages of this methodology and emphasizing the proposed solutions to overcome its drawbacks.

Remark 1.1.1. *Throughout this chapter, the time-harmonic dependence for the pressure field (and also for the rest of the physical quantities) has been settled as $\pi(\mathbf{p}, t) = \text{Re}(\Pi(\mathbf{p})e^{i\omega t})$, being π the time-dependent acoustic pressure field, Π the complex-valued time-harmonic acoustic pressure field, ω the angular frequency, t the time variable, \mathbf{p} the Cartesian coordinates of the spatial position, $\text{Re}(\cdot)$ the real part function of a complex number, and i the imaginary unit.*

1.2 Mathematical models

To compute the mechanical response of the porous materials, a variety of configurations are considered, such as fluid-porous-rigid wall, fluid-porous-fluid, fluid-rigid plate-porous-rigid wall,... In what follows, the mathematical models of the layers and the coupling conditions used in these configurations are described in detail.

1.2.1 Compressible fluid

If the acoustic pressure field (understood as the Lagrangian fluctuation of the total pressure field) is considered as primal unknown, then the time-dependent linear equation of motion of a compressible fluid (which is assumed inviscid and isentropic) is given by

$$\frac{1}{\rho_F c_F^2} \frac{\partial^2 \pi}{\partial t^2} - \text{div} \left(\frac{1}{\rho_F} \nabla \pi \right) = 0,$$

where π is the pressure field, and ρ_F and c_F are the mass density and the sound velocity, respectively, at the equilibrium state of reference. Imposing harmonic solutions, i.e., if $\pi(\mathbf{p}, t) = \text{Re}(e^{i\omega t}\Pi(\mathbf{p}))$, being ω the angular frequency and \mathbf{p} the spatial coordinates vector, the harmonic pressure field Π satisfies

$$-\frac{\omega^2}{\rho_F c_F^2} \Pi - \text{div} \left(\frac{1}{\rho_F} \nabla \Pi \right) = 0,$$

and if ρ_F is assumed constant, it holds

$$-\frac{\omega^2}{c_F^2}\Pi - \Delta\Pi = 0.$$

1.2.2 Classical rigid-frame porous models

The acoustic behavior of a rigid-frame porous material at the time-harmonic regime can be represented by an equivalent fluid wave equation, written in terms of the pressure field Π , given by

$$-\omega^2\rho_{eq}(\omega)\Pi - K_{eq}(\omega)\Delta\Pi = 0,$$

where ω is the angular frequency, $\rho_{eq}(\omega)$ is the equivalent dynamic mass density, and $K_{eq}(\omega)$ is the equivalent dynamic bulk modulus of the porous material. This model described above is the so-called fluid-equivalent formulation. Both equivalent coefficients are not only depending on the angular frequency but also other intrinsic material-dependent parameters such as the bulk mass density, the porosity, the static airflow resistivity, the tortuosity, the static thermal permeability, and the viscous and thermal characteristic length, among others.

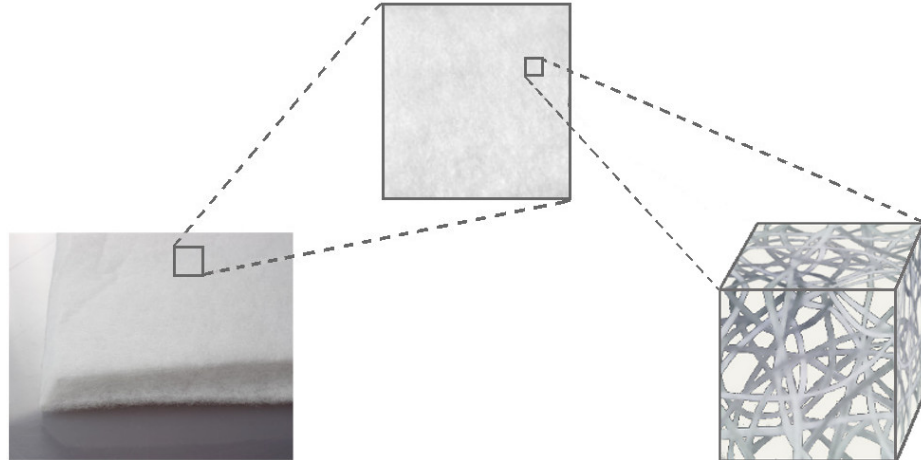


Figure 1.1: Example of a representative elementary volume of a polyethylene terephthalate fibers material.

To describe each one of these parameters, it is essential to take into account the concept of a representative elementary volume (REV), which is the smallest volume over which an experimental measurement (or an analytical computation taking into account the microstructure of the material) can be made to obtain a proper representative value of the whole sample material at a macroscopic scale. In Figure 2.1, a cube of foam material has been considered as REV. The total representative elementary volume Ω is divided into two disjoint parts: the grey region is the solid domain Ω_S of the representative elementary volume, and the transparent part of the representative volume is the domain Ω_F occupied by the interstitial fluid.

Intrinsic parameters definition

In order to describe the sound propagation in porous media, it is necessary to determine a set of intrinsic macroscopic acoustical parameters such as bulk mass density, porosity, flow resistivity, tortuosity, permeability, or characteristic length. In what follows, each one of these parameters is defined in detail.

Definition 1.2.1 (Bulk mass density). *The bulk mass density ρ of a porous material is given by*

$$\rho = \frac{1}{\text{vol}(\Omega)} \int_{\Omega_S} \rho_S(\mathbf{p}) dV_p, \quad (1.1)$$

where ρ_S is the mass density of the solid part of the representative volume Ω , and $\text{vol}(\cdot)$ is the volume function of a three-dimensional domain.

Definition 1.2.2 (Porosity). *The open porosity ϕ is defined as the ratio of the interconnected pore fluid volume (the volume of the fluid phase) to the total bulk volume of the porous aggregate. It can also be expressed in terms of the fluid and solid part of a REV as (see [7])*

$$\phi = \frac{\text{vol}(\Omega_F)}{\text{vol}(\Omega)} = 1 - \frac{\text{vol}(\Omega_S)}{\text{vol}(\Omega)}, \quad (1.2)$$

where recall that the REV domain Ω is split in the fluid and solid part, i.e., $\Omega = \Omega_F \cup \Omega_S$.

Since the mass density of the solid part in the REV is assumed constant microscopically, from (1.1) it holds $\text{vol}(\Omega_S) = \rho \text{vol}(\Omega)/\rho_S$ and so the porosity (1.2) can be rewritten in terms of the bulk mass density ρ and the solid mass density ρ_S :

$$\phi = 1 - \frac{\rho}{\rho_S}.$$

For the particular case of a porous material having q cylindrical pores of radius R per unit area of cross-section, the porosity is given by (see [7])

$$\phi = q\pi R^2. \quad (1.3)$$

The absorption in a porous material is related to the resistance of the material to an airflow passing through (the flow resistivity). Then, let us also assume that the REV has two fronted parallel faces, Γ_0 and Γ_1 and that a fluid flow is imposed in the porous sample, which produces a jump on the total pressure field at both faces of the REV. On each of these boundaries, the total fluid pressure and the velocity \mathbf{W} are assumed constant. Since both faces share the same unit normal vector \mathbf{n} (exterior to Ω on Γ_1) and the fluid is supposed incompressible at the microscopic scale, the normal velocity is identical on both boundaries. Thereby the flow resistivity can be defined as

Definition 1.2.3 (Flow resistivity). *The flow resistivity σ is defined as the quotient of the fluid pressure jump on the fronted parallel boundaries of a REV (which are induced by a*

fluid flow) divided by the thickness sample h and the normal velocity $\mathbf{W} \cdot \mathbf{n}$ (see [7]), this is,

$$\sigma = \frac{\Pi|_{\Gamma_1} - \Pi|_{\Gamma_0}}{h(\mathbf{W} \cdot \mathbf{n})|_{\Gamma_0}}.$$

For a porous material, with cylindrical pores of radius R , the flow resistivity can be written as (see [7])

$$\sigma = \frac{8\eta}{R^2\phi}, \quad (1.4)$$

where η is the dynamic viscosity of the fluid in the porous sample, and ϕ is the porosity given by (1.3).

Definition 1.2.4 (Tortuosity). *The geometrical parameter called tortuosity α_∞ is related to the apparent increase in the mass density when the fluid saturates a porous structure and is given by (see [7])*

$$\alpha_\infty = \frac{\frac{1}{\text{vol}(\Omega_F)} \int_{\Omega_F} ||\mathbf{W}(\mathbf{p})||^2 dV_p}{\left(\frac{1}{\text{vol}(\Omega_F)} \int_{\Omega_F} ||\mathbf{W}(\mathbf{p})|| dV_p \right)^2},$$

where \mathbf{W} is the induced microscopic velocity field in the fluid part Ω_F of a REV assuming that it is filled by an incompressible fluid.

It is commonly assumed in the scientific literature that for fibrous materials with porosity ϕ close to one, $\alpha_\infty = 1$ (see [7]).

Definition 1.2.5 (Static viscous tortuosity). *This parameter accounts for the additional inertial influence on the viscous effects at low frequencies, and it is defined by (see [110])*

$$\alpha_0 = \frac{\frac{1}{\text{vol}(\Omega_F)} \int_{\Omega_F} ||\mathbf{W}_0(\mathbf{p})||^2 dV_p}{\left(\frac{1}{\text{vol}(\Omega_F)} \int_{\Omega_F} ||\mathbf{W}_0(\mathbf{p})|| dV_p \right)^2},$$

where \mathbf{W}_0 is the induced microscopic static velocity field in the fluid part Ω_F of a REV assuming that it is filled by an incompressible fluid.

Definition 1.2.6 (Static viscous permeability). *The static viscous permeability k_0 , which is related to the flow resistivity σ by using (see [110])*

$$k_0 = \frac{\eta}{\sigma},$$

where η is the dynamic viscosity of the saturating fluid.

The static viscous permeability is an intrinsic parameter which depends only on the microstructure of the porous frame.

Definition 1.2.7 (Static thermal permeability). *The thermal dissipation effects at low frequencies are described by the static thermal permeability k'_0 , which is the solution of the Poisson equation (see [110])*

$$\begin{cases} -\Delta k'_0 = 1 & \text{in } \Omega_F, \\ k'_0 = 0 & \text{on } \Gamma. \end{cases}$$

For cylindrical pores, the static thermal permeability verify (see [111])

$$k'_0 = k_0 = \frac{\eta}{\sigma},$$

where η is the dynamic viscosity of the saturating fluid, and σ is the flow resistivity given by (1.4).

Definition 1.2.8 (Static thermal tortuosity). *This parameter accounts for the additional inertial influence on the thermal effects at low frequencies, and it is defined by (see [110])*

$$\alpha'_0 = \frac{\frac{1}{\text{vol}(\Omega_F)} \int_{\Omega_F} (k'_0)^2 dV_p}{\left(\frac{1}{\text{vol}(\Omega_F)} \int_{\Omega_F} k'_0 dV_p \right)^2},$$

where k'_0 is the static thermal permeability.

Definition 1.2.9 (Viscous characteristic length). *The viscous characteristic length Λ describes the viscous dissipation effects at medium and high frequencies. It is computed from (see [100])*

$$\Lambda = 2 \frac{\int_{\Omega_F} \|\mathbf{W}(\mathbf{p})\|^2 dV_p}{\int_{\Gamma} \|\mathbf{W}(\mathbf{p})\|^2 dA_p},$$

where \mathbf{W} is the induced microscopic velocity field in the fluid part Ω_F of a REV assuming that is filled by an incompressible fluid and Γ is the interface boundary between the fluid and the solid part of the REV.

Notice that this definition only depends on the geometry of the solid frame of the porous microstructure [100]. If the pores (the fluid part of the REV) consists of isolated identical cylindrical-like tubes, quantities σ , ϕ , Λ , and α_∞ are related as follows (see [55]):

$$\Lambda = M \sqrt{\frac{8\alpha_\infty \eta}{\sigma \phi}}, \quad (1.5)$$

where η is the dynamic viscosity of the saturating fluid, and M is a parameter that depends on the geometry of the pores and whose value lies between 0.25 and 1 for most porous

materials. At the microscopical level, if the cylinders are considered arranged perpendicular to an incident acoustic field then $M = 1$ (see [55]), and taking into account (1.3), (1.4), and (1.5), viscous characteristic length is given by

$$\Lambda = \sqrt{\frac{8\alpha_\infty\eta}{\sigma\phi}} = \sqrt{\frac{8\eta}{\frac{8\eta}{R^2(q\pi R^2)}q\pi R^2}} = R,$$

where q is the number of cylindrical pores of radius R per unit area of cross-section of the porous sample.

Definition 1.2.10 (Thermal characteristic length). *The thermal characteristic length Λ' describes the thermal dissipation effects at medium and high frequencies and is given by (see [55])*

$$\Lambda' = 2 \frac{\int_{\Omega_F} dV_p}{\int_{\Gamma} dS_p},$$

where Γ is the interface boundary between the fluid and the solid part of the REV.

Analogous to the definition of the viscous characteristic length, this definition only depends on the geometry of the microstructure of the porous sample [100]. If the pores (the fluid part of the REV) consists of disjoint identical cylindrical-like tubes, physical quantities σ , ϕ , Λ' , and α_∞ are related as follows (see [55]):

$$\Lambda' = M' \sqrt{\frac{8\alpha_\infty\eta}{\sigma\phi}}, \quad (1.6)$$

where η is the dynamic viscosity of the saturating fluid, and M' is a parameter that depends on the geometry of the pores. In fact, for straight cylindrical pores perpendicular to the surface of the porous sample, $M' = 1$ (see [55]), and taking into account (1.3), (1.4), and (1.6), thermal characteristic length reduces to

$$\Lambda' = \sqrt{\frac{8\alpha_\infty\eta}{\sigma\phi}} = \sqrt{\frac{8\eta}{\frac{8\eta}{R^2(q\pi R^2)}q\pi R^2}} = R,$$

where q is the number of cylindrical pores of radius R per unit area of cross-section.

There exists a wide variety of fluid-equivalent models in the scientific literature, depending on different physical parameters used to describe the mathematical models and the assumptions required for the microstructure. Among many other models, it can be cited: the Zwikker-Kosten model [182] based on one parameter $\{\phi\}$, the Delany-Bazley model [69] based on one parameter $\{\sigma\}$, the Delany-Bazley-Miki model [126] based on one parameter $\{\sigma\}$, the Darcy's like model [26, 175] based on two parameters $\{\phi, \sigma\}$, the general Miki model [125] based on four parameters $\{\sigma, \phi, \alpha_\infty, M''\}$, the Attenborough model [12]

based on four parameters $\{\phi, \sigma, \alpha_\infty, M''\}$, the Wilson model [177] based on four parameters $\{\rho_\infty, K_\infty, \tau_{\text{vor}}, \tau_{\text{ent}}\}$, the Johnson-Champoux-Allard model [55, 100] based on five parameters $\{\sigma, \phi, \alpha_\infty, \Lambda, \Lambda'\}$, the Johnson-Champoux-Allard-Lafarge [55, 100, 111] model based on six parameters $\{\sigma, \phi, \alpha_\infty, \Lambda, \Lambda', k'_0\}$, and the Johnson-Champoux-Allard-Pride-Lafarge [55, 100, 111, 147] model based on eight parameters $\{\sigma, \phi, \alpha_\infty, \Lambda, \Lambda', k'_0, \alpha_0, \alpha'_0\}$. All these models are described below.

Equivalent dynamic mass density and bulk modulus

In this section, the expressions of the equivalent dynamic mass density $\rho_{\text{eq}}(\omega)$, and the equivalent dynamic bulk modulus $K_{\text{eq}}(\omega)$ for each of the models cited in the section above are described in detail. Some of these models (specifically those derived from the Delany-Bazley model) provide expressions for the complex wave number $k(\omega)$, and the characteristic impedance $Z(\omega)$. In this case, taking into account that $Z(\omega) = \sqrt{K_{\text{eq}}(\omega)\rho_{\text{eq}}(\omega)\phi^2}$, and $K_{\text{eq}}(\omega) = \omega^2\rho_{\text{eq}}(\omega)/(k(\omega))^2$, the equivalent mass density, and the equivalent bulk modulus are computed as $\rho_{\text{eq}}(\omega) = k(\omega)Z(\omega)/(\omega\phi)$, and $K_{\text{eq}}(\omega) = \omega Z(\omega)/(\phi k(\omega))$, respectively.

Zwikker-Kosten model This classical model [182] only takes into account the viscosity effects in cylindrical tubes, having a circular cross-section of radius R . The equivalent dynamic mass density is written as follows

$$\rho_{\text{eq}}(\omega) = \frac{\rho_F}{\phi} \left(1 - \frac{2}{s\sqrt{-i}} \frac{J_1(s\sqrt{-i})}{J_0(s\sqrt{-i})} \right)^{-1},$$

where ϕ is the porosity of the material, $J_n(\cdot)$ are the cylindrical Bessel functions (see [4]) of order $n = 0, 1$, respectively, ρ_F is the mass density of the fluid and $s = \sqrt{\omega\rho_F R^2/\eta}$, being η the dynamic viscosity of the saturating fluid. The equivalent dynamic bulk modulus is given by

$$K_{\text{eq}}(\omega) = \frac{\pi_0\gamma}{\phi} \left(1 + (\gamma - 1) \frac{2}{s\sqrt{-i}\text{Pr}} \frac{J_1(s\sqrt{-i}\text{Pr})}{J_0(s\sqrt{-i}\text{Pr})} \right)^{-1},$$

where π_0 is the fluid equilibrium pressure, γ is the ratio of specific heats, and Pr is the Prandtl number defined by $\text{Pr} = \eta C_p/\kappa$, being κ the thermal conductivity, and C_p the specific heat at constant pressure.

Delany-Bazley model Delany and Bazley computed an empirical model for fibrous materials with porosity close to one which is valid for those materials whose fibers are uniformly distributed [69]. In this model, the complex wave number $k(\omega)$ and the characteristic impedance $Z(\omega)$ are computed as a function of the flow resistivity σ . The empirical laws described by Delany and Bazley were established after measurements made by using the Kundt's tube for some materials of varying resistivity and performing a least-square fitting of the experimental results. The Delany-Bazley model is suitable for fibrous materials within the range $0.01 < \omega/(2\pi\sigma) < 10$. The empirical expressions for $k(\omega)$ and $Z(\omega)$

are respectively given by

$$k(\omega) = \frac{\omega}{c_F} \left(1 + 0.0987 \left(\frac{\rho_F \omega}{2\pi\sigma} \right)^{-0.70} - i0.189 \left(\frac{\rho_F \omega}{2\pi\sigma} \right)^{-0.595} \right),$$

$$Z(\omega) = \rho_F c_F \left(1 + 0.0571 \left(\frac{\rho_F \omega}{2\pi\sigma} \right)^{-0.754} - i0.087 \left(\frac{\rho_F \omega}{2\pi\sigma} \right)^{-0.732} \right),$$

where ρ_F , and c_F are the fluid mass density, and sound speed, respectively.

Attenborough model This model is proposed to describe the behavior of rigid-porous media in which identical circular-cylindrical pores run normal to the surface [12]. The equivalent dynamic mass density is given by

$$\rho_{eq}(\omega) = \rho_F \frac{\alpha_\infty}{\phi} \left(1 - \frac{2}{s\sqrt{-i}} \frac{J_1(s\sqrt{-i})}{J_0(s\sqrt{-i})} \right)^{-1},$$

where ϕ , and α_∞ are the porosity, and the tortuosity of the material, $J_n(\cdot)$ are the cylindrical Bessel functions (see [4]) of order $n = 0, 1$, respectively, ρ_F is the mass density of the fluid, and $s = \sqrt{(8\rho_F \alpha_\infty \omega) / (\phi \sigma) / M''}$, being σ the flow resistivity of the material, and M'' the pore shape factor ratio, which is an adjustable parameter for real materials with complex pore geometry. The equivalent dynamic bulk modulus is given by

$$K_{eq}(\omega) = \frac{\pi_0 \gamma}{\phi} \left(1 + (\gamma - 1) \frac{2}{s\sqrt{-i} \text{Pr}} \frac{J_1(s\sqrt{-i} \text{Pr})}{J_0(s\sqrt{-i} \text{Pr})} \right)^{-1},$$

where π_0 is the fluid equilibrium pressure, γ is the ratio of specific heats, and Pr is the Prandtl number defined by $\text{Pr} = \eta C_p / \kappa$, being η the dynamic viscosity coefficient, κ the thermal conductivity, and C_p the specific heat at constant pressure.

Darcy's like model Based on the classical Darcy's model for incompressible flow in porous material [26, 175], if the inertial and isothermal compressional effects are included, the following expression for the equivalent dynamic mass density is obtained:

$$\rho_{eq}(\omega) = \frac{1}{\phi} \left(\rho_F - i \frac{\sigma}{\omega} \right),$$

where ϕ and σ are the porosity, and the flow resistivity of the material, respectively, and ρ_F is the fluid mass density. In the same manner, the equivalent bulk modulus is given by

$$K_{eq}(\omega) = \frac{\rho_F c_F^2}{\phi^2 \gamma},$$

being c_F the fluid sound speed, and γ the ratio of specific heats.

Delany-Bazley-Miki model To extend the valid range of application of the original Delany-Bazley model [69] at low frequencies, where the real part of the characteristic impedance could reach negative values, Miki and coworkers proposed a modification of the classical Delany-Bazley model [126]. The expression for the values of the complex wave number $k(\omega)$ and the characteristic impedance $Z(\omega)$ are respectively given by

$$k(\omega) = \frac{\omega}{c_F} \left(1 + 0.109 \left(\frac{\omega}{2\pi\sigma} \right)^{-0.618} - i0.16 \left(\frac{\omega}{2\pi\sigma} \right)^{-0.618} \right),$$

$$Z(\omega) = \rho_F c_F \left(1 + 0.07 \left(\frac{\omega}{2\pi\sigma} \right)^{-0.632} - i0.107 \left(\frac{\omega}{2\pi\sigma} \right)^{-0.632} \right),$$

where ρ_F and c_F are the fluid mass density and sound speed, respectively, and σ is the flow resistivity of the material. As the classical Delany-Bazley model, this model is suitable for fibrous materials with porosity close to one but now in the extended frequency range $\omega/(2\pi\sigma) < 0.01$ (see [126] for more details).

Miki model Although the Delany-Bazley-Miki model [126] provides a good prediction of the acoustic behavior of porous materials even for low-frequency range where the classical Delany-Bazley model [69] is not applicable, both models still suffer the restriction that the porosity must be close to one. The new model proposed by Miki [125] generalizes these empirical models by introducing the porosity ϕ , the tortuosity α_∞ , and the pore shape factor ratio M'' given by Attenborough [11] as intrinsic parameters in the model. Expressions for the values of the complex wave number $k(\omega)$, and the characteristic impedance $Z(\omega)$ are, respectively, given by

$$k(\omega) = \frac{\omega}{c_F} \sqrt{\alpha_\infty} \left(1 + 0.109 \left(\frac{\alpha_\infty \omega}{2\pi\sigma\phi M''^2} \right)^{-0.618} - i0.16 \left(\frac{\alpha_\infty \omega}{2\pi\sigma\phi M''^2} \right)^{-0.618} \right),$$

$$Z(\omega) = \frac{\rho_F c_F}{\phi} \sqrt{\alpha_\infty} \left(1 + 0.07 \left(\frac{\alpha_\infty \omega}{2\pi\sigma\phi M''^2} \right)^{-0.632} - i0.107 \left(\frac{\alpha_\infty \omega}{2\pi\sigma\phi M''^2} \right)^{-0.632} \right),$$

where ρ_F , and c_F are the fluid mass density and sound speed, respectively.

Johnson-Champoux-Allard model This model is proposed to describe the complex density of a porous material with a motionless skeleton having arbitrary pore shapes [55, 100]. The model assumes that the thermal effects depend on the frequency. The equivalent dynamic mass density is given by

$$\rho_{eq}(\omega) = \frac{\rho_F}{\phi} \alpha_\infty \left(1 - i \frac{\sigma\phi}{\omega\rho_F\alpha_\infty} \sqrt{1 + i \frac{4\alpha_\infty^2 \eta \rho_F \omega}{\sigma^2 \Lambda^2 \phi^2}} \right),$$

where ϕ , σ , α_∞ , and Λ are the porosity, the flow resistivity, the tortuosity, and the viscous characteristic length of the material, ρ_F is the mass density of the fluid, and η the dynamic viscosity. The equivalent dynamic bulk modulus is given by

$$K_{\text{eq}}(\omega) = \frac{\gamma\pi_0/\phi}{\gamma - (\gamma - 1) \left(1 - i \frac{8\eta}{\rho_F \Lambda'^2 \omega \text{Pr}} \sqrt{1 + i \frac{\rho_F \Lambda'^2 \omega \text{Pr}}{16\eta}} \right)^{-1}},$$

where Λ' is the thermal characteristic length of the material, π_0 is the fluid equilibrium pressure, Pr is the Prandtl number, and γ is the ratio of specific heats.

Johnson-Champoux-Allard-Lafarge model This model is a slight modification of the Johnson-Champoux-Allard model, and hence it is a reliable model to describe the complex density of a porous material with a motionless skeleton, having arbitrary pore shapes [55, 100, 111]. The expression for the effective dynamic mass density is identical to the one included in the Johnson-Champoux-Allard model, i.e.,

$$\rho_{\text{eq}}(\omega) = \frac{\rho_F}{\phi} \alpha_\infty \left(1 - i \frac{\sigma\phi}{\omega\rho_F\alpha_\infty} \sqrt{1 + i \frac{4\alpha_\infty^2 \eta \rho_F \omega}{\sigma^2 \Lambda^2 \phi^2}} \right),$$

where ϕ , σ , α_∞ , and Λ are the porosity, the flow resistivity, the tortuosity, and the viscous characteristic length of the material, ρ_F is the mass density of the fluid, and η the dynamic viscosity. On the contrary, the expression of K_{eq} provided by the Johnson-Champoux-Allard model [55] is modified to include the thermal effects at low frequencies. Thus, the expression of the effective dynamic bulk modulus is given by

$$K_{\text{eq}}(\omega) = \frac{\gamma\pi_0/\phi}{\gamma - (\gamma - 1) \left(1 - i \frac{\eta\phi}{\rho_F k'_0 \omega \text{Pr}} \sqrt{1 + i \frac{4k'_0{}^2 \rho_F \omega \text{Pr}}{\eta \Lambda'^2 \phi^2}} \right)^{-1}},$$

where Λ' , and k'_0 are the thermal characteristic length, and the static thermal permeability of the material, π_0 is the fluid equilibrium pressure, Pr is the Prandtl number, and γ is the ratio of specific heats.

Johnson-Champoux-Allard-Pride-Lafarge model This fluid-equivalent model is proposed to describe precisely the visco-inertial dissipative effects generated in the interstitial fluid of porous media [55, 100, 111, 147]. This model introduces corrections, at low frequencies, to the dynamic mass density and bulk modulus through viscous and thermal behavior, improving the JCA model. The expression for the effective dynamic mass density is given by

$$\rho_{\text{eq}}(\omega) = \frac{\rho_F \alpha_\infty}{\phi} \left(1 - i \frac{\eta\phi}{\omega\rho_F k_0 \alpha_\infty} \left(1 - \frac{2k_0 \alpha_\infty^2}{(\alpha_0 - \alpha_\infty) \phi \Lambda^2} \left(1 - \sqrt{1 - i \frac{\omega \rho_F \Lambda^2 (\alpha_0 - \alpha_\infty)^2}{\alpha_\infty^2 \eta}} \right) \right) \right),$$

being ϕ , σ , α_∞ , Λ , and k_0 are the porosity, the flow resistivity, the tortuosity, the viscous characteristic length, and the static viscous permeability of the material, ρ_F the mass density, η the dynamic viscosity of the fluid, π_0 the fluid equilibrium pressure, Pr the Prandtl number, and γ the ratio of specific heats. The equivalent dynamic bulk modulus is given by

$$K_{\text{eq}}(\omega) = \frac{1}{\phi} \frac{\gamma \pi_0}{\gamma - (\gamma - 1) \left(1 - \frac{i\eta\phi}{\omega\rho_F\text{Pr}k'_0} \left(1 - \frac{2k'_0}{\phi\Lambda'^2(\alpha'_0-1)} \left(1 - \sqrt{1 - \frac{i\omega\rho_F\text{Pr}\Lambda'^2(\alpha'_0-1)^2}{\eta}} \right) \right) \right)^{-1}},$$

where Λ' , k'_0 , and α'_0 are the thermal characteristic length, the static thermal permeability, and the static thermal tortuosity of the material, π_0 the fluid equilibrium pressure, Pr the Prandtl number, and γ the ratio of specific heats.

Wilson model This model is adequate to describe the dissipation behavior of porous materials with arbitrary pore shapes but without significant pore cross-section variations. Its derivation is based on the fact that viscous and thermal dissipation effects of an acoustic wave propagating through a porous medium can be described as a relaxation process (see [177] for further details). The equivalent mass density and bulk modulus coefficients are given by

$$\rho_{\text{eq}}(\omega) = \rho_\infty \frac{\sqrt{1 + i\omega\tau_{\text{vor}}}}{\sqrt{1 + i\omega\tau_{\text{vor}}} - 1}, \quad (1.7)$$

$$K_{\text{eq}}(\omega) = K_\infty \frac{\sqrt{1 + i\omega\tau_{\text{ent}}}}{\sqrt{1 + i\omega\tau_{\text{ent}}} + \gamma - 1}, \quad (1.8)$$

where

$$\rho_\infty = \frac{\rho_F\alpha_\infty}{\phi}, \quad K_\infty = \frac{\pi_0\gamma}{\phi}, \quad \tau_{\text{vor}} = \frac{2\rho_F\alpha_\infty}{\phi\sigma}, \quad \tau_{\text{ent}} = \frac{2\rho_F\alpha_\infty\text{Pr}}{\phi\sigma}, \quad (1.9)$$

being ϕ , σ , and α_∞ are the porosity, the flow resistivity, and the tortuosity of the material, ρ_F the fluid mass density, π_0 the fluid equilibrium pressure, Pr the Prandtl number, γ the ratio of specific heats, τ_{vor} , and τ_{ent} the vorticity-mode relaxation time and the entropy-mode relaxation time, respectively, and ρ_∞ and K_∞ the mass density and the bulk modulus, respectively, for the infinite frequency limit. To rewrite (1.7) and (1.8) with the intrinsic parameters defined in Section 1.2.2, the auxiliary expressions in (1.9) are inserted in (1.7)

and (1.8), obtaining

$$\rho_{\text{eq}}(\omega) = \frac{\rho_F}{\phi} \alpha_\infty \frac{\sqrt{1 + i \frac{2\omega\rho_F\alpha_\infty}{\sigma\phi}}}{\sqrt{1 + i \frac{2\omega\rho_F\alpha_\infty}{\sigma\phi}} - 1},$$

$$K_{\text{eq}}(\omega) = \frac{\gamma\pi_0}{\phi} \frac{\sqrt{1 + i \frac{2\omega\rho_F\alpha_\infty \text{Pr}}{\sigma\phi}}}{\sqrt{1 + i \frac{2\omega\rho_F\alpha_\infty \text{Pr}}{\sigma\phi}} - 1}.$$

1.3 Coupling conditions

Once the mathematical models have been reviewed, it is necessary to describe the coupling conditions between different media. Besides, coupling conditions between two media can also be used to model the presence of thin layers of other materials.

1.3.1 Contact interface

Since the rigid-frame porous materials can be modeled by using a fluid-equivalent model, contact interfaces between two fluids, two rigid-frame porous, or a fluid and a rigid-frame porous are included in this section.

Where two media are in contact, the first condition to be imposed is the continuity of normal displacements to the interface, that is,

$$\mathbf{U}_-(\mathbf{p}) \cdot \mathbf{n} = \mathbf{U}_+(\mathbf{p}) \cdot \mathbf{n} \quad \text{on } \Gamma, \quad (1.10)$$

where \mathbf{U}_- and \mathbf{U}_+ are the displacement fields in the left, and in the right media, respectively, Γ is the contact interface between both media and \mathbf{n} is the normal vector to Γ . It is necessary to take into account that the displacement field in a rigid-frame porous modeled by using a fluid-equivalent model is given by $\phi\mathbf{U}$ where ϕ is the porosity of the porous material.

The second condition to be imposed is the continuity of pressures on the interface, that is,

$$\Pi_- = \Pi_+ \quad \text{on } \Gamma, \quad (1.11)$$

where Π_- and Π_+ are the pressure fields in the left, and in the right media, respectively.

1.3.2 Rigid wall

When a medium is in contact with a rigid wall, the contact condition is that the normal displacement is null, that is,

$$\mathbf{U}(\mathbf{p}) \cdot \mathbf{n} = 0 \quad \text{on } \Gamma,$$

where \mathbf{U} is the displacement field in the medium, Γ is the interface where the rigid wall condition is imposed, and \mathbf{n} is the normal vector to Γ .

1.3.3 Radiation conditions

In order to ensure there are no waves coming from the last medium towards the previous one, an outgoing radiation condition is imposed on the displacement field \mathbf{U}_N when p_1 tends to infinity, this is,

$$\lim_{p_1 \rightarrow +\infty} \left(\frac{\partial \mathbf{U}_N(\mathbf{p})}{\partial p_1} - ik_N \mathbf{U}_N(\mathbf{p}) \right) = \mathbf{0},$$

where k_N and \mathbf{U}_N are the wave number, and the displacement field in the last medium. Moreover, to guarantee no waves are coming from the first medium towards the second one, an incoming radiation condition is imposed on the displacement field \mathbf{U}_1 when p_1 tends to infinity, this is,

$$\lim_{p_1 \rightarrow +\infty} \left(\frac{\partial \mathbf{U}_1(\mathbf{p})}{\partial p_1} - ik_1 \mathbf{U}_1(\mathbf{p}) \right) = \mathbf{0},$$

where k_1 and \mathbf{U}_1 are the wave number, and the displacement field in the first medium.

1.3.4 Thin media models

In addition to the contact conditions between two media, it is possible to include some media that are supposed infinitely thin, that is, their thickness is much smaller than the thickness of the media surrounding it.

Rigid plate

It is supposed that the plate is located in Γ . Let $\chi(t)$ be the normal displacement of the plate at time t . The movement equation of the plate (see [76]) is

$$m \frac{d^2 \chi}{dt^2}(t) + s \frac{d\chi}{dt}(t) + r \chi(t) = f(t),$$

where m is the surface mass density, s is the viscosity coefficient, r is the elasticity coefficient, and f is the superficial load. Imposing harmonic solutions, i.e., if $\chi(t) = \text{Re}(e^{i\omega t} X)$, the rigid plate equation in the frequency domain results

$$-m\omega^2 X + i\omega s X + rX = F.$$

If the rigid plate is located between two media in contact, where the continuity of the displacements (see Equation (1.10)) is imposed, the coupling condition results

$$\mathbf{U}_-(\mathbf{p}) \cdot \mathbf{n} = \mathbf{U}_+(\mathbf{p}) \cdot \mathbf{n} = X \quad \text{on } \Gamma.$$

Viscoelastic panel

Sometimes, the medium appearing between two media is a pretty thin viscoelastic medium. In this case, the elastic response is assumed to be proportional to the jump

in the displacements, while the viscous response is proportional to the jump in the velocities when crossing the interface Γ where the panel is located (see [21, 140]). If the panel is located between a compressible fluid and another compressible fluid or a rigid-frame porous, the continuity of pressures on Γ is given by (1.11). The continuity of the normal displacement (1.10) is not required, but the pressure on Γ is supposed linearly dependent on the jumps of the displacements, and the velocity on the interface, that is,

$$-\Pi_- = -\Pi_+ = i\omega Z(\omega)(\mathbf{U}_+ - \mathbf{U}_-) \quad \text{on } \Gamma,$$

where $Z(\omega) = \beta - i\frac{\alpha}{\omega}$ is the impedance surface of the viscoelastic panel.

1.4 Plane wave analysis

In this section, considering a plane-wave framework, the pressure and the displacement fields of a fluid (or a rigid-frame porous) are described. In the frequency domain, the pressure field of a fluid (or a rigid-frame porous) Π_F , at oblique incidence, can be written as

$$\Pi_F(\mathbf{p}) = A_1 e^{ik_F(-\cos \theta_F p_1 + \sin \theta_F p_2)} + A_2 e^{ik_F(\cos \theta_F p_1 + \sin \theta_F p_2)},$$

where A_1 , and A_2 , are frequency-dependent complex constants which can be viewed as the reflection and transmission coefficients between each medium, and θ_F is the incident angle in the fluid. The wave number of the medium k_F is given by $k_F = \omega/c_F$ in a compressible fluid, and by $k_F = \sqrt{\omega^2 \rho_{eq}(\omega)/K_{eq}(\omega)}$ in a porous medium modeled following a fluid-equivalent model. It is useful to write the displacement field in the fluid \mathbf{U}_F in terms of the pressure field as follows

$$\begin{aligned} \mathbf{U}_F(\mathbf{p}) = & \frac{i}{\omega Z_F} (-A_1 e^{ik_F(-\cos \theta_F p_1 + \sin \theta_F p_2)} + A_2 e^{ik_F(\cos \theta_F p_1 + \sin \theta_F p_2)}) \cos \theta_F \mathbf{e}_1 \\ & + (A_1 e^{ik_F(-\cos \theta_F p_1 + \sin \theta_F p_2)} + A_2 e^{ik_F(\cos \theta_F p_1 + \sin \theta_F p_2)}) \sin \theta_F \mathbf{e}_2, \end{aligned}$$

being Z_F the characteristic impedance of the medium, given by $Z_F = \rho_F c_F$ in a compressible fluid, and $Z_F(\omega) = \sqrt{\rho_{eq}(\omega) K_{eq}(\omega) \phi^2}$ in a porous media modeled following a fluid-equivalent model.

The available experimental data are the frequency response of the absorption coefficient and the transmission loss of different porous materials. Throughout this section, two different problems are described: a multilayer problem formed by several layers of porous materials with a rigid backend, to compute the absorption coefficient, and a multilayer problem where the first and the last layer are fluids, to compute the transmission loss. For the sake of simplicity, the dependency of ω in the physical quantities related to the porous media such as wave number, and characteristic impedance, is omitted below.

1.4.1 Absorption problem: multilayer medium backed by a rigid surface

Firstly, let us consider a coupling problem used to characterize the absorbing properties of a multilayer system. This problem consists of a planar configuration formed by one or several porous layers surrounded by fluid in the front face and backed by a rigid wall (see Figure 1.2). The fluid is placed in an unbounded domain (half-space), and the thicknesses of the samples are finite (denoted by h_j with $j = 1, \dots, N - 1$) but unbounded in the other two Cartesian coordinates. In this simple geometrical configuration, if an incident plane wave is impinging on the first layer at normal incidence, the complex-valued displacement in each medium is given by a linear combination of transmitted, and reflected plane waves. The coupled interfaces $\Gamma_1, \Gamma_2, \dots, \Gamma_N$ are defined by

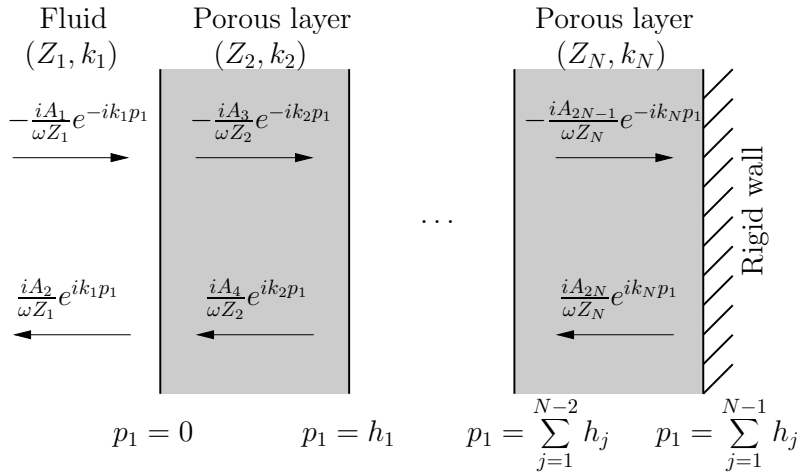


Figure 1.2: Geometrical configuration of the absorption problem formed by a fluid, $N - 1$ porous layers (highlighted in gray), and a rigid wall. Arrows from left to right denote the propagative direction of the incident waves in each medium. Analogously, arrows from right to left denote the propagative direction of the reflected waves in each medium. The coefficients $\pm iA_m/(\omega Z_j)$ with $j = 1, \dots, N$, and $m = 1, \dots, 2N$, are the frequency-dependent complex amplitudes that correspond to the reflection, and transmission coefficients associated with the displacement fields.

$$\begin{aligned}
\Gamma_1 &= \{\mathbf{p} = (p_1, p_2, p_3) \in \mathbb{R}^3 : p_1 = 0\}, \\
\Gamma_2 &= \{\mathbf{p} = (p_1, p_2, p_3) \in \mathbb{R}^3 : p_1 = h_1\}, \\
&\vdots \\
\Gamma_{N-1} &= \{\mathbf{p} = (p_1, p_2, p_3) \in \mathbb{R}^3 : p_1 = h_1 + h_2 + \dots + h_{N-2}\} \\
\Gamma_N &= \{\mathbf{p} = (p_1, p_2, p_3) \in \mathbb{R}^3 : p_1 = h_1 + h_2 + \dots + h_{N-1}\}.
\end{aligned} \tag{1.12}$$

All these interfaces are perpendicular to the Cartesian p_1 -axis, so the unit normal vector on Γ_j with $j = 1, \dots, N$ is $\mathbf{n} = \mathbf{e}_1$. Following the contact coupling condition explained in

Section 1.3, the interface conditions are the continuity of normal displacements and pressure fields on Γ_j with $j = 1, \dots, N - 1$. On Γ_N a rigid wall condition is imposed. Taking into account the coupling conditions, to determine the complex constants A_1, \dots, A_{2N} , a linear system is solved.

1.4.2 Transmission problem: multilayer medium surrounded by a fluid

To compute the transmission properties, let us consider a coupling problem consists of a planar configuration formed by one or several porous layers surrounded by fluid (see Figure 1.3). The first, and the last fluids are placed in an unbounded domain (half-space) and the thicknesses of the samples are finite (denoted by h_j with $j = 1, \dots, N - 1$) but unbounded in the other two Cartesian coordinates. In this configuration, if an incident plane wave is impinging on the first layer at normal incidence, the complex-valued displacement in each medium is given by a linear combination of transmitted and reflected plane waves. The

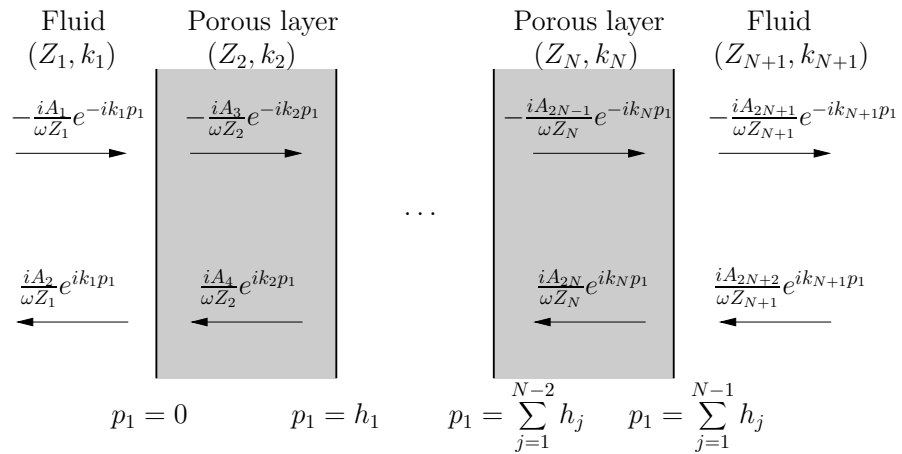


Figure 1.3: Geometrical configuration of the transmission problem formed by a fluid, $N - 1$ porous layers (highlighted in gray), and another fluid. Arrows from left to right denote the propagative direction of the incident waves in each medium. Analogously, arrows from right to left denote the propagative direction of the reflected waves in each medium. The coefficients $\pm iA_m/(\omega Z_j)$ with $j = 1, \dots, N + 1$, and $m = 1, \dots, 2(N + 1)$, are the frequency-dependent complex amplitudes that correspond to the reflection, and transmission coefficients associated with the displacement fields.

coupled interfaces $\Gamma_1, \Gamma_2, \dots, \Gamma_N$ are defined as in the absorption problem (1.12). Following the contact coupling condition explained in Section 1.3, the interface conditions are the continuity of normal displacements, and pressure fields on Γ_j with $j = 1, \dots, N$. Once again, to determine the complex constants A_1, \dots, A_{2N+2} , a linear system is solved.

1.5 Acoustic quantities

Once the mathematical models and the coupling conditions have been introduced and the multilayer configurations used in this chapter have been described, it is possible to compute some acoustic quantities of interest related to the acoustic response of a layer with a finite thickness. In this section, some acoustic quantities are defined, such as the reflection and the transmission coefficient, the surface impedance, the absorption coefficient, and the transmission loss.

Definition 1.5.1. *The reflection coefficient \mathcal{R} on Γ_1 is the ratio of the root mean square value of the reflected, and the incident pressure field, that is,*

$$|\mathcal{R}| = \left| \frac{(\Pi_{\text{ref}})_{\text{rms}}}{(\Pi_{\text{inc}})_{\text{rms}}} \right|_{\Gamma_1}, \quad (1.13)$$

where Π_{ref} , and Π_{inc} are the reflected, and the incident pressure field in the first fluid medium, respectively. The root mean square value (or RMS value) of a pressure field π is given by

$$(\Pi)_{\text{rms}}(\mathbf{p}) = \sqrt{\frac{1}{T} \int_0^T \pi^2(\mathbf{p}, t) dt},$$

where $T = \frac{2\pi}{\omega}$ is the period of the harmonic fields, being ω the angular frequency.

Definition 1.5.2. *The absorption coefficient at normal incidence is given by*

$$\alpha(0) = 1 - |\mathcal{R}|^2, \quad (1.14)$$

where the reflection coefficient \mathcal{R} is given by (1.13).

Definition 1.5.3. *Following [109], the absorption coefficient in the presence of a diffuse field, i.e., under a uniformly distributed incidence, is given by*

$$\alpha_d = \int_0^{\pi/2} \alpha(\theta) \sin(2\theta) d\theta,$$

where $\alpha(\theta)$ is the absorption coefficient at oblique incidence given by (1.14), which depends on the angle of incidence θ in the first medium.

Definition 1.5.4. *The surface impedance Z_s (see [32]) is the ratio of the pressure field at a point \mathbf{p} to the particle velocity at the same point. Then, the surface impedance at oblique incidence θ on the coupling interface Γ_1 is defined by the ratio*

$$Z_s(\theta) = \left| \frac{\Pi_1(\mathbf{p})}{i\omega \mathbf{U}_1(\mathbf{p}) \cdot \mathbf{n}} \right|_{\mathbf{p} \in \Gamma_1} = \left| \frac{\Pi_1(\mathbf{p})}{\frac{i}{\omega \rho_F} \nabla \Pi_1(\mathbf{p}) \cdot \mathbf{n}} \right|_{\mathbf{p} \in \Gamma_1},$$

where Π_1 and \mathbf{U}_1 are the pressure, and the displacement fields in the first medium.

Definition 1.5.5. *The transmission coefficient is defined as the ratio of the root mean square value of the transmitted, and the incident pressure field, and is given by*

$$|\mathcal{T}| = \frac{(\Pi_{\text{transm}})_{\text{rms}}}{(\Pi_{\text{inc}})_{\text{rms}}},$$

where Π_{transm} is the pressure transmitted in the last fluid medium, and Π_{inc} is the incident pressure in the first medium.

Definition 1.5.6. *The transmission loss (see [32]), understood as an acoustic quantity that depends on the intensity field (or the acoustic power) is defined as*

$$\text{TL} = 10 \log_{10} \left(\frac{1}{\tau} \right),$$

where

$$\tau = \frac{\| \mathbf{I}_{N+1}(\mathbf{p})|_{\mathbf{p} \in \Gamma_N} \|}{\| \mathbf{I}_1(\mathbf{p})|_{\mathbf{p} \in \Gamma_1} \|},$$

being \mathbf{I}_{N+1} and \mathbf{I}_1 the acoustic intensity field in the last, and the first fluid medium, respectively.

1.6 Numerical procedure to solve the inverse problems

To characterize acoustically the materials under consideration, it is necessary to compute the solution of inverse problems, which fits a discrete set of frequency-dependent experimental measurements of the absorption coefficient of a single layer or a multilayer configuration. Then, for a fixed frequency value, the inverse problem is written as a minimization problem, where the cost function is the relative error between the experimental measurements and the absorption coefficient computed with the propagation problem described in Section 1.4.1. In this chapter, two kinds of materials have been considered: porous or fibrous materials, modeled by using a fluid-equivalent model, and films which have been modeled by using a rigid plate model. The fitting problems used for each one of these materials are explained as follows.

1.6.1 Absorbing materials

Porous materials used in this chapter can be modeled by using a fluid-equivalent model (see Section 1.2.2 for more details). In general, if it is supposed that \vec{p} is the vector with the intrinsic parameters of the model, all of them unknown, the fitting problem solved in each case is, find \vec{p}^* that minimize the difference between the experimental and the analytical

values, i.e.,

$$\vec{p}^* = \arg \min_{\vec{p}} \sum_{m=1}^M \left(\frac{\sum_{j=1}^N |\alpha_{jm} - \alpha_{\text{anl}}(\omega_j, \vec{p}, h_m)|^2}{\sum_{j=1}^N |\alpha_{jm}|^2} \right), \quad (1.15)$$

where α_{jm} are the experimental absorption values of a material with thickness h_m available for each angular frequency ω_j with $j = 1, \dots, N$, and $\alpha_{\text{anl}}(\omega_j, \vec{p}, h_m)$ are the analytic absorption coefficients computed numerically by determining the acoustic propagation of plane waves through a multilayer medium, as it has been explained in Section 1.4.1.

For example, if the porous layer follows a Miki model, the fitting problem (1.15) consists in finding the values ϕ^* , σ^* , α_∞^* , and M''^* that minimize the difference between the experimental and the analytical values, i.e.,

$$(\phi^*, \sigma^*, \alpha_\infty^*, M''^*) = \arg \min_{\substack{0 < \phi < 1, \sigma > 0 \\ \alpha_\infty > 0, 0.6 < M'' < 1}} \sum_{m=1}^M \left(\frac{\sum_{j=1}^N |\alpha_{jm} - \alpha_{\text{anl}}(\omega_j, \phi, \sigma, \alpha_\infty, M'', h_m)|^2}{\sum_{j=1}^N |\alpha_{jm}|^2} \right), \quad (1.16)$$

where ϕ , σ , α_∞ , and M'' are the porosity, the flow resistivity, the tortuosity, and the pore shape factor ratio, respectively, which are the intrinsic parameters of the Miki model (see Section 1.2.2 for more details).

1.6.2 Films

Due to the difficulties of repeating the measurements of the absorption coefficient for films, to characterize them, it is necessary to consider that they are part of a multilayer medium which is formed by other known layers. A rigid plate model has been used for the characterization of these films. The fitting problem consists in finding the values m^* , s^* , r^* that minimize the difference between the experimental and the analytical values, i.e.,

$$(m^*, s^*, r^*) = \arg \min_{\substack{m > 0, s > 0 \\ r > 0}} \left(\frac{\sum_{j=1}^N |\alpha_j - \alpha_{\text{anl}}(\omega_j, m, s, r, h)|^2}{\sum_{j=1}^N |\alpha_j|^2} \right), \quad (1.17)$$

where m , s , and r are the surface mass density, the viscosity coefficient, and the elastic coefficient, respectively. These coefficients are the parameters of the rigid plate model (see Section 1.3.4 for more details).

Sometimes, the surface mass density of the material is known. In this case, the fitting problem (1.17) can be modifying to use this known value. The fitting problem consists in finding the values s^* , r^* that minimize the difference between the experimental and the analytical values, i.e.,

$$(s^*, r^*) = \arg \min_{s > 0, r > 0} \left(\frac{\sum_{j=1}^N |\alpha_j - \alpha_{\text{anl}}(\omega_j, s, r, h)|^2}{\sum_{j=1}^N |\alpha_j|^2} \right). \quad (1.18)$$

Remark 1.6.1. *Throughout this chapter, the well or ill-posedness of these problems is not discussed. However, in Chapter 2, a detailed study about why these problems are ill-posed, is done. The main idea is that the available experimental data are not enough to ensure the uniqueness of the solution.*

1.7 Numerical results

In this section, some porous, fibrous materials and films have been characterized by using the parametric models described in Section 1.2. The considered materials are both single and multilayer materials, and the numerical results are compared with the experimental data measured in the Kundt's tube (see [1]). To characterize these materials, a Python code has been developed, following an Object-oriented paradigm. The code has been designed as an efficient computer tool to simulate the plane wave propagation through a multilayer medium numerically. The use of this code requires to define a coupled problem formed by a finite set of layers, by using the models described in Section 1.2 and interface coupling conditions between layers, by using the conditions described in Section 1.3. Once the multilayer problem is settled, the code allows us to compute and plot several acoustic quantities from both the multilayer problem and also from each layer independently, by using the acoustic quantities described in Section 1.5. Hence, numerical comparisons between the computed results and the experimental values are performed. Finally, the code also includes optimization capabilities (based on state of the art AMPL solvers), allowing to create a multilayer problem with some unknown parameters, whose values can be identified from experimental data.

1.7.1 Porous materials

In this section, some porous and fibrous materials have been characterized. Figure 2.5 shows some of the materials under study. Although these materials can be modeled with most of the fluid-equivalent models explained in Section 1.2.2, all of them have been modeled by using the Miki model. This model does not have any limitations respect to the frequency range, as happens with the Delany-Bazley family models and it allows fitting accurate without so many parameters as in the JCA family models.



Figure 1.4: Top left: material made from recycled fibers. Top middle: material made from polypropylene (PP) fibers. Top right: polyurethane foam (PU). Bottom left: PU with a foam. Bottom middle: Foam. Bottom right: Film of thickness $180\ \mu\text{m}$.

The experimental data have been measured in the Kundt's tube by a company¹. The frequency range considered in all simulations is from 500 to 5000 Hz, measured in third-octave. In the first simulation, a material made from recycled fibers and natural white wool is used (sample 1). This material is available in three different thicknesses $h_1 = 8\text{ mm}$, $h_2 = 10\text{ mm}$, and $h_3 = 12\text{ mm}$. By using the fitting problem (1.16) with $M = 3$, the obtained optimal values are $\phi = 0.94$, $\sigma = 2.08 \times 10^5\ \text{Nm}^{-4}\text{s}$, $\alpha_\infty = 1.11$, and $M'' = 0.64$. With these optimal values, the relative errors are $\varepsilon_8 = 10.8\%$, $\varepsilon_{10} = 2.57\%$, and $\varepsilon_{12} = 5.6\%$. In left plot of Figure 1.5, the values of the absorption coefficient computed by using the optimal values (dashed lines) for different thicknesses are compared with the experimental data (solid lines). In right plot of Figure 1.5, the values of the real (solid lines), and the imaginary part (dashed lines) of the surface impedance of sample 1, computed by using the optimal values, are shown.

In the second simulation, a material made from polyethylene terephthalate fibers is considered (sample 2). The material is available in two different thicknesses $h_1 = 10\text{ mm}$, and $h_2 = 20\text{ mm}$. By using the fitting problem (1.16) with $M = 2$, the obtained optimal values are $\phi = 0.98$, $\sigma = 9.91 \times 10^3\ \text{Nm}^{-4}\text{s}$, $\alpha_\infty = 0.38$, and $M'' = 1$. With these optimal values, the relative errors are $\varepsilon_{10} = 24.3\%$ and $\varepsilon_{20} = 16.59\%$. In left plot of Figure 1.6, the values of the absorption coefficient computed by using the optimal values of the parameters (dashed lines) for different thicknesses are compared with the experimental data (solid lines). In right plot of Figure 1.6, the values of the real (solid lines), and the imaginary

¹Due to the confidentiality agreement with the company, neither the name of the company nor the name of the materials are published. All the samples are identified by the material they are made of.

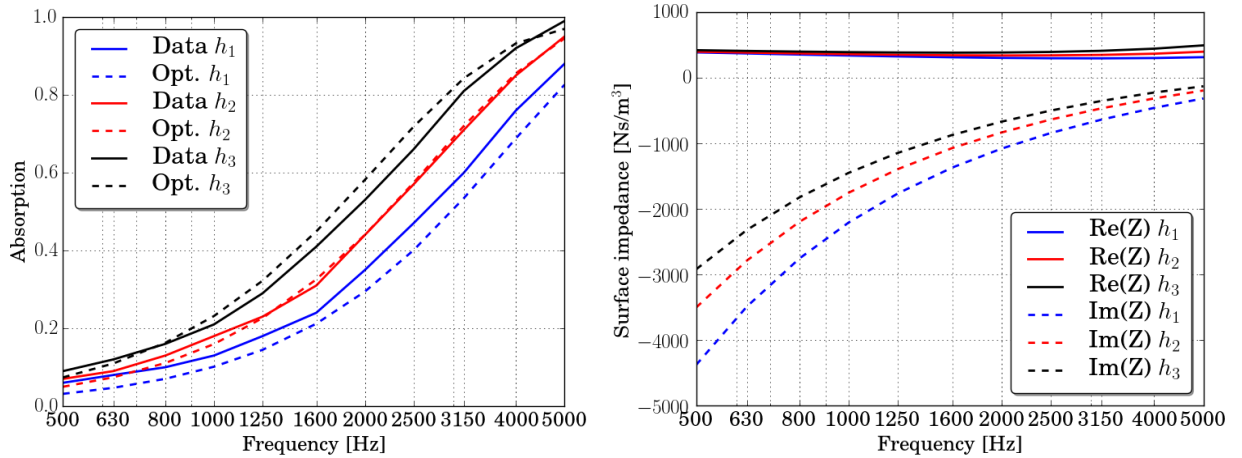


Figure 1.5: Left: Absorption coefficient of the sample 1 with thicknesses $h_1 = 8\text{ mm}$ (in blue), $h_2 = 10\text{ mm}$ (in red), and $h_3 = 12\text{ mm}$ (in black). The solid lines show the experimental values, and the dashed lines show the optimized values. Right: Real (solid lines), and imaginary part (dashed lines) of the surface impedance of sample 1, plotted with respect to the frequency. The results are computed by using the Miki model, and the optimal values obtained with the fitting problem described in (1.16), that is, $\phi = 0.94$, $\sigma = 2.08 \times 10^5 \text{ Nm}^{-4}\text{s}$, $\alpha_\infty = 1.11$, and $M'' = 0.64$.

part (dashed lines) of the surface impedance of sample 2 are shown.

Now, a material made from polypropylene fibers with thickness $h_1 = 20\text{ mm}$ is considered (sample 3). Again, the Miki model has been used for its characterization. By using the fitting problem (1.16) with $M = 1$, the obtained optimal values are $\phi = 0.83$, $\sigma = 2.29 \times 10^4 \text{ Nm}^{-4}\text{s}$, $\alpha_\infty = 1.02$, and $M'' = 0.95$. The relative error obtained with these optimal values is $\varepsilon = 4.05\%$. In left plot of Figure 1.7, the values of the computed absorption coefficient (dashed line) are compared with the experimental data (solid line), and in right plot of Figure 1.7, the values of the real (solid line), and the imaginary part (dashed line) of the surface impedance of sample 3 are shown.

Now, a polyester material with thickness $h_1 = 15\text{ mm}$ has been characterized (sample 4). In this simulation, the available experimental data come from a problem with one and with two layers of the material, first of all, the problem under study is formed by one layer of the sample 4 with a rigid backend. Once again, the fitting problem considered is (1.16) with $M = 1$. The obtained optimal values are $\phi = 0.9906$, $\alpha_\infty = 2.079$, $\sigma = 1.1818 \times 10^4 \text{ Nm}^{-4}\text{s}$, and $M'' = 1$. The relative error obtained with these optimal values is $\varepsilon = 7.49\%$. In left plot of Figure 1.8, the values of the absorption coefficient computed (dashed line) are compared with the experimental data (solid line). In right plot of Figure 1.8, the values of the real (solid line), and the imaginary part (dashed line) of the surface impedance of sample 4 are shown. Once the optimal values of the intrinsic parameters are obtained, the absorption values of a multilayer formed by two layers of sample 4 in contact can be computed. The relative error obtained is $\varepsilon = 5.68\%$. In left plot of Figure 1.9, the values of the absorption

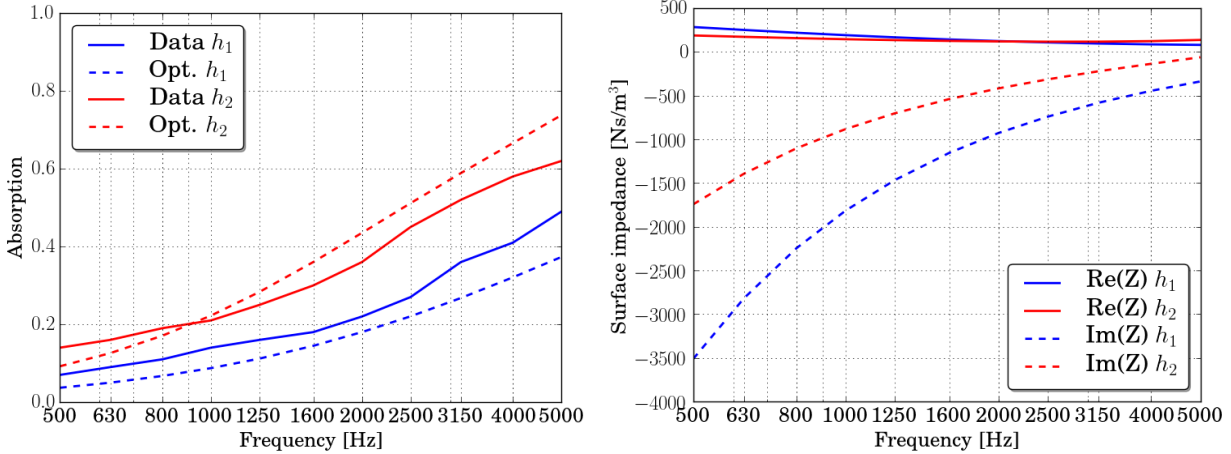


Figure 1.6: Left: Absorption coefficient of the sample 2 with thicknesses $h_1 = 10$ mm (in blue), and $h_2 = 20$ mm (in red). The solid lines show the experimental values, and the dashed lines show the optimized values. Right: Real (solid lines), and imaginary part (dashed lines) of the surface impedance of sample 2, plotted with respect to the frequency. The results are computed by using the Miki model, and the optimal values obtained with the fitting problem described in (1.16), that is, $\phi = 0.98$, $\sigma = 9.91 \times 10^3 \text{ Nm}^{-4}\text{s}$, $\alpha_\infty = 0.38$, and $M'' = 1$.

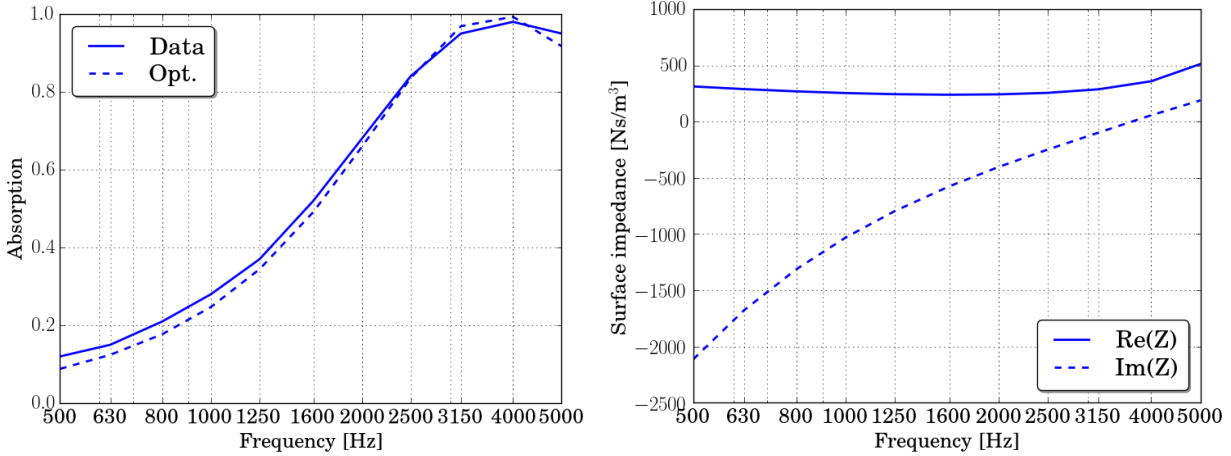


Figure 1.7: Left: Absorption coefficient of the sample 3 with thickness $h_1 = 20$ mm. The solid line shows the experimental values, and the dashed line shows the computed values. Right: Real (solid line), and imaginary part (dashed line) of the surface impedance of sample 3 plotted with respect to the frequency. The results are computed by using the Miki model, and the optimal values obtained with the fitting problem described in (1.16), that is, $\phi = 0.83$, $\sigma = 2.29 \times 10^4 \text{ Nm}^{-4}\text{s}$, $\alpha_\infty = 1.02$, and $M'' = 0.95$.

coefficient computed in the problem with two layers (dashed line) are compared with the experimental data (solid line), showing a good agreement. In right plot of Figure 1.9, the

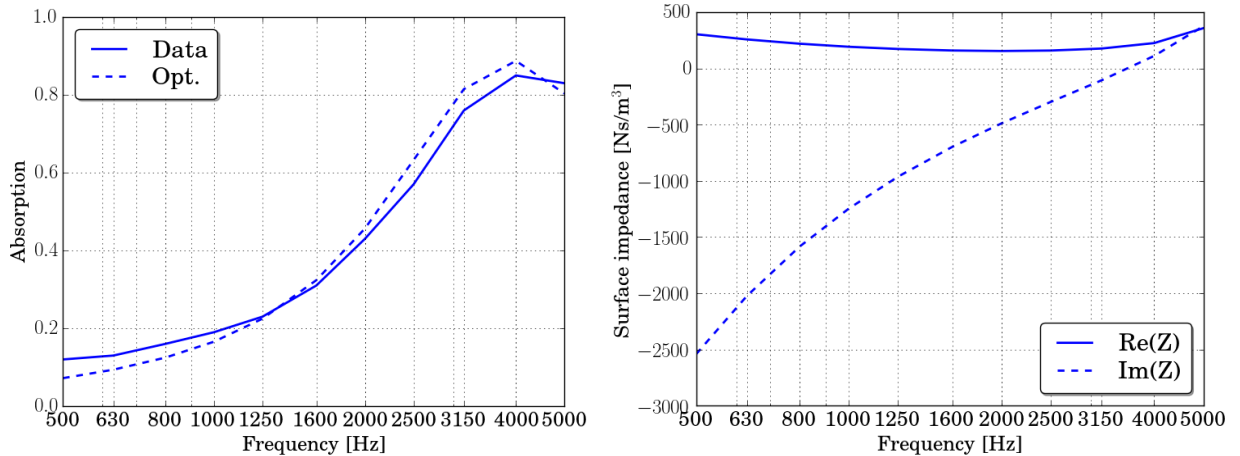


Figure 1.8: Left: Absorption coefficient of sample 4 with thickness $h_1 = 15$ mm. The solid line shows the experimental values, and the dashed line shows the computed values. Right: Real (solid line), and imaginary part (dashed line) of the surface impedance of sample 4 plotted with respect to the frequency. The results are computed by using the Miki model, and the optimal values obtained with the fitting problem described in (1.16), that is, $\phi = 0.9906$, $\alpha_\infty = 2.079$, $\sigma = 1.1818 \times 10^4 \text{ Nm}^{-4}\text{s}$, and $M'' = 1$.

values of the real (solid line), and the imaginary part (dashed line) of the surface impedance of the multilayer with two layers of sample 4 in contact are shown.

1.7.2 Films

The characterization of films and other thin materials should be treated independently due to the difficulty of repeating the measurements in the Kundt's tube. For this reason, films considered in this section are part of a multilayer medium which is formed by other known layers (some of the layers characterized in Section 1.7.1). Since these films are pretty thin, all of them are modeled following a rigid plate model (see Section 1.3.4 for more details).

The first material under consideration is a polyethylene (PE) film (film 1) with thickness $h = 80 \mu\text{m}$ as part of a multilayer medium formed by this film surrounded by the polyester (sample 4) studied in Section 1.7.1. Then, using the parameters of the Miki model for the sample 4 computed previously, that is, $\phi = 0.9906$, $\alpha_\infty = 2.079$, $\sigma = 1.1818 \times 10^4 \text{ Nm}^{-4}\text{s}$, and $M'' = 1$, and the fitting problem (1.17), the optimal values for the parameters of the film 1 are $m = 0.0589 \text{ kg/m}^2$, $s = 1.58 \times 10^3 \text{ kg/ms}$, and $r = 5.496 \times 10^6 \text{ kg/m}^2$. The relative error obtained with these optimal values is $\varepsilon = 3.61\%$. Once, the intrinsic parameters of sample 4 and the PE film $80 \mu\text{m}$ have been computed, the absorption coefficient of a multilayer medium formed by three layers of sample 4 and two layers of the PE film $80 \mu\text{m}$ among them is calculated. The parameters of the Miki model for sample 4 are those computed in Section 1.7.1, and the values of the rigid plate model are those computed

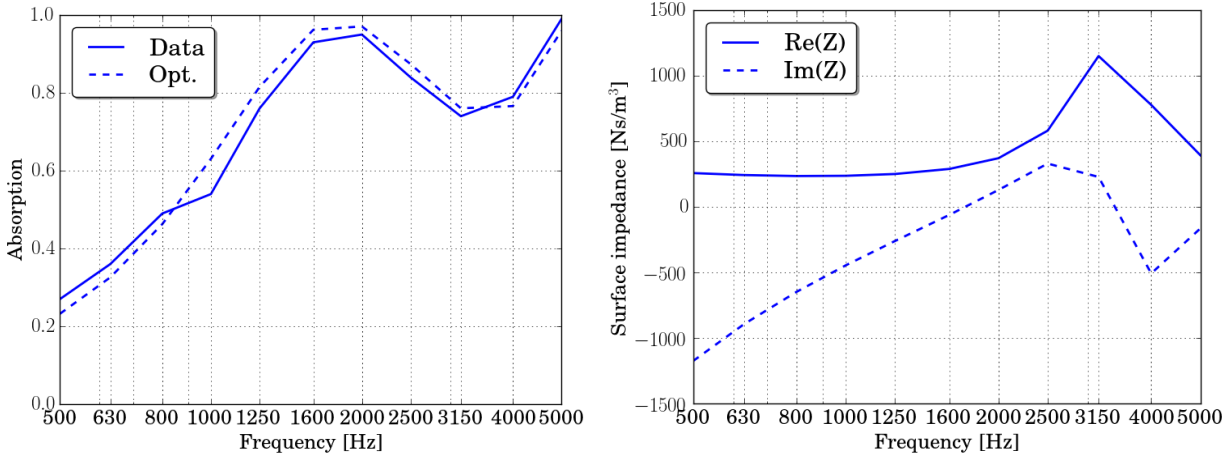


Figure 1.9: Left: Absorption coefficient of a multilayer formed by two layers of sample 4 with thickness $h_1 = 15$ mm in contact. The solid line shows the values computed considering the optimal values of the parameters, obtained in the one-layer fitting, and the dashed line shows the experimental data. Right: Real (solid line), and imaginary part (dashed line) of the surface impedance of the multilayer formed by two layers of sample 4 in contact, plotted with respect to the frequency. The results are computed by using the Miki model, and the optimal values obtained with the fitting problem described in (1.16), that is, $\phi = 0.9906$, $\alpha_\infty = 2.079$, $\sigma = 1.1818 \times 10^4 \text{ Nm}^{-4}\text{s}$, and $M'' = 1$.

above. The relative error obtained with these optimal values is $\varepsilon = 10.72\%$. The numerical results of the fitting problem with two layers of sample 4, and the film 1 between them are shown in left plot of Figure 1.10, and with three layers of sample 4, and two layers of film among them are shown in the plot of Figure 1.10.

Now, the material under consideration is a polypropylene (PP) film (film 2) with thickness $h = 125 \mu\text{m}$ as part of a multilayer medium formed by this film surrounded by the polyester (sample 4) studied in Section 1.7.1. Then, using the parameters of the Miki model for sample 4 computed previously, that is, $\phi = 0.9906$, $\alpha_\infty = 2.079$, $\sigma = 1.1818 \times 10^4 \text{ Nm}^{-4}\text{s}$, and $M'' = 1$, and the fitting problem (1.17), the optimal values for the parameters are $m = 0.0609 \text{ kg/m}^2$, $s = 1.09 \times 10^3 \text{ kg/ms}$, and $r = 3.574 \times 10^6 \text{ kg/m}^2$. The relative error with these optimal values is $\varepsilon = 2.43\%$.

Once this configuration has been completely characterized, the absorption coefficient of a multilayer medium formed by three layers of sample 4, and two layers of PP film 125 μm among them. The parameters of the Miki model for sample 4 are those computed in Section 1.7.1, and the values of the rigid plate model are those computed above. The relative error obtained with these optimal values is $\varepsilon = 10.38\%$. The numerical results of the fitting problem with two layers of sample 4, and the film 2 between them are shown in left plot of Figure 1.11, and with three layers of sample 4, and two layers of film among them are shown in right plot of Figure 1.11.

The next material under consideration is a polyethylene (PE) film (film 3) with thickness

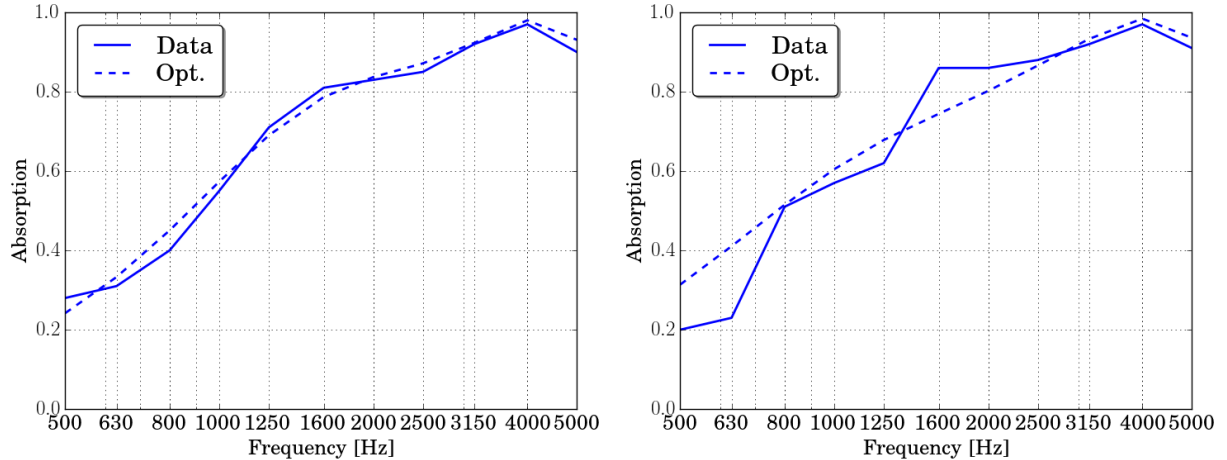


Figure 1.10: Left: Absorption coefficient of a multilayer medium formed by the film 1 with thickness $80 \mu\text{m}$ surrounded by the sample 4 with thickness $h = 15 \text{ mm}$. Right: Absorption coefficient of a multilayer medium formed by three layers of sample 4 with two layers of film 1 among them, plotted with respect to the frequency. In both cases, the porous layer (sample 4) follows a Miki model with optimal values $\phi = 0.9906$, $\alpha_\infty = 1.9$, $\sigma = 2.11 \times 10^4 \text{ Nm}^{-4}$, and $M'' = 0.7402$. The film has been modeled by using a rigid plate model with optimal values $m = 0.0589 \text{ kg/m}^2$, $s = 1.58 \times 10^3 \text{ kg/ms}$, and $r = 5.496 \times 10^6 \text{ kg/m}^2$. The solid line shows the computed values, and the dashed line shows the experimental ones.

$h = 180 \mu\text{m}$ as part of a multilayer medium formed by this film surrounded by the sample 4. Using the parameters of the Miki model for the sample 4 computed previously, and the fitting problem (1.17), the obtained optimal values for the parameters are $m = 0.1561 \text{ kg/m}^2$, $s = 2.77 \times 10^3 \text{ kg/ms}$ and $r = 3.169 \times 10^7 \text{ kg/m}^2$. The relative error obtained with these optimal values is $\varepsilon = 7.41\%$. Once this configuration has been completely characterized, the absorption coefficient of a multilayer medium formed by three layers of the sample 4, and two layers of the PE film $180 \mu\text{m}$ among them is calculated. The parameters of the Miki model for the sample 4 are those computed in Section 1.7.1, and the values of the rigid plate model are those computed above. The relative error obtained with these optimal values is $\varepsilon = 11.61\%$. The numerical results of the fitting problem with two layers of the sample 4 and the film 3 between them are shown in left plot of Figure 1.12, and with three layers of the sample 4, and two layers of film among them are shown in right plot of Figure 1.12.

1.7.3 Foam

As it happens with films, this material is thin enough to be modeled following a rigid plate model (see Section 1.3.4 for more details). The material under consideration is a polypropylene (PP) foam (sample 5) with thickness $h = 2.2 \mu\text{m}$, and surface density of $m = 0.110 \text{ kg/m}^2$, as part of a multilayer medium formed by this foam surrounded by the sample 4. Since the surface density is known, the fitting problem used

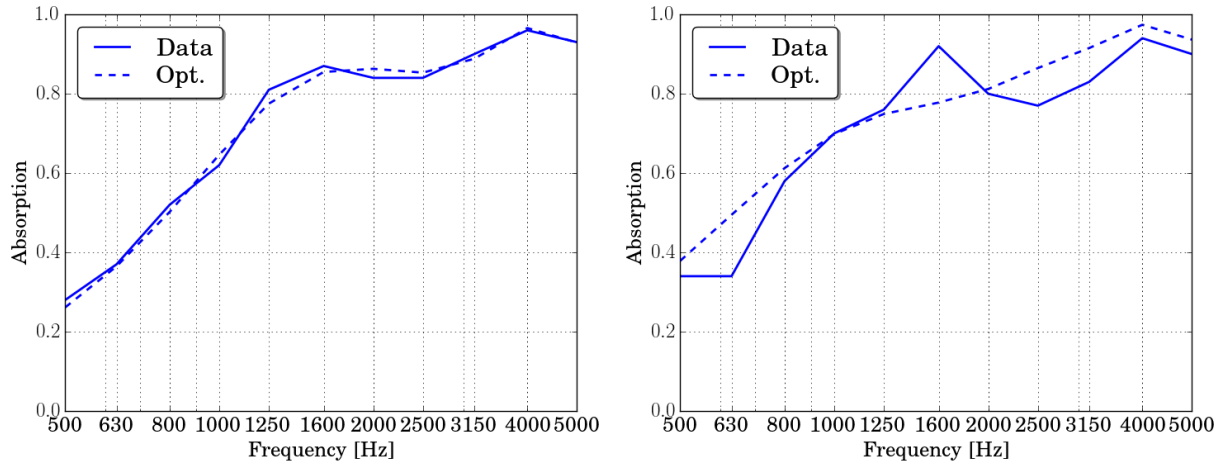


Figure 1.11: Left: Absorption coefficient of a multilayer medium formed by the film 2 with thickness $125 \mu\text{m}$ surrounded by the sample 4. Right: Absorption coefficient of a multilayer medium formed by three layers of the sample 4 with two layers of the film 2 among them, plotted with respect to the frequency. In both cases, the porous layer (sample 4) follows a Miki model with optimal values $\phi = 0.9906$, $\alpha_\infty = 1.9$, $\sigma = 2.11 \times 10^4 \text{ Nm}^{-4}$, and $M'' = 0.7402$. The film has been modeled by using a rigid plate model with optimal values $m = 0.0609 \text{ kg/m}^2$, $s = 1.09 \times 10^3 \text{ kg/ms}$, and $r = 3.574 \times 10^6 \text{ kg/m}^2$. The solid line shows the computed values, and the dashed line shows the experimental ones.

is (1.18). The obtained optimal values for the parameters are $s = 3.34 \times 10^3 \text{ kg/ms}$, and $r = 4.516 \times 10^7 \text{ kg/m}^2$, and the relative error with these optimal values is $\varepsilon = 7.09\%$. Once this configuration has been completely characterized, the absorption coefficient of a multilayer medium formed by the sample 4, the film 2, the foam, and the sample 4 has been computed. The parameters of the Miki model for the sample 4 are those computed in Section 1.7.1, the parameters of the film 2 are those computed in Section 1.7.2, and the parameter of the foam are those computed above. The relative error obtained with these optimal values is $\varepsilon = 8.77\%$. The numerical results of the fitting problem with two layers of the sample 4, and the foam between them are shown in left plot of Figure 1.13, and with the sample 4, the film 2, the foam, and the sample 4 are shown in right plot of Figure 1.13.

1.8 Conclusions

Since most of the rigid-frame porous materials can be modeled by using a fluid-equivalent model, in this chapter, the most common fluid-equivalent models used in the acoustic characterization of porous and fibrous materials, have been reviewed. First of all, each model has been described in detail, including the definition of their intrinsic physical parameters and explaining the restrictions of each model. Moreover, a description of the coupling con-

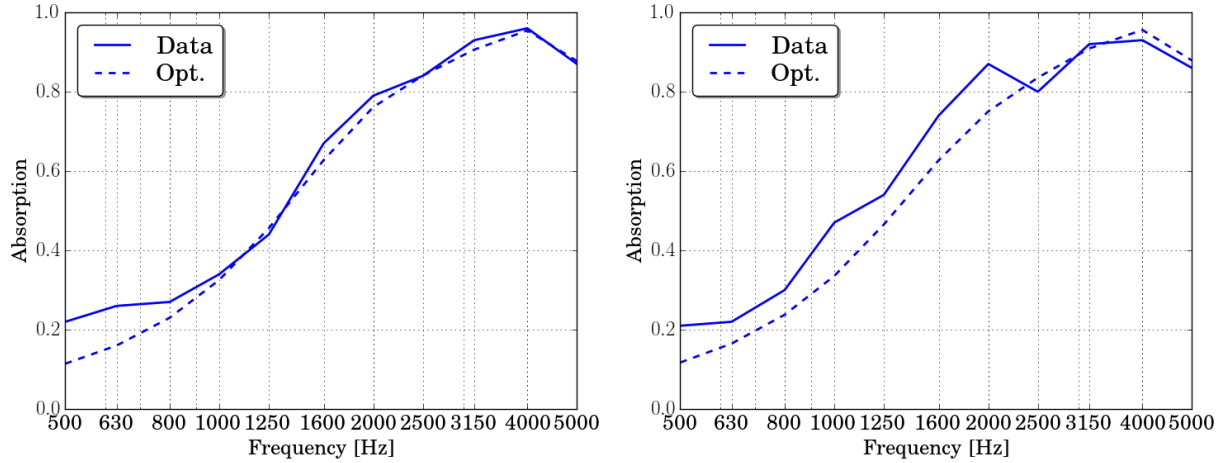


Figure 1.12: Left: Absorption coefficient of a multilayer medium formed by the film 3 with thickness $180\ \mu\text{m}$ surrounded by the sample 4. Right: Absorption coefficient of a multilayer medium formed by three layers of the sample 4 with two layers of the film 3 among them, plotted with respect to the frequency. In both cases, the porous layer (sample 4) follows a Miki model with optimal values $\phi = 0.9906$, $\alpha_\infty = 1.9$, $\sigma = 2.11 \times 10^4\ \text{Nm}^{-4}$, and $M'' = 0.7402$. The film has been modeled by using a rigid plate model with optimal values $m = 0.1561\ \text{kg/m}^2$, $s = 2.77 \times 10^3\ \text{kg/ms}$, and $r = 3.169 \times 10^7\ \text{kg/m}^2$. The solid line shows the computed values, and the dashed line shows the experimental ones.

ditions and a definition of some acoustic quantities of interest have been given. To compute these acoustic quantities, two multilayer media have been studied: one for the computation of the absorption coefficient, and another one, for the calculation of the transmission coefficient.

To characterize the available porous and fibrous materials, several inverse problems have been defined. Some numerical simulations are shown in order to illustrate the advantages and disadvantages of the parametric fitting methodology. On the one hand, these parametric fluid-equivalent models are well-known but have some limitations: some of them are only for fibrous materials [12, 69], the Delany-Bazley family models [69, 126] are only for materials with porosity close to 1, the JCA family models [55, 100, 111, 147] need a large number of parameters what can be a challenge for the solver used to perform the optimization. Although in some cases the numerical results for the single layers are smaller than 10% (see left plot in Figures 1.7 and 1.8), the incessant develop of new materials, such as recycled materials, which can not follow a concrete model or which may have an uncertain nature, can lead us to choose a wrong model or even to need a more complex fluid-equivalent model (see, for example, left plot in Figures 1.5 and 1.6, where errors are much bigger). Moreover, it may be interesting to consider other acoustic quantities different from the absorption or the transmission coefficient which are real-valued, in order to improve the results or even to have experimental data of varying multilayer configurations involving the material under study, to have a well-posed optimization problem [54]. In the

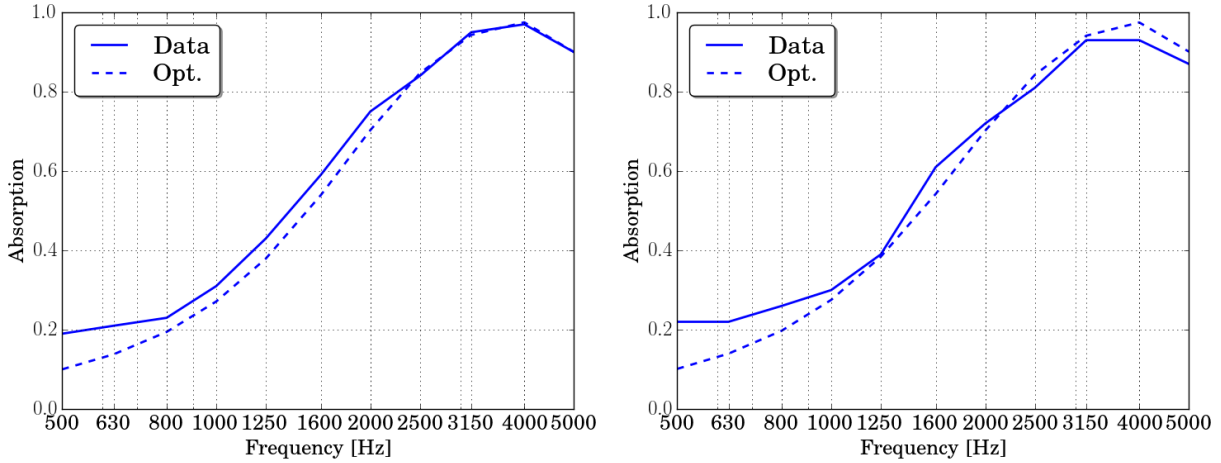


Figure 1.13: Left: Absorption coefficient of a multilayer medium formed by the foam with thickness $2.2 \mu\text{m}$ (sample 5) surrounded by the sample 4. Right: Absorption coefficient of a multilayer medium formed by the sample 4, the film 2, the foam, and the sample 4, plotted with respect to the frequency. In both cases, the porous layer (sample 4) follows a Miki model with optimal values $\phi = 0.9906$, $\alpha_\infty = 1.9$, $\sigma = 2.11 \times 10^4 \text{ Nm}^{-4}$, and $M'' = 0.7402$. The film has been modeled by using a rigid plate model with optimal values $m = 0.0609 \text{ kg/m}^2$, $s = 1.095 \times 10^3 \text{ kg/ms}$, and $r = 3.574 \times 10^7 \text{ kg/m}^2$. The solid line shows the computed values, and the dashed line shows the experimental ones.

next chapter, a non-parametric fluid-equivalent approach is used to overcome the issues that appear with the parametric models, and the posedness of the optimization problems is studied.

Chapter 2

A non-parametric fluid-equivalent approach for the acoustic characterization of rigid porous materials

Contents

2.1	Introduction	37
2.2	Harmonic response of a rigid porous material	39
2.2.1	Macroscopic description	39
2.2.2	Experimental characterization	40
2.3	Acoustic characterization of a single porous layer using a fixed-frequency inverse problem	42
2.3.1	Statement of the direct propagation problem	42
2.3.2	Characterization with absorption datasets	46
2.3.3	Characterization with surface impedance datasets	48
2.4	Acoustic characterization of a double porous layer using a fixed-frequency inverse problem	50
2.4.1	Statement of the direct propagation problem	50
2.4.2	Characterization with four surface admittance datasets	52
2.5	Numerical procedure to solve the inverse problems	54
2.5.1	Non-parametric approach	54
2.5.2	Parametric JCAL approach	57
2.6	Characterization results	57
2.6.1	Spurious oscillations	58

2.6.2	Single layer case	60
2.6.3	Double layer case	62
2.7	Conclusions	66

2.1 Introduction

Rigid porous materials are widely used for noise mitigation in a large number of engineering applications in building and environmental acoustics. In this context, it is of great interest to predict the acoustic properties of these materials when they are part of noise control devices (e.g., noise barriers [13], isolation walls [75]). As it is explained in Chapter 1, these materials are modeled on a macroscopic scale as an equivalent fluid, and its effective acoustic coefficients can be determined by using a parametric prediction model (e.g., [55, 69, 93, 100]). The main drawback of this parametric methodology is that these minimization procedures require using multiple frequency values for the adjustment, which may constrain the solution of the inverse problem given by a specific parametric model.

Moreover, the chosen parametric model could not be suitable for a particular material (e.g., the use of a single-parameter model [69] may not be accurate enough to describe the acoustic behavior of a rigid porous material properly). Although many parametric models exist in the literature [7, 11, 55, 69, 93, 100], the constant development of new materials poses the need for alternative predictive tools and fitting methods. Regarding the specific measurement procedures, some authors have proposed other methods based on ultrasonic [78, 79], or impedance tube arrangements [34, 70, 169, 171] for measuring the acoustic properties of porous materials. Unfortunately, most of them rely on the use of a parametric model [78, 79], require complementary appliances or other equipment configurations [34, 70, 169, 171] different from the setting described in ISO-10534 standard [1].

In this chapter, a novel non-parametric approach for the characterization of rigid porous materials is proposed. Unlike the above approaches, the proposed procedure avoids any parametric assumption on the coefficients of the fluid-equivalent model (see Definition 2.2.1 for further details) or the need to determine intrinsic physical parameters (required by the parametric models) using sophisticated laboratory equipment. Instead, this non-parametric approach uses a standardized impedance tube setup [1] data to solve a fixed-frequency propagation problem and thus estimate the effective properties of the material under study using a reduced amount of wideband experimental data. Notice that no novelties are introduced in the use of classical fluid-equivalent models (and its associated assumption of rigid solid-skeleton). This fluid-equivalent model is governed by a partial differential equation, which is written in terms of different effective (frequency-dependent) coefficients, namely, e.g., the dynamic mass density and the dynamic bulk modulus. Each of these parametric models uses different assumptions to write these effective coefficients in terms of different expressions (depending on the parametric model used), which involve intrinsic parameters of the materials (such as porosity, flow resistivity, or tortuosity). On the contrary, the present work analyzes how to avoid this rewriting procedure in terms of parameters and compute the effective coefficients directly from the available measured data.

The work described in this chapter is a collaboration with Jesús Carbajo and Jaime Ramis from the Department of Physics, System Engineering, and Signal Theory of the University of Alicante. All the materials under study are provided by this research group, and the available experimental data are measured in the laboratory of the research group

to which they belong. Moreover, part of this chapter has been published in [54].

In order to validate the proposed non-parametric approach, the effective acoustic properties associated to different single and multilayer configurations of porous materials were determined from simple surface impedance data, the results being compared to those obtained with one of these methods (specifically, the two-cavity method proposed by Utsuno et al. [171]). An excellent agreement was found between the numerically fitted results and the experimental measurements. Besides, results were also compared to those obtained using the JCAL (Johnson-Champoux-Allard-Lafarge) parametric model, the accuracy being potentially decreased in this latter case.

Hence, on the one hand, the proposed non-parametric methodology does not depend on the physical nature of the rigid porous material itself, so that it is expected to be more generic than the traditional predictive parametric approaches and may be applied to any porous material (i.e., fibrous, granular, where different parametric models should be used [93]). On the other hand, the proposed approach was found to be extensible to the analysis of multilayered systems containing thin or light rigid porous layers, which may serve to tackle the laboratory difficulties associated with the accurate characterization of the latter alone using an impedance tube.

Given that the use of multilayered or stratified media is of great interest in real-life engineering applications (from a thermal [181] and an acoustic [102] point of view), this feature is highly relevant for practical purposes. Therefore, this novel numerical methodology may be regarded as a simple and straightforward alternative for the characterization of rigid porous materials to be used in the design stage thereof. Besides, to write the acoustic propagation problems using a uniform approach valid for different multilayer configurations, the inverse problems stated throughout this chapter have been written in terms of the surface admittance values, in addition to using the classical absorption values or the surface impedance values [7, 75, 171]). The mathematical analysis of the well-posed inverse problem associated with the characterization of the porous materials has been made in a classical multi-modal approach, which is valid not only for the standard plane wave propagation but also for the case of higher-order modes in a Kundt's tube (see [148]).

This chapter is organized as follows: Section 2.2 describes the acoustic quantities used to characterize rigid porous materials, as well as the experimental setup used to measure these. In Section 2.3, the mathematical statement of the inherent propagation problem is fully described. Then, the inverse problem methodology used to obtain the effective acoustic coefficients associated with a rigidly backed single porous layer is described in detail. Four different strategies are outlined: each of them successively overcoming the limitations of the traditional fitting procedures used for the same purpose. Section 2.4 presents an extension of that methodology but for the case of a double porous layer configuration. In Section 2.5, the numerical procedure followed to solve the well-posed inverse problems is described. Section 2.6 presents the numerical results obtained, both for the single and double layer configurations, showing a good agreement when compared to measured data. Finally, Section 2.7 summarizes the main conclusions of the proposed approach.

Remark 2.1.1. Throughout this chapter, time-harmonic dependence for the acoustic pressure and displacement fields is assumed. In this manner, it has been settled formally that $\pi(\mathbf{p}, t) = \text{Re}(\Pi(\mathbf{p})e^{i\omega t})$, being π the time-dependent acoustic pressure field, Π the complex-valued time-harmonic acoustic pressure field, ω the angular frequency, t the time variable, \mathbf{p} the Cartesian coordinates of the spatial position, $\text{Re}(\cdot)$ the real part function of a complex number, and $i = \sqrt{-1}$ the imaginary unit.

2.2 Harmonic response of a rigid porous material

To characterize the rigid porous materials, it is necessary to use some acoustic quantities. These quantities, called effective coefficients, are described in this section emphasizing the differences approaches to obtain them. Also, the experimental setup used to measure the experimental data is described.

2.2.1 Macroscopic description

Linear theory regarding the propagation of sound in air-saturated rigid porous media has been extensively studied in the last decades (see, for instance, [7]). Basically, rigid porous materials attenuate sound mainly due to viscous friction and thermal conductivity in their pore network. If the pore size is small compared to the wavelength of an impinging sound wave, the air inside a layer of porous material with rigid solid frame (i.e., motionless skeleton) can be modeled accurately on a macroscopic scale as an equivalent compressible fluid. The acoustical behavior of the material is then fully characterized by the complex-valued and frequency-dependent effective coefficient pair: dynamic mass density $\rho_P(\omega)$ and dynamic bulk modulus $K_P(\omega)$. Alternatively, the acoustic response of this fluid-equivalent model can be determined from the effective coefficient pair: dynamic characteristic impedance, $Z_P(\omega)$, and dilatational (compressional) wave number, $k_P(\omega)$, these being related to the previous ones by (see [7]),

$$Z_P(\omega) = \sqrt{\rho_P(\omega)K_P(\omega)}, \quad (2.1)$$

$$k_P(\omega) = \omega\sqrt{\rho_P(\omega)/K_P(\omega)}. \quad (2.2)$$

Both effective coefficients can be handle using parametric techniques and the proposed non-parametric approach. The following definition provides a detailed definition of these two methodologies in the framework of the mathematical modeling of rigid porous materials:

Definition 2.2.1. The frequency-dependent values of the characteristic impedance and the wave number, respectively $\rho_P(\omega)$ and $K_P(\omega)$, involved in a fluid-equivalent model follows:

- i) a parametric approach if there exist two response functions $\hat{\rho}_P$ and \hat{K}_P (known in closed-form) and a finite number of constant parameters a_1, \dots, a_m such that $\hat{\rho}_P :$

$(a_1, \dots, a_m) \mapsto \hat{\rho}_P(a_1, \dots, a_m) \in \mathcal{C}((0, \infty), \mathbb{C})$ and $\hat{K}_P : (a_1, \dots, a_m) \mapsto \hat{K}_P(a_1, \dots, a_m) \in \mathcal{C}((0, \infty), \mathbb{C})$, and it holds

$$\rho_P(\omega) = [\hat{\rho}_P(a_1, \dots, a_m)](\omega), \quad K_P(\omega) = [\hat{K}_P(a_1, \dots, a_m)](\omega).$$

- ii) a non-parametric approach if both values $\rho_P(\omega)$ and $K_P(\omega)$ are only assumed given by arbitrary complex-valued continuous functions, this is, $\rho_P, K_P \in \mathcal{C}((0, \infty), \mathbb{C})$.

Bearing in mind the definition above, and using the parametric Johnson-Champoux-Allard-Lafarge model introduced in Section 1.2.2 in Chapter 1, the response function for the complex-valued dynamic mass density and for the dynamic bulk modulus are defined in a finite dimensional parametric space ($m = 5$) by

$$[\hat{\rho}_{JCAL}(\phi, \sigma, \alpha_\infty, \Lambda, \Lambda')](\omega) = \frac{\rho_F}{\phi} \alpha_\infty \left(1 - i \frac{\sigma \phi}{\omega \rho_F \alpha_\infty} \sqrt{1 + i \frac{4\alpha_\infty^2 \eta \rho_F \omega}{\sigma^2 \Lambda^2 \phi^2}} \right), \quad (2.3)$$

$$[\hat{K}_{JCAL}(\phi, \sigma, \alpha_\infty, \Lambda, \Lambda')](\omega) = \frac{\gamma P_F / \phi}{\gamma - (\gamma - 1) \left(1 - i \frac{\eta \phi}{\rho_F k'_0 \omega \text{Pr}} \sqrt{1 + i \frac{4k'^2 \rho_F \omega \text{Pr}}{\eta \Lambda'^2 \phi^2}} \right)^{-1}}, \quad (2.4)$$

where ρ_F is the mass density of the fluid, η is the dynamic viscosity, P_F is the fluid equilibrium pressure, Pr is the Prandtl number, and γ is the ratio of specific heats. Then, the proposed non-parametric approach will be described in detail in Sections 2.3 and 2.4.

2.2.2 Experimental characterization

Experimental methods frequently used for the acoustic characterization of porous materials use an impedance tube arrangement [70, 169, 171]. Particularly, Utsuno et al. [171] proposed the so-called two-cavity method whose experimental setup is shown in Figure 2.1 to estimate the effective acoustic properties associated with a single porous layer configuration. In brief, a source (typically an audio speaker) generates plane waves that impinge on the porous material positioned on the other end of the tube. By moving the rigid piece behind the sample, the surface impedance is measured twice: with a rigid backing and with a backing air cavity. The characteristic impedance (2.1) and the wave number (2.2) of the material under test are determined then from the surface impedance data obtained with a pair of microphones flush mounted in the tube for these two configurations. This method was chosen in the present work because of its easiness of practical implementation with a standard impedance tube without the need for modified arrangements [70, 169]. Consequently, this method can be used to determine either the surface impedance of a rigid porous material following the standardized method (rigid backed) [1] or its effective quantities of interest following the two-cavity method (rigid and air-cavity backed) [171].

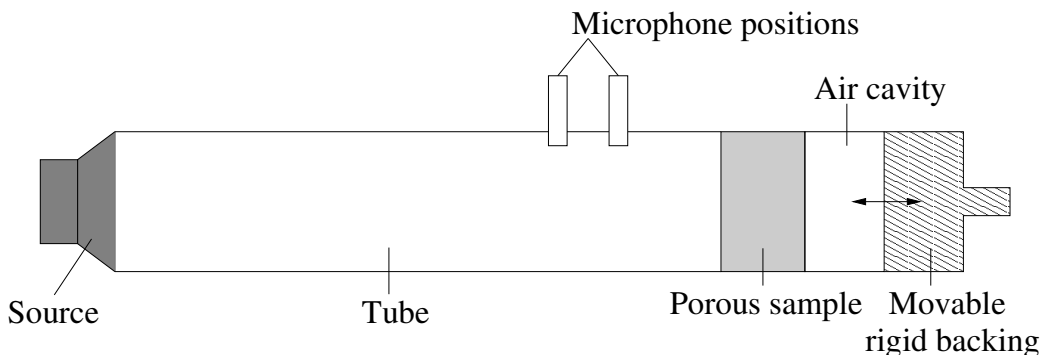


Figure 2.1: Impedance tube setup proposed by Utsuno et al. [171] to determine the characteristic impedance and wave number of porous materials in a single layer configuration.

Figure 2.2 shows some pictures of the impedance tube and its respective appliances used for these measurements in the present work. It consists of a stainless steel tube of circular cross-section with an inner thickness of 6 mm and an inner diameter of 100 mm, the microphones being spaced 85 mm (cut-off frequency around 1800 Hz). The acquisition system was composed of the system OR34 Compact Analyzer (which integrates a random noise generator), a 5M30 Beyma dynamic speaker, and two Brüel & Kjær type 4188 1/2 inch microphones. Acquisition data was post-processed to obtain the surface impedance of the sample under study.

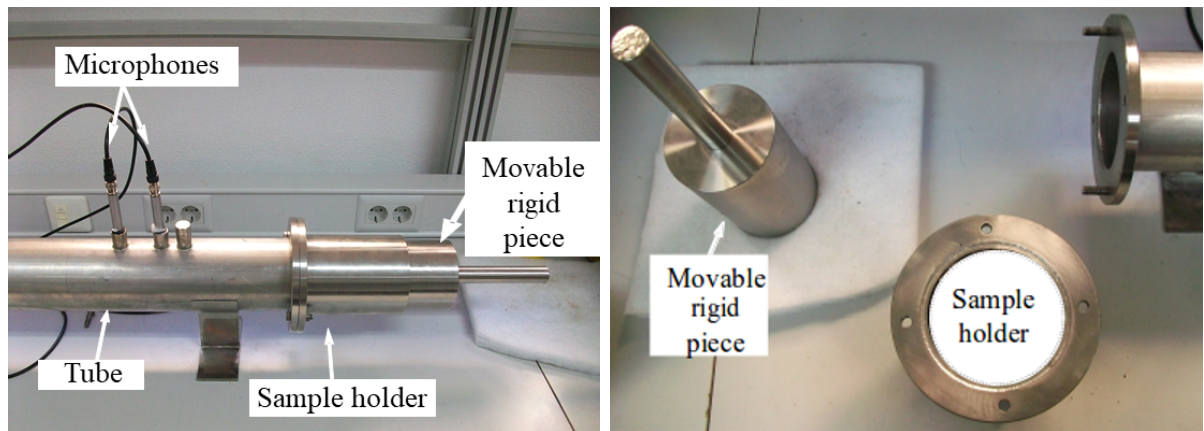


Figure 2.2: Impedance tube used for the experimental measurements. (Left) General view; (Right) Detailed view of the movable rigid piece and the sample holder in which the sample under test is placed.

2.3 Acoustic characterization of a single porous layer using a fixed-frequency inverse problem

Once the effective acoustic coefficients that characterize a rigid porous material and the experimental method used to measure these were outlined in Section 2.2, a description of the mathematical model of the associated inverse problem and subsequently the inherent direct propagation problem is given below.

2.3.1 Statement of the direct propagation problem

When the porous medium with rigid solid frame is assumed to be homogeneous and isotropic on a macroscopic scale, its intrinsic effective acoustic properties are considered spatially constant, and so the classical Helmholtz and momentum equations describing the acoustic wave propagation in such medium (written in terms of the corresponding pair of coefficients $\rho_P(\omega)$ and $k_P(\omega)$) are given by

$$-k_P^2(\omega)\Pi_P - \Delta\Pi_P = 0, \quad (2.5)$$

$$-\omega^2\rho_P(\omega)\mathbf{U}_P - \nabla\Pi_P = \mathbf{0}, \quad (2.6)$$

where Π_P and \mathbf{U}_P are the acoustic pressure and displacement fields in the porous medium, respectively.

In order to model the acoustic wave propagation mathematically throughout a rigid-backed porous layer placed inside an impedance tube, a multilayer planar configuration formed by a porous layer surrounded by a compressible fluid in the front face (air in the case under study), is considered. Figure 2.3 shows a two-dimensional cut of the computational domain whose boundaries and the fluid and porous subdomains depicted are described below. Let Ω_F and Ω_P be the three-dimensional domains occupied by the fluid and the porous layer, respectively. Both, the fluid and the porous layer of thickness d are placed in the interior of a tube with constant cross-section \mathcal{S} . The porous layer is located at distance l from the acoustic source. The coupled interface Γ_F denotes the common boundary between the fluid and the porous layer. The rigid lateral walls of the tube are denoted by Γ_W (assumed as being acoustically rigid, i.e., $\mathbf{U}_P \cdot \boldsymbol{\eta} = 0$, being $\boldsymbol{\eta}$ the unit normal vector on the boundary), the back boundary of the porous layer is denoted by Γ_B , and the acoustic pressure source (audio speaker in practice) is placed on boundary Γ_L .

To write the differential formulation of the coupled problem, both the compressible fluid and the porous models have been expressed in terms of the pressure field. Since the acoustic behavior of a rigid-frame porous material could be represented by a fluid-equivalent model (2.5)-(2.6), then the differential formulation for this coupled problem is given by: for a fixed angular frequency $\omega > 0$, a prescribed surface admittance operator Y_B for the back boundary, and an acoustic pressure source G , find the acoustic pressure and displacement fields in the fluid, Π_F and \mathbf{U}_F , and the acoustic pressure and displacement fields in the porous medium, Π_P and \mathbf{U}_P , such that

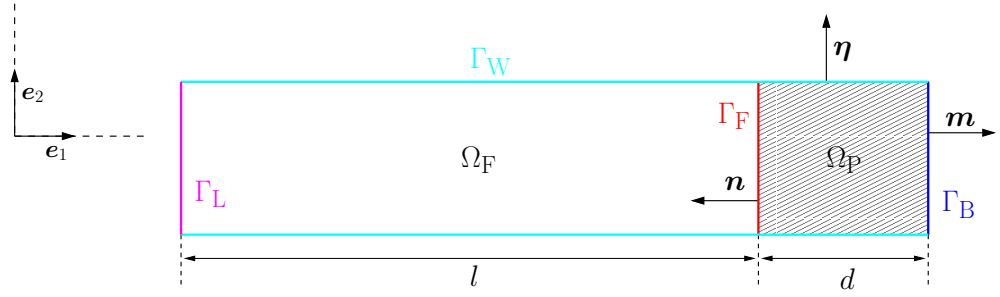


Figure 2.3: Schematic two-dimensional cut of the computational domain where the fluid (air in the case under study) and the porous subdomains, Ω_F and Ω_P , are marked in white and dashed regions, respectively. Their boundaries are highlighted with different colors: Γ_F in red, Γ_W in cyan, Γ_L in magenta, and Γ_B in blue.

$$\left\{ \begin{array}{ll} -k_F^2(\omega)\Pi_F - \Delta\Pi_F = 0 & \text{in } \Omega_F, \\ -\omega^2\rho_F\mathbf{U}_F - \nabla\Pi_F = \mathbf{0} & \text{in } \Omega_F, \\ -k_P^2(\omega)\Pi_P - \Delta\Pi_P = 0 & \text{in } \Omega_P, \\ -\omega^2\rho_P(\omega)\mathbf{U}_P - \nabla\Pi_P = \mathbf{0} & \text{in } \Omega_P, \\ \mathbf{U}_F \cdot \mathbf{n} = \mathbf{U}_P \cdot \mathbf{n} & \text{on } \Gamma_F, \\ \Pi_F = \Pi_P & \text{on } \Gamma_F, \\ i\omega\mathbf{U}_P \cdot \mathbf{m} = Y_B\Pi_P & \text{on } \Gamma_B, \\ \mathbf{U}_F \cdot \boldsymbol{\eta} = 0 & \text{on } \Gamma_W \cap \partial\Omega_F, \\ \mathbf{U}_P \cdot \boldsymbol{\eta} = 0 & \text{on } \Gamma_W \cap \partial\Omega_P, \\ \Pi_F = G & \text{on } \Gamma_L, \end{array} \right.$$

where $k_F(\omega) = \omega/c_F$, being c_F the sound velocity and ρ_F the mass density in the fluid domain (air), which are assumed to have no frequency dependence (air in ambient conditions). Finally, \mathbf{n} , \mathbf{m} , and $\boldsymbol{\eta}$ are respectively the unit normal vectors on boundaries Γ_F , Γ_B , and Γ_W . These normal vectors are outward to the porous domain (on those boundaries where it is applicable). Notice that the system of equations written above involves the standard continuity assumption of the pressure and the normal displacements on Γ_F (see [7, Chapter 11]).

Equivalently, the coupled problem stated above can be reformulated only in terms of the acoustic pressure field Π_F in the fluid domain and the acoustic pressure field Π_P in the porous layer:

$$\left\{ \begin{array}{ll} -k_F^2(\omega)\Pi_F - \Delta\Pi_F = 0 & \text{in } \Omega_F, \\ -k_P^2(\omega)\Pi_P - \Delta\Pi_P = 0 & \text{in } \Omega_P, \\ \frac{1}{\rho_F}\frac{\partial\Pi_F}{\partial\mathbf{n}} = \frac{1}{\rho_P(\omega)}\frac{\partial\Pi_P}{\partial\mathbf{n}} & \text{on } \Gamma_F, \\ \Pi_F = \Pi_P & \text{on } \Gamma_F, \\ \frac{1}{i\omega\rho_P(\omega)}\frac{\partial\Pi_P}{\partial\mathbf{m}} = Y_B\Pi_P & \text{on } \Gamma_B, \\ \frac{\partial\Pi_F}{\partial\boldsymbol{\eta}} = 0 & \text{on } \Gamma_W \cap \partial\Omega_F, \\ \frac{\partial\Pi_P}{\partial\boldsymbol{\eta}} = 0 & \text{on } \Gamma_W \cap \partial\Omega_P, \\ \Pi_F = G & \text{on } \Gamma_L. \end{array} \right. \quad (2.7)$$

The multimodal decomposition described further is similar to the work written in [90]. There, a method for solving the acoustic time-harmonic wave equation in a non-uniform waveguide is proposed. The multimodal method is based on the use of a spectral basis in each transverse section of the guide, using Fourier-like series (see [94]).

Following standard arguments to model waveguides [120], the transversal section \mathcal{S} of the impedance tube is assumed constant along its axis (in the p_1 -direction), the acoustic pressure source is placed on the plane $p_1 = -l$, and the coupling interface and the back surface are placed on planes $p_1 = 0$ and $p_1 = d$, respectively. Hence, $\Omega_F = (-l, 0) \times \mathcal{S}$ and $\Omega_P = (0, d) \times \mathcal{S}$ and then the $L^2(S)$ -Hilbert basis $\{\varphi_n\}_{n \in \mathbb{N}}$ of transverse modes associated to the impedance tube [62] can be computed as the eigenmodes of the two-dimensional problem on the $p_2 - p_3$ coordinate plane

$$\left\{ \begin{array}{ll} -\lambda_n^2\varphi_n - \frac{d^2\varphi_n}{dp_2^2} - \frac{d^2\varphi_n}{dp_3^2} = 0 & \text{in } \mathcal{S}, \\ \frac{\partial\varphi_n}{\partial\mathbf{r}} = 0 & \text{on } \partial\mathcal{S}, \end{array} \right.$$

where λ_n is the transverse eigenvalue associated to the n -th mode φ_n , and \mathbf{r} denotes the unit normal vector on boundary $\partial\mathcal{S}$ exterior to \mathcal{S} (\mathbf{r} is determined by the last two components of normal vector $\boldsymbol{\eta}$). Since the coupling boundary Γ_F and the back surface Γ_B are assumed planar and placed on $p_1 = 0$ and $p_1 = d$, respectively, then the unit outward normal vectors are given by $\mathbf{n} = -\mathbf{e}_1$ and $\mathbf{m} = \mathbf{e}_1$, being $\{\mathbf{e}_1, \mathbf{e}_2, \mathbf{e}_3\}$ the canonical vector basis of the Cartesian system. Hence, the solution of the pressure fields (written in Cartesian coordinates $\mathbf{p} = (p_1, p_2, p_3)$) are given by

$$\Pi_F(\mathbf{p}) = \sum_{n=0}^{\infty} (A_F^n e^{-i\beta_F^n(\omega)p_1} + B_F^n e^{i\beta_F^n(\omega)p_1}) \varphi_n(p_2, p_3) \quad \text{for } \mathbf{p} \in \Omega_F, \quad (2.8)$$

$$\Pi_P(\mathbf{p}) = \sum_{n=0}^{\infty} (A_P^n e^{-i\beta_P^n(\omega)p_1} + B_P^n e^{i\beta_P^n(\omega)p_1}) \varphi_n(p_2, p_3) \quad \text{for } \mathbf{p} \in \Omega_P, \quad (2.9)$$

where $A_F^n, B_F^n, A_P^n, B_P^n$ are the modal coefficients associated to n -th mode for the acoustic pressure in the fluid and porous subdomains, respectively; $\beta_F^n(\omega) = \sqrt{k_F^2(\omega) - \lambda_n^2}$ and $\beta_P^n(\omega) = \sqrt{k_P^2(\omega) - \lambda_n^2}$ for $n \in \mathbb{N}$ (notice that the square root is computed with the positive criterion $\text{Re}(\sqrt{z}) \geq 0$).

In addition, the pressure induced by the active boundary of the acoustic pressure source, Γ_L , can be represented by $G = \sum_{n=0}^{\infty} g_n \varphi_n$, where g_n is the projection of function G into the basis element φ_n . Consequently, the action of the surface admittance operator Y_B , which can be read as a Dirichlet-to-Neumann (DtN) operator on Γ_B associated to problem (2.7) (see for instance [85, 96]), can be expressed by

$$F = \sum_{n=0}^{\infty} f_n \varphi_n \mapsto Y_B F = \sum_{n=0}^{\infty} Y_B^n(\omega) f_n \varphi_n.$$

Consequently, problem (2.7) can be decoupled in terms of the transverse modes, and hence the modal coefficients $\{A_F^n, B_F^n, A_P^n, B_P^n\}_{n \in \mathbb{N}}$ are the solution of the following sequence of linear algebraic system of equations:

$$\begin{cases} \rho_P(\omega) \beta_P^n(\omega) (-A_F^n + B_F^n) = \rho_F \beta_F^n(\omega) (-A_P^n + B_P^n), \\ A_F^n + B_F^n = A_P^n + B_P^n, \\ \frac{\beta_P^n(\omega)}{\omega \rho_P(\omega)} (-A_P^n e^{-i\beta_P^n(\omega)d} + B_P^n e^{i\beta_P^n(\omega)d}) = Y_B^n(\omega) (A_P^n e^{-i\beta_P^n(\omega)d} + B_P^n e^{i\beta_P^n(\omega)d}), \\ A_F^n e^{i\beta_F^n(\omega)l} + B_F^n e^{-i\beta_F^n(\omega)l} = g_n, \end{cases}$$

for each $n \in \mathbb{N}$.

Once the solution of the modal coefficients $\{A_F^n(\omega), B_F^n(\omega), A_P^n(\omega), B_P^n(\omega)\}_{n \in \mathbb{N}}$ have been computed, from (2.8)-(2.9), the surface impedance operator on boundary Γ_F can be defined as the trace of the pressure field associated to a prescribed normal velocity on Γ_F . This functional operator Z_I is completely described by its action on the trace of each basis element φ_n as follows:

$$F = \sum_{n=0}^{\infty} f_n \varphi_n \mapsto Z_I F = \sum_{n=0}^{\infty} Z_I^n(\omega) f_n \varphi_n \quad \text{with} \quad Z_I^n(\omega) = Z_F \frac{A_F^n(\omega) + B_F^n(\omega)}{A_F^n(\omega) - B_F^n(\omega)}, \quad (2.10)$$

where f_n is the projection of F into the basis element φ_n , Z_F is the characteristic impedance of the fluid medium, and $Z_I^n(\omega)$ is the surface impedance of the porous layer for each mode $n \in \mathbb{N}$.

Analogously, the sound absorption coefficient of the porous layer can be computed as a scalar quantity associated to each transverse mode. So, for each mode $n \in \mathbb{N}$, the n -th modal sound absorption coefficient is given by

$$\alpha_n(\omega) = 1 - \left| \frac{Z_I^n(\omega) - Z_F}{Z_I^n(\omega) + Z_F} \right|^2 = 1 - \left| \frac{Y_F - Y_I^n(\omega)}{Y_F + Y_I^n(\omega)} \right|^2, \quad (2.11)$$

where the modal admittance values are given by $Y_I^n(\omega) = 1/Z_I^n(\omega)$ and the characteristic admittance by $Y_F = 1/Z_F$. Notice that, in the case of $n = 0$, $\alpha_0(\omega)$ coincides with the absorption coefficient computed in the classical plane wave analysis at normal incidence.

The main concern for practitioners consists of ensuring an adequate choice of the parametric porous model. The most accurate selection is not always possible to be known *a priori*, since it depends on the acoustic nature of the material samples. In fact, an inadequate model selection could ruin any parameter model fitting. As a partial remedy of these drawbacks, in the present chapter, the proposed non-parametric methodology avoids the choice and the use of parametric models. More precisely, it is not required to impose any functional dependency on the acoustic quantities used in (2.1)-(2.2) in terms of the frequency, and it is only based on the experimental measurements. Throughout the following sections, different strategies are described in detail, showing their drawbacks and the potential applicability for the characterization of the porous material properties.

2.3.2 Characterization with absorption datasets

In this characterization strategy, for a fixed frequency value ω , it is assumed that the propagation problem (2.7) is solved with only a back admittance operator, whose coefficients $\{Y_B^n(\omega)\}_{n \in \mathbb{N}}$ and the absorbing coefficients $\{\alpha_n(\omega)\}_{n \in \mathbb{N}}$ are known. So, the characterization problem can be stated as follows.

Problem 2.3.1 (Inverse problem with a single absorption dataset). *For a fixed frequency value ω and a fixed transverse mode n_0 , find the complex-valued coefficients $k_P(\omega)$ and $Z_P(\omega)$ assuming only known the absorption value $\alpha_{n_0}(\omega)$ obtained by solving problem (2.7) with the back admittance value $Y_B^{n_0}(\omega)$ on Γ_B .*

Lemma 2.3.2. *Problem 2.3.1 is ill-posed in the sense that there exists an innumerable number of solutions due to the lack of observation data.*

Proof. Firstly, despite $\alpha_{n_0}(\omega)$ only depends on the absolute value of a quotient of complex-valued expressions involving the surface admittance values, let us consider for simplicity the most favorable case where the surface admittance Y_I is also known in phase and modulus in addition to the absorption quantity. In this case, the pressure field Π_P , which is solution of the propagation problem (2.7), satisfies the boundary conditions

$$\frac{1}{i\omega\rho_P(\omega)} \frac{\partial\Pi_P}{\partial\mathbf{n}} = Y_I\Pi_P \quad \text{on } \Gamma_F, \quad \frac{1}{i\omega\rho_P(\omega)} \frac{\partial\Pi_P}{\partial\mathbf{m}} = Y_B\Pi_P \quad \text{on } \Gamma_B.$$

Hence, the porous coefficients $A_P^{n_0}$ and $B_P^{n_0}$ hold

$$\begin{cases} -\frac{\beta_P^{n_0}(\omega)}{\omega\rho_P(\omega)} (-A_P^{n_0} + B_P^{n_0}) = Y_I^{n_0}(\omega) (A_P^{n_0} + B_P^{n_0}), \\ \frac{\beta_P^{n_0}(\omega)}{\omega\rho_P(\omega)} \left(-A_P^{n_0} e^{-i\beta_P^{n_0}(\omega)d} + B_P^{n_0} e^{i\beta_P^{n_0}(\omega)d} \right) \\ \qquad \qquad \qquad = Y_B^{n_0}(\omega) \left(A_P^{n_0} e^{-i\beta_P^{n_0}(\omega)d} + B_P^{n_0} e^{i\beta_P^{n_0}(\omega)d} \right), \end{cases}$$

where $Y_I^{n_0}(\omega) = 1/Z_I^{n_0}(\omega)$. From both equations, if the quotient $B_P^{n_0}/A_P^{n_0}$ is solved for both equations, it holds

$$\frac{Y_B^{n_0}(\omega) + A(\omega)}{Y_B^{n_0}(\omega) - A(\omega)B(\omega)} = \frac{A(\omega) + Y_I^{n_0}(\omega)}{A(\omega) - Y_I^{n_0}(\omega)}$$

with $A(\omega) = \beta_P^{n_0}(\omega)/(\omega\rho_P(\omega))$ and $B(\omega) = e^{2i\beta_P^{n_0}(\omega)d}$. Obviously, the equation written above has uncountable solutions since, for each fixed arbitrary value of $B(\omega)$, there are different solution values for $A(\omega)$. The same conclusion is derived for the pair of coefficients $(\beta_P^{n_0}(\omega), \rho_P(\omega))$ and consequently also for $(k_P(\omega), Z_P(\omega))$ taking into account the definition of wave number $\beta_P^{n_0}$, this is, $k_P(\omega) = \sqrt{(\beta_P^{n_0}(\omega))^2 + \lambda_{n_0}^2}$ and $Z_P(\omega) = \rho_P(\omega)\omega/k_P(\omega)$. \square

The ill-posedness of the inverse problem stated above could be tentatively medicated adding new absorption observations with a second different back admittance leading to the following strategy:

Problem 2.3.3 (Inverse problem with two absorption datasets). *For a fixed frequency value ω and a fixed transverse mode n_0 , find the complex-valued coefficients $k_P(\omega)$ and $Z_P(\omega)$ assuming known the absorption values $\alpha_{n_0}(\omega)$ and $\tilde{\alpha}_{n_0}(\omega)$ obtained respectively by solving problem (2.7) with two different back admittance values $Y_B^{n_0}(\omega)$ and $\tilde{Y}_B^{n_0}(\omega)$ on Γ_B .*

However, even with an additional absorption dataset, the inverse problem to be solved is still ill-posed.

Lemma 2.3.4. *Problem 2.3.3 is ill-posed in the sense that there exists an uncountable number of solutions due to the lack of phase information on the observation data.*

Proof. Firstly, let us consider for simplicity the most favorable case where the surface admittance Y_I and \tilde{Y}_I are known in phase and modulus in addition to the absorption quantities $\alpha_{n_0}(\omega)$ and $\tilde{\alpha}_{n_0}(\omega)$, respectively. In this case, the pressure fields Π_P and $\tilde{\Pi}_P$, which are respectively solutions of propagation problem (2.7) with admittance operators Y_B and \tilde{Y}_B , satisfy the boundary conditions

$$\begin{aligned} \frac{1}{i\omega\rho_P(\omega)} \frac{\partial\Pi_P}{\partial\mathbf{n}} &= Y_I\Pi_P \quad \text{on } \Gamma_F, & \frac{1}{i\omega\rho_P(\omega)} \frac{\partial\Pi_P}{\partial\mathbf{m}} &= Y_B\Pi_P \quad \text{on } \Gamma_B, \\ \frac{1}{i\omega\rho_P(\omega)} \frac{\partial\tilde{\Pi}_P}{\partial\mathbf{n}} &= \tilde{Y}_I\tilde{\Pi}_P \quad \text{on } \Gamma_F, & \frac{1}{i\omega\rho_P(\omega)} \frac{\partial\tilde{\Pi}_P}{\partial\mathbf{m}} &= \tilde{Y}_B\tilde{\Pi}_P \quad \text{on } \Gamma_B. \end{aligned}$$

Hence, the modal coefficients $A_P^{n_0}$ and $B_P^{n_0}$ associated to Π_P hold

$$\left\{ \begin{array}{l} -\frac{\beta_P^{n_0}(\omega)}{\omega\rho_P(\omega)} (-A_P^{n_0} + B_P^{n_0}) = Y_I^{n_0}(\omega) (A_P^{n_0} + B_P^{n_0}), \\ \frac{\beta_P^{n_0}(\omega)}{\omega\rho_P(\omega)} \left(-A_P^{n_0} e^{-i\beta_P^{n_0}(\omega)d} + B_P^{n_0} e^{i\beta_P^{n_0}(\omega)d} \right) \\ \qquad = Y_B^{n_0}(\omega) \left(A_P^{n_0} e^{-i\beta_P^{n_0}(\omega)d} + B_P^{n_0} e^{i\beta_P^{n_0}(\omega)d} \right), \end{array} \right.$$

and analogously those modal coefficients $\tilde{A}_P^{n_0}$ and $\tilde{B}_P^{n_0}$ associated to $\tilde{\Pi}_P$ hold

$$\begin{cases} -\frac{\beta_P^{n_0}(\omega)}{\omega\rho_P(\omega)} \left(-\tilde{A}_P^{n_0} + \tilde{B}_P^{n_0} \right) = \tilde{Y}_I^{n_0}(\omega) \left(\tilde{A}_P^{n_0} + \tilde{B}_P^{n_0} \right), \\ \frac{\beta_P^{n_0}(\omega)}{\omega\rho_P(\omega)} \left(-\tilde{A}_P^{n_0} e^{-i\beta_P^{n_0}(\omega)d} + \tilde{B}_P^{n_0} e^{i\beta_P^{n_0}(\omega)d} \right) \\ \quad = \tilde{Y}_B^{n_0}(\omega) \left(\tilde{A}_P^{n_0} e^{-i\beta_P^{n_0}(\omega)d} + \tilde{B}_P^{n_0} e^{i\beta_P^{n_0}(\omega)d} \right), \end{cases}$$

where $Y_I^{n_0}(\omega) = 1/Z_I^{n_0}(\omega)$ and $\tilde{Y}_I^{n_0}(\omega) = 1/\tilde{Z}_I^{n_0}(\omega)$. Following straightforward computations (analogous to those ones described, for instance, in [171] where impedance-dependent expressions are used instead), it leads to

$$A(\omega) = \sqrt{\frac{Y_I^{n_0}(\omega)\tilde{Y}_I^{n_0}(\omega) \left(\tilde{Y}_B^{n_0}(\omega) - Y_B^{n_0}(\omega) \right) + Y_B^{n_0}(\omega)\tilde{Y}_B^{n_0}(\omega) \left(\tilde{Y}_I^{n_0}(\omega) - Y_I^{n_0}(\omega) \right)}{\left(\tilde{Y}_B^{n_0}(\omega) - Y_B^{n_0}(\omega) \right) + \left(\tilde{Y}_I^{n_0}(\omega) - Y_I^{n_0}(\omega) \right)}}, \quad (2.12)$$

$$\beta_P^{n_0}(\omega) = \frac{1}{2id} \ln \left(\frac{Y_I^{n_0}(\omega) - A(\omega)}{Y_I^{n_0}(\omega) + A(\omega)} \frac{Y_B^{n_0}(\omega) - A(\omega)}{Y_B^{n_0}(\omega) + A(\omega)} \right), \quad \rho_P(\omega) = \frac{\beta_P^{n_0}(\omega)}{\omega A(\omega)}, \quad (2.13)$$

and consequently there exists a solution for $Z_P(\omega)$ and $k_P(\omega)$ (given by $Z_P(\omega) = \rho_P(\omega)\omega/k_P(\omega)$ and $k_P(\omega) = \sqrt{(\beta_P^{n_0}(\omega))^2 + \lambda_{n_0}^2}$). Now, coming back to the original absorption datasets of Problem 2.3.3, it is easy to show that the inverse problem is ill-posed using the solution described above: since $\alpha_{n_0}(\omega)$ (2.11) only depends on the absolute value of a complex-valued expressions, if the value of $Y_I^{n_0}(\omega)$ in (2.11) is replaced by

$$Y_F \frac{Y_F(e^{i\gamma} - 1) - Y_I^{n_0}(\omega)(e^{i\gamma} + 1)}{Y_I^{n_0}(\omega)(e^{i\gamma} - 1) - Y_F(e^{i\gamma} + 1)},$$

for any arbitrary value $\gamma \in (-\pi, \pi]$, then the absorption values will be identical for any arbitrary value of γ . The same argument can be applied to the absorption coefficient $\tilde{\alpha}_{n_0}(\omega)$ replacing the values of $\tilde{Y}_I^{n_0}(\omega)$ in (2.11). In conclusion, the inverse problem based on absorption datasets has an infinite uncountable number of solutions varying simply γ . \square

2.3.3 Characterization with surface impedance datasets

Since the inverse problem described in the previous section is still ill-posed, a new characterization strategy is used, considering surface impedance values instead of absorption values. Since the surface impedance data are complex-valued while the absorption data are real-valued, the strategy possesses more input information and the ill-posedness of the inverse problem could be overcome. So, in this characterization strategy, for a fixed frequency value ω , it is assumed that only a propagation problem (2.7) is solved with only

a back admittance operator, whose coefficients are $\{Y_B^n(\omega)\}_{n \in \mathbb{N}}$ and the surface admittance values $\{Y_I^n(\omega)\}_{n \in \mathbb{N}}$ are known. So, the characterization problem can be stated as follows.

Problem 2.3.5 (Inverse problem with a single surface admittance dataset). *For a fixed frequency value ω and a fixed transverse mode n_0 , find the complex-valued coefficients $k_P(\omega)$ and $Z_P(\omega)$ assuming only known the surface admittance value $Y_I^{n_0}(\omega)$ on Γ_F obtained by solving problem (2.7) with the back admittance value $Y_B^{n_0}(\omega)$ on Γ_B .*

Lemma 2.3.6. *Problem 2.3.5 is ill-posed in the sense that there exist innumerable solutions due to the lack of observation data.*

Proof. The same arguments described in the proof of Lemma 2.3.2 lead to the conclusion that there exists an uncountable number of solutions. \square

The ill-posedness of the inverse problem stated above can be overcome adding an additional surface admittance observation with a second different back admittance leading to the following characterization approach:

Problem 2.3.7 (Inverse problem with two surface impedance datasets). *For a fixed frequency value ω and a fixed transverse mode n_0 , find the complex-valued coefficients $k_P(\omega)$ and $Z_P(\omega)$ assuming known the surface admittance values $Y_I^{n_0}(\omega)$ and $\tilde{Y}_I^{n_0}(\omega)$ on Γ_F obtained respectively by solving problem (2.7) with two different back admittance values $Y_B^{n_0}(\omega)$ and $\tilde{Y}_B^{n_0}(\omega)$ on Γ_B .*

However, even with two frequency response curves associated with surface admittance values, the inverse problem to be solved will have an infinite (but countable) number of solutions.

Lemma 2.3.8. *Problem 2.3.7 is well-posed in the sense that there exists an infinite (but countable) number of solutions due to the periodicity of the wave number values.*

Proof. Following identical arguments to those ones used in the proof of Lemma 2.3.4, the existence of solution of the inverse problem is ensured from the expressions of $A(\omega)$, $\beta_P^{n_0}(\omega)$ and $\rho_P(\omega)$ in (2.12)-(2.13). The uniqueness of solution for the expression $A(\omega)$ is straightforward taking into account that it is the root of a quadratic polynomial, where only the solution with positive real part is considered. However, from (2.13), it is clear that due to the periodicity (with respect to the imaginary axis) of the complex-valued exponential function, the wave number admits the solutions

$$\beta_P^{n_0}(\omega) = \frac{1}{2id} \ln \left(\frac{Y_I^{n_0}(\omega) - A(\omega)}{Y_I^{n_0}(\omega) + A(\omega)} \frac{Y_B^{n_0}(\omega) - A(\omega)}{Y_B^{n_0}(\omega) + A(\omega)} \right) + \frac{\pi\ell(\omega)}{d} \quad \text{for } \ell(\omega) \in \mathbb{Z}, \quad (2.14)$$

which leads to an infinite (but countable) number of solutions for $\beta_P^{n_0}(\omega)$. The same conclusions hold for $\rho_P(\omega)$ and $Z_P(\omega)$. \square

Remark 2.3.9. To overcome the lack of uniqueness in the previous inverse problem, the value of the integer parameter $\ell(\omega)$ should be fixed. In that case, the inverse Problem 2.3.7 would be well-posed and it would have a unique solution. For this purpose, two assumptions are considered: (i) the frequency response function associated to $\beta_P^{n_0}(\omega)$ is continuous (so, no discontinuities are allowed in its frequency response) and (ii) the integer value $\ell(\omega)$ is assumed known at a given frequency.

Taking into account the strategy devised in Remark 2.3.9, to overcome the lack of uniqueness of solution in (2.13) the value of ℓ should be fixed. In practice, there are different possible alternatives for this purpose. For instance, it would be enough to know the low-frequency limit of the dynamic mass density, i.e., $\lim_{\omega \rightarrow 0} \rho_P(\omega) = \rho_{P0}$ (see, for instance, the relevance of this low-frequency limits for rigid and limp frame porous materials in [144, 162]). Alternatively, since $\beta_P^{n_0}(\omega) = \sqrt{(\omega/c_P(\omega))^2 - \lambda_{n_0}^2}$, being $c_P(\omega)$ the sound speed in the porous material, if it is assumed that $c_P(\omega)$ is not null in the limit case when $\omega \rightarrow 0$, then it can be fixed ℓ at the low-frequency regime to ensure the static limit $\beta_P^{n_0}(0) = \lambda_{n_0}$. Subsequently, $\ell(\omega)$ is updated at higher frequencies to guarantee no discontinuities are presented on the frequency response of $\beta_P^{n_0}(\omega)$. This latter procedure has been used throughout all the numerical results shown in this chapter (in particular, once it is fixed $n_0 = 0$, it holds $\beta_P^{n_0}(\omega) \rightarrow 0$ and also $\ell(\omega) \rightarrow 0$ when ω tends to 0).

2.4 Acoustic characterization of a double porous layer using a fixed-frequency inverse problem

In most of the acoustic engineering applications, absorbing materials are stratified, and hence they are composed by a number of different porous layers. The characterization strategy described in the previous section can be adapted to deal with this multilayer configuration. For the sake of conciseness, a double multilayer configuration composed of two different porous materials is presented in this section. However, similar arguments could be applied to stratified porous media with a higher number of layers (see Remark 2.4.4).

2.4.1 Statement of the direct propagation problem

The mathematical model of the time-harmonic wave propagation problem is analogous to (2.7) described in Section 2.3.1 for a single layer case. More precisely, for a double layer configuration, let Ω_F be three-dimensional domain occupied by the fluid and Ω_P and Ω_Q be respectively the three-dimensional domains occupied by two porous layers (see Figure 2.4 for a better understanding of the notation). The coupling boundary between both porous layers is denoted by Γ_Q , located on the plane $p_1 = h$. Notation on the rest of exterior and coupling boundaries and also on the unit normal vectors is identical to that one used in Section 2.3.

Hence, the differential formulation of the coupled problem with a double porous layer is given by the following problem: for a fixed angular frequency $\omega > 0$, a prescribed

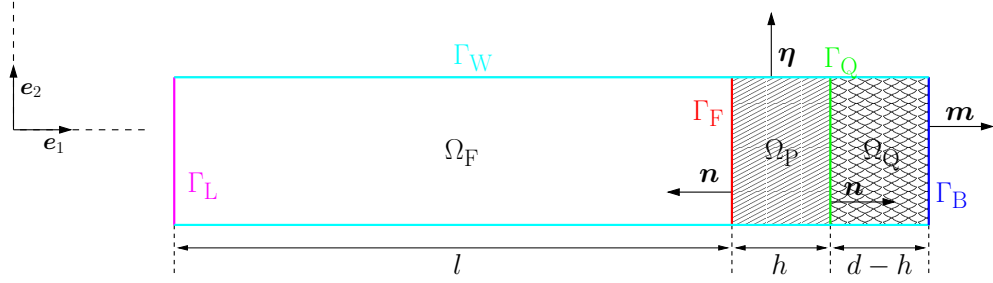


Figure 2.4: Schematic two-dimensional cut of the impedance tube where the fluid (air in the case under study) and the two porous subdomains, Ω_F , Ω_P , and Ω_Q , are marked with different patterns. The boundaries are highlighted with different colors: Γ_F in red, Γ_W in cyan, Γ_L in magenta, Γ_Q in green, and Γ_B in blue.

back surface admittance operator Y_B , and an acoustic pressure source G , find the acoustic pressure field in the fluid Π_F and in the porous media Π_P and Π_Q such that

$$\left\{ \begin{array}{ll} -k_F^2(\omega)\Pi_F - \Delta\Pi_F = 0 & \text{in } \Omega_F, \\ -k_P^2(\omega)\Pi_P - \Delta\Pi_P = 0 & \text{in } \Omega_P, \\ -k_Q^2(\omega)\Pi_Q - \Delta\Pi_Q = 0 & \text{in } \Omega_Q, \\ \frac{1}{\rho_F} \frac{\partial\Pi_F}{\partial\mathbf{n}} = \frac{1}{\rho_P(\omega)} \frac{\partial\Pi_P}{\partial\mathbf{n}} & \text{on } \Gamma_F, \\ \Pi_F = \Pi_P & \text{on } \Gamma_F, \\ \frac{1}{\rho_P(\omega)} \frac{\partial\Pi_P}{\partial\mathbf{n}} = \frac{1}{\rho_Q(\omega)} \frac{\partial\Pi_Q}{\partial\mathbf{n}} & \text{on } \Gamma_Q, \\ \Pi_P = \Pi_Q & \text{on } \Gamma_Q, \\ \frac{1}{i\omega\rho_Q(\omega)} \frac{\partial\Pi_Q}{\partial\mathbf{m}} = Y_B \Pi_Q & \text{on } \Gamma_B, \\ \frac{\partial\Pi_F}{\partial\boldsymbol{\eta}} = 0 & \text{on } \Gamma_W \cap \partial\Omega_F, \\ \frac{\partial\Pi_P}{\partial\boldsymbol{\eta}} = 0 & \text{on } \Gamma_W \cap \partial\Omega_P, \\ \frac{\partial\Pi_Q}{\partial\boldsymbol{\eta}} = 0 & \text{on } \Gamma_W \cap \partial\Omega_Q, \\ \Pi_F = G & \text{on } \Gamma_L, \end{array} \right. \quad (2.15)$$

where $k_F(\omega) = \omega/c_F$ being ρ_F the mass density and the sound velocity in the fluid, $\rho_P(\omega)$, $\rho_Q(\omega)$ and $k_P(\omega)$, $k_Q(\omega)$ are the frequency-dependent equivalent dynamic mass density and the frequency-dependent wave number of the porous materials located respectively in the layers Ω_P and Ω_Q . Unit vectors \mathbf{n} , \mathbf{m} , and $\boldsymbol{\eta}$ are respectively normal on boundaries $\Gamma_F \cup \Gamma_Q$, Γ_B , and Γ_W , and outward to the porous layer Ω_P (on the boundaries

where it is applicable).

The direct propagation problem (2.15) can be decoupled in terms of the transverse modes (as it has been described in detail for a single layer in Section 2.3). Consequently, the modal coefficients $\{A_F^n, B_F^n, A_P^n, B_P^n, A_Q^n, B_Q^n\}_{n \in \mathbb{N}}$ associated respectively with the acoustic pressure fields Π_F , Π_P , and Π_Q are the solution of the following sequence of linear algebraic system of equations: for each $n \in \mathbb{N}$, it holds

$$\left\{ \begin{array}{l} \rho_P(\omega)\beta_F^n(\omega)(-A_F^n + B_F^n) = \rho_F\beta_P^n(\omega)(-A_P^n + B_P^n), \\ A_F^n + B_F^n = A_P^n + B_P^n, \\ \rho_Q(\omega)\beta_P^n(\omega)(-A_P^n e^{-i\beta_P^n(\omega)h} + B_P^n e^{i\beta_P^n(\omega)h}) \\ \quad = \rho_P(\omega)\beta_Q^n(\omega)(-A_Q^n e^{-i\beta_Q^n(\omega)h} + B_Q^n e^{i\beta_Q^n(\omega)h}), \\ A_P^n e^{-i\beta_P^n(\omega)h} + B_P^n e^{i\beta_P^n(\omega)h} = A_Q^n e^{-i\beta_Q^n(\omega)h} + B_Q^n e^{i\beta_Q^n(\omega)h}, \\ \frac{\beta_Q^n(\omega)}{\omega\rho_Q(\omega)} \left(-A_Q^n e^{-i\beta_Q^n(\omega)d} + B_Q^n e^{i\beta_Q^n(\omega)d} \right) = Y_B^n(\omega) \left(A_Q^n e^{-i\beta_Q^n(\omega)d} + B_Q^n e^{i\beta_Q^n(\omega)d} \right), \\ A_F^n e^{i\beta_F^n(\omega)l} + B_F^n e^{-i\beta_F^n(\omega)l} = g_n, \end{array} \right.$$

where $\beta_Q^n(\omega) = \sqrt{k_Q^2(\omega) - \lambda_n^2}$ for $n \in \mathbb{N}$, and the notation is analogous to that one used in problem (2.8)-(2.9). Once these modal coefficients are computed solving the above linear system for a fixed $n \in \mathbb{N}$, the contribution of the n -th mode to the surface impedance (2.10) on Γ_F or the absorption coefficient (2.11) of the double porous layer configuration can be computed straightforwardly.

2.4.2 Characterization with four surface admittance datasets

In sections presented above, Problems 2.3.1, 2.3.3, 2.3.5, and 2.3.7 deal with the characterization of a single porous layer. However, the numerical methodology proposed in this chapter can be applied to frameworks much more complex where two porous materials can be characterized simultaneously. Obviously, the datasets to be used in the inverse problem should be doubled. Notice also that the present strategy combined with a Transfer Matrix Method (TMM) [7, Chapter 11] applied to each modal contribution could be used in a general multilayer configuration but at the expense of increasing the number of datasets used in the inverse characterization problem. Consequently, for a multilayer sample formed by two layers of different porous materials, “P” and “Q”, the characterization problem can be stated as follows.

Problem 2.4.1 (Inverse problem with four surface impedance datasets). *For a fixed frequency value ω and a fixed transverse mode n_0 , find the complex-valued coefficients of the characteristic impedance and the wave number, $Z_P(\omega)$, and $k_P(\omega)$ (resp. $Z_Q(\omega)$, and $k_Q(\omega)$), associated to the porous layer “P” (resp. “Q”) assuming known:*

(i)-(ii) *The surface admittance values $Y_I^{n_0}(\omega)$ (respectively $\tilde{Y}_I^{n_0}(\omega)$) on Γ_F , obtained by solving a single layer configuration problem (2.7) with the porous material “P” (resp. “Q”) and the back admittance values $Y_B^{n_0}(\omega)$ (resp. $\tilde{Y}_B^{n_0}(\omega)$) on Γ_B .*

(iii)-(iv) The surface admittance values $\hat{Y}_I^{n_0}(\omega)$ (respectively $\check{Y}_I^{n_0}(\omega)$) on Γ_F , obtained by solving a double layer configuration problem (2.15), being materials “P” and “Q” (resp. “Q” and “P”) placed on the right and left layers, and the back admittance value $\hat{Y}_B^{n_0}(\omega)$ (resp. $\check{Y}_B^{n_0}(\omega)$) on Γ_B .

Remark 2.4.2. Other choices of surface admittance datasets could be considered in the definition of Problem 2.4.1 (for instance, datasets involving only double layer configurations and two different back admittance conditions). In fact, since single and double layer configurations are used in Problem 2.4.1, possibly the same back admittance operator could be considered in all the datasets i)-iv).

As it is expected from the results shown related to Problem 2.3.7, even with the use of four surface impedance datasets, the inverse problem characterizing the double layer configuration has an infinite (but countable) number of solutions.

Lemma 2.4.3. Problem 2.4.1 is well-posed in the sense that there exists an infinite (but countable) number of solutions due to the periodicity of the wave number values.

Proof. Firstly, consider the datasets i) and iii) and assume that the complex-valued properties $(Z_Q(\omega), k_Q(\omega))$ are known. For instance, from dataset iii) can be understood as the surface admittance data coming from a single layer configuration where the back admittance data can be computed as the input admittance of the porous layer $(Z_P(\omega), k_P(\omega))$ backed with the admittance $\check{Y}_B^{n_0}(\omega)$. More precisely, the back surface admittance on Γ_Q associated to the front boundary of a layer of porous material $(Z_Q(\omega), k_Q(\omega))$ of thickness $d - h$ and supported on its back-end boundary with admittance $\check{Y}_B^{n_0}(\omega)$ is given by

$$\tilde{\check{Y}}_B^{n_0}(\omega) = \frac{1}{Y_Q(\omega)} \frac{Y_Q(\omega) + \check{Y}_B^{n_0}(\omega) \tanh(\beta_Q^{n_0}(\omega)(d-h))}{\check{Y}_B^{n_0}(\omega) + Y_Q(\omega) \tanh(\beta_Q^{n_0}(\omega)(d-h))}, \quad (2.16)$$

where $Y_Q(\omega) = 1/Z_Q(\omega)$. Hence, applying the arguments of the proof in Lemma 2.3.8, the values $(Z_P(\omega), k_P(\omega))$ are uniquely determined except for the phase changes in the wave number coefficient (see (2.14)). Analogous arguments are also applicable to dataset i).

Once the phase of the wave number is fixed using a given criterion (see Remark 2.3.9), the existence and uniqueness of solution of single layer Problem 2.3.7 with datasets i) and iii) ensures that the mapping $\mathcal{X} : (Z_Q, k_Q) \mapsto (Z_P, k_P)$ is well-defined and injective. In addition, since expressions involved in (2.12)-(2.13) and (2.16) are continuous, this mapping is also continuous in \mathbb{C}^2 . Analogous arguments can be used to conclude that if (Z_P, k_P) are assumed known then the complex-valued coefficients (Z_Q, k_Q) can be uniquely determined from datasets ii) and iv) (except for the phase changes in the wave number coefficient). Hence, the mapping $\mathcal{Y} : (Z_P, k_P) \mapsto (Z_Q, k_Q)$ is well-defined, injective and continuous. In addition, since the single layer problems which are involved in mappings \mathcal{X} and \mathcal{Y} involves datasets iii) and iv) respectively, for an arbitrary complex disc $D \subset \mathbb{C}^2$, it holds $\mathcal{X}(\mathcal{Y}(D)) = D$ (otherwise, it would imply that one of the datasets is not compatible with the rest of them).

Consequently, the inverse Problem 2.4.1 can be formulated as a fixed point problem: find $(Z_P(\omega), k_P(\omega))$ such that $(Z_P(\omega), k_P(\omega)) = (\mathcal{X} \circ \mathcal{Y})(Z_P(\omega), k_P(\omega))$. Hence, the existence of solution is guaranteed from the classical Brouwer fixed-point theorem [168] applied on a disc of sufficiently large radius D in \mathbb{C}^2 . The uniqueness of this fixed point is clear from the injective character of \mathcal{X} and \mathcal{Y} . Once $(Z_P(\omega), k_P(\omega))$ is determined, the values of $(Z_Q(\omega), k_Q(\omega))$ are computed straightforwardly using $(Z_Q(\omega), k_Q(\omega)) = \mathcal{Y}(Z_P(\omega), k_P(\omega))$. In conclusion, except for a phase change in the wave numbers (which leads to a countable infinite number of solutions on $k_P(\omega)$ and $k_Q(\omega)$), the inverse Problem 2.4.1 is well-posed.

□

Despite the proof of the existence and uniqueness of Problem 2.4.1 relies on the use of a fixed-point theorem, the numerical resolution of both inverse Problems 2.3.7 and 2.4.1, (with single and double layer configurations) involves the same numerical method whose main characteristics are: the rewritten of the modal linear system in terms of robust primal unknowns and the use of a TMM method combined with a derivative-free optimization method to find the solution of each inverse problem. This numerical procedure is described in detail in the following section.

Remark 2.4.4. *Although this chapter is mainly focused on a single and double layer configuration, an analogous non-parametric procedure could be designed to characterize numerically an arbitrary stratified medium composed by N layers. In this case, the numerical results obtained for this general configuration confirm that $2N$ complex-valued datasets (surface impedances or admittances) would be required to state a well-posed inverse problem as in the case of the double layer configuration.*

2.5 Numerical procedure to solve the inverse problems

The proposed approach for determining the characteristic impedance and the wave number associated to a fluid-equivalent rigid porous model uses intensively the numerical solution of a sequence of inverse problems, which fits a discrete set of frequency-dependent experimental measurements of the surface admittance of a single or double layer configuration. With this aim, for a fixed frequency value and a given modal contribution, the inverse problem is rewritten as a minimization problem where the cost function is the relative error between the experimental measurements and the surface admittance computed with the direct propagation problem. Both the proposed non-parametric approach and the parametric JCAL model have been compared within the same framework and using the same amount of experimental data.

2.5.1 Non-parametric approach

Since the fluid-equivalent equations can be written in terms of any pair of the dynamic coefficients introduced in Section 2.3.1, there exists a variety of model coefficients which

could be used as primal unknowns in the cost function used in the minimization problem to be solved numerically. For instance, the surface admittance could be computed naively in terms of the real and the imaginary part of the mass density $\rho_P(\omega)$ and the bulk modulus $K_P(\omega)$ as primal unknowns (see Section 2.6.1 for check the numerical results). In this case, despite relative fitting error are almost negligible, spurious oscillations distort the parameter frequency-response due to the exponential dependence of the TMM matrix coefficients with respect to these acoustic quantities (see [53] for details).

In order to mitigate this situation, instead of using the dynamic mass density and the dynamic bulk modulus as primal unknowns, the minimization problem has been rewritten replacing the real and imaginary part of the bulk modulus by a novel pair of primal unknowns: $\delta_P(\omega) = \text{Re}(\beta_P^{n_0}(\omega))d$ and $M_P(\omega) = e^{\text{Im}(\beta_P^{n_0}(\omega))d}$, which involves the wave number $\beta_P^{n_0}(\omega)$ of the porous material associated to the n_0 -th transverse mode and the thickness of the porous layer d . Hence, since the acoustic quantity measurements chosen for fitting is the surface admittance in Problem 2.3.7, the values of $M_P(\omega)$, $\delta_P(\omega)$, $\text{Re}(\rho_P(\omega))$, and $\text{Im}(\rho_P(\omega))$ are computed as the solution of the minimization problem

$$\begin{aligned} & (M_P(\omega), \delta_P(\omega), \text{Re}(\rho_P(\omega)), \text{Im}(\rho_P(\omega))) \\ &= \arg \min_{\substack{M_P, \delta_P > 0 \\ \text{Re}(\rho_P) > 0 \\ \text{Im}(\rho_P) < 0}} \left(\frac{|Y_I(\omega) - Y_I^{\text{TMM}}(\omega, n_0, Y_B^{n_0}(\omega), M_P, \delta_P, \text{Re}(\rho_P), \text{Im}(\rho_P))|^2}{|Y_I(\omega)|^2} \right. \\ &\quad \left. + \frac{|\tilde{Y}_I(\omega) - Y_I^{\text{TMM}}(\omega, n_0, \tilde{Y}_B^{n_0}(\omega), M_P, \delta_P, \text{Re}(\rho_P), \text{Im}(\rho_P))|^2}{|\tilde{Y}_I(\omega)|^2} \right), \end{aligned} \quad (2.17)$$

where $Y_I^{\text{TMM}}(\omega, n_0, Y_B^{n_0}, M_P, \delta_P, \text{Re}(\rho_P), \text{Im}(\rho_P))$ is the surface admittance computed by solving the linear problem (2.7) (single layer configuration) with back admittance $Y_B^{n_0}$ using the TMM method for the n_0 -th modal contribution. Similarly, the minimization problem with a double multilayer configuration can be written as follows:

$$\begin{aligned} & (M_P(\omega), M_Q(\omega), \delta_P(\omega), \delta_Q(\omega), \text{Re}(\rho_P(\omega)), \text{Re}(\rho_Q(\omega)), \text{Im}(\rho_P(\omega)), \text{Im}(\rho_Q(\omega))) \\ &= \arg \min_{\substack{M_P, M_Q, \delta_P, \delta_Q > 0 \\ \text{Re}(\rho_P), \text{Re}(\rho_Q) > 0 \\ \text{Im}(\rho_P), \text{Im}(\rho_Q) < 0}} \left(\frac{|Y_I(\omega) - Y_I^{\text{TMM}}(\omega, n_0, Y_B^{n_0}(\omega), M_P, \delta_P, \text{Re}(\rho_P), \text{Im}(\rho_P))|^2}{|Y_I(\omega)|^2} \right. \\ &\quad \left. + \frac{|\tilde{Y}_I(\omega) - Y_I^{\text{TMM}}(\omega, n_0, \tilde{Y}_B^{n_0}(\omega), M_Q, \delta_Q, \text{Re}(\rho_Q), \text{Im}(\rho_Q))|^2}{|\tilde{Y}_I(\omega)|^2} \right. \\ &\quad \left. + \frac{|\hat{Y}_I(\omega) - Y_I^{\text{TMM}}(\omega, n_0, \hat{Y}_B^{n_0}(\omega), M_P, M_Q, \delta_P, \delta_Q, \text{Re}(\rho_P), \text{Re}(\rho_Q), \text{Im}(\rho_P), \text{Im}(\rho_Q))|^2}{|\hat{Y}_I(\omega)|^2} \right. \\ &\quad \left. + \frac{|\check{Y}_I(\omega) - Y_I^{\text{TMM}}(\omega, n_0, \check{Y}_B^{n_0}(\omega), M_P, M_Q, \delta_P, \delta_Q, \text{Re}(\rho_P), \text{Re}(\rho_Q), \text{Im}(\rho_P), \text{Im}(\rho_Q))|^2}{|\check{Y}_I(\omega)|^2} \right), \end{aligned} \quad (2.18)$$

where $\delta_Q(\omega) = \text{Re}(\beta_Q^{n_0}(\omega))(d - h)$ and $M_Q(\omega) = e^{\text{Im}(\beta_Q^{n_0}(\omega))(d - h)}$ are the pair of primal unknowns related to the second porous layer involving its wave number $\beta_Q^{n_0}$ and its thickness $d - h$ and Y_I^{TMM} denotes the surface admittance computed by solving the linear problem (2.15) (double multilayer configuration) with back admittance $\tilde{Y}_B^{n_0}$ using the TMM method [37] for the n_0 -th modal contribution. Due to the reduced dimension of the minimization problem and to keep the computational cost of this minimization procedure as low as possible, the Nelder-Mead Simplex Method has been used [112]. Also, to preserve the restrictions on the arguments of the minimization problem (i.e., the right sign on M_P , δ_P , $\text{Re}(\rho_P)$, and $\text{Im}(\rho_P)$), a classical quadratic transformation [153, Chapter 7] has been used to handle these constrained optimization problems.

Consequently, since this fitting procedure is repeated in a frequency-by-frequency sweeping, the use of this kind of derivative-free optimization algorithms guarantee the overall efficiency of this methodology. Obviously, other optimization strategies could be used for this purpose, such as genetic algorithms [157] or efficient global optimization procedures [129].

As it has been highlighted in Remark 2.3.9, the inverse problem solved for the characterization of porous materials has infinite (but countable) solutions due to phase changes on the wave number values. Since, the primal unknowns $\delta_P(\omega)$ and $\delta_Q(\omega)$ drive the complex phase of $\beta_P^{n_0}(\omega)$ and $\beta_Q^{n_0}(\omega)$, respectively, the drawback of multiple solutions could lead to a discontinuous behavior with respect to the frequency of these unknowns in the solution of the minimization problems (2.17) and (2.18). Consequently, to guarantee a continuous behavior of the primal unknowns with respect to the frequency, five simultaneous strategies have been utilized to complement the use of the Nelder-Mead method: (a) for a given set of angular frequency values, problems (2.17) and (2.18) are solved sequentially from the highest frequency to the lowest one; (b) the initial guess in the minimization method for the highest frequency have been computed (see Remark 2.5.1) by assuming that $\beta_P^{n_0} \approx \beta_F^{n_0} - 10i$ and $Z_P \approx Z_F - i\text{Re}(1/Y_I)$ (analogous considerations are made for the initial guesses of quantities related to the second porous layer in Ω_Q); (c) the initial guess for subsequent frequencies are given by the solution of the previous solution for a higher frequency; (d) the low-frequency limit of the real part of the dynamic mass density is assumed known (in order to fix the value of the wave number phase at lowest frequencies as it is described in Remark 2.3.9), and (e) an unwrapping procedure is performed on the frequency dependent values of $\beta_P(\omega)$ and $\beta_Q(\omega)$ to avoid possible jump discontinuities. All these strategies have been used to obtain the numerical results presented in the following section.

Remark 2.5.1. *The initial guesses for the imaginary parts of the porous wave number and characteristic impedance have been derived from the expression of the input impedance of a porous layer of thickness d backed by a rigid wall, $Z_I(\omega) = Z_P(\omega)/\tanh(i\beta_P^{n_0}(\omega)d)$. Assuming that the porous layer is highly absorbing at high frequencies, then $\text{Im}(\beta_P^{n_0}(\omega)) \ll 0$, and so $|\tanh(i\beta_P^{n_0}(\omega)d)| \approx 1$. Due to the exponential decreasing behavior of \tanh , it is enough to assume $\text{Im}(\beta_P^{n_0}(\omega)) \approx -10$ to obtain $|\tanh(i\beta_P^{n_0}(\omega)d)| \approx 1$. On the other hand, at the frequency range of the present chapter, $\text{Re}(\beta_P^{n_0}(\omega)d) \gg \text{Im}(\beta_P^{n_0}(\omega)d)$. Hence, neglecting the imaginary part of the wave number, $\tanh(i\beta_P^{n_0}(\omega)d) \approx \tanh(i\text{Re}(\beta_P^{n_0}(\omega))d)$*

whose real part is null. So, $Z_I(\omega) \approx iZ_P(\omega)|\tanh(i\text{Re}(\beta_P^{n_0}(\omega))d)| \approx iZ_P(\omega)$ and hence $\text{Im } Z_P \approx -\text{Re}(1/Y_I)$.

2.5.2 Parametric JCAL approach

As it is explained in Section 1.2.2 in Chapter 1, the parametric JCAL model involves six intrinsic parameters: α_∞ , σ , ϕ , Λ , Λ' , and k'_0 . Hence, instead of using a fitting procedure which computes a frequency-by-frequency inverse problem independently (as in the non-parametric approach), in the JCAL case, the six constant parameters are fitted using the entire frequency band data in a unique global optimization problem as follows. In the single layer configuration, if a set of M different frequency values $\{\omega_j\}_{j=1}^M$ are considered, the minimization problem is given by

$$\begin{aligned} & (\alpha_\infty, \sigma, \phi, \Lambda, \Lambda', k'_0) \\ &= \arg \min_{\substack{\tilde{\alpha}_\infty, \tilde{\sigma}, \tilde{k}'_0 > 0 \\ 0 < \tilde{\phi}, \tilde{\Lambda}, \tilde{\Lambda}' < 1}} \sum_{j=1}^M \left(\frac{|Y_I(\omega_j) - Y_I^{\text{JCAL}}(\omega_j, n_0, Y_B^{n_0}(\omega), \tilde{\alpha}_\infty, \tilde{\sigma}, \tilde{\phi}, \tilde{\Lambda}, \tilde{\Lambda}', \tilde{k}'_0)|^2}{|Y_I(\omega_j)|^2} \right. \\ & \quad \left. + \frac{|\tilde{Y}_I(\omega_j) - Y_I^{\text{JCAL}}(\omega_j, n_0, \tilde{Y}_B^{n_0}(\omega_j), \tilde{\alpha}_\infty, \tilde{\sigma}, \tilde{\phi}, \tilde{\Lambda}, \tilde{\Lambda}', \tilde{k}'_0)|^2}{|\tilde{Y}_I(\omega_j)|^2} \right), \end{aligned} \quad (2.19)$$

where $Y_I^{\text{JCAL}}(\omega, n_0, Y_B^{n_0}, \tilde{\alpha}_\infty, \tilde{\sigma}, \tilde{\phi}, \tilde{\Lambda}, \tilde{\Lambda}', \tilde{k}'_0)$ is the surface admittance computed solving the linear problem (2.7) with back admittance $Y_B^{n_0}$. The JCAL model (2.3)-(2.4) has been used to replace the mass density $\rho_P(\omega)$ by $\rho_P(\omega) = \hat{\rho}_{\text{JCAL}}(\tilde{\alpha}_\infty, \tilde{\sigma}, [\tilde{\phi}, \tilde{\Lambda}, \tilde{\Lambda}', \tilde{k}'_0])(\omega)$, and the wave number $k_P(\omega)$ by $k_P(\omega) = \omega \sqrt{[\hat{\rho}_{\text{JCAL}}(\tilde{\alpha}_\infty, \tilde{\sigma}, \tilde{\phi}, \tilde{\Lambda}, \tilde{\Lambda}', \tilde{k}'_0)](\omega) / [\hat{K}_{\text{JCAL}}(\tilde{\alpha}_\infty, \tilde{\sigma}, \tilde{\phi}, \tilde{\Lambda}, \tilde{\Lambda}', \tilde{k}'_0)](\omega)}$. Again, as in the non-parametric case, the TMM method has been used to compute the n_0 -th modal contribution. The minimization problem with a double multilayer configuration can be written similarly.

In the non-parametric approach, the initial guess used in the iterative optimization procedure is computed following the estimates described in Remark 2.5.1. However, in the case of the JCAL model, these estimates are not feasible, and a generic initial guess has been considered for its six parameters, namely, $\alpha_\infty = 1.06$, $\sigma = 40 \times 10^3 \text{ Nm}^{-4}\text{s}$, $\phi = 0.94$, $\Lambda = 5.6 \times 10^{-6} \text{ m}$, $\Lambda' = 1.1 \times 10^{-8} \text{ m}$, $k'_0 = 1.2 \text{ m}^2$ in all the numerical simulations included in Section 2.6.

2.6 Characterization results

In this section, some characterization results obtained with the proposed methodology for different single and double layer configurations are analyzed. Surface admittance data (the inverse of the surface impedance measured with the standardized impedance tube method [1]) were used as input data for the proposed approach (open-access available online), being the resulting effective acoustic properties compared with those obtained

using the JCAL model and the two-cavity method worked out by Utsuno et al. [171]. In all the results, it has been considered the frequency range in which the acoustic pressure source excites only the first transverse mode of the impedance tube and the model coefficients in the fluid are given by the typical reference values taken from air, this is, $\rho_F = 1.213 \text{ kg/m}^3$ and $c_F = 343 \text{ m/s}$ (and those air-related values necessary for the parametric JCAL model (2.3)-(2.4): $\eta = 1.84 \times 10^{-5} \text{ Pa s}$, $P_F = 101320 \text{ Pa}$, $\Pr = 0.702$, and $\gamma = 1.4$). Figure 2.5 shows the samples of porous materials used in the experimental measurements in both single and double layer configurations.

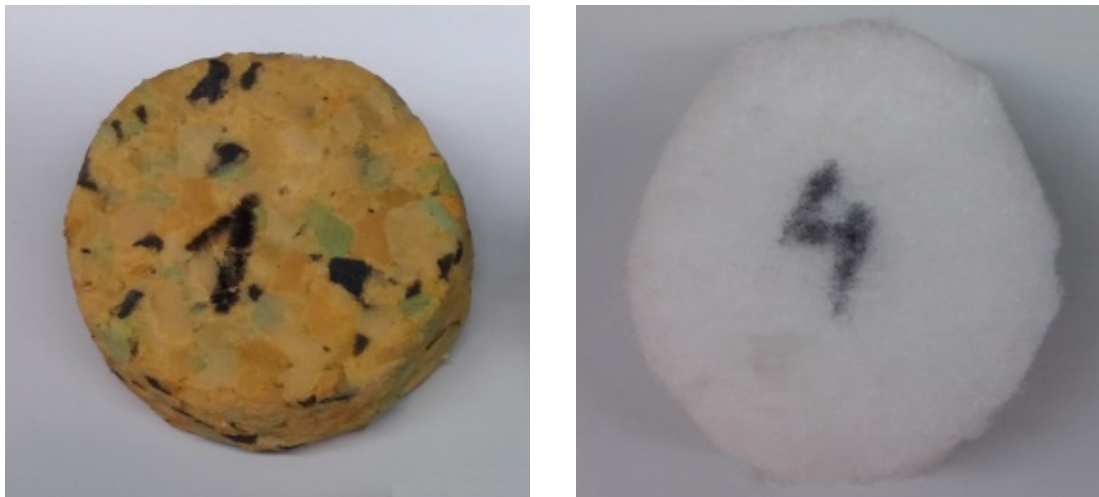


Figure 2.5: Porous materials whose results are shown in this chapter: Recycled foam (#1) (left); Recycled fibrous material (#4) (right) [150].

In the numerical comparison of the proposed non-parametric approach and the JCAL parametric model, the same optimization procedure has been used with identical threshold values in the convergence criteria, i.e., the convergence is considered reached once the value of the cost function in problems (2.17) and (2.18) is smaller than 10^{-10} .

2.6.1 Spurious oscillations

As it has been explained in Section 2.5, there exists a variety of coefficients which come from the parametric models that could be used as primal unknowns in the minimization problem. An incorrect choice of these primal unknowns can ruin the results of the fitting, or can lead to unusual behaviors of the unknowns. For instance, if the surface admittance is computed in terms of the real and the imaginary part of the mass density $\rho_P(\omega)$, and the bulk modulus $K_P(\omega)$ as primal unknowns, the relative fitting error is $\varepsilon = 6.25\%$ (see Figure 2.6). However, although the error is small, as it is shown in Figures 2.7 and 2.8, spurious oscillations distort the parameter frequency-response due to the exponential dependence of the TMM matrix coefficients with respect to these acoustic quantities.

To mitigate this situation, instead of using the dynamic mass density and the dynamic

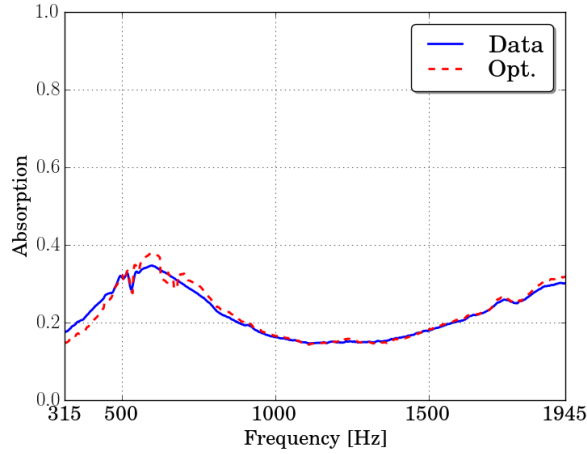


Figure 2.6: Comparison of the experimental absorption values (solid blue line) with the computed ones obtained by using the proposed non-parametric approach (dashed red line). The chosen primal unknowns in the fitting problem are the real and the imaginary parts of the mass density $\rho_P(\omega)$ and the bulk modulus $K_P(\omega)$.

bulk modulus as primal unknowns, a novel pair of unknowns are chosen and the minimization problem is rewritten by using $\delta_P(\omega) = \text{Re}(\beta_P^{n_0}(\omega))d$ and $M_P(\omega) = e^{\text{Im}(\beta_P^{n_0}(\omega))d}$, where $\beta_P^{n_0}(\omega)$ is the wave number of the porous material associated to the n_0 -th transverse mode and d is the thickness of the porous layer (in Section 2.5.1 a detailed description of the new unknowns and the minimization problem is given).

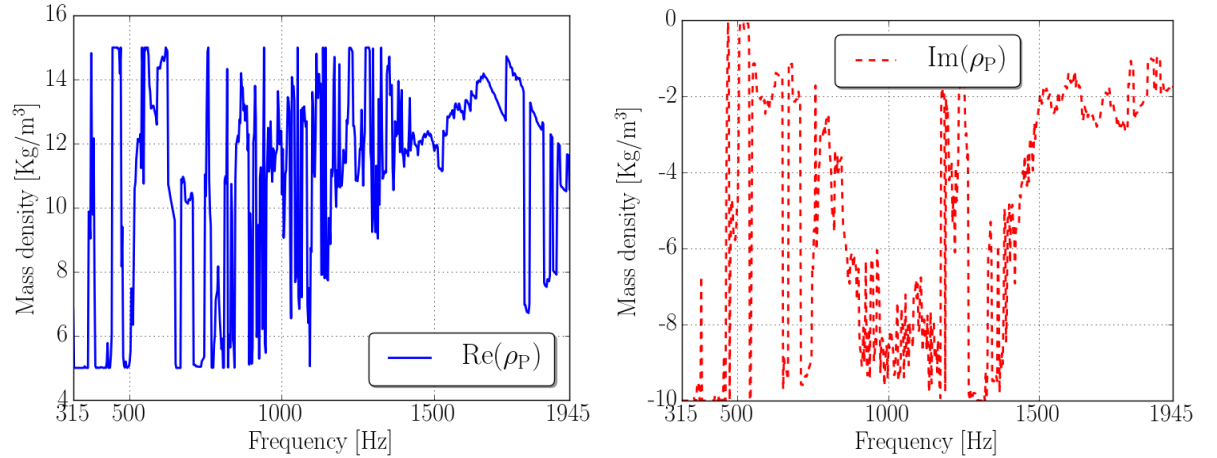


Figure 2.7: Frequency response of the real (left) and the imaginary (right) parts of the mass density $\rho_P(\omega)$, which is one of the unknowns of the fitting problem, obtained using the non-parametric approach.

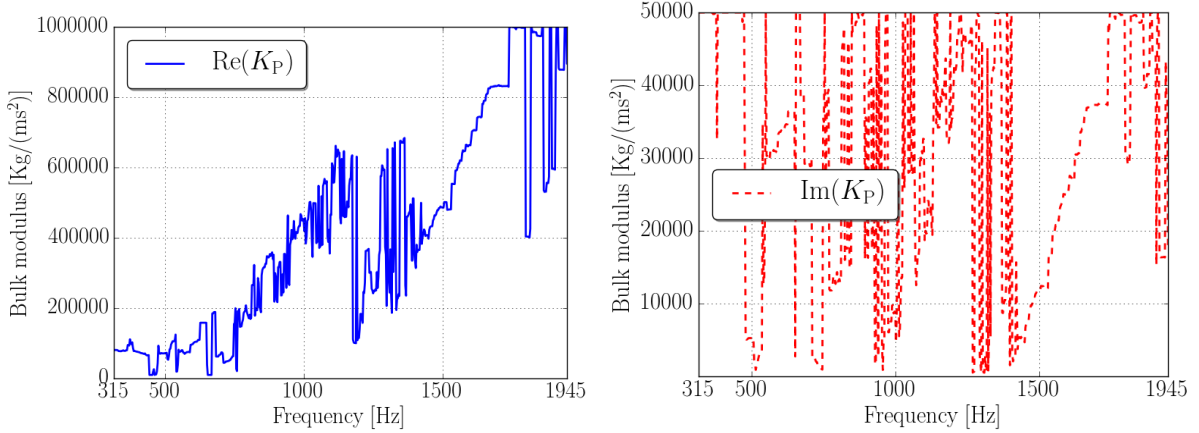


Figure 2.8: Frequency response of the real (left) and the imaginary (right) parts of the bulk modulus $K_p(\omega)$, which is one of the unknowns of the fitting problem, obtained using the non-parametric approach.

2.6.2 Single layer case

Results for two different types of materials are shown: recycled foam (#1) of thickness $d = 32$ mm and recycled fibrous material (#4) of thickness $d = 45$ mm (see Figure 2.5). The experimental data used for the predictions are the surface admittance of a setup with the single porous layer where the two datasets $Y_I(\omega)$ and $\tilde{Y}_I(\omega)$ involve a rigid backing respectively, this is, $Y_B^0 = 0$ and an air gap of thickness $d = 0.02$ m between the porous layer and the rigid backing (so straightforward computations lead to $\tilde{Y}_B^0(\omega) = Y_F(\omega)/\tanh(i\beta_F^0(\omega)d)$ following the two-cavity method [171]).

Accordingly, the experimental data used in the fitting problem (2.17) are the surface admittance of the setup with and without an air gap for each sample. Both the proposed non-parametric method and the JCAL model (fitting problem (2.19)) use the same data.

In both cases for materials #1 and #4, the relative errors resulting from this fitting are around $10^{-13}\%$ for the non-parametric approach (in the errors computed from the admittance and the absorption responses). Figure 2.9 shows the absorption fitting computed by using the non-parametric optimization procedure (labeled as “Opt”), using the Utsuno’s two-cavity method [171], and computed with the parametric JCAL model for the material #1 and #4. A similar comparison is also shown in Figure 2.10 for the characteristic impedance and the wave number related to the porous layer. The accurate agreement between the Utsuno closed-form expressions and the solution computed with the optimization procedure described in Section 2.5 confirms the accuracy of the proposed general approach for the analyzed cases. In the case of the parametric JCAL model, the computed frequency-dependent values reproduce qualitatively the trends exhibited by the characteristic impedance and the wave number for material #1 and #4 above 1000 Hz. However, for lower frequency values, between 500 Hz and 1000 Hz, the JCAL estimates are not accurate, and potentially it suffers from large deviations, reaching around 100% deviations with re-

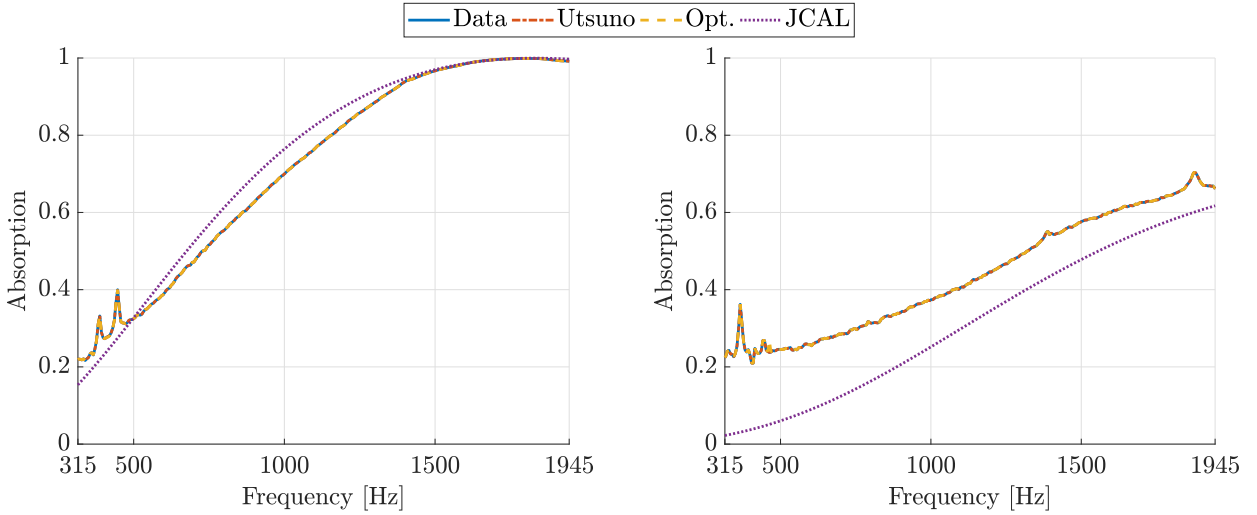


Figure 2.9: Comparison of the obtained absorption coefficient using the two-cavity method (dot-dashed line), the non-parametric approach (dashed line), and the JCAL model (dotted line) for the single layer porous material #1 (left) and material #4 (right).

spect to the actual value in the characteristic impedance related to the material #1 (see Figure 2.10).

From the data used in this single case configuration, it can be observed the presence of some perturbations at the low-frequency regime (below 500 Hz). So, the robustness of the proposed non-parametric model has been studied with respect to the presence of noise on the dataset used in the fitting problem (2.17). Firstly, the error variance on the surface impedance data has been estimated (by considering a standard local linear Gaussian kernel regression method [36]). Then, a sampling method has been used to replicate 500 frequency-dependent curves, which have been used independently as input data in the fitting problem.

Figures 2.11 and 2.12 show the variability band of the surface impedance data (left plots) and the characteristic impedance obtained utilizing the Utsuno closed-form expressions, the proposed non-parametric methodology, and the JCAL model. It can be observed that a wide variability on the surface impedance data leads to mild deviations on the fitted frequency-dependent values. In fact, the variability bands obtained for the Utsuno closed-form expressions and the proposed non-parametric approach nearly overlap, and they have a similar extension since both procedures depend on computations performed within a frequency-by-frequency algorithm. On the contrary, the variability band associated with the JCAL model is negligible since the fitting problem to compute its six parameters uses all the frequency-dependent input data at once, reducing the dependency of its parameter values on the noisy low-frequency data exhibits by the surface impedance data.

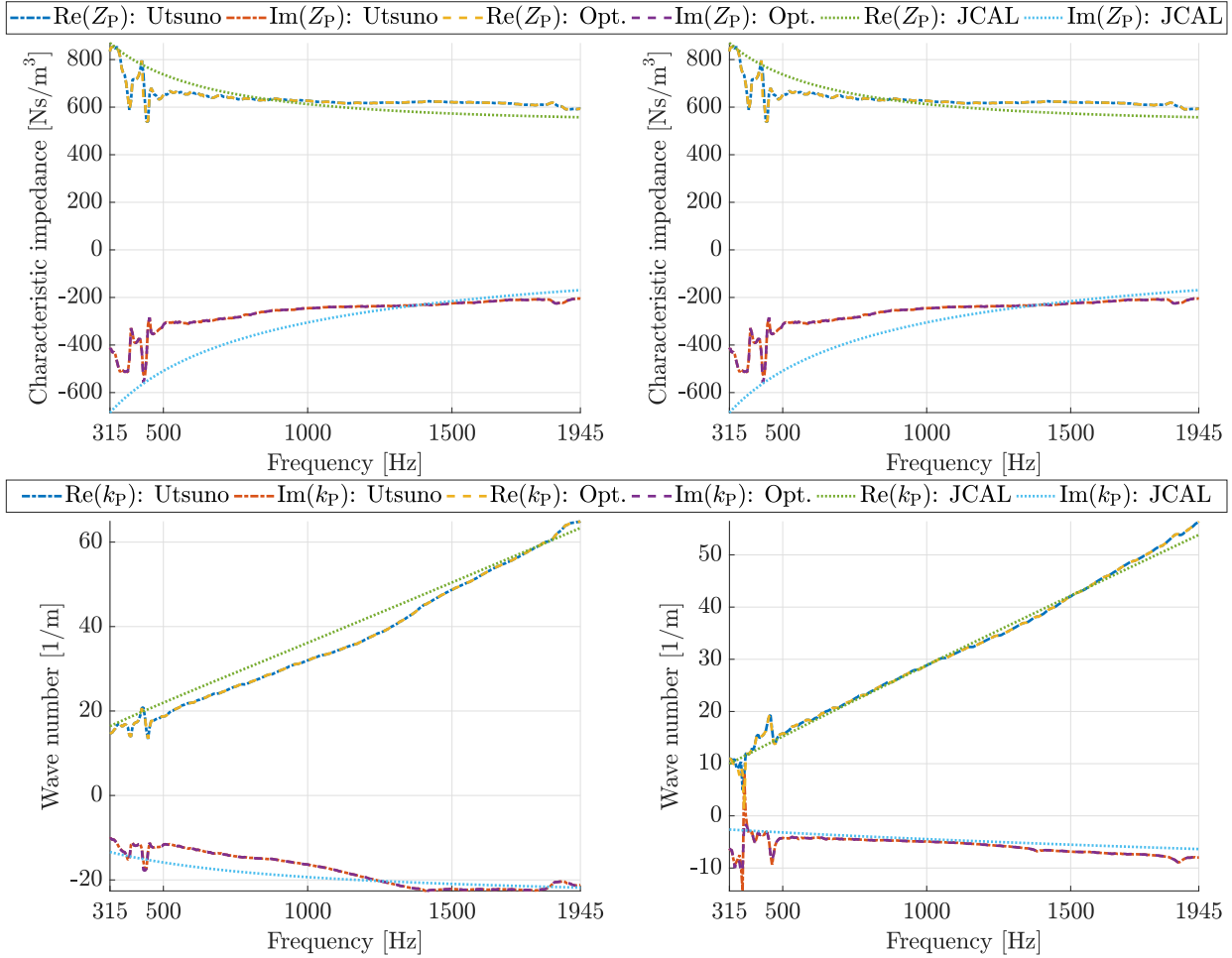


Figure 2.10: Comparison of the obtained characteristic impedance (top) and wave number (bottom) using the two-cavity method (dot-dashed line), the non-parametric approach (dashed line), and the JCAL model (dotted line) for the single layer porous material #1 (left) and material #4 (right).

2.6.3 Double layer case

The data used in the previous single layer configuration needs to perform measurements with a cavity behind the samples to determine its effective acoustic properties [171]. To avoid such limitation, which is of great interest especially for thin lightweight samples as mentioned previously, a double layer configuration can be analyzed. Obviously, the Utsuno closed-form expressions are no longer valid, and fitting approaches are required. In what follows, both the parametric JCAL model and the proposed non-parametric methodology are compared in this double layer setting.

The multilayer problem under consideration is formed by the two porous layers of the previous section (see Figure 2.5). Since now the unknown effective acoustic properties are the dynamic mass density and the wave number of the two layers, i.e., $\text{Re}(\rho_P)$, $\text{Im}(\rho_P)$, M_P ,

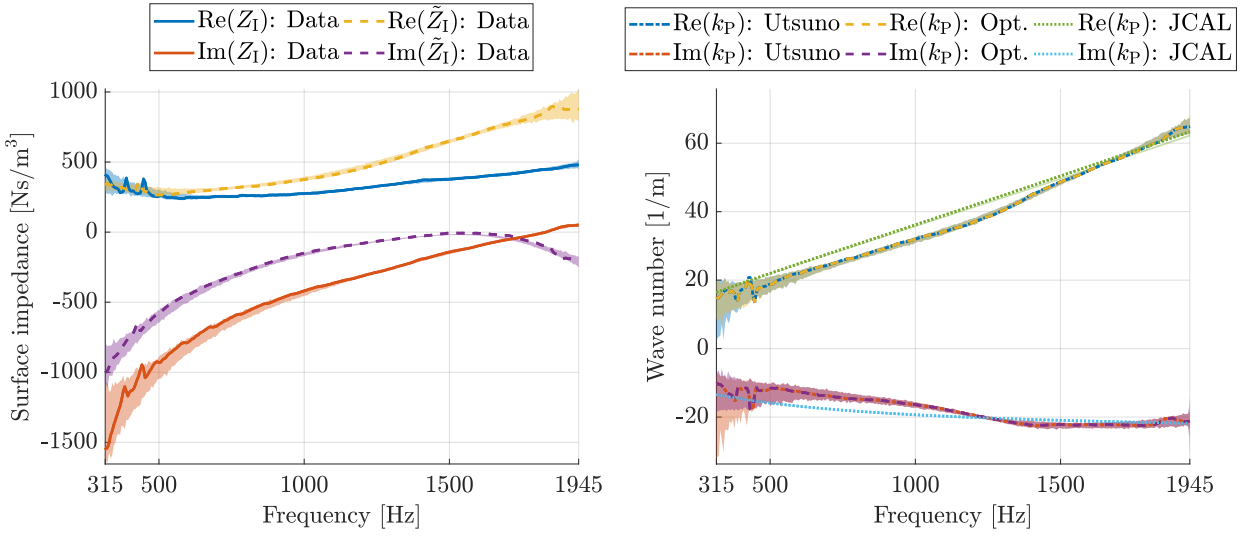


Figure 2.11: Comparison of the surface impedance data (left), and the wave number (right), obtained by using the two-cavity method (dot-dashed line), the non-parametric approach (dashed line), and the JCAL model (dotted line) for the single layer porous material #1. The shadow regions highlight the variability bands on the data and the computed frequency values responses.

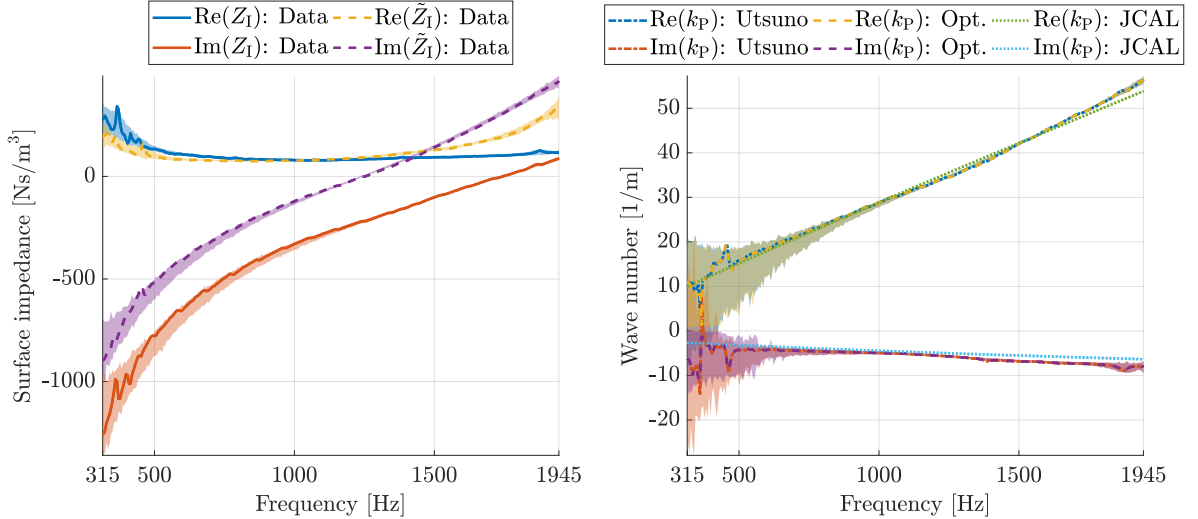


Figure 2.12: Comparison of the surface impedance data (left), and the wave number (right) obtained using the two-cavity method (dot-dashed line), the non-parametric approach (dashed line), and the JCAL model (dotted line) for the single layer porous material #4. The shadow regions highlight the variability bands on the data and the computed frequency values responses.

δ_P , and $\text{Re}(\rho_Q)$, $\text{Im}(\rho_Q)$, M_Q , and δ_Q , it is necessary to consider four surface admittance datasets instead of two for the solution of the minimization problem (2.18). Note that in

this case, the size of the fitting problem using the JCAL model increases to a total of twelve parameters (six for each layer). In the present study, the experimental data used in the fitting problem are the surface admittance of each porous layer separately with rigid back admittance ($Y_B^0 = 0$ and $\tilde{Y}_B^0 = 0$ in the datasets i) and iii) of the inverse Problem 2.4.1) and additionally, the surface admittance data of two different double multilayer configurations (only in the proposed approach), where the order of the porous layers have been inverted (datasets ii) and iv) of the inverse Problem 2.4.1). In both of them, the backing condition is assumed rigid, this is, $\hat{Y}_B^0 = 0$ and $\check{Y}_B^0 = 0$. Once the minimization problem (2.18) has been solved using these four datasets, the effective acoustic coefficients can be identified.

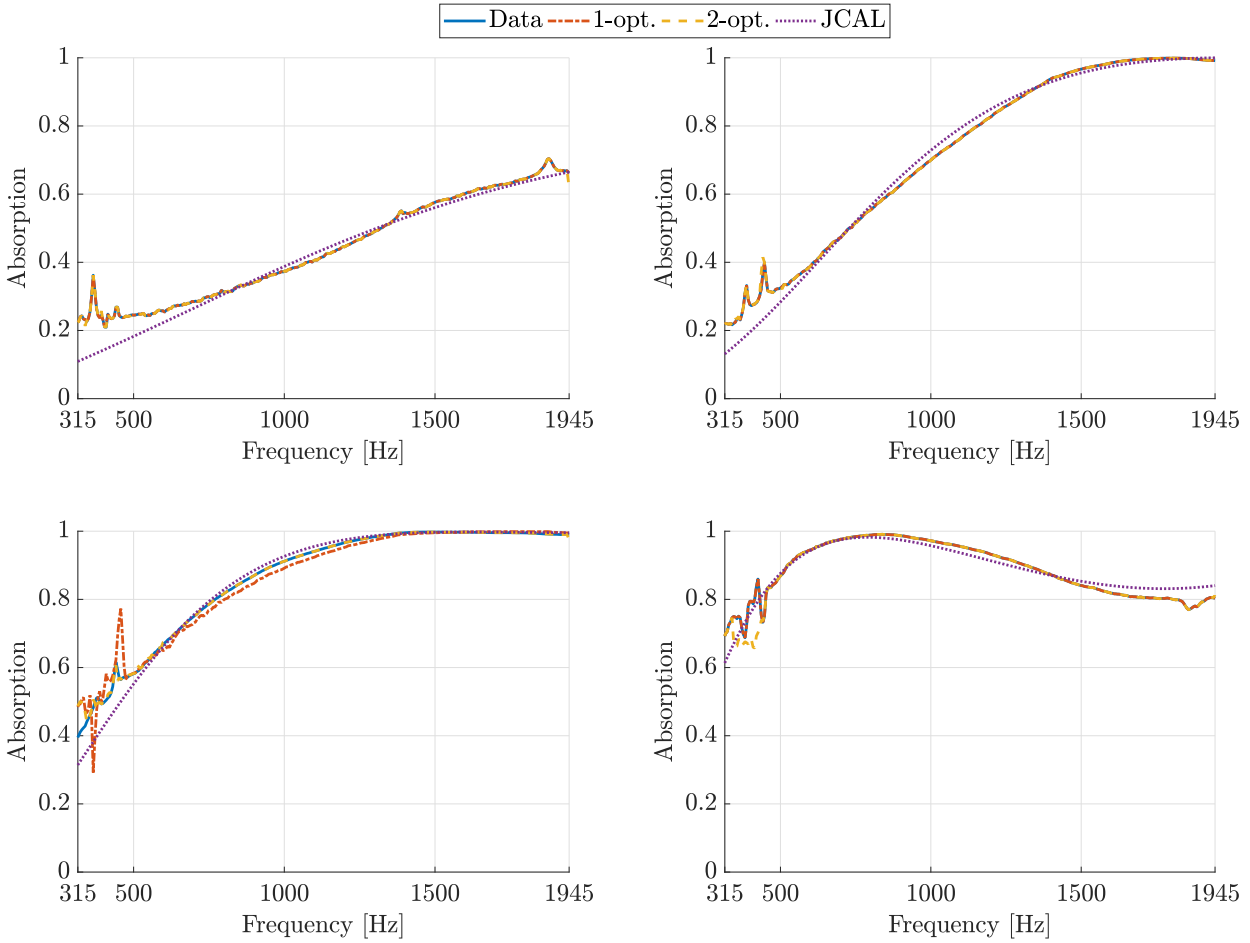


Figure 2.13: Comparison of the absorption coefficient associated with each of the four admittance values Y_B^0 (top-left), \tilde{Y}_B^0 (top-right), \hat{Y}_B^0 (bottom-left), and \check{Y}_B^0 (bottom-right) with respect to the fitted values obtained from the non-parametric approach with the double layer configuration (label “2-opt”, dot-dashed line), the non-parametric approach with the single layer configuration (label “1-opt”, dashed line), and the JCAL model with the double layer configuration (dotted line).

To illustrate the accuracy of the proposed non-parametric model, the absorption co-

efficients associated with each admittance value have been plotted in Figure 2.13, taking into account the non-parametric approach with the double layer configuration, the non-parametric approach with the single layer configuration, and the JCAL model with the double layer configuration. Figures 2.14 and 2.15 show the characteristic impedance and the wave number of both porous materials in this double layer configuration. Again, the frequency-dependent responses for these values are compared using the non-parametric approach (with double and single configurations), and the parametric JCAL model (in a double layer case). In all cases, the predicted values in this double layer configuration reproduce consistently the fitted values obtained in the one layer configuration with negligible differences above 500 Hz. For lower frequency values, the use of four different data sets reduces notably the perturbations presented in the fitted values below 500 Hz (see the wave number curves in the left plots of Figures 2.14 and 2.15).

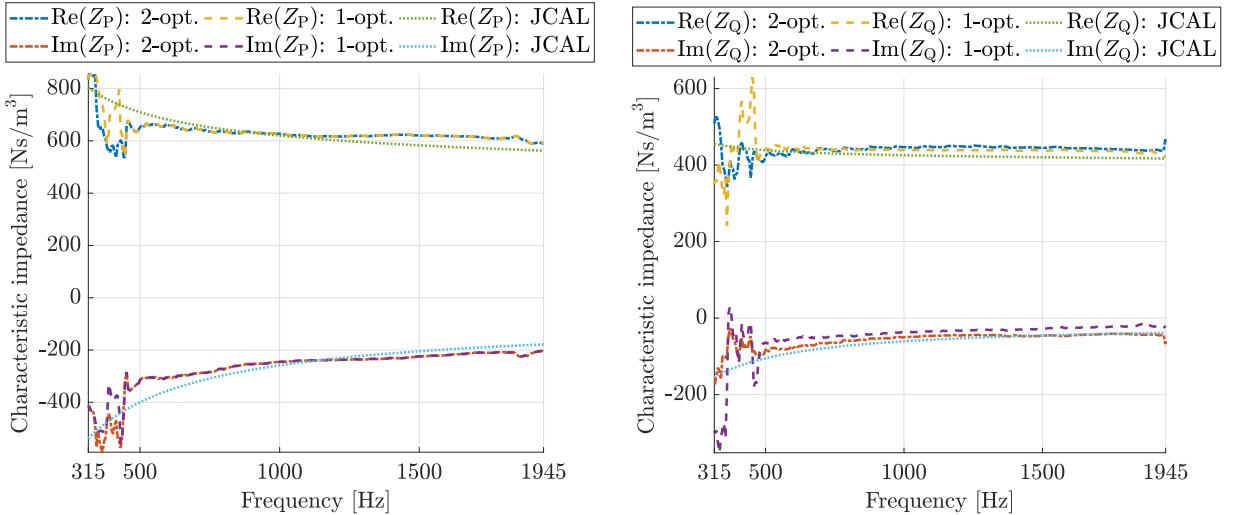


Figure 2.14: Comparison of the characteristic impedance of the first layer ($Z_P(\omega)$ on the left) and the second layer ($Z_Q(\omega)$ on the right) obtained using the non-parametric approach with the double layer configuration (label “2-opt”, dot-dashed line), the non-parametric approach with the single layer configuration (label “1-opt”, dashed line), and the JCAL model with the double layer configuration (dotted line).

In addition, it can be seen that the use of a larger amount of input data in the double configuration yields to a much better agreement with the JCAL model when compared to the analogous results obtained in a single layer configuration (see, for instance, the more accurate results obtained in the absorption profile of layer of material #4 in the top-right plot of Figure 2.13 in comparison with respect to the analogous values reported in the right plot shown in Figure 2.9).

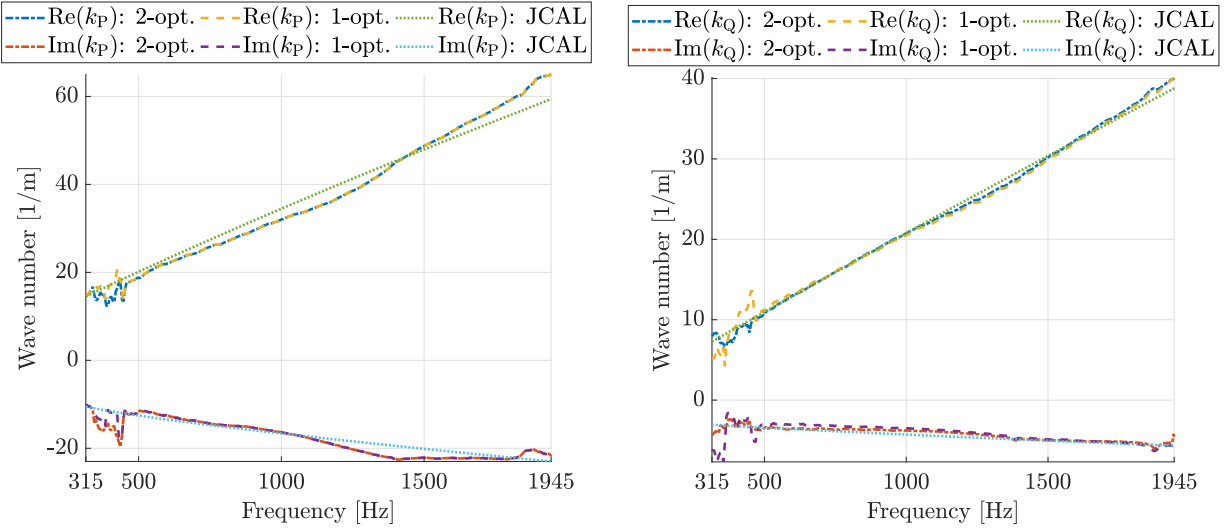


Figure 2.15: Comparison of the wave number of the first layer ($k_P(\omega)$ on the left) and the second layer ($k_Q(\omega)$ on the right) obtained using the non-parametric approach with the double layer configuration (label “2-opt”, dot-dashed line), the non-parametric approach with the single layer configuration (label “1-opt”, dashed line), and the JCAL model with the double layer configuration (dotted line).

2.7 Conclusions

A non-parametric approach was proposed to predict the effective acoustic properties associated with a standard fluid-equivalent model, which governs the time-harmonic vibrations of porous materials with a rigid solid frame. The adopted procedure is based on solving a sequence of frequency-by-frequency well-posed inverse problems, but without the requirement of using any theoretical parametric model (e.g., the widely used parametric JCAL model). Hence, it is not necessary to determine intrinsic physical parameters (required by the parametric models), and consequently, avoiding the use of sophisticated laboratory equipment to measure those intrinsic parameters experimentally.

The main advantages of the proposed non-parametric approach are: i) no need for sophisticated laboratory equipment but only a standard impedance tube rig; ii) avoid the constraints resulting from using a frequency-dependent parametric model in favor of a sequential frequency-by-frequency strategy, which may be of great interest when characterizing non-traditional porous materials whose acoustic properties have singular responses (e.g., metamaterials) or when the assumptions of the standard parametric models are not completely fulfilled; iii) reducing the number of unknowns in the fitting procedure when compared to other inversion techniques requiring multiple parameters, especially when analyzing multilayer configurations.

The well-posedness of the inverse problem has been analyzed in detail in Section 2.3 and 2.4 showing that the acoustic properties of a porous material can be accurately identified both for single and double porous layer configurations. At the contrary of other

inversion techniques, which uses large datasets or real-valued experimental datasets (such as absorption curves), thanks to the detailed analysis of the well-posedness character of the inverse problems in the single and double layer configurations, the proposed approach makes use of the minimal amount of experimental complex-valued data (in the frequency regime) obtained using only a standard two-microphone impedance tube setup.

The proposed methodology produces relative fitting errors smaller when compared with those obtained using a parametric JCAL model, thus improving the characterization procedure. Also, this method has been compared with the results obtained using the two-cavity method proposed by Utsuno *et al.* for single layer configurations, showing a good agreement. In comparison, the proposed methodology not only avoids the assumptions made by the former but also allows broader applicability to single and multiple layer configurations. In this latter regard, the need for characterization procedures that let tackle with light and thin porous layers is of great interest because of the associated technical difficulties in the experimental measurements, thus making this approach an interesting tool in the design stage of multilayer porous materials. In conclusion, and even though further research is necessary to assess its range of applicability, the present work shows that the acoustic properties of porous materials can be accurately predicted by adopting this non-parametric methodology.

Part II

Characterization of viscoelastic materials in underwater environments

Chapter 3

Non-parametric characterization of viscoelastic materials

Contents

3.1	Introduction	73
3.2	Mathematical modeling	75
3.2.1	Mathematical models	75
3.2.2	Coupled problem	76
3.2.3	Acoustic quantities of interest	77
3.3	Statement of the direct problem: wave propagation in a multilayer medium	78
3.3.1	Integral representation of pressure fields	79
3.3.2	Computation of reflection and transmission coefficients by using a plane-wave framework	83
3.4	Acoustic characterization of a viscoelastic solid using an inverse problem	86
3.4.1	Constitutive laws for the primal unknowns	86
3.4.2	Adjoint problem	92
3.5	Numerical results	93
3.5.1	Code validation	94
3.5.2	Experimental data	104
3.5.3	Numerical simulation considering a parametric model	105
3.5.4	Numerical simulation considering a non-parametric approach	106
3.6	Conclusions	118
Appendices		123
3.A	Integral approximation	123

3.B Derivatives	126
------------------------	------------

3.1 Introduction

Elastomeric materials appear in many applications in the automotive, aerospace, or naval industries because they can be used in passive structural vibration control, or noise radiation techniques [114, 149, 152, 172]. These materials are polymers with a viscoelastic mechanical behavior at ultrasound frequencies [80, 98]. The continuous arising of new materials in industrial problems, many of them with unknown properties, makes it necessary a complete description of their acoustic behavior. In this chapter, a real-world scenario is studied, considering a coupled problem formed by an absorbing tile with a viscoelastic behavior surrounded by a fluid (water in this case). This viscoelastic layer has been numerically characterized by using the frequency response of the echo reduction level, the insertion loss, and the fractional power dissipation at ultrasonic frequencies. In order to simplify the problem under study, a viscoelastic material with a planar surface has been considered (in Chapter 4 the original non-planar surface of the viscoelastic material is taken into account).

To perform the material characterization, a suitable choice of the viscoelastic model is fundamental: the more appropriate the model is, the more accurate its mechanical response will be in comparison with the experimental data. Well-known viscoelastic material models such as Maxwell, Zener, and Kelvin-Voigt models [58, 81, 121], or the more recent fractional derivative viscoelasticity models [14, 104] are common choices for modeling linear wave propagation in viscoelastic materials. Usually, to estimate the unknown parameters, the constitutive laws are first fixed, and then the available experimental data are fitted with the response of the mathematical model. However, in this chapter, a data-driven approach is considered [64, 86, 105]. This methodology avoids the need of choosing a constitutive law for fitting. Instead of this, the fitting problem consists of minimizing the distance between a set of experimental data and the computed values. Therefore, the choice of the viscoelastic model is based only on the experimental ultrasound measurements, and not on imposing any functional dependence of the parameters in terms of frequency.

In this chapter, a viscoelastic material has been characterized by using a data-driven approach instead of a classical parametric model. This material is part of a coupled problem formed by the material surrounded by water. In Section 3.2, an analysis of the mathematical modeling of the problem has been performed. First of all, in Section 3.2.1, the mathematical models used in this chapter are described, including the classical parametric models, emphasizing the differences between the parametric and the non-parametric approaches. Then, the coupled problem under consideration is described, and the acoustic quantities of interest, such as the reflection and the transmission coefficients, the echo reduction level, the insertion loss, and the fractional power dissipation, are defined. The direct problem of wave propagation in the multilayer medium is described in Section 3.3. A complete description of the pressure fields (incident, scattered, and transmitted) by using an integral representation is given in Section 3.3.1. Moreover, in Section 3.3.2, the reflection and the transmission coefficients are computed in a plane wave framework. In Section 3.4, the inverse problems for parametric and non-parametric approaches are described, taking

into account different constitutive laws for the primal unknowns of the fitting problem, and emphasizing the advantages and disadvantages of each used law. When the real and the imaginary parts of the Young modulus are used as unknowns, the frequency response of the levels under consideration presents spurious oscillations. Therefore, a change in the primal unknowns is necessary, and the fitting problem in terms of these new unknowns is described. Since to solve the fitting problems, a trust-region reflective algorithm is used, and this algorithm needs the derivatives of the cost function, in Section 3.4.2, the adjoint method is described. This method is used to compute the derivatives of the cost function effectively. Section 3.5 is devoted to presenting some numerical results. To validate the code, some simulations with manufactured data are shown in Section 3.5.1. Then, a real-world viscoelastic material is characterized by using the proposed methodology. In Section 3.5.2, the available experimental data are presented. Figure 3.1 shows the material under consideration, which is an absorbing tile of Apltile SF5048 material (see [5]). Sections 3.5.3 and 3.5.4 show the numerical results obtained by using parametric and non-parametric approaches, respectively. Hence, it is possible to compare them and to illustrate the efficiency of the proposed approach. Section 3.6 shows the conclusions about the methodology. At the end of this chapter, in Appendix 3.A, some considerations about the approximation of the integrals used in the definition of the levels under consideration and in Appendix 3.B, the computation of the derivatives of the cost functions are explained.

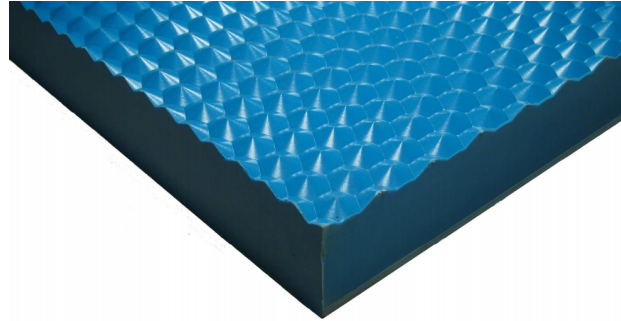


Figure 3.1: Detail of the absorbing tile of Apltile SF5048 material (see [5]).

Remark 3.1.1. Throughout this chapter, the time-harmonic dependence for the pressure field (and for the displacement field) has been settled as $\pi(\mathbf{p}, t) = \text{Re}(\Pi(\mathbf{p})e^{-i\omega t})$, being π the time-dependent acoustic pressure field, Π the complex-valued time-harmonic acoustic pressure field, ω the angular frequency, t the time variable, \mathbf{p} the Cartesian coordinates of the spatial position, $\text{Re}(\cdot)$ the real part function of a complex number, and i the imaginary unit.

3.2 Mathematical modeling

To characterize the viscoelastic material, a coupled fluid-structure problem has been considered. Then, in this section, the mathematical models of the layers involved in the coupled problem are given, the coupled problem is described, and the acoustic quantities of interest in this problem are defined.

3.2.1 Mathematical models

The coupled problem under study involves a viscoelastic layer (with the same parameters as the absorbing tile), and a compressible fluid surrounding it. In what follows, the constitutive laws of both models are described in detail.

Compressible dissipative fluid

Taking into account the fluid dissipation (see [140] for further details), and considering the acoustic pressure field π as the primal unknown, the time-dependent equation of motion of a compressible dissipative fluid (which is assumed isentropic) is given by

$$\frac{1}{\rho_F c_F^2} \frac{\partial^2 \pi}{\partial t^2} + \frac{\alpha^2}{\rho_F} \frac{\partial^4 \pi}{\partial t^4} + \frac{2\alpha}{\rho_F c_F} \frac{\partial^3 \pi}{\partial t^3} - \operatorname{div} \left(\frac{1}{\rho_F} \nabla \pi \right) = 0,$$

where α is the attenuation coefficient, and ρ_F and c_F are the mass density and the sound speed of the fluid, respectively. Assuming harmonic solutions, $\pi(\mathbf{p}, t) = \operatorname{Re}(e^{-i\omega t} \Pi(\mathbf{p}))$, the motion equation is given by

$$-\frac{\omega^2}{\rho_F c_F^2} \Pi + \frac{\alpha^2 \omega^4}{\rho_F} \Pi + \frac{2i\alpha\omega^3}{\rho_F c_F} \Pi - \operatorname{div} \left(\frac{1}{\rho_F} \nabla \Pi \right) = 0.$$

If it is assumed that ρ_F is constant, and taking into account $\operatorname{div} \nabla \Pi = \Delta \Pi$, it holds

$$\left[-\frac{\omega^2}{c_F^2} + \alpha \omega^4 + \frac{2i\alpha\omega^2}{c_F} \right] \Pi - \Delta \Pi = - \left[\frac{\omega}{c_F} - i\alpha\omega^2 \right]^2 \Pi - \Delta \Pi = 0. \quad (3.1)$$

If $k_F(\omega) = \frac{\omega}{c_F} - i\alpha\omega^2$ is the complex-valued wave number, then (3.1) can be written as

$$-k_F^2(\omega) \Pi - \Delta \Pi = 0,$$

which is the so-called Helmholtz equation.

Viscoelastic solid

Under the small deformations hypothesis (see [113]), the time-dependent linear equation of motion for a viscoelastic solid (which is assumed homogeneous and isotropic), written in terms of the displacement, is given by

$$\rho_V \frac{\partial^2 \mathbf{u}}{\partial t^2} - \operatorname{div}(\boldsymbol{\sigma}) = \mathbf{0},$$

where ρ_V is the mass density at the equilibrium state of reference, \mathbf{u} is the displacement field, and $\boldsymbol{\sigma}$ is the stress tensor. To choose the constitutive law for the stress tensor, two different approaches can be followed: a parametric approach using well-known models, such as the Maxwell or the Kelvin-Voigt model, or a non-parametric approach where it is not required an a priori knowledge on the constitutive relations. The constitutive relation for the stress tensor in the viscoelastic solid (see [88]) can be written as the time convolution product

$$\sigma_{ij}(\mathbf{p}, t) = \int_{-\infty}^t c_{ijkl}(t - \tau) \frac{\partial \varepsilon_{kl}}{\partial t}(\mathbf{p}, \tau) d\tau,$$

where $\varepsilon = \frac{\nabla \mathbf{u} + \nabla \mathbf{u}^t}{2}$ is the strain tensor, and c is the linear elasticity tensor. Once a time-harmonic dependency is prescribed on the viscoelastic model, i.e., $c(t) = \text{Re}(e^{-i\omega t} C(\omega))$ and $\mathbf{u}(\mathbf{p}, t) = \text{Re}(e^{-i\omega t} \mathbf{U}(\mathbf{p}))$, and drawing an analogy with Hooke's law in the frequency regime, the action of the tensor C on any tensor R (assuming Einstein notation) is given by

$$C_{ijkl}(\omega) R_{kl} = \frac{\nu E(\omega)}{(1 - 2\nu)(1 + \nu)} R_{kk} \delta_{ij} + \frac{E(\omega)}{(1 + \nu)} R_{ij},$$

where ν is the Poisson's ratio, $E(\omega)$ is the complex-valued Young modulus of the viscoelastic material, and δ_{ij} is the Kronecker's delta. Hence, the time-harmonic displacement field satisfies

$$-\omega^2 \rho_V \mathbf{U} - \text{div}(C(\omega) \Sigma(\mathbf{U})) = \mathbf{0},$$

being $\Sigma(\mathbf{U}) = \frac{\nabla \mathbf{U} + \nabla \mathbf{U}^t}{2}$.

3.2.2 Coupled problem

Once the mathematical models of the media involved in the problem under study have been introduced, a multilayer planar configuration formed by a viscoelastic solid surrounded by a compressible dissipative fluid (water in the case under study) is considered (see Figure 3.4). Let Ω_1 and Ω_3 be the domains occupied by the fluid, and Ω_V the domain where the viscoelastic layer is located. Both fluids are placed on unbounded domains (half-spaces), and the thickness of viscoelastic tile is finite (denoted by l) but unbounded in the other two Cartesian coordinates. The coupled interfaces Γ_1 and Γ_2 , between the first fluid and the viscoelastic solid, and between the viscoelastic solid and the second fluid, respectively, are located on the planes $p_1 = 0$ and $p_1 = l$, i.e., Γ_1 and Γ_2 are defined by

$$\begin{aligned} \Gamma_1 &= \{\mathbf{p} = (p_1, p_2, p_3) \in \mathbb{R}^3 : p_1 = 0\}, \\ \Gamma_2 &= \{\mathbf{p} = (p_1, p_2, p_3) \in \mathbb{R}^3 : p_1 = l\}. \end{aligned}$$

Both interfaces are perpendicular to the Cartesian p_1 -axis, so the unit normal vector on Γ_1 and Γ_2 is $\mathbf{n} = \mathbf{e}_1$. On both interfaces, kinetic and kinematic coupled conditions are considered to preserve the continuity of normal displacements and the normal tensions. To

write the formulation of the coupled problem, the equation of motion of the compressible fluid has been expressed in terms of the pressure field, and the equation of motion of the viscoelastic model in terms of the displacement field. This coupled problem is given by: for a fixed angular frequency $\omega > 0$, find the acoustic pressure fields in the first and last fluid $\Pi_{\text{tot},1} = \Pi_{\text{scat}} + \Pi_{\text{inc}}$ and $\Pi_{\text{tot},3} = \Pi_{\text{transm}}$, and the displacement field \mathbf{U}_V in the viscoelastic medium such that

$$\left. \begin{array}{lcl} -k_F^2(\omega)(\Pi_{\text{tot},1}) - \Delta\Pi_{\text{tot},1} & = & 0 \\ -\omega^2\rho_V \mathbf{U}_V - \text{div}(\mathbf{C}(\omega)\Sigma(\mathbf{U}_V)) & = & \mathbf{0} \\ -k_F^2(\omega)\Pi_{\text{tot},3} - \Delta\Pi_{\text{tot},3} & = & 0 \\ \mathbf{U}_1 \cdot \mathbf{n} & = & \mathbf{U}_V \cdot \mathbf{n} \\ -\Pi_{\text{tot},1} & = & \mathbf{C}(\Sigma(\mathbf{U}_V))\mathbf{n} \cdot \mathbf{n} \\ \mathbf{U}_V \cdot \mathbf{n} & = & \mathbf{U}_3 \cdot \mathbf{n} \\ \mathbf{C}(\Sigma(\mathbf{U}_V))\mathbf{n} \cdot \mathbf{n} & = & -\Pi_{\text{tot},3} \end{array} \right\} \quad (3.2)$$

where \mathbf{U}_1 and \mathbf{U}_3 are the displacement field in the first and last fluid, respectively, and $\Sigma(\mathbf{U}_V)$ is the strain tensor in the frequency regime. Additionally, in order to guarantee there is no waves coming from the second fluid towards the viscoelastic solid, a radiation condition is imposed on the displacement field on the displacement field \mathbf{U}_3 at infinity.

3.2.3 Acoustic quantities of interest

In this section, some coefficients and levels of interest for the problem under studied are defined. Since an underwater environment is considered, the acoustic pressure field is measured by using a hydrophone, located at the field point $\mathbf{p}_m = (p_{1m}, p_{2m}, p_{3m})$.

Definition 3.2.1 (Reflection coefficient). *The reflection coefficient on the interface Γ_1 is the ratio of the scattered pressure to that of the incident pressure, that is,*

$$\mathcal{R}(\mathbf{p}_m) = \frac{\Pi_{\text{scat}}(\mathbf{p}_m)}{\Pi_{\text{inc}}(\mathbf{p}_m)} \Big|_{\Gamma_1}, \quad \mathbf{p}_m \in \Omega_1, \quad (3.3)$$

where Π_{scat} and Π_{inc} are the acoustic pressure scattered from the sample and the acoustic pressure incident upon the sample, respectively.

Definition 3.2.2 (Transmission coefficient). *The transmission coefficient is defined as the ratio of the transmitted pressure to that of the incident pressure.*

$$\mathcal{T}(\mathbf{p}_m) = \frac{\Pi_{\text{transm}}(\mathbf{p}_m)}{\Pi_{\text{inc}}(\mathbf{p}_m)}, \quad \mathbf{p}_m \in \Omega_3, \quad (3.4)$$

where Π_{transm} is the acoustic pressure transmitted from the sample and Π_{inc} is the acoustic pressure incident upon the sample.

Definition 3.2.3 (Echo Reduction). *The Echo Reduction level (ER) is given by*

$$\text{ER}(\mathbf{p}_m) = -20 \log_{10} |\mathcal{R}(\mathbf{p}_m)|, \quad (3.5)$$

where \mathcal{R} is the reflection coefficient defined in (3.3).

Definition 3.2.4 (Insertion Loss). *The Insertion Loss (IL) is defined by*

$$\text{IL}(\mathbf{p}_m) = -20 \log_{10} |\mathcal{T}(\mathbf{p}_m)|, \quad (3.6)$$

where \mathcal{T} is the transmission coefficient defined in (3.4).

Definition 3.2.5 (Fractional Power Dissipation). *The Fractional Power Dissipation (FPD) is given by*

$$\text{FPD}(\mathbf{p}_m) = 1 - |\mathcal{R}(\mathbf{p}_m)|^2 - |\mathcal{T}(\mathbf{p}_m)|^2, \quad (3.7)$$

where \mathcal{R} and \mathcal{T} are the reflection and the transmission coefficients, respectively.

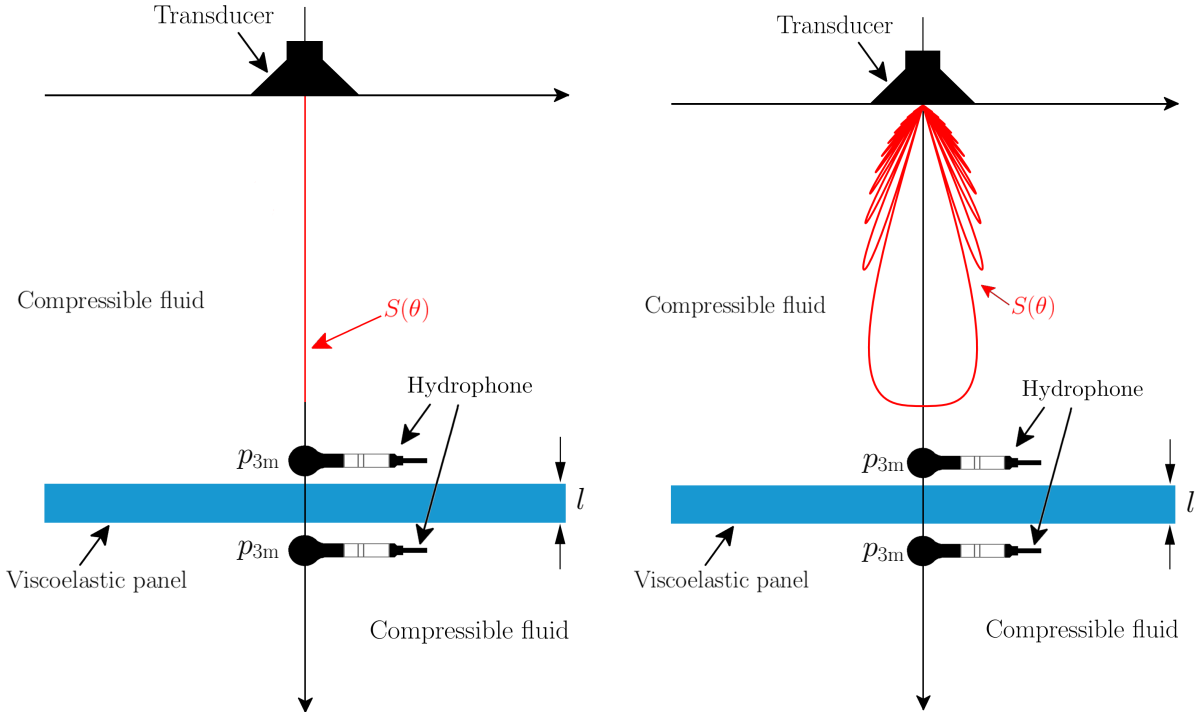


Figure 3.2: Experimental setup used to measure the incident, scattered, and transmitted pressure fields. The viscoelastic material is highlighted in blue. The position p_{3m} in the p_3 -axis is the position of the hydrophone which is located in front of, or behind the sample depending on the measured coefficient. The directivity pattern $S(\theta)$ is highlighted in red. Left: The considered acoustic source is a plane wave. Right: The acoustic source has a non-planar directivity pattern.

3.3 Statement of the direct problem: wave propagation in a multilayer medium

To obtain a complete characterization of the viscoelastic material, the frequency response of the echo reduction level, the insertion loss, and the fractional power dissipation

have been considered. Although the acoustic propagation in a multilayer medium can be computed by using plane waves, since the available experimental data have been measured in an NPL Acoustic Pressure Vessel, instead of using a conventional linear source transducer, a parametric array is used as the acoustic source, following [17]. Since the acoustic field is represented in terms of a linear combination of plane waves with different angles of incidence, the effect of the panel under test in each component of the spectrum is considered. In this section, the computation of the incident, scattered, and transmitted pressure fields are described by using an integral representation. The reflection and the transmission coefficients in a plane-wave framework are involved in the computation of these pressure fields. Hence, in this section, a plane wave propagation problem is described, explaining how the reflection and the transmission coefficients are calculated.

3.3.1 Integral representation of pressure fields

In this section, the incident, the scattered, and the transmitted pressure fields are represented in terms of a plane wave spectrum. When a non-planar wave impinges in a plane interface between two media, difficulties can arise due to the difference between the form of the boundary and the symmetry of the wave. To overcome the problem, the non-planar wave is expanded into plane waves, following [37]. In what follows, the media are assumed dissipative compressible fluids to ensure that the wave number k is complex-valued. Such a feature implies that the fundamental solutions (spherical waves) are spatially damped, and hence belong to $L^2(\mathbb{R}^3)$. Consequently, a Fourier analysis approach can be applied in this context rigorously.

The spherical wave can be written as e^{ikR}/R , where k is the wave number, and assuming that the source is located at the origin, $R = |\mathbf{p}| = \sqrt{p_1^2 + p_2^2 + p_3^2}$. If the plane $p_3 = 0$ is considered, the spherical wave can be written as e^{ikr}/r , where $r = \sqrt{p_1^2 + p_2^2}$. This field can be expanded by using the inverse Fourier transform

$$\frac{e^{ikr}}{r} = \int_{-\infty}^{\infty} \int_{-\infty}^{\infty} A(\xi_1, \xi_2) e^{i(\xi_1 p_1 + \xi_2 p_2)} d\xi_1 d\xi_2, \quad (3.8)$$

being

$$A(\xi_1, \xi_2) = \frac{1}{(2\pi)^2} \int_{-\infty}^{\infty} \int_{-\infty}^{\infty} \frac{e^{i(kr - \xi_1 p_1 - \xi_2 p_2)}}{r} dp_1 dp_2, \quad (3.9)$$

and using polar coordinates

$$\begin{aligned} \xi_1 &= \xi \cos \psi, & \xi_2 &= \xi \sin \psi, & \xi &= \sqrt{\xi_1^2 + \xi_2^2}, \\ p_1 &= r \cos \phi, & p_2 &= r \sin \phi. \end{aligned}$$

Then, Equation (3.9) results

$$A(\xi_1, \xi_2) = \frac{1}{(2\pi)^2} \int_0^{2\pi} d\phi \int_0^{\infty} e^{ir(k - \xi \cos(\psi - \phi))} dr. \quad (3.10)$$

Since a dissipative compressible fluid is considered, $\text{Im}k > 0$, so $e^{ikr} \rightarrow 0$ at $r \rightarrow \infty$, and the integral over r results

$$\int_0^\infty e^{ir(k-\xi \cos(\psi-\phi))} dr = \frac{i}{k - \xi \cos(\psi - \phi)},$$

and (3.10) can be written as

$$A(\xi_1, \xi_2) = \frac{i}{(2\pi)^2} \int_0^{2\pi} \frac{1}{k - \xi \cos(\psi - \phi)} d\phi = \frac{i}{(2\pi)^2} \int_0^{2\pi} \frac{1}{k - \xi \cos \tilde{\phi}} d\tilde{\phi} = \frac{i}{2\pi \sqrt{k^2 - \xi^2}}.$$

Therefore, if it is considered the notation $\xi_3 = \sqrt{k^2 - \xi^2}$, (3.8) results

$$\frac{e^{ikr}}{r} = \frac{i}{2\pi} \int_{-\infty}^\infty \int_{-\infty}^\infty \frac{e^{i(\xi_1 p_1 + \xi_2 p_2)}}{\xi_3} d\xi_1 d\xi_2.$$

This expression, which describes the field in the $p_3 = 0$ plane, can be extended into the whole space. Each Fourier component corresponds to a plane wave in the space. To achieve this, it is necessary to add the $i\xi_3 p_3$ term in the exponent in the integrand, when $p_3 > 0$, which corresponds to the waves propagating in the positive p_3 -axis, and to add the term $-i\xi_3 p_3$ when $p_3 < 0$, which corresponds to the waves propagating in the negative p_3 -axis, that is,

$$\frac{e^{ikR}}{R} = \frac{i}{2\pi} \int_{-\infty}^\infty \int_{-\infty}^\infty \frac{e^{i(\xi_1 p_1 + \xi_2 p_2 + \xi_3 |p_3|)}}{\xi_3} d\xi_1 d\xi_2. \quad (3.11)$$

This expression is the expansion of a spherical wave into plane waves. Now, it is possible to compute (3.11) over the angles θ and ϕ (see Figure 3.3) by using the spherical coordinates

$$\xi_1 = k \sin \theta \cos \phi, \quad \xi_2 = k \sin \theta \sin \phi, \quad \xi_3 = k \cos \theta,$$

where $\phi \in [0, 2\pi]$. Now, the limits of θ are computed. By the definition of ξ_3 , $\xi_3 = \sqrt{k^2 - \xi^2} = \sqrt{k^2 - \xi_1^2 - \xi_2^2}$. If $\xi_1 = \xi_2 = 0$ then $\xi_3 = 0$ and $\theta = \frac{\pi}{2}$. If $\xi_1 \rightarrow \pm\infty$ and $\xi_2 \rightarrow \pm\infty$, $\xi_3 = \sqrt{-\infty} = i\infty$ and $\theta = \frac{\pi}{2} - i\infty$. Then, $\xi_3 \in [0, i\infty]$ and $\theta \in [0, \frac{\pi}{2} - i\infty]$. Moreover,

$$\frac{d\xi_1 d\xi_2}{d\theta d\phi} = \begin{vmatrix} k \cos \theta \cos \phi & -k \sin \theta \sin \phi \\ k \cos \theta \sin \phi & k \sin \theta \cos \phi \end{vmatrix} = k^2 \sin \theta \cos \theta. \quad (3.12)$$

By using (3.12), the integral in (3.11) can be calculated over the angles θ and ϕ as follows

$$\frac{e^{ikR}}{R} = \frac{i}{2\pi} \int_0^{\pi/2-i\infty} \int_0^{2\pi} e^{i(\xi_1 p_1 + \xi_2 p_2 + \xi_3 |p_3|)} \sin \theta d\phi d\theta. \quad (3.13)$$

Considering the geometry in Figure 3.3, and following [95], if $\mathbf{s} = (0, 0, s)$ is the position of an element of the line array, the incident pressure field at a field point $\mathbf{p}_m = (p_{1m}, p_{2m}, p_{3m})$

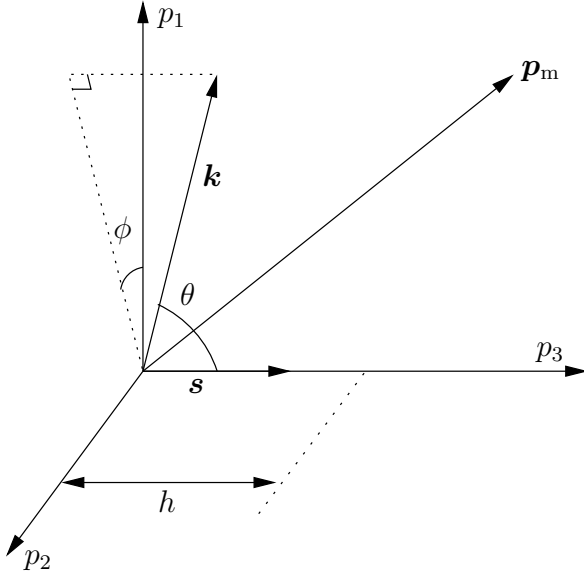


Figure 3.3: Scheme of the geometry used to compute the plane wave spectrum of the parametric array.

in front of the panel can be calculated by integrating over the incident field components. That is, the incident pressure field can be written as

$$\Pi_{\text{inc}}(\mathbf{p}_m) = Q_0 \int_0^h e^{ik_F(\omega)s} \frac{e^{ik_F(\omega)r}}{r} ds, \quad (3.14)$$

where $k_F(\omega)$ is the wave number of the fluid, $\mathbf{r} = \mathbf{R} - \mathbf{s}$, h is the length of the parametric array, and Q_0 is a constant determined by the strength of the array. For the sake of simplicity, the dependency of ω in the fluid wave number k_F is omitted below. Taking into account (3.13), the spherical wave term $\frac{e^{ik_F r}}{r}$ can be expanded into plane waves, and using spherical coordinates, results

$$\frac{e^{ik_F r}}{r} = \frac{ik_F}{2\pi} \int_0^{\pi/2-i\infty} \int_0^{2\pi} e^{i\mathbf{k}\cdot\mathbf{r}} \sin \theta d\phi d\theta, \quad (3.15)$$

where (θ, ϕ) is the direction of the wave vector \mathbf{k} , $k_F = |\mathbf{k}|$, with θ the angle measured from p_3 -axis and ϕ the angle measured from p_1 -axis. Considering (3.15), the incident pressure field (3.14) results

$$\Pi_{\text{inc}}(\mathbf{p}_m) = \frac{ik_F}{2\pi} \int_0^{\pi/2-i\infty} \int_0^{2\pi} S(\theta, \phi) e^{i\mathbf{k}\cdot\mathbf{r}} \sin \theta d\phi d\theta, \quad (3.16)$$

where $S(\theta, \phi)$ is the plane wave spectrum of the truncated parametric array of length h ,

and is given by

$$S(\theta, \phi) = Q_0 \int_0^h e^{ik_F s} e^{-i\mathbf{k} \cdot \mathbf{s}} ds.$$

In the considered geometry (see Figure 3.3), $\mathbf{k} \cdot \mathbf{s} = k_F s \cos \theta$, and

$$S(\theta) = Q_0 \int_0^h e^{ik_F s(1-\cos \theta)} ds = Q_0 \frac{e^{ik_F h(1-\cos \theta)} - 1}{ik_F(1-\cos \theta)}, \quad (3.17)$$

that is, the plane wave spectrum is a function of θ only. Then, considering p_{3m} the field point on the p_3 -axis in front of the sample and the symmetry of the acoustic field about the p_3 -axis, the incident pressure field, given by (3.16), can be written as

$$\Pi_{\text{inc}}(\mathbf{p}_m) = ik_F \int_0^{\frac{\pi}{2}-i\infty} S(\theta) e^{ik_F p_{3m} \cos \theta} \sin \theta d\theta. \quad (3.18)$$

Following a similar argument, the transmitted acoustic pressure field, $\Pi_{\text{transm}}(\mathbf{p}_m)$, at a field point \mathbf{p}_m beyond the sample, can be calculated by integrating over the transmitted field components (see [95]), that is,

$$\Pi_{\text{transm}}(\mathbf{p}_m) = \frac{ik_F}{2\pi} \int_0^{\frac{\pi}{2}-i\infty} \int_0^{2\pi} S(\theta, \phi) \mathcal{T}(\mathbf{p}_m) e^{i\mathbf{k} \cdot \mathbf{p}_m} \sin \theta d\phi d\theta, \quad (3.19)$$

where $\mathcal{T}(\mathbf{p}_m)$ is the transmission coefficient of the inserted panel, given by (3.4). Since in the considered geometry the plane wave spectrum is a function of θ only, the transmitted acoustic pressure field (3.19), at a field point p_{3m} on the p_3 -axis beyond the sample, is

$$\Pi_{\text{transm}}(\mathbf{p}_m) = ik_F \int_0^{\frac{\pi}{2}-i\infty} S(\theta) \mathcal{T}(\mathbf{p}_m) e^{ik_F p_{3m} \cos \theta} \sin \theta d\theta, \quad (3.20)$$

where $S(\theta)$ the plane wave spectrum given by (3.17).

The scattered pressure field Π_{scat} at a field point \mathbf{p}_m in front of the sample can be calculated by integrating over the scattered field components, that is,

$$\Pi_{\text{scat}}(\mathbf{p}_m) = \frac{ik_F}{2\pi} \int_0^{\frac{\pi}{2}-i\infty} \int_0^{2\pi} S(\theta, \phi) \mathcal{R}(\mathbf{p}_m) e^{i\mathbf{k} \cdot \mathbf{p}_m} \sin \theta d\phi d\theta, \quad (3.21)$$

where $\mathcal{R}(\mathbf{p}_m)$ is the reflection coefficient of the inserted panel, given by (3.3). Considering the geometry described in Figure 3.3, the scattered acoustic pressure field (3.21), at a field point p_{3m} on the p_3 -axis in front of the sample, can be written as

$$\Pi_{\text{scat}}(\mathbf{p}_m) = ik_F \int_0^{\frac{\pi}{2}-i\infty} S(\theta) \mathcal{R}(\mathbf{p}_m) e^{ik_F p_{3m} \cos \theta} \sin \theta d\theta, \quad (3.22)$$

where $S(\theta)$ the plane wave spectrum given by (3.17).

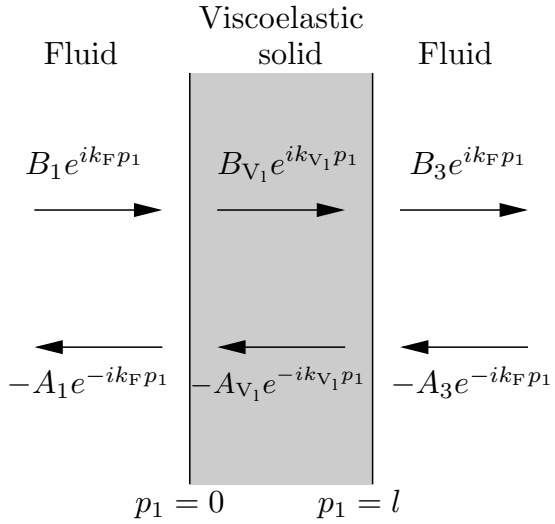


Figure 3.4: Geometrical configuration of the considered multilayer problem, which is formed by a viscoelastic solid, surrounded by a fluid. Arrows from left to right (resp., from right to left) denote the propagative direction of the incident waves (resp. reflected waves) in each medium. The coefficients A_j and B_j with $j = 1, 3$ (resp. A_{V1} and B_{V1}) are the frequency-dependent complex amplitudes, which corresponds to the reflection and transmission coefficients associated with the displacement fields in the fluids (resp. in the viscoelastic solid).

3.3.2 Computation of reflection and transmission coefficients by using a plane-wave framework

Integral expressions used to compute scattered and transmitted pressure fields described in the previous section involve the reflection and the transmission coefficient of the panel for an oblique incident wave. To describe these coefficients, a multilayer medium formed by a fluid, a viscoelastic layer, and another fluid is studied. If an incident plane wave is impinging on the viscoelastic layer with an incidence angle θ_1 , the complex-valued displacement in each medium is given by a linear combination of transmitted and reflected plane waves. In fact, the displacement fields in both fluids are given only by a linear combination of longitudinal waves. However, straightforward computations show that the displacement field in the viscoelastic solid is given not only by longitudinal waves but also by transversal waves.

In the frequency domain, the displacement field in both fluids (medium 1 and medium 3) at oblique incidence can be written as

$$\begin{aligned} \mathbf{U}_j(\mathbf{p}) = & (-A_j e^{ik_F(-\cos \theta_j p_1 + \sin \theta_j p_2)} + B_j e^{ik_F(\cos \theta_j p_1 + \sin \theta_j p_2)}) \cos \theta_j \mathbf{e}_1 \\ & + (A_j e^{ik_F(-\cos \theta_j p_1 + \sin \theta_j p_2)} + B_j e^{ik_F(\cos \theta_j p_1 + \sin \theta_j p_2)}) \sin \theta_j \mathbf{e}_2, \quad j = 1, 3, \end{aligned}$$

where A_j and B_j with $j = 1, 3$, are frequency-dependent complex constants which can be viewed as the reflection and transmission coefficients between each medium, θ_1 and θ_3 are the incident angles in the first and the last fluid, respectively, and k_F is the wave number of the fluid, given by $k_F = \omega/c_F$, being c_F the sound velocity in the fluid.

Since the pressure field is defined as

$$\Pi_j = -\rho_F c_F^2 \operatorname{div} \mathbf{U}_j, \quad j = 1, 3,$$

the pressure field of both fluids Π_j with $j = 1, 3$, at oblique incidence can be written as

$$\Pi_j(\mathbf{p}) = -i\omega Z_F (A_j e^{ik_F(-\cos \theta_j p_1 + \sin \theta_j p_2)} + B_j e^{ik_F(\cos \theta_j p_1 + \sin \theta_j p_2)}),$$

being Z_F the characteristic impedance of the medium, given by $Z_F = \rho_F c_F$.

The displacement field of a viscoelastic solid \mathbf{U}_V is given by a linear combination of longitudinal waves, where the oscillations occur in the direction of wave propagation, and transverse waves, where the particles displacement due to the plane wave is perpendicular to the direction of propagation. Then the displacement field at oblique incidence can be written as

$$\begin{aligned} \mathbf{U}_V(\mathbf{p}) &= \mathbf{U}_{V_l}(\mathbf{p}) + \mathbf{U}_{V_t}(\mathbf{p}) \\ &= [(-A_{V_l} e^{ik_{V_l}(-\cos \theta_{V_l} p_1 + \sin \theta_{V_l} p_2)} + B_{V_l} e^{ik_{V_l}(\cos \theta_{V_l} p_1 + \sin \theta_{V_l} p_2)}) \cos \theta_{V_l} \\ &\quad + (A_{V_t} e^{ik_{V_t}(-\cos \theta_{V_t} p_1 + \sin \theta_{V_t} p_2)} - B_{V_t} e^{ik_{V_t}(\cos \theta_{V_t} p_1 + \sin \theta_{V_t} p_2)}) \sin \theta_{V_t}] \mathbf{e}_1 \\ &\quad + [(A_{V_l} e^{ik_{V_l}(-\cos \theta_{V_l} p_1 + \sin \theta_{V_l} p_2)} + B_{V_l} e^{ik_{V_l}(\cos \theta_{V_l} p_1 + \sin \theta_{V_l} p_2)}) \sin \theta_{V_l} \\ &\quad + (A_{V_t} e^{ik_{V_t}(-\cos \theta_{V_t} p_1 + \sin \theta_{V_t} p_2)} + B_{V_t} e^{ik_{V_t}(\cos \theta_{V_t} p_1 + \sin \theta_{V_t} p_2)}) \cos \theta_{V_t}] \mathbf{e}_2, \end{aligned}$$

where A_{V_l} , B_{V_l} , A_{V_t} , and B_{V_t} , are frequency-dependent complex constants which can be viewed as the reflection and transmission coefficients between each medium, θ_{V_l} and θ_{V_t} are the incident angles of the longitudinal and transverse waves in the viscoelastic solid, and

k_{V_l} and k_{V_t} are the wave numbers given by $k_{V_l} = \frac{\omega}{c_{V_l}}$ and $k_{V_t} = \frac{\omega}{c_{V_t}}$ where $c_{V_l} = \sqrt{\frac{\lambda + 2\mu}{\rho_V}}$

is the sound velocity of the longitudinal waves, and $c_{V_t} = \sqrt{\frac{\mu}{\rho_V}}$ is the sound velocity of the transverse waves, being ρ_V is the mass density of the viscoelastic solid, and λ and μ the Lamé coefficients associated to the material, given by $\lambda = \frac{\nu E}{(1 - 2\nu)(1 + \nu)}$ and $\mu = \frac{E}{2(1 + \nu)}$, respectively.

To compute the constants which determine the plane waves, it is necessary to solve the propagation problem (3.2). Introducing the characteristic impedances, $Z_F = \rho_F c_F$ and $Z_V = \rho_V c_{V_t}$, the linear system to solve is

$$\left. \begin{aligned}
& -\cos \theta_1 A_1 + \cos \theta_{V_1} A_{V_1} - \cos \theta_{V_1} B_{V_1} - \sin \theta_{V_t} A_{V_t} + \sin \theta_{V_t} B_{V_t} = -\cos \theta_1 B_1, \\
& \frac{Z_F}{Z_V} A_1 - \left(\frac{2\mu}{2\mu + \lambda} \cos^2 \theta_{V_1} + \frac{\lambda}{2\mu + \lambda} \right) A_{V_1} \\
& \quad - \left(\frac{2\mu}{2\mu + \lambda} \cos^2 \theta_{V_1} + \frac{\lambda}{2\mu + \lambda} \right) B_{V_1} \\
& + \frac{2\mu}{2\mu + \lambda} \frac{k_{V_t}}{k_{V_1}} \sin \theta_{V_t} \cos \theta_{V_t} A_{V_t} + \frac{2\mu}{2\mu + \lambda} \frac{k_{V_t}}{k_{V_1}} \sin \theta_{V_t} \cos \theta_{V_t} B_{V_t} = -\frac{Z_F}{Z_V} B_1, \\
& -2 \sin \theta_{V_1} \cos \theta_{V_1} A_{V_1} + 2 \sin \theta_{V_1} \cos \theta_{V_1} B_{V_1} - \frac{k_{V_t}}{k_{V_1}} (\cos^2 \theta_{V_t} - \sin^2 \theta_{V_t}) A_{V_t} \\
& \quad + \frac{k_{V_t}}{k_{V_1}} (\cos^2 \theta_{V_t} - \sin^2 \theta_{V_t}) B_{V_t} = 0, \\
& -\cos \theta_{V_1} e^{-ik_{V_1} \cos \theta_{V_1} l} A_{V_1} + \cos \theta_{V_1} e^{ik_{V_1} \cos \theta_{V_1} l} B_{V_1} + \sin \theta_{V_t} e^{-ik_{V_t} \cos \theta_{V_t} l} A_{V_t} \\
& \quad - \sin \theta_{V_t} e^{ik_{V_t} \cos \theta_{V_t} l} B_{V_t} - \cos \theta_3 e^{ik_F \cos \theta_3 l} B_3 = 0, \\
& \left(\frac{2\mu}{2\mu + \lambda} \cos^2 \theta_{V_1} + \frac{\lambda}{2\mu + \lambda} \right) e^{-ik_{V_1} \cos \theta_{V_1} l} A_{V_1} \\
& + \left(\frac{2\mu}{2\mu + \lambda} \cos^2 \theta_{V_1} + \frac{\lambda}{2\mu + \lambda} \right) e^{ik_{V_1} \cos \theta_{V_1} l} B_{V_1} \\
& - \frac{2\mu}{2\mu + \lambda} \frac{k_{V_t}}{k_{V_1}} \sin \theta_{V_t} \cos \theta_{V_t} e^{-ik_{V_t} \cos \theta_{V_t} l} A_{V_t} \\
& - \frac{2\mu}{2\mu + \lambda} \frac{k_{V_t}}{k_{V_1}} \sin \theta_{V_t} \cos \theta_{V_t} e^{ik_{V_t} \cos \theta_{V_t} l} B_{V_t} - \frac{Z_F}{Z_V} e^{ik_F \cos \theta_3 l} B_3 = 0, \\
& -2 \sin \theta_{V_1} \cos \theta_{V_1} e^{-ik_{V_1} \cos \theta_{V_1} l} A_{V_1} + 2 \sin \theta_{V_1} \cos \theta_{V_1} e^{ik_{V_1} \cos \theta_{V_1} l} B_{V_1} \\
& \quad - \frac{k_{V_t}}{k_{V_1}} (\cos^2 \theta_{V_t} - \sin^2 \theta_{V_t}) e^{-ik_{V_t} \cos \theta_{V_t} l} A_{V_t} \\
& \quad + \frac{k_{V_t}}{k_{V_1}} (\cos^2 \theta_{V_t} - \sin^2 \theta_{V_t}) e^{ik_{V_t} \cos \theta_{V_t} l} B_{V_t} = 0,
\end{aligned} \right. \tag{3.23}$$

where the unknowns are the constants $A_1, A_3, B_3, A_{V_1}, B_{V_1}, A_{V_t}, B_{V_t}$, and B_1 is the amplitude of the incident wave in the first compressible fluid that spreads to other media, which has been assumed as known.

Once the system (3.23), by using the solutions $A_1, B_1, A_3, B_3, A_{V_1}, B_{V_1}, A_{V_t}, B_{V_t}$ is straightforward to compute the reflection and the transmission coefficients taking into account

$$\begin{aligned}
\Pi_{\text{inc}} &= -i\omega Z_F A_1, \\
\Pi_{\text{scat}} &= -i\omega Z_F B_1, \\
\Pi_{\text{transm}} &= -i\omega Z_F B_3.
\end{aligned}$$

3.4 Acoustic characterization of a viscoelastic solid using an inverse problem

Once the acoustic mathematical models have been described, the multilayer problem under study has been explained and the acoustic quantities have been defined, the following section focuses on the numerical solution of an inverse problem. The only known data of the polymer tile are its dimensions, its mass density, and the frequency response of the echo reduction level, the insertion loss, and the fractional power dissipation. Since to get the acoustic characterization of an absorbing tile by using a viscoelastic model, it is necessary to know its Poisson's ratio and its Young modulus, the purpose of this inverse problem is to find the values of the real and the imaginary parts of Young modulus, E' y E'' , respectively, which provide a frequency response as close as possible to that provided by experimental measurements. In the numerical simulations, the value of Poisson's ratio is supposed known according to the literature (see Remark 3.4.1).

Remark 3.4.1. *It is well-known that the Lamé coefficients associated to the material, λ and μ , are given by*

$$\begin{aligned}\lambda &= \frac{\nu E}{(1 - 2\nu)(1 + \nu)}, \\ \mu &= \frac{E}{2(1 + \nu)}.\end{aligned}$$

Then, the Poisson's ratio is given by $\nu = \frac{\lambda}{2(\lambda + \mu)}$. Since the numerator and the denominator depend on the Young modulus, it is redundant to consider the Poisson's ratio as unknown.

3.4.1 Constitutive laws for the primal unknowns

In this section, a detailed study about different constitutive laws that can be assumed for the primal unknowns is shown. First of all, a discussion about the ill-posedness of the optimization problem is given. Then, different constitutive laws for the primal unknowns are considered, some of them following a parametric model and other ones following a non-parametric approach. Moreover, a study about the primal unknowns of the problem is done. Firstly, the unknowns are the real and the imaginary parts of the Young modulus. By using these unknowns appear spurious oscillations which are overcome considering a new pair of unknowns depending on the wave number and the thickness of the material. The inverse problem to solve and the cost function to be minimized have been described in each case.

Characterization with real-valued datasets

For a fixed frequency value ω , it is assumed that the propagation problem (3.2) is solved with the values of one real-valued level $L(\omega)$ (in this chapter ER, IL, or FPD). The

characterization problem can be stated as follows:

Problem 3.4.2 (Inverse problem with a real-valued level dataset). *For a fixed frequency value ω , find the complex-valued coefficients $E(\omega)$, assuming that only the values of one level $L(\omega)$ is known, obtained by solving the problem (3.2).*

Lemma 3.4.3. *Problem 3.4.2 is ill-posed in the sense that there exists an innumerable number of solutions due to the lack of observation data.*

Proof. The simplest case is considered, that is, a plane wave with incidence angle $\theta_1 = 0$ and amplitude 1 is considered. Then, $B_1 = 1$, and the system (3.23) results

$$-A_1 + A_{V_1} - B_{V_1} = -1, \quad (3.24)$$

$$A_1 - \frac{Z_V}{Z_F} A_{V_1} - \frac{Z_V}{Z_F} B_{V_1} = -1, \quad (3.25)$$

$$-e^{-ik_{V_1}l} A_{V_1} + e^{ik_{V_1}l} B_{V_1} - e^{ik_F l} B_3 = 0, \quad (3.26)$$

$$e^{-ik_{V_1}l} \frac{Z_V}{Z_F} A_{V_1} + e^{ik_{V_1}l} \frac{Z_V}{Z_F} B_{V_1} - e^{ik_F l} B_3 = 0. \quad (3.27)$$

By definition, the echo reduction level is $ER = -20 \log 10 \frac{|A_1|}{|B_1|} = -20 \log_{10} |A_1|$. To proof that the problem is ill-posed, it is enough to proof that there exist infinite values of A_1 which lead to the same echo reduction level. Subtracting (3.24) and (3.25), and (3.26) and (3.27),

$$A_1 = \frac{1}{2} \left[\left(1 + \frac{Z_V}{Z_F} \right) A_{V_1} + \left(-1 + \frac{Z_V}{Z_F} \right) B_{V_1} \right], \quad (3.28)$$

$$A_{V_1} = \frac{\left(1 - \frac{Z_V}{Z_F} \right)}{\left(1 + \frac{Z_V}{Z_F} \right)} B_{V_1} e^{2ik_{V_1}l}. \quad (3.29)$$

By using (3.29) in (3.24), and in (3.28),

$$\begin{aligned} A_1 &= A_{V_1} - B_{V_1} + 1 = \frac{\left(1 - \frac{Z_V}{Z_F} \right)}{\left(1 + \frac{Z_V}{Z_F} \right)} B_{V_1} e^{2ik_{V_1}l} - B_{V_1} + 1 \\ &= \left(\frac{Z_F - Z_V}{Z_F + Z_V} e^{2ik_{V_1}l} - 1 \right) B_{V_1} + 1. \end{aligned} \quad (3.30)$$

$$A_1 = \frac{1}{2} \left(1 - \frac{Z_V}{Z_F} \right) (e^{2ik_{V_1}l} - 1) B_{V_1} \Rightarrow B_{V_1} = \frac{A_1}{\frac{1}{2} \left(1 - \frac{Z_V}{Z_F} \right) (e^{2ik_{V_1}l} - 1)}. \quad (3.31)$$

By using (3.31), Equation (3.30) results

$$\begin{aligned} A_1 &= 1 + \left(\frac{Z_F - Z_V}{Z_F + Z_V} e^{2ik_{V_1}l} - 1 \right) \frac{A_1}{\frac{1}{2} \left(1 - \frac{Z_V}{Z_F} \right) (e^{2ik_{V_1}l} - 1)} \\ &\Rightarrow A_1 \left[1 - \frac{2Z_F \left(\frac{Z_F - Z_V}{Z_F + Z_V} e^{2ik_{V_1}l} - 1 \right)}{(Z_F - Z_V) (e^{2ik_{V_1}l} - 1)} \right] = 1. \end{aligned}$$

Now, the goal is to find \tilde{Z}_V and \tilde{k}_{V_1} such that

$$1 - \frac{2Z_F \left(\frac{Z_F - \tilde{Z}_V}{Z_F + \tilde{Z}_V} e^{2i\tilde{k}_{V_1}l} - 1 \right)}{(Z_F - \tilde{Z}_V) (e^{2i\tilde{k}_{V_1}l} - 1)} = e^{i\phi} \left[1 - \frac{2Z_F \left(\frac{Z_F - Z_V}{Z_F + Z_V} e^{2ik_{V_1}l} - 1 \right)}{(Z_F - Z_V) (e^{2ik_{V_1}l} - 1)} \right],$$

with ϕ arbitrary, $\phi \in [-\pi, \pi)$. Solving \tilde{Z}_V and assuming $\tilde{k}_{V_1} = k_{V_1}$,

$$\begin{aligned} &\tilde{Z}_V^2 [(e^{2ik_{V_1}l} - 1) (Z_F^2 - Z_V^2) (e^{i\phi} - 1) + 2Z_F e^{i\phi} ((Z_F + Z_V) - (Z_F - Z_V) e^{2ik_{V_1}l})] \\ &+ \tilde{Z}_V [2Z_F (Z_F^2 - Z_V^2) (e^{2ik_{V_1}l} + 1)] - Z_F^2 (e^{2ik_{V_1}l} - 1) (Z_F^2 - Z_V^2) (e^{i\phi} - 3) \\ &+ 2Z_F^3 e^{i\phi} ((Z_F - Z_V) e^{2ik_{V_1}l} - (Z_F + Z_V)) = 0. \end{aligned}$$

Since ϕ is arbitrary, there are infinite solutions for \tilde{Z}_V . Then, There exist an innumerable number of solutions of A_1 with arbitrary phases and the same modulus. \square

Parametric optimization

First of all, a parametric optimization has been performed. The Young modulus, which is the considered primal unknown, is a linear function of the frequency, following the Kelvin-Voigt model [58, 81, 121]. Then, the real and the imaginary parts of Young modulus are considered constants. More precisely, following [124], it was considered that the Young modulus of the polymer tile could be written as

$$E = E' - i\omega E'',$$

where E' and E'' are assumed constant. Let L_j^{exp} be the experimental values obtained by measuring the level under study, for $j = 1, \dots, N_L$, being N_L the number of considered frequencies, and let $\hat{L}(E', E'', \omega_j)$ be the computed numerical values of the level under consideration, for $j = 1, \dots, N_L$, where E' and E'' are the real and the imaginary parts of

the Young modulus, and ω_j is the studied angular frequency. If the cost function is defined as

$$\Phi_L(E', E'') = \frac{\sqrt{\sum_{j=1}^{N_L} |L_j^{\text{exp}} - \hat{L}(E', E'', \omega_j)|^2}}{\sqrt{\sum_{j=1}^{N_L} |L_j^{\text{exp}}|^2}}, \quad (3.32)$$

the fitting problem is stated as follows: Find the values $E'_* \geq 0$ and $E''_* \geq 0$, such that minimize the difference between the experimental and the numerical values, i.e.,

$$(E'_*, E''_*) = \arg \min_{E', E'' > 0} \Phi_L(E', E''), \quad (3.33)$$

where $E = E' - i\omega E''$ is the Young modulus with E' and E'' constants, and L is the level that is fitted (in this chapter L can be the echo reduction level, the insertion loss or the fractional power dissipation).

The used optimization strategy, which is based on exhaustive search algorithms, consists of minimizing a cost function on progressively finer grids. Although the algorithm is computationally more expensive, this strategy allows us to find the absolute minimum of a function of two variables in successive refined two-dimensional Cartesian discrete grids. This strategy performs an exhaustive multigrid search among the values reached by the objective function in a discrete set of positions. The implemented function has as input the lower (a_m and b_m) and the upper endpoints (A_m and B_m) of the interval where the real and the imaginary parts of the Young modulus are looking for. A grid of points contained in $[a_m, A_m] \times [b_m, B_m]$, in the iteration m , is generated to evaluate the cost function and find the minimum at these points. The endpoints of the intervals in which the minimum is searched in both variables are chosen as follows: firstly, a grid of points is considered, covering a rectangle region where the location of the absolute minimum is guessed. Then, an exhaustive search algorithm finds the absolute minimum on the grid points. Finally, the rectangle region is reduced by a fixed factor, but always centering on the grid point where the absolute minimum on the grid is placed. So, in a finite number of iterations, the minimum value is located with a given tolerance, determined by the distance between the grid points.

Non-parametric optimization

In order to improve the results obtained by assuming that both the real and the imaginary parts of the Young modulus are constants, it is assumed that the Young modulus is governed by an arbitrary smooth frequency-dependent function, that is, the real and the imaginary parts of the Young modulus are governed by an arbitrary function that depends on the angular frequency. Let L_j^{exp} be the experimental values obtained by measuring the level under study, for $j = 1, \dots, N_L$, being N_L the number of considered frequencies, and

let $\widehat{L}(E'_j, E''_j, \omega_j)$ be the computed numerical values of the level, for $j = 1, \dots, N_L$, where E'_j and E''_j are the real and the imaginary parts of the Young modulus for each value of the angular frequency ω_j . For each value of ω_j , the cost function is defined as

$$\Psi_L(E'_j, E''_j, \omega_j) = \frac{|L_j^{\text{exp}} - \widehat{L}(E'_j, E''_j, \omega_j)|^2}{|L_j^{\text{exp}}|^2}, \quad \forall j = 1, \dots, N_L. \quad (3.34)$$

Then, the fitting problem is stated as follows: Find the values $E'_{j*} \geq 0$ and $E''_{j*} \geq 0$, such that minimize the difference between the experimental and the numerical values, i.e.,

$$(E'_{j*}, E''_{j*}) = \arg \min_{E'_j, E''_j > 0} \Psi_L(E'_j, E''_j, \omega_j), \quad \forall j = 1, \dots, N_L, \quad (3.35)$$

where $E_j = E'_j - iE''_j$, and L is the level that is fitted (in this chapter L can be the echo reduction level, the insertion loss, or the fractional power dissipation). As in the parametric approach, a brute-force fitting is used to solve the optimization problem. After performing the fittings shown above, it is observed that the use of E' and E'' as primal unknowns leads to results where both the real and the imaginary parts of the Young modulus present spurious oscillations (see Section 3.5.4 for more details). In order to overcome the problem, and to get smoother frequency responses of the parameters, new unknowns should be chosen.

To choose the new unknowns properly, it is necessary to highlight that the oscillatory behavior comes from the computation of the scattered and the transmitted pressure fields. As it can be observed in Equations (3.22) and (3.20), the reflection and the transmission coefficients of a plane wave propagation problem are involved in these integral expressions, and both coefficients are computed by using the linear system (3.23). In this linear system, the exponential dependence of the coefficients with respect to the value of the Young modulus can be fully appreciated. This fact also implies that the fitting results are highly dependent on the initial guess: small changes in the initial guess lead to pretty different numerical results. To mitigate this situation, instead of using the unknowns E' and E'' in the fitting procedure, a novel pair of unknowns, $\delta = \text{Re}(k_{V_1})l$ and $M = e^{\text{Im}(k_{V_1})l}$, has been considered, where recall that k_{V_1} is the wave number of the longitudinal waves in the viscoelastic medium, and l is the thickness of the viscoelastic layer. Hence, the exponential dependence of the transmission and reflection coefficients with respect to the unknowns is avoided.

The exponential terms depending on the Young modulus in the system (3.23) can be rewritten in terms of $\delta = \text{Re}(k_{V_1})l$ and $M = e^{\text{Im}(k_{V_1})l}$. Then, keeping in mind that $Z_V = \rho_V c_{V_t} = \rho_V \frac{\omega}{k_{V_t}} = \frac{\rho_V \omega l}{\delta + i \log M}$, the system (3.23) is rewritten as

$$\left\{
\begin{aligned}
& -\cos \theta_1 A_1 + \cos \theta_{V_1} A_{V_1} - \cos \theta_{V_1} B_{V_1} - \sin \theta_{V_t} A_{V_t} + \sin \theta_{V_t} B_{V_t} = -\cos \theta_1 B_1, \\
& \frac{Z_F}{Z_V} A_1 - \left(\frac{2\mu}{2\mu + \lambda} \cos^2 \theta_{V_1} + \frac{\lambda}{2\mu + \lambda} \right) A_{V_1} \\
& \quad - \left(\frac{2\mu}{2\mu + \lambda} \cos^2 \theta_{V_1} + \frac{\lambda}{2\mu + \lambda} \right) B_{V_1} \\
& + \frac{2\mu}{2\mu + \lambda} \frac{k_{V_t}}{k_{V_1}} \sin \theta_{V_t} \cos \theta_{V_t} A_{V_t} + \frac{2\mu}{2\mu + \lambda} \frac{k_{V_t}}{k_{V_1}} \sin \theta_{V_t} \cos \theta_{V_t} B_{V_t} = -\frac{Z_F}{Z_V} B_1, \\
& -2 \sin \theta_{V_1} \cos \theta_{V_1} A_{V_1} + 2 \sin \theta_{V_1} \cos \theta_{V_1} B_{V_1} - \frac{k_{V_t}}{k_{V_1}} (\cos^2 \theta_{V_t} - \sin^2 \theta_{V_t}) A_{V_t} \\
& \quad + \frac{k_{V_t}}{k_{V_1}} (\cos^2 \theta_{V_t} - \sin^2 \theta_{V_t}) B_{V_t} = 0, \\
& -\cos \theta_{V_1} M^{\cos \theta_{V_1}} e^{-i\delta \cos \theta_{V_1}} A_{V_1} + \cos \theta_{V_1} \frac{e^{i\delta \cos \theta_{V_1}}}{M^{\cos \theta_{V_1}}} B_{V_1} \\
& + \sin \theta_{V_t} M^{\frac{\text{Im} k_{V_t}}{\text{Im} k_{V_1}} \cos \theta_{V_t}} e^{-i\delta \frac{\text{Re} k_{V_t}}{\text{Re} k_{V_1}} \cos \theta_{V_t}} A_{V_t} - \sin \theta_{V_t} \frac{e^{i\delta \frac{\text{Re} k_{V_t}}{\text{Re} k_{V_1}} \cos \theta_{V_t}}}{M^{\frac{\text{Im} k_{V_t}}{\text{Im} k_{V_1}} \cos \theta_{V_t}}} B_{V_t} \\
& \quad - \cos \theta_3 e^{i k_F \cos \theta_3 l} B_3 = 0, \\
& \left(\frac{2\mu}{2\mu + \lambda} \cos^2 \theta_{V_1} + \frac{\lambda}{2\mu + \lambda} \right) M^{\cos \theta_{V_1}} e^{-i\delta \cos \theta_{V_1}} A_{V_1} \\
& \quad + \left(\frac{2\mu}{2\mu + \lambda} \cos^2 \theta_{V_1} + \frac{\lambda}{2\mu + \lambda} \right) \frac{e^{i\delta \cos \theta_{V_1}}}{M^{\cos \theta_{V_1}}} B_{V_1} \\
& - \frac{2\mu}{2\mu + \lambda} \frac{k_{V_t}}{k_{V_1}} \sin \theta_{V_t} \cos \theta_{V_t} M^{\frac{\text{Im} k_{V_t}}{\text{Im} k_{V_1}} \cos \theta_{V_t}} e^{-i\delta \frac{\text{Re} k_{V_t}}{\text{Re} k_{V_1}} \cos \theta_{V_t}} A_{V_t} \\
& - \frac{2\mu}{2\mu + \lambda} \frac{k_{V_t}}{k_{V_1}} \sin \theta_{V_t} \cos \theta_{V_t} \frac{e^{i\delta \frac{\text{Re} k_{V_t}}{\text{Re} k_{V_1}} \cos \theta_{V_t}}}{M^{\frac{\text{Im} k_{V_t}}{\text{Im} k_{V_1}} \cos \theta_{V_t}}} B_{V_t} - \frac{Z_F}{Z_V} e^{i k_F \cos \theta_3 l} B_3 = 0, \\
& -2 \sin \theta_{V_1} \cos \theta_{V_1} M^{\cos \theta_{V_1}} e^{-i\delta \cos \theta_{V_1}} A_{V_1} + 2 \sin \theta_{V_1} \cos \theta_{V_1} \frac{e^{i\delta \cos \theta_{V_1}}}{M^{\cos \theta_{V_1}}} B_{V_1} \\
& - \frac{k_{V_t}}{k_{V_1}} (\cos^2 \theta_{V_t} - \sin^2 \theta_{V_t}) M^{\frac{\text{Im} k_{V_t}}{\text{Im} k_{V_1}} \cos \theta_{V_t}} e^{-i\delta \frac{\text{Re} k_{V_t}}{\text{Re} k_{V_1}} \cos \theta_{V_t}} A_{V_t} \\
& + \frac{k_{V_t}}{k_{V_1}} (\cos^2 \theta_{V_t} - \sin^2 \theta_{V_t}) \frac{e^{i\delta \frac{\text{Re} k_{V_t}}{\text{Re} k_{V_1}} \cos \theta_{V_t}}}{M^{\frac{\text{Im} k_{V_t}}{\text{Im} k_{V_1}} \cos \theta_{V_t}}} B_{V_t} = 0,
\end{aligned} \tag{3.36}
\right.$$

where B_1 is the amplitude of the incident wave in the first compressible fluid that spreads to other media, which has been assumed as known.

Then, by using this change of unknowns, the reflection and the transmission coefficients can be computed, avoiding the spurious oscillations. Once these two coefficients are calculated, the scattered and the transmitted field are obtained by using the expressions (3.22) and (3.20). Now, it is necessary to rewrite the fitting problem considering this new pair of unknowns. Let L_j^{\exp} be the experimental values obtained by measuring the level under study, for $j = 1, \dots, N_L$, being N_L the number of considered frequencies, and let $\widehat{L}(M_j, \delta_j, \omega_j)$ be the computed numerical values of the level under consideration, for $j = 1, \dots, N_L$, where M_j and δ_j are the novel unknowns, and ω_j is the fixed angular frequency. If the cost function is defined as

$$\Upsilon_L(M_j, \delta_j, \omega_j) = \frac{|L_j^{\exp} - \widehat{L}(M_j, \delta_j, \omega_j)|^2}{|L_j^{\exp}|^2}, \quad \forall j = 1, \dots, N_L, \quad (3.37)$$

the fitting problem is stated as follows: Find the values $M_{j*} \geq 0$ and $\delta_{j*} \geq 0$ such that minimize the difference between the experimental and the numerical values, i.e.,

$$(M_{j*}, \delta_{j*}) = \arg \min_{M_j, \delta_j > 0} \Upsilon_L(M_j, \delta_j, \omega_j), \quad \forall j = 1, \dots, N_L, \quad (3.38)$$

where M_j and δ_j are the novel unknowns given by $M_j = e^{\text{Im}(k_{V_1j})l}$ and $\delta_j = \text{Re}(k_{V_1j})l$, and L is the fitted level (in this chapter L can be the echo reduction level, the insertion loss, or the fractional power dissipation).

In this new strategy, an algorithm of type trust-region reflective (see [59]) has been used to solve the minimization problem (3.38). This algorithm is based in the interior-reflective Newton method (see [60] and [61] for more details), and requires the computation of the gradient of the functional to be minimized. Then, in the next section, the adjoint method is explained.

3.4.2 Adjoint problem

Since the optimization problem with the new unknowns is solved by using an algorithm which requires the computation of the gradient of the objective function, the adjoint method is used to reduce the computational cost [73, 84, 136].

Let $\mathbf{C} = (A_1, B_1, A_{V_1}, B_{V_1}, A_{V_t}, B_{V_t}, A_3, B_3)$ be the solution of the system (3.36) (state variables), and $\mathbf{q} = (M, \delta)$ the parameters in the model (control variables). The equation of state can be written as follows

$$\mathbf{g}(\mathbf{C}, \mathbf{q}) = A(\mathbf{q})\mathbf{C}(\mathbf{q}) - \mathbf{b}(\mathbf{q}) = \mathbf{0}, \quad (3.39)$$

where A is the matrix of the system (3.36), and \mathbf{b} is the right-hand side. If the parameters \mathbf{q} are known, the solution of (3.39) could be computed by using the direct problem explained in Section 3.3. However, the solution of the inverse problem could be difficult. To approximate the gradient of the state equation (3.39), it is possible to use methods such as finite differences over the parameters, increasing the computational cost of the problem. Adjoint

methods give an efficient way to evaluate the derivative of (3.39), with a cost independent of the number of parameters, and that usually is no greater than solving the state equation once.

It is supposed that \mathbf{C} is the solution of the system of linear equations $A\mathbf{C} = \mathbf{b}$, where A , \mathbf{C} , and \mathbf{b} depend on the parameters \mathbf{q} . Then, to evaluate the gradient of \mathbf{g} ,

$$\begin{aligned}\nabla_{\mathbf{q}}\mathbf{g} &= \mathbf{g}_{\mathbf{q}} + \mathbf{g}_{\mathbf{C}}\mathbf{C}_{\mathbf{q}} \\ &= \left(\frac{\partial \mathbf{g}}{\partial q_1}, \frac{\partial \mathbf{g}}{\partial q_2}, \dots, \frac{\partial \mathbf{g}}{\partial q_{N_q}} \right) + \left(\frac{\partial \mathbf{g}}{\partial C_1}, \frac{\partial \mathbf{g}}{\partial C_2}, \dots, \frac{\partial \mathbf{g}}{\partial C_{N_C}} \right) \begin{pmatrix} \frac{\partial C_1}{\partial q_1} & \frac{\partial C_1}{\partial q_2} & \dots & \frac{\partial C_1}{\partial q_{N_q}} \\ \vdots & \vdots & & \vdots \\ \frac{\partial C_{N_C}}{\partial q_1} & \frac{\partial C_{N_C}}{\partial q_2} & \dots & \frac{\partial C_{N_C}}{\partial q_{N_q}} \end{pmatrix},\end{aligned}\quad (3.40)$$

where $\mathbf{g}_{\mathbf{q}}$ and $\mathbf{g}_{\mathbf{C}}$ are the gradient of \mathbf{g} with respect to the parameters (p_1, \dots, p_{N_p}) and the variables (C_1, \dots, C_{N_C}) , respectively. Once the function \mathbf{g} is given, $\mathbf{g}_{\mathbf{p}}$ and $\mathbf{g}_{\mathbf{C}}$ are easy to compute, but the computation of $\mathbf{C}_{\mathbf{p}}$ is challenging. Taking into account $A\mathbf{C} = \mathbf{b}$,

$$\frac{\partial A}{\partial q_i} \mathbf{C} + A \frac{\partial \mathbf{C}}{\partial q_i} = \frac{\partial \mathbf{b}}{\partial q_i} \Rightarrow \frac{\partial \mathbf{C}}{\partial q_i} = A^{-1} \left(\frac{\partial \mathbf{b}}{\partial q_i} - \frac{\partial A}{\partial q_i} \mathbf{C} \right), \quad \forall i = 1, \dots, N_q. \quad (3.41)$$

Then, to solve the derivative of \mathbf{C} with respect to the parameters \mathbf{q} , it is necessary to solve a system of $M_C \times M_C$ equations for each component of the parameters vector. To overcome these difficulties the adjoint equation is solved

$$A^T \lambda = \mathbf{g}_{\mathbf{C}}^T \Rightarrow \mathbf{g}_{\mathbf{C}} = \lambda^T A. \quad (3.42)$$

Taking into account (3.41) and (3.42),

$$\begin{aligned}\mathbf{g}_{\mathbf{C}}\mathbf{C}_{\mathbf{q}} &= \mathbf{g}_{\mathbf{C}}(A^{-1}(\mathbf{b}_{\mathbf{q}} - A_{\mathbf{q}}\mathbf{C})) = (\mathbf{g}_{\mathbf{C}}A^{-1})(\mathbf{b}_{\mathbf{q}} - A_{\mathbf{q}}\mathbf{C}) = (\lambda^T AA^{-1})(\mathbf{b}_{\mathbf{q}} - A_{\mathbf{q}}\mathbf{C}) \\ &= \lambda^T(\mathbf{b}_{\mathbf{q}} - A_{\mathbf{q}}\mathbf{C}).\end{aligned}\quad (3.43)$$

By using (3.43), the gradient of \mathbf{g} given by (3.40) results

$$\nabla_{\mathbf{q}}\mathbf{g} = \mathbf{g}_{\mathbf{q}} + \mathbf{g}_{\mathbf{C}}\mathbf{C}_{\mathbf{q}} = \mathbf{g}_{\mathbf{q}} - \lambda^T(\mathbf{b}_{\mathbf{q}} - A_{\mathbf{q}}\mathbf{C}).$$

All the details of the computation of the gradient of the cost function with ER, IL, and FPD are shown in the Appendix 3.B.

3.5 Numerical results

Once the different constitutive laws over the Young modulus have been explained, and the objective functions have been described, the following section focuses on the numerical simulations of the inverse problem. First of all, code validation is performed to ensure the robustness of the methodology. For this purpose, some manufactured data have been

created. Then, the available experimental data are described, and these data are used to perform both the parametric and the non-parametric simulations. The numerical results are shown considering two different acoustic sources: a plane wave with an oblique incidence angle, and a source with a non-planar directivity pattern.

In all the numerical simulations, to compute the mass density of the water in terms of the hydrostatic pressure and the temperature, the standard IAPWS95 is used, *International Association for the Properties of Water and Steam, Formulation 1995*, (see [101] and [97] for more details). Also, it is supposed that the sound speed is given by a response function depending on the hydrostatic pressure and the temperature, following [20]. According to [23], the attenuation coefficient of the water results

$$\alpha = 0.11 \times 10^{-12} \frac{\ln 10}{(2\pi)^2} = 6.42 \times 10^{-16}.$$

Following [95], the length of the parametric array is $h = 1.88$ m and the constant $Q_0 = 1$.

3.5.1 Code validation

To validate the code, some simulations with manufactured data have been performed. Since a viscoelastic material is manufactured, it is necessary to consider the values of the Young modulus and the Poisson's ratio, which describe the elastic behavior of the material as well as the thickness and the mass density. In this case, it is considered the mass density $\rho_V = 2100$ kg/m³, the thickness $l = 0.05$ m, and the Poisson's ratio $\nu = 0.48$. It is supposed that the Young modulus is governed by an arbitrary frequency-dependent function (see Figure 3.5), that is, $E_j = E'_j - iE''_j$, $\forall j = 1, \dots, N_L$, where N_L is the number of considered frequencies.

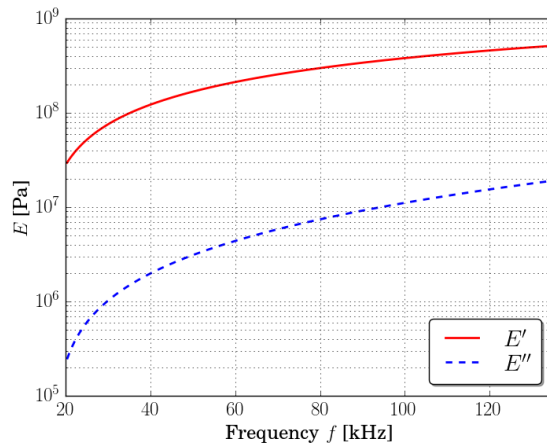


Figure 3.5: Values of the real and the imaginary parts (solid blue and dashed red line, respectively), which have been chosen as the Young modulus of the manufactured material.

Plane waves

By using the values of the Young modulus shown in Figure 3.5, and considering a plane wave as the acoustic source, it is possible to calculate the echo reduction level, the insertion loss, and the fractional power dissipation of the material by using the definitions appearing in Section 3.2.3 with $S(\theta) = \delta_{\theta_0}$. The resulting manufactured data are shown in Figure 3.6. The validation code is done considering the fitting problem with the unknowns $\delta = \text{Re}(k_{V_1})l$

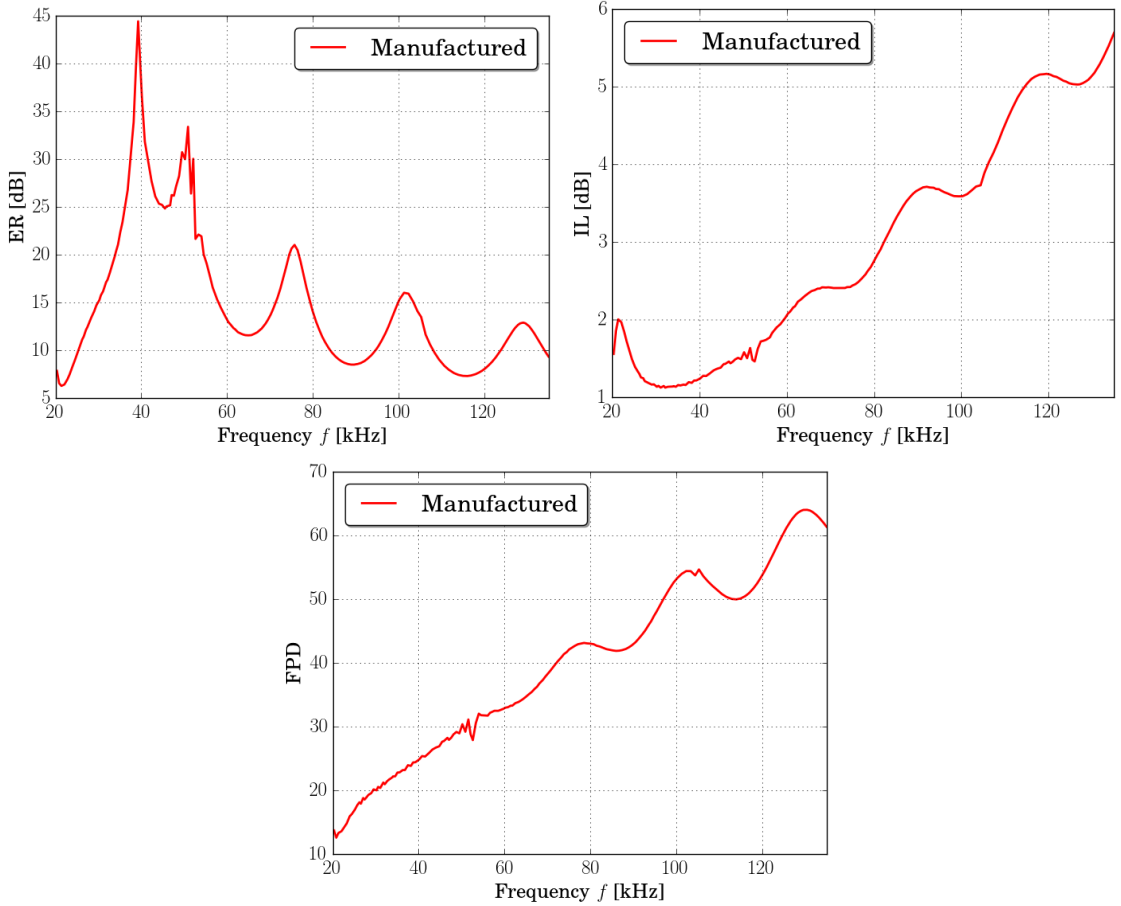


Figure 3.6: Manufactured values of the frequency response of a material with mass density $\rho_V = 2100 \text{ kg/m}^3$, thickness $l = 0.05 \text{ m}$, Poisson's ratio $\nu = 0.48$, and Young modulus shown in Figure 3.5, for the echo reduction level (top left), insertion loss level (top right), and fractional power dissipation (bottom).

and $M = e^{\text{Im}(k_{V_1})l}$ (see Section 3.4.1 for more details). The fitting is performed for each level individually by using a trust-region reflective algorithm. The initial guess for the solver has been computed, finding the absolute minimum of a function of two variables in a two-dimensional Cartesian discrete grid for the higher frequency. The considered grid is $(M, \delta) \in [10^{-2}, 10^2] \times [1, 100]$, and the cost function is (3.44). With this strategy, the guess value of the Young modulus is $E = 5.14 \times 10^8 - i1.91 \times 10^7 \text{ Pa}$. The results of the fitting of the echo reduction level, the insertion loss, and the fractional power dissipation

are shown in Figures 3.7, 3.8, and 3.9, respectively. In the left plots, the manufactured data, with solid blue line, and the optimized values, with dashed red line of each level are plotted with respect to the frequency. In the right plots, the real and the imaginary parts of the Young modulus are plotted. The fitting problem solved to obtain the optimized values is given by (3.38), and the relative errors are $\varepsilon_{\text{ER}} = 5.68\%$, $\varepsilon_{\text{IL}} = 4.04 \times 10^{-11}\%$, and $\varepsilon_{\text{FPD}} = 2.86 \times 10^{-1}\%$. Table 3.1 shows the relative errors in the single fittings. The cells

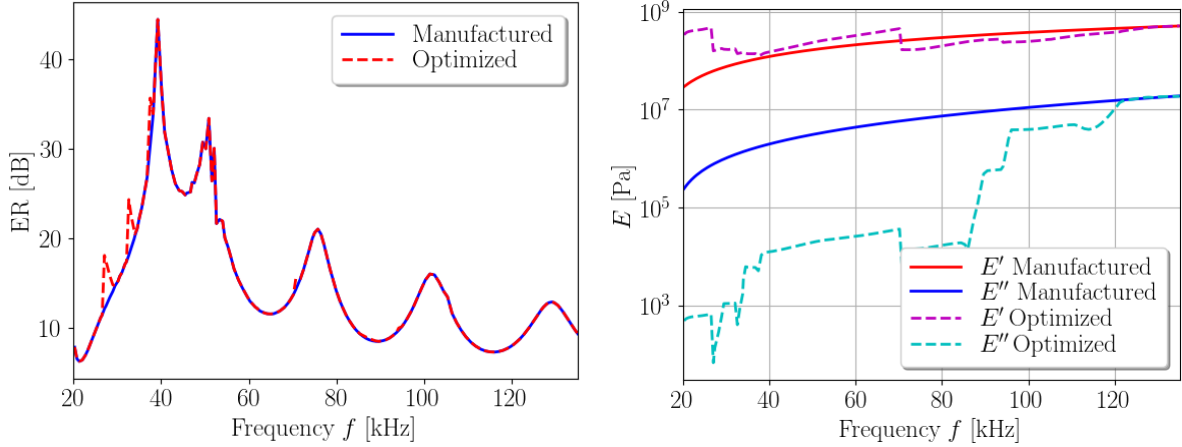


Figure 3.7: Left: Manufactured (solid blue line) and optimized (dashed red line) values of the echo reduction level plotted with respect to the frequency. Right: Values of the real and imaginary parts of the Young modulus (solid line: manufactured data, dashed line: optimized ones). The fitting problem under consideration is (3.38) where $L = \text{ER}$. The relative error is $\varepsilon_{\text{ER}} = 5.68\%$.

	ER fitting	IL fitting	FPD fitting
ε_{ER}	5.68%	71.43%	65.75%
ε_{IL}	54.45%	$4.04 \times 10^{-11}\%$	27.41%
ε_{FPD}	67.25%	16.20%	$2.86 \times 10^{-1}\%$

Table 3.1: Relative errors in the single fitting, using the primal unknowns M and δ . The minimization problem is given by (3.38). The relative errors are computed by using (3.37), where L is ER, IL, and FPD, respectively.

highlighted in grey are the errors due to the single fitting. The rest of the errors in the same column are obtained from computing the values of the rest of the levels with the optimal values of the single fitting. These errors are smaller than 1% for IL and FPD fittings, and lower than 6% for ER. Moreover, as it can be observed in the right plots of Figures 3.13 and 3.14, the obtained real and imaginary parts of the Young modulus have similar behavior than the manufactured one given in Figure 3.5. However, for the ER fitting, the behavior is quite different and non-smooth. For this reason, a joint fitting is performed. The considered minimization problem is (3.44). The numerical results are shown in Figure 3.15.

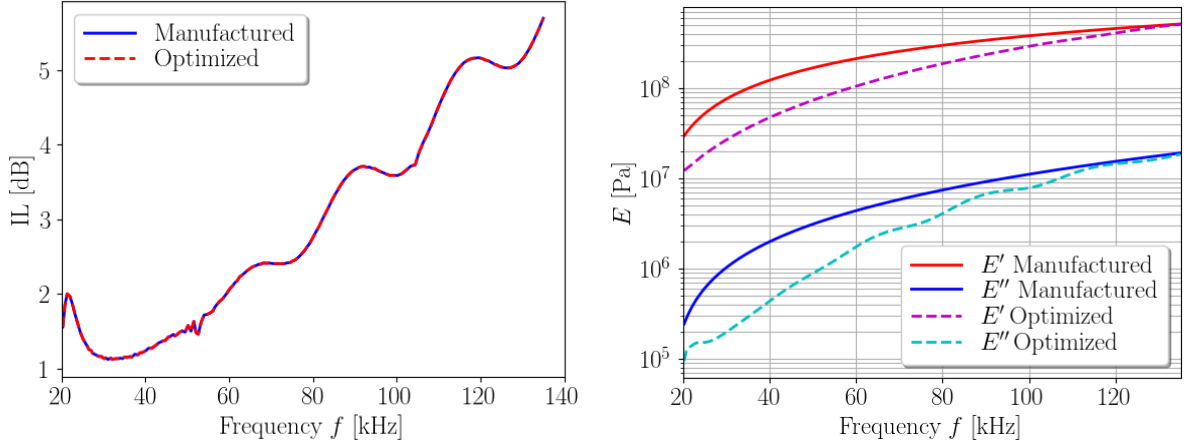


Figure 3.8: Left: Manufactured (solid blue line) and optimized (dashed red line) values of the insertion loss level plotted with respect to the frequency. Right: Values of the real and imaginary parts of the Young modulus (solid line: manufactured data, dashed line: optimized ones). The fitting problem is given by (3.38) where $L = IL$. The relative error is $\varepsilon_{IL} = 4.04 \times 10^{-11}\%$.

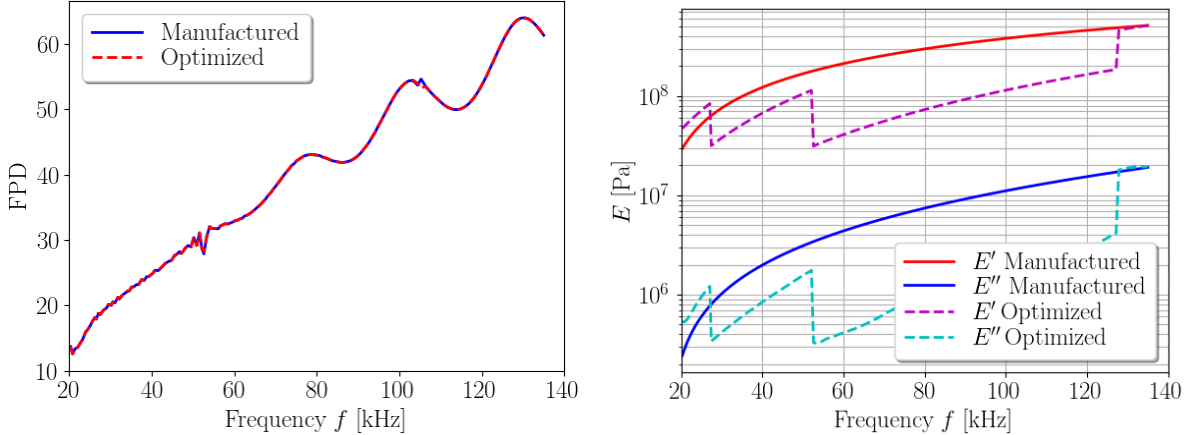


Figure 3.9: Left: Manufactured (solid blue line) and optimized (dashed red line) values of the fractional power dissipation plotted with respect to the frequency. Right: Values of the real and imaginary parts of the Young modulus (solid line: manufactured data, dashed line: optimized ones). The considered fitting problem is (3.38) where $L = FPD$. The relative error is $\varepsilon_{FPD} = 2.86 \times 10^{-1}\%$.

The comparison between the experimental data and the optimized ones is shown in the top left, top right, and bottom left plots of Figure 3.10 for the echo reduction level, the insertion loss, and the fractional power dissipation, respectively. In the bottom right plot, the real and the imaginary parts of the Young modulus are plotted. The relative errors of single fittings computed by using (3.37) are $\varepsilon_{ER} = 30.76\%$, $\varepsilon_{IL} = 3.97\%$, and $\varepsilon_{FPD} = 4.96\%$.

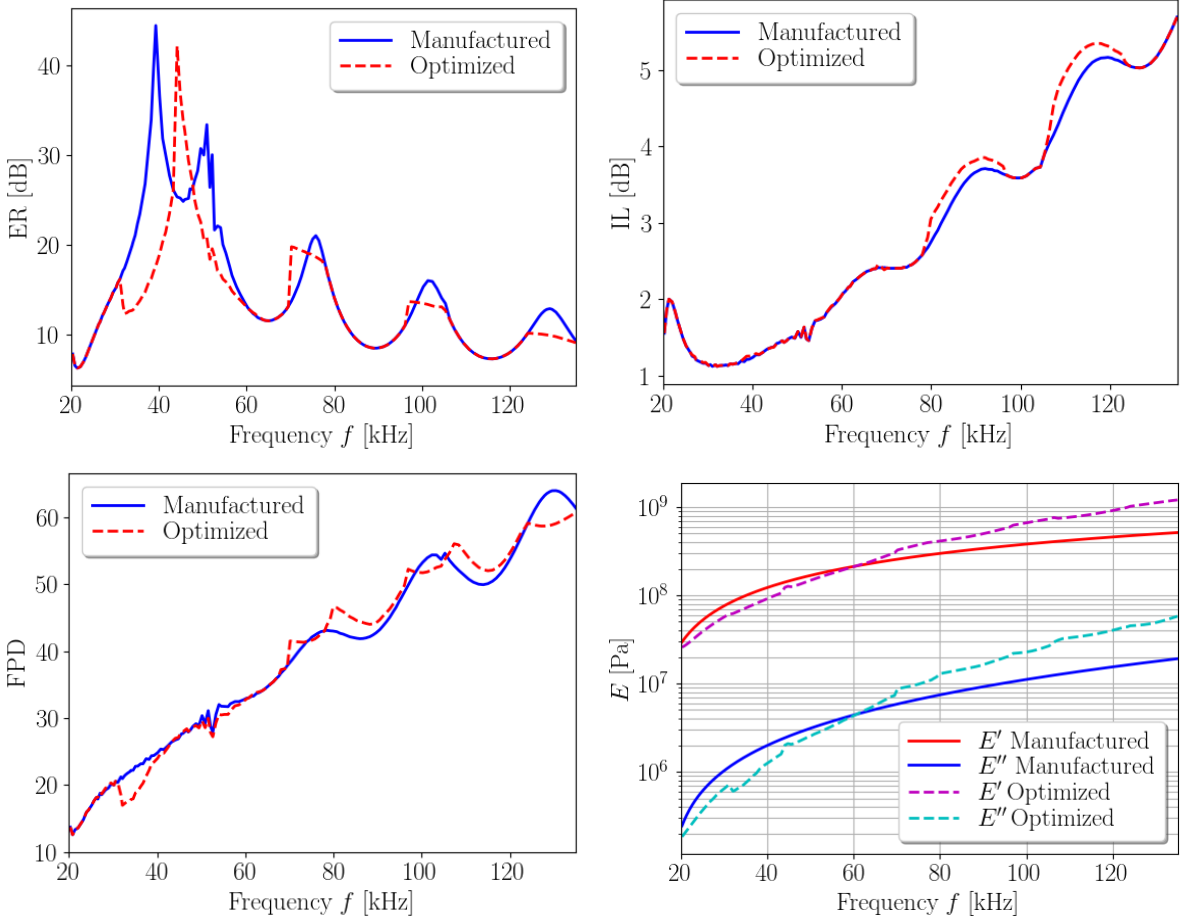


Figure 3.10: Manufactured (solid blue line) and optimized (dashed red line) values of the echo reduction level (top left), insertion loss (top right), and fractional power dissipation (bottom left) plotted with respect to the frequency for the joint fitting. Bottom right: Values of the real and imaginary parts of the Young modulus (solid line: manufactured data, dashed line: optimized ones). The considered fitting problem is (3.44). The relative errors are $\varepsilon_{\text{ER}} = 30.76\%$, $\varepsilon_{\text{IL}} = 3.97\%$, and $\varepsilon_{\text{FPD}} = 4.96\%$.

With the joint fitting, the Young modulus presents a smoother behavior than with the single fitting, but the error with the ER level is higher.

Acoustic source with a non-planar directivity pattern

By using the values of the Young modulus shown in Figure 3.5, and taking into account the directivity pattern of the acoustic source described in (3.17), the experimental data for the echo reduction, insertion loss, and fractional power dissipation can be computed by using the definitions appearing in Section 3.2.3. The resulting manufactured data are shown in Figure 3.11. The validation of the code is performed considering the fitting

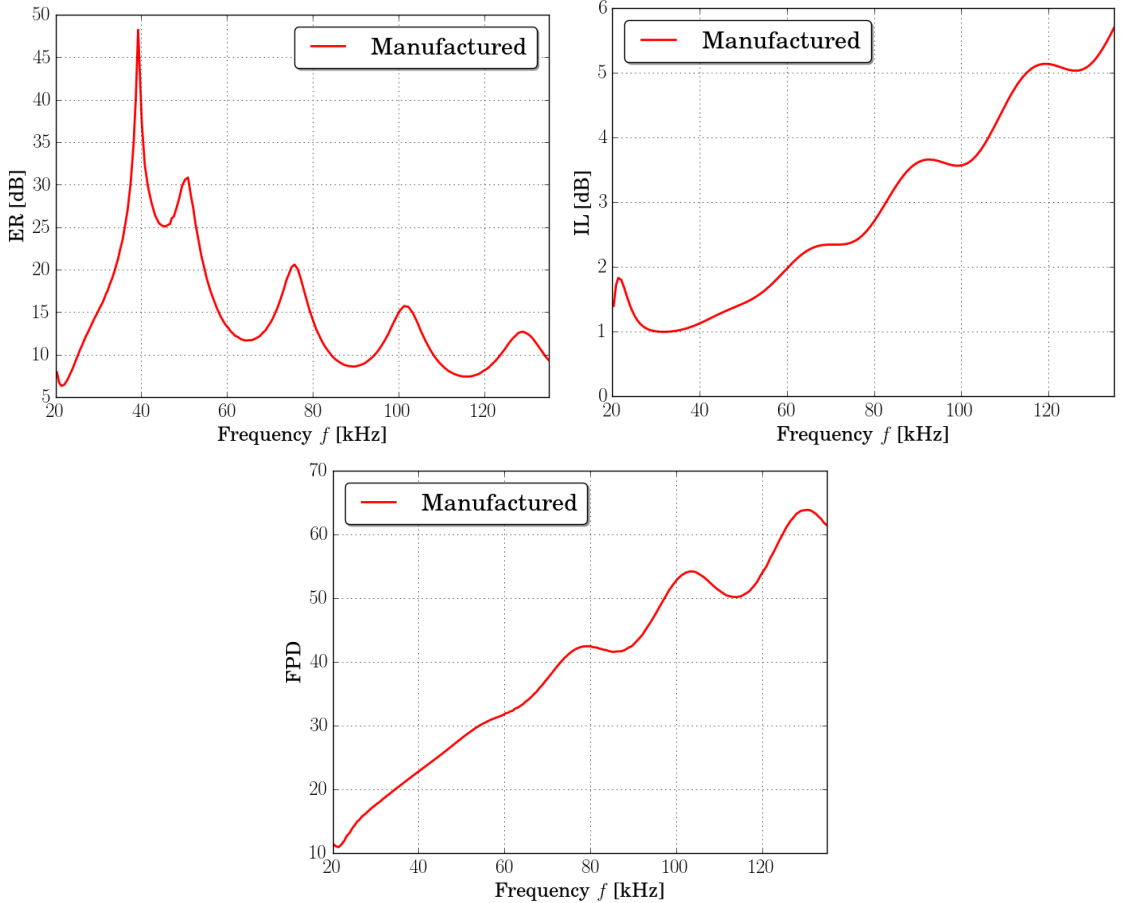


Figure 3.11: Manufactured values of the frequency response of a material with mass density $\rho_V = 2100 \text{ kg/m}^3$, thickness $l = 0.05 \text{ m}$, Poisson's ratio $\nu = 0.48$, and Young modulus shown in Figure 3.5, for the echo reduction level (top left), insertion loss level (top right), and fractional power dissipation (bottom).

problem with the unknowns $\delta = \operatorname{Re}(k_{V_1})l$ and $M = e^{\operatorname{Im}(k_{V_1})l}$ (see Section 3.4.1 for more details), and with the fitting of each level individually. To solve the fitting problem, a trust-region reflective algorithm has been used. The initial guess has been computed, finding the absolute minimum of a function of two variables in a two-dimensional Cartesian discrete grid for the higher frequency. The considered grid is $(M, \delta) \in [10^{-2}, 10^2] \times [1, 100]$, and the cost function is given by (3.44). With this strategy, the guess value of the Young modulus is $E = 5.09 \times 10^8 - i1.84 \times 10^7 \text{ Pa}$. The results of the fitting of the echo reduction level, the insertion loss, and the fractional power dissipation are shown in Figures 3.12, 3.13, and 3.14, respectively. In left plots, the experimental data, with solid blue line, and the optimized values, with dashed red line) of each level are plotted with respect to the frequency. In the right plots, the real and the imaginary parts of the Young modulus are plotted. The fitting problem solved to obtain the optimized values is given by (3.38), and the relative errors are $\varepsilon_{\text{ER}} = 23.76\%$, $\varepsilon_{\text{IL}} = 4.21 \times 10^{-11}\%$, and $\varepsilon_{\text{FPD}} = 4.65 \times 10^{-10}\%$.

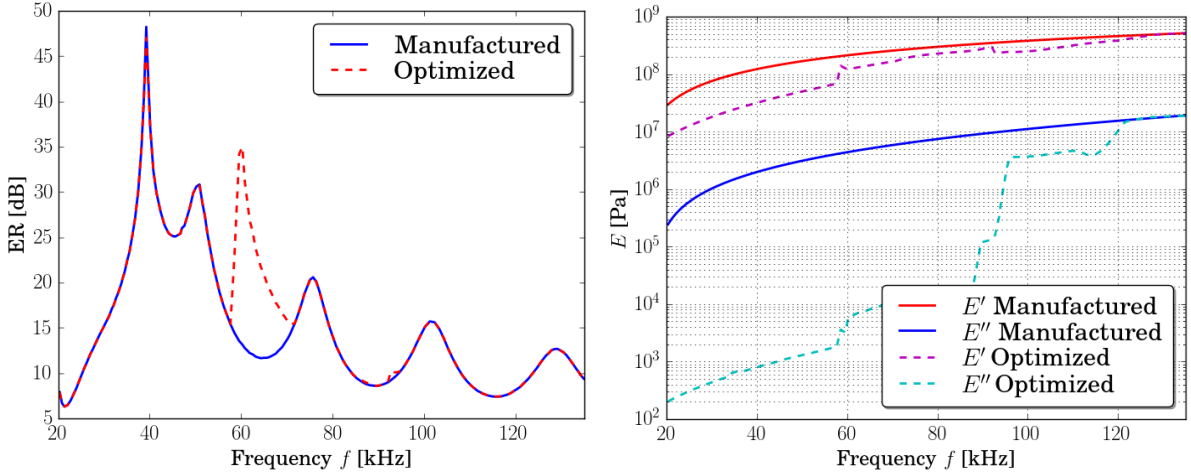


Figure 3.12: Left: Manufactured (solid blue line) and optimized (dashed red line) values of the echo reduction level plotted with respect to the frequency. Right: Values of the real and imaginary parts of the Young modulus (solid line: manufactured data, dashed line: optimized ones). The fitting problem under consideration is (3.38) where $L = ER$. The relative error is $\varepsilon_{ER} = 23.76\%$.

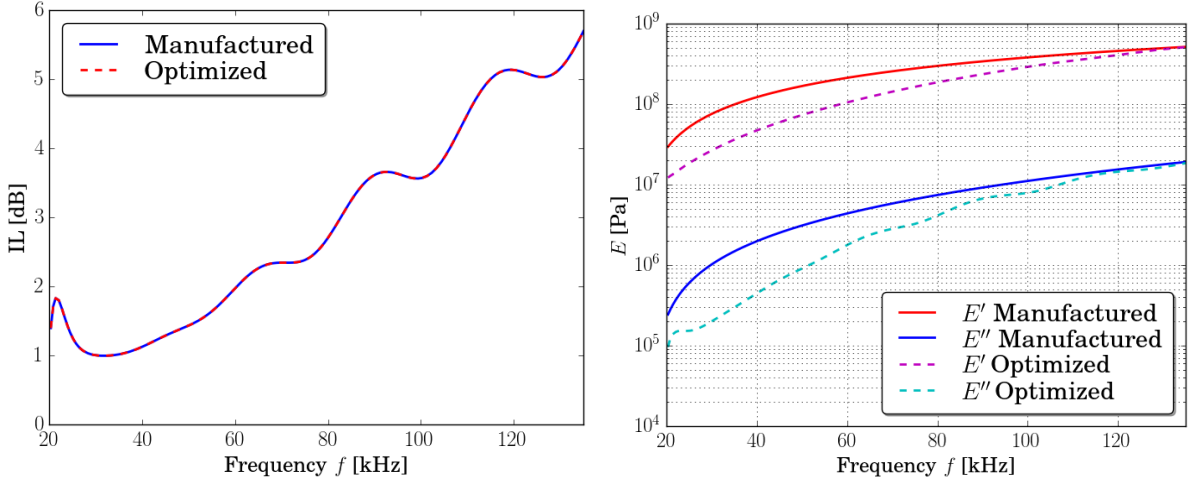


Figure 3.13: Left: Manufactured (solid blue line) and optimized (dashed red line) values of the insertion loss level plotted with respect to the frequency. Right: Values of the real and imaginary parts of the Young modulus (solid line: manufactured data, dashed line: optimized ones). The fitting problem is given by (3.38) where $L = IL$. The relative error is $\varepsilon_{IL} = 4.21 \times 10^{-11}\%$.

In Table 3.2, the relative errors obtained in the single fittings are given. The highlighted cells are the errors due to the single fitting. The rest of the errors in the same column are obtained from computing the values of the rest of the levels with the optimal values of the

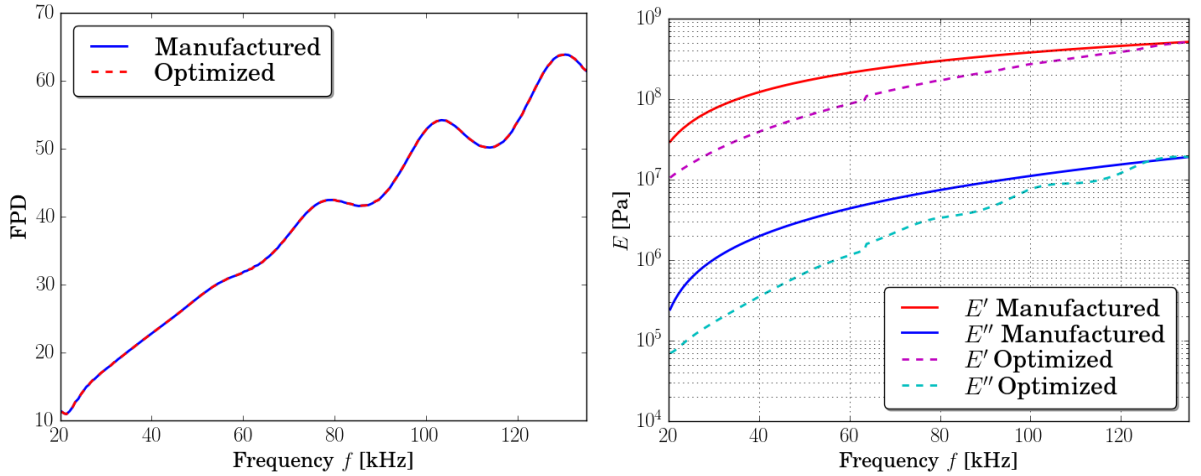


Figure 3.14: Left: Manufactured (solid blue line) and optimized (dashed red line) values of the fractional power dissipation plotted with respect to the frequency. Right: Values of the real and imaginary parts of the Young modulus (solid line: manufactured data, dashed line: optimized ones). The considered fitting problem is (3.38) where $L = \text{FPD}$. The relative error is $\varepsilon_{\text{FPD}} = 4.65 \times 10^{-10}\%$.

	ER fitting	IL fitting	FPD fitting
ε_{ER}	23.76%	70.88%	59.93%
ε_{IL}	57.80%	$4.21 \times 10^{-11}\%$	26.49%
ε_{FPD}	71.77%	16.16%	$4.65 \times 10^{-10}\%$

Table 3.2: Relative errors in the single fitting, using the primal unknowns M and δ . The minimization problem is given by (3.38). The relative errors are computed by using (3.37), where L is ER, IL, and FPD, respectively.

fitting. These errors are negligible for the IL and the FPD fittings. However, the error for the ER fitting is larger than 20%. Moreover, as it can be observed in the the right plots of Figures 3.13 and 3.14, the obtained real and imaginary parts of the Young modulus have similar behavior than the manufactured ones given in Figure 3.5. However, for the ER fitting, the behavior is quite different and non-smooth. For this reason, a joint fitting is performed. The considered minimization problem is (3.44). The numerical results are shown in Figure 3.15. The comparison between the experimental data and the optimized ones is shown in the top left, top right, and bottom left plots of Figure 3.15 for the echo reduction level, the insertion loss, and the fractional power dissipation, respectively. In the bottom right plot, the real and the imaginary parts of the Young modulus are plotted. The relative errors of single fittings computed by using (3.37) are $\varepsilon_{\text{ER}} = 8.87\%$, $\varepsilon_{\text{IL}} = 5.62\%$, and $\varepsilon_{\text{FPD}} = 2.49\%$. Although this problem is ill-posed because the experimental data are real (see Lemma 3.4.3), joint fitting errors smaller than 10% are achieved in all the levels. Moreover, the obtained Young modulus has similar behavior to the manufactured one, and

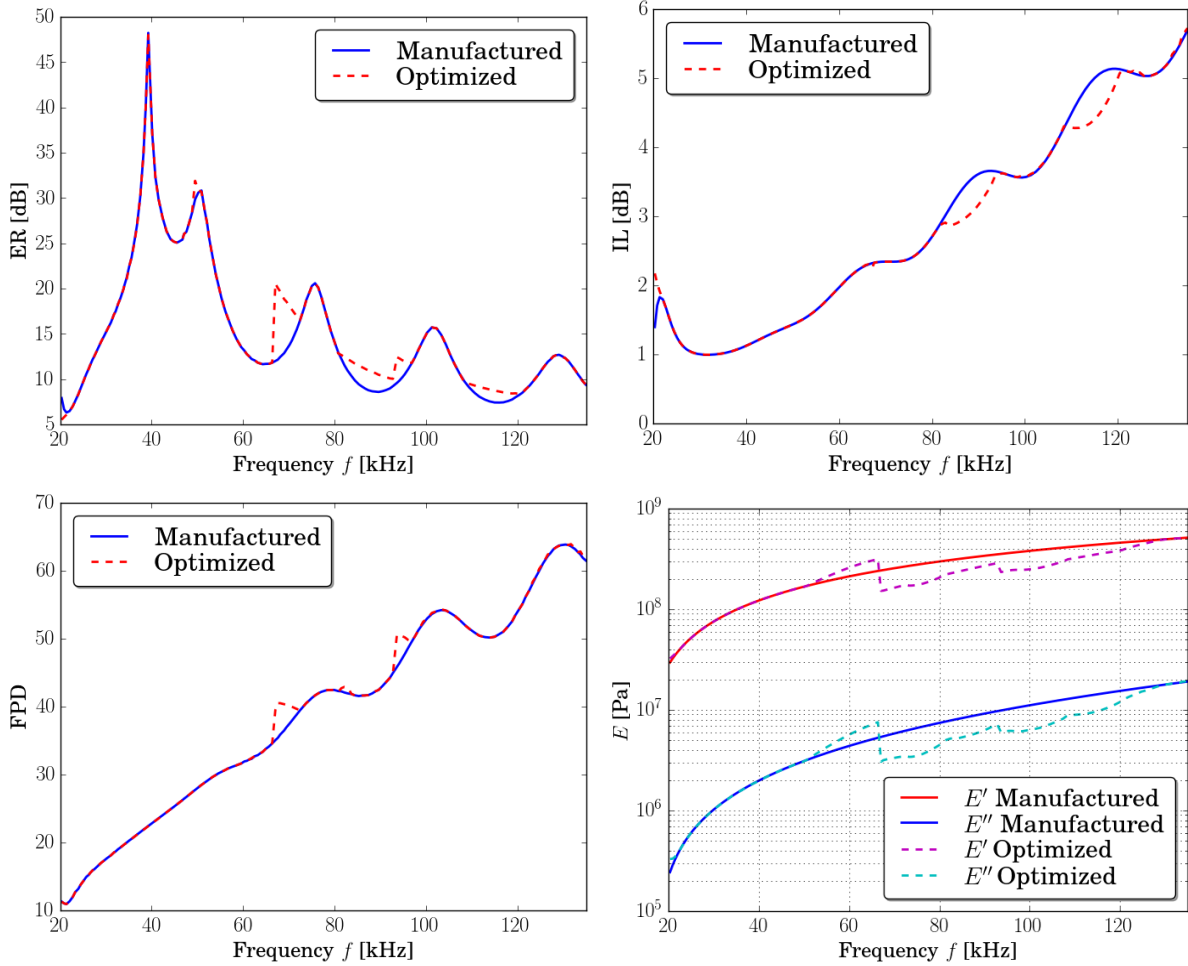


Figure 3.15: Manufactured (solid blue line) and optimized (dashed red line) values of the echo reduction level (top left), insertion loss (top right), and fractional power dissipation (bottom left) plotted with respect to the frequency for the joint fitting. Bottom right: Values of the real and imaginary parts of the Young modulus (solid line: manufactured data, dashed line: optimized ones). The considered fitting problem is (3.44). The relative errors are $\varepsilon_{\text{ER}} = 8.87\%$, $\varepsilon_{\text{IL}} = 5.62\%$, and $\varepsilon_{\text{FPD}} = 2.49\%$.

it is smooth (see Figure 3.5).

To illustrate the robustness of the proposed methodology with respect to the selected initial guess (used in the frequency-by-frequency non-linear optimization), a variety of initial iterants has been considered in a log-scaled 10×10 grid around the exact value. The fitting curves for the quantities of interest ER, IL, and FPD and also the real and imaginary parts of the Young modulus are plotted in Figure 3.16. To show a sharp estimation of the variability of this frequency response function, functional medians of these sets of functions have been computed. These functional medians correspond to curves that can be obtained for a particular initial guess. On the contrary, the computation of the pointwise-mean curve

would lead to a fictitious curve (see [151] for a detailed discussion), which does not represent any realization of the optimization procedure described in the sections above.

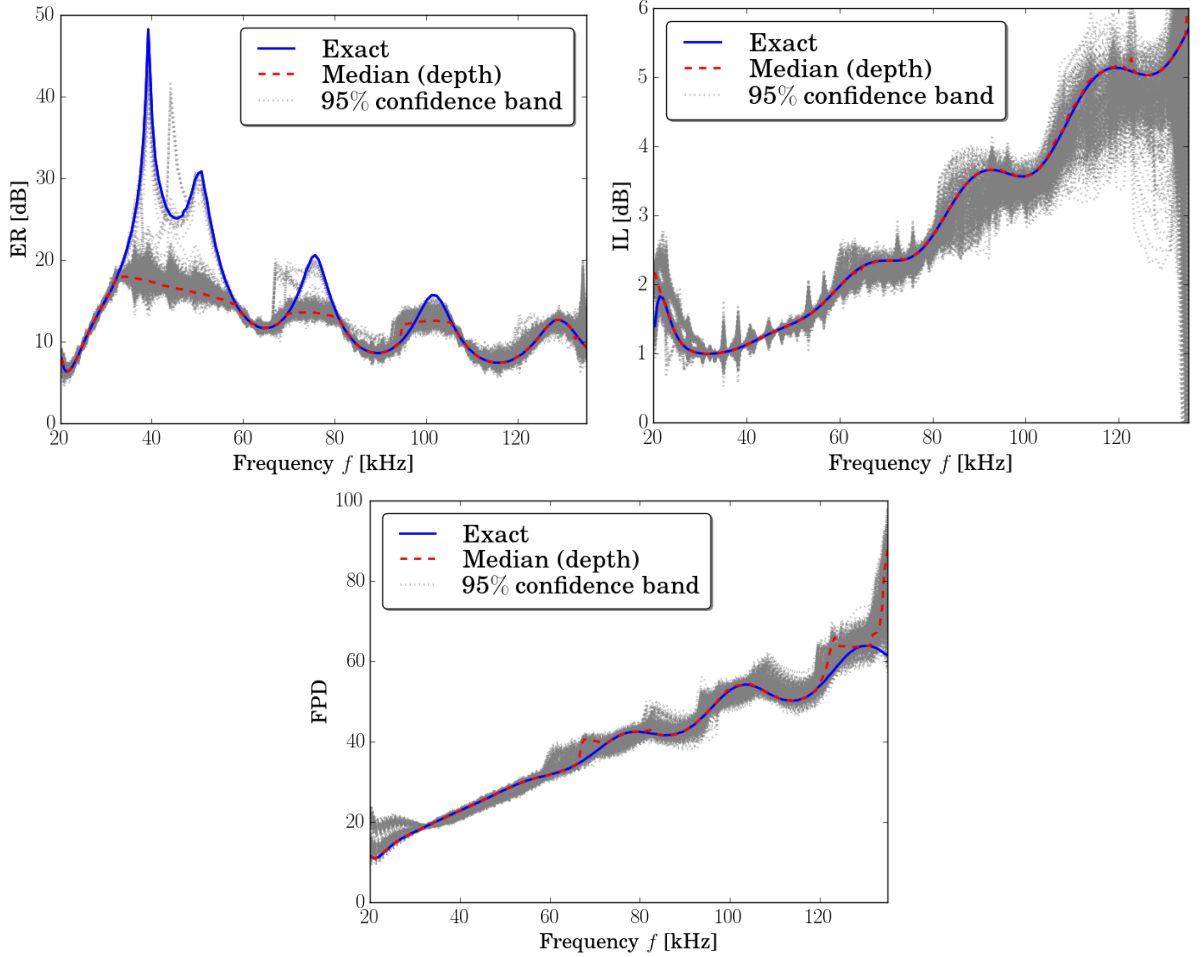


Figure 3.16: Manufactured values (solid blue line) of the echo reduction level (top left), insertion loss (top right), and fractional power dissipation (bottom) plotted with respect to the frequency for the joint fitting. Shaded grey lines represent the 95% confidence level bands computed by using the functional medians of sets of optimized curves, which are obtained by using different initial guesses in a grid. The dashed red line corresponds with the depth median. The fitting problem is given by (3.44).

Additionally, the associated functional 95% confidence level bands using the modal depth have also been computed (see [67] for further details). These functional computations have been performed using a bootstrap procedure with 500 resamples, and the smoothing parameter for the bootstrap samples, which is settled as a proportion of the sample variance matrix, has been fixed to 0.1 (more precisely, the R package fda.usc [77] has been used in the implementation).

As it can be observed in Figures 3.16 and 3.17, slight changes on the initial guess lead

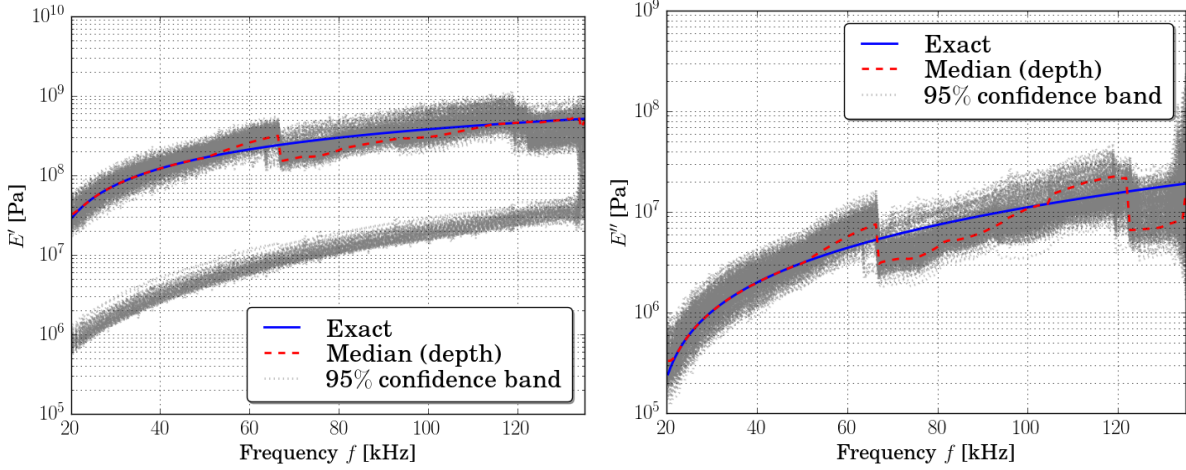


Figure 3.17: Manufactured values (solid blue line) of the real (left plot), and imaginary (right plot) parts of the Young modulus. Shaded grey lines represent the 95% confidence level bands computed by using the functional medians of sets of optimized curves, which are obtained by using different initial guesses in a grid. The dashed red line corresponds with the depth median. The used fitting problem is (3.44).

us to such different results in the fitting. Moreover, it is clear that not all the initial guess yields to the same optimal value for the Young modulus, which is consistent with the fact that the functional cost exhibits multiple local minima.

3.5.2 Experimental data

The material under consideration is the AptFlex SF5048 (see [5]). This material is a polymer and the company *Precision Acoustics* provides its dimensions, its mass density, and some frequency response plots of the Echo Reduction level (ER), the Insertion Loss (IL), and the Fractional Power Dissipation (FPD). In Figure 3.18, the frequency response of this polymeric plate is shown in a frequency range between 20 and 135 kHz, for ER (top left), IL (top right), and FPD (bottom).

In order to get the acoustic characterization of AptFlex SF5048 by using a viscoelastic model, it is necessary to compute the value of the two parameters, which describe the elastic behavior of the material, that is, the Poisson's ratio and the Young modulus. The main goal is to find the values of the elastic parameters which provide a frequency response as close as possible to the experimental measurements. For this purpose, the inverse problems described in Section 3.4 are solved. In all the numerical simulations, the Poisson's ratio is supposed known (see Remark 3.4.1 for more details), with value $\nu = 0.48$, following the work [98], which is the generic value for polyurethane elastomers. Besides, following the technical specifications provided by the supplier of the material Aptflex SF5048 (see [5]), the polymer mass density is $\rho_V = 2100 \text{ kg/m}^3$, and the thickness $l = 0.05 \text{ m}$.

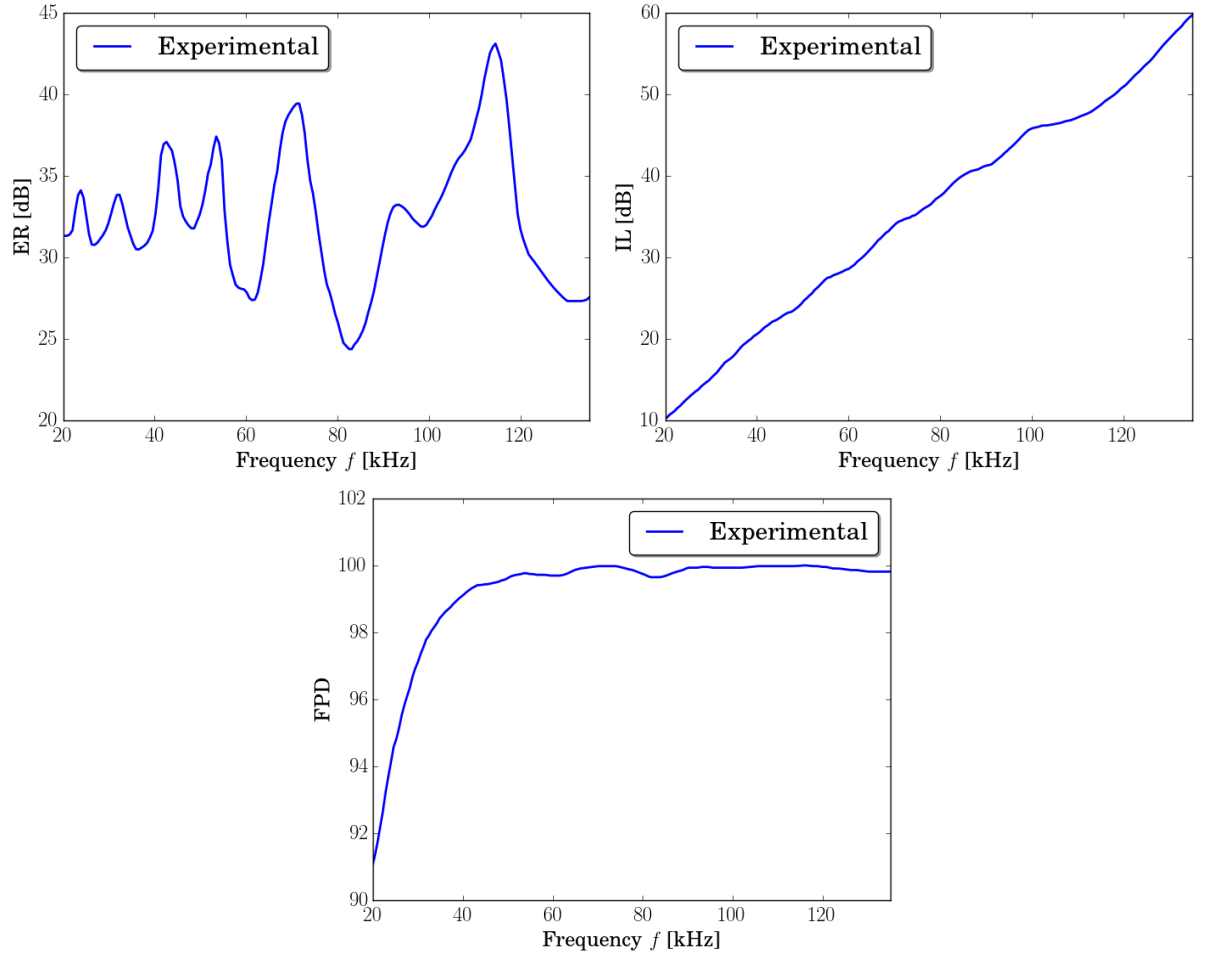


Figure 3.18: Experimental values of the frequency response of the AptFlex SF5048 for the echo reduction level (top left), the insertion loss (top right), and the fractional power dissipation (bottom).

3.5.3 Numerical simulation considering a parametric model

In this section, the numerical simulations are performed with the available experimental data, shown in Figure 3.18, by using the Kelvin-Voigt model and considering a plane wave with an oblique incidence angle as the acoustic source.

On the first hypothesis, the real and the imaginary parts of Young modulus are considered constants. More precisely, following [124], it was considered that the Young modulus of the polymer tile could be written as

$$E = E' - i\omega E''$$

where E' and E'' are assumed constant, that is, the used parametric model is the Kelvin-Voigt model. This fitting is performed by using an exhaustive search algorithm. Since the range for the real and the imaginary parts of the Young modulus is extensive, an

optimization strategy based on brute-force has been implemented. Although the algorithm is computationally more expensive, this strategy allows us to find the absolute minimum of a function of two variables in successive refined two-dimensional Cartesian discrete grids (see Section 3.4.1 for more details).

A multigrid of 300×300 points is considered, where $E' \in [10^4, 10^{10}]$, and $E'' \in [10^2, 10^8]$. The values of the cost function at each point of the multigrid have been computed, and the absolute minimum of these values is chosen as the optimal. This optimal value corresponds with a value of E'_1 and E''_1 . For performing a new iteration, it is necessary to give new limits for the multigrid. The new endpoints of the intervals are chosen fixing the optimal values of the Young modulus as the center of the interval, that is, a new multigrid of 300×300 points is considered, where $E' \in [E'_1 \times 10^{-0.5}, E'_1 \times 10^{0.5}]$ and $E'' \in [E''_1 \times 10^{-0.5}, E''_1 \times 10^{0.5}]$. Two iterations have been considered because the two obtained minima in these two iterations are closer than 10^{-2} .

	ER fitting	IL fitting	FPD fitting
E' [Pa]	1.0975×10^8	1.2328×10^9	7.5646×10^7
E'' [Pa]	14.1747	5.5908×10^3	114.9757
ε_{ER}	15.44%	89.93%	49.88%
ε_{IL}	66.64%	3.14%	238.53%
ε_{FPD}	39.41%	49.63%	2.86%

Table 3.3: Real and imaginary parts of the Young modulus, and relative errors in every single fitting, assuming than the Young modulus is a linear function of the frequency. The minimization problem under consideration is (3.33), and it has been solved by using an exhaustive search. The relative errors are computed by using (3.32), where L is ER, IL, and FPD.

The comparison between the experimental data and the optimized ones is shown in Figure 3.19 (top left: echo reduction level; top right: insertion loss; bottom: fractional power dissipation). Although the fitting for IL and FPD shows good agreement, the fitting for ER shows many oscillations in the frequency response of the optimization values. Table 3.3 shows the real and the imaginary parts of the Young modulus obtained with the minimization problem (3.33), and the relative error computed by using (3.32). Since the results are not good enough, especially for the acoustic coefficients that are not fitting, so a new strategy is considered.

3.5.4 Numerical simulation considering a non-parametric approach

In order to improve the results obtained with the parametric model, a non-parametric approach is considered in this section. As in the previous section, two different types of acoustic sources have been used: a plane wave with an oblique angle of incidence, and a parametric array with a non-planar directivity pattern. Different constitutive laws over the primal unknowns are used to overcome the difficulties.

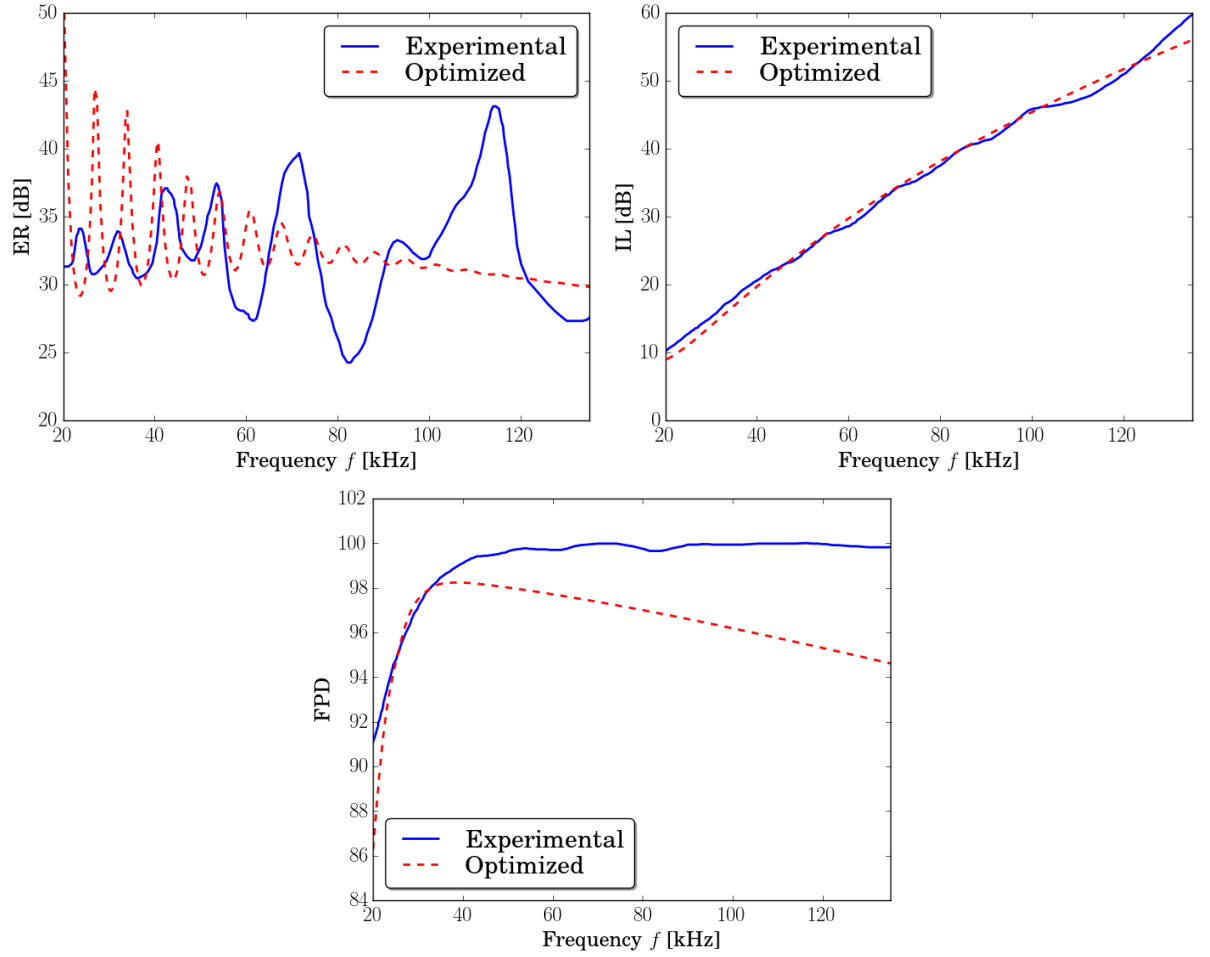


Figure 3.19: Experimental (solid blue line) and optimized (dashed red line) values of the echo reduction level (top left), the insertion loss (top right), and the fractional power dissipation (bottom) plotted with respect to the frequency. The considered fitting problem is (3.33), and an exhaustive search strategy is used. E' and E'' are considered constants, and the Young modulus is given by $E = E' - i\omega E''$. The optimal Young modulus and the relative errors are given in Table 3.3.

Plane waves

To improve the obtained results when both the real and the imaginary parts of the Young modulus are constants, it is here assumed that the real and the imaginary parts of the Young modulus are governed by an arbitrary smooth function that depends on the angular frequency, that is,

$$E(\omega) = E'(\omega) - iE''(\omega).$$

As in the previous case, to calculate the solution of the minimization problem (3.35) for the different acoustic quantities under consideration (ER, IL, and FPD), an optimization

strategy based on brute-force has been implemented. The parameters for the algorithm are the same as in the previous case, but in this case, three iterations are necessary to achieve than the two last obtained minima are closer than 10^{-2} .

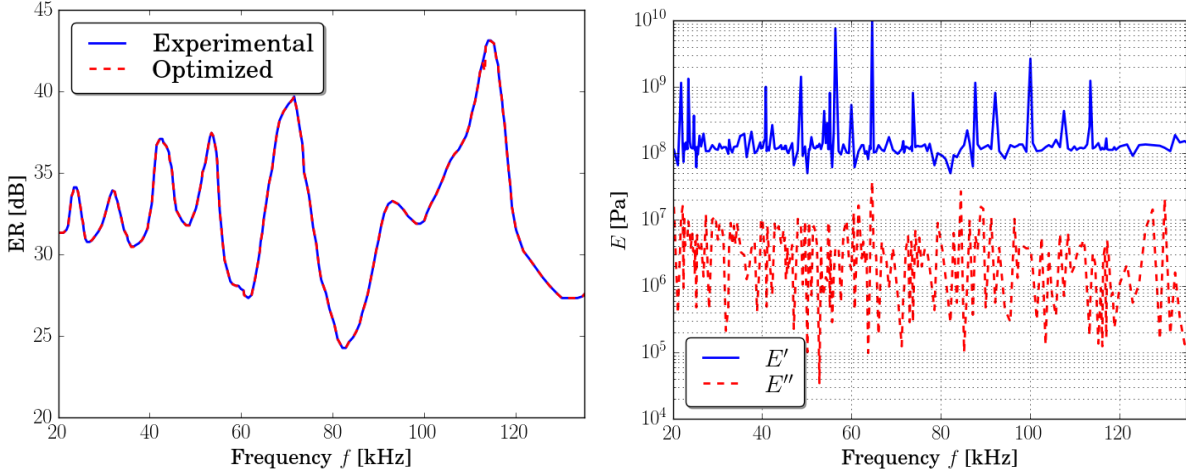


Figure 3.20: Left: Experimental (solid blue line) and optimized (dashed red line) values of the echo reduction level plotted with respect to the frequency. Right: Values of the real (solid blue line) and imaginary (dashed red line) part of the Young modulus. The considered fitting problem is (3.35) where $L = ER$ and an exhaustive search strategy is used. The relative errors are given in the first column in Table 3.4.

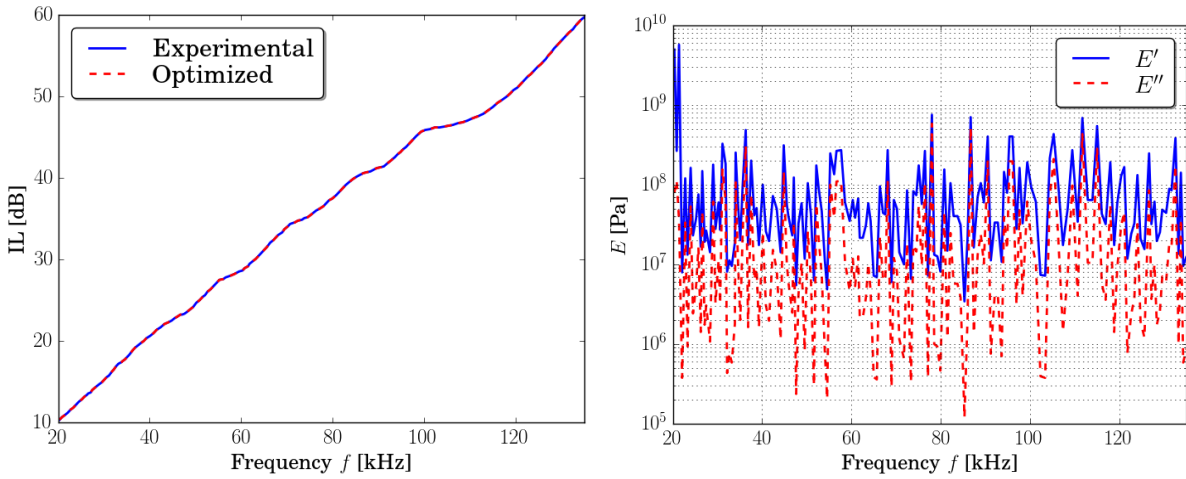


Figure 3.21: Left: Experimental (solid blue line) and optimized (dashed red line) values of the insertion loss level plotted with respect to the frequency. Right: Values of the real (solid blue line) and imaginary (dashed red line) part of the Young modulus. The considered fitting problem is given by (3.35) where $L = IL$ and an exhaustive search strategy is used. The relative errors are given in the second column in Table 3.4.

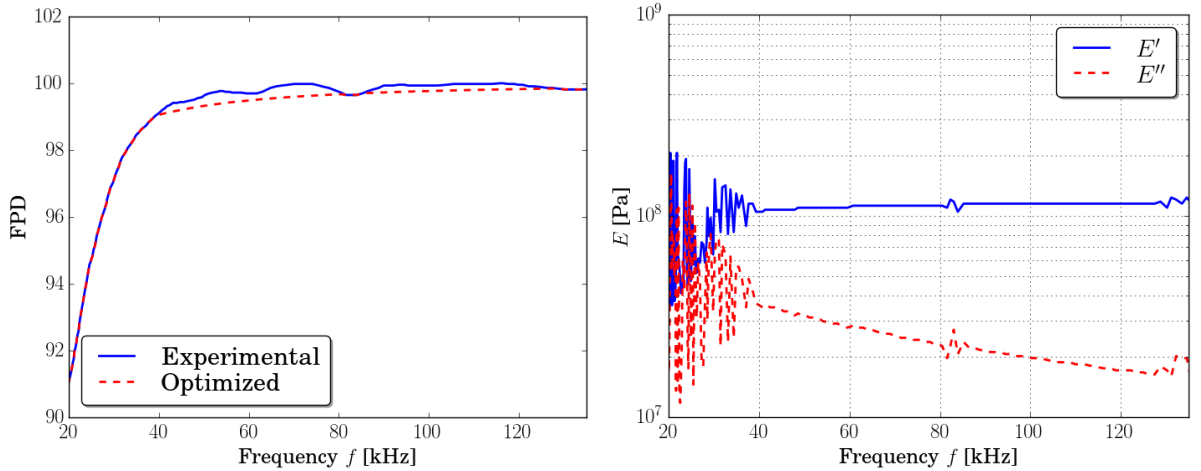


Figure 3.22: Left: Experimental (solid blue line) and optimized (dashed red line) values of the fractional power dissipation plotted with respect to the frequency. Right: Values of the real (solid blue line) and imaginary (dashed red line) part of the Young modulus. The fitting problem under consideration is (3.35) where $L = \text{FPD}$ and an exhaustive search strategy is used. The relative errors are given in the third column in Table 3.4.

	ER fitting	IL fitting	FPD fitting
ε_{ER}	0.24%	66.31%	39.24%
ε_{IL}	89.84%	$1.8166 \times 10^{-2}\%$	47.48%
ε_{FPD}	64.80%	19.75%	0.17%

Table 3.4: Relative errors in the single fitting, assuming than the Young modulus is governed by an arbitrary frequency-dependent function. The considered minimization problem is (3.35), and an exhaustive search strategy is used. The relative errors are computed by using (3.34), where L is ER, IL, and FPD, respectively.

The comparison between the experimental data and the optimized ones is shown in the left plot of Figures 3.20, 3.21, and 3.22 for the echo reduction level, the insertion loss, and the fractional power dissipation, respectively, showing a good agreement with the experimental data. In the right plot, the real and the imaginary parts of the Young modulus are plotted, showing an oscillatory behavior. As it is shown in Table 3.4, the relative errors computed by using (3.34) for the single fittings (highlighted in grey) are smaller than when a parametric model is used, but this fitting leads to results where both the real and the imaginary parts of the Young modulus present spurious oscillations. Notice that the behavior of the complex-valued Young modulus is qualitatively different from the smooth behavior shown in [98] for other polymeric materials.

To improve the results and get a smoother frequency response of the acoustic levels under study, instead of using the unknowns E' and E'' in the fitting procedure a novel pair of unknowns, depending on the wave number of the longitudinal waves in the viscoelastic

medium, k_{V_1} , and the thickness of the absorbing tile, l , have been chosen. It has been considered $\delta = \text{Re}(k_{V_1})l$ and $M = e^{\text{Im}(k_{V_1})l}$. As it has been explained in Section 3.4.1, an algorithm of type trust-region reflective (see [59]) has been used to solve the minimization problem. This algorithm requires the computation of the gradient of the functional to be minimized. In order to achieve better results, the fitting problem has been solved from upper to lower frequencies. To choose the initial guess, a multigrid exhaustive search algorithm has been used. One iteration in a multigrid with 500×500 points has been considered where $E' \in [E'_1 \times 10^{-0.5}, E'_1 \times 10^{0.5}]$ and $E'' \in [E''_1 \times 10^{-0.5}, E''_1 \times 10^{0.5}]$. Moreover, at each frequency, the previous optimal value is chosen as guess for the next frequency. Figure 3.23

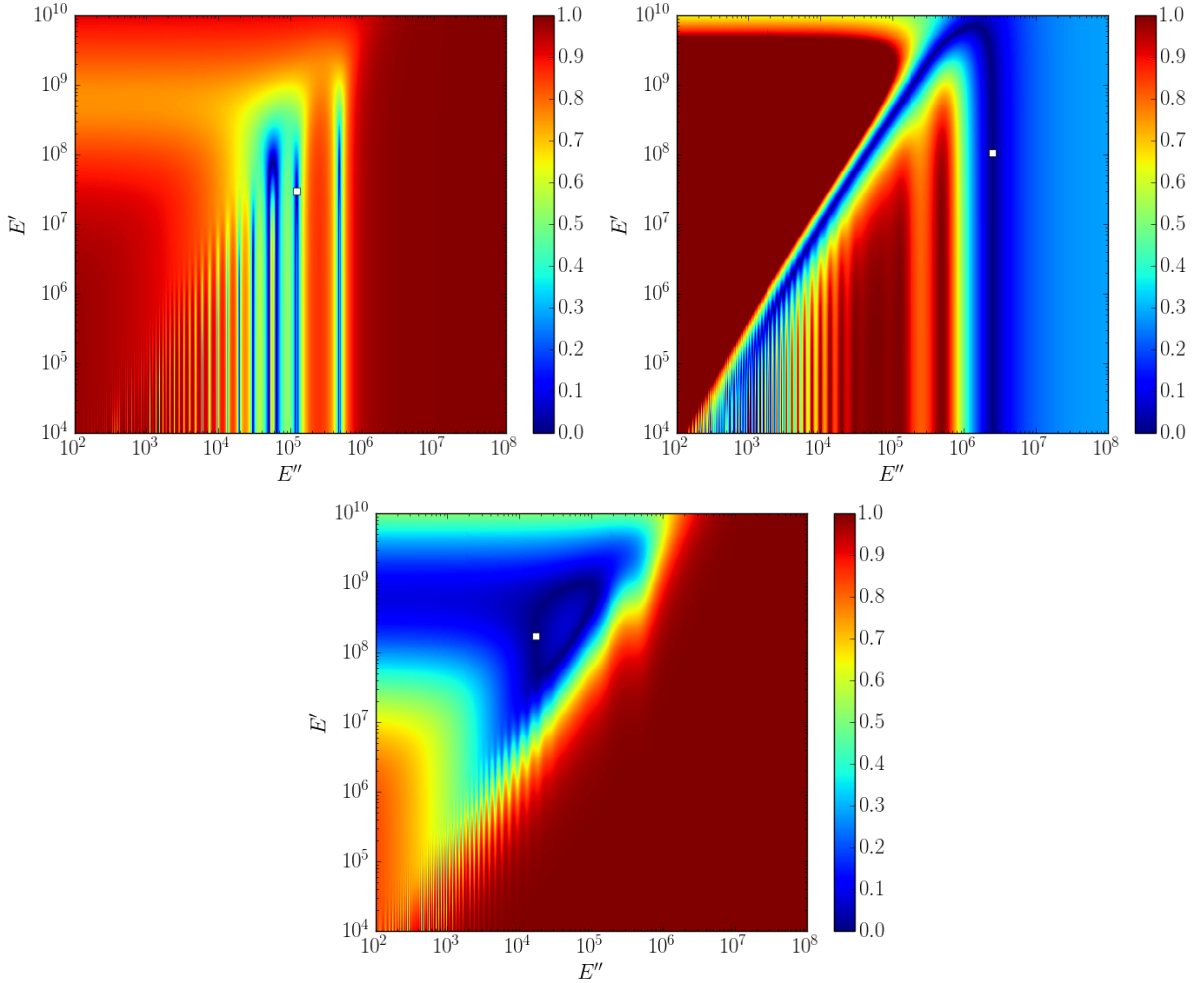


Figure 3.23: Values of the relative error for ER (top left plot), IL (top right plot), and FPD (bottom plot) for different values of E' and E'' at $f = 135$ kHz. The white square is the minimum value of the cost function.

shows the values of the cost function for different values of E' and E'' for ER (top left plot), IL (top right plot), and FPD (bottom plot), and what is the position where the local

minimum is located, marked with a white square. This minimum is chosen as the initial guess for the algorithm explained above. As it can be observed, the levels under study present several local minima, which makes the problem more difficult to solve. Although the relative errors in these fitting are small, the difficulties appear because the frequency response can show oscillations or can be smooth but presents jumps at some frequencies.

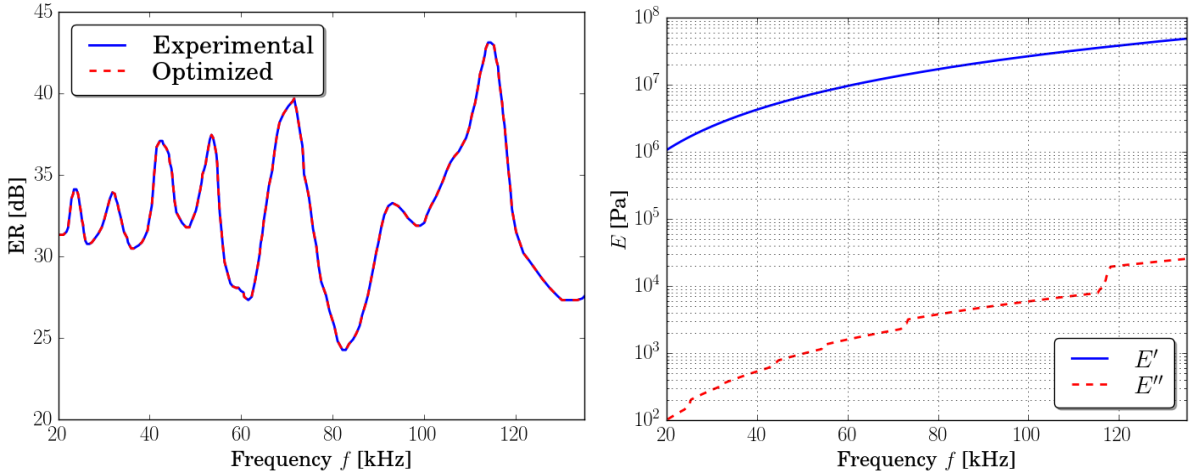


Figure 3.24: Left: Experimental (solid blue line) and optimized (dashed red line) values of the echo reduction level plotted with respect to the frequency. Right: Values of the real (solid blue line) and imaginary (dashed red line) part of the Young modulus. The considered fitting problem is (3.38) where $L = ER$. The relative error is $\varepsilon_{ER} = 4.0717 \times 10^{-10}\%$.

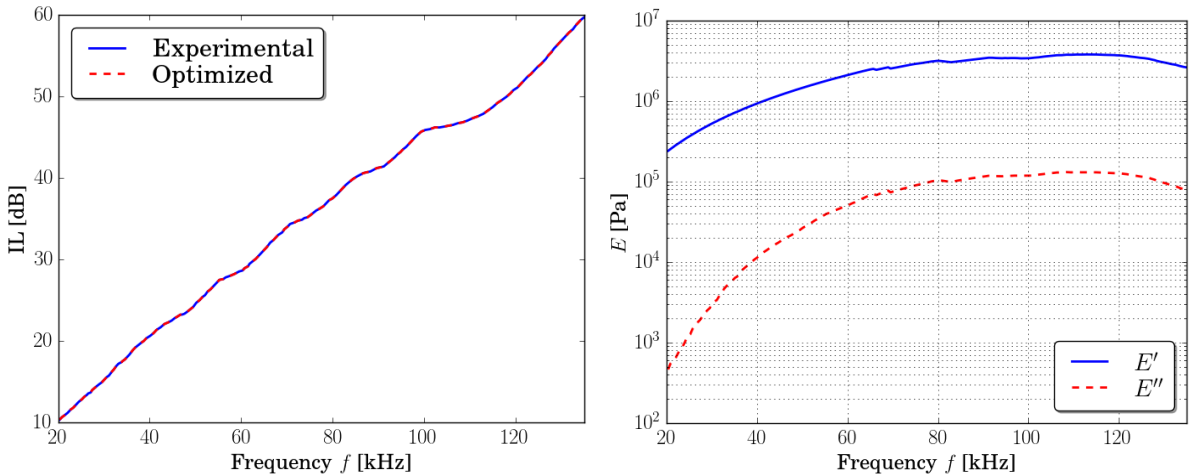


Figure 3.25: Left: Experimental (solid blue line) and optimized (dashed red line) values of the insertion loss level plotted with respect to the frequency. Right: Values of the real (solid blue line) and imaginary (dashed red line) part of the Young modulus. The fitting problem under consideration is (3.38) where $L = IL$. The relative error is $\varepsilon_{IL} = 2.6181 \times 10^{-12}\%$.

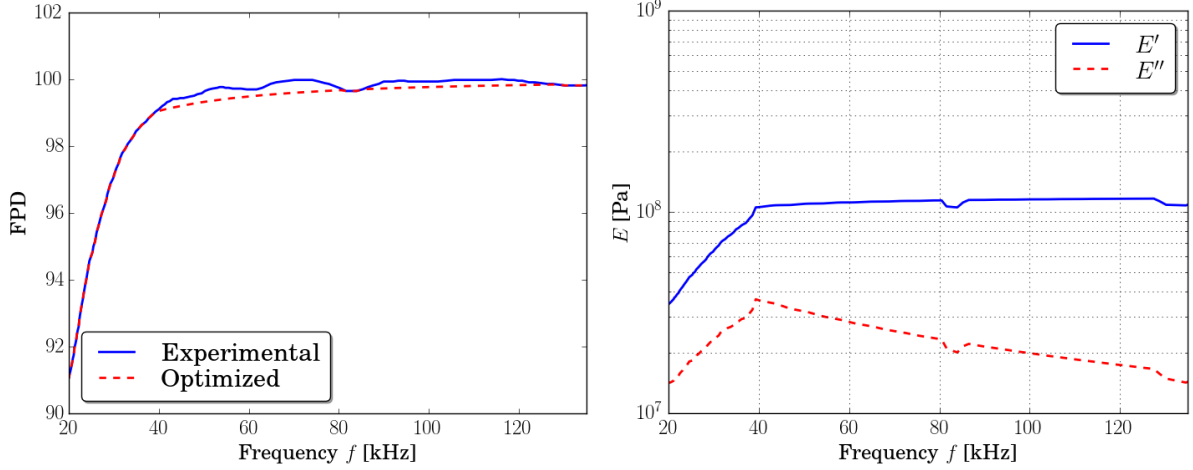


Figure 3.26: Left: Experimental (solid blue line) and optimized (dashed red line) values of the fractional power dissipation plotted with respect to the frequency. Right: Values of the real (solid blue line) and imaginary (dashed red line) part of the Young modulus. The fitting problem is given by (3.38) where $L = \text{FPD}$. The relative error is $\varepsilon_{\text{FPD}} = 0.15\%$.

	ER fitting	IL fitting	FPD fitting
ε_{ER}	$4.0717 \times 10^{-10}\%$	92.19%	99.82%
ε_{IL}	99.59%	$2.6181 \times 10^{-12}\%$	100.17%
ε_{FPD}	96.62%	56.71%	0.15%

Table 3.5: Relative errors in the single fitting, using the novel primal unknowns M and δ . The minimization problem is given by (3.38). The relative errors are computed by using (3.37), where L is ER, IL, and FPD, respectively.

The comparison between the experimental data and the optimized ones is shown in the left plots of Figures 3.24, 3.25, and 3.26 for the echo reduction level, the insertion loss, and the fractional power dissipation, respectively. In the right plot the real and the imaginary parts of the Young modulus are plotted. The relative errors of each single fitting computed by using (3.37) are $\varepsilon_{\text{ER}} = 4.0717 \times 10^{-10}\%$, $\varepsilon_{\text{IL}} = 2.6181 \times 10^{-12}\%$, and $\varepsilon_{\text{FPD}} = 0.15\%$. In Table 3.5 are given all the relative errors. The highlighted cells are the errors due to single fittings. The rest of the errors in the same column are obtained from computing the values of the rest of the levels with the optimal values obtained from each single fitting. Although these relative errors are slightly larger than those obtained with previous strategies, as it can be observed in the right plots of Figures 3.24, 3.25, and 3.26, the real and the imaginary parts of the Young modulus have a smoother frequency response than those obtained when the unknowns in the minimization problem are E' and E'' . In fact, these frequency responses qualitatively reproduce the mechanical behavior of polymeric materials described in the work [98], in which it can be seen that both the real part and the imaginary part of Young module decrease rapidly as the frequency decreases.

However, the values of the E' and E'' obtained for each level are different. They do not have the same behavior, and even do not have the same magnitude order. To overcome this problem, a joint fitting is performed, where the fitting problem consists in finding the values $M_{j*} \geq 0$ and $\delta_{j*} \geq 0$, such that minimize the difference between the experimental and the numerical values, i.e., $\forall j = 1, \dots, N$

$$(M_{j*}, \delta_{j*}) = \arg \min_{M_j, \delta_j > 0} [\Upsilon_{\text{ER}}(M_j, \delta_j, \omega_j) + \Upsilon_{\text{IL}}(M_j, \delta_j, \omega_j) + \Upsilon_{\text{FPD}}(M_j, \delta_j, \omega_j)], \quad (3.44)$$

where Υ_{L} is given by (3.37), M_j and δ_j are the novel unknowns given by $M_j = e^{\text{Im}(k_{V_{1j}})l}$ and $\delta_j = \text{Re}(k_{V_{1j}})l$, ER^{exp} , IL^{exp} , and FPD^{exp} are the experimental echo reduction level, insertion loss, and fractional power dissipation, respectively. Once again, to choose the initial guess, a multigrid exhaustive search algorithm has been used. One iteration in a multigrid with 500×500 points has been considered where $E' \in [E'_1 \times 10^{-0.5}, E'_1 \times 10^{0.5}]$ and $E'' \in [E''_1 \times 10^{-0.5}, E''_1 \times 10^{0.5}]$. Figure 3.27 shows the values of the cost function for

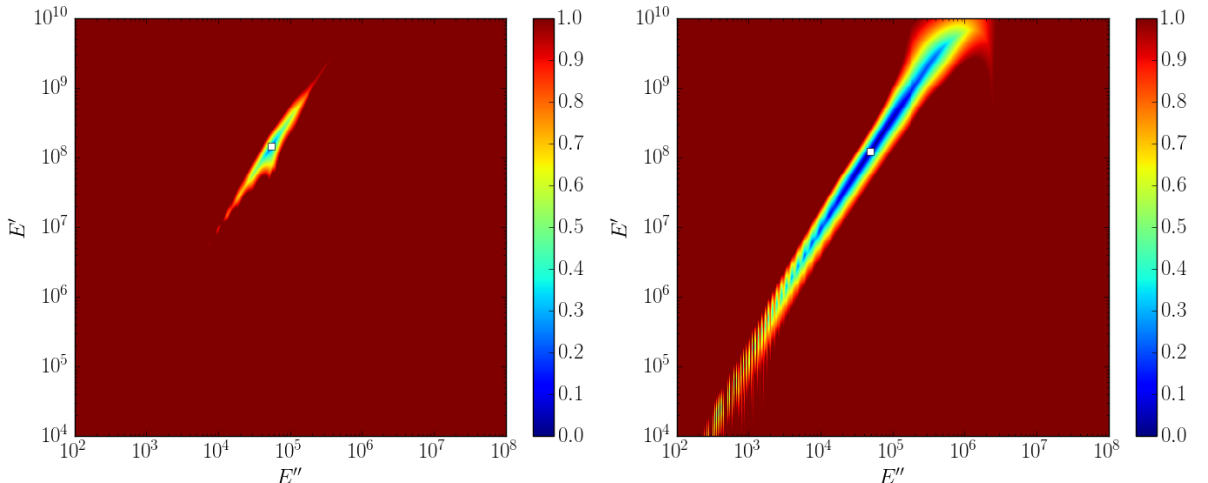


Figure 3.27: Values of the relative error for the joint fitting (left) and for the joint without considering ER (right), for different values of E' and E'' at $f = 135$ kHz. The white square is the minimum value of the cost function.

different values of E' and E'' for the joint fitting (left plot), and for the joint fitting without ER (right plot), and what is the position where the local minimum is located, marked with a white square. This minimum is chosen as the initial guess for the algorithm explained above. Although in the joint fitting, the cost function presents a global minimum well identified, in the joint fitting without ER the zone where the minimum can be located is bigger. The comparison between the experimental data and the optimized ones is shown in the top left, top right, and bottom left plots of Figure 3.28 for the echo reduction level, the insertion loss, and the fractional power dissipation, respectively. In the bottom right plot, the real and the imaginary parts of the Young modulus are plotted. The relative errors of single fittings computed by using (3.37) are $\varepsilon_{\text{ER}} = 29.44\%$, $\varepsilon_{\text{IL}} = 3.6536 \times 10^{-2}\%$, and

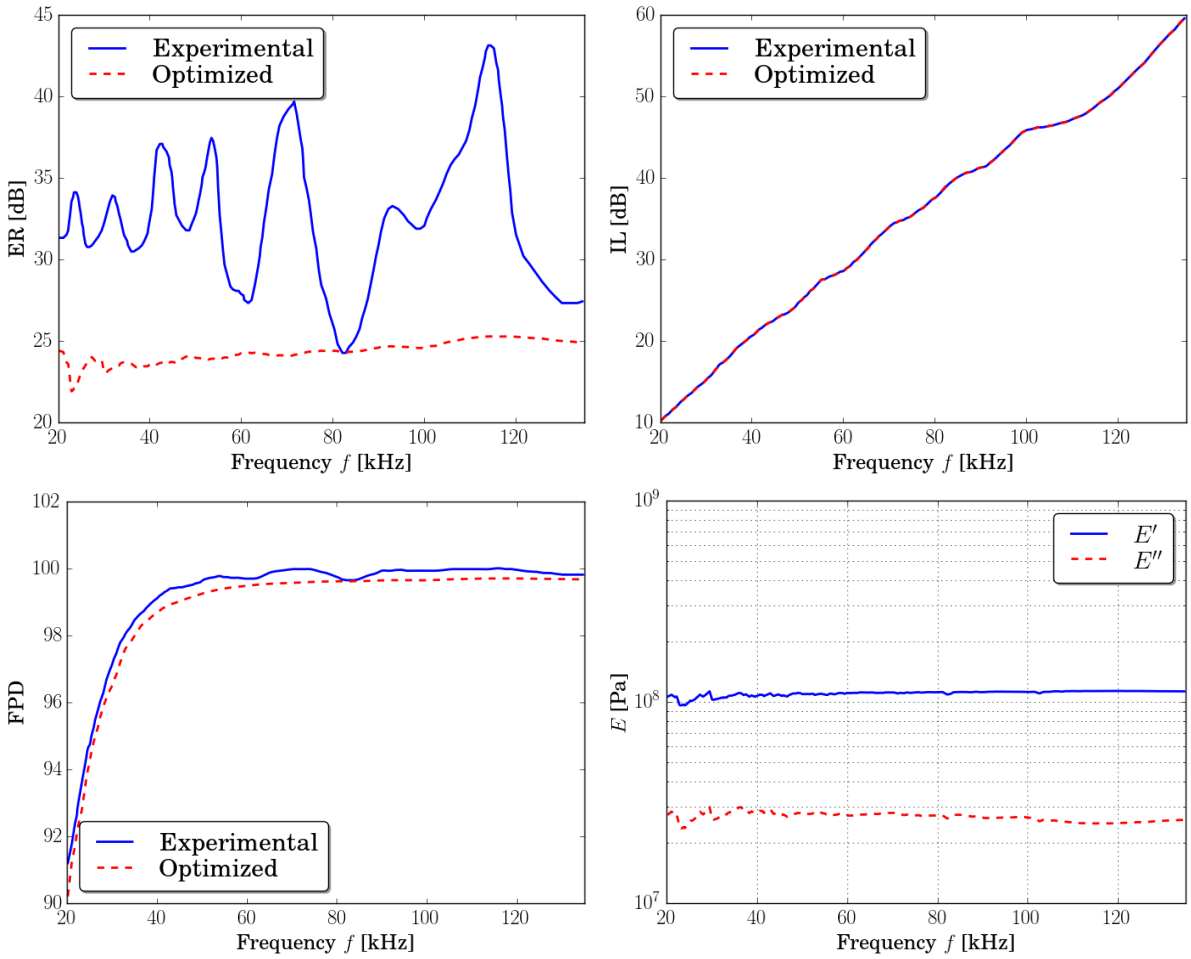


Figure 3.28: Experimental (solid blue line) and optimized (dashed red line) values of the echo reduction level (top left plot), insertion loss (top right plot), and fractional power dissipation (bottom left plot) plotted with respect to the frequency for the joint fitting. Bottom right: Values of the real (solid blue line) and imaginary (dashed red line) part of the Young modulus. The used fitting problem is (3.44). The relative errors are $\varepsilon_{\text{ER}} = 29.44\%$, $\varepsilon_{\text{IL}} = 3.6536 \times 10^{-2}\%$, and $\varepsilon_{\text{FPD}} = 0.39\%$.

$\varepsilon_{\text{FPD}} = 0.39\%$. With this fitting, common values for the Young modulus are obtained, but the relative errors have grown. Since the relative error for the echo reduction level is several orders larger than the error in the other two levels, a joint fitting without considering the echo reduction level is performed. Then, the fitting problem consists in finding the values $M_{j*} \geq 0$ and $\delta_{j*} \geq 0$, such that minimize the difference between the experimental and the numerical values, i.e., $\forall j = 1, \dots, N$

$$(M_{j*}, \delta_{j*}) = \arg \min_{M_j, \delta_j > 0} [\Upsilon_{\text{IL}}(M_j, \delta_j, \omega_j) + \Upsilon_{\text{FPD}}(M_j, \delta_j, \omega_j)]. \quad (3.45)$$

The comparison between the experimental data and the optimized ones is shown in the

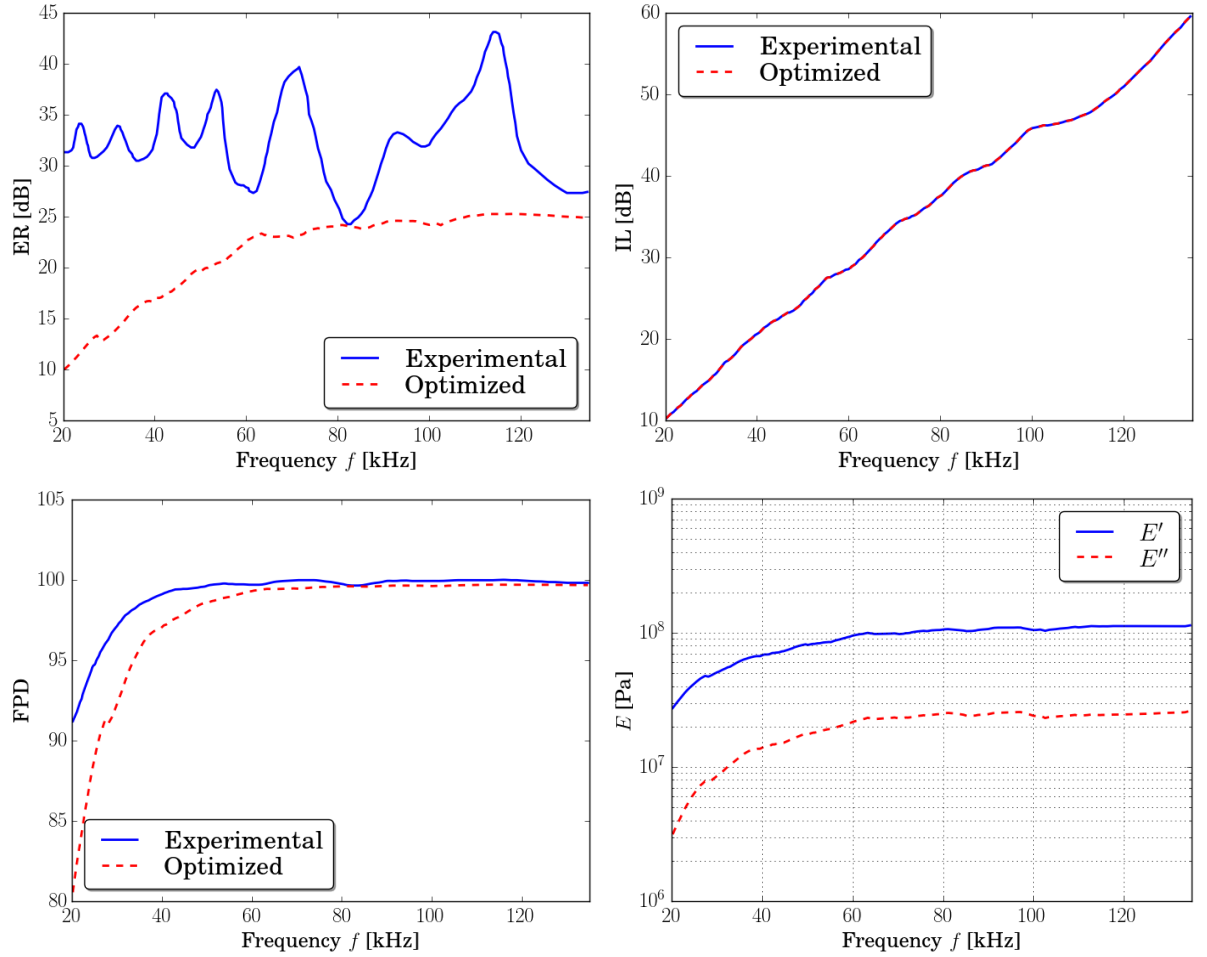


Figure 3.29: Experimental (solid blue line) and optimized (dashed red line) values of the echo reduction level (top left), insertion loss (top right), and fractional power dissipation (bottom left) plotted with respect to the frequency for the joint fitting without considering the ER level in the fitting. Bottom right: Values of the real (solid blue line) and imaginary (dashed red line) part of the Young modulus. The fitting problem is given by (3.45). The relative errors are $\varepsilon_{\text{ER}} = 41.64\%$, $\varepsilon_{\text{IL}} = 2.3538 \times 10^{-10}\%$, and $\varepsilon_{\text{FPD}} = 2.76\%$.

top left, top right, and bottom left plots of Figure 3.29 for the echo reduction level, the insertion loss, and the fractional power dissipation, respectively. In the bottom right plot, the real and the imaginary parts of the Young modulus are plotted. The frequency response of E' and E'' in Figure 3.29 qualitatively reproduce the mechanical behavior of polymeric materials described in the work [98], in which it can be seen that both the real part and the imaginary part of Young module decrease as the frequency decreases. The relative errors of single fittings computed by using (3.37) are $\varepsilon_{\text{ER}} = 41.64\%$, $\varepsilon_{\text{IL}} = 2.3538 \times 10^{-10}\%$, and $\varepsilon_{\text{FPD}} = 2.76\%$. As it can be observed, the relative error for IL has decreased, but for FPD and ER have grown (in fact, the error for ER is double than with the joint fitting).

Comparing the values of the relative error for the joint fitting and the joint fitting without ER (see Figure 3.27), this situation is what expected because when the ER is omitted in the fitting, the minimum is less seated.

Acoustic source with a non-planar directivity pattern

In this section, it is considered that the acoustic source is a parametric array with a non-planar directivity pattern. The considered plane wave spectrum is described in Section 3.3.1. As it has been explained in Section 3.4, to improve the results of the previous sections, and get a smoother frequency response of the acoustic levels under study, instead of using the unknowns E' and E'' in the fitting procedure, $\delta = \text{Re}(k_{V_1})l$ and $M = e^{\text{Im}(k_{V_1})l}$ have been considered (see Section 3.4.1 for more details). An algorithm of type trust-region reflective (see [59]) has been used to solve the minimization problem, so the computation of the gradient of the functional is necessary. First of all, each level is fitting separately, considering the minimization problem given by (3.38). As in previous simulations, the fitting problem has been solved from upper to lower frequencies. The numerical results for

	ER fitting	IL fitting	FPD fitting
ε_{ER}	$3.002 \times 10^{-5}\%$	51.10%	30.77%
ε_{IL}	81.29%	$2.156 \times 10^{-6}\%$	32.61%
ε_{FPD}	78.29%	8.60%	0.188%

Table 3.6: Relative errors in the single fitting, using the novel primal unknowns M and δ . The minimization problem under consideration is (3.38). The relative errors are computed by using (3.37), where L is ER, IL, and FPD, respectively.

the echo reduction level, the insertion loss, and the fractional power dissipation are shown in Figures 3.30, 3.31, and 3.32. In the left plots, the experimental data in solid blue line and the optimized ones in dashed red line are plotted with respect to the frequency, and in the right plots, the real and the imaginary parts of the Young modulus (in solid blue line and in dashed red line, respectively) are shown. The relative errors of single fittings computed by using (3.37) are $\varepsilon_{\text{ER}} = 3.002 \times 10^{-5}\%$, $\varepsilon_{\text{IL}} = 2.156 \times 10^{-6}\%$, and $\varepsilon_{\text{FPD}} = 0.188\%$, and in Table 3.5, the relative errors committed for each fitting are shown.

Table 3.6 shows the relative errors. Those cells highlighted in grey represent the errors obtained with every single fitting. By using the obtained optimal values of the parameters, it is possible to compute the rest of the levels, and therefore to calculate the relative errors. As it can be observed, the relative errors due to the single fittings are smaller than 1% but are larger than those computed with plane waves. Moreover, the frequency response of the real and the imaginary parts of the Young modulus are smooth and qualitatively similar to those computed when the acoustic source is an oblique plane wave (see right plots of Figures 3.30, 3.31, and 3.32). However, the values of E' and E'' present different orders for each level. To overcome this difficulty, the joint fitting, given by (3.44), is performed. The comparison between the experimental data and the optimized ones is shown in the top left,

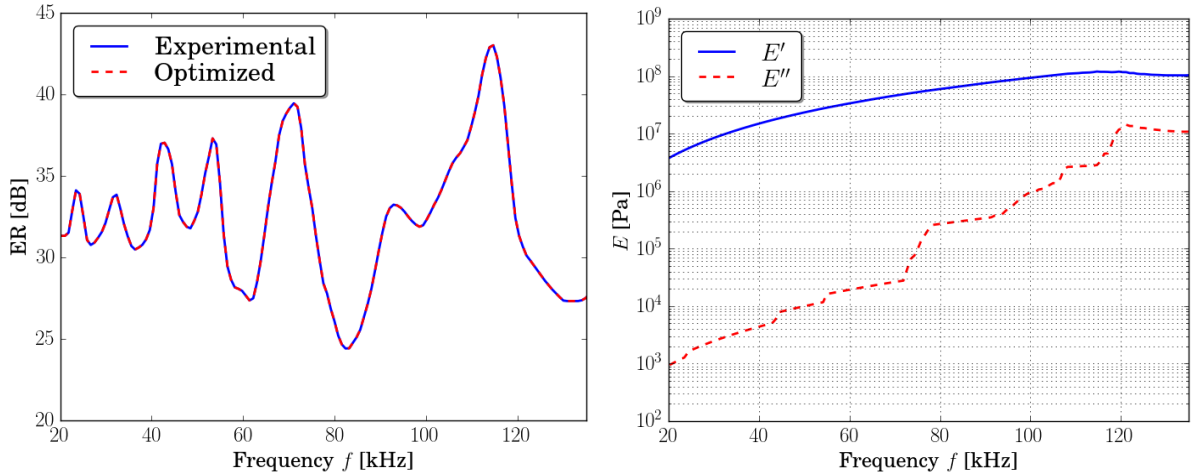


Figure 3.30: Left: Experimental (solid blue line) and optimized (dashed red line) values of the echo reduction level plotted with respect to the frequency. Right: Values of the real (solid blue line) and imaginary part (dashed red line) of the Young modulus. The fitting problem is given by (3.38) where $L = ER$. The relative error is $\varepsilon_{ER} = 3.002 \times 10^{-5}\%$.

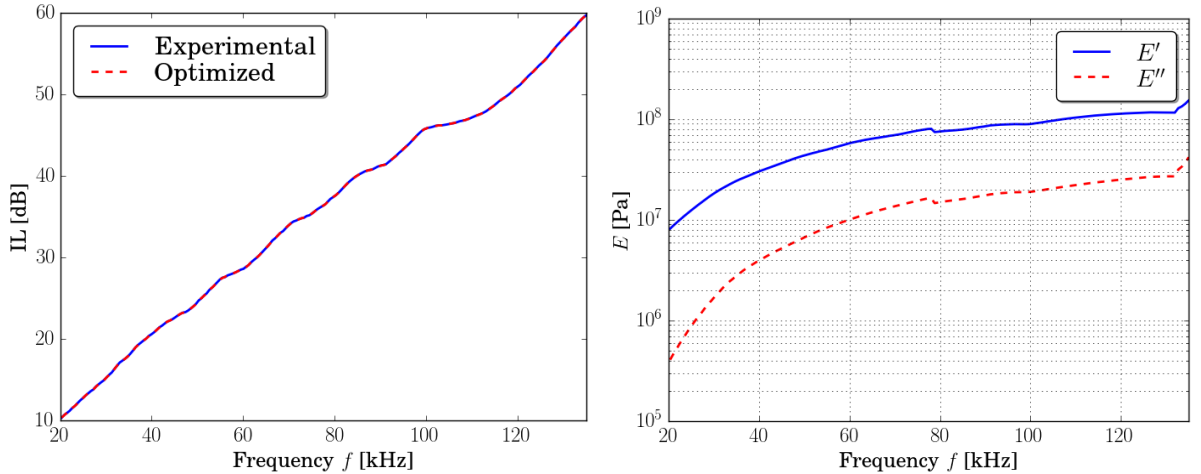


Figure 3.31: Left: Experimental (solid blue line) and optimized (dashed red line) values of the insertion loss level plotted with respect to the frequency. Right: Values of the real (solid blue line) and imaginary part (dashed red line) of the Young modulus. The fitting problem under consideration is (3.38) where $L = IL$. The relative error is $\varepsilon_{IL} = 2.156 \times 10^{-6}\%$.

top right, and bottom left plots of Figure 3.33 for the echo reduction level, the insertion loss, and the fractional power dissipation, respectively. In the bottom right plot, the real and the imaginary parts of the Young modulus are plotted. The relative errors of single fittings computed by using (3.38) are $\varepsilon_{ER} = 27.09\%$, $\varepsilon_{IL} = 3.94 \times 10^{-2}\%$, and $\varepsilon_{FPD} = 0.34\%$. The behavior is the same observed when the acoustic source is a plane wave: the relative errors are grown with respect to those obtained with single fittings, and the error for ER is

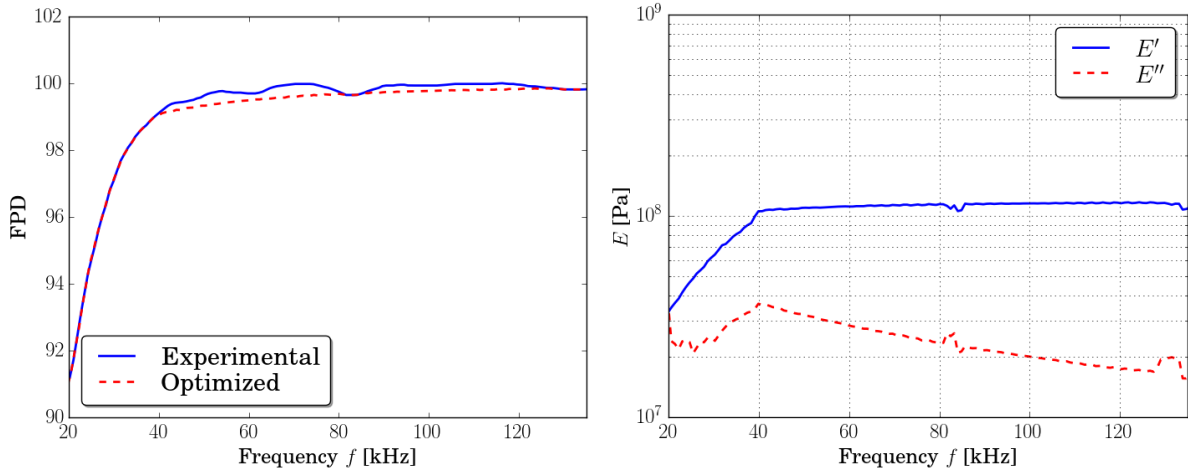


Figure 3.32: Left: Experimental (solid blue line) and optimized (dashed red line) values of the fractional power dissipation plotted with respect to the frequency. Right: Values of the real (solid blue line) and imaginary part (dashed red line) of the Young modulus. The considered fitting problem is (3.38) where $L = \text{FPD}$. The relative error is $\varepsilon_{\text{FPD}} = 0.188\%$.

several orders higher than for the other two levels. Then, a joint fitting without considering the echo reduction level is performed by using the fitting problem (3.45). The comparison between the experimental data and the optimized ones is shown in the top left, top right, and bottom left plots of Figure 3.34 for the echo reduction level, the insertion loss, and the fractional power dissipation, respectively. In the bottom right plot, the real and the imaginary parts of the Young modulus are plotted. The relative errors of single fittings computed by using (3.45) are $\varepsilon_{\text{ER}} = 38.33\%$, $\varepsilon_{\text{IL}} = 1.75 \times 10^{-6}\%$, and $\varepsilon_{\text{FPD}} = 3.35\%$. Once again, the behavior is the same as when a plane wave is considered as the acoustic source: the relative error for IL decreases, but for the other two levels grows. Since in all simulations, errors in the echo reduction fitting are larger than in the other two levels, and the obtained Young modulus for this level presents significant differences with respect to the obtained with the other levels, some doubts about the reliability of the echo reduction data appear. Moreover, the frequency response of E' and E'' in Figure 3.34 decreases as the frequency decreases, as expected.

3.6 Conclusions

In this chapter, a viscoelastic material has been numerically characterized by using the frequency response of the echo reduction level, the insertion loss, and the fractional power dissipation. The main purpose of this chapter is to use a non-parametric methodology to characterize the viscoelastic model. Then, a data-driven approach has been considered to determine the frequency-dependent parameters of the material under consideration. By using this approach, the choice of a parametric model for fitting is avoided, and the fitting

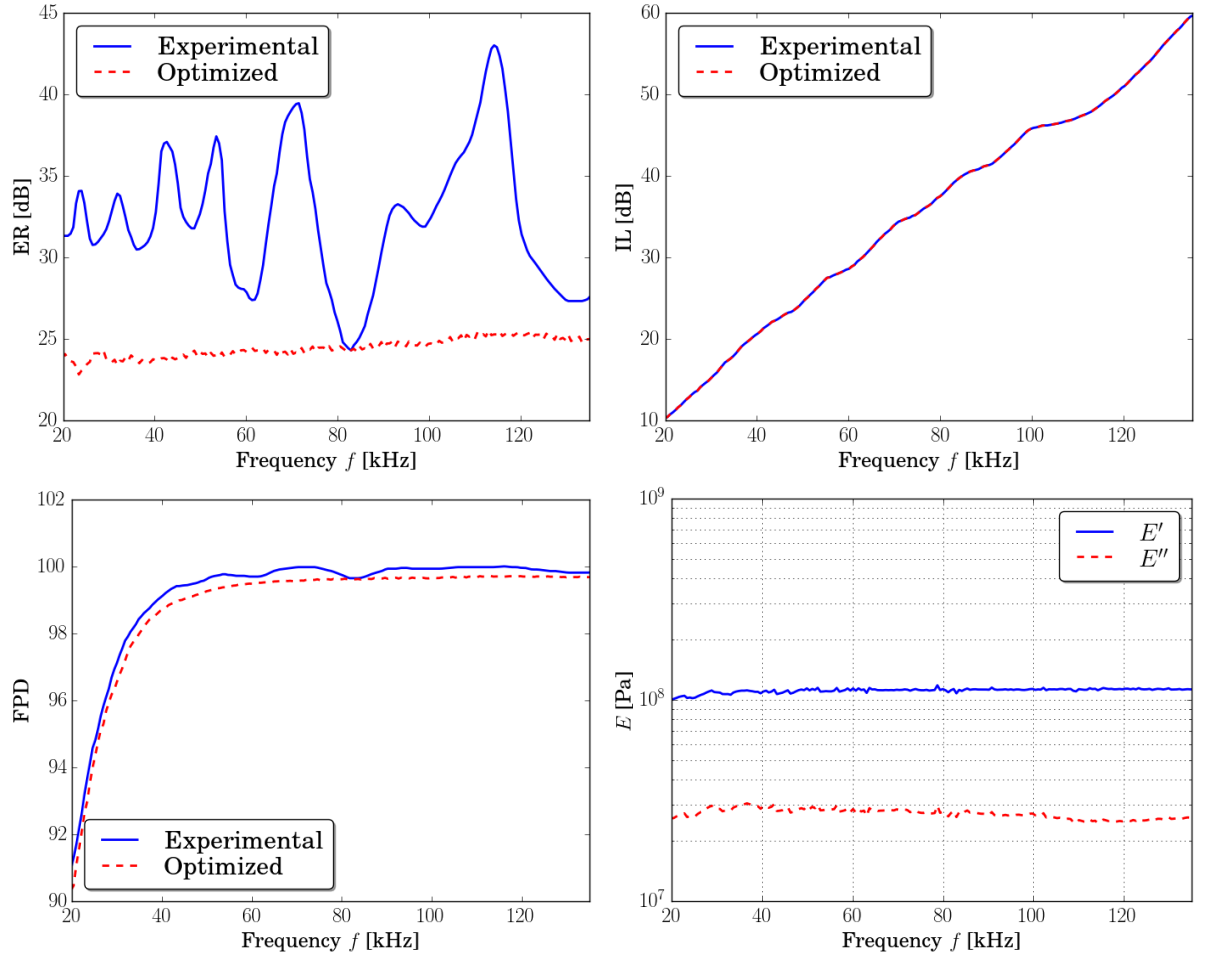


Figure 3.33: Experimental (solid blue line) and optimized (dashed red line) values of the echo reduction level (top left), insertion loss (top right), and fractional power dissipation (bottom left) plotted with respect to the frequency for the joint fitting. Bottom right: Values of the real (solid blue line) and imaginary part (dashed red line) of the Young modulus. The fitting problem is given by (3.44). The relative errors are $\varepsilon_{\text{ER}} = 27.09\%$, $\varepsilon_{\text{IL}} = 3.94 \times 10^{-2}\%$, and $\varepsilon_{\text{FPD}} = 0.34\%$.

is performed, minimizing the distance between the experimental data and the computed values.

Taking into account the setup, which is used to measure the experimental data, a multilayer medium formed by the viscoelastic material, surrounded by a fluid, is studied. For this purpose, at the beginning of this chapter, the mathematical models of the compressible fluid, and the viscoelastic solid are studied. Then, the coupled problem and the acoustic quantities of interest for this problem have been described.

The direct problem of wave propagation in the multilayer medium has been studied. Since the available experimental data are measured in a setup where the acoustic source

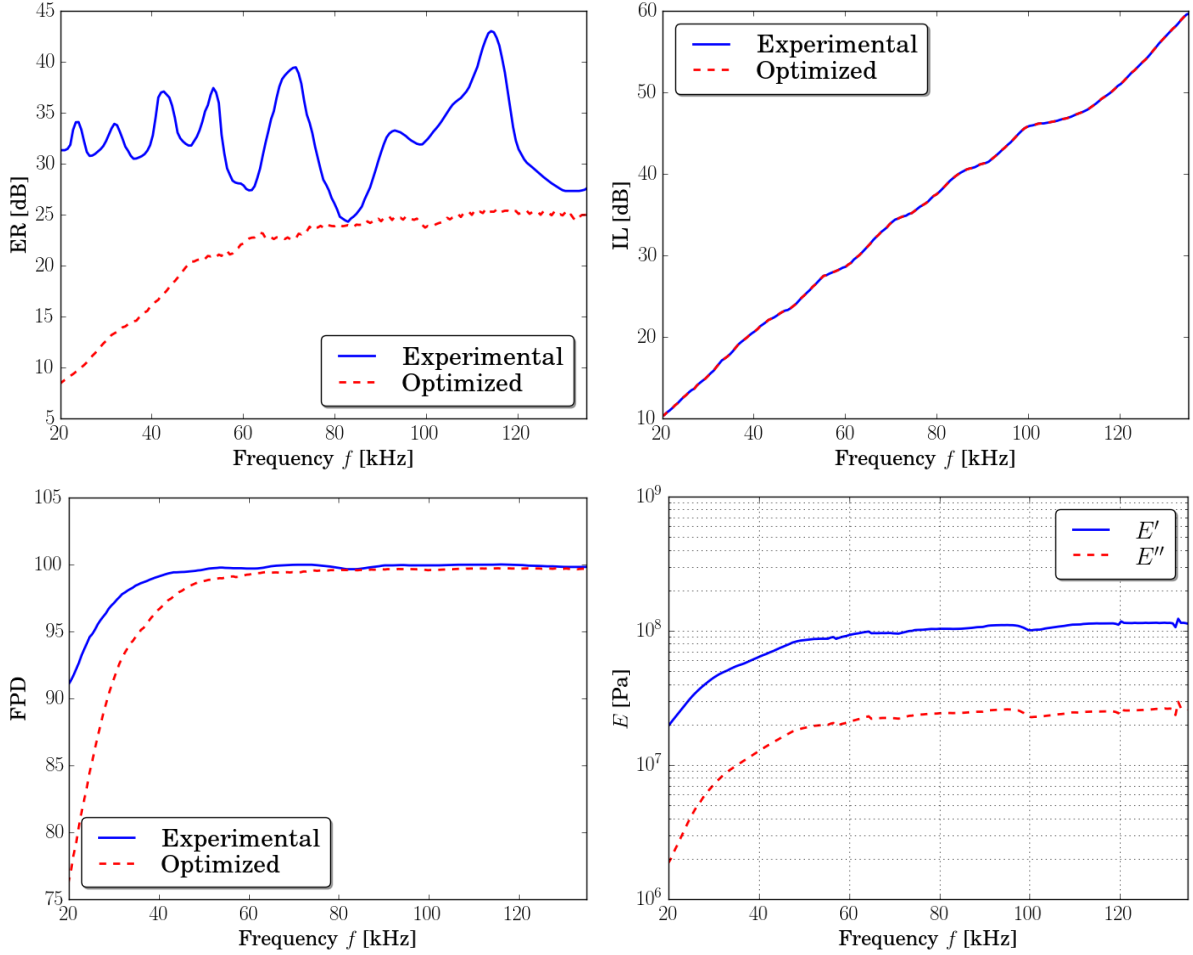


Figure 3.34: Experimental (solid blue line) and optimized (dashed red line) values of the echo reduction level (top left), insertion loss (top right) and fractional power dissipation (bottom left) plotted with respect to the frequency for the joint fitting without considering the ER level in the fitting. Bottom right: Values of the real (solid blue line) and imaginary part (dashed red line) of the Young modulus. The used fitting problem is (3.45). The relative errors are $\varepsilon_{\text{ER}} = 38.33\%$, $\varepsilon_{\text{IL}} = 1.75 \times 10^{-6}\%$, and $\varepsilon_{\text{FPD}} = 3.35\%$.

is a parametric array with a non-planar directivity pattern, the incident, scattered, and transmitted fields have been described by using an integral representation. These integrals involve a plane wave spectrum and the reflection and transmission coefficients in a plane wave framework. Then, the computation of these two coefficients considering a propagation problem of plane waves is shown.

Since to characterize the material, some inverse problems are solved, the choice of the primal unknowns for the fitting problem is highly relevant. In this chapter, a variety of constitutive laws over the unknowns has been considered, such as considering that the Young modulus is a linear function of the frequency, or that is governed by an arbitrary

frequency-dependent function. With these assumptions, when the fitting results present good agreement with the experimental data, the unknowns present an oscillatory behavior. Then, a new pair of unknowns, depending on the wave number and the thickness of the material, has been considered. To solve this fitting problem, a trust-region reflective algorithm has been used. This algorithm requires the computation of the gradient of the functional cost. To achieve a lower computational cost, the adjoint method is used to calculate the derivatives of the functional cost.

Finally, numerical simulations have been performed. The code has been validated by using manufactured data. Then, a real-world viscoelastic material has been characterized, considering a parametric model and a non-parametric approach. The results with both methodologies have been compared, showing that the non-parametric approach allows us to improve the frequency response of the unknowns, achieving relative errors similar to the parametric methodology. Concluding, the viscoelastic material has been characterizing, with errors less than 10%, and with a smooth frequency response of the real and imaginary parts of the Young modulus similar to those appearing in the literature.

It is important to recall that the fitting may be improved considering the non-planar surface of the material (see Chapter 4). But, despite the problem is ill-posed (see Lemma 3.4.3), the proposed methodology has contributed to characterized the absorbing tile “Apltile SF5048” (see[5]) as a viscoelastic material.

Appendix

3.A Integral approximation

The computation of the levels ER, IL, and FPD with the expressions (3.5), (3.6), and (3.7), presents some difficulties due to the integral representations (3.18), (3.20), and (3.22). In this section, a brief explanation about how the integral is approximated is given. The difficulties appearing in the approximation are shown, and the used solutions to overcome them are given.

First of all, the change of variable $u = 1 - \cos \theta$ is considered. Then, the incident pressure field, defined by (3.18), results

$$\Pi_{\text{inc}}(\mathbf{p}_m) = ik_F \int_0^{1-i\infty} \tilde{S}(u) e^{ik_F p_{3m}(1-u)} du, \quad (3.A.1)$$

where k_F is the wave number of the fluid, p_{3m} is the measurement point in the p_3 -axis, located in front of the sample, and \tilde{S} is the plane wave spectrum in terms of u , given by

$$\tilde{S}(u) = Q_0 \frac{e^{ik_F hu} - 1}{ik_F u}. \quad (3.A.2)$$

Now, it is possible to split the integral (3.A.1) in two parts to compute the integral over the real and the imaginary path, that is,

$$\Pi_{\text{inc}}(\mathbf{p}_m) = \underbrace{ik_F \int_0^1 \tilde{S}(u) e^{ik_F p_{3m}(1-u)} du}_{I_1} + \underbrace{ik_F \int_1^{1-i\infty} \tilde{S}(u) e^{ik_F p_{3m}(1-u)} du}_{I_2} = I_1 + I_2.$$

The difficulties appearing in the computation of I_2 are related to the endpoint of the complex path. As it is shown in right plot in Figure 3.35, there is an exponential decay on the complex path. As the contribution from the complex path decreases rapidly due to the exponential that appears in the integrand, it is possible to calculate the imaginary part of the contour only over the interval $(1, 1 + Aj)$ where A is chosen according to each problem details.

On the other hand, the difficulties appearing in the computation of I_1 are related to the highly oscillatory behavior of this integral over $[0, 1]$. As it is shown in left plot in

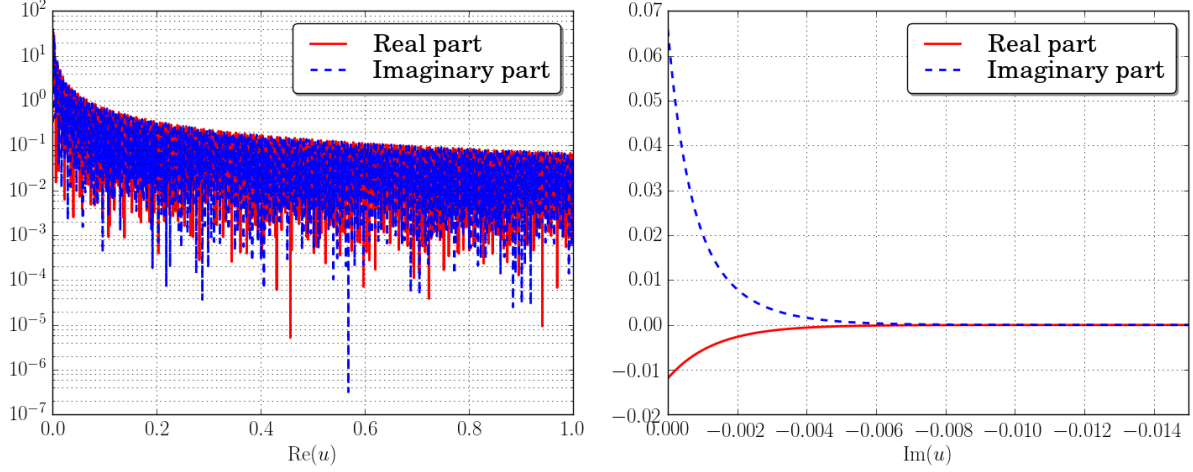


Figure 3.35: Real and imaginary parts of the integrand of Π_{inc} over the real path (left plot) and over the complex path (right plot) at $f = 135 \text{ kHz}$.

Figure 3.35, both the real and the imaginary parts of the integrand of I_1 are highly oscillatory. Then, to get the desired accuracy by using a classical quadrature rule, a huge amount of quadrature nodes is necessary, increasing the computational cost of the Gaussian quadrature.

Remark 3.A.1. In the simulations shown in this chapter, $A = \frac{\log(10^{-16})}{-p_{3m}\text{Re}(k_F)}$ to guarantee that the complex path of the integral is truncated at that point u such that $|e^{ik_F p_{3m} u}| < 10^{-16}$. To approximate the integrals, a Simpson method is used, and the number of quadrature points is $N = 100000$ for the real path and $N = 1000$ for the imaginary path.

The same arguments can be followed to compute the scattered and the transmitted fields. If the change of variable $u = 1 - \cos \theta$ is considered, the scattered pressure field, defined by (3.22), results

$$\begin{aligned} \Pi_{\text{scat}}(\mathbf{p}_m) &= ik_F \int_0^{1-i\infty} \tilde{S}(u) \mathcal{R}(\mathbf{p}_m) e^{ik_F p_{3m}(1-u)} du \\ &= ik_F \underbrace{\int_0^1 \tilde{S}(u) \mathcal{R}(\mathbf{p}_m) e^{ik_F p_{3m}(1-u)} du}_{I_3} + ik_F \underbrace{\int_1^{1-i\infty} \tilde{S}(u) \mathcal{R}(\mathbf{p}_m) e^{ik_F p_{3m}(1-u)} du}_{I_4}, \end{aligned}$$

and the transmitted pressure field, defined by (3.20), results

$$\begin{aligned} \Pi_{\text{transm}}(\mathbf{p}_m) &= ik_F \int_0^{1-i\infty} \tilde{S}(u) \mathcal{T}(\mathbf{p}_m) e^{ik_F p_{3m}(1-u)} du \\ &= ik_F \underbrace{\int_0^1 \tilde{S}(u) \mathcal{T}(\mathbf{p}_m) e^{ik_F p_{3m}(1-u)} du}_{I_5} + ik_F \underbrace{\int_1^{1-i\infty} \tilde{S}(u) \mathcal{T}(\mathbf{p}_m) e^{ik_F p_{3m}(1-u)} du}_{I_6}, \end{aligned}$$

where \mathcal{R} and \mathcal{T} are the reflection and the transmission coefficient of the inserted panel. As it happens with the incident pressure field, the complex path is truncated, and I_4 and I_6 are computed over the interval $(1, 1 + Aj)$ (see the right plots in Figures 3.36 and 3.37). The left plots of Figures 3.36 and 3.37 show that the integrand of I_3 and I_5 are highly oscillatory. Then, to get the desired accuracy it is necessary to use a classical quadrature rule with a large number of quadrature nodes.

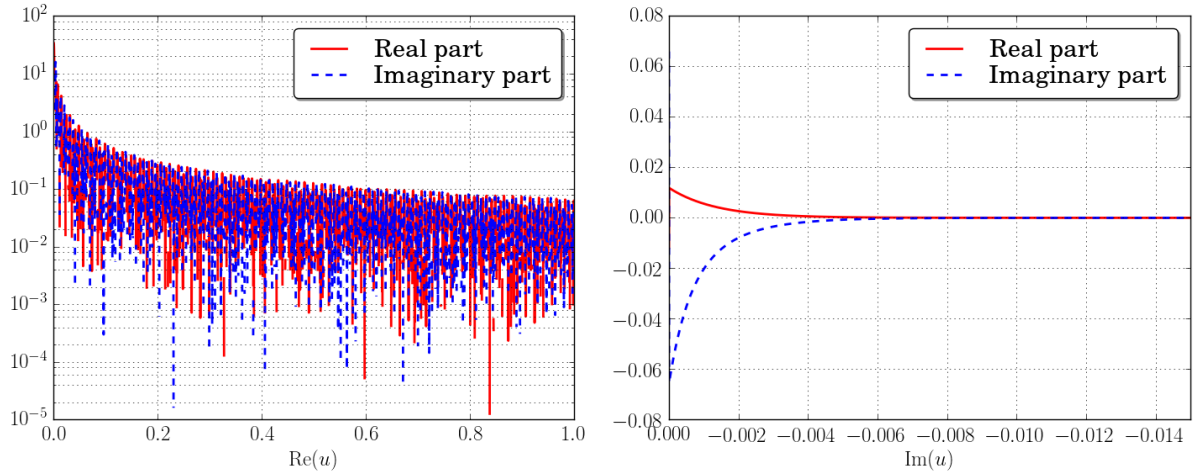


Figure 3.36: Real and imaginary parts of the integrand of Π_{scat} over the real (left plot) and the complex path (right plot) at $f = 135 \text{ kHz}$.

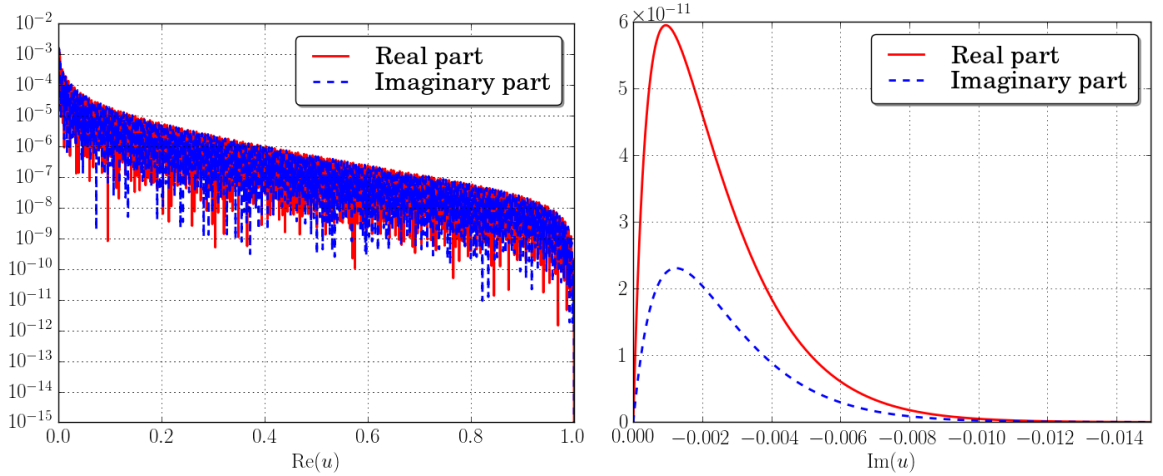


Figure 3.37: Real and imaginary parts of the integrand of Π_{transm} over the real (left plot) and the complex path (right plot) at $f = 135 \text{ kHz}$.

3.B Derivatives

In Section 3.4.1, an optimization problem has been described, in term of two new unknowns M and δ . This problem has been solved by using a trust-region reflective algorithm. This method is based in the interior-reflective Newton method, and requires the computation of the gradient of the cost function. Although each one of these derivatives can be calculated separately, the adjoint method described in Section 3.4.2 is used to compute the gradient efficiently.

Now, the derivatives of L with respect to the two parameters M and δ are described to be used in the computation of the gradient of the objective function (3.38), where L could be ER, IL, or FPD. The system (3.36) can be written as $A\mathbf{C} = \mathbf{b}$. If the parameters are q_i with $i = 1, 2$, where $q_1 = M$ and $q_2 = \delta$, the derivative of the system solution \mathbf{C} with respect to q_i could be computed by using

$$\frac{\partial A}{\partial q_i} \mathbf{C} + A \frac{\partial \mathbf{C}}{\partial q_i} = \frac{\partial \mathbf{b}}{\partial q_i}, \quad i = 1, 2.$$

Once the partial derivatives $\frac{\partial \mathbf{C}}{\partial q_i}$ are computed, it is possible to calculate the gradient of the cost function. Following (3.38), the cost function can be defined as

$$\Upsilon_L(M_j, \delta_j, \omega_j) = \frac{|L_j^{\text{exp}} - \hat{L}(M_j, \delta_j, \omega_j)|^2}{|L_j^{\text{exp}}|^2}, \quad \forall j = 1, \dots, N_L,$$

and the partial derivative with respect to the parameter q_i is given by

$$\begin{aligned} \frac{\partial \Upsilon_L}{\partial q_i}(M_j, \delta_j, \omega_j) &= \frac{2 \text{sign} \left(L_j^{\text{exp}} - \hat{L}(M_j, \delta_j, \omega_j) \right) |L_j^{\text{exp}} - \hat{L}(M_j, \delta_j, \omega_j)|}{|L_j^{\text{exp}}|^2} \\ &\times \frac{\partial \hat{L}}{\partial q_i}(M_j, \delta_j, \omega_j), \quad \forall j = 1, \dots, N_L, \end{aligned}$$

where the computation of $\frac{\partial \hat{L}}{\partial q_i}$ is detailed below to consider the differences when the level L is ER, IL, or FPD. For the sake of simplicity, the dependency of M_j , δ_j , and ω_j in Π_{scat} and Π_{transm} is omitted below. Taking into account the definition of the echo reduction level (3.5) and the insertion loss (3.6), the gradients of ER and IL are given as

$$\begin{aligned} \nabla_{\delta, M} \widehat{\text{ER}} &= \frac{-10}{|\widehat{\Pi}_{\text{scat}}|^2 \log 10} \nabla_{\delta, M} |\widehat{\Pi}_{\text{scat}}|^2, \\ \nabla_{\delta, M} \widehat{\text{IL}} &= \frac{-10}{|\widehat{\Pi}_{\text{transm}}|^2 \log 10} \nabla_{\delta, M} |\widehat{\Pi}_{\text{transm}}|^2, \end{aligned}$$

being $\nabla_{\delta, M}$ the gradient respect to δ and M , and

$$\nabla_{\delta, M} |\hat{\Pi}_{\text{scat}}|^2 = 2 \begin{pmatrix} \text{Re}(\hat{\Pi}_{\text{scat}}) \text{Re} \left(\frac{\partial \hat{\Pi}_{\text{scat}}}{\partial M} \right) + \text{Im}(\hat{\Pi}_{\text{scat}}) \text{Im} \left(\frac{\partial \hat{\Pi}_{\text{scat}}}{\partial M} \right) \\ \text{Re}(\hat{\Pi}_{\text{scat}}) \text{Re} \left(\frac{\partial \hat{\Pi}_{\text{scat}}}{\partial \delta} \right) + \text{Im}(\hat{\Pi}_{\text{scat}}) \text{Im} \left(\frac{\partial \hat{\Pi}_{\text{scat}}}{\partial \delta} \right) \end{pmatrix}, \quad (3.B.1)$$

$$\nabla_{\delta, M} |\hat{\Pi}_{\text{transm}}|^2 = 2 \begin{pmatrix} \text{Re}(\hat{\Pi}_{\text{transm}}) \text{Re} \left(\frac{\partial \hat{\Pi}_{\text{transm}}}{\partial M} \right) + \text{Im}(\hat{\Pi}_{\text{transm}}) \text{Im} \left(\frac{\partial \hat{\Pi}_{\text{transm}}}{\partial M} \right) \\ \text{Re}(\hat{\Pi}_{\text{transm}}) \text{Re} \left(\frac{\partial \hat{\Pi}_{\text{transm}}}{\partial \delta} \right) + \text{Im}(\hat{\Pi}_{\text{transm}}) \text{Im} \left(\frac{\partial \hat{\Pi}_{\text{transm}}}{\partial \delta} \right) \end{pmatrix}, \quad (3.B.2)$$

where, following (3.20) and (3.22),

$$\begin{aligned} \frac{\partial}{\partial M} \hat{\Pi}_{\text{scat}} &= ik_F \frac{\partial}{\partial M} \int_0^{1-i\infty} \tilde{S}(u) \mathcal{R}(\mathbf{p}_m) e^{ik_F p_{3m}(1-u)} du \\ &= ik_F \int_0^{1-i\infty} \tilde{S}(u) \frac{\partial C_1}{\partial M}(\mathbf{p}_m) e^{ik_F p_{3m}(1-u)} du, \end{aligned}$$

$$\begin{aligned} \frac{\partial}{\partial \delta} \hat{\Pi}_{\text{scat}} &= ik_F \frac{\partial}{\partial \delta} \int_0^{1-i\infty} \tilde{S}(u) \mathcal{R}(\mathbf{p}_m) e^{ik_F p_{3m}(1-u)} du \\ &= ik_F \int_0^{1-i\infty} \tilde{S}(u) \frac{\partial C_1}{\partial \delta}(\mathbf{p}_m) e^{ik_F p_{3m}(1-u)} du, \end{aligned}$$

$$\begin{aligned} \frac{\partial}{\partial M} \hat{\Pi}_{\text{transm}} &= ik_F \frac{\partial}{\partial M} \int_0^{1-i\infty} \tilde{S}(u) \mathcal{T}(\mathbf{p}_m) e^{ik_F p_{3m}(1-u)} du \\ &= ik_F \int_0^{1-i\infty} \tilde{S}(u) \frac{\partial C_8}{\partial M}(\mathbf{p}_m) e^{ik_F p_{3m}(1-u)} du, \end{aligned}$$

$$\begin{aligned} \frac{\partial}{\partial \delta} \hat{\Pi}_{\text{transm}} &= ik_F \frac{\partial}{\partial \delta} \int_0^{1-i\infty} \tilde{S}(u) \mathcal{T}(\mathbf{p}_m) e^{ik_F p_{3m}(1-u)} du \\ &= ik_F \int_0^{1-i\infty} \tilde{S}(u) \frac{\partial C_8}{\partial \delta}(\mathbf{p}_m) e^{ik_F p_{3m}(1-u)} du, \end{aligned}$$

where $\tilde{S}(u)$ is the plane wave spectrum of the truncated parametric source, given by (3.A.2), $\mathcal{R}(\mathbf{p}_m)$ and $\mathcal{T}(\mathbf{p}_m)$ are the plane wave reflection and transmission coefficients, respectively, given by (3.3) and (3.4), and C_1 and C_8 are the amplitudes of scattered and transmitted waves, respectively, obtained from the resolution of the system (3.36), in terms of δ and M .

On the other hand, taking into account the definition of the fractional power dissipation (3.7), the gradient of FPD is given as

$$\nabla_{\delta, M} \widehat{\text{FPD}}(M_j, \delta_j, \omega_j) = \frac{-2}{|\widehat{\Pi}_{\text{inc}}|^2} \left[\nabla_{\delta, M} |\widehat{\Pi}_{\text{transm}}|^2 + \nabla_{\delta, M} |\widehat{\Pi}_{\text{scat}}|^2 \right],$$

being $\nabla_{\delta, M}$ the gradient respect to δ and M , and $\nabla_{\delta, M} |\widehat{\Pi}_{\text{scat}}|^2$ and $\nabla_{\delta, M} |\widehat{\Pi}_{\text{transm}}|^2$ are given by (3.B.1) and (3.B.2).

Chapter 4

Numerical simulation of layered materials with non-planar geometries

Contents

4.1	Introduction	131
4.2	Sound-soft periodic surface with a single-layer representation	132
4.2.1	Statement of the problem	132
4.2.2	Classical quasi-periodic Green function	134
4.2.3	Slow-rise windowing Green function	134
4.2.4	Shifted quasi-periodic Green function	136
4.2.5	Integral formulation	138
4.3	Sound-soft periodic surface with a double-layer representation	142
4.3.1	Integral formulation	142
4.4	Transmission problem	146
4.4.1	Statement of the problem	146
4.4.2	Shifted quasi-periodic Green function	149
4.4.3	Integral formulation	149
4.5	Discretization	161
4.5.1	MKN quadrature rules	161
4.5.2	Efficiency computation	162
4.5.3	Discrete problems	166
4.6	Numerical results	171
4.6.1	Numerical results for the scattering problem by a sound-soft boundary with a single-layer formulation	172

4.6.2	Numerical results for the scattering problem by a sound-soft boundary with a double-layer formulation	175
4.6.3	Numerical results for the transmission problem	178
4.7	Conclusions	186
	Appendices	191
4.A	Bessel functions	191
4.B	Kernel decomposition in a periodic setting	193
4.B.1	Single-layer potential	193
4.B.2	Double-layer potential	195
4.B.3	Adjoint double-layer potential	198
4.B.4	Hypersingular formulation	201
4.C	Perfectly Matched Layers	211
4.C.1	Statement of the quasi-periodic problem	211
4.C.2	Variational formulation	214
4.C.3	Finite element discretization	215

4.1 Introduction

In Chapter 3, a viscoelastic material has been characterized considering two different acoustic sources: a plane wave and an acoustic source with a non-planar directivity pattern. In that chapter, it has been considered that the material has a planar surface. The main goal of this chapter is the acoustic characterization of this viscoelastic material with a non-planar surface. Since there exist many difficulties, some simplifications are considered to deal with them, such as to consider that the acoustic source is a plane wave or to consider that the viscoelastic material can only be deformed on tension/compression mechanical stresses (neglecting possible shear effects).

The problem of acoustic wave scattering by a periodic coupling surface between two different media, under plane wave excitation, is deeply studied in a wide range of fields in science and engineering [9, 118, 134, 146, 174, 176]. Many of the used approaches are based on the use of integral equation methods due to the need of discretizing only the boundary of the domain. The slow convergence of the classical expansions for quasi-periodic Green functions is well-known (in fact, do not converge at Wood anomalies [39]). There is a variety of efficient integral equation methods that allow computing solutions accurately with reduced computing times [52, 116, 117]. Particularly in [42, 43], highly accurate solutions of some challenging transverse electric and transverse magnetic scattering problems are obtained with short computational times. The Windowing Green Function method for scattering problems by a periodic perfect conductor is introduced in [39]. The problem is given in the context of electromagnetic wave propagation problems, and plane wave illumination is considered. The methodology is based on the use of quasi-periodic Green functions, in conjunction with a smooth-windowing technique, and presents fast convergence even at and around Wood anomaly configurations where the classical quasi-periodic Green function ceases to exist. The same shifted Green function can be used to solve a problem of scattering by a periodic array of cylinders with fast convergence even at and around Wood anomalies (see [40] for more details). In [41], the windowing technique, in conjunction with free-space Green functions, is applied to transmission problems with superalgebraically convergence.

In this chapter, a fast convergent integral equation method, that solves the problem of acoustic wave scattering by two media in contact in a periodic setting, is introduced. The proposed integral method uses a shifted quasi-periodic Green function and a smooth-windowing technique to achieve the fast convergence. In Section 4.2, the problem of wave scattering by a periodic sound-soft surface is solved, describing the shifted quasi-periodic Green functions and the windowing technique used to achieve the superalgebraically convergence. In this section, a single-layer representation is used. In Section 4.3, the same scattering problem by a periodic sound-soft surface is studied, but in this case, using a double-layer representation. Section 4.4 is devoted to studying the wave scattering problem by a periodic coupling interface between two media, including the integral equation formulation. Section 4.5 shows the discretization of each problem under study, the quadrature rules used to approximate the integrals, and the description of the efficiency test used

to illustrate the convergence order. In Section 4.6, numerical results are presented to illustrate the fast convergence of the proposed method. Finally, in Section 4.7, some conclusions about the methodology are discussed. This chapter has three appendices. Appendix 4.A presents some relevant results about the Bessel functions, which are used widely throughout the sections of this chapter. Appendix 4.B describes the decomposition of the kernels involved in the integral formulation of single-layer, double-layer, adjoint double-layer, and hypersingular representations are detailed. These decompositions are useful to deal with the kernels appearing in the integral formulation. In Appendix 4.C, some relevant questions about Perfectly Matched Layers (PML) are described because the results obtained with the proposed method are compared with the solution computed by using the Finite Element Method (FEM) and the PML technique.

The work presented in this chapter has been carried out during a visit of fourteen weeks at the California Institute of Technology, under the supervision of the professor Oscar P. Bruno.

4.2 Sound-soft periodic surface with a single-layer representation

In this section, the acoustic wave scattering problem (see Figure 4.1) by a sound-soft periodic surface is considered. It is supposed that a plane wave with a concrete incident angle is impinging on the periodic surface. An integral formulation is used to solve the scattering problem, and a single-layer representation is considered. The classical quasi-periodic Green function is introduced in order to show the problems appearing at Wood anomaly frequencies. Moreover, a shifted quasi-periodic Green function is fully described, and used to achieve a fast convergence order.

4.2.1 Statement of the problem

The problem of scattering of a plane wave (see Figure 4.1) by a sound-soft periodic surface is considered

$$\Gamma = \{(x, f(x)), x \in \mathbb{R}\} \text{ with } f \in \mathcal{C}_{\text{per}}^r \left(\left[-\frac{L}{2}, \frac{L}{2} \right] \right), r \geq 2,$$

where $\mathcal{C}_{\text{per}}^r \left(\left[-\frac{L}{2}, \frac{L}{2} \right] \right)$ is the set of L -periodic, and r -times continuously differentiable functions in the real line. The propagation domain is $\Omega = \{(x, y) \in \mathbb{R}^2 : y > f(x)\}$, the incident plane wave is

$$U^{\text{inc}}(x, y) = e^{ik(x \sin \theta - y \cos \theta)} = e^{i(\alpha x - \beta y)}, \quad (4.1)$$

where $\theta \in [-\pi/2, \pi/2]$ is the incidence angle measured from the vertical, and k is the wave number in the propagation domain Ω . Given the incident field U^{inc} (solution of the Helmholtz equation), the problem under consideration is to find a solution $U = U^{\text{inc}} + U^s$ of the Helmholtz equation in Ω such that the scattered field U^s satisfies a Rayleigh expansion

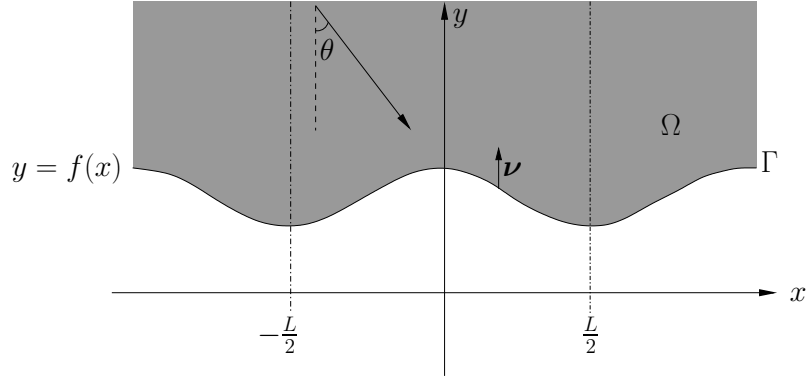


Figure 4.1: Scheme of the problem. The propagation domain Ω is highlighted in grey. Γ is the periodic surface, with period L , and θ is the incidence angle.

radiation condition [146] at infinity, and the quasi-periodicity condition. Moreover, the total field U satisfies the boundary condition $U = 0$ on Γ . That is, the aim is to compute the scattered field $U^s \in C^2(\Omega) \cap C(\bar{\Omega})$ solution of the Helmholtz equation

$$\Delta U^s + k^2 U^s = 0 \text{ in } \Omega,$$

which satisfies

$$\begin{aligned} U^s &= -U^{\text{inc}} \text{ on } \Gamma, \\ U^s(x+L, y) &= U^s(x, y)e^{i\alpha L} \text{ with } (x, y) \in \Gamma. \end{aligned}$$

U^s is required to satisfy a Rayleigh expansion radiation condition [146], that is, the scattered field can be expanded as an infinite sum of plane waves

$$U^s(x, y) = \sum_{n \in \mathbb{N}} a_n e^{i(\alpha_n x + \beta_n y)}, \quad \text{with } (x, y) \in [-L/2, L/2] \times (H, \infty), \quad (4.2)$$

where the Rayleigh coefficients $a_n \in \mathbb{C}$ and $H = \max_{x \in [-L/2, L/2]} f(x)$. Here

$$\alpha_n = \alpha + n \frac{2\pi}{L}, \quad (4.3)$$

and

$$\beta_n = \begin{cases} \sqrt{k^2 - \alpha_n^2} & \text{if } \alpha_n^2 \leq k^2, \\ i\sqrt{\alpha_n^2 - k^2} & \text{otherwise.} \end{cases} \quad (4.4)$$

If the subset of integer numbers $\Lambda = \{n \in \mathbb{Z} : \alpha_n^2 < k^2\}$ is defined, then for $n \in \Lambda$, $e^{i\alpha_n x + i\beta_n y}$ is a propagative plane wave. If $\alpha_n^2 > k^2$, $e^{i\alpha_n x + i\beta_n y}$ are evanescent, that is, they decrease exponentially as $y \rightarrow \infty$. If $\alpha_n^2 = k^2$, $\beta_n = 0$ so $e^{i\alpha_n x + i\beta_n y} = e^{i\alpha_n x}$ is a grazing plane wave, i.e., a plane wave that propagates parallel to the grating, and in that case, k is a value of the so-called Wood anomaly frequency (see [155, 179]). For a fixed L and θ , the set of Wood frequencies can be defined as

$$\mathcal{K} = \{k \in \mathbb{R} : k = \pm \alpha_n, n \in \mathbb{Z}\}.$$

Remark 4.2.1. In what follows, for the sake of simplicity on the exposition of the integral kernels, for $x, x' \in \Omega$ and $y, y' \in \Omega$, it will be defined $X = x - x'$ and $Y = y - y'$.

4.2.2 Classical quasi-periodic Green function

Let $(X, Y) \in \mathbb{R}^2$, $k \notin \mathcal{K}$, that is, k is not a Wood anomaly. Let G be the two-dimensional free space Green function

$$G(X, Y) = \frac{i}{4} H_0^{(1)}(k\sqrt{X^2 + Y^2}), \quad (4.5)$$

where $H_0^{(1)}$ is the first kind Hankel function of order 0 (see (4.A.4) in Appendix 4.A). The quasi-periodic Green function G^q can be constructed as an infinite sum of free-space Green functions (with periodically distributed monopole singularities) (see [44] for further details), that is,

$$G^q(X, Y) = \sum_{n \in \mathbb{Z}} e^{-i\alpha n L} G(X + nL, Y).$$

It may be easily verified that G^q possesses the quasi-periodic property, that is,

$$G^q(X + nL, Y) = e^{i\alpha n L} G^q(X, Y), (X, Y) \in \mathbb{R}^2.$$

It can be defined $\mathcal{B} = \{(x, y) \in \mathbb{R}^2 : (x, y) \neq (mL, 0), m \in \mathbb{Z}\}$. The series $G^q(X, Y)$ converges for $(X, Y) \in \mathcal{B}$ (see [44]), and the regular part of the series can be defined as

$$R^q(X, Y) = \sum_{n \in \mathbb{Z}, |n| \geq 2} e^{-i\alpha n L} G(X + nL, Y),$$

which converges uniformly for (X, Y, k) in any compact subset of $\mathcal{B} \times \bar{\mathcal{K}}$. Moreover, the Green function also admits the Rayleigh expansion (see theorem 4.4 in [44]), that is, can be expressed in spectral form as

$$G^q(X, Y) = \sum_{n \in \mathbb{Z}} \frac{e^{i\alpha_n X + i\beta_n |Y|}}{\beta_n}.$$

This expression is only valid provided $\beta_n \neq 0$ for all $n \in \mathbb{Z}$.

4.2.3 Slow-rise windowing Green function

Following [128], a smooth windowing function S (see Figure 4.2) is introduced. This function is non-zero in an interval of length $2A$ and has a slow rise (is equal to zero for $|x| > A$, is equal to 1 for $|x| < cA$, and decreases from 1 to 0 in a slow and smooth manner: its derivatives tend to zero as $A \rightarrow \infty$ throughout the region of decrease $cA \leq |x| \leq A$ with $0 < c < 1$). This windowing function is given by

$$S(x, cA, A) = \begin{cases} 1 & \text{if } |x| \leq cA, \\ e^{\frac{2e^{-1/u}}{u-1}} & \text{if } cA \leq |x| < A, \\ 0 & \text{if } |x| \geq A. \end{cases} \quad u = \frac{|x| - cA}{A - cA}, \quad (4.6)$$

By using the smooth windowing function (4.6), for wave numbers k that are not Wood

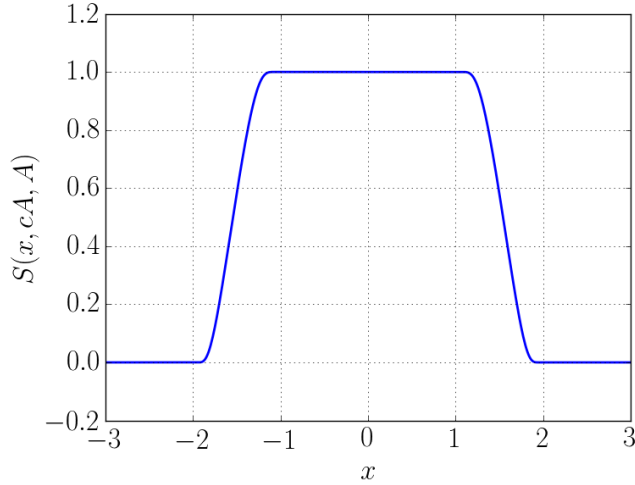


Figure 4.2: Windowing function $S(x, cA, A)$ for $cA = 1$ and $A = 2$.

anomaly values, $k \notin \mathcal{K}$, if $A > L$ then an approximate periodic Green function is defined as follows:

$$G_A^q(X, Y) = \sum_{n \in \mathbb{Z}} e^{-i\alpha nL} G(X + nL, Y) S(X + nL, cA, A),$$

where $0 < c < 1$. Similarly, it is possible to define an approximation of its normal derivative. If $\boldsymbol{\nu}$ is the unit normal to the interface Γ , defined by

$$\boldsymbol{\nu}_x = \frac{(-f'(x), 1)}{\sqrt{1 + f'(x)^2}}, \quad (4.7)$$

the approximation of the normal derivative of G^q is defined as

$$H_A^q(X, Y) = \sum_{n \in \mathbb{Z}} e^{-i\alpha nL} \frac{\partial G}{\partial \boldsymbol{\nu}_{x'}}(X + nL, Y) S(X + nL, cA, A).$$

Theorem 4.2.2. *If k is not a Wood anomaly, f is a smooth function and μ is an α quasi-periodic smooth function, the integral*

$$\int_{-L/2}^{L/2} G_A^q(x - x', y - f(x')) \mu(x') \sqrt{1 + f'(x')^2} dx'$$

converges superalgebraically fast as the truncation radius A tends to infinity, that is, it converges faster than any power of the ratio $\frac{1}{A}$, to

$$\int_{-L/2}^{L/2} G^q(x - x', y - f(x')) \mu(x') \sqrt{1 + f'(x')^2} dx',$$

uniformly for $(x, y) \in [-L/2, L/2] \times \mathbb{R}$ (see [128] for the complete proof). A similar numerical behavior is observed for the integral

$$\int_{-L/2}^{L/2} H_A^q(x - x', y - f(x')) \mu(x') \sqrt{1 + f'(x')^2} dx',$$

which converges superalgebraically fast as A tends to infinity to

$$\int_{-L/2}^{L/2} \frac{\partial G^q}{\partial \nu_{x'}}(x - x', y - f(x')) \mu(x') \sqrt{1 + f'(x')^2} dx',$$

uniformly for $(x, y) \in [-L/2, L/2] \times \mathbb{R}$, where $\nu_{x'}$ is given by (4.7).

4.2.4 Shifted quasi-periodic Green function

To overcome the convergence problem at and around Wood anomaly frequencies, and to solve the scattering problem at all frequencies, the shifted quasi-periodic Green function introduced in [39] is used. The fast decay of this function is proof in [39] for a two-dimensional context, and in [47], and [48] for a three-dimensional case. The fast convergence of the function is achieved adding a number J of Green function poles outside the physical propagation domain. In this chapter, these poles are located outside of Ω vertically below the original Green function pole at distances $h, 2h, \dots, Jh$, that is, the set of shifted poles is given by

$$\mathcal{P}_J = \{(X, Y) \in \mathbb{R}^2 : (X, Y) = (0, -lh) \text{ for some } l \in \mathbb{Z}, \text{ with } 1 \leq l \leq J\}.$$

To define this shifted quasi-periodic Green function, it is necessary to define the rapidly decaying half-space Green functions G_J . If $k \in \bar{\mathcal{K}}$, for a given shift distance $h > 0$, and $J \in \mathbb{N}$, the J -th rapidly-decaying half-space Green function is defined by

$$G_J(X, Y) = \frac{i}{4} \sum_{l=0}^J (-1)^l \binom{J}{l} H_0^{(1)}(k\sqrt{X^2 + (Y + lh)^2}), \quad (4.8)$$

for $(X, Y) \in \mathbb{R}^2$, $(X, Y) \neq (0, -lh)$, $l = 0, \dots, J$. This function G_J is a J -dependent half-space Green function which decays rapidly as X tends to infinity, and is constructed as linear combination of J free-space Green functions (4.5) with shifted arguments. For example, if $J = 1$,

$$G_1(X, Y) = H_0^{(1)}(k\sqrt{X^2 + Y^2}) - H_0^{(1)}(k\sqrt{X^2 + (Y + h)^2}).$$

Then, similarly to the classical case, the new quasi-periodic Green function G_J^q can be constructed as an infinite sum of half-space Green functions (with periodically distributed monopole singularities), that is,

$$G_J^q(X, Y) = \sum_{n \in \mathbb{Z}} e^{-i\alpha n L} G_J(X + nL, Y). \quad (4.9)$$

G_J^q possesses the quasi-periodic property, that is,

$$G_J^q(X + nL, Y) = e^{i\alpha n L} G_J^q(X, Y).$$

Let $\mathcal{B} = \{(x, y) \in \mathbb{R}^2 : (x, y) \neq (mL, 0), m \in \mathbb{Z}\}$. By using (4.8), the quasi-periodic Green function (4.9) is given by

$$G_J^q(X, Y) = \frac{i}{4} \sum_{n \in \mathbb{Z}} e^{-i\alpha n L} \sum_{l=0}^J (-1)^l \binom{J}{l} H_0^{(1)}(k \sqrt{(X + nL)^2 + (Y + lh)^2}),$$

which converges for $(X, Y) \in \mathcal{B}$ (see [44] for more details). Further, the regular part of the series can be defined as

$$R_J^q(X, Y) = \sum_{n \in \mathbb{Z}, |n| \geq 2} e^{-i\alpha n L} G_J(X + nL, Y),$$

which converges uniformly for (X, Y, k) over compact subsets of $\mathcal{B} \times \bar{\mathcal{K}}$. Moreover, for $Y \geq 0$, the Green function G_J^q admits a Rayleigh expansion (see [39]), that is, can be expressed in spectral form as

$$G_J^q(X, Y) = \sum_{n \in \mathbb{Z}} \frac{i}{2L\beta_n} \left(\sum_{l=0}^J (-1)^l \binom{J}{l} e^{i\beta_n lh} \right) e^{i\alpha_n X + i\beta_n |Y|}. \quad (4.10)$$

This expression is only valid provided $\beta_n \neq 0$ for all $n \in \mathbb{Z}$.

Theorem 4.2.3. *Let $J \in \mathbb{N}$ be given. If $A > L$, and k is not a Wood anomaly, by using the smooth windowing function (4.6), an approximate periodic Green function can be defined by*

$$G_{JA}^q(X, Y) = \sum_{n \in \mathbb{Z}} e^{-i\alpha n L} G_J(X + nL, Y) S(X + nL, cA, A),$$

which converges to the quasi-periodic Green function G_J^q faster than any power of the ratio $\frac{1}{A}$ (see [47]), uniformly for $(X, Y) \in [-L/2, L/2] \times \mathbb{R}$. Moreover, if $\boldsymbol{\nu}$ is the unit normal to the interface, the approximation of the normal derivative of G_J can be defined as

$$H_{JA}^q(X, Y) = \sum_{n \in \mathbb{Z}} e^{-i\alpha n L} \frac{\partial G_J}{\partial \boldsymbol{\nu}_{x'}}(X + nL, Y) S(X + nL, cA, A),$$

which converges uniformly for $(X, Y) \in [-L/2, L/2] \times \mathbb{R}$, to the normal derivative of the quasi-periodic Green function $\frac{\partial G_J^q}{\partial \boldsymbol{\nu}_{x'}}$ superalgebraically fast as the truncation radius A tends to infinity.

Convergence at and around Wood anomalies G_J^q converges far away from Wood anomalies. In many cases, the integral operators involved in the integral formulation of the problems are not invertible at Wood anomalies (the integral operators are not invertible for any values of the shift h) or for some values of the shift h (they are not invertible at any value of k). In these cases, a finite number of Rayleigh modes in the spectral expansion of G_J^q (4.10) presents difficulties because their denominators tend to zero as a Wood anomaly is approached. If these terms are excluded of the infinite sum (4.10), then G_J^q converges for each $(X, Y) \in \mathcal{B}$. To overcome these difficulties at and around Wood anomalies, in [39] a modification of G_J^q is described, when a double-layer formulation is used. [40] shows another modification of G_J^q , but in this case, a linear combination of a single- and double-layer formulation is used. In [48], a modified shifted quasi-periodic Green function for a three-dimensional case is shown considering a linear combination of a single- and double-layer formulation. In this chapter, the convergence order is studied in the frequencies far away from Wood anomalies. The study of the proposed methodology at and around Wood anomalies will be considered for a further research.

4.2.5 Integral formulation

Once the shifted quasi-periodic Green function has been defined, the acoustic wave propagation by a periodic sound-soft boundary is studied over one period. Let $\Omega^\#$ and $\Gamma^\#$ be the intersection of Ω and Γ , respectively with the set $(-L/2, L/2) \times \mathbb{R}$ (see Figure 4.3), that is

$$\begin{aligned}\Omega^\# &= \left\{ (x, y) \in \left(-\frac{L}{2}, \frac{L}{2}\right) \times \mathbb{R} : y > f(x) \right\}, \\ \Gamma^\# &= \left\{ (x, f(x)), x \in \left(-\frac{L}{2}, \frac{L}{2}\right) \right\}.\end{aligned}$$

The Dirichlet scattering problem described in Section 4.2.1 can be reduced to second kind integral equations on the curve $\Gamma^\#$ (see [106, 146] for a detailed study), and it can be written by using a variety of integral formulations. In this case, the scattered field is given in the form of a single-layer potential as

$$U^s(x, y) = \int_{-L/2}^{L/2} -G_J^q(x - x', y - f(x')) \varphi^q(x') \sqrt{1 + f'(x')^2} dx', \quad (x, y) \in \Omega^\#, \quad (4.11)$$

with φ^q a quasi-periodic and continuous density, solution of the integral equation

$$\int_{-L/2}^{L/2} G_J^q(x - x', f(x) - f(x')) \varphi^q(x') \sqrt{1 + f'(x')^2} dx' = U^{\text{inc}}(x, f(x)), \quad (x, f(x)) \in \Gamma^\#, \quad (4.12)$$

where U^{inc} is the incident plane wave given in (4.1). In order to solve (4.12), it is necessary to compute the integral in the left-hand side. A modification of the Nyström approach

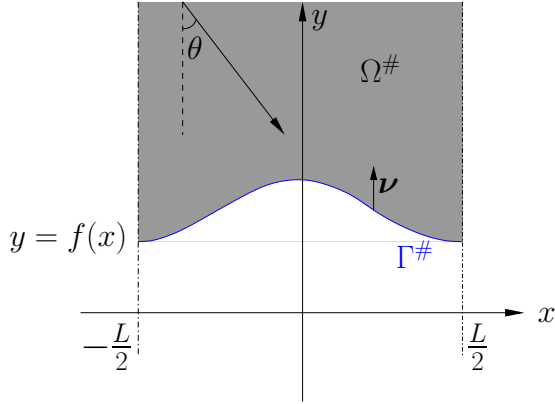


Figure 4.3: Scheme of the periodic problem. The intersection between the propagation domain Ω , and the set $[-L/2, L/2] \times \mathbb{R}$ is denoted by $\Omega^\#$, and is highlighted in grey. $\Gamma^\#$ is the intersection between the interface Γ , and $[-L/2, L/2] \times \mathbb{R}$ (highlighted in blue), where L is the period, and θ is the angle of incidence of the impinging plane wave.

is used [138] to approximate this integral in order to achieve a high-order evaluation of logarithmic integral operators. This method is based on the use of periodic unknowns [39]. Then, considering the change of unknown

$$\varphi^{\text{per}}(x) = \varphi^q(x)e^{-i\alpha x}, \quad (4.13)$$

where, since φ^q is a quasi-periodic function,

$$\varphi^{\text{per}}(x+L) = \varphi^q(x+L)e^{-i\alpha(x+L)} = e^{i\alpha L}\varphi^q(x)e^{-i\alpha x}e^{-i\alpha L} = \varphi^q(x)e^{-i\alpha x},$$

it results that φ^{per} is a periodic function. Then, Equation (4.12) results

$$\int_{-L/2}^{L/2} G_J^q(x-x', f(x)-f(x')) \varphi^{\text{per}}(x') \gamma(x, x') \sqrt{1+f'(x')^2} dx' = U^{\text{inc}}(x, f(x)) e^{-i\alpha x}, \quad (4.14)$$

where $\gamma(x, x') = e^{-i\alpha(x-x')}$.

Lemma 4.2.4. *Let μ be a continuous and periodic density, and f a periodic function, with period L . Taking into account the definition of the shifted quasi-periodic function (4.9),*

$$\begin{aligned} I(x) &= \int_{-L/2}^{L/2} G_J^q(x-x', f(x)-f(x')) \gamma(x, x') \mu(x') \sqrt{1+f'(x')^2} dx' \\ &= \int_{-L/2}^{L/2} \sum_{n \in \mathbb{Z}} e^{-i\alpha n L} G_J(x-x'+nL, f(x)-f(x')) \gamma(x, x') \mu(x') \sqrt{1+f'(x')^2} dx' \\ &= \sum_{n \in \mathbb{Z}} e^{-i\alpha n L} \int_{-L/2}^{L/2} G_J(x-x'+nL, f(x)-f(x')) \gamma(x, x') \mu(x') \sqrt{1+f'(x')^2} dx'. \end{aligned}$$

Considering the change of variable $z' = x' - nL$,

$$\begin{aligned} I(x) &= \sum_{n \in \mathbb{Z}} e^{-i\alpha n L} \int_{-L/2-nL}^{L/2+nL} G_J(x - z', f(x) - f(z' + nL)) \gamma(x, z' + nL) \mu(z' + nL) \\ &\quad \times \sqrt{1 + f'(z' + nL)^2} dz' = \sum_{n \in \mathbb{Z}} \int_{-L/2-nL}^{L/2+nL} G_J(x - z', f(x) - f(z')) \gamma(x, z') \mu(z') \\ &\quad \times \sqrt{1 + f'(z')^2} dz' = \int_{-\infty}^{\infty} G_J(x - z', f(x) - f(z')) \gamma(x, z') \mu(x') \sqrt{1 + f'(z')^2} dz'. \end{aligned}$$

By using Lemma 4.2.4, the left-hand side of (4.14) can be written as (see [39, 128] for more details)

$$\begin{aligned} &\int_{-L/2}^{L/2} G_J^q(x - x', f(x) - f(x')) \varphi^{\text{per}}(x') \gamma(x, x') \sqrt{1 + f'(x')^2} dx' \\ &= \int_{-\infty}^{\infty} G_J(x - x', f(x) - f(x')) \varphi^{\text{per}}(x') \gamma(x, x') \sqrt{1 + f'(x')^2} dx'. \end{aligned}$$

This integral can be truncated by using the window function described in Section 4.2.3, and using Theorem 4.2.3, it is possible to obtain superalgebraically convergence, and it results

$$\begin{aligned} &\int_{-L/2}^{L/2} G_J^q(x - x', f(x) - f(x')) \varphi^{\text{per}}(x') \gamma(x, x') \sqrt{1 + f'(x')^2} dx' \\ &\approx \int_{-\infty}^{\infty} \underbrace{S(x - x', cA, A) G_J(x - x', f(x) - f(x')) \gamma(x, x') \sqrt{1 + f'(x')^2}}_{M_w(x, x'; J)} \varphi^{\text{per}}(x') dx' \\ &= \int_{-\infty}^{\infty} M_w(x, x'; J) \varphi^{\text{per}}(x') dx' = \int_{x-A}^{x+A} M_w(x, x'; J) \varphi^{\text{per}}(x') dx'. \end{aligned} \tag{4.15}$$

Then, Equation (4.14) can be approximated considering (4.15). To achieve a high order accuracy is fundamental to deal with the logarithmic singularity appearing in M_w at $x = x'$. Then, the decomposition of the kernel M_w is studied as follows (the reader is referred to Section 4.B.1 in Appendix 4.B to have a complete and detailed decomposition of a single-layer potential in a periodic setting). To deduce the decomposition of M_w in (4.15), the same steps than in the decomposition of the kernel M (see (4.B.1) in Appendix 4.B) is followed, splitting the kernel in a smooth kernel and a logarithmic part. The difficulties appear whenever $x - x'$ is a multiple of 2π because M_w presents singularities (see Section 4.2.4 for more details). Since the integral (4.15) is solved for $-A < x - x' < A$, the condition $|x - x'| < 2\pi$ is not always satisfied, and hence, an additional cut-off function P_l (see [39]) that vanishes outside a sufficiently small local neighborhood of the singular point $x = x'$ is used. This function is introduced in M_{wl} (see (4.18)), and it can be defined as:

$$P_l(x - x', d_l, A_l) = S(x - x', d_l A_l, A_l), \text{ with } 0 < A_l < L/2, 0 < d_l < 1. \tag{4.16}$$

This local window function is nonzero in an interval of length $2A_l$, and its derivatives tend to zero as $A_l \rightarrow \infty$ throughout the region of decrease $d_l A \leq x - x' \leq A_l$. Then, it is possible to decompose the kernel M_w in (4.15) as the sum of a smooth kernel M_{wr} and a logarithm part as follows

$$\begin{aligned} M_w(x, x'; J) &= S(x - x', cA, A) G_J(x - x', f(x) - f(x')) \gamma(x, x') \sqrt{1 + f'(x')^2} \\ &= M_{wl}(x, x'; J) \ln \left(4 \sin^2 \left(\frac{\pi}{L}(x - x') \right) \right) + M_{wr}(x, x'; J). \end{aligned} \quad (4.17)$$

Remark 4.2.5. The subscript wr denotes the regular part, and wl is used to denote the singular part.

Problem without shifts As in the decomposition of M (see Section (4.B.1) in Appendix 4.B), first of all the problem without shifts is considered, that is, $J = 0$. In a similar way to the kernel decomposition of (4.B.1), considering (4.17) the logarithmic part and the smooth kernel result,

$$M_{wl}(x, x'; 0) = -\frac{1}{4\pi} P_l(x - x', d_l, A_l) J_0 \left(k \sqrt{(x - x')^2 + (f(x) - f(x'))^2} \right) \sqrt{1 + f'(x')^2}, \quad (4.18)$$

$$M_{wr}(x, x'; 0) = M_w(x, x'; 0) - M_{wl}(x, x'; 0) \ln \left(4 \sin^2 \left(\frac{\pi}{L}(x - x') \right) \right), \quad (4.19)$$

where

$$\begin{aligned} M_w(x, x'; 0) &= S(x - x', cA, A) G_J(x - x', f(x) - f(x')) \gamma(x, x') \sqrt{1 + f'(x')^2} \\ &= \frac{i}{4} S(x - x', cA, A) H_0^{(1)} \left(k \sqrt{(x - x')^2 + (f(x) - f(x'))^2} \right) \gamma(x, x') \sqrt{1 + f'(x')^2}. \end{aligned} \quad (4.20)$$

When $x' \rightarrow x$, $\gamma(x, x) = 1$, and the local window (4.16) results $P_l(x, x) = 1$. Then, considering (4.18), and (4.A.9), the values of the function M_{wl} at $x = x'$ result

$$M_{wl}(x, x; 0) = -\frac{1}{4\pi} \sqrt{1 + f'(x)^2},$$

and considering (4.18), (4.19), and (4.20), and proceeding in a similar way to (4.B.4), the values of M_{wr} at $x = x'$ can be computed as

$$\begin{aligned} M_{wr}(x, x; 0) &= \lim_{x' \rightarrow x} M_{wr}(x, x'; 0) = \lim_{x' \rightarrow x} \left[M_w(x, x'; 0) - M_{wl}(x, x'; 0) \ln \left(4 \sin^2 \left(\frac{\pi}{L}(x - x') \right) \right) \right] \\ &= \left[\frac{i}{4} - \frac{C}{2\pi} - \frac{1}{2\pi} \ln \left(\frac{kL}{4\pi} \sqrt{1 + f'(x)^2} \right) \right] \sqrt{1 + f'(x)^2}, \end{aligned}$$

where C is the Euler's constant given by (4.A.3).

Problem with shifts Now the problem with shifts is considered, that is, $J > 0$. Similarly to the problem without shifts, $M_{\text{wl}}(x, x'; J)$ and $M_{\text{wr}}(x, x'; J)$ are defined as in (4.18) and (4.19), but in this case, M_{w} is given by

$$\begin{aligned} M_{\text{w}}(x, x'; J) &= S(x - x', cA, A) G_J(x - x', f(x) - f(x')) \gamma(x, x') \sqrt{1 + f'(x')^2} \\ &= \frac{i}{4} S(x - x', cA, A) \sum_{l=0}^J (-1)^l \binom{J}{l} H_0^{(1)} \left(k \sqrt{(x - x')^2 + (f(x) - f(x') + lh)^2} \right) \\ &\quad \times \gamma(x, x') \sqrt{1 + f'(x')^2}. \end{aligned} \quad (4.21)$$

Considering (4.18), (4.19), and (4.21), and working similarly to (4.B.5), the values of the function $M_{\text{wr}}(x, x; J)$ at $x = x'$ can be computed as

$$\begin{aligned} M_{\text{wr}}(x, x; J) &= \lim_{x' \rightarrow x} M_{\text{wr}}(x, x'; J) = \lim_{x' \rightarrow x} \left[M_{\text{w}}(x, x'; J) - M_{\text{wl}}(x, x'; J) \ln \left(4 \sin^2 \left(\frac{\pi}{L}(x - x') \right) \right) \right] \\ &= \left[\frac{i}{4} - \frac{C}{2\pi} - \frac{1}{2\pi} \ln \left(\frac{kL}{4\pi} \sqrt{1 + f'(x)^2} \right) + \frac{i}{4} \sum_{l=1}^J (-1)^l \binom{J}{l} H_0^{(1)}(klh) \right] \sqrt{1 + f'(x)^2}, \end{aligned}$$

where C is the Euler's constant given by (4.A.3).

4.3 Sound-soft periodic surface with a double-layer representation

In this section, the same problem of scattering of a plane wave by a sound-soft periodic surface studied in Section 4.2.1 is considered (see Figure 4.1). In this case, instead of using a single-layer formulation, a double-layer representation is considered.

4.3.1 Integral formulation

As in Section 4.2.5, the acoustic wave propagation problem by a periodic sound-soft boundary is studied over one period. Let $\Omega^\#$ and $\Gamma^\#$ be the intersection of Ω , and Γ , respectively, with the set $x \in (-L/2, L/2) \times \mathbb{R}$ (see Figure 4.3). In this section, the Dirichlet scattering problem described in Section 4.2.1 is solved by using an integral formulation considering that the scattered field is given in the form of a double-layer potential [107]. Then, the scattered field may be written as

$$U^s(x, y) = \int_{-L/2}^{L/2} \frac{\partial G_J^q}{\partial \nu_{x'}}(x - x', f(x) - f(x')) \varphi^q(x') \sqrt{1 + f'(x')^2} dx', \quad (x, y) \in \Omega^\#, \quad (4.22)$$

with φ^q a quasi-periodic and continuous density, solution of the integral equation

$$\varphi^q(x) + 2 \int_{-L/2}^{L/2} \frac{\partial G_J^q}{\partial \nu_{x'}}(x - x', f(x) - f(x')) \varphi^q(x') \sqrt{1 + f'(x')^2} dx' = -2U^{\text{inc}}(x, f(x)),$$

$$(x, f(x)) \in \Gamma^\#, \quad (4.23)$$

being ν the unit normal vector to the interface $\Gamma^\#$ defined by (4.7). To solve (4.23), it is necessary to compute the integral in the left-hand side. As in Section 4.2.5, to approximate this integral, a modification of the Nyström approach, based on use of periodic unknowns, is used (see [39] for further information). Then, using the change of unknown defined in (4.13), Equation (4.23) results

$$\begin{aligned} \varphi^{\text{per}}(x) + 2 \int_{-L/2}^{L/2} \frac{\partial G_J^q}{\partial \nu_{x'}}(x - x', f(x) - f(x')) \varphi^{\text{per}}(x') \gamma(x, x') \sqrt{1 + f'(x')^2} dx' \\ = -2U^{\text{inc}}(x, f(x)) e^{-i\alpha x}, \end{aligned} \quad (4.24)$$

where $\gamma(x, x') = e^{-i\alpha(x-x')}$. By using Lemma 4.2.4, the integral in the left-hand side of (4.24) can be written as

$$\begin{aligned} & \int_{-L/2}^{L/2} \frac{\partial G_J^q}{\partial \nu_{x'}}(x - x', f(x) - f(x')) \varphi^{\text{per}}(x') \gamma(x, x') \sqrt{1 + f'(x')^2} dx' \\ &= \int_{-\infty}^{\infty} \frac{\partial G_J}{\partial \nu_{x'}}(x - x', f(x) - f(x')) \varphi^{\text{per}}(x') \gamma(x, x') \sqrt{1 + f'(x')^2} dx'. \end{aligned}$$

This integral can be truncated by using the window function described in Section 4.2.3. Taking into account Theorem 4.2.3, superalgebraically convergence is obtained. Then, the previous integral results

$$\begin{aligned} & \int_{\Gamma^\#} \frac{\partial G_J^q}{\partial \nu_{x'}}(x - x', f(x) - f(x')) \varphi^{\text{per}}(x') \gamma(x, x') ds(x') \\ & \approx \underbrace{\int_{-\infty}^{\infty} S(x - x', cA, A) \frac{\partial G_J}{\partial \nu_{x'}}(x - x', f(x) - f(x')) \gamma(x, x') \sqrt{1 + f'(x')^2} \varphi^{\text{per}}(x') dx'}_{L_w(x, x'; J)} \\ &= \int_{-\infty}^{\infty} L_w(x, x'; J) \varphi^{\text{per}}(x') dx' = \int_{x-A}^{x+A} L_w(x, x'; J) \varphi^{\text{per}}(x') dx'. \end{aligned} \quad (4.25)$$

Equation (4.24) can be approximated by using (4.25). In order to achieve a high-order accuracy, it is necessary to deal with the logarithmic singularity that appears in L_w at $x = x'$. For this purpose, the decomposition of L_w is studied as follows. To get a complete comprehension of the decomposition, the reader is referred to Section 4.B.2 in Appendix 4.B where a complete and detailed decomposition of a double-layer potential in a periodic setting

is shown. Following the same steps applied for L (see (4.B.6) in Appendix 4.B), the kernel L_w can be split in a smooth kernel, and a logarithmic part. Moreover, wherever $x - x'$ is a multiple of 2π , L_w presents singularities (see Section 4.2.4 for more details) and, since the integration interval is $-A < x - x' < A$, the condition $|x - x'| < 2\pi$ is not always satisfied. As in the single-layer formulation, the additional cut-off function P_l defined in (4.16) is introduced in L_{wl} (see (4.27)). Consequently, the integrand in (4.25) may be rewritten as the sum of a smooth kernel, and a logarithm part (recall that the function P_l vanishes outside a sufficiently small local neighborhood of the singular point $x = x'$). Then, L_w is given by

$$\begin{aligned} L_w(x, x'; J) &= S(x - x', cA, A) \frac{\partial G_J}{\partial \nu_{x'}}(x - x', f(x) - f(x')) \gamma(x, x') \sqrt{1 + f'(x')^2} \\ &= \frac{i}{4} S(x - x', cA, A) \sum_{l=0}^J (-1)^l \binom{J}{l} \frac{\partial H_0^{(1)}}{\partial \nu_{x'}} \left(k \sqrt{(x - x')^2 + (f(x) - f(x') + lh)^2} \right) \\ &\quad \times \gamma(x, x') \sqrt{1 + f'(x')^2} \\ &= \frac{ik}{4} S(x - x', cA, A) \sum_{l=0}^J \left[(-1)^l \binom{J}{l} H_1^{(1)} \left(k \sqrt{(x - x')^2 + (f(x) - f(x') + lh)^2} \right) \right. \\ &\quad \left. \times \frac{-f'(x')(x - x') + f(x) - f(x') + lh}{\sqrt{(x - x')^2 + (f(x) - f(x') + lh)^2}} \right] \gamma(x, x'). \end{aligned} \quad (4.26)$$

Problem without shifts As in the decomposition of the kernel L , first of all the problem without shifts is considered, that is, $J = 0$. Considering (4.26), and in a similar manner to the decomposition of (4.B.6), the logarithmic part, and the smooth kernel L_{wr} (see Remark 4.2.5 for subscript notation) are given by

$$\begin{aligned} L_{wl}(x, x'; 0) &= -\frac{k}{4\pi} P_l(x - x', d_l, A_l) J_1 \left(k \sqrt{(x - x')^2 + (f(x) - f(x'))^2} \right) \\ &\quad \times \frac{-f'(x')(x - x') + f(x) - f(x')}{\sqrt{(x - x')^2 + (f(x) - f(x'))^2}}, \end{aligned} \quad (4.27)$$

$$L_{wr}(x, x'; 0) = L_w(x, x'; 0) - L_{wl}(x, x') \ln \left(4 \sin^2 \left(\frac{\pi}{L}(x - x') \right) \right), \quad (4.28)$$

where

$$\begin{aligned} L_w(x, x'; 0) &= S(x - x', cA, A) \frac{\partial G_J}{\partial \nu_{x'}}(x - x', f(x) - f(x')) \gamma(x, x') \sqrt{1 + f'(x')^2} \\ &= \frac{i}{4} S(x - x', cA, A) \frac{\partial H_0^{(1)}}{\partial \nu_{x'}} \left(k \sqrt{(x - x')^2 + (f(x) - f(x'))^2} \right) \gamma(x, x') \sqrt{1 + f'(x')^2}. \end{aligned} \quad (4.29)$$

When $x = x'$, $\gamma(x, x) = 1$, and $P_l(x, x) = 1$. Then, taking into account the definition of L_{wl} (4.27), the asymptotic behavior of the Bessel function $J_1(t)$ when $t \rightarrow 0$ (see (4.A.10)

in Appendix 4.A), and proceeding in a similar way to (4.B.9), the values of the kernel L_{wl} at $x = x'$ can be computed as

$$L_{\text{wl}}(x, x; 0) = \lim_{x' \rightarrow x} L_{\text{wl}}(x, x'; 0) = \lim_{x' \rightarrow x} -\frac{k^2}{8\pi} P_l(x-x', d_l, A_l)(-f'(x')(x-x') + f(x) - f(x')) = 0,$$

and considering (4.27), (4.28), and (4.29), and proceeding in a similar manner to (4.B.12), the values of L_{wr} at $x = x'$ can be calculated by

$$\begin{aligned} L_{\text{wr}}(x, x; 0) &= \lim_{x' \rightarrow x} L_{\text{wr}}(x, x'; 0) = \lim_{x' \rightarrow x} \left[L_{\text{w}}(x, x'; 0) - L_{\text{wl}}(x, x'; 0) \ln \left(4 \sin^2 \left(\frac{\pi}{L}(x-x') \right) \right) \right] \\ &= \lim_{x' \rightarrow x} \left[\frac{ik}{4} S(x-x', cA, A) H_1^{(1)} \left(k \sqrt{(x-x')^2 + (f(x) - f(x'))^2} \right) \gamma(x, x') \right. \\ &\quad \times \frac{-f'(x')(x-x') + f(x) - f(x')}{\sqrt{(x-x')^2 + (f(x) - f(x'))^2}} + \frac{k}{4\pi} P_l(x-x', d_l, A_l) \\ &\quad \times \ln \left(4 \sin^2 \left(\frac{\pi}{L}(x-x') \right) \right) J_1 \left(k \sqrt{(x-x')^2 + (f(x) - f(x'))^2} \right) \\ &\quad \left. \times \frac{-f'(x')(x-x') + f(x) - f(x')}{\sqrt{(x-x')^2 + (f(x) - f(x'))^2}} \right] = \frac{f''(x)}{4\pi(1 + f'(x)^2)}. \end{aligned}$$

Problem with shifts Now, the problem with shifts is considered, that is, $J > 0$. Similarly to the problem without shifts, L_{wl} and L_{wr} are defined as in (4.27) and (4.28), but in this case, L_{w} is given by (4.26). Taking into account (4.26), (4.27), and (4.28), the value of the function $L_{\text{wr}}(x, x)$ when x coincides with x' is given by

$$\begin{aligned} L_{\text{wr}}(x, x; J) &= \lim_{x' \rightarrow x} L_{\text{wr}}(x, x'; J) = \lim_{x' \rightarrow x} \left[L_{\text{w}}(x, x'; J) - L_{\text{wl}}(x, x'; J) \ln \left(4 \sin^2 \left(\frac{\pi}{L}(x-x') \right) \right) \right] \\ &= \lim_{x' \rightarrow x} \left[\frac{ik}{4} \sum_{l=0}^J \left[(-1)^l \binom{J}{l} H_1^{(1)} \left(k \sqrt{(x-x')^2 + (f(x) - f(x') + lh)^2} \right) \right. \right. \\ &\quad \times \frac{-f'(x')(x-x') + f(x) - f(x') + lh}{\sqrt{(x-x')^2 + (f(x) - f(x') + lh)^2}} \left. \right] \gamma(x, x') S(x-x', cA, A) \\ &\quad + \frac{k}{4\pi} \ln \left(4 \sin^2 \left(\frac{\pi}{L}(x-x') \right) \right) J_1 \left(k \sqrt{(x-x')^2 + (f(x) - f(x'))^2} \right) \\ &\quad \left. \times P_l(x-x', d_l, A_l) \frac{-f'(x')(x-x') + f(x) - f(x')}{\sqrt{(x-x')^2 + (f(x) - f(x'))^2}} \right]. \end{aligned}$$

The singularities in the Hankel function $H_1^{(1)}$ appear when $l = 0$ so, the sum is split into two parts: $l = 0$ and $l > 0$. The values of L_{wr} at $x = x'$ are given by

$$\begin{aligned} L_{\text{wr}}(x, x; J) &= \lim_{x' \rightarrow x} L_{\text{wr}}(x, x'; J) = \lim_{x' \rightarrow x} \frac{k}{4} (iS(x - x', cA, A)\gamma(x, x') \\ &\quad \times H_1^{(1)}\left(k\sqrt{(x - x')^2 + (f(x) - f(x'))^2}\right) \frac{-f'(x')(x - x') + f(x) - f(x')}{\sqrt{(x - x')^2 + (f(x) - f(x'))^2}} \\ &\quad + \frac{1 - f'(x')(x - x') + f(x) - f(x')}{\pi \sqrt{(x - x')^2 + (f(x) - f(x'))^2}} J_1\left(k\sqrt{(x - x')^2 + (f(x) - f(x'))^2}\right) \\ &\quad \times P_l(x - x', d_l, A_l) \ln\left(4\sin^2\left(\frac{\pi}{L}(x - x')\right)\right) + iS(x - x', cA, A)\gamma(x, x') \\ &\quad \times \sum_{l=1}^J \left[(-1)^l \binom{J}{l} H_1^{(1)}\left(k\sqrt{(x - x')^2 + (f(x) - f(x') + lh)^2}\right) \right. \\ &\quad \left. \times \frac{-f'(x')(x - x') + f(x) - f(x') + lh}{\sqrt{(x - x')^2 + (f(x) - f(x') + lh)^2}} \right] = \frac{f''(x)}{4\pi(1 + f'(x)^2)} \\ &\quad + \frac{ik}{4} \sum_{l=1}^J (-1)^l \binom{J}{l} H_1^{(1)}(klh). \end{aligned}$$

4.4 Transmission problem

In this section, the wave propagation between two periodic media in contact is considered. The scattering problem by a periodic coupling interface is described (see Figure 4.4). As in previous sections, it is supposed that a plane wave with a given incident angle is impinging on the periodic interface. An integral formulation is used to solve the scattering problem considering a linear combination of a single- and a double-layer representations.

4.4.1 Statement of the problem

The transmission problem (see Figure 4.4) of a plane wave by a periodic surface is considered.

$$\Gamma = \{(x, f(x)), x \in \mathbb{R}\} \text{ with } f \in C_{\text{per}}^r \left(\left[-\frac{L}{2}, \frac{L}{2} \right] \right), r \geq 2.$$

The propagation domains of the scattered and the transmitted field are, respectively,

$$\begin{aligned} \Omega_+ &= \{(x, y) \in \mathbb{R}^2 : y > f(x)\}, \\ \Omega_- &= \{(x, y) \in \mathbb{R}^2 : y < f(x)\}. \end{aligned}$$

The incident plane wave is

$$U^{\text{inc}}(x, y) = e^{ik^+(x \sin \theta^+ - y \cos \theta^+)} = e^{i(\alpha x - \beta y)}, \quad (4.30)$$

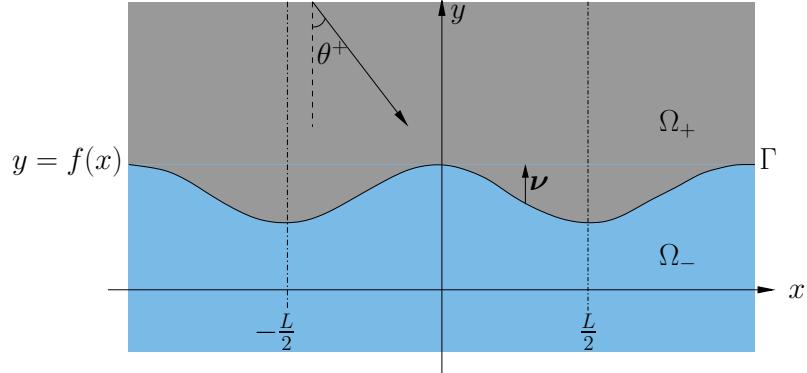


Figure 4.4: Scheme of the transmission problem between two media. The propagation domain of the scattered field Ω_+ is highlighted in grey, and the propagation domain of the transmitted field Ω_- is highlighted in cyan. Γ is the periodic surface with period L , and θ^+ is the incidence angle in Ω_+ .

where $\theta^+ \in (-\pi/2, \pi/2)$ is the incidence angle in Ω_+ measured from the vertical and k^+ is the wave number in the propagation domain Ω_+ . Given the incident field U^{inc} (solution of the Helmholtz equation), the problem under consideration is to find $U_+ = U^s + U^{\text{inc}}$ and U_- solutions to the Helmholtz equation in Ω_+ and Ω_- , respectively, that is,

$$\begin{aligned}\Delta U_+ + (k^+)^2 U_+ &= 0 \text{ in } \Omega_+, \\ \Delta U_- + (k^-)^2 U_- &= 0 \text{ in } \Omega_-,\end{aligned}$$

where k^- is the wave number in the propagation domain Ω_- . The aim is to compute the scattered field $U^s \in \mathcal{C}^2(\Omega_+) \cap \mathcal{C}^1(\overline{\Omega}_+)$ solution of the Helmholtz equation

$$\Delta U^s + (k^+)^2 U^s = 0 \text{ in } \Omega_+, \quad (4.31)$$

and the transmitted field $U_- \in \mathcal{C}^2(\Omega_-) \cap \mathcal{C}^1(\overline{\Omega}_-)$ solution of the Helmholtz equation

$$\Delta U_- + (k^-)^2 U_- = 0 \text{ in } \Omega_-, \quad (4.32)$$

such that

$$U^s - U_- = -U^{\text{inc}} \quad \text{on } \Gamma, \quad (4.33)$$

$$\frac{\partial U^s}{\partial \nu} - \frac{\partial U_-}{\partial \nu} = -\frac{\partial U^{\text{inc}}}{\partial \nu} \quad \text{on } \Gamma, \quad (4.34)$$

$$U^s(x + L, y) = U^s(x, y)e^{i\alpha L} \quad \text{with } (x, y) \in \Gamma, \quad (4.35)$$

$$U_-(x + L, y) = U_-(x, y)e^{i\alpha L} \quad \text{with } (x, y) \in \Gamma, \quad (4.36)$$

where ν is the unit normal vector to the interface Γ defined by

$$\nu_x = \frac{(-f'(x), 1)}{\sqrt{1 + f'(x)^2}}. \quad (4.37)$$

U^s is required to satisfy a Rayleigh expansion radiation condition [146], that is, the scattered field can be expanded as an infinite sum of plane waves

$$U^s(x, y) = \sum_{n \in \mathbb{Z}} a_n^+ e^{i(\alpha_n^+ x + \beta_n^+ y)}, \text{ with } (x, y) \in [-L/2, L/2] \times (H, \infty), \quad (4.38)$$

where the Rayleigh coefficients $a_n^+ \in \mathbb{C}$, and $H = \max_{x \in [-\frac{L}{2}, \frac{L}{2}]} f(x)$. Here

$$\alpha_n^+ = \alpha + n \frac{2\pi}{L}$$

and

$$\beta_n^+ = \begin{cases} \sqrt{(k^+)^2 - (\alpha_n^+)^2} & \text{if } |\alpha_n^+| \leq k^+, \\ i\sqrt{(\alpha_n^+)^2 - (k^+)^2} & \text{if } |\alpha_n^+| > k^+. \end{cases} \quad (4.39)$$

Let $\Lambda_+ = \{n \in \mathbb{Z} : (\alpha_n^+)^2 < (k^+)^2\}$. For $n \in \Lambda_+$, $e^{i\alpha_n^+ x + i\beta_n^+ y}$ is a propagative plane wave. If $(\alpha_n^+)^2 > (k^+)^2$, $e^{i\alpha_n^+ x + i\beta_n^+ y}$ are evanescent waves, that is, they decrease exponentially as $y \rightarrow \infty$. If $(\alpha_n^+)^2 = (k^+)^2$, $\beta_n^+ = 0$ so $e^{i\alpha_n^+ x + i\beta_n^+ y} = e^{i\alpha_n^+ x}$ is a grazing plane wave, i.e., a plane wave that propagates parallel to the grating, and k^+ is a Wood anomaly frequency (see [155, 179]).

Similarly, U_- is required to satisfy a Rayleigh expansion radiation condition [146], that is, the transmitted field can be expanded as an infinite sum of plane waves

$$U_-(x, y) = \sum_{n \in \mathbb{Z}} a_n^- e^{i(\alpha_n^- x - \beta_n^- y)}, \text{ with } (x, y) \in [-L/2, L/2] \times (-\infty, h), \quad (4.40)$$

where the Rayleigh coefficients $a_n^- \in \mathbb{C}$, and $h = \min_{x \in [-\frac{L}{2}, \frac{L}{2}]} f(x)$. Here

$$\alpha_n^- = \gamma + n \frac{2\pi}{L},$$

where $\gamma = k^- \sin \theta^- = k^+ \sin \theta^+ = \alpha$ to preserve the continuity on the interface, being θ^- the incident angle in Ω_- , that is, $\alpha_n^+ = \alpha_n^-$, and

$$\beta_n^- = \begin{cases} \sqrt{(k^-)^2 - (\alpha_n^-)^2} & \text{if } |\alpha_n^-| \leq k^-, \\ i\sqrt{(\alpha_n^-)^2 - (k^-)^2} & \text{if } |\alpha_n^-| > k^-. \end{cases} \quad (4.41)$$

Let $\Lambda_- = \{n \in \mathbb{Z} : (\alpha_n^-)^2 < (k^-)^2\}$. For $n \in \Lambda_-$, $e^{i\alpha_n^- x - i\beta_n^- y}$ is a propagative plane wave. If $(\alpha_n^-)^2 > (k^-)^2$, $e^{i\alpha_n^- x - i\beta_n^- y}$ are evanescent waves, that is, they decrease exponentially as $y \rightarrow -\infty$. If $(\alpha_n^-)^2 = (k^-)^2$, $\beta_n^- = 0$ so $e^{i\alpha_n^- x + i\beta_n^- y} = e^{i\alpha_n^- x}$ is a grazing plane wave, i.e., a plane wave that propagates parallel to the grating, and k^- is a Wood anomaly frequency

4.4.2 Shifted quasi-periodic Green function

The definition of the shifted quasi-periodic Green functions in Ω_+ and Ω_- is given as in Section 4.2.4: they can be constructed as an infinite sum of half-space Green functions (with periodically distributed monopole singularities), and the fast convergence of the method is achieved adding a number J of Green function poles outside the propagation domain. The shifted poles for the Green function G_{J+}^q are located in Ω_- vertically below the original Green function pole at distances $h^+, 2h^+, \dots, Jh^+$, and those for the Green function G_{J-}^q are located in Ω_+ vertically above the original Green function pole at distances $h^-, 2h^-, \dots, Jh^-$, that is, the sets of shifted poles are given by

$$\begin{aligned}\mathcal{P}_J^+ &= \{(X, Y) \in \mathbb{R}^2 : (X, Y) = (0, -lh^+) \text{ for some } l \in \mathbb{Z}, \text{ with } 1 \leq l \leq J\}, \\ \mathcal{P}_J^- &= \{(X, Y) \in \mathbb{R}^2 : (X, Y) = (0, lh^-) \text{ for some } l \in \mathbb{Z}, \text{ with } 1 \leq l \leq J\}.\end{aligned}$$

Then, the shifted quasi-periodic Green functions in Ω_\pm are given by

$$G_{J\pm}^q(X, Y) = \sum_{n \in \mathbb{Z}} e^{-i\alpha n L} G_{J\pm}(X + nL, Y), \quad (4.42)$$

where for $(X, Y) \in \mathbb{R}^2$, $(X, Y) \neq (0, \mp lh^\pm)$, $l = 0, \dots, J$, it holds

$$G_{J\pm}(X, Y) = \frac{i}{4} \sum_{l=0}^J (-1)^l \binom{J}{l} H_0^{(1)}(k^\pm \sqrt{X^2 + (Y \pm lh^\pm)^2}). \quad (4.43)$$

The functions $G_{J\pm}$ are the J -th rapidly-decaying half-space Green functions in Ω_+ and Ω_- , where the values $h^+ > 0$ and $h^- > 0$ are the shift distances in Ω_+ and Ω_- . Then, the shifted quasi-periodic Green functions (4.42) are given by

$$G_{J\pm}^q(X, Y) = \frac{i}{4} \sum_{n \in \mathbb{Z}} e^{-i\alpha n L} \sum_{l=0}^J (-1)^l \binom{J}{l} H_0^{(1)}(k^\pm \sqrt{(X + nL)^2 + (Y \pm lh^\pm)^2}). \quad (4.44)$$

4.4.3 Integral formulation

Once the transmission problem is described, to work with the quasi-periodic Green function it is necessary to consider domains formed only by a period. Let $\Omega_+^\#$, $\Omega_-^\#$ and $\Gamma^\#$ be the intersection of Ω_+ , Ω_- and Γ , respectively with the set $(-L/2, L/2) \times \mathbb{R}$ (see Figure 4.5),

$$\begin{aligned}\Omega_+^\# &= \{(x, y) \in (-L/2, L/2) \times \mathbb{R} : y > f(x)\}, \\ \Omega_-^\# &= \{(x, y) \in (-L/2, L/2) \times \mathbb{R} : y < f(x)\}, \\ \Gamma^\# &= \{(x, f(x)) \mid x \in (-L/2, L/2)\}.\end{aligned}$$

The transmission problem described in Section 4.4.1 can be reduced to a system of sec-

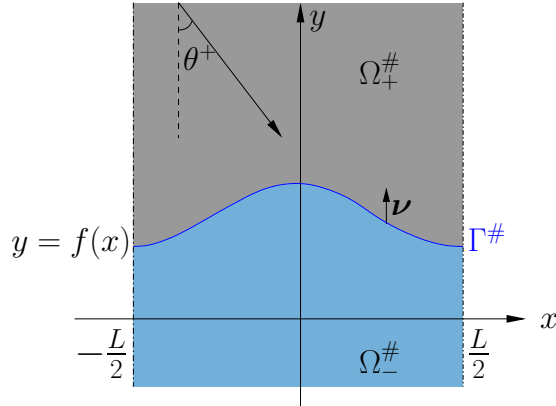


Figure 4.5: Scheme of the periodic transmission problem. The intersection between the propagation domain Ω_+ (resp. Ω_-) and the set $[-L/2, L/2] \times \mathbb{R}$ is denoted by $\Omega_+^\#$ (resp. $\Omega_-^\#$), and is highlighted in grey (resp. in cyan). $\Gamma^\#$ is the intersection between the interface Γ and the set $[-L/2, L/2] \times \mathbb{R}$ (highlighted in blue), where L is the period, and θ^+ is the incidence angle.

ond kind integral equations over the curve $\Gamma^\#$. The scattered field, written as a linear combination of a single- and double-layer potential, is given by

$$U^s(x, y) = \int_{-L/2}^{L/2} \left[\frac{\partial G_{J+}^q}{\partial \nu_{x'}}(x - x', y - f(x')) \varphi^q(x') - G_{J+}^q(x - x', y - f(x')) \phi^q(x') \right] \\ \times \sqrt{1 + f'(x')^2} dx', \quad (x, y) \in \Omega_+^\#, \quad (4.45)$$

and the transmitted field, given as a linear combination of a single- and double-layer potential, is written as

$$U_-(x, y) = \int_{-L/2}^{L/2} \left[-\frac{\partial G_{J-}^q}{\partial \nu_{x'}}(x - x', y - f(x')) \varphi^q(x') + G_{J-}^q(x - x', y - f(x')) \phi^q(x') \right] \\ \times \sqrt{1 + f'(x')^2} dx', \quad (x, y) \in \Omega_-^\#, \quad (4.46)$$

where ν is the normal vector to $\Gamma^\#$, pointing outwards $\Omega_-^\#$, which is defined in (4.37), $G_{J\pm}^q$ are the shifted quasi-periodic Green functions given in (4.44), and φ^q, ϕ^q are quasi-periodic and continuous densities, solution of the system of integral equations (see [41] for further details)

$$\begin{cases} \varphi^q + (D_- - D_+) \varphi^q + (S_+ - S_-) \phi^q = U^{\text{inc}}(x, f(x)), \\ \phi^q + (N_- - N_+) \varphi^q + (K_+ - K_-) \phi^q = \frac{\partial U^{\text{inc}}}{\partial \nu_x}(x, f(x)), \end{cases} \quad (x, f(x)) \in \Gamma^\#, \quad (4.47)$$

where U^{inc} is the incident plane wave given in (4.30).

The integral operators S_{\pm} , D_{\pm} , N_{\pm} , and K_{\pm} are defined as follows:

$$\begin{aligned} S_{\pm}[\mu](x, y) &= \int_{-L/2}^{L/2} G_{J\pm}^q(x - x', y - f(x')) \mu(x') \sqrt{1 + f'(x')^2} dx', \\ D_{\pm}[\mu](x, y) &= \int_{-L/2}^{L/2} \frac{\partial G_{J\pm}^q}{\partial \nu_{x'}}(x - x', y - f(x')) \mu(x') \sqrt{1 + f'(x')^2} dx', \\ N_{\pm}[\mu](x, y) &= \int_{-L/2}^{L/2} \frac{\partial^2 G_{J\pm}^q}{\partial \nu_x \partial \nu_{x'}}(x - x', y - f(x')) \mu(x') \sqrt{1 + f'(x')^2} dx', \\ K_{\pm}[\mu](x, y) &= \int_{-L/2}^{L/2} \frac{\partial G_{J\pm}^q}{\partial \nu_x}(x - x', y - f(x')) \mu(x') \sqrt{1 + f'(x')^2} dx', \end{aligned}$$

where S_{\pm} are single-layer potentials, D_{\pm} are double-layer potentials, N_{\pm} are hypersingular potentials and K_{\pm} are adjoint double-layer potentials (see [107] for more details).

As in the sound-soft periodic problem, to solve (4.47) the integral operators are approximated by using a modification of the Nyström approach, based on the use of periodic unknowns. Then, taking into account the changes of unknowns $\varphi^{\text{per}}(x) = \varphi^q(x)e^{-i\alpha x}$, and $\phi^{\text{per}}(x) = \phi^q(x)e^{-i\alpha x}$, the system of integral equations (4.47) results

$$\begin{aligned} \varphi^{\text{per}}(x) + \int_{-L/2}^{L/2} \left(\frac{\partial G_{J-}^q}{\partial \nu_{x'}}(x - x', f(x) - f(x')) - \frac{\partial G_{J+}^q}{\partial \nu_{x'}}(x - x', f(x) - f(x')) \right) \\ \times \varphi^{\text{per}}(x') \gamma(x, x') \sqrt{1 + f'(x')^2} dx' + \int_{-L/2}^{L/2} \left(G_{J+}^q(x - x', f(x) - f(x')) \right. \\ \left. - G_{J-}^q(x - x', f(x) - f(x')) \right) \phi^{\text{per}}(x') \gamma(x, x') \sqrt{1 + f'(x')^2} dx' = U^{\text{inc}}(x, f(x)) e^{-i\alpha x}, \end{aligned} \quad (4.48)$$

$$\begin{aligned} \phi^{\text{per}}(x) + \int_{-L/2}^{L/2} \left(\frac{\partial^2 G_{J-}^q}{\partial \nu_x \partial \nu_{x'}}(x - x', f(x) - f(x')) - \frac{\partial^2 G_{J+}^q}{\partial \nu_x \partial \nu_{x'}}(x - x', f(x) - f(x')) \right) \\ \times \varphi^{\text{per}}(x') \gamma(x, x') \sqrt{1 + f'(x')^2} dx' + \int_{-L/2}^{L/2} \left(\frac{\partial G_{J+}^q}{\partial \nu_x}(x - x', f(x) - f(x')) \right. \\ \left. - \frac{\partial G_{J-}^q}{\partial \nu_x}(x - x', f(x) - f(x')) \right) \phi^{\text{per}}(x') \gamma(x, x') \sqrt{1 + f'(x')^2} dx' = \frac{\partial U^{\text{inc}}}{\partial \nu_x}(x, f(x)) e^{-i\alpha x}, \end{aligned} \quad (4.49)$$

where $\gamma(x, x') = e^{-i\alpha(x-x')}$. To solve (4.48) and (4.49), first of all it is necessary to compute the integrals in the left-hand side, that is,

$$I_1(x) = \int_{-L/2}^{L/2} \left[\left(\frac{\partial G_{J-}^q}{\partial \boldsymbol{\nu}_{x'}}(x - x', f(x) - f(x')) - \frac{\partial G_{J+}^q}{\partial \boldsymbol{\nu}_{x'}}(x - x', f(x) - f(x')) \right) \varphi^{\text{per}}(x') \times \gamma(x, x') \sqrt{1 + f'(x')^2} \right] dx', \quad (4.50)$$

$$I_2(x) = \int_{-L/2}^{L/2} \left[(G_{J+}^q(x - x', f(x) - f(x')) - G_{J-}^q(x - x', f(x) - f(x'))) \phi^{\text{per}}(x') \gamma(x, x') \times \sqrt{1 + f'(x')^2} \right] dx', \quad (4.51)$$

$$I_3(x) = \int_{-L/2}^{L/2} \left[\left(\frac{\partial^2 G_{J-}^q}{\partial \boldsymbol{\nu}_x \partial \boldsymbol{\nu}_{x'}}(x - x', f(x) - f(x')) - \frac{\partial^2 G_{J+}^q}{\partial \boldsymbol{\nu}_x \partial \boldsymbol{\nu}_{x'}}(x - x', f(x) - f(x')) \right) \times \varphi^{\text{per}}(x') \gamma(x, x') \sqrt{1 + f'(x')^2} \right] dx', \quad (4.52)$$

$$I_4(x) = \int_{-L/2}^{L/2} \left[\left(\frac{\partial G_{J+}^q}{\partial \boldsymbol{\nu}_x}(x - x', f(x) - f(x')) - \frac{\partial G_{J-}^q}{\partial \boldsymbol{\nu}_x}(x - x', f(x) - f(x')) \right) \phi^{\text{per}}(x') \times \gamma(x, x') \sqrt{1 + f'(x')^2} \right] dx'. \quad (4.53)$$

The integral operator involved in the definition of $I_1(x)$ is a double-layer potential. Then, following a similar reasoning as in Section 4.3.1, integral (4.50) can be approximated by using a windowing procedure as follows:

$$I_1(x) = \int_{-L/2}^{L/2} \left[\left(\frac{\partial G_{J-}^q}{\partial \boldsymbol{\nu}_{x'}}(x - x', f(x) - f(x')) - \frac{\partial G_{J+}^q}{\partial \boldsymbol{\nu}_{x'}}(x - x', f(x) - f(x')) \right) \varphi^{\text{per}}(x') \times \gamma(x, x') \sqrt{1 + f'(x')^2} \right] dx' \approx \int_{-\infty}^{\infty} [S(x - x', cA, A) \varphi^{\text{per}}(x') \gamma(x, x') \times \left(\frac{\partial G_{J-}^q}{\partial \boldsymbol{\nu}_{x'}}(x - x', f(x) - f(x')) - \frac{\partial G_{J+}^q}{\partial \boldsymbol{\nu}_{x'}}(x - x', f(x) - f(x')) \right) \sqrt{1 + f'(x')^2}] dx',$$

where, in a similar manner to Section 4.3.1, $L_{w\pm}$ are defined as

$$L_{w\pm}(x, x') = S(x - x', cA, A) \frac{\partial G_{J\pm}}{\partial \boldsymbol{\nu}_{x'}}(x - x', f(x) - f(x')) \gamma(x, x') \sqrt{1 + f'(x')^2},$$

and using Lemma 4.2.4,

$$\begin{aligned} I_1(x) &= \int_{-\infty}^{\infty} (L_{w-}(x, x') - L_{w+}(x, x')) \varphi^{\text{per}}(x') dx' \\ &= \int_{x-A}^{x+A} (L_{w-}(x, x') - L_{w+}(x, x')) \varphi^{\text{per}}(x') dx'. \end{aligned}$$

The integral operator involved in the definition of $I_2(x)$ is a single-layer potential. Then, following a similar reasoning as in Section 4.2.5, integral (4.51) can be approximated by using a windowing technique as follows:

$$\begin{aligned} I_2(x) &= \int_{-L/2}^{L/2} \left[(G_{J+}^q(x - x', f(x) - f(x')) - G_{J-}^q(x - x', f(x) - f(x'))) \phi^{\text{per}}(x') \gamma(x, x') \right. \\ &\quad \times \sqrt{1 + f'(x')^2} \Big] dx' \approx \int_{-\infty}^{\infty} [S(x - x', cA, A) \phi^{\text{per}}(x') \gamma(x, x') \\ &\quad \times (G_{J+}(x - x', f(x) - f(x')) - G_{J-}(x - x', f(x) - f(x'))) \sqrt{1 + f'(x')^2}] dx', \end{aligned}$$

where, in a similar manner to Section 4.2.5, $M_{w\pm}$ are defined as

$$M_{w\pm}(x, x') = S(x - x', cA, A) G_{J\pm}(x - x', f(x) - f(x')) \gamma(x, x') \sqrt{1 + f'(x')^2},$$

and considering Lemma 4.2.4,

$$\begin{aligned} I_2(x) &= \int_{-\infty}^{\infty} (M_{w-}(x, x') - M_{w+}(x, x')) \phi^{\text{per}}(x') dx' \\ &= \int_{x-A}^{x+A} (M_{w-}(x, x') - M_{w+}(x, x')) \phi^{\text{per}}(x') dx'. \end{aligned}$$

Both integrals have been truncated considering the window function described in Section 4.2.3, and following Theorem 4.2.3, superalgebraically convergence is obtained. Since in Sections 4.2.5 and 4.3.1, the kernel decomposition of a single-layer potential, and a double-layer potentials have been described, following similar arguments the decomposition of the adjoint double-layer potential, and the hypersingular potential are described.

Adjoint double-layer potential

This section is devoted to describing the kernel decomposition of the adjoint double-layer potential. For the sake of simplicity, in Section 4.B.3 in Appendix 4.B a detailed decomposition of an adjoint double-layer potential in a periodic setting is described (the reader is referred to this section in order to obtain more details). The integral considered, taking into account Lemma 4.2.4, is

$$\begin{aligned} &\int_{-L/2}^{L/2} \frac{\partial G_J^q}{\partial \nu_x}(x - x', f(x) - f(x')) \phi^{\text{per}}(x') \gamma(x, x') \sqrt{1 + f'(x')^2} dx' \\ &= \int_{-\infty}^{\infty} \frac{\partial G_J}{\partial \nu_x}(x - x', f(x) - f(x')) \phi^{\text{per}}(x') \gamma(x, x') \sqrt{1 + f'(x')^2} dx', \end{aligned}$$

which involves an adjoint double-layer potential. This integral, following Theorem 4.2.3, can be truncated to obtain superalgebraically convergence far away from Wood anomalies,

by using the window function described in Section 4.2.3, and it results

$$\begin{aligned}
& \int_{-L/2}^{L/2} \frac{\partial G_J^q}{\partial \nu_x}(x - x', f(x) - f(x')) \phi^{\text{per}}(x') \gamma(x, x') \sqrt{1 + f'(x')^2} dx' \\
& \approx \int_{-\infty}^{\infty} \underbrace{S(x - x', cA, A) \frac{\partial G_J}{\partial \nu_x}(x - x', f(x) - f(x')) \gamma(x, x') \sqrt{1 + f'(x')^2}}_{H_w(x, x'; J)} \phi^{\text{per}}(x') dx' \\
& = \int_{-\infty}^{\infty} H_w(x, x'; J) \phi^{\text{per}}(x') dx' = \int_{-A}^{x+A} H_w(x, x'; J) \phi^{\text{per}}(x') dx'. \tag{4.54}
\end{aligned}$$

As it has been explained in previous sections, the decomposition of H_w in (4.54) is necessary to deal with the logarithmic singularity appearing at $x = x'$. In Section 4.B.3 in Appendix 4.B, a detailed decomposition of an adjoint-double-layer potential in a periodic setting is explained. The decomposition of H shown in that section can be used by the reader to obtain better comprehension of this section. Then, following the same steps applied for H , the kernel H_w can be split in a smooth and a logarithmic part. When $x - x'$ is an integer multiple of 2π , the kernel H_w presents singularities (see Section 4.2.4 for the study of the convergence of G_J), and in this case, since the integration interval is $-A < x - x' < A$, $|x - x'| < 2\pi$ is not always satisfied. To overcome these difficulties, the additional cut-off function P_l defined in (4.16) is used in H_{wl} (see (4.56)). Then, the integrand in (4.54) can be rewritten as the sum of a smooth kernel H_{wr} , and a logarithm part (see Remark 4.2.5 for subscript notation) in the form

$$\begin{aligned}
H_w(x, x'; J) &= S(x - x', cA, A) \frac{\partial G_J}{\partial \nu_x}(x - x', f(x) - f(x')) \gamma(x, x') \sqrt{1 + f'(x')^2} \\
&= \frac{i}{4} S(x - x', cA, A) \sum_{l=0}^J (-1)^l \binom{J}{l} \frac{\partial H_0^{(1)}}{\partial \nu_x} \left(k \sqrt{(x - x')^2 + (f(x) - f(x') + lh)^2} \right) \\
&\quad \times \gamma(x, x') \sqrt{1 + f'(x')^2} = -\frac{ik}{4} S(x - x', cA, A) \gamma(x, x') \frac{\sqrt{1 + f'(x')^2}}{\sqrt{1 + f'(x)^2}} \\
&\quad \times \sum_{l=0}^J \left[(-1)^l \binom{J}{l} H_1^{(1)} \left(k \sqrt{(x - x')^2 + (f(x) - f(x') + lh)^2} \right) \right. \\
&\quad \times \left. \frac{-f'(x)(x - x') + f(x) - f(x') + lh}{\sqrt{(x - x')^2 + (f(x) - f(x') + lh)^2}} \right] \\
&= H_{wl}(x, x') \ln \left(4 \sin^2 \left(\frac{\pi}{L} (x - x') \right) \right) + H_{wr}(x, x'). \tag{4.55}
\end{aligned}$$

Problem without shifts As in the decomposition of kernels L and M in Sections 4.2.5 and 4.3.1, respectively, first of all the problem without shifts is considered, that is, $J = 0$.

In a similar way to the kernel decomposition described in (4.B.13), considering (4.55) the logarithmic part and the smooth kernel H_{wr} result,

$$\begin{aligned} H_{\text{wl}}(x, x'; 0) &= \frac{k}{4\pi} P_l(x - x', d_l, A_l) J_1 \left(k \sqrt{(x - x')^2 + (f(x) - f(x'))^2} \right) \\ &\quad \times \frac{-f'(x)(x - x') + f(x) - f(x')}{\sqrt{(x - x')^2 + (f(x) - f(x'))^2}} \frac{\sqrt{1 + f'(x')^2}}{\sqrt{1 + f'(x)^2}}, \end{aligned} \quad (4.56)$$

$$H_{\text{wr}}(x, x'; 0) = H_w(x, x'; 0) - H_{\text{wl}}(x, x'; 0) \ln \left(4 \sin^2 \left(\frac{\pi}{L}(x - x') \right) \right), \quad (4.57)$$

where

$$\begin{aligned} H_w(x, x'; 0) &= S(x - x', cA, A) \frac{\partial G_J}{\partial \nu_x}(x - x', f(x) - f(x')) \gamma(x, x') \sqrt{1 + f'(x')^2} \\ &= \frac{i}{4} S(x - x', cA, A) \frac{\partial H_0^{(1)}}{\partial \nu_x} \left(k \sqrt{(x - x')^2 + (f(x) - f(x'))^2} \right) \gamma(x, x') \sqrt{1 + f'(x')^2} \\ &= -\frac{ik}{4} S(x - x', cA, A) H_1^{(1)} \left(k \sqrt{(x - x')^2 + (f(x) - f(x'))^2} \right) \gamma(x, x') \\ &\quad \times \frac{-f'(x)(x - x') + f(x) - f(x')}{\sqrt{(x - x')^2 + (f(x) - f(x'))^2}} \frac{\sqrt{1 + f'(x')^2}}{\sqrt{1 + f'(x)^2}}. \end{aligned} \quad (4.58)$$

When $x' \rightarrow x$, $\gamma(x, x) = 1$, and $P_l(x, x) = 1$. Then, taking into account the definition of H_{wl} (4.56), and the limit of the Bessel function $J_1(t)$ when $t \rightarrow 0$ (see (4.A.10) in Appendix 4.A), and proceeding in a similar way to (4.B.16), the values of the kernel H_{wl} at $x = x'$ result

$$H_{\text{wl}}(x, x; 0) = \lim_{x' \rightarrow x} H_{\text{wl}}(x, x'; 0) = \lim_{x' \rightarrow x} \frac{k^2}{8\pi} P_l(x - x', d_l, A_l) (-f'(x')(x - x') + f(x) - f(x')) = 0.$$

Considering (4.56), (4.57), and (4.58), and proceeding in a similar manner to (4.B.18), the values of H_{wr} at $x = x'$ are

$$\begin{aligned} H_{\text{wr}}(x, x; 0) &= \lim_{x' \rightarrow x} H_{\text{wr}}(x, x'; 0) = \lim_{x' \rightarrow x} \left[H_w(x, x'; 0) - H_{\text{wl}}(x, x'; 0) \ln \left(4 \sin^2 \left(\frac{\pi}{L}(x - x') \right) \right) \right] \\ &= \frac{f''(x)}{4\pi(1 + f'(x)^2)}. \end{aligned} \quad (4.59)$$

Problem with shifts Now, the problem with shifts is considered, that is, $J > 0$. Similarly to the problem without shifts, $H_{\text{wl}}(x, x'; J)$ and $H_{\text{wr}}(x, x', J)$ are defined as in (4.56) and (4.57), but in this case, H_w is given by (4.55). At $x = x'$, $\gamma(x, x) = 1$ and $P_l(x, x) = 1$. Taking into account (4.55), (4.56), and (4.57), the values of the function $H_{\text{wr}}(x, x; J)$ at

$x = x'$ can be written as

$$\begin{aligned}
H_{\text{wr}}(x, x; J) &= \lim_{x' \rightarrow x} H_{\text{wr}}(x, x'; J) = \lim_{x' \rightarrow x} \left[H_{\text{w}}(x, x'; J) - H_{\text{wl}}(x, x'; J) \ln \left(4 \sin^2 \left(\frac{\pi}{L}(x - x') \right) \right) \right] \\
&= \lim_{x' \rightarrow x} \left[-\frac{ik}{4} S(x - x', cA, A) \gamma(x, x') \frac{\sqrt{1 + f'(x')^2}}{\sqrt{1 + f'(x)^2}} \right. \\
&\quad \times \sum_{l=0}^J \left[(-1)^l \binom{J}{l} H_1^{(1)} \left(k \sqrt{(x - x')^2 + (f(x) - f(x') + lh)^2} \right) \right. \\
&\quad \times \frac{-f'(x)(x - x') + f(x) - f(x') + lh}{\sqrt{(x - x')^2 + (f(x) - f(x') + lh)^2}} \left. \right] - \frac{k}{4\pi} \ln \left(4 \sin^2 \left(\frac{\pi}{L}(x - x') \right) \right) \\
&\quad \times P_l(x - x', d_l, A_l) J_1 \left(k \sqrt{(x - x')^2 + (f(x) - f(x'))^2} \right) \\
&\quad \left. \times \frac{-f'(x)(x - x') + f(x) - f(x')}{\sqrt{(x - x')^2 + (f(x) - f(x'))^2}} \right].
\end{aligned}$$

The singularities in the Hankel function $H_1^{(1)}$ appear when $l = 0$ so, the summation is separated in two parts: when $l = 0$, and (4.59) can be used, and when $l > 0$. Then, the values of H_{wr} at $x = x'$ are

$$\begin{aligned}
H_{\text{wr}}(x, x; J) &= \lim_{x' \rightarrow x} H_{\text{wr}}(x, x'; J) = \lim_{x' \rightarrow x} \left[-\frac{ik}{4} S(x - x', cA, A) \gamma(x, x') \frac{\sqrt{1 + f'(x')^2}}{\sqrt{1 + f'(x)^2}} \right. \\
&\quad \times H_1^{(1)} \left(k \sqrt{(x - x')^2 + (f(x) - f(x'))^2} \right) \frac{-f'(x)(x - x') + f(x) - f(x')}{\sqrt{(x - x')^2 + (f(x) - f(x'))^2}} \\
&\quad - \frac{k}{4\pi} P_l(x - x', d_l, A_l) \ln \left(4 \sin^2 \left(\frac{\pi}{L}(x - x') \right) \right) \\
&\quad \times J_1 \left(k \sqrt{(x - x')^2 + (f(x) - f(x'))^2} \right) \frac{-f'(x)(x - x') + f(x) - f(x')}{\sqrt{(x - x')^2 + (f(x) - f(x'))^2}} \\
&\quad - \frac{ik}{4} \gamma(x, x') \sum_{l=1}^J \left[(-1)^l \binom{J}{l} H_1^{(1)} \left(k \sqrt{(x - x')^2 + (f(x) - f(x') + lh)^2} \right) \right. \\
&\quad \left. \times \frac{-f'(x)(x - x') + f(x) - f(x') + lh}{\sqrt{(x - x')^2 + (f(x) - f(x') + lh)^2}} \right] S(x - x', cA, A) \frac{\sqrt{1 + f'(x')^2}}{\sqrt{1 + f'(x)^2}} \\
&= \frac{f''(x)}{4\pi(1 + f'(x)^2)} - \frac{ik}{4} \sum_{l=1}^J (-1)^l \binom{J}{l} H_1^{(1)}(klh).
\end{aligned}$$

Hypersingular formulation

This section is devoted to describing the kernel decomposition of the normal derivative of a double-layer potential (hypersingular potential). In order to deal with this operator, the difference of hypersingular potentials is considered because, in such a way, the singularities appearing in the kernels disappear. Moreover, since the hypersingular kernel appearing in the original problem uses the shifting and windowing methods (described in Sections 4.2.3 and 4.2.4) what can difficult the comprehension of the decomposition, the reader is referred to Section 4.B.4 in Appendix 4.B to get a detail and complete description of the decomposition of the difference of two hypersingular kernel in a periodic setting.

Now, the integral with the difference of the hypersingular potentials appearing in the transmission problem is considered. Once again, taking into account Lemma 4.2.4, the integral results

$$\begin{aligned} I(x) &= \int_{-L/2}^{L/2} \left[\left(\frac{\partial^2 G_{J-}^q}{\partial \boldsymbol{\nu}_x \partial \boldsymbol{\nu}_{x'}}(x - x', f(x) - f(x')) - \frac{\partial^2 G_{J+}^q}{\partial \boldsymbol{\nu}_x \partial \boldsymbol{\nu}_{x'}}(x - x', f(x) - f(x')) \right) \varphi^{\text{per}}(x') \right. \\ &\quad \times \gamma(x, x') \sqrt{1 + f'(x')^2} \Big] dx' = \int_{-\infty}^{\infty} \left[\left(\frac{\partial^2 G_{J-}^q}{\partial \boldsymbol{\nu}_x \partial \boldsymbol{\nu}_{x'}}(x - x', f(x) - f(x')) \right. \right. \\ &\quad \left. \left. - \frac{\partial^2 G_{J+}^q}{\partial \boldsymbol{\nu}_x \partial \boldsymbol{\nu}_{x'}}(x - x', f(x) - f(x')) \right) \varphi^{\text{per}}(x') \gamma(x, x') \sqrt{1 + f'(x')^2} \right] dx'. \end{aligned}$$

By using the window function described in Section 4.2.3, last integral can be truncated, and superalgebraically convergence can be achieved far away from Wood anomalies (see Theorem 4.2.3), and it results

$$\begin{aligned} I(x) &\approx \int_{-\infty}^{\infty} \left[\gamma(x, x') \left(\frac{\partial^2 G_{J-}^q}{\partial \boldsymbol{\nu}_x \partial \boldsymbol{\nu}_{x'}}(x - x', f(x) - f(x')) - \frac{\partial^2 G_{J+}^q}{\partial \boldsymbol{\nu}_x \partial \boldsymbol{\nu}_{x'}}(x - x', f(x) - f(x')) \right) \right. \\ &\quad \times \varphi^{\text{per}}(x') S(x - x', cA, A) \sqrt{1 + f'(x')^2} \Big] dx', \end{aligned} \quad (4.60)$$

where K_w is defined as

$$\begin{aligned} K_w(x, x'; J) &= \left(\frac{\partial^2 G_{J-}^q}{\partial \boldsymbol{\nu}_x \partial \boldsymbol{\nu}_{x'}}(x - x', f(x) - f(x')) - \frac{\partial^2 G_{J+}^q}{\partial \boldsymbol{\nu}_x \partial \boldsymbol{\nu}_{x'}}(x - x', f(x) - f(x')) \right) \\ &\quad \times S(x - x', cA, A) \gamma(x, x') \sqrt{1 + f'(x')^2}, \end{aligned}$$

and then

$$I(x) = \int_{-\infty}^{\infty} K_w(x, x'; J) \varphi^{\text{per}}(x') dx' = \int_{x-A}^{x+A} K_w(x, x'; J) \varphi^{\text{per}}(x') dx'.$$

To deal with the logarithmic singularity appearing at $x = x'$, it is necessary to study the decomposition of the kernel K_w . The reader is referred to Section 4.B.4 in Appendix 4.B

to get a better comprehension of the decomposition below (in the appendix a detailed decomposition of the difference of two hypersingular potentials in a periodic setting is given). Following the same steps applied for K , the kernel K_w can be split in a smooth and a logarithmic part. When $x - x'$ is an integer multiple of 2π , the kernel K_w presents singularities (see Section 4.4.2 for the study of the convergence of $G_{J\pm}$) and, since the integration interval is $-A < x - x' < A$, the condition $|x - x'| < 2\pi$ is not always satisfied. Then, it is necessary to use the additional cut-off function P_l , defined in (4.16), in K_{wl}^1 and K_{wl}^2 (see (4.62) and (4.64)). Hence, the integrand in (4.60) can be rewritten as the sum of a smooth kernel and a logarithm part (see Remark 4.2.5 for subscript notation) in the following form:

$$\begin{aligned} K_w(x, x'; J) &= K_w^1(x, x'; J) + K_w^2(x, x'; J) = S(x - x', cA, A)\gamma(x, x')\sqrt{1 + f'(x')^2} \\ &\times \left(\frac{\partial^2 G_{J-}}{\partial \nu_x \partial \nu_{x'}}(x - x', f(x) - f(x')) - \frac{\partial^2 G_{J+}}{\partial \nu_x \partial \nu_{x'}}(x - x', f(x) - f(x')) \right) \\ &= (K_{wl}^1(x, x'; J) + K_{wl}^2(x, x'; J)) \ln \left(4 \sin^2 \left(\frac{\pi}{L}(x - x') \right) \right) \\ &+ (K_{wr}^1(x, x'; J) + K_{wr}^2(x, x'; J)). \end{aligned} \quad (4.61)$$

Problem without shifts As in the decomposition of the kernel L , M and H , first of all the problem without shifts is considered, that is, $J = 0$. In a similar way to the kernel decompositions of (4.B.25) and (4.B.26), considering (4.61), the logarithmic part and the smooth kernel K_{wr}^1 and K_{wr}^2 result,

$$\begin{aligned} K_{wl}^1(x, x'; 0) &= \frac{1}{4\pi} P_l(x - x', d_l, A_l) \left[k_-^2 J_2 \left(k_- \sqrt{(x - x')^2 + (f(x) - f(x'))^2} \right) \right. \\ &\quad \left. - k_+^2 J_2 \left(k_+ \sqrt{(x - x')^2 + (f(x) - f(x'))^2} \right) \right] \chi(x, x'; 0) \\ &\times \tilde{\chi}(x, x'; 0) \sqrt{1 + f'(x')^2}, \end{aligned} \quad (4.62)$$

$$K_{wr}^1(x, x'; 0) = K_w^1(x, x'; 0) - K_{wl}^1(x, x'; 0) \ln \left(4 \sin^2 \left(\frac{x - x'}{2} \right) \right), \quad (4.63)$$

$$\begin{aligned} K_{wl}^2(x, x'; 0) &= -\frac{1}{4\pi} P_l(x - x', d_l, A_l) \left[k_-^+ J_1 \left(k_- \sqrt{(x - x')^2 + (f(x) - f(x'))^2} \right) \right. \\ &\quad \left. - k_+^+ J_1 \left(k_+ \sqrt{(x - x')^2 + (f(x) - f(x'))^2} \right) \right] \xi(x, x'; 0), \end{aligned} \quad (4.64)$$

$$K_{wr}^2(x, x'; 0) = K_w^2(x, x'; 0) - K_{wl}^2(x, x'; 0) \ln \left(4 \sin^2 \left(\frac{x - x'}{2} \right) \right), \quad (4.65)$$

where $\chi(x, x'; \delta)$, $\tilde{\chi}(x, x'; \delta)$, and $\xi(x, x'; \delta)$ are the functions (4.B.20), (4.B.22), and (4.B.23), respectively, defined in Section 4.B.4 in Appendix 4.B.

The kernels $K_w^1(x, x'; 0)$ and $K_w^2(x, x'; 0)$ are given by

$$\begin{aligned} K_w^1(x, x'; 0) = & -\frac{i}{4} S(x - x', cA, A) \gamma(x, x') \left[k_-^2 H_2^{(1)} \left(k^- \sqrt{(x - x')^2 + (f(x) - f(x'))^2} \right) \right. \\ & \left. - k_+^2 H_2^{(1)} \left(k^+ \sqrt{(x - x')^2 + (f(x) - f(x'))^2} \right) \right] \chi(x, x'; 0) \\ & \times \tilde{\chi}(x, x'; 0) \sqrt{1 + f'(x')^2}, \end{aligned} \quad (4.66)$$

$$\begin{aligned} K_w^2(x, x'; 0) = & \frac{i}{4} S(x - x', cA, A) \left[k^- H_1^{(1)} \left(k^- \sqrt{(x - x')^2 + (f(x) - f(x'))^2} \right) \right. \\ & \left. - k^+ H_1^{(1)} \left(k^+ \sqrt{(x - x')^2 + (f(x) - f(x'))^2} \right) \right] \xi(x, x'; 0) \gamma(x, x'). \end{aligned} \quad (4.67)$$

When $x' \rightarrow x$, $\gamma(x, x) = 1$, and $P_l(x, x) = 1$. Then, using the asymptotic value of χ and $\tilde{\chi}$ when $x = x'$ (see (4.B.31) and (4.B.32) in the Appendix), the values of the kernel K_{wl}^1 at $x = x'$ results

$$K_{wl}^1(x, x; 0) = \lim_{x' \rightarrow x} K_{wl}^1(x, x'; 0) = 0,$$

and considering (4.62), (4.63), and (4.66), the values of K_{wr}^1 at $x = x'$ result

$$K_{wr}^1(x, x; 0) = \lim_{x' \rightarrow x} K_{wr}^1(x, x'; 0) = 0.$$

To compute the values of K_{wl}^2 and K_{wr}^2 when $x = x'$, a similar reasoning than in (4.B.33) is used. Taking into account (4.64),

$$\begin{aligned} K_{wl}^2(x, x; 0) = & \lim_{x' \rightarrow x} K_{wl}^2(x, x'; 0) = \lim_{x' \rightarrow x} -\frac{1}{4\pi} \left(k^- J_1 \left(k^- \sqrt{(x - x')^2 + (f(x) - f(x'))^2} \right) \right. \\ & \left. - k^+ J_1 \left(k^+ \sqrt{(x - x')^2 + (f(x) - f(x'))^2} \right) \right) \xi(x, x'; 0) \\ = & -\frac{1}{8\pi} ((k^-)^2 - (k^+)^2) \sqrt{1 + f'(x)^2}, \end{aligned}$$

and considering (4.64), (4.65), and (4.67),

$$\begin{aligned} K_{wr}^2(x, x; 0) = & \lim_{x' \rightarrow x} K_{wr}^2(x, x'; 0) = \lim_{x' \rightarrow x} \left[K_w^2(x, x'; 0) - K_{wl}^2(x, x'; 0) \ln \left(4 \sin^2 \left(\frac{x - x'}{2} \right) \right) \right] \\ = & \left(\left(\frac{i}{8} - \frac{C}{4\pi} + \frac{1}{8\pi} \right) (k_-^2 - k_+^2) - \frac{1}{4\pi} \left[k_-^2 \ln \left(\frac{k_-}{2} \sqrt{1 + f'(x)^2} \right) \right. \right. \\ & \left. \left. - k_+^2 \ln \left(\frac{k^+}{2} \sqrt{1 + f'(x)^2} \right) \right] \right) \sqrt{1 + f'(x)^2}, \end{aligned}$$

where C is the Euler's constant given by (4.A.3).

Problem with shifts Now, the problem with shifts is considered, that is, $J > 0$. Similarly to the problem without shifts, K_{wl}^1 , K_{wr}^1 , K_{wl}^2 , and K_{wr}^2 are defined as in (4.62), (4.63), (4.64), and (4.65), but in this case, K_w^1 and K_w^2 are given by

$$\begin{aligned} K_w^1(x, x'; J) = & -\frac{i}{4} S(x - x', cA, A) \gamma(x, x') \sqrt{1 + f'(x')^2} \left(\sum_{l=0}^J \left[(-1)^l \binom{J}{l} \right. \right. \\ & \times \left[k_-^2 H_2^{(1)} \left(k^- \sqrt{(x - x')^2 + (f(x) - f(x') - lh^-)^2} \right) \chi(x, x'; -lh^-) \tilde{\chi}(x, x'; -lh^-) \right. \\ & \left. \left. - k_+^2 H_2^{(1)} \left(k^+ \sqrt{(x - x')^2 + (f(x) - f(x') + lh^+)^2} \right) \chi(x, x'; lh^+) \tilde{\chi}(x, x'; lh^+) \right] \right], \end{aligned} \quad (4.68)$$

$$\begin{aligned} K_w^2(x, x'; J) = & \frac{i}{4} \gamma(x, x') S(x - x', cA, A) \frac{1 + f'(x)f'(x')}{\sqrt{1 + f'(x)^2}} \\ & \times \sum_{l=0}^J \left[(-1)^l \binom{J}{l} \left[k^- \frac{H_1^{(1)} \left(k^- \sqrt{(x - x')^2 + (f(x) - f(x') - lh^-)^2} \right)}{\sqrt{(x - x')^2 + (f(x) - f(x') - lh^-)^2}} \right. \right. \\ & \left. \left. - k^+ \frac{H_1^{(1)} \left(k^+ \sqrt{(x - x')^2 + (f(x) - f(x') + lh^+)^2} \right)}{\sqrt{(x - x')^2 + (f(x) - f(x') + lh^+)^2}} \right] \right]. \end{aligned} \quad (4.69)$$

When $x = x'$ $\gamma(x, x) = 1$, and $P_l(x, x) = 1$. Taking into account (4.62), (4.63), and (4.68), the values of the kernel $K_{\text{wr}}^1(x, x; J)$ at $x = x'$ can be computed as

$$\begin{aligned} K_{\text{wr}}^1(x, x; J) &= \lim_{x' \rightarrow x} K_{\text{wr}}^1(x, x'; J) = \lim_{x' \rightarrow x} \left[K_w^1(x, x'; J) - K_{\text{wl}}^1(x, x'; J) \ln \left(4 \sin^2 \left(\frac{x - x'}{2} \right) \right) \right] \\ &= -\frac{i}{4} \sum_{l=1}^J (-1)^l \binom{J}{l} \frac{\left[k_-^2 H_2^{(1)}(-k^- lh^-) - k_+^2 H_2^{(1)}(k^+ lh^+) \right]}{\sqrt{1 + f'(x)^2}}. \end{aligned}$$

Moreover, considering (4.64), (4.65), and (4.69), the values of $K_{\text{wr}}^2(x, x; J)$ at $x = x'$ can be calculated as

$$\begin{aligned} K_{\text{wr}}^2(x, x; J) &= \lim_{x' \rightarrow x} K_{\text{wr}}^2(x, x'; J) = \lim_{x' \rightarrow x} \left(K_w^2(x, x'; J) - K_{\text{wl}}^2(x, x'; J) \ln \left(4 \sin^2 \left(\frac{x - x'}{2} \right) \right) \right) \\ &= \left(\left(\frac{i}{8} - \frac{C}{4\pi} + \frac{1}{8\pi} \right) (k_-^2 - k_+^2) - \frac{1}{4\pi} \left[k_-^2 \ln \left(\frac{k^-}{2} \sqrt{1 + f'(x)^2} \right) \right. \right. \\ &\quad \left. \left. - k_+^2 \ln \left(\frac{k^+}{2} \sqrt{1 + f'(x)^2} \right) \right] + \frac{i}{4} \sum_{l=1}^J (-1)^l \binom{J}{l} \left[k^- \frac{H_1^{(1)}(-k^- lh^-)}{-lh^-} \right. \right. \\ &\quad \left. \left. - k^+ \frac{H_1^{(1)}(k^+ lh^+)}{lh^+} \right] \right) \sqrt{1 + f'(x)^2}, \end{aligned}$$

where C is the Euler's constant given by (4.A.3).

4.5 Discretization

The numerical method described in this chapter uses the windowing function method, and the shifted Green function detailed in Section 4.2.4. This method is based on a Nyström approach, and on the use of periodic unknowns. An analogous method applied to a simpler setting was firstly introduced in [39]. Throughout the following sections, the quadrature rules used for an efficient evaluation of integral operators appearing along this chapter are described. Moreover, a convergence test used to study the convergence order of the proposed method is detailed. Taking into account the quadrature rules, it is possible to give a discretization of the problems appearing in this chapter.

4.5.1 MKN quadrature rules

By using the Nyström method [138], and the Martensen and Kussmaul decompositions [108, 122], the integrals can be approximated by quadrature formulas. In the present case, for the L -periodic integrands, an equidistant discretization mesh containing an even number n_I of points per period of the scattering surface is chosen. Thus, the $(2N + 1)n_I$ discretization points x_j are defined by

$$x_j := \left(-\frac{L}{2} - NL \right) + (j - 1) \frac{L}{n_I}, \quad j = 1, \dots, (2N + 1)n_I, \quad (4.70)$$

where $N = \lceil \frac{A}{L} \rceil$ is the number of periodic intervals contained in the integration domain to the right of the point $x = \frac{L}{2}$. Since the integrands in the $(-\infty, \infty)$ integrals are compactly supported functions with supports contained in the interval $(x - A_l, x + A_l)$, the integrals related to the logarithm part are approximated by means of the quadrature rule

$$\begin{aligned} I_l(x) &= \int_{-\infty}^{\infty} \ln \left(4 \sin^2 \left(\frac{\pi}{L}(x - x') \right) \right) T_{wl}(x, x') \Phi^{\text{per}}(x') dx' \\ &= \int_{x-A_l}^{x+A_l} \ln \left(4 \sin^2 \left(\frac{\pi}{L}(x - x') \right) \right) T_{wl}(x, x') \Phi^{\text{per}}(x') dx' \\ &\approx \frac{L}{2\pi} \sum_{|x-x_j| \leq A_l} R_{j,n_I} \left(\frac{2\pi x}{L} \right) T_{wl}(x, x_j) \Phi^{\text{per}}(x_j), \end{aligned} \quad (4.71)$$

where Φ^{per} is a periodic function of period L , T_{wl} is a smooth function of x and x' , which may be one of the kernels previously studied (L_{wl} , M_{wl} , H_{wl} , K_{wl}^1 , or K_{wl}^2), and R_{j,n_I} are the quadrature weights (see [107] for further details) given by

$$R_{j,n_I}(t) = \frac{1}{n_I} \sum_{q=-\frac{n_I}{2}+1}^{\frac{n_I}{2}} \int_0^{2\pi} e^{iq(\frac{2\pi x_j}{L} + \tau - t)} \ln \left(4 \sin^2 \frac{\tau}{2} \right) d\tau,$$

which using the expression

$$\frac{1}{2\pi} \int_0^{2\pi} \ln \left(4 \sin^2 \frac{\tau}{2} \right) e^{im\tau} d\tau = \begin{cases} 0 & \text{if } m = 0, \\ -\frac{1}{m} & \text{if } m \in \mathbb{N}, n > 0, \end{cases}$$

it results

$$R_{j,n_I}(t) = -\frac{4\pi}{n_I} \left[\sum_{q=1}^{\frac{n_I}{2}-1} \frac{1}{q} \cos \left(q \left(\frac{2\pi}{L}(x - x_j) \right) \right) \right] - \frac{4\pi}{n_I^2} \cos \left(\frac{n_I}{2} \left(\frac{2\pi}{L}(x - x_j) \right) \right).$$

On the other hand, the integrals related to the smooth kernels are approximated by means of the composite trapezoidal rule

$$\begin{aligned} I_r(x) &= \int_{-\infty}^{\infty} T_{wr}(x, x') \Phi^{per}(x') dx' = \int_{x-A}^{x+A} T_{wr}(x, x') \Phi^{per}(x') dx' \\ &\approx \frac{L}{n_I} \sum_{|x-x_j| \leq A} T_{wr}(x, x_j) \Phi^{per}(x_j), \end{aligned} \quad (4.72)$$

where Φ^{per} is a periodic function of period L , and T_{wr} is a smooth function of x and x' , which may be one of the kernels previously studied (L_{wr} , M_{wr} , H_{wr} , K_{wr}^1 , or K_{wr}^2).

Remark 4.5.1. Let $f(x) \in C^2[-\frac{L}{2}, \frac{L}{2}]$ be a L -periodic function, and an equidistant set of $n_I + 1$ points $x_k = -\frac{L}{2} + k \frac{L}{n_I}$, with $k = 0, \dots, n_I$. Then, the composite trapezoidal rule is given by

$$\begin{aligned} \int_{-L/2}^{L/2} f(x) dx &\approx \frac{L}{n_I} \left[\frac{f(-\frac{L}{2}) + f(\frac{L}{2})}{2} + \sum_{k=1}^{n_I-1} f(x_j) \right] = \frac{L}{n_I} \left[f\left(-\frac{L}{2}\right) + \sum_{k=1}^{n_I-1} f(x_j) \right] \\ &= \frac{L}{n_I} \sum_{k=0}^{n_I-1} f(x_j), \end{aligned}$$

and the error can be estimated by $\varepsilon = \frac{1}{12} \frac{(b-a)^3}{n_I^2} f''(\xi)$, $\xi \in \left[-\frac{L}{2}, \frac{L}{2}\right]$.

4.5.2 Efficiency computation

In order to perform a convergence test for the numerical solution of the scattering problem in a sound-soft boundary, and of the transmission problem, a relation between the Rayleigh coefficients of the solution is used (see (4.2) to recall the definition of the scattered field in terms of the Rayleigh coefficients in the sound-soft boundary problem, and (4.38), and (4.40) to recall the definition of the scattered, and the transmitted field in terms of the Rayleigh coefficients in the transmission problem). This relation is given by the principle of conservation of energy (see [123]).

Sound-soft boundary

Following [45], for each $n \in \Lambda = \{n \in \mathbb{Z} : \alpha_n^2 < k^2\}$, where α_n is defined in (4.3), and k the wave number of the propagation medium, the n th-order efficiency is defined as

$$e_n = |a_n|^2 \frac{\beta_n}{\beta_0}, \quad (4.73)$$

where β_n is defined in (4.4). The energy balance criterion is given by

$$\sum_{n \in \Lambda} e_n = 1 \Leftrightarrow \sum_{n \in \Lambda} |a_n|^2 \beta_n = \beta_0, \quad (4.74)$$

where a_n are the Rayleigh coefficients.

When a single-layer formulation is considered, as it is explained in Section 4.2.5, the scattered field is given by

$$U^s(x, y) = \int_{-L/2}^{L/2} -G_J^q(x - x', y - f(x')) \varphi^q(x') \sqrt{1 + f'(x')^2} dx', \quad (4.75)$$

and considering the Rayleigh expansion of the Green function G_J^q given in (4.10), the expression (4.75) results

$$\begin{aligned} U^s(x, y) = & \int_{-L/2}^{L/2} - \left[\sum_{n \in \mathbb{Z}} \frac{i}{2L\beta_n} \left(\sum_{l=0}^J (-1)^l \binom{J}{l} e^{i\beta_n l h} \right) e^{i\alpha_n(x-x')+i\beta_n(y-f(x'))} \varphi^q(x') \right. \\ & \times \left. \sqrt{1 + f'(x')^2} \right] dx'. \end{aligned}$$

Since $\{e^{i\alpha_n x}\}_{n \in \mathbb{N}}$ is an orthogonal system in $L^2(-L/2, L/2)$, taking into account (4.2), for a fixed $y = y_0$, it holds

$$U^s(x, y_0) = \sum_{n \in \mathbb{Z}} a_n e^{i(\alpha_n x + \beta_n y_0)},$$

with a_n the Rayleigh coefficients given by

$$a_n = -\frac{i}{2L\beta_n} \left(\sum_{l=0}^J (-1)^l \binom{J}{l} e^{i\beta_n l h} \right) \int_{-L/2}^{L/2} e^{-i\alpha_n x' - i\beta_n f(x')} \varphi^q(x') \sqrt{1 + f'(x')^2} dx'. \quad (4.76)$$

When a double-layer formulation is considered, as it is explained in Section 4.3.1, the scattered field is given by

$$U^s(x, y) = \int_{-L/2}^{L/2} \frac{\partial G_J^q}{\partial \nu_{x'}}(x - x', y - f(x')) \varphi^q(x') \sqrt{1 + f'(x')^2} dx', \quad (4.77)$$

and considering the Rayleigh expansion of the Green function G_J^q given in (4.10), it is possible to compute the normal derivative $\frac{\partial G_J^q}{\partial \nu_{x'}}$ as

$$\frac{\partial G_J^q}{\partial \nu_{x'}}(x - x', y - f(x')) = \sum_{n \in \mathbb{Z}} \frac{1}{2L\beta_n} \left(\sum_{l=0}^J (-1)^l \binom{J}{l} e^{i\beta_n l h} \right) \frac{-\alpha_n f'(x') + \beta_n}{\sqrt{1 + f'(x')^2}} e^{i\alpha_n(x-x')+i\beta_n(y-f(x'))}.$$

Then, the expression (4.77) results

$$\begin{aligned} U^s(x, y) = & \int_{-L/2}^{L/2} \left[\sum_{n \in \mathbb{Z}} \frac{1}{2L\beta_n} \left(\sum_{l=0}^J (-1)^l \binom{J}{l} e^{i\beta_n l h} \right) e^{i\alpha_n(x-x')+i\beta_n(y-f(x'))} (-\alpha_n f'(x') + \beta_n) \right. \\ & \times \varphi^q(x')] dx'. \end{aligned}$$

Since $\{e^{i\alpha_n x}\}_{n \in \mathbb{N}}$ is an orthogonal system in $L^2(-L/2, L/2)$, taking into account (4.2), for a fixed $y = y_0$, it holds

$$U^s(x, y_0) = \sum_{n \in \mathbb{Z}} a_n e^{i(\alpha_n x + \beta_n y_0)},$$

where the Rayleigh coefficients a_n are defined by

$$a_n = \frac{1}{2L\beta_n} \left(\sum_{l=0}^J (-1)^l \binom{J}{l} e^{i\beta_n l h} \right) \int_{-L/2}^{L/2} (-\alpha_n f'(x') + \beta_n) e^{-i\alpha_n x' - i\beta_n f(x')} \varphi^q(x') dx'. \quad (4.78)$$

Transmission problem

Following [46], for each $n \in \Lambda_{\pm} = \{n \in \mathbb{Z} : (\alpha_n^{\pm})^2 < (k^{\pm})^2\}$, the n th-order efficiency in Ω_{\pm} is defined as

$$e_n^{\pm} = |a_n^{\pm}|^2 \frac{\beta_n^{\pm}}{\beta_0^{\pm}}, \quad (4.79)$$

where β_n^+ , and β_n^- are defined by (4.39), and (4.41), respectively. Then, the energy balance criterion is given by

$$\sum_{n \in \Lambda_-} e_n^- + \sum_{n \in \Lambda_+} e_n^+ = 1 \Leftrightarrow \sum_{n \in \Lambda_-} |a_n^-|^2 \frac{\beta_0^-}{\beta_0^+} + \sum_{n \in \Lambda_+} |a_n^+|^2 \frac{\beta_0^+}{\beta_0^-} = 1. \quad (4.80)$$

In the transmission problem described in Section 4.4.3, the scattered field is given by

$$\begin{aligned} U^s(x, y) = & \int_{-L/2}^{L/2} \left(\left[\frac{\partial G_{J+}^q}{\partial \boldsymbol{\nu}_{x'}}(x - x', y - f(x')) \varphi^q(x') \right. \right. \\ & \left. \left. - G_{J+}^q(x - x', y - f(x')) \phi^q(x') \right] \sqrt{1 + f'(x')^2} \right) dx'. \end{aligned} \quad (4.81)$$

Considering the Rayleigh expansion of the Green function G_J^q given by (4.10), it holds

$$G_{J\pm}^q(x - x', y - f(x')) = \sum_{n \in \mathbb{Z}} \frac{i}{2L\beta_n^{\pm}} \left(\sum_{l=0}^J (-1)^l \binom{J}{l} e^{i\beta_n^{\pm} l h^{\pm}} \right) e^{i\alpha_n^{\pm}(x-x') \pm i\beta_n^{\pm}(y-f(x'))}, \quad (4.82)$$

$$\begin{aligned} \frac{\partial G_{J\pm}^q}{\partial \boldsymbol{\nu}_{x'}}(x - x', y - f(x')) = & \sum_{n \in \mathbb{Z}} \left[\frac{1}{2L\beta_n^{\pm}} \left(\sum_{l=0}^J (-1)^l \binom{J}{l} e^{i\beta_n^{\pm} l h^{\pm}} \right) \frac{-\alpha_n^{\pm} f'(x') \pm \beta_n^{\pm}}{\sqrt{1 + f'(x')^2}} \right. \\ & \left. \times e^{i\alpha_n^{\pm}(x-x') \pm i\beta_n^{\pm}(y-f(x'))} \right]. \end{aligned} \quad (4.83)$$

By using (4.82) and (4.83), the expression (4.81) results

$$U^s(x, y) = \int_{-L/2}^{L/2} \left[\sum_{n \in \mathbb{Z}} \frac{1}{2L\beta_n^+} \left(\sum_{l=0}^J (-1)^l \binom{J}{l} e^{i\beta_n^+ l h^+} \right) \left(\frac{-\alpha_n^+ f'(x') + \beta_n^+}{\sqrt{1 + f'(x')^2}} \varphi^q(x') - i\phi^q(x') \right) e^{i\alpha_n(x-x') + i\beta_n(y-f(x'))} \sqrt{1 + f'(x')^2} \right] dx'.$$

Since $\{e^{i\alpha_n x}\}_{n \in \mathbb{N}}$ is an orthogonal system in $L^2(-L/2, L/2)$, taking into account (4.38), for a fixed $y = y_0$, it holds

$$U^s(x, y_0) = \sum_{n \in \mathbb{Z}} a_n^+ e^{i(\alpha_n^+ x + \beta_n^+ y_0)},$$

with a_n^+ the Rayleigh coefficients given by

$$a_n^+ = \frac{1}{2L\beta_n^+} \left(\sum_{l=0}^J (-1)^l \binom{J}{l} e^{i\beta_n^+ l h^+} \right) \int_{-L/2}^{L/2} \left[\left(\frac{-\alpha_n^+ f'(x') + \beta_n^+}{\sqrt{1 + f'(x')^2}} \varphi^q(x') - i\phi^q(x') \right) e^{-i\alpha_n^+ x' - i\beta_n^+ f(x')} \sqrt{1 + f'(x')^2} \right] dx'. \quad (4.84)$$

On the other hand, the transmitted field is given by

$$U_-(x, y) = \int_{-L/2}^{L/2} \left(\left[-\frac{\partial G_{J-}^q}{\partial \nu_{x'}}(x - x', y - f(x')) \varphi^q(x') + G_{J-}^q(x - x', y - f(x')) \phi^q(x') \right] \sqrt{1 + f'(x')^2} \right) dx', \quad (4.85)$$

and considering (4.82) and (4.83), the expression (4.85) results

$$U^s(x, y) = \int_{-L/2}^{L/2} \left[\sum_{n \in \mathbb{Z}} \frac{1}{2L\beta_n^-} \left(\sum_{l=0}^J (-1)^l \binom{J}{l} e^{i\beta_n^- l h^-} \right) \left(\frac{\alpha_n^- f'(x') + \beta_n^-}{\sqrt{1 + f'(x')^2}} \varphi^q(x') + i\phi^q(x') \right) e^{i\alpha_n^-(x-x') - i\beta_n^-(y-f(x'))} \sqrt{1 + f'(x')^2} \right] dx'.$$

Since $\{e^{i\alpha_n x}\}_{n \in \mathbb{N}}$ is an orthogonal system in $L^2(-L/2, L/2)$, taking into account (4.40), for a fixed $y = y_0$, it holds

$$U^s(x, y_0) = \sum_{n \in \mathbb{Z}} a_n^- e^{i(\alpha_n^- x - \beta_n^- y_0)},$$

where the Rayleigh coefficients a_n^- are given as follows

$$a_n^- = \frac{1}{2L\beta_n^-} \left(\sum_{l=0}^J (-1)^l \binom{J}{l} e^{i\beta_n^- l h^-} \right) \int_{-L/2}^{L/2} \left[\left(\frac{\alpha_n^- f'(x') + \beta_n^-}{\sqrt{1 + f'(x')^2}} \varphi^q(x') + i\phi^q(x') \right) e^{-i\alpha_n^- x' + i\beta_n^- f(x')} \sqrt{1 + f'(x')^2} \right] dx'. \quad (4.86)$$

4.5.3 Discrete problems

Considering the quadrature rules described in Section 4.5.1, it is possible to give the discrete formulation of the scattering problem in a sound-soft boundary, and of the transmission problem. In the present chapter, the Nyström method with an equidistant and even number n_I of collocation points is used. These points x_k are defined by

$$x_k := \frac{L}{n_I}(k-1) - \frac{L}{2}, \quad k = 1, \dots, n_I.$$

Scattering problem in a sound-soft boundary with a single-layer formulation

As it has been described in Section 4.2.5, the integral equation of the scattering problem with the single-layer formulation is given by

$$\int_{-L/2}^{L/2} G_J^q(x - x', f(x) - f(x')) \varphi^{\text{per}}(x') \gamma(x, x') \sqrt{1 + f'(x')^2} dx' = U^{\text{inc}}(x, f(x)) e^{-i\alpha x}, \quad (4.87)$$

with $x \in [-L/2, L/2]$, and considering the truncated integral (4.15), and the decomposition (4.17), the integral equation (4.87) results

$$\begin{aligned} & \int_{x-A}^{x+A} \left[M_{\text{wl}}(x, x'; J) \ln \left(4 \sin^2 \left(\frac{\pi}{L}(x - x') \right) \right) + M_{\text{wr}}(x, x'; J) \right] \varphi^{\text{per}}(x') \sqrt{1 + f'(x')^2} dx' \\ &= U^{\text{inc}}(x, f(x)) e^{-i\alpha x}, \text{ with } x \in [-L/2, L/2], \end{aligned} \quad (4.88)$$

where $2A$ is the window size used to truncate the integral. Considering the discrete space $V_h = \{\phi \in \mathcal{C}^{\text{per}}([-L/2, L/2]) : \phi|_{[x_k, x_{k+1}]} \in \mathbb{P}^1\}$, since the functional space $\mathcal{C}^{\text{per}}([-L/2, L/2])$ can be replaced by the discrete space V_h , Equation (4.88) can be approximated by:

$$\begin{aligned} & \int_{x-A}^{x+A} \left[M_{\text{wl}}(x, x'; J) \ln \left(4 \sin^2 \left(\frac{\pi}{L}(x - x') \right) \right) + M_{\text{wr}}(x, x'; J) \right] \varphi_h^{\text{per}}(x') \sqrt{1 + f'(x')^2} dx' \\ &= U^{\text{inc}}(x, f(x)) e^{-i\alpha x}, \text{ with } x \in [-L/2, L/2], \end{aligned} \quad (4.89)$$

with $\varphi_h^{\text{per}} \in V_h$. Let $\overrightarrow{\varphi_h^{\text{per}}}$ be the column vector of coefficients of φ^{per} in the basis associated with V_h , $\varphi_h^{\text{per}}(x) = \sum_{k=1}^{n_I} [\overrightarrow{\varphi_h^{\text{per}}}]_k W_k(x)$. Then, the matrix formulation of the problem (4.89) is

$$A_M \overrightarrow{\varphi_h^{\text{per}}} = B,$$

where the coefficients of the matrix A_M , and the vector B are given by

$$\begin{aligned} [A_M]_k &= \int_{x-A}^{x+A} M_{\text{wl}}(x_k, x'; J) \ln \left(4 \sin^2 \left(\frac{\pi}{L}(x_k - x') \right) \right) W_k(x') \sqrt{1 + f'(x')^2} dx' \\ &+ \int_{x-A}^{x+A} M_{\text{wr}}(x_k, x'; J) W_k(x') \sqrt{1 + f'(x')^2} dx', \end{aligned}$$

$$[B]_k = U^{\text{inc}}(x_k, f(x_k)) e^{-i\alpha x_k},$$

for $k = 1, \dots, n_I$. Now, choosing the discretization points (4.70), and applying the quadrature rules (4.71) to M_{wl} , and (4.72) to M_{wr} , the integral equation (4.88) can be replaced by the approximated equation

$$\left[\frac{L}{2\pi} \sum_{|x_k - x_j| \leq A_l} R_{j,n_I} \left(\frac{2\pi x_k}{L} \right) M_{\text{wl}}(x_k, x_j; J) W_k(x_j) + \frac{L}{n_I} \sum_{|x_k - x_j| \leq A} M_{\text{wr}}(x_k, x_j; J) W_k(x_j) \right] \overrightarrow{\varphi_h^{\text{per}}} = U^{\text{inc}}(x_k, f(x_k)) e^{-i\alpha x_k},$$

for $k = 1, \dots, n_I$.

Scattering problem in a sound-soft boundary with a double-layer formulation

As it has been described in Section 4.3.1, the integral equation solved with the double-layer formulation is

$$\begin{aligned} \varphi^{\text{per}}(x) + 2 \int_{L/2}^{L/2} \frac{\partial G_J^q}{\partial \nu_{x'}}(x - x', f(x) - f(x')) \varphi^{\text{per}}(x') \gamma(x, x') \sqrt{1 + f'(x')^2} dx' \\ = -2U^{\text{inc}}(x, f(x)) e^{-i\alpha x}, \text{ with } x \in [-L/2, L/2], \end{aligned} \quad (4.90)$$

and considering the truncated integral (4.25), and the decomposition (4.26), the integral equation (4.90) results

$$\begin{aligned} \varphi^{\text{per}}(x) + 2 \int_{x-A}^{x+A} \left([L_{\text{wl}}(x, x'; J) \ln \left(4 \sin^2 \left(\frac{\pi}{L}(x - x') \right) \right) + L_{\text{wr}}(x, x'; J)] \right. \\ \times \varphi^{\text{per}}(x') \left. \right) \sqrt{1 + f'(x')^2} dx' = -2U^{\text{inc}}(x, f(x)) e^{-i\alpha x}, \text{ with } x \in [-L/2, L/2], \end{aligned} \quad (4.91)$$

where $2A$ is the size of the window used in the windowing method considered to obtain the fast convergence of the results. Let $V_h = \{\phi \in \mathcal{C}^{\text{per}}([-L/2, L/2]) : \phi|_{[x_k, x_{k+1}]} \in \mathbb{P}^1\}$. Since the functional space $\mathcal{C}^{\text{per}}([-L/2, L/2])$ can be replaced by the discrete space V_h , the approximation of Equation (4.91) is defined by:

$$\begin{aligned} \varphi_h^{\text{per}}(x) + 2 \int_{x-A}^{x+A} \left([L_{\text{wl}}(x, x'; J) \ln \left(4 \sin^2 \left(\frac{\pi}{L}(x - x') \right) \right) + L_{\text{wr}}(x, x'; J)] \right. \\ \times \varphi_h^{\text{per}}(x') \left. \right) \sqrt{1 + f'(x')^2} dx' = -2U^{\text{inc}}(x, f(x)) e^{-i\alpha x}, \text{ with } x \in [-L/2, L/2], \end{aligned} \quad (4.92)$$

with $\varphi_h^{\text{per}} \in V_h$. Let $\overrightarrow{\varphi_h^{\text{per}}}$ be the column vector of coefficients of φ^{per} in the basis associated with V_h , $\varphi_h^{\text{per}}(x) = \sum_{k=1}^{n_I} [\overrightarrow{\varphi_h^{\text{per}}}]_k W_k(x)$. Then, the matrix formulation of the problem (4.92) is

$$(I + 2A_L) \overrightarrow{\varphi_h^{\text{per}}} = -2B,$$

where I is the identity matrix of size n_I , and the coefficients of the matrix A_L , and the vector B are given by

$$\begin{aligned}[A_L]_k &= \int_{x-A}^{x+A} L_{\text{wl}}(x_k, x'; J) \ln \left(4 \sin^2 \left(\frac{\pi}{L}(x_k - x') \right) \right) W_k(x') \sqrt{1 + f'(x')^2} dx' \\ &\quad + \int_{x-A}^{x+A} L_{\text{wr}}(x_k, x'; J) W_k(x') \sqrt{1 + f'(x')^2} dx', \\ [B]_k &= U^{\text{inc}}(x_k, f(x_k)) e^{-i\alpha x_k},\end{aligned}$$

for $k = 1, \dots, n_I$. Now, choosing the discretization points (4.70), and applying the quadrature rules (4.71) to L_{wl} , and (4.72) to L_{wr} , the integral equation (4.91) can be replaced by the approximated equation

$$\begin{bmatrix} W_k(x_k) + \frac{L}{\pi} \sum_{|x_k - x_j| \leq A_l} R_{j,n_I} \left(\frac{2\pi x_k}{L} \right) L_{\text{wl}}(x_k, x_j; J) W_k(x_j) \\ + \frac{2L}{n_I} \sum_{|x_k - x_j| \leq A} L_{\text{wr}}(x_k, x_j; J) W_k(x_j) \end{bmatrix} \overrightarrow{\varphi_h^{\text{per}}} = -2U^{\text{inc}}(x_k, f(x_k)) e^{-i\alpha x_k},$$

for $k = 1, \dots, n_I$.

Transmission problem

As it has been described in Section 4.4.3, the system of integral equations used to solve the transmission problem using a combination of single- and double-layer formulations is

$$\begin{aligned}\varphi^{\text{per}}(x) + \int_{-L/2}^{L/2} \left[\left(\frac{\partial G_{J-}^{\text{q}}}{\partial \boldsymbol{\nu}_{x'}}(x - x', f(x) - f(x')) - \frac{\partial G_{J+}^{\text{q}}}{\partial \boldsymbol{\nu}_{x'}}(x - x', f(x) - f(x')) \right) \varphi^{\text{per}}(x') \gamma(x, x') \right] \\ \times \sqrt{1 + f'(x')^2} dx' + \int_{-L/2}^{L/2} \left[(G_{J+}^{\text{q}}(x - x', f(x) - f(x')) - G_{J-}^{\text{q}}(x - x', f(x) - f(x'))) \right. \\ \left. \times \phi^{\text{per}}(x') \gamma(x, x') \right] \sqrt{1 + f'(x')^2} dx' = U^{\text{inc}}(x, f(x)) e^{-i\alpha x},\end{aligned}\quad (4.93)$$

$$\begin{aligned}\phi^{\text{per}}(x) + \int_{-L/2}^{L/2} \left[\left(\frac{\partial^2 G_{J-}^{\text{q}}}{\partial \boldsymbol{\nu}_x \partial \boldsymbol{\nu}_{x'}}(x - x', f(x) - f(x')) - \frac{\partial^2 G_{J+}^{\text{q}}}{\partial \boldsymbol{\nu}_x \partial \boldsymbol{\nu}_{x'}}(x - x', f(x) - f(x')) \right) \varphi^{\text{per}}(x') \right. \\ \left. \times \gamma(x, x') \right] \sqrt{1 + f'(x')^2} dx' + \int_{-L/2}^{L/2} \left[\phi^{\text{per}}(x') \gamma(x, x') \left(\frac{\partial G_{J+}^{\text{q}}}{\partial \boldsymbol{\nu}_x}(x - x', f(x) - f(x')) \right. \right. \\ \left. \left. - \frac{\partial G_{J-}^{\text{q}}}{\partial \boldsymbol{\nu}_x}(x - x', f(x) - f(x')) \right) \right] \sqrt{1 + f'(x')^2} dx' = \frac{\partial U^{\text{inc}}}{\partial \boldsymbol{\nu}_x}(x, f(x)) e^{-i\alpha x},\end{aligned}\quad (4.94)$$

with $x \in [-L/2, L/2]$, and considering (4.17), (4.26), (4.55), and (4.61), the integral equations (4.93) and (4.94) result

$$\begin{aligned}
& \varphi^{\text{per}}(x) + \int_{x-A}^{x+A} \left[(L_{\text{wl}-}(x, x'; J) - L_{\text{wl}+}(x, x'; J)) \ln \left(4 \sin^2 \left(\frac{\pi}{L}(x - x') \right) \right) \right. \\
& \quad \left. + (L_{\text{wr}-}(x, x'; J) - L_{\text{wr}+}(x, x'; J)) \right] \varphi^{\text{per}}(x') \sqrt{1 + f'(x')^2} dx' \\
& + \int_{x-A}^{x+A} \left[(M_{\text{wl}+}(x, x'; J) - M_{\text{wl}-}(x, x'; J)) \ln \left(4 \sin^2 \left(\frac{\pi}{L}(x - x') \right) \right) \right. \\
& \quad \left. + (M_{\text{wr}+}(x, x'; J) - M_{\text{wr}-}(x, x'; J)) \right] \phi^{\text{per}}(x') \sqrt{1 + f'(x')^2} dx' \\
& = U^{\text{inc}}(x, f(x)) e^{-i\alpha x}, \text{ with } x \in [-L/2, L/2], \tag{4.95}
\end{aligned}$$

$$\begin{aligned}
& \phi^{\text{per}}(x) + \int_{x-A}^{x+A} \left[K_{\text{wl}}(x, x'; J) \ln \left(4 \sin^2 \left(\frac{\pi}{L}(x - x') \right) \right) + K_{\text{wr}}(x, x'; J) \right] \varphi^{\text{per}}(x') \sqrt{1 + f'(x')^2} dx' \\
& + \int_{x-A}^{x+A} \left[(H_{\text{wl}+}(x, x'; J) - H_{\text{wl}-}(x, x'; J)) \ln \left(4 \sin^2 \left(\frac{\pi}{L}(x - x') \right) \right) \right. \\
& \quad \left. + (H_{\text{wr}+}(x, x'; J) - H_{\text{wr}-}(x, x'; J)) \right] \phi^{\text{per}}(x') \sqrt{1 + f'(x')^2} dx' \\
& = \frac{\partial U^{\text{inc}}}{\partial \boldsymbol{\nu}_x}(x, f(x)) e^{-i\alpha x}, \text{ with } x \in [-L/2, L/2]. \tag{4.96}
\end{aligned}$$

Let $V_h = \{\phi \in C^{\text{per}}([-L/2, L/2]) : \phi|_{[x_k, x_{k+1}]} \in \mathbb{P}^1\}$. The functional space $C^{\text{per}}([-L/2, L/2])$ can be replaced by the discrete space V_h . Then, the approximation of Equations (4.95) and (4.96) is defined by:

$$\begin{aligned}
& \varphi_h^{\text{per}}(x) + \int_{x-A}^{x+A} \left[(L_{\text{wl}-}(x, x'; J) - L_{\text{wl}+}(x, x'; J)) \ln \left(4 \sin^2 \left(\frac{\pi}{L}(x - x') \right) \right) \right. \\
& \quad \left. + (L_{\text{wr}-}(x, x'; J) - L_{\text{wr}+}(x, x'; J)) \right] \varphi_h^{\text{per}}(x') \sqrt{1 + f'(x')^2} dx' \\
& + \int_{x-A}^{x+A} \left[(M_{\text{wl}+}(x, x'; J) - M_{\text{wl}-}(x, x'; J)) \ln \left(4 \sin^2 \left(\frac{\pi}{L}(x - x') \right) \right) \right. \\
& \quad \left. + (M_{\text{wr}+}(x, x'; J) - M_{\text{wr}-}(x, x'; J)) \right] \phi_h^{\text{per}}(x') \sqrt{1 + f'(x')^2} dx' \\
& = U^{\text{inc}}(x, f(x)) e^{-i\alpha x}, \text{ with } x \in [-L/2, L/2], \tag{4.97}
\end{aligned}$$

$$\begin{aligned}
& \phi_h^{\text{per}}(x) + \int_{x-A}^{x+A} \left[K_{\text{wl}}(x, x'; J) \ln \left(4 \sin^2 \left(\frac{\pi}{L}(x - x') \right) \right) + K_{\text{wr}}(x, x'; J) \right] \varphi_h^{\text{per}}(x') \sqrt{1 + f'(x')^2} dx' \\
& + \int_{x-A}^{x+A} \left[(H_{\text{wl}+}(x, x'; J) - H_{\text{wl}-}(x, x'; J)) \ln \left(4 \sin^2 \left(\frac{\pi}{L}(x - x') \right) \right) \right. \\
& \quad \left. + (H_{\text{wr}+}(x, x'; J) - H_{\text{wr}-}(x, x'; J)) \right] \phi_h^{\text{per}}(x') \sqrt{1 + f'(x')^2} dx' \\
& = \frac{\partial U^{\text{inc}}}{\partial \boldsymbol{\nu}_x}(x, f(x)) e^{-i\alpha x}, \text{ with } x \in [-L/2, L/2], \tag{4.98}
\end{aligned}$$

with $\varphi_h^{\text{per}}, \phi_h^{\text{per}} \in (V_h \times V_h)$. Let $\overrightarrow{\varphi_h^{\text{per}}}$ be the column vector of coefficients of φ^{per} in the basis associated with V_h , $\varphi_h^{\text{per}}(x) = \sum_{k=1}^{n_I} [\overrightarrow{\varphi_h^{\text{per}}}]_k W_k(x)$ and $\overrightarrow{\phi_h^{\text{per}}}$ be the column vector of coefficients of ϕ^{per} in the basis associated with V_h , $\phi_h^{\text{per}}(x) = \sum_{k=1}^{n_I} [\overrightarrow{\phi_h^{\text{per}}}]_k W_k(x)$. Then, the matrix formulation of the problem formed by Equations (4.97) and (4.98) is

$$\left(I + \begin{pmatrix} A_L & A_M \\ A_K & A_H \end{pmatrix} \right) \begin{pmatrix} \overrightarrow{\varphi_h^{\text{per}}} \\ \overrightarrow{\phi_h^{\text{per}}} \end{pmatrix} = \begin{pmatrix} B \\ C \end{pmatrix},$$

where I is the identity matrix of size $2n_I$, and the coefficients of the matrices A_L, A_M, A_H, A_K , and the vectors B and C are given by

$$\begin{aligned} [A_L]_k &= \int_{x-A}^{x+A} \left[(L_{\text{wl}-}(x_k, x'; J) - L_{\text{wl}+}(x_k, x'; J)) \ln \left(4 \sin^2 \left(\frac{\pi}{L} (x_k - x') \right) \right) \right. \\ &\quad \left. + (L_{\text{wr}-}(x_k, x'; J) - L_{\text{wr}+}(x_k, x'; J)) \right] W_k(x') \sqrt{1 + f'(x')^2} dx', \\ [A_M]_k &= \int_{x-A}^{x+A} \left[(M_{\text{wl}+}(x_k, x'; J) - M_{\text{wl}-}(x_k, x'; J)) \ln \left(4 \sin^2 \left(\frac{\pi}{L} (x_k - x') \right) \right) \right. \\ &\quad \left. + (M_{\text{wr}+}(x_k, x'; J) - M_{\text{wr}-}(x_k, x'; J)) \right] W_k(x') \sqrt{1 + f'(x')^2} dx', \\ [A_K]_k &= \int_{x-A}^{x+A} \left[K_{\text{wl}}(x_k, x'; J) \ln \left(4 \sin^2 \left(\frac{\pi}{L} (x_k - x') \right) \right) + K_{\text{wr}}(x_k, x'; J) \right] W_k(x') \\ &\quad \times \sqrt{1 + f'(x')^2} dx', \\ [A_H]_k &= \int_{x-A}^{x+A} \left[(H_{\text{wl}+}(x_k, x'; J) - H_{\text{wl}-}(x_k, x'; J)) \ln \left(4 \sin^2 \left(\frac{\pi}{L} (x_k - x') \right) \right) \right. \\ &\quad \left. + (H_{\text{wr}+}(x_k, x'; J) - H_{\text{wr}-}(x_k, x'; J)) \right] W_k(x') \sqrt{1 + f'(x')^2} dx', \\ [B]_k &= U^{\text{inc}}(x_k, f(x_k)) e^{-i\alpha x_k}, \\ [C]_k &= \frac{\partial U^{\text{inc}}}{\partial \boldsymbol{\nu}_x}(x_k, f(x_k)) e^{-i\alpha x_k}, \end{aligned}$$

for $k = 1, \dots, n_I$. Now, choosing the discretization points (4.70), and applying the quadrature rule (4.71) to the integrals which have the logarithmic part (the integrals which involve $L_{\text{wl}+}, L_{\text{wl}-}, M_{\text{wl}+}, M_{\text{wl}-}, K_{\text{wl}}, H_{\text{wl}+}$, and $H_{\text{wl}-}$), and the quadrature rule (4.72) to the smooth integrals (those integrals which involve $L_{\text{wr}+}, L_{\text{wr}-}, M_{\text{wr}+}, M_{\text{wr}-}, K_{\text{wr}}, H_{\text{wr}+}$, and $H_{\text{wr}-}$), the integral equations (4.95) and (4.96) can be replaced by the approximated equations

$$\begin{aligned}
& \left[W_k(x_k) + \frac{L}{\pi} \sum_{|x_k - x_j| \leq A_l} R_{j,n_I} \left(\frac{2\pi x_k}{L} \right) (L_{\text{wl-}}(x_k, x_j; J) - L_{\text{wl+}}(x_k, x_j; J)) W_k(x_j) \right. \\
& \quad \left. + \frac{2L}{n_I} \sum_{|x_k - x_j| \leq A} (L_{\text{wr-}}(x_k, x_j; J) - L_{\text{wr+}}(x_k, x_j; J)) W_k(x_j) \right] \overrightarrow{\varphi_h^{\text{per}}} \\
& \quad + \left[\frac{L}{\pi} \sum_{|x_k - x_j| \leq A_l} R_{j,n_I} \left(\frac{2\pi x_k}{L} \right) (M_{\text{wl+}}(x_k, x_j; J) - M_{\text{wl-}}(x_k, x_j; J)) W_k(x_j) \right. \\
& \quad \left. + \frac{2L}{n_I} \sum_{|x_k - x_j| \leq A} (M_{\text{wr+}}(x_k, x_j; J) - M_{\text{wr-}}(x_k, x_j; J)) W_k(x_j) \right] \overrightarrow{\phi_h^{\text{per}}} \\
& = U^{\text{inc}}(x_k, f(x_k)) e^{-i\alpha x_k}, \quad \text{for } k = 1, \dots, n_I, \\
& \left[\frac{L}{\pi} \sum_{|x_k - x_j| \leq A_l} R_{j,n_I} \left(\frac{2\pi x_k}{L} \right) K_{\text{wl}}(x_k, x_j; J) W_k(x_j) + \frac{2L}{n_I} \sum_{|x_k - x_j| \leq A} K_{\text{wr}}(x_k, x_j; J) W_k(x_j) \right] \overrightarrow{\varphi_h^{\text{per}}} \\
& \quad + \left[W_k(x_k) + \frac{L}{\pi} \sum_{|x_k - x_j| \leq A_l} R_{j,n_I} \left(\frac{2\pi x_k}{L} \right) (H_{\text{wl+}}(x_k, x_j; J) - H_{\text{wl-}}(x_k, x_j; J)) W_k(x_j) \right. \\
& \quad \left. + \frac{2L}{n_I} \sum_{|x_k - x_j| \leq A} (H_{\text{wr+}}(x_k, x_j; J) - H_{\text{wr-}}(x_k, x_j; J)) W_k(x_j) \right] \overrightarrow{\phi_h^{\text{per}}} \\
& = \frac{\partial U^{\text{inc}}}{\partial \boldsymbol{\nu}_x}(x_k, f(x_k)) e^{-i\alpha x_k}, \quad \text{for } k = 1, \dots, n_I.
\end{aligned}$$

4.6 Numerical results

In this section, numerical results are presented to illustrate the fast convergence of the proposed method in two different problems: the wave scattering problem by a sound-soft periodic surface considering a single-layer, and also a double-layer representation, and the wave propagation between two periodic media in contact. Two different test are performed in each problem. In the first test, the convergence order of the method is analyzed with respect to the size of the window considered, and with respect to the number of points per period. In the second one, the efficiencies e_n of the propagative modes are computed using different number of shifts J .

To obtain the numerical results, the linear systems described in the previous section has been solved by using the iterative solver GMRES [159]. The method is restarted every 50 inner iterations, with a tolerance of 10^{-12} , and with the LU factorization as preconditioner.

The periodic coupling interface considered is the sinusoidal grating parametrized by the equation (4.99) (see Figure 4.6), with $L = 2\pi$.

$$y = \frac{L}{2} \cos \left(\frac{2\pi x}{L} \right). \tag{4.99}$$

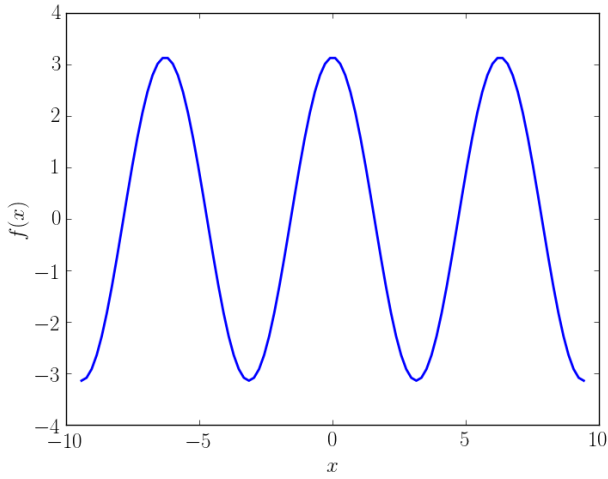


Figure 4.6: Sinusoidal grating (4.99) with $L = 2\pi$, used in the numerical simulations

The efficiencies e_n in the scattering problem by a periodic sound-soft boundary have been computed by using (4.73), and the error is given by

$$\varepsilon = \left| 1 - \sum_{n \in \Lambda} e_n \right|,$$

following the energy balance criterion (4.74). The efficiencies e_n^\pm in the transmission problem have been computed by using (4.79), and following the energy balance criterion (4.80), the error is computed by

$$\varepsilon = \left| 1 - \sum_{n \in \Lambda_+} e_n^+ - \sum_{n \in \Lambda_-} e_n^- \right|.$$

4.6.1 Numerical results for the scattering problem by a sound-soft boundary with a single-layer formulation

In this section, the problem under consideration is the scattering problem by a sound-soft boundary with a single-layer formulation introduced in Section 4.2. The periodic sinusoidal grating used is (4.99) with period $L = 2\pi$, and the incident angle of the plane wave is $\theta = \pi/4$. In order to illustrate the convergence of the numerical solution of each problem, the energy balance criterion (4.74) has been used. The efficiencies of the propagative modes have been computed by using (4.73), and to compute the Rayleigh coefficients in the single-layer formulation, Equation (4.76) has been considered.

Efficiencies considering a sinusoidal grating

In this section, the efficiencies e_n have been computed using different number of shifts J . Tables 4.1 and 4.2 show the energy balance error for a small wave number, $k = 1.5$, and

for a large wave number, $k = 8.5$, respectively, considering a number of points per period n_I , and a window size $2A$. The value of the shift distance considered when $J \neq 0$ is $h = 2.5$ for the small wave number, and $h = 5$ for the large one, and the parameters of the windows are $c = 0.1$, $A_l = L/4$, and $d_l = 0.2$. As it can be observed, a smaller error is achieved increasing the number of points per period, and the window size.

J	$n_I = 128$ $A = 400$	$n_I = 256$ $A = 800$	$n_I = 512$ $A = 1600$	$n_I = 1024$ $A = 3200$
0	2.271×10^{-7}	1.937×10^{-10}	3.312×10^{-12}	7.048×10^{-11}
1	2.519×10^{-6}	3.102×10^{-7}	3.876×10^{-8}	4.772×10^{-9}
2	1.083×10^{-5}	1.354×10^{-6}	1.692×10^{-7}	2.107×10^{-8}
3	3.329×10^{-5}	4.164×10^{-6}	5.204×10^{-7}	6.496×10^{-8}
4	7.630×10^{-5}	9.540×10^{-6}	1.192×10^{-6}	1.489×10^{-7}

Table 4.1: Energy balance error (following (4.74)) in the scattering problem with a single-layer formulation for a small wave number, $k = 1.5$. Solutions are computed using n_I number of points per period, and the window size is $2A$. The value of shift considered when $J > 0$, is $h = 2.5$, and the parameters for the windows are $c = 0.1$, $A_l = L/4$, and $d_l = 0.2$.

J	$n_I = 128$ $A = 400$	$n_I = 256$ $A = 800$	$n_I = 512$ $A = 1600$	$n_I = 1024$ $A = 3200$
0	8.111×10^{-6}	1.041×10^{-7}	1.537×10^{-9}	4.377×10^{-11}
1	9.104×10^{-4}	1.071×10^{-4}	1.326×10^{-5}	1.655×10^{-6}
2	2.165×10^{-2}	2.097×10^{-3}	2.509×10^{-4}	3.108×10^{-5}
3	5.576×10^{-2}	2.340×10^{-3}	2.148×10^{-4}	2.544×10^{-5}
4	2.099×10^{-1}	3.692×10^{-2}	7.178×10^{-3}	9.437×10^{-4}

Table 4.2: Energy balance error (following (4.74)) in the scattering problem with a single-layer formulation for $k = 8.5$. The number of points per period, and the window size used are n_I and $2A$, respectively. The value of shift considered when $J > 0$, is $h = 5$, and the parameters for the windows are $c = 0.1$, $A_l = L/4$, and $d_l = 0.2$.

Since in the previous simulations, the chosen wave number is not a Wood anomaly, now, the error for $k_w = \frac{2\pi}{L(1-\sin(\pi/4))} \approx 3.414$, which is a Wood anomaly, is computed. Table 4.3 shows the error for different values of the shift J , to illustrate that the error is larger when the wave number is approached to the Wood anomaly.

Convergence analysis considering a sinusoidal grating

In this section, some numerical results are shown to illustrate the convergence of the method introduced in Section 4.2. Tables 4.4 and 4.5 show the computed energy balance error for a small wave number, $k = 1.5$, by using $J = 0$ and $J = 2$, respectively, by

	$j = 0$	$j = 1$	$j = 2$	$j = 6$	$j = 8$
$k_w - 10^0$	2.456×10^{-8}	1.590×10^{-8}	4.957×10^{-7}	4.201×10^{-5}	3.023×10^{-4}
$k_w - 10^{-1}$	1.182×10^{-5}	5.306×10^{-6}	2.423×10^{-6}	1.049×10^{-5}	1.052×10^{-4}
$k_w - 10^{-2}$	1.520×10^{-3}	1.475×10^{-3}	6.483×10^{-5}	2.508×10^{-3}	1.235×10^{-2}
$k_w - 10^{-3}$	1.299×10^{-2}	1.046×10^{-2}	6.671×10^{-3}	5.655×10^{-2}	9.110×10^{-2}
$k_w - 10^{-4}$	1.511×10^{-2}	1.269×10^{-2}	1.265×10^{-2}	5.530×10^{-2}	9.153×10^{-2}

Table 4.3: Energy balance error in the scattering problem with a single-layer formulation for wave numbers closed to the Wood anomaly $k_w = \frac{2\pi}{L(1-\sin(\pi/4))} \approx 3.414$. The value of shift when $J > 0$ is $h = 2.5$, the number of points per period is $n_I = 1024$, and the parameters for the windows are $A = 1600$, $c = 0.1$, $A_l = L/4$, and $d_l = 0.2$.

using a number of points per period n_I , and a window size $2A$. The value of the shift distance considered when $J = 2$ is $h = 2.5$, and the parameters of the windows are $c = 0.1$, $A_l = L/4$, and $d_l = 0.2$. As it has been defined in Theorem 4.2.3, the method converges superalgebraically fast as the truncation radius A tends to infinity.

n_I	$A = 200$	$A = 400$	$A = 800$	$A = 1600$
32	3.978×10^{-5}	3.258×10^{-7}	5.534×10^{-7}	5.536×10^{-7}
64	3.923×10^{-5}	2.193×10^{-7}	7.804×10^{-9}	8.001×10^{-9}
128	3.922×10^{-5}	2.271×10^{-7}	7.837×10^{-11}	1.251×10^{-10}
256	3.922×10^{-5}	2.272×10^{-7}	1.937×10^{-10}	5.241×10^{-12}
512	3.922×10^{-5}	2.272×10^{-7}	1.955×10^{-10}	3.312×10^{-12}

Table 4.4: Energy balance error (following (4.74)) in the scattering problem with a single-layer formulation for a small wave number, $k = 1.5$. Solutions are computed using n_I number of points per period, and the window size is $2A$. None shifts are considered, that is, $J = 0$, and the parameters for the windows are $c = 0.1$, $A_l = L/4$, and $d_l = 0.2$.

n_I	$A = 200$	$A = 400$	$A = 800$	$A = 1600$
32	4.911×10^{-5}	6.405×10^{-5}	6.406×10^{-5}	6.406×10^{-5}
64	3.731×10^{-6}	1.114×10^{-5}	1.114×10^{-5}	1.114×10^{-5}
128	1.358×10^{-5}	1.278×10^{-6}	1.280×10^{-6}	1.280×10^{-6}
256	1.472×10^{-5}	1.423×10^{-7}	1.437×10^{-7}	1.438×10^{-7}
512	1.485×10^{-5}	8.495×10^{-9}	9.891×10^{-9}	9.912×10^{-9}

Table 4.5: Energy balance error (following (4.74)) in the scattering problem with a single-layer formulation for a small wave number, $k = 1.5$. Solutions are computed using n_I number of points per period, and the window size is $2A$. The value of the shift distance is $h = 2.5$, the number of shifts is $J = 2$, and the parameters for the windows are $c = 0.1$, $A_l = L/4$, and $d_l = 0.2$.

Tables 4.6 and 4.7 show the computed energy balance error for a large wave number, $k = 8.5$, by using $J = 0$ and $J = 2$, respectively, by using a number of points per period n_I , and a window size $2A$. The value of the shift distance considered when $J = 2$ is $h = 5$, and the parameters of the windows are $c = 0.1$, $A_l = L/4$, and $d_l = 0.2$. As it can be observed, to increase the number of points per period is more important when k is large, and to increase the window size is more important when k is small to achieve a fast convergence.

n_I	$A = 200$	$A = 400$	$A = 800$	$A = 1600$
64	7.690×10^{-3}	7.693×10^{-3}	7.693×10^{-3}	7.693×10^{-3}
128	3.598×10^{-6}	8.111×10^{-6}	8.375×10^{-6}	8.375×10^{-6}
256	4.525×10^{-6}	1.597×10^{-7}	1.041×10^{-7}	1.041×10^{-7}
512	4.611×10^{-6}	2.622×10^{-7}	1.537×10^{-9}	1.548×10^{-9}
1024	4.611×10^{-6}	2.638×10^{-7}	1.525×10^{-11}	2.697×10^{-11}

Table 4.6: Energy balance error (following (4.74)) in the scattering problem with a single-layer formulation for a large wave number, $k = 8.5$. Solutions are computed using n_I number of points per period, and the window size is $2A$. None shifts are considered, that is, $J = 0$, and the parameters for the windows are $c = 0.1$, $A_l = L/4$, and $d_l = 0.2$.

n_I	$A = 200$	$A = 400$	$A = 800$	$A = 1600$
64	1.247×10^{-1}	1.232×10^{-1}	1.232×10^{-1}	1.232×10^{-1}
128	2.266×10^{-2}	2.165×10^{-2}	2.165×10^{-2}	2.165×10^{-2}
256	2.931×10^{-3}	2.098×10^{-3}	2.097×10^{-3}	2.097×10^{-3}
512	1.068×10^{-3}	2.519×10^{-4}	2.511×10^{-4}	2.511×10^{-4}
1024	8.455×10^{-4}	3.201×10^{-5}	3.117×10^{-5}	3.117×10^{-5}

Table 4.7: Energy balance error (following (4.74)) in the scattering problem with a single-layer formulation for $k = 8.5$. Solutions are computed using n_I number of points per period, and the window size is $2A$. The value of the shift distance is $h = 5$, the number of shifts is $J = 2$, and the parameters for the windows are $c = 0.1$, $A_l = L/4$, and $d_l = 0.2$.

4.6.2 Numerical results for the scattering problem by a sound-soft boundary with a double-layer formulation

In this section, the scattering problem by a sound-soft boundary with a double-layer formulation introduced in Section 4.3 is considered. The periodic sinusoidal grating used is (4.99) with period $L = 2\pi$, and the incident angle of the plane wave is $\theta = \pi/4$. As in single-layer simulations, to illustrate the convergence of the numerical solution of the problem, the energy balance criterion (4.74) has been used, and the efficiencies of the propagative modes have been computed by using (4.73), where the Rayleigh coefficients in the double-layer formulation are obtained by using Equation (4.76).

Efficiencies sinusoidal grating

In this section, the efficiencies e_n have been computed using different number of shifts J . Tables 4.8 and 4.9 show the energy balance error for a small wave number, $k = 1.5$, and for a large wave number, $k = 8.5$, respectively, considering a number of points per period n_I , and a window size $2A$. The value of the shift distance considered when $J \neq 0$ is $h = 2.5$ for the small wave number, and $h = 5$ for the large one, and the parameters of the windows are $c = 0.1$, $A_l = L/4$, and $d_l = 0.2$. As it can be observed, a smaller error is achieved increasing the number of points per period, and the window size.

J	$n_I = 128$ $A = 400$	$n_I = 256$ $A = 800$	$n_I = 512$ $A = 1600$	$n_I = 1024$ $A = 3200$
0	3.695×10^{-7}	2.389×10^{-10}	1.377×10^{-11}	7.075×10^{-11}
1	2.298×10^{-8}	2.298×10^{-10}	9.773×10^{-12}	7.070×10^{-11}
2	1.122×10^{-7}	2.350×10^{-10}	3.545×10^{-12}	7.099×10^{-11}
3	2.932×10^{-7}	1.100×10^{-9}	3.110×10^{-11}	7.146×10^{-11}
4	6.002×10^{-7}	2.647×10^{-9}	7.994×10^{-11}	7.201×10^{-11}

Table 4.8: Energy balance error (following (4.74)) in the scattering problem with a double-layer formulation for a small wave number, $k = 1.5$. Solutions are computed by using n_I number of points per period, and the window size is $2A$. The value of shift considered, when $J > 0$ is $h = 2.5$, and the parameters for the windows are $c = 0.1$, $A_l = L/4$, and $d_l = 0.2$.

J	$n_I = 128$ $A = 400$	$n_I = 256$ $A = 800$	$n_I = 512$ $A = 1600$	$n_I = 1024$ $A = 3200$
0	7.071×10^{-6}	1.816×10^{-7}	5.444×10^{-9}	2.396×10^{-10}
1	5.860×10^{-6}	1.565×10^{-7}	4.703×10^{-9}	2.175×10^{-10}
2	1.189×10^{-5}	3.693×10^{-7}	1.113×10^{-8}	4.064×10^{-10}
3	1.088×10^{-5}	3.312×10^{-6}	9.948×10^{-8}	3.098×10^{-9}
4	5.702×10^{-3}	1.370×10^{-6}	4.160×10^{-8}	1.295×10^{-9}

Table 4.9: Energy balance error (following (4.74)) in the scattering problem with a double-layer formulation for a large wave number, $k = 8.5$. Solutions are computed using n_I number of points per period, and the window size is $2A$. The value of shift considered, when $J > 0$ is $h = 5$, and the parameters for the windows are $c = 0.1$, $A_l = L/4$, and $d_l = 0.2$.

In the previous simulations, the chosen wave number is not a Wood anomaly. Now, the error for $k_w = \frac{2\pi}{L(1-\sin(\pi/4))} \approx 3.414$, which is a Wood anomaly, is computed. Table 4.10 shows the error for different values of the shift J , to illustrate that the error is larger when the wave number is approached to the Wood anomaly.

	$j = 0$	$j = 1$	$j = 2$	$j = 5$	$j = 7$
$k_w - 10^0$	6.019×10^{-8}	4.813×10^{-10}	1.041×10^{-9}	2.667×10^{-9}	1.130×10^{-8}
$k_w - 10^{-1}$	3.614×10^{-5}	3.848×10^{-6}	8.031×10^{-8}	5.861×10^{-7}	4.765×10^{-6}
$k_w - 10^{-2}$	1.117×10^{-3}	2.540×10^{-3}	2.889×10^{-3}	5.226×10^{-3}	3.751×10^{-2}
$k_w - 10^{-3}$	1.658×10^{-2}	7.415×10^{-3}	2.087×10^{-3}	2.892×10^{-2}	5.233×10^{-2}
$k_w - 10^{-4}$	2.002×10^{-2}	1.114×10^{-2}	9.436×10^{-3}	3.263×10^{-2}	4.973×10^{-2}

Table 4.10: Energy balance error in the scattering problem with a double-layer formulation for wave numbers closed to the Wood anomaly $k_w = \frac{2\pi}{L(1-\sin(\pi/4))} \approx 3.414$. The value of shift when $J > 0$ is $h = 1.5$, the number of points per period is $n_I = 1024$, and the parameters for the windows are $A = 1600$, $c = 0.1$, $A_l = L/4$, and $d_l = 0.2$.

Convergence analysis considering a sinusoidal grating

In this section, to illustrate the convergence of the method introduced in Section 4.3, numerical results are shown. Tables 4.11 and 4.12 show the computed energy balance error for $k = 1.5$, with $J = 0$ and $J = 2$, respectively, using n_I number of points per period, and a window size $2A$. The shift distance when $J = 2$ is $h = 1.5$, and the window parameters are $c = 0.1$, $A_l = L/4$, and $d_l = 0.2$. Following Theorem 4.2.3, the method converges superalgebraically fast as the truncation radius A tends to infinity.

n_I	$A = 200$	$A = 400$	$A = 800$	$A = 1600$
32	1.105×10^{-5}	1.519×10^{-6}	1.900×10^{-6}	1.900×10^{-6}
64	1.273×10^{-5}	1.679×10^{-7}	2.129×10^{-7}	2.134×10^{-7}
128	1.294×10^{-5}	3.695×10^{-7}	1.135×10^{-8}	1.193×10^{-8}
256	1.295×10^{-5}	3.811×10^{-7}	2.389×10^{-10}	3.372×10^{-10}
512	1.295×10^{-5}	3.814×10^{-7}	5.622×10^{-10}	1.377×10^{-11}

Table 4.11: Energy balance error (following (4.74)) in the scattering problem with a double-layer formulation for a small wave number, $k = 1.5$. Solutions are computed using n_I number of points per period, and the window size is $2A$. None shifts are considered, that is, $J = 0$, and the parameters for the windows are $c = 0.1$, $A_l = L/4$, and $d_l = 0.2$.

n_I	$A = 200$	$A = 400$	$A = 800$	$A = 1600$
32	3.435×10^{-4}	3.443×10^{-4}	3.443×10^{-4}	3.443×10^{-4}
64	5.965×10^{-7}	2.071×10^{-7}	2.303×10^{-7}	2.303×10^{-7}
128	8.282×10^{-7}	2.467×10^{-8}	1.445×10^{-9}	1.417×10^{-9}
256	8.269×10^{-7}	2.331×10^{-8}	8.007×10^{-11}	5.610×10^{-11}
512	8.268×10^{-7}	2.325×10^{-8}	2.251×10^{-11}	1.454×10^{-12}

Table 4.12: Energy balance error (following (4.74)) in the scattering problem with a double-layer formulation for a small wave number, $k = 1.5$. Solutions are computed using n_I number of points per period, and the window size is $2A$. The value of shift is $h = 2.5$ and $J = 2$, and the parameters for the windows are $c = 0.1$, $A_l = L/4$, and $d_l = 0.2$.

Tables 4.13 and 4.14 show the computed energy balance error for a large wave number, $k = 8.5$, by using $J = 0$ and $J = 2$, respectively, by using a number of points per period n_I and a window size $2A$. The value of the shift distance considered when $J = 2$ is $h = 5$, and the parameters of the windows are $c = 0.1$, $A_l = L/4$, and $d_l = 0.2$. As it can be observed, the method possesses superalgebraically convergence as the truncation radius A tends to infinity.

n_I	$A = 200$	$A = 400$	$A = 800$	$A = 1600$
64	2.213×10^{-3}	2.211×10^{-3}	2.211×10^{-3}	2.211×10^{-3}
128	4.927×10^{-6}	7.071×10^{-6}	6.945×10^{-6}	6.945×10^{-6}
256	1.837×10^{-6}	3.081×10^{-7}	1.816×10^{-7}	1.818×10^{-7}
512	2.013×10^{-6}	1.318×10^{-7}	5.282×10^{-9}	5.443×10^{-9}
1024	2.019×10^{-6}	1.265×10^{-7}	3.298×10^{-10}	1.655×10^{-10}

Table 4.13: Energy balance error (following (4.74)) in the scattering problem with a double-layer formulation for a large wave number, $k = 8.5$. Solutions are computed using n_I number of points per period, and the window size is $2A$. None shifts are considered, that is, $J = 0$, and the parameters for the windows are $c = 0.1$, $A_l = L/4$, and $d_l = 0.2$.

n_I	$A = 200$	$A = 400$	$A = 800$	$A = 1600$
64	2.120×10^{-3}	5.199×10^{-3}	5.201×10^{-3}	5.201×10^{-3}
128	2.963×10^{-3}	1.189×10^{-5}	1.378×10^{-5}	1.378×10^{-5}
256	2.977×10^{-3}	1.524×10^{-6}	3.693×10^{-7}	3.692×10^{-7}
512	2.977×10^{-3}	1.882×10^{-6}	1.123×10^{-8}	1.113×10^{-8}
1024	2.977×10^{-3}	1.893×10^{-6}	4.437×10^{-10}	3.417×10^{-10}

Table 4.14: Energy balance error (following (4.74)) in the scattering problem with a double-layer formulation for a large wave number, $k = 8.5$. Solutions are computed using n_I number of points per period, and the window size is $2A$. The value of shift is $h = 5$ and $J = 2$, and the parameters for the windows are $c = 0.1$, $A_l = L/4$, and $d_l = 0.2$.

4.6.3 Numerical results for the transmission problem

In this section, some numerical results are shown to illustrate the efficiency of the method. First of all, some validation test have been performed. Considering a plane interface between the media, the solution of the proposed method has been compared with the exact solution. When a sinusoidal grating is considered, since an exact solution can not be computed, the solution has been compared with the solution obtained by using the Finite Element Method (FEM). Once the code has been validated, a convergence analysis of the proposed method is shown.

Validation code with a planar interface

In this section, the code has been validated considering a planar interface. If the incident wave is a plane wave with an oblique incidence angle, it is possible to compute the scattered

wave and the transmitted wave analytically. In all these simulations, the planar interface $y = 0$ is considered, and it is supposed that the incidence angle of the plane wave is $\theta^+ = \pi/4$. The parameters to perform the simulations are $n_I = 256$, $A = 400$, $c = 0.1$, $A_l = L/4$, and $d_l = 0.2$.

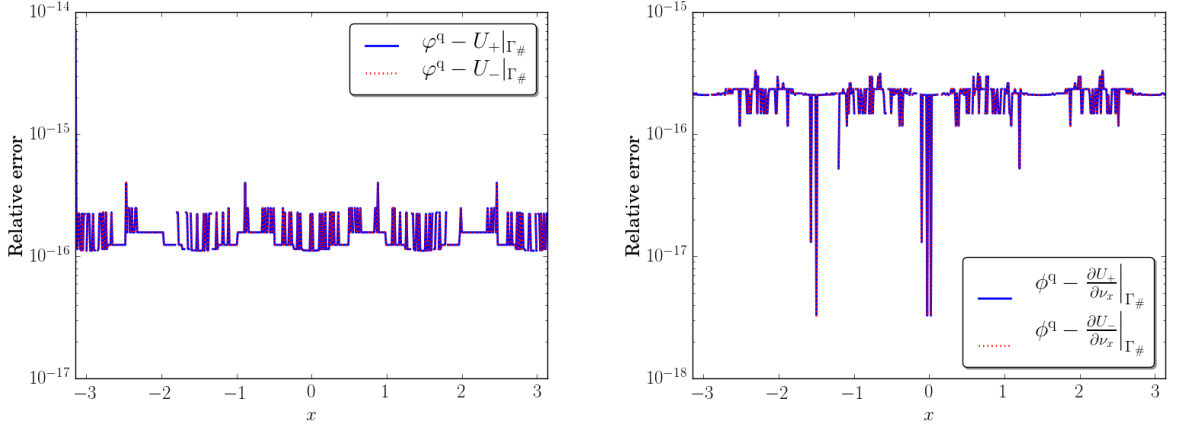


Figure 4.7: Relative error for the solution φ^q (left plot), and for the solution ϕ^q (right plot). In both cases, errors are computed comparing with the exact solution in the propagation domain Ω_+ (solid blue line), and comparing with the exact solution in the propagation domain Ω_- (dotted red line), considering a planar interface, and an incident plane wave with an incidence angle $\theta^+ = \pi/4$. The values of the wave numbers are $k^+ = k^- = 1.5$.

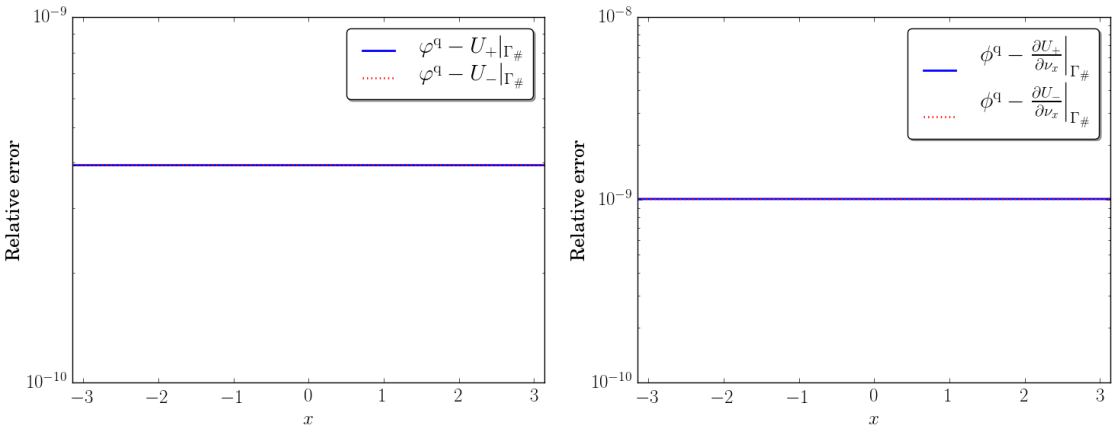


Figure 4.8: Relative error for the solution φ^q (left plot), and for the solution ϕ^q (right plot). In both cases, errors are computed comparing with the exact solution in the propagation domain Ω_+ (solid blue line), and comparing with the exact solution in the propagation domain Ω_- (dotted red line), considering a planar interface, and an incident plane wave with an incidence angle $\theta^+ = \pi/4$. The wave numbers are $k^+ = 1.5$, and $k^- = 2.5$.

As it is well-known, the solutions of the system (4.47), φ^q and ϕ^q , can be computed as $\varphi^q = U_+|_{\Gamma^\#} = U_-|_{\Gamma^\#}$ and $\phi^q = \frac{\partial U_+}{\partial \nu_x}|_{\Gamma^\#} = \frac{\partial U_-}{\partial \nu_x}|_{\Gamma^\#}$. Figures 4.7, 4.8, and 4.9 show the relative error in the solution of the system (4.47) comparing with the analytic exact solution when

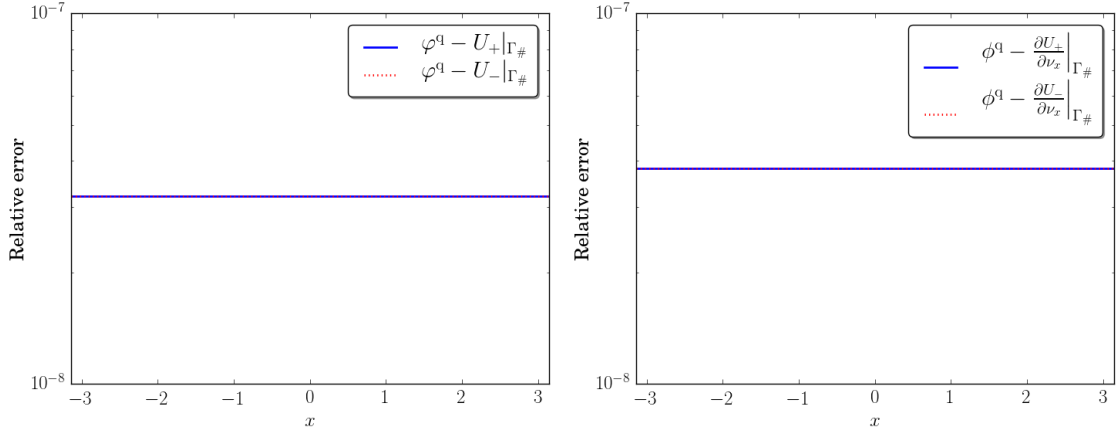


Figure 4.9: Relative error for the solution φ^q (left plot), and for the solution ϕ^q (right plot). In both cases, errors are computed comparing with the exact solution in the propagation domain Ω_+ (solid blue line), and comparing with the exact solution in the propagation domain Ω_- (dotted red line), considering a planar interface, and an incident plane wave with an incidence angle $\theta^+ = \pi/4$. The wave numbers are $k^+ = 2.5$, and $k^- = 1.5$.

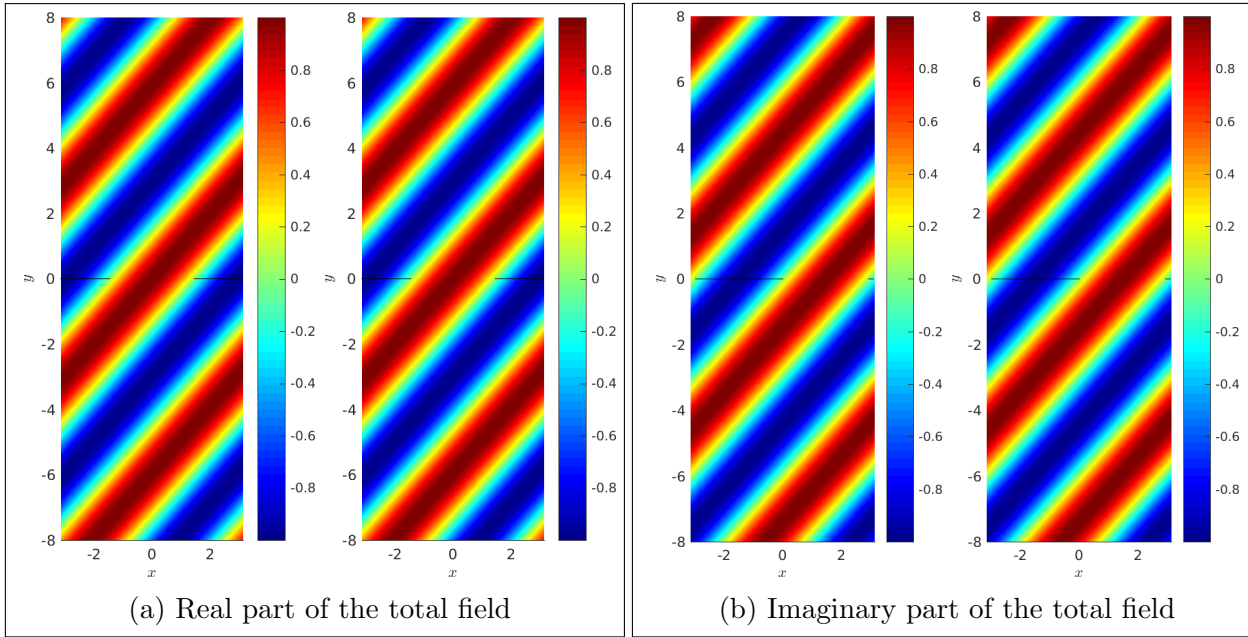


Figure 4.10: Real and imaginary part of the total field. Left: Exact solution. Right: Solution computed by using the integral equation method described in Section 4.4.3. The wave numbers are $k^+ = k^- = 1.5$.

$k^+ = k^-$, $k^+ < k^-$, and $k^+ > k^-$, respectively. As it can be observed, in the worst case, the relative errors in the solution of the system are less than 10^{-7} .

Figures 4.10, 4.11, and 4.12 show the comparison between the integral equation method

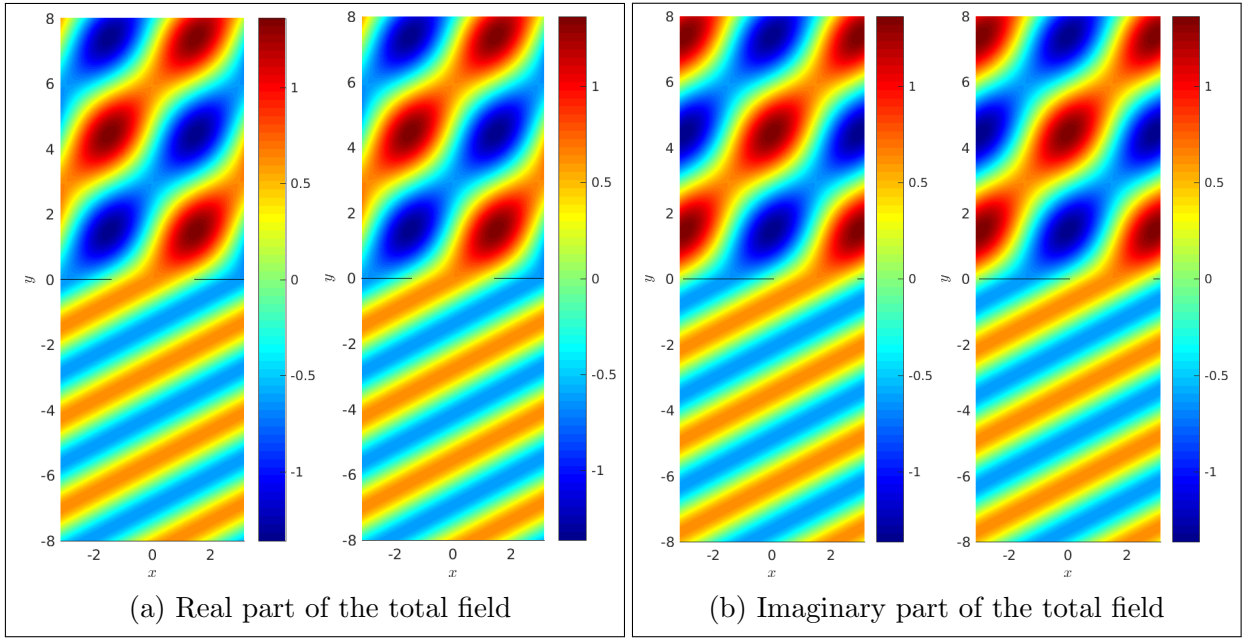


Figure 4.11: Real and imaginary part of the total field. Left: Exact solution. Right: Solution computed by using the integral equation method described in Section 4.4.3. The wave numbers are $k^+ = 1.5$ and $k^- = 2.5$.

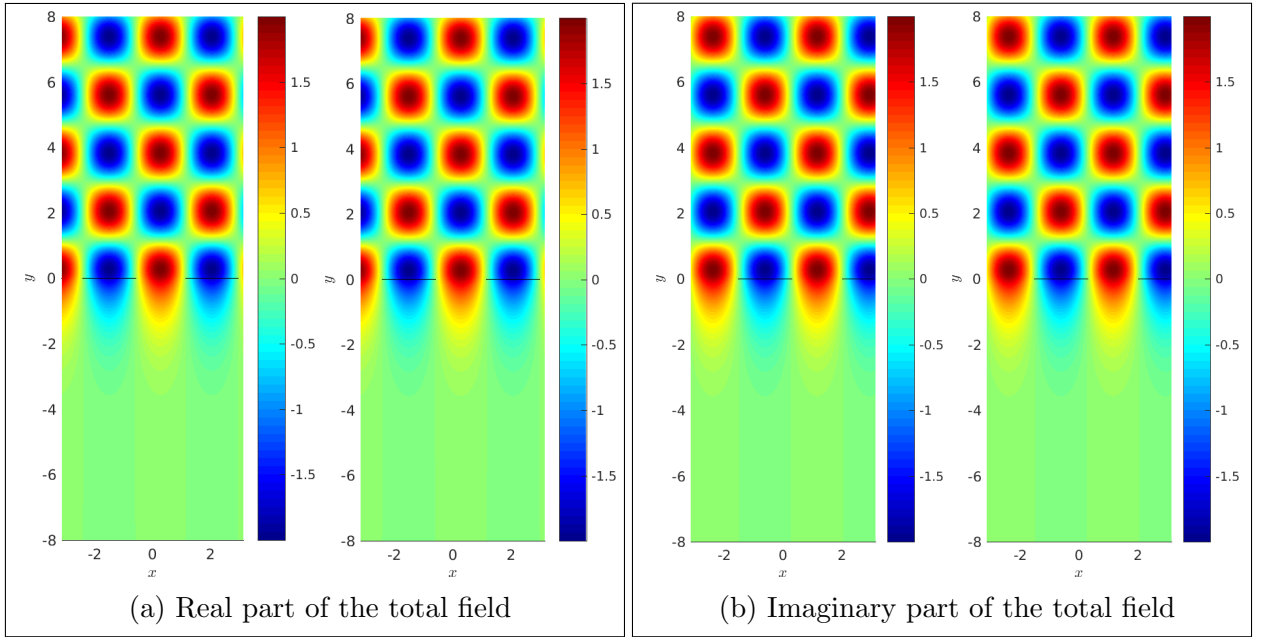


Figure 4.12: Real and imaginary part of the total field. Left: Exact solution. Right: Solution computed by using the integral equation method described in Section 4.4.3. The wave numbers are $k^+ = 2.5$ and $k^- = 1.5$.

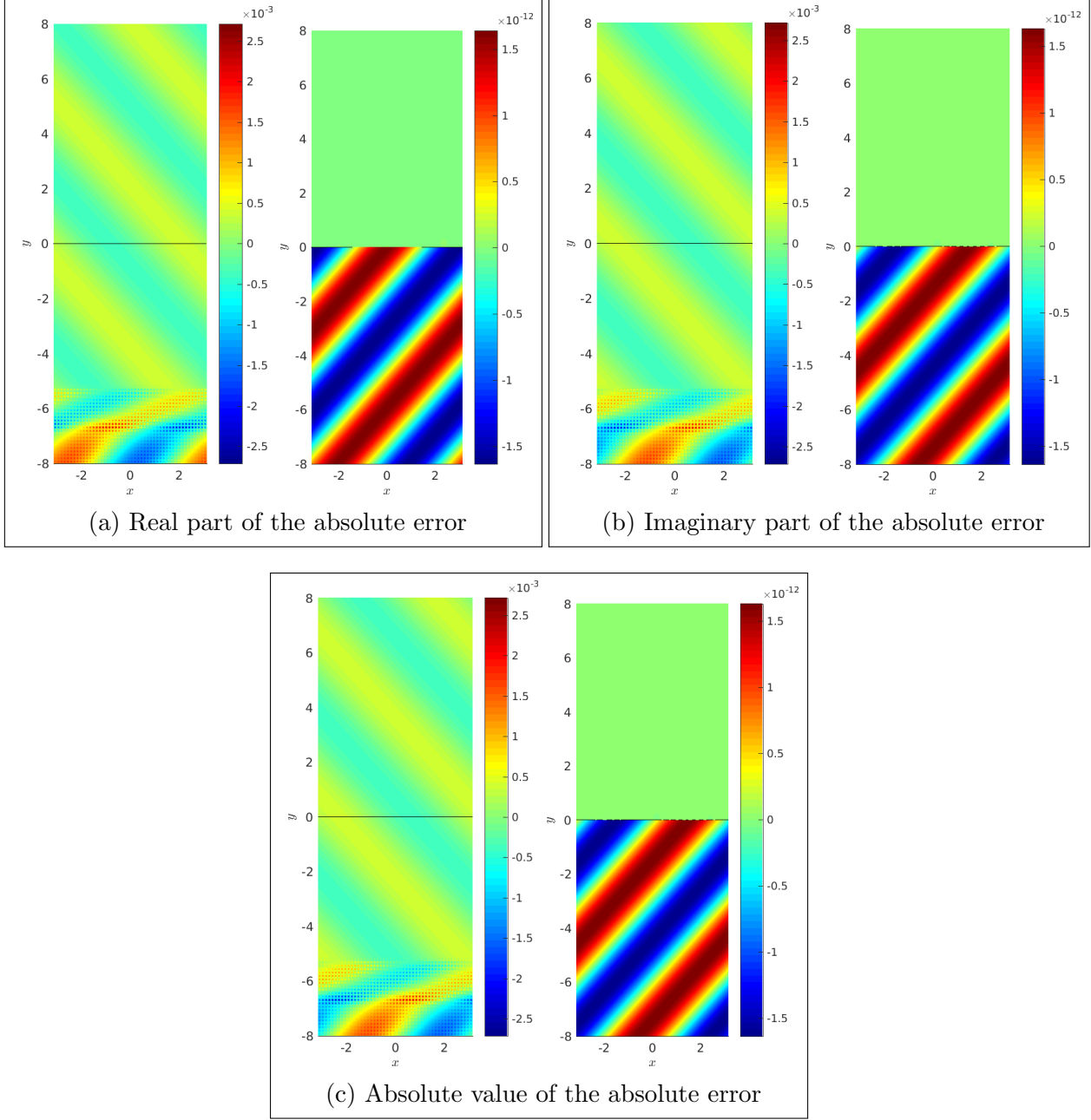


Figure 4.13: Subplots (a), (b) and (c) are real, imaginary part, and absolute value of the absolute error. Left: solution computed with FEM. Right: solution computed with the integral equation method described in Section 4.4.3. The wave numbers are $k^+ = k^- = 1.5$.

described in this chapter and the exact solution, when $k^+ = k^-$, $k^+ < k^-$, and $k^+ > k^-$, respectively. The shown values are the real (subplot (a)), and the imaginary part (subplot (b)) of the scattered field in $\Omega_+^\#$, and the transmitted field in $\Omega_-^\#$. When the

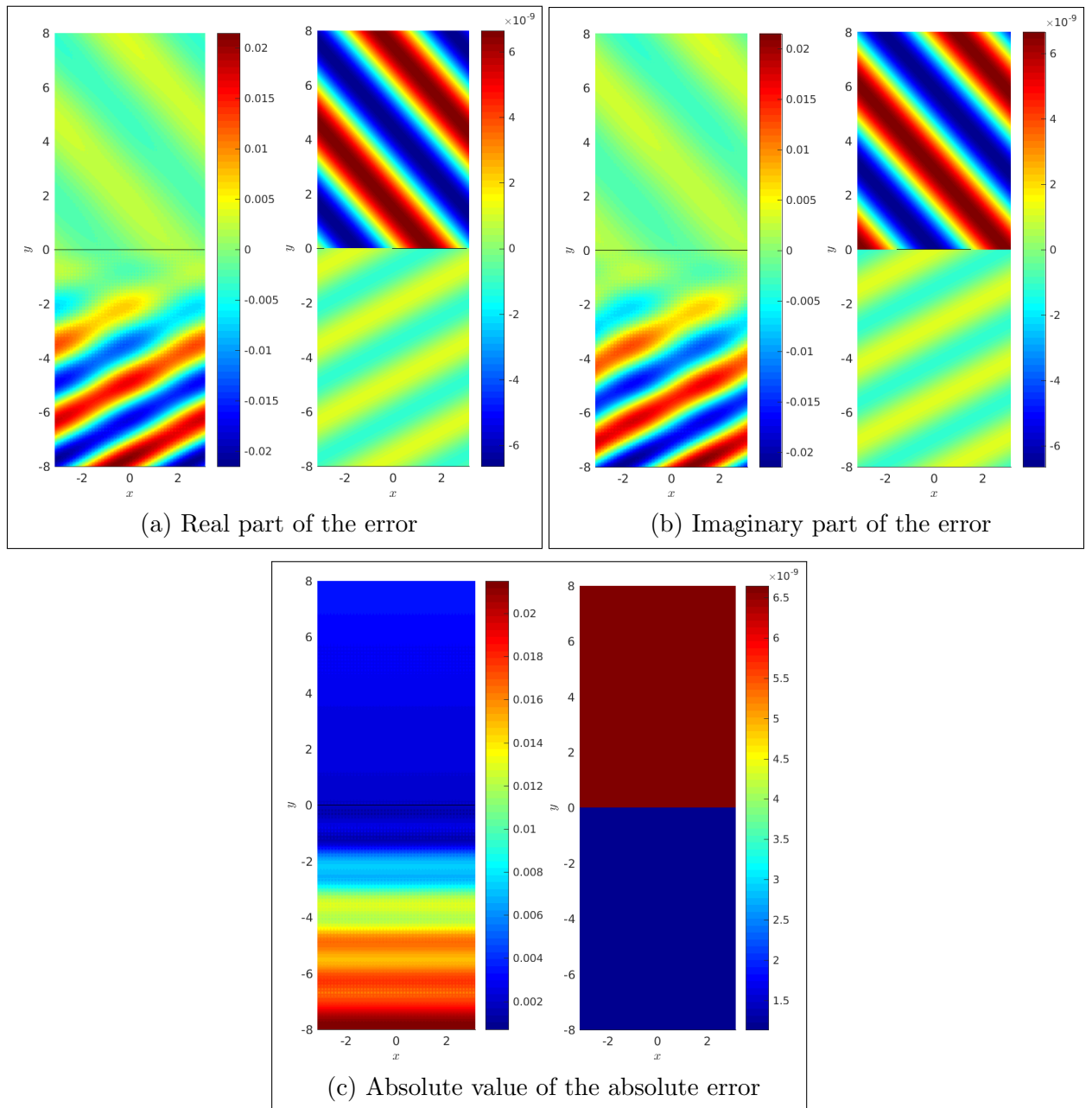


Figure 4.14: Subplots (a), (b) and (c) are real, imaginary part, and absolute value of the absolute error. Left: solution computed with FEM. Right: solution computed with the integral equation method described in Section 4.4.3. The wave numbers are $k^+ = 1.5$, and $k^- = 2.5$.

solution is computed by using the integral equation method described in Section 4.4.3, following (4.38) and (4.40), the solution can be computed in the interval $(-\infty, h) \cup (H, \infty)$ where $H = \max_{x \in [-\frac{L}{2}, \frac{L}{2}]} f(x)$, and $h = \min_{x \in [-\frac{L}{2}, \frac{L}{2}]} f(x)$. The infinite sums (4.38) and (4.40) are

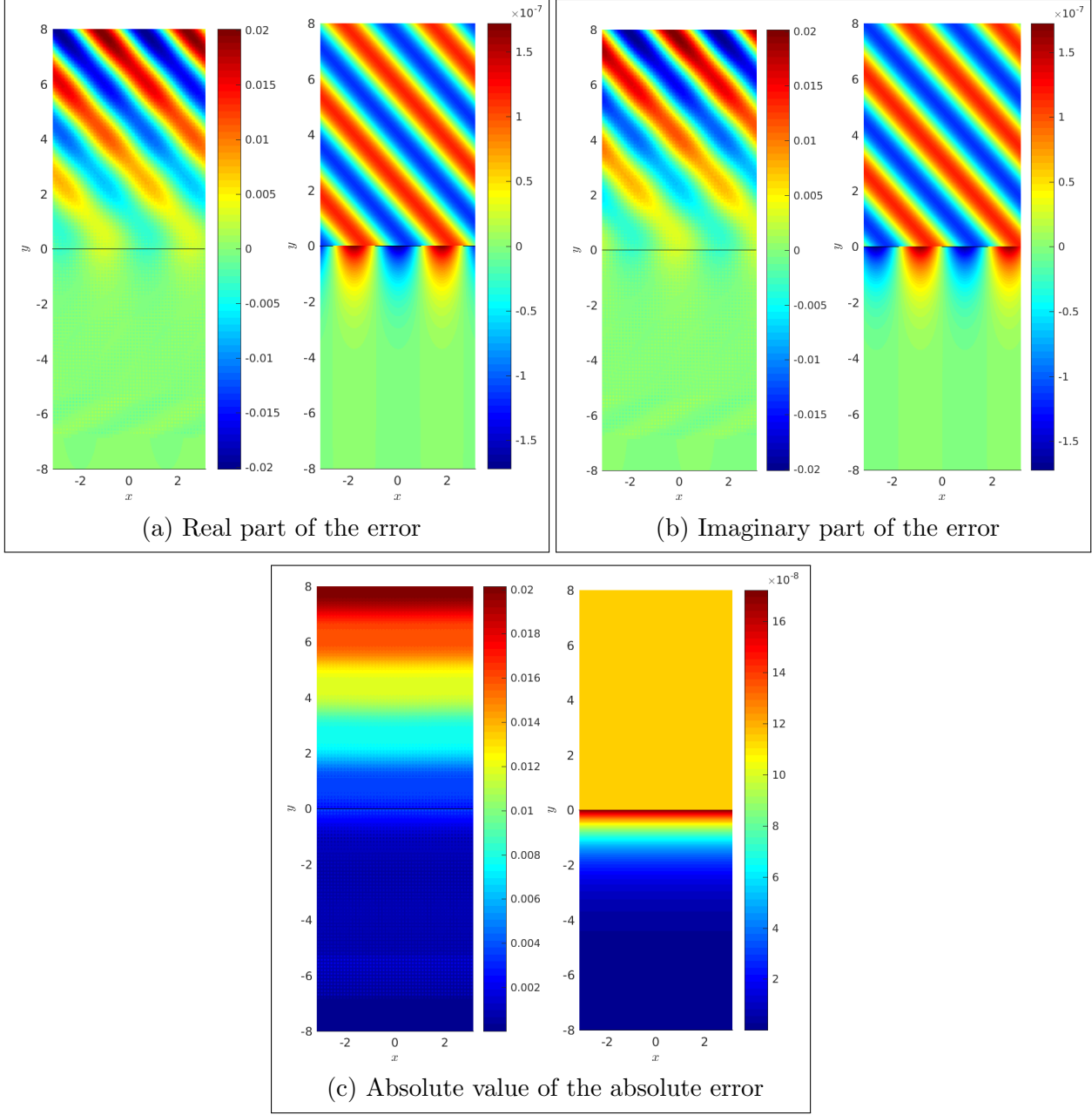


Figure 4.15: Subplots (a), (b) and (c) are real, imaginary part, and absolute value of the absolute error. Left: solution computed with FEM. Right: solution computed with the integral equation method described in Section 4.4.3. The wave numbers are $k^+ = 2.5$, and $k^- = 1.5$.

computed by using a truncated series with 41 terms. These figures show a good agreement between the computed solution by using the proposed method, and the exact solution.

In order to illustrate the committed error, the real, the imaginary part, and the absolute

value of the absolute error are plotted. Moreover, to show the advantages of the method, the error has been compared with the committed error when the solution is computed by using the Finite Element Method (FEM). The reader is referred to Appendix 4.C to get a complete description of how the problem has been solved by using FEM and Perfectly Matched Layers (PML). The plane grating $y = 0$ is considered and it is supposed that the incidence angle of the plane wave is $\theta^+ = \pi/4$. Figure 4.13 shows the real (subplot (a)), the imaginary part (subplot (b)), and the absolute value (subplot (c)) of the absolute error between the computed solution by using the integral equation method described in Section 4.4.3 (right plots), and the FEM (left plots), for $k^+ = k^- = 1.5$. As it can be observed, the error with the integral equation method is around 10^{-12} while the error with FEM is 10^{-3} .

Figure 4.14 shows the real (subplot (a)), the imaginary part (subplot (b)), and the absolute value (subplot (c)) of the absolute error between the computed solution by using the integral equation method described in Section 4.4.3 (right plots), and the FEM (left plots), for $k^+ = 1.5$, and $k^- = 2.5$. As in the previous case, the error with the integral equation method is smaller than with FEM (around 10^{-9} with the integral method, and around 10^{-2} with FEM).

Figure 4.15 shows the real (subplot (a)), the imaginary part (subplot (b)), and the absolute values (subplot (c)) of the absolute error between the computed solution by using the integral equation method described in Section 4.4.3 (right plots), and the FEM (left plots), for $k^+ = 2.5$, and $k^- = 1.5$. As in previous cases, the error with the integral equation method is smaller than with FEM (around 10^{-8} with the integral method, and around 10^{-2} with FEM).

Validation code considering a sinusoidal grating

In this section, a code validation has been performed considering a sinusoidal grating. Since it is not possible to compute the exact solution, the results with the proposed method are compared with the solution obtained with a FEM, and using PML (see Appendix 4.C for more details). In the simulations, the sinusoidal grating considered is given by (4.99) with $L = 2\pi$, and it is supposed that the incidence angle of the plane wave is $\theta^+ = \pi/4$. The parameters to perform the simulations are $n_I = 256$, $A = 400$, $c = 0.1$, $A_l = L/4$, and $d_l = 0.2$.

Figures 4.16, 4.17, and 4.18 show the comparison between the integral equation method described in this chapter and the FEM, when $k^+ = k^-$, $k^+ < k^-$, and $k^+ > k^-$, respectively. Following (4.38) and (4.40), the solution can be computed in the interval $(-\infty, h) \cup (H, \infty)$ where $H = \max_{x \in [-\frac{L}{2}, \frac{L}{2}]} f(x)$, and $h = \min_{x \in [-\frac{L}{2}, \frac{L}{2}]} f(x)$. The infinite sums (4.38) and (4.40) are computed by using a truncated series with 41 terms.

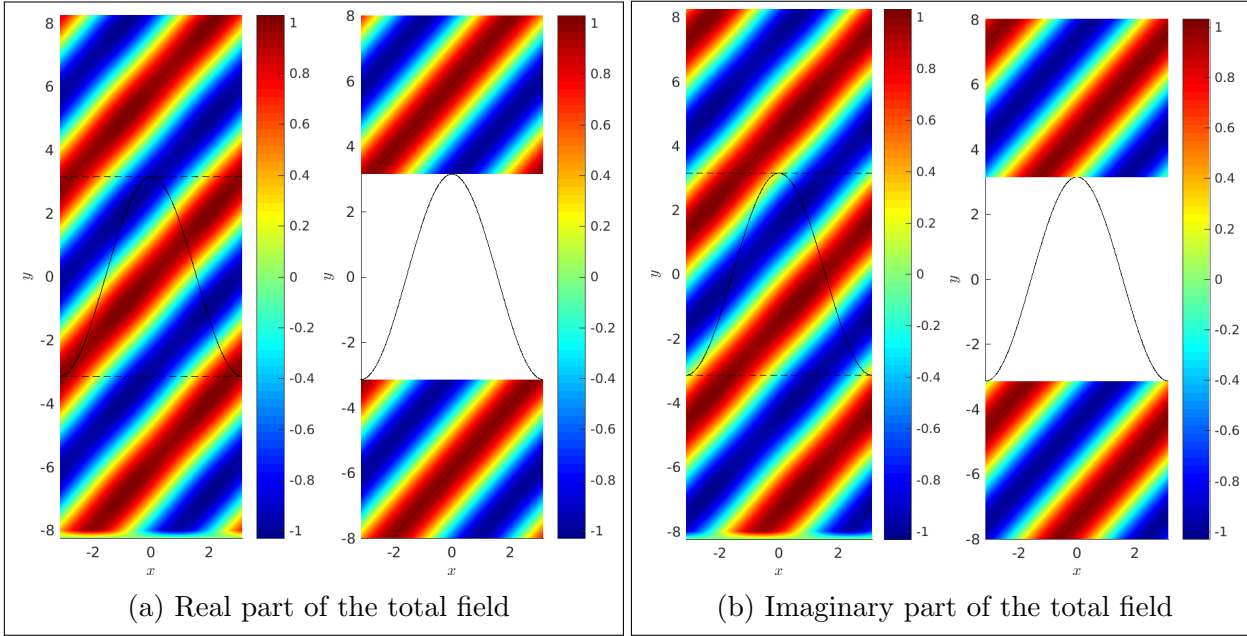


Figure 4.16: Real (subplot (a)) and imaginary part (subplot (b)) of the total field. Left: Solution computed by using FEM and PML. Right: Solution computed by using the integral equation method described in Section 4.4.3, where the series (4.38) and (4.40) are truncated to 41 terms. The wave numbers are $k^+ = k^- = 1.5$.

Convergence analysis considering a sinusoidal grating

To illustrate the convergence of the method introduced in Section 4.4, some numerical results are shown. The problem under consideration is the transmission problem by the periodic sinusoidal grating (4.99) with period $L = 2\pi$, and the incident angle is $\theta^+ = \pi/4$. Tables 4.15, 4.16, and 4.17 show the computed energy balance error for $k^+ = k^-$, $k^+ < k^-$, and $k^+ > k^-$, respectively, by using $J = 0$, a number of points per period n_I , and a window size $2A$. The parameters of the windows are $c = 0.1$, $A_l = L/4$, and $d_l = 0.2$.

4.7 Conclusions

In this chapter, a fast convergent integral equation method to solve a transmission problem is introduced. This method solves the problem of acoustic wave scattering by two media with a periodic coupling surface. The integral method proposed is based on the use of quasi-periodic Green functions in combination with a smooth-windowing technique. First of all, the definition of a slow-rise windowing function has been introduced, showing how this function can improve the convergence of the classical quasi-periodic Green function. This function presents convergence problems at and around Wood anomalies. Then, a shifted quasi-periodic Green function has been described to overcome the convergence problem at and around Wood anomaly frequencies.

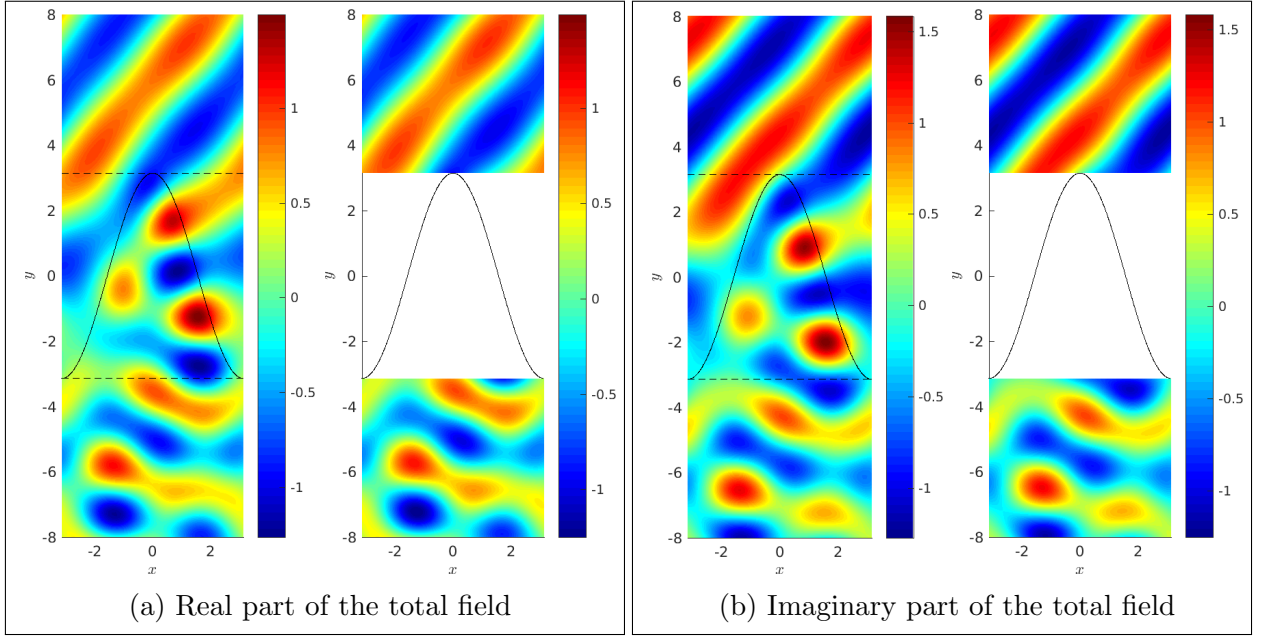


Figure 4.17: Real (subplot (a)) and imaginary part (subplot (b)) of the total field. Left: Solution computed by using FEM and PML. Right: Solution computed by using the integral equation method described in Section 4.4.3, where the series (4.38) and (4.40) are truncated to 41 terms. The wave numbers are $k^+ = 1.5$, and $k^- = 2.5$.

n_I	$A = 200$	$A = 400$	$A = 800$	$A = 1600$
32	8.082×10^{-14}	2.136×10^{-13}	2.141×10^{-13}	9.929×10^{-13}
64	2.096×10^{-13}	2.127×10^{-13}	9.507×10^{-13}	1.368×10^{-12}
128	2.092×10^{-13}	9.475×10^{-13}	1.370×10^{-12}	3.260×10^{-12}
256	9.490×10^{-13}	1.368×10^{-12}	3.267×10^{-12}	3.252×10^{-12}
512	1.370×10^{-12}	3.266×10^{-12}	3.265×10^{-12}	3.266×10^{-12}
1024	3.269×10^{-12}	3.264×10^{-12}	3.259×10^{-12}	3.266×10^{-12}

Table 4.15: Energy balance error (following (4.80)) in the transmission problem for $k^+ = k^- = 1.5$. Solutions are computed using n_I number of points per period, and the window size is $2A$. None shifts are considered, that is, $J = 0$, and the parameters for the windows are $c = 0.1$, $A_l = L/4$, and $d_l = 0.2$.

For the sake of completeness, the acoustic wave scattering problem by a sound-soft periodic surface is studied, with a single-, and a double-layer representations. The computation of the solution of both problems involves the approximation of some integrals with logarithmic singularities, which appear due to the definition of the Hankel functions. To achieve a high-order evaluation of logarithmic integral operators, a modification of the Nyström approach is used. The most important point to deal with this method is to split each kernel

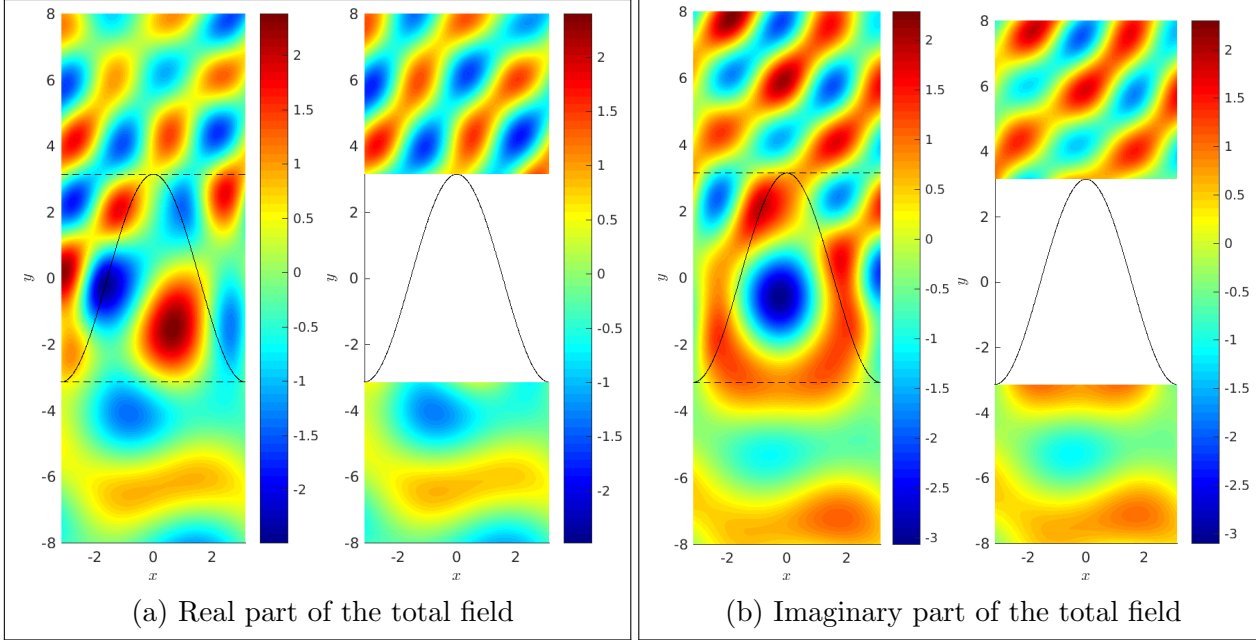


Figure 4.18: Real (subplot (a)) and imaginary part (subplot (b)) of the total field. Left: Solution computed by using FEM and PML. Right: Solution computed by using the integral equation method described in Section 4.4.3, where the series (4.38) and (4.40) are truncated to 41 terms. The wave numbers are $k^+ = 2.5$, and $k^- = 1.5$.

n_I	$A = 200$	$A = 400$	$A = 800$	$A = 1600$
32	1.097×10^{-3}	1.093×10^{-3}	1.092×10^{-3}	1.092×10^{-3}
64	1.145×10^{-4}	1.075×10^{-4}	1.072×10^{-4}	1.072×10^{-4}
128	2.078×10^{-5}	1.356×10^{-5}	1.326×10^{-5}	1.326×10^{-5}
256	9.210×10^{-6}	1.958×10^{-6}	1.655×10^{-6}	1.654×10^{-6}
512	7.767×10^{-6}	5.108×10^{-7}	2.072×10^{-7}	2.067×10^{-7}
1024	7.586×10^{-6}	3.299×10^{-7}	2.634×10^{-8}	2.583×10^{-8}

Table 4.16: Energy balance error (following (4.80)) in the transmission problem for $k^+ = 1.5$, and $k^- = 2.5$. Solutions are computed using n_I number of points per period, and the window size is $2A$. None shifts are considered, that is, $J = 0$, and the parameters for the windows are $c = 0.1$, $A_l = L/4$, and $d_l = 0.2$.

into a smooth kernel, and a logarithmic part. Once the kernel decomposition in the single- and the double-layer representation has been detailed, the transmission problem has been studied, emphasizing the kernel decomposition of the adjoint double-layer potential, and the difference of hypersingular potentials.

Moreover, the discretization of each problem, describing the quadrature rules used to

n_I	$A = 200$	$A = 400$	$A = 800$	$A = 1600$
32	2.363×10^{-3}	3.689×10^{-4}	3.279×10^{-4}	3.280×10^{-4}
64	2.089×10^{-3}	8.727×10^{-5}	4.643×10^{-5}	4.659×10^{-5}
128	2.050×10^{-3}	4.669×10^{-5}	5.861×10^{-6}	6.021×10^{-6}
256	2.044×10^{-3}	4.142×10^{-5}	5.976×10^{-7}	7.579×10^{-7}
512	2.044×10^{-3}	4.076×10^{-5}	6.545×10^{-8}	9.481×10^{-8}
1024	2.044×10^{-3}	4.067×10^{-5}	1.485×10^{-7}	1.179×10^{-8}

Table 4.17: Energy balance error (following (4.80)) in the transmission problem for $k^+ = 2.5$, and $k^- = 1.5$. Solutions are computed using n_I number of points per period, and the window size is $2A$. None shifts are considered, that is, $J = 0$, and the parameters for the windows are $c = 0.1$, $A_l = L/4$, and $d_l = 0.2$.

approximate the integrals, is explained. Finally, in order to illustrate the fast convergence of the method, some numerical results are presented. The code has been validated, taking into account two different boundaries. If a plane interface between media is considered, the exact solution can be calculated, and it has been compared with the computed solution with the proposed integral method. If a sinusoidal grating is considered, since the exact solution can not be obtained, the computed solution is compared with the approximated solution calculated by using FEM and PML. In both cases, a good agreement is shown. In the end, the results of the convergence analysis of the proposed method are given, showing the fast convergence of the method when the window size is increased.

Appendix

4.A Bessel functions

The solutions to Bessel's equation are defined as [4, 63, 115]

$$J_n(t) := \sum_{p=0}^{\infty} \frac{(-1)^p}{p!(n+p)!} \left(\frac{t}{2}\right)^{n+2p}, \quad n = 0, 1, 2, \dots \quad (4.A.1)$$

which are known as Bessel functions of order n , and are analytic functions in the complex-plane (in particular \mathcal{C}^∞ -functions in the real line).

$$\begin{aligned} Y_n(t) := & \frac{2}{\pi} \left(\ln \frac{t}{2} + C \right) J_n(t) - \frac{1}{\pi} \sum_{p=0}^{n-1} \frac{(n-1-p)!}{p!} \left(\frac{2}{t}\right)^{n-2p} \\ & - \frac{1}{\pi} \sum_{p=0}^{\infty} \frac{(-1)^p}{p!(n+p)!} \left(\frac{t}{2}\right)^{n+2p} (\psi(p+n) + \psi(p)), \quad n = 0, 1, 2, \dots \end{aligned} \quad (4.A.2)$$

where

$$C = \lim_{p \rightarrow \infty} \left(\sum_{m=1}^p \frac{1}{m} - \ln p \right) \quad (4.A.3)$$

is the Euler's constant, and

$$\psi(p) = \sum_{m=1}^p \frac{1}{m}, \quad p = 1, 2, \dots, \quad \psi(0) = 0.$$

The functions (4.A.2) are known as Neumann functions of order n , and they belong to $\mathcal{C}^\infty(0, \infty)$. By using (4.A.1) and (4.A.2), the Hankel functions of first kind of order n are defined as

$$H_n^{(1)}(t) := J_n(t) + iY_n(t). \quad (4.A.4)$$

When $n = 0$, considering the definition (4.A.4), the Hankel function of first kind of order 0 results $H_0^{(1)} = J_0(t) + iY_0(t)$ where

$$\begin{aligned} J_0(t) &= \sum_{p=0}^{\infty} \frac{(-1)^p}{(p!)^2} \left(\frac{t}{2}\right)^{2p}, \\ Y_0(t) &= \frac{2}{\pi} \left(\ln \left(\frac{t}{2}\right) + C \right) J_0(t) - \frac{2}{\pi} \sum_{p=0}^{\infty} \frac{(-1)^p}{(p!)^2} \left(\frac{t}{2}\right)^{2p} \psi(p). \end{aligned}$$

Then, the Hankel function of order 0 can be written as

$$\begin{aligned} H_0^{(1)}(t) &= J_0(t) + iY_0(t) \\ &= J_0(t) + \frac{2i}{\pi} \left(\ln \frac{t}{2} + C \right) J_0(t) - \frac{2i}{\pi} \sum_{p=0}^{\infty} \frac{(-1)^p}{(p!)^2} \left(\frac{t}{2}\right)^{2p} \psi(p) \\ &= J_0(t) \left(1 + \frac{2i}{\pi} \left(\ln \frac{t}{2} + C \right) \right) - \frac{2i}{\pi} \sum_{p=0}^{\infty} \frac{(-1)^p}{(p!)^2} \left(\frac{t}{2}\right)^{2p} \psi(p). \end{aligned} \quad (4.A.5)$$

Following the same argument, the Hankel function of order 1 can be written as

$$\begin{aligned} H_1^{(1)}(t) &= J_1(t) + iY_1(t) = J_1(t) + \frac{2i}{\pi} \left(\ln \frac{t}{2} + C \right) J_1(t) - \frac{2i}{\pi t} \\ &\quad - \frac{it}{2\pi} \sum_{p=0}^{\infty} \frac{(-1)^p}{p!(1+p)!} \left(\frac{t}{2}\right)^{2p} (\psi(p+1) + \psi(p)) \\ &= J_1(t) \left(1 + \frac{2i}{\pi} \left(\ln \frac{t}{2} + C \right) \right) - \frac{2i}{\pi t} - \frac{it}{2\pi} \Sigma_1(t), \end{aligned} \quad (4.A.6)$$

where $\Sigma_n(t)$ is given by

$$\Sigma_n(t) = \sum_{p=0}^{\infty} \frac{(-1)^p}{p!(n+p)!} \left(\frac{t}{2}\right)^{2p} (\psi(p+n) + \psi(p)). \quad (4.A.7)$$

Taking into account (4.A.4), the Hankel function of order 2 is given by

$$\begin{aligned} H_2^{(1)}(t) &= J_2(t) + iY_2(t) = J_2(t) + \frac{2i}{\pi} \left(\ln \frac{t}{2} + C \right) J_2(t) - \frac{4i}{\pi t^2} \left(1 + \frac{t^2}{4} \right) \\ &\quad - \frac{it^2}{4\pi} \sum_{p=0}^{\infty} \frac{(-1)^p}{p!(2+p)!} \left(\frac{t}{2}\right)^{2p} (\psi(p+2) + \psi(p)) \\ &= J_2(t) \left(1 + \frac{2i}{\pi} \left(\ln \frac{t}{2} + C \right) \right) - \frac{4i}{\pi t^2} \left(1 + \frac{t^2}{4} \right) - \frac{it^2}{4\pi} \Sigma_2(t). \end{aligned} \quad (4.A.8)$$

Considering the definition (4.A.1)

$$J_0(0) = 1, \quad (4.A.9)$$

and

$$\lim_{t \rightarrow 0} \frac{J_1(kt)}{t} = k J'_0(0) = -J_1(0)k/2 = \frac{k}{2}. \quad (4.A.10)$$

Moreover, the derivative of the Hankel functions are given by

$$[H_0^{(1)}]'(t) = -H_1^{(1)}(t), \quad (4.A.11)$$

$$[H_1^{(1)}]'(t) = -H_2^{(1)}(t) + \frac{1}{t} H_1^{(1)}(t). \quad (4.A.12)$$

4.B Kernel decomposition in a periodic setting

In this section, the decomposition of kernels associated with a single-layer, a double-layer, an adjoint double-layer, and a hypersingular potentials is detailed. The goal of this section is to help further understanding of the decomposition of kernels M_w , L_w , H_w , and K_w , appearing in Sections 4.2.5, 4.3.1, and 4.4.3.

4.B.1 Single-layer potential

To understand the decomposition of the kernel M_w in Section 4.2.5, a simple single-layer potential is considered, avoiding the shifting and windowing techniques. The kernel considered is formed by the half-space Green function G_J given by (4.8) multiplied by the norm of the normal vector to the boundary, that is,

$$\int_{-L/2}^{L/2} \underbrace{G_J(x - x', f(x) - f(x')) \sqrt{1 + f'(x')^2}}_{M(x, x'; J)} \varphi(x') dx' = \int_{-L/2}^{L/2} M(x, x'; J) \varphi(x') dx',$$

where φ is a continuous density. Then, taking into account the definition of G_J , the kernel M is given by

$$\begin{aligned} M(x, x'; J) &= G_J(x - x', f(x) - f(x')) \sqrt{1 + f'(x')^2} \\ &= \frac{i}{4} \sum_{l=0}^J (-1)^l \binom{J}{l} H_0^{(1)} \left(k \sqrt{(x - x')^2 + (f(x) - f(x') + lh)^2} \right) \sqrt{1 + f'(x')^2}. \end{aligned} \quad (4.B.1)$$

The kernel M presents a logarithmic singularity at $x = x'$ when $l = 0$ due to the Bessel function of the second kind $Y_0(x)$ (see the asymptotic behavior of the Hankel function of order 0 at the origin in (4.A.5)). Then, following Martensen [122] and Kussmaul [108], the

integral kernel M given by (4.B.1) can be split in a smooth kernel M_r , and a logarithmic part, that is,

$$M(x, x'; J) = M_s(x, x'; J) \ln \left(4 \sin^2 \left(\frac{x - x'}{2} \right) \right) + M_r(x, x'; J),$$

where

$$\begin{aligned} M_s(x, x'; J) &= -\frac{1}{4\pi} J_0 \left(k \sqrt{(x - x')^2 + (f(x) - f(x'))^2} \right) \sqrt{1 + f'(x')^2}, \\ M_r(x, x'; J) &= M(x, x'; J) - M_s(x, x'; J) \ln \left(4 \sin^2 \left(\frac{x - x'}{2} \right) \right). \end{aligned} \quad (4.B.2)$$

Remark 4.B.1. The subscript r is used to denote the regular part and s denotes the singular one.

In order to deal with the singularities appearing in the Bessel functions, it is necessary to study the behavior of the function M at $x = x'$ when shifts are not considered ($J = 0$), and when they are used ($J > 0$). If $J = 0$, using (4.B.1) the kernel M is given by

$$M(x, x'; 0) = \frac{i}{4} H_0^{(1)} \left(k \sqrt{(x - x')^2 + (f(x) - f(x'))^2} \right) \sqrt{1 + f'(x')^2}. \quad (4.B.3)$$

Then, taking into account (4.B.2), (4.B.3), and the asymptotic expansion of $H_0^{(1)}$ around the origin (see (4.A.5) for more details), the value of the smooth kernel M_r when $x = x'$ can be computed as

$$\begin{aligned} M_r(x, x; 0) &= \lim_{x' \rightarrow x} M_r(x, x'; 0) = \lim_{x' \rightarrow x} \left[M(x, x'; 0) - M_s(x, x'; 0) \ln \left(4 \sin^2 \left(\frac{x - x'}{2} \right) \right) \right] \\ &= \lim_{x' \rightarrow x} \left[\frac{i}{4} H_0^{(1)} \left(k \sqrt{(x - x')^2 + (f(x) - f(x'))^2} \right) \right. \\ &\quad \left. + \frac{1}{4\pi} J_0 \left(k \sqrt{(x - x')^2 + (f(x) - f(x'))^2} \right) \ln \left(4 \sin^2 \left(\frac{x - x'}{2} \right) \right) \right] \sqrt{1 + f'(x')^2} \\ &= \lim_{x' \rightarrow x} \left[\frac{i}{4} \left(1 + \frac{2iC}{\pi} + \frac{2i}{\pi} \left(\ln \frac{k \sqrt{(x - x')^2 + (f(x) - f(x'))^2}}{2} \right) \right) \right. \\ &\quad \left. + \frac{1}{4\pi} \ln \left(4 \sin^2 \left(\frac{x - x'}{2} \right) \right) \right] \sqrt{1 + f'(x')^2} \\ &= \lim_{x' \rightarrow x} \left[\frac{i}{4} - \frac{C}{2\pi} - \frac{1}{4\pi} \ln \left(\frac{\frac{k^2((x-x')^2+(f(x)-f(x'))^2)}{4}}{4 \sin^2 \left(\frac{x-x'}{2} \right)} \right) \right] \sqrt{1 + f'(x')^2} \\ &= \left[\frac{i}{4} - \frac{C}{2\pi} - \frac{1}{2\pi} \ln \left(\frac{k}{2} \sqrt{1 + f'(x)^2} \right) \right] \sqrt{1 + f'(x)^2}, \end{aligned} \quad (4.B.4)$$

where C is the Euler's constant given by (4.A.3). On the other hand, when $J > 0$, the kernel M is given by (4.B.1). Then, taking into account (4.B.2), the value of the kernel M_r at $x = x'$ can be computed as

$$\begin{aligned} M_r(x, x; J) &= \lim_{x' \rightarrow x} M_r(x, x'; J) = \lim_{x' \rightarrow x} \left[M(x, x'; J) - M_s(x, x'; J) \ln \left(4 \sin^2 \left(\frac{x - x'}{2} \right) \right) \right] \\ &= \lim_{x' \rightarrow x} \left[\frac{i}{4} \sum_{l=0}^J (-1)^l \binom{J}{l} H_0^{(1)}(k\sqrt{(x-x')^2 + (f(x)-f(x')+lh)^2}) \right. \\ &\quad \left. + \frac{1}{4\pi} J_0(k\sqrt{(x-x')^2 + (f(x)-f(x'))^2}) \ln \left(4 \sin^2 \left(\frac{x - x'}{2} \right) \right) \right] \\ &\quad \times \sqrt{1 + f'(x')^2}. \end{aligned}$$

Since, the singularities in the Hankel functions appear only when $l = 0$, the sum is split in two parts: $l = 0$ and $l > 0$. Then, the value of the kernel M_r at $x = x'$ is given by

$$\begin{aligned} M_r(x, x; J) &= \lim_{x' \rightarrow x} M_r(x, x'; J) = \lim_{x' \rightarrow x} \left[\frac{i}{4} H_0^{(1)}(k\sqrt{(x-x')^2 + (f(x)-f(x'))^2}) \right. \\ &\quad \left. + \frac{1}{4\pi} J_0(k\sqrt{(x-x')^2 + (f(x)-f(x'))^2}) \ln \left(4 \sin^2 \left(\frac{x - x'}{2} \right) \right) \right] \sqrt{1 + f'(x')^2} \\ &\quad + \lim_{x' \rightarrow x} \left[\frac{i}{4} \sum_{l=1}^J (-1)^l \binom{J}{l} H_0^{(1)}(k\sqrt{(x-x')^2 + (f(x)-f(x')+lh)^2}) \right] \sqrt{1 + f'(x')^2} \\ &= \left[\frac{i}{4} - \frac{C}{2\pi} - \frac{1}{2\pi} \ln \left(\frac{k}{2} \sqrt{1 + f'(x)^2} \right) + \frac{i}{4} \sum_{l=1}^J (-1)^l \binom{J}{l} H_0^{(1)}(klh) \right] \sqrt{1 + f'(x)^2}, \end{aligned} \tag{4.B.5}$$

where C is the Euler's constant given by (4.A.3).

4.B.2 Double-layer potential

To understand the decomposition of the kernel L_w in Section 4.3.1, similar arguments to previous section are followed, but in this case, a double-layer potential is considered. Once again, to avoid the shifting and windowing techniques, a simple kernel is taking into account. This kernel is formed by the normal derivative of the half-space Green function G_J (given by (4.8)), multiplied by the norm of the normal vector to the boundary, that is,

$$\underbrace{\int_{-L/2}^{L/2} \frac{\partial G_J}{\partial \nu_{x'}}(x - x', f(x) - f(x')) \sqrt{1 + f'(x')^2} \varphi(x') dx'}_{L(x, x'; J)} = \int_{-L/2}^{L/2} L(x, x'; J) \varphi(x') dx'.$$

Taking into account the definition of G_J and the derivative of $H_0^{(1)}$ (see (4.A.11)),

$$\begin{aligned} L(x, x'; J) &= \frac{\partial G_J}{\partial \nu_{x'}}(x - x', f(x) - f(x')) \sqrt{1 + f'(x')^2} \\ &= \frac{ik}{4} \sum_{l=0}^J \left[(-1)^l \binom{J}{l} H_1^{(1)} \left(k \sqrt{(x - x')^2 + (f(x) - f(x') + lh)^2} \right) \right. \\ &\quad \left. \times \frac{-f'(x')(x - x') + f(x) - f(x') + lh}{\sqrt{(x - x')^2 + (f(x) - f(x') + lh)^2}} \right]. \end{aligned} \quad (4.B.6)$$

Considering the asymptotic expansion of the Hankel function of order 1 at the origin (see (4.A.6)), the kernel L presents logarithmic singularities at $x = x'$ when $l = 0$. Then, following Martensen [122] and Kussmaul [108], the kernel L (4.B.6) can be split in a smooth kernel L_s , and a logarithmic part (see Remark 4.B.1 for subscript notation), that is,

$$L(x, x'; J) = L_s(x, x'; J) \ln \left(4 \sin^2 \left(\frac{x - x'}{2} \right) \right) + L_r(x, x'; J),$$

where

$$L_s(x, x'; J) = -\frac{k}{4\pi} J_1 \left(k \sqrt{(x - x')^2 + (f(x) - f(x'))^2} \right) \frac{-f'(x')(x - x') + f(x) - f(x')}{\sqrt{(x - x')^2 + (f(x) - f(x'))^2}}, \quad (4.B.7)$$

$$L_r(x, x'; J) = L(x, x'; J) - L_s(x, x'; J) \ln \left(4 \sin^2 \left(\frac{x - x'}{2} \right) \right). \quad (4.B.8)$$

In order to deal with the singularities appearing in the Bessel functions around the origin, it is necessary to analyze the behavior of the kernels L_s and L_r at $x = x'$. Taking into account (4.B.7), and the limit of the Bessel function $J_1(t)$ at $t \rightarrow 0$ (see (4.A.10)), the value of L_s at $x = x'$ can be computed as

$$\begin{aligned} L_s(x, x; J) &= \lim_{x' \rightarrow x} L_s(x, x'; J) = \lim_{x' \rightarrow x} -\frac{k}{4\pi} J_1 \left(k \sqrt{(x - x')^2 + (f(x) - f(x'))^2} \right) \\ &\quad \times \frac{-f'(x')(x - x') + f(x) - f(x')}{\sqrt{(x - x')^2 + (f(x) - f(x'))^2}} \\ &= \lim_{x' \rightarrow x} -\frac{k^2}{8\pi} (-f'(x')(x - x') + f(x) - f(x')) = 0. \end{aligned} \quad (4.B.9)$$

To analyze the behavior of the kernel L_r when x is equal to x' , it has been considered what happens when shifts are not used ($J = 0$), and when shifts are used ($J > 0$). If $J = 0$, using (4.B.6), the function L is given by

$$L(x, x'; 0) = \frac{ik}{4} H_1^{(1)} \left(k \sqrt{(x - x')^2 + (f(x) - f(x'))^2} \right) \frac{-f'(x')(x - x') + f(x) - f(x')}{\sqrt{(x - x')^2 + (f(x) - f(x'))^2}}. \quad (4.B.10)$$

Considering the asymptotic expansion of the Hankel function $H_1^{(1)}$ at the origin (see (4.A.6)), and taking into account (4.B.7), (4.B.8), and (4.B.10), the values of the smooth kernel L_r at $x = x'$ can be computed as

$$\begin{aligned}
L_r(x, x; 0) &= \lim_{x' \rightarrow x} L_r(x, x'; 0) = \lim_{x' \rightarrow x} \left[L(x, x'; 0) - L_s(x, x'; 0) \ln \left(4 \sin^2 \left(\frac{x - x'}{2} \right) \right) \right] \\
&= \lim_{x' \rightarrow x} \left[\left(\frac{ik}{4} \left(1 + \frac{2i}{\pi} (C + \ln(2)) \right) \frac{J_1 \left(k \sqrt{(x - x')^2 + (f(x) - f(x'))^2} \right)}{\sqrt{(x - x')^2 + (f(x) - f(x'))^2}} \right. \right. \\
&\quad + \frac{k^2}{8\pi} \Sigma_1 \left(k \sqrt{(x - x')^2 + (f(x) - f(x'))^2} \right) (-f'(x')(x - x') + f(x) - f(x')) \\
&\quad + \lim_{x' \rightarrow x} \frac{-f'(x')(x - x') + f(x) - f(x')}{2\pi ((x - x')^2 + (f(x) - f(x'))^2)} \\
&\quad + \lim_{x' \rightarrow x} \left[\frac{k}{4\pi} \left(-\ln \left(k^2 ((x - x')^2 + (f(x) - f(x'))^2) \right) + \ln \left(4 \sin^2 \left(\frac{x - x'}{2} \right) \right) \right) \right. \\
&\quad \times \left. \left. \frac{J_1 \left(k \sqrt{(x - x')^2 + (f(x) - f(x'))^2} \right)}{\sqrt{(x - x')^2 + (f(x) - f(x'))^2}} (-f'(x')(x - x') + f(x) - f(x')) \right] \right], \tag{4.B.11}
\end{aligned}$$

where C is the Euler's constant given by (4.A.3), and Σ_1 is defined in (4.A.7). Since

$$\begin{aligned}
\lim_{x' \rightarrow x} \frac{-f'(x')(x - x') + f(x) - f(x')}{(x - x')^2 + (f(x) - f(x'))^2} &= \lim_{x' \rightarrow x} \left[\frac{f(x') + f'(x')(x - x') + \frac{1}{2} f''(x')(x - x')^2}{(x - x')^2 + (f(x) - f(x'))^2} \right. \\
&\quad \left. + \frac{\mathcal{O}((x - x')^3) - f'(x')(x - x') - f(x')}{(x - x')^2 + (f(x) - f(x'))^2} \right] = \frac{f''(x)}{2(1 + f'(x)^2)},
\end{aligned}$$

(see Section 2.2.3 in [128] for more details), (4.B.11) results

$$\begin{aligned}
\lim_{x' \rightarrow x} L_r(x, x'; 0) &= \lim_{x' \rightarrow x} \left[\frac{-f'(x')(x - x') + f(x) - f(x')}{2\pi ((x - x')^2 + (f(x) - f(x'))^2)} \right. \\
&\quad \left. - \frac{k^2}{8\pi} (-f'(x')(x - x') + f(x) - f(x')) \times \ln \left(\frac{k^2 ((x - x')^2 + (f(x) - f(x'))^2)}{4 \sin^2 \left(\frac{x - x'}{2} \right)} \right) \right] \\
&= \frac{f''(x)}{4\pi(1 + f'(x)^2)}. \tag{4.B.12}
\end{aligned}$$

When the shifts are used, that is, if $J > 0$, the kernel L is given by (4.B.6). Then, taking into account (4.B.7) and (4.B.8), the values of the smooth kernel L_r at $x = x'$ are computed

as follows:

$$\begin{aligned}
L_r(x, x; J) &= \lim_{x' \rightarrow x} L_r(x, x'; J) \\
&= \lim_{x' \rightarrow x} \left[\frac{ik}{4} \sum_{l=0}^J \left[(-1)^l \binom{J}{l} H_1^{(1)}(k\sqrt{(x-x')^2 + (f(x)-f(x')+lh)^2}) \right. \right. \\
&\quad \times \frac{-f'(x')(x-x') + f(x) - f(x') + lh}{\sqrt{(x-x')^2 + (f(x)-f(x')+lh)^2}} \left. \right] + \frac{k}{4\pi} \ln \left(4 \sin^2 \left(\frac{x-x'}{2} \right) \right) \\
&\quad \times J_1 \left(k\sqrt{(x-x')^2 + (f(x)-f(x'))^2} \right) \frac{-f'(x')(x-x') + f(x) - f(x')}{\sqrt{(x-x')^2 + (f(x)-f(x'))^2}} \left. \right].
\end{aligned}$$

Since the singularities in the Hankel function $H_1^{(1)}$ appear when $l = 0$, the sum has been split in two parts: $l = 0$, to use (4.B.12), and $l > 0$. Then, the values of L_r when x is equal to x' are computed as

$$\begin{aligned}
L_r(x, x; J) &= \lim_{x' \rightarrow x} L_r(x, x'; J) = \lim_{x' \rightarrow x} \left[\frac{k}{4} \frac{-f'(x')(x-x') + f(x) - f(x')}{\sqrt{(x-x')^2 + (f(x)-f(x'))^2}} \right. \\
&\quad \times \ln \left(4 \sin^2 \left(\frac{x-x'}{2} \right) \right) \left(iH_1^{(1)} \left(k\sqrt{(x-x')^2 + (f(x)-f(x'))^2} \right) \right. \\
&\quad \left. \left. + \frac{1}{\pi} J_1 \left(k\sqrt{(x-x')^2 + (f(x)-f(x'))^2} \right) \right) \right] \\
&\quad + \lim_{x' \rightarrow x} \left(\frac{ik}{4} \sum_{l=1}^J \left[(-1)^l \binom{J}{l} H_1^{(1)} \left(k\sqrt{(x-x')^2 + (f(x)-f(x')+lh)^2} \right) \right. \right. \\
&\quad \times \frac{-f'(x')(x-x') + f(x) - f(x') + lh}{\sqrt{(x-x')^2 + (f(x)-f(x')+lh)^2}} \left. \right] \left. \right) = \frac{f''(x)}{4\pi(1+f'(x)^2)} \\
&\quad + \frac{ik}{4} \sum_{l=1}^J (-1)^l \binom{J}{l} H_1^{(1)}(klh).
\end{aligned}$$

4.B.3 Adjoint double-layer potential

This section is devoted to describing the kernel decomposition of the adjoint double-layer potential by using a similar procedure to the arguments applied to the double-layer potential. As in the single- and double-layer representations, and for simplicity, the kernel decomposition in a periodic setting is detailed, without including windowing and shifting methods. The considered kernel is formed by the normal derivative of the half-space Green function G_J (given by (4.8)) multiplied by the norm of the normal vector to the boundary,

that is,

$$\int_{-L/2}^{L/2} \underbrace{\frac{\partial G_J}{\partial \nu_x}(x - x', f(x) - f(x')) \sqrt{1 + f'(x')^2} \varphi(x') dx'}_{H(x, x'; J)} = \int_{-L/2}^{L/2} H(x, x'; J) \varphi(x') dx',$$

where taking into account the definition of G_J , given by (4.8), and the derivative of the Hankel function $H_0^{(1)}$ (see (4.A.11)), it holds

$$\begin{aligned} H(x, x'; J) &= \frac{\partial G_J}{\partial \nu_x}(x - x', f(x) - f(x')) \sqrt{1 + f'(x')^2} \\ &= -\frac{ik}{4} \left(\sum_{l=0}^J \left[(-1)^l \binom{J}{l} H_1^{(1)} \left(k \sqrt{(x - x')^2 + (f(x) - f(x') + lh)^2} \right) \right. \right. \\ &\quad \times \left. \left. \frac{-f'(x)(x - x') + f(x) - f(x') + lh}{\sqrt{(x - x')^2 + (f(x) - f(x') + lh)^2}} \right] \frac{\sqrt{1 + f'(x')^2}}{\sqrt{1 + f'(x)^2}} \right). \end{aligned} \quad (4.B.13)$$

Considering the asymptotic expansion of the Hankel function of order 1 at the origin (see (4.A.6)), the kernel H presents logarithmic singularities at $x = x'$ when $l = 0$. Then, following Martensen [122] and Kussmaul [108], the kernel H can be split into a smooth kernel H_r , and a logarithmic part (see Remark 4.B.1 for subscript notation), that is,

$$H(x, x'; J) = H_s(x, x'; J) \ln \left(4 \sin^2 \left(\frac{x - x'}{2} \right) \right) + H_r(x, x'; J),$$

where

$$\begin{aligned} H_s(x, x'; J) &= \frac{k}{4\pi} J_1 \left(k \sqrt{(x - x')^2 + (f(x) - f(x'))^2} \right) \frac{-f'(x)(x - x') + f(x) - f(x')}{\sqrt{(x - x')^2 + (f(x) - f(x'))^2}} \\ &\quad \times \frac{\sqrt{1 + f'(x')^2}}{\sqrt{1 + f'(x)^2}}, \end{aligned} \quad (4.B.14)$$

$$H_r(x, x'; J) = H(x, x'; J) - H_s(x, x'; J) \ln \left(4 \sin^2 \left(\frac{x - x'}{2} \right) \right). \quad (4.B.15)$$

To deal with the singularities appearing in the Bessel function when $x = x'$, it is necessary to compute the values of H_s and H_r when x coincides with x' . Considering (4.B.14), and the limit of the Bessel function $J_1(t)$ when $t \rightarrow 0$ (see (4.A.10)), the values of H_s at $x = x'$ result

$$\begin{aligned}
H_s(x, x; J) &= \lim_{x' \rightarrow x} H_s(x, x'; J) = \lim_{x' \rightarrow x} \left[\frac{k}{4\pi} J_1 \left(k \sqrt{(x - x')^2 + (f(x) - f(x'))^2} \right) \right. \\
&\quad \times \left. \frac{-f'(x)(x - x') + f(x) - f(x')}{\sqrt{(x - x')^2 + (f(x) - f(x'))^2}} \frac{\sqrt{1 + f'(x')^2}}{\sqrt{1 + f'(x)^2}} \right] \\
&= \lim_{x' \rightarrow x} \frac{k^2}{8\pi} (-f'(x')(x - x') + f(x) - f(x')) = 0. \tag{4.B.16}
\end{aligned}$$

The values of H_r at $x = x'$ have been computed in two different cases: when shifts are not considered ($J = 0$), and when they are used ($J > 0$). If $J = 0$, using (4.B.13), the kernel H results

$$\begin{aligned}
H(x, x'; 0) &= -\frac{ik}{4} H_1^{(1)} \left(k \sqrt{(x - x')^2 + (f(x) - f(x'))^2} \right) \frac{-f'(x)(x - x') + f(x) - f(x')}{\sqrt{(x - x')^2 + (f(x) - f(x'))^2}} \\
&\quad \times \frac{\sqrt{1 + f'(x')^2}}{\sqrt{1 + f'(x)^2}}. \tag{4.B.17}
\end{aligned}$$

Similarly to the double-layer potential, and considering (4.B.14), (4.B.15), and (4.B.17), the values of the smooth kernel H_r when x is equal to x' can be computed as

$$\begin{aligned}
H_r(x, x; 0) &= \lim_{x' \rightarrow x} H_r(x, x'; 0) = \lim_{x' \rightarrow x} \left[H(x, x'; 0) - H_s(x, x'; 0) \ln \left(4 \sin^2 \left(\frac{x - x'}{2} \right) \right) \right] \\
&= \lim_{x' \rightarrow x} \left[\left(-\frac{ik}{4} \left(1 - \frac{2i}{\pi} (C + \ln(2)) \right) \frac{J_1 \left(k \sqrt{(x - x')^2 + (f(x) - f(x'))^2} \right)}{\sqrt{(x - x')^2 + (f(x) - f(x'))^2}} \right. \right. \\
&\quad \left. \left. - \frac{k^2}{8\pi} \Sigma_1 \left(k \sqrt{(x - x')^2 + (f(x) - f(x'))^2} \right) \right) + \frac{k}{4\pi} \frac{\sqrt{1 + f'(x')^2}}{\sqrt{1 + f'(x)^2}} \right. \\
&\quad \times \frac{J_1 \left(k \sqrt{(x - x')^2 + (f(x) - f(x'))^2} \right)}{\sqrt{(x - x')^2 + (f(x) - f(x'))^2}} (-f'(x)(x - x') + f(x) - f(x')) \\
&\quad \times \ln \left(\frac{k^2 ((x - x')^2 + (f(x) - f(x'))^2)}{4 \sin^2 \left(\frac{x - x'}{2} \right)} \right) \left. \right] \\
&\quad - \lim_{x' \rightarrow x} \frac{-f'(x)(x - x') + f(x) - f(x')}{2\pi ((x - x')^2 + (f(x) - f(x'))^2)} \frac{\sqrt{1 + f'(x')^2}}{\sqrt{1 + f'(x)^2}} = \frac{f''(x)}{4\pi (1 + f'(x)^2)}, \tag{4.B.18}
\end{aligned}$$

where C is the Euler's constant given by (4.A.3), and Σ_1 is defined in (4.A.7). When $J > 0$ is considered, the kernel H is given by (4.B.13). Then, taking into account (4.B.14),

and (4.B.15), the values of H_r at $x = x'$ result

$$\begin{aligned}
H_r(x, x; J) &= \lim_{x' \rightarrow x} H_r(x, x'; J) = \lim_{x' \rightarrow x} \left[H(x, x'; J) - H_s(x, x'; J) \ln \left(4 \sin^2 \left(\frac{x - x'}{2} \right) \right) \right] \\
&= \lim_{x' \rightarrow x} \left[\left(-\frac{ik}{4} \left(\sum_{l=0}^J \left[(-1)^l \binom{J}{l} H_1^{(1)}(k \sqrt{(x - x')^2 + (f(x) - f(x') + lh)^2}) \right. \right. \right. \right. \right. \\
&\quad \times \frac{-f'(x)(x - x') + f(x) - f(x') + lh}{\sqrt{(x - x')^2 + (f(x) - f(x') + lh)^2}} \left. \left. \left. \left. \right] \right) - \frac{k}{4\pi} \ln \left(4 \sin^2 \left(\frac{x - x'}{2} \right) \right) \right. \\
&\quad \times J_1 \left(k \sqrt{(x - x')^2 + (f(x) - f(x'))^2} \right) \frac{-f'(x)(x - x') + f(x) - f(x')}{\sqrt{(x - x')^2 + (f(x) - f(x'))^2}} \left. \left. \left. \right. \right) \\
&\quad \times \frac{\sqrt{1 + f'(x')^2}}{\sqrt{1 + f'(x)^2}} \left. \right].
\end{aligned}$$

The singularities in the Hankel function $H_1^{(1)}$ appear when $l = 0$ so, the summation is separated in two parts: one of them when $l = 0$, to use (4.B.18), and another one when $l > 0$. Then, the values of H_r at $x = x'$ are

$$\begin{aligned}
H_r(x, x; J) &= \lim_{x' \rightarrow x} H_r(x, x'; J) \\
&= - \lim_{x' \rightarrow x} \left(\frac{ik}{4} \sum_{l=1}^J \left[(-1)^l \binom{J}{l} H_1^{(1)} \left(k \sqrt{(x - x')^2 + (f(x) - f(x') + lh)^2} \right) \right. \right. \\
&\quad \times \frac{-f''(x')(x - x') + f(x) - f(x') + lh}{\sqrt{(x - x')^2 + (f(x) - f(x') + lh)^2}} \left. \left. \right] \frac{\sqrt{1 + f'(x')^2}}{\sqrt{1 + f'(x)^2}} \right) \frac{f''_1(x)}{4\pi(1 + f'(x)^2)} \\
&= \frac{f''_1(x)}{4\pi(1 + f'(x)^2)} - \frac{ik}{4} \sum_{l=1}^J (-1)^l \binom{J}{l} H_1^{(1)}(klh).
\end{aligned}$$

4.B.4 Hypersingular formulation

This section is devoted to describing the kernel decomposition of the normal derivative of a double-layer potential (also called, hypersingular potential). In order to deal with this operator, the difference of hypersingular potentials is considered because thus, the singularities appearing in the kernels disappear. As in the single-, double-, and adjoint double-layer potential, to ease the understanding, neither shifting nor windowing methods are considered. The kernel considered is formed by the difference of the second normal derivative of the half-space Green function $G_{J\pm}$, given by (4.43), multiplied by the norm of

the normal vector to the boundary. Then, the integral considered is

$$\begin{aligned} I(x) &= \int_{-L/2}^{L/2} \left[\left(\frac{\partial^2 G_{J-}}{\partial \boldsymbol{\nu}_x \partial \boldsymbol{\nu}_{x'}}(x - x', f(x) - f(x')) - \frac{\partial^2 G_{J+}}{\partial \boldsymbol{\nu}_x \partial \boldsymbol{\nu}_{x'}}(x - x', f(x) - f(x')) \right) \right. \\ &\quad \times \left. \sqrt{1 + f'(x')^2} \varphi(x') \right] dx'. \end{aligned}$$

To follow same arguments than before, it is called K to

$$K(x, x'; J) = \left(\frac{\partial^2 G_{J-}}{\partial \boldsymbol{\nu}_x \partial \boldsymbol{\nu}_{x'}}(x - x', f(x) - f(x')) - \frac{\partial^2 G_{J+}}{\partial \boldsymbol{\nu}_x \partial \boldsymbol{\nu}_{x'}}(x - x', f(x) - f(x')) \right) \sqrt{1 + f'(x')^2},$$

and then

$$I(x) = \int_{-L/2}^{L/2} K(x, x'; J) \varphi(x') dx'.$$

In order to compute the decomposition of K , the difference of double-layer potentials is considered. Taking into account the definition of $G_{J\pm}$, given by (4.43), the difference of these potentials results

$$\begin{aligned} &\left(\frac{\partial G_{J-}}{\partial \boldsymbol{\nu}_{x'}}(x - x', f(x) - f(x')) - \frac{\partial G_{J+}}{\partial \boldsymbol{\nu}_{x'}}(x - x', f(x) - f(x')) \right) \\ &= \frac{i}{4} \left(\sum_{l=0}^J \left[(-1)^l \binom{J}{l} \left[k^- H_1^{(1)} \left(k^- \sqrt{(x - x')^2 + (f(x) - f(x') - lh^-)^2} \right) \right. \right. \right. \\ &\quad \times \frac{(x - x', f(x) - f(x') - lh^-)}{\sqrt{(x - x')^2 + (f(x) - f(x') - lh^-)^2}} \cdot \frac{(-f'(x'), 1)}{\sqrt{1 + f'(x')^2}} \\ &\quad - k^+ H_1^{(1)} \left(k^+ \sqrt{(x - x')^2 + (f(x) - f(x') + lh^+)^2} \right) \\ &\quad \left. \left. \left. \times \frac{(x - x', f(x) - f(x') + lh^+)}{\sqrt{(x - x')^2 + (f(x) - f(x') + lh^+)^2}} \cdot \frac{(-f'(x'), 1)}{\sqrt{1 + f'(x')^2}} \right] \right] \right) \\ &= \frac{i}{4} \left(\sum_{l=0}^J \left[(-1)^l \binom{J}{l} \left[k^- H_1^{(1)} \left(k^- \sqrt{(x - x')^2 + (f(x) - f(x') - lh^-)^2} \right) \chi(x, x'; -lh^-) \right. \right. \right. \\ &\quad - k^+ H_1^{(1)} \left(k^+ \sqrt{(x - x')^2 + (f(x) - f(x') + lh^+)^2} \right) \chi(x, x'; lh^+) \left. \right] \right], \quad (4.B.19) \end{aligned}$$

where

$$\chi(x, x'; \delta) = \frac{(x - x', f(x) - f(x') + \delta)}{\sqrt{(x - x')^2 + (f(x) - f(x') + \delta)^2}} \cdot \frac{(-f'(x'), 1)}{\sqrt{1 + f'(x')^2}}. \quad (4.B.20)$$

Considering the derivative of the Hankel function $H_1^{(1)}$ (see (4.A.12)), the normal derivative of the difference of double-layer potentials (4.B.19) is given by

$$\begin{aligned}
K(x, x'; J) &= \frac{\partial^2 G_{J-}}{\partial \boldsymbol{\nu}_x \partial \boldsymbol{\nu}_{x'}}(x - x', f(x) - f(x')) - \frac{\partial^2 G_{J+}}{\partial \boldsymbol{\nu}_x \partial \boldsymbol{\nu}_{x'}}(x - x', f(x) - f(x')) \\
&= \frac{i}{4} \left(\sum_{l=0}^J \left[(-1)^l \binom{J}{l} \left[\left(-k_-^2 H_2^{(1)} \left(k^- \sqrt{(x-x')^2 + (f(x)-f(x')-lh^-)^2} \right) \right. \right. \right. \right. \right. \\
&\quad \left. \left. \left. \left. \left. \left. + \frac{k^- H_1^{(1)} \left(k^- \sqrt{(x-x')^2 + (f(x)-f(x')+lh^-)^2} \right)}{\sqrt{(x-x')^2 + (f(x)-f(x')-lh^-)^2}} \right) \chi(x, x'; -lh^-) \right. \right. \right. \right. \\
&\quad \times \tilde{\chi}(x, x'; -lh^-) - \left(-k_+^2 H_2^{(1)} \left(k^+ \sqrt{(x-x')^2 + (f(x)-f(x')+lh^+)^2} \right) \right. \\
&\quad \left. \left. \left. \left. \left. \left. + \frac{k^+ H_1^{(1)} \left(k^+ \sqrt{(x-x')^2 + (f(x)-f(x')+lh^+)^2} \right)}{\sqrt{(x-x')^2 + (f(x)-f(x')+lh^+)^2}} \right) \right. \right. \right. \right. \\
&\quad \times \chi(x, x'; lh^+) \tilde{\chi}(x, x'; lh^+) \right] \right) \\
&\quad + \frac{i}{4} \left(\sum_{l=0}^J \left[(-1)^l \binom{J}{l} \left[k^- H_1^{(1)} \left(k^- \sqrt{(x-x')^2 + (f(x)-f(x')-lh^-)^2} \right) \right. \right. \right. \\
&\quad \times \frac{\partial \chi}{\partial \boldsymbol{\nu}_x}(x, x'; -lh^-) - k^+ \frac{\partial \chi}{\partial \boldsymbol{\nu}_x}(x, x'; lh^+) \\
&\quad \times \left. \left. \left. H_1^{(1)} \left(k^+ \sqrt{(x-x')^2 + (f(x)-f(x')+lh^+)^2} \right) \right] \right] \right) \\
&= \frac{i}{4} \left(\sum_{l=0}^J \left[(-1)^l \binom{J}{l} \left[-k_-^2 H_2^{(1)} \left(k^- \sqrt{(x-x')^2 + (f(x)-f(x')-lh^-)^2} \right) \right. \right. \right. \\
&\quad \times \chi(x, x'; -lh^-) \tilde{\chi}(x, x'; -lh^-) + k_+^2 H_2^{(1)} \left(k^+ \sqrt{(x-x')^2 + (f(x)-f(x')+lh^+)^2} \right) \\
&\quad \times \chi(x, x'; lh^+) \tilde{\chi}(x, x'; lh^+) \right] \right) + \frac{i}{4} \left(\sum_{l=0}^J \left[(-1)^l \binom{J}{l} \right. \right. \\
&\quad \times \left. \left. \left[k^- H_1^{(1)} \left(k^- \sqrt{(x-x')^2 + (f(x)-f(x')-lh^-)^2} \right) \xi(x, x'; -lh^-) \right. \right. \right. \\
&\quad \left. \left. \left. - k^+ H_1^{(1)} \left(k^+ \sqrt{(x-x')^2 + (f(x)-f(x')+lh^+)^2} \right) \xi(x, x'; lh^+) \right] \right] \right), \tag{4.B.21}
\end{aligned}$$

where χ is given by (4.B.20), and

$$\tilde{\chi}(x, x'; \delta) = \frac{(x' - x, f(x') - f(x) + \delta)}{\sqrt{(x' - x)^2 + (f(x') - f(x) + \delta)^2}} \cdot \frac{(-f'(x), 1)}{\sqrt{1 + f'(x)^2}}, \quad (4.B.22)$$

$$\xi(x, x'; \delta) = \frac{\chi(x, x'; \delta) \tilde{\chi}(x, x'; \delta)}{\sqrt{(x - x')^2 + (f(x) - f(x') + \delta)^2}} + \frac{\partial \chi}{\partial \nu_x}(x, x'; \delta). \quad (4.B.23)$$

The normal derivative of χ is given by

$$\begin{aligned} & \frac{\partial \chi}{\partial \nu_x}(x, x'; \delta) \\ &= \left(\frac{-f'(x') ((x - x')^2 + (f(x) - f(x') + \delta)^2) - (x - x') (-f'(x')(x - x') + f(x) - f(x') + \delta)}{\sqrt{(x - x')^2 + (f(x) - f(x') + \delta)^2}^3 \sqrt{1 + f'(x')^2} \sqrt{1 + f'(x)^2}}, \right. \\ & \quad \left. \frac{((x - x')^2 + (f(x) - f(x') + \delta)^2) - (-f'(x')(x - x') + f(x) - f(x') + \delta) (f(x) - f(x') + \delta)}{\sqrt{(x - x')^2 + (f(x) - f(x') + \delta)^2}^3 \sqrt{1 + f'(x')^2} \sqrt{1 + f'(x)^2}} \right) \\ &= \frac{f'(x) f'(x') (f(x) - f(x') + \delta)^2 + (x - x')^2 + (x - x') (f(x) - f(x') + \delta) (f'(x) + f'(x'))}{\sqrt{(x - x')^2 + (f(x) - f(x') + \delta)^2}^3 \sqrt{1 + f'(x')^2} \sqrt{1 + f'(x)^2}}. \end{aligned} \quad (4.B.24)$$

By using (4.B.20), (4.B.22), and (4.B.24), the expression (4.B.23) results

$$\begin{aligned} \xi(x, x'; \delta) &= \frac{\chi(x, x'; \delta) \tilde{\chi}(x, x'; \delta)}{\sqrt{(x - x')^2 + (f(x) - f(x') + \delta)^2}} + \frac{\partial \chi}{\partial \nu_x}(x, x'; \delta) \\ &= \frac{(-f'(x')(x - x') + f(x) - f(x') + \delta) (-f'(x)(x - x') + f(x) - f(x') + \delta)}{\sqrt{(x - x')^2 + (f(x) - f(x') + \delta)^2}^3 \sqrt{1 + f'(x')^2} \sqrt{1 + f'(x)^2}} \\ &= \frac{(x - x')^2 (1 + f'(x) f'(x')) + (f(x) - f(x') + \delta) (1 + f'(x) f'(x'))}{\sqrt{(x - x')^2 + (f(x) - f(x') + \delta)^2}^3 \sqrt{1 + f'(x')^2} \sqrt{1 + f'(x)^2}} \\ &= \frac{1 + f'(x) f'(x')}{\sqrt{(x - x')^2 + (f(x) - f(x') + \delta)^2} \sqrt{1 + f'(x')^2} \sqrt{1 + f'(x)^2}}. \end{aligned}$$

Then, the difference of hypersingular kernels (4.B.21) is given by

$$\begin{aligned}
K(x, x'; J) &= \frac{\partial^2 G_{J-}}{\partial \boldsymbol{\nu}_x \partial \boldsymbol{\nu}_{x'}}(x - x', f(x) - f(x')) - \frac{\partial^2 G_{J+}}{\partial \boldsymbol{\nu}_x \partial \boldsymbol{\nu}_{x'}}(x - x', f(x) - f(x')) \\
&= -\frac{i}{4} \left(\sum_{l=0}^J \left[(-1)^l \binom{J}{l} \left[k_-^2 H_2^{(1)} \left(k^- \sqrt{(x - x')^2 + (f(x) - f(x') - lh^-)^2} \right) \right. \right. \right. \\
&\quad \times \chi(x, x'; -lh^-) \tilde{\chi}(x, x'; -lh^-) - k_+^2 H_2^{(1)} \left(k^+ \sqrt{(x - x')^2 + (f(x) - f(x') + lh^+)^2} \right) \\
&\quad \times \chi(x, x'; lh^+) \tilde{\chi}(x, x'; lh^+) \left. \right] \left. \right] + \frac{i}{4} \left(\sum_{l=0}^J \left[(-1)^l \binom{J}{l} \right. \right. \\
&\quad \times \left[k^- \frac{H_1^{(1)} \left(k^- \sqrt{(x - x')^2 + (f(x) - f(x') - lh^-)^2} \right)}{\sqrt{(x - x')^2 + (f(x) - f(x') - lh^-)^2}} \right. \\
&\quad \left. \left. - k^+ \frac{H_1^{(1)} \left(k^+ \sqrt{(x - x')^2 + (f(x) - f(x') + lh^+)^2} \right)}{\sqrt{(x - x')^2 + (f(x) - f(x') + lh^+)^2}} \right] \right] \\
&\quad \times \frac{1 + f'(x) f'(x')}{\sqrt{1 + f'(x')^2} \sqrt{1 + f'(x)^2}} \right) = K^1(x, x'; J) + K^2(x, x'; J),
\end{aligned}$$

where

$$\begin{aligned}
K^1(x, x'; J) &= -\frac{i}{4} \left(\sum_{l=0}^J \left[(-1)^l \binom{J}{l} \left[k_-^2 H_2^{(1)} \left(k^- \sqrt{(x - x')^2 + (f(x) - f(x') - lh^-)^2} \right) \right. \right. \right. \\
&\quad \times \chi(x, x'; -lh^-) \tilde{\chi}(x, x'; -lh^-) \\
&\quad - k_+^2 H_2^{(1)} \left(k^+ \sqrt{(x - x')^2 + (f(x) - f(x') + lh^+)^2} \right) \chi(x, x'; lh^+) \\
&\quad \times \tilde{\chi}(x, x'; lh^+) \left. \right] \left. \right] \sqrt{1 + f'(x')^2}, \tag{4.B.25}
\end{aligned}$$

$$\begin{aligned}
K^2(x, x'; J) &= \frac{i}{4} \left(\sum_{l=0}^J \left[(-1)^l \binom{J}{l} \left[k^- \frac{H_1^{(1)} \left(k^- \sqrt{(x - x')^2 + (f(x) - f(x') - lh^-)^2} \right)}{\sqrt{(x - x')^2 + (f(x) - f(x') - lh^-)^2}} \right. \right. \right. \\
&\quad \left. \left. - k^+ \frac{H_1^{(1)} \left(k^+ \sqrt{(x - x')^2 + (f(x) - f(x') + lh^+)^2} \right)}{\sqrt{(x - x')^2 + (f(x) - f(x') + lh^+)^2}} \right] \right] \right) \frac{1 + f'(x) f'(x')}{\sqrt{1 + f'(x)^2}}. \tag{4.B.26}
\end{aligned}$$

Taking into account the asymptotic expansion of the Hankel function of order 1 and 2 at the origin (see (4.A.6) and (4.A.8)), the kernels K^1 and K^2 present logarithmic singularities at $x = x'$ when $l = 0$, and following Martensen [122] and Kussmaul [108], the kernels K^1

and K^2 can be split into a smooth kernel K_r^1 and K_r^2 , respectively, and a logarithmic part (see Remark 4.B.1 for subscript notation), that is,

$$\begin{aligned} K^1(x, x'; J) &= K_s^1(x, x'; J) \ln \left(4 \sin^2 \left(\frac{x - x'}{2} \right) \right) + K_r^1(x, x'; J), \\ K^2(x, x'; J) &= K_s^2(x, x'; J) \ln \left(4 \sin^2 \left(\frac{x - x'}{2} \right) \right) + K_r^2(x, x'; J), \end{aligned}$$

where

$$\begin{aligned} K_s^1(x, x'; J) &= \frac{1}{4\pi} \sqrt{1 + f'(x')^2} \left[k_-^2 J_2 \left(k^- \sqrt{(x - x')^2 + (f(x) - f(x'))^2} \right) \right. \\ &\quad \left. - k_+^2 J_2 \left(k^+ \sqrt{(x - x')^2 + (f(x) - f(x'))^2} \right) \right] \\ &\quad \times \frac{(x - x', f(x) - f(x'))}{\sqrt{(x - x')^2 + (f(x) - f(x'))^2}} \cdot \frac{(-f'(x'), 1)}{\sqrt{1 + f'(x')^2}} \\ &\quad \times \frac{(x - x', f(x) - f(x'))}{\sqrt{(x - x')^2 + (f(x) - f(x'))^2}} \cdot \frac{(-f'(x), 1)}{\sqrt{1 + f'(x)^2}} \\ &= \frac{1}{4\pi} \chi(x, x'; 0) \tilde{\chi}(x, x'; 0) \left[k_-^2 J_2 \left(k^- \sqrt{(x - x')^2 + (f(x) - f(x'))^2} \right) \right. \\ &\quad \left. - k_+^2 J_2 \left(k^+ \sqrt{(x - x')^2 + (f(x) - f(x'))^2} \right) \right] \sqrt{1 + f'(x')^2}, \quad (4.B.27) \end{aligned}$$

$$\begin{aligned} K_s^2(x, x'; J) &= -\frac{1}{4\pi} \left[\frac{k^- J_1 \left(k^- \sqrt{(x - x')^2 + (f(x) - f(x'))^2} \right)}{\sqrt{(x - x')^2 + (f(x) - f(x'))^2}} \right. \\ &\quad \left. - \frac{k^+ J_1 \left(k^+ \sqrt{(x - x')^2 + (f(x) - f(x'))^2} \right)}{\sqrt{(x - x')^2 + (f(x) - f(x'))^2}} \right] \frac{1 + f'(x)f'(x')}{\sqrt{1 + f'(x)^2}} \\ &= -\frac{1}{4\pi} \left[k^- J_1 \left(k^- \sqrt{(x - x')^2 + (f(x) - f(x'))^2} \right) \right. \\ &\quad \left. - k^+ J_1 \left(k^+ \sqrt{(x - x')^2 + (f(x) - f(x'))^2} \right) \right] \xi(x, x'; 0), \quad (4.B.28) \end{aligned}$$

$$K_r^1(x, x'; J) = K^1(x, x'; J) - K_s^1(x, x'; J) \ln \left(4 \sin^2 \left(\frac{x - x'}{2} \right) \right), \quad (4.B.29)$$

$$K_r^2(x, x'; J) = K^2(x, x'; J) - K_s^2(x, x'; J) \ln \left(4 \sin^2 \left(\frac{x - x'}{2} \right) \right). \quad (4.B.30)$$

To deal with the singularities appearing in the Bessel functions at the origin, it is necessary to work separately with the values of the kernels K_s^1 , K_r^1 , K_s^2 , and K_r^2 , at $x = x'$. The values of K_s^1 when $x = x'$ can be computed as

$$K_s^1(x, x; J) = \lim_{x' \rightarrow x} K_s^1(x, x'; J) = 0$$

since

$$\begin{aligned} \lim_{x' \rightarrow x} \chi(x, x'; 0) &= \lim_{x' \rightarrow x} \frac{(x - x', f(x) - f(x'))}{\sqrt{(x - x')^2 + (f(x) - f(x'))^2}} \cdot \frac{(-f'(x'), 1)}{\sqrt{1 + f'(x')^2}} \\ &= \lim_{x' \rightarrow x} \frac{-f'(x') + \frac{f(x) - f(x')}{x - x'}}{\sqrt{1 + \frac{(f(x) - f(x'))^2}{(x - x')^2}} \sqrt{1 + f'(x')^2}} = 0. \end{aligned} \quad (4.B.31)$$

$$\lim_{x' \rightarrow x} \tilde{\chi}(x, x'; 0) = 0 \quad (4.B.32)$$

Now, taking into account (4.B.28), and the limit of the Bessel function $J_1(t)$ when $t \rightarrow 0$ (see (4.A.10)),

$$\begin{aligned} K_s^2(x, x; J) &= \lim_{x' \rightarrow x} K_s^2(x, x'; J) = \lim_{x' \rightarrow x} -\frac{1}{4\pi} \left(k^- J_1 \left(k^- \sqrt{(x - x')^2 + (f(x) - f(x'))^2} \right) \right. \\ &\quad \left. - k^+ J_1 \left(k^+ \sqrt{(x - x')^2 + (f(x) - f(x'))^2} \right) \right) \xi(x, x', 0) \\ &= -\frac{1}{8\pi} ((k^-)^2 - (k^+)^2) \sqrt{1 + f'(x)^2}. \end{aligned} \quad (4.B.33)$$

Then the values of the kernel K_s when x coincides with x' are computed by using

$$K_s(x, x; J) = K_s^1(x, x; J) + K_s^2(x, x; J) = -\frac{1}{8\pi} ((k^-)^2 - (k^+)^2) \sqrt{1 + f'(x)^2}.$$

The values of K_r^1 and K_r^2 at $x = x'$ have been computed in two different cases: when shifts are not used ($J = 0$) and when shifts are used ($J > 0$). If $J = 0$, using (4.B.25) the kernel K^1 results

$$\begin{aligned} K^1(x, x'; 0) &= -\frac{i}{4} \chi(x, x'; 0) \tilde{\chi}(x, x'; 0) \left[k_-^2 H_2^{(1)} \left(k^- \sqrt{(x - x')^2 + (f(x) - f(x'))^2} \right) \right. \\ &\quad \left. - k_+^2 H_2^{(1)} \left(k^+ \sqrt{(x - x')^2 + (f(x) - f(x'))^2} \right) \right] \sqrt{1 + f'(x')^2}. \end{aligned}$$

Then, considering the asymptotic behavior of χ and $\tilde{\chi}$ at $x = x'$ (see (4.B.31), and (4.B.32)), it holds

$$K_r^1(x, x; 0) = \lim_{x' \rightarrow x} K_r^1(x, x'; 0) = 0. \quad (4.B.34)$$

On the other hand, when $J = 0$ using (4.B.26) the kernel K^2 results

$$\begin{aligned} K^2(x, x'; 0) &= \frac{i}{4} \left[k^- H_1^{(1)} \left(k^- \sqrt{(x - x')^2 + (f(x) - f(x'))^2} \right) \right. \\ &\quad \left. - k^+ H_1^{(1)} \left(k^+ \sqrt{(x - x')^2 + (f(x) - f(x'))^2} \right) \right] \xi(x, x'; 0). \end{aligned} \quad (4.B.35)$$

Considering the asymptotic expansion of the Hankel function $H_1^{(1)}$ (see (4.A.6) for more details) and taking into account (4.B.28), (4.B.30), and (4.B.35), the values of the smooth kernel K_r^2 at $x = x'$ can be computed as

$$\begin{aligned}
K_r^2(x, x; J) &= \lim_{x' \rightarrow x} K_r^2(x, x'; J) = \lim_{x' \rightarrow x} \left[K^2(x, x'; J) - K_s^2(x, x'; J) \ln \left(4 \sin^2 \left(\frac{x - x'}{2} \right) \right) \right] \\
&= \lim_{x' \rightarrow x} \left(\left(\frac{i}{4} - \frac{C}{2\pi} \right) \frac{1}{\sqrt{(x - x')^2 + (f(x) - f(x'))^2}} \right. \\
&\quad \times \left[k^- J_1 \left(k^- \sqrt{(x - x')^2 + (f(x) - f(x'))^2} \right) - k^+ J_1 \left(k^+ \sqrt{(x - x')^2 + (f(x) - f(x'))^2} \right) \right] \\
&\quad + \frac{1}{2\pi ((x - x')^2 + (f(x) - f(x'))^2)} \left[\frac{k^-}{k^-} - \frac{k^+}{k^+} \right] \\
&\quad + \frac{1}{8\pi} \left[k_-^2 \Sigma_1 \left(k^- \sqrt{(x - x')^2 + (f(x) - f(x'))^2} \right) - k_+^2 \Sigma_1 \left(k^+ \sqrt{(x - x')^2 + (f(x) - f(x'))^2} \right) \right] \\
&\quad - \frac{1}{4\pi} \left[k^- \ln \left(\frac{k_-^2 ((x - x')^2 + (f(x) - f(x'))^2)}{4} \right) \frac{J_1 \left(k^- \sqrt{(x - x')^2 + (f(x) - f(x'))^2} \right)}{\sqrt{(x - x')^2 + (f(x) - f(x'))^2}} \right. \\
&\quad \left. - k^+ \ln \left(\frac{k_+^2 ((x - x')^2 + (f(x) - f(x'))^2)}{4} \right) \frac{J_1 \left(k^+ \sqrt{(x - x')^2 + (f(x) - f(x'))^2} \right)}{\sqrt{(x - x')^2 + (f(x) - f(x'))^2}} \right] \\
&\quad + \frac{1}{4\pi} \ln \left(4 \sin^2 \left(\frac{x - x'}{2} \right) \right) \left[\frac{k^- J_1 \left(k^- \sqrt{(x - x')^2 + (f(x) - f(x'))^2} \right)}{\sqrt{(x - x')^2 + (f(x) - f(x'))^2}} \right. \\
&\quad \left. - \frac{k^+ J_1 \left(k^+ \sqrt{(x - x')^2 + (f(x) - f(x'))^2} \right)}{\sqrt{(x - x')^2 + (f(x) - f(x'))^2}} \right] \right) \frac{1 + f'(x)f'(x')}{\sqrt{1 + f'(x)^2}} \\
&= \left(\left(\frac{i}{8} - \frac{C}{4\pi} + \frac{1}{8\pi} \right) (k_-^2 - k_+^2) - \frac{1}{4\pi} \lim_{x' \rightarrow x} \left[\frac{k_-^2}{2} \ln \left(\frac{\frac{k_-^2 ((x - x')^2 + (f(x) - f(x'))^2)}{4}}{4 \sin^2 \left(\frac{x - x'}{2} \right)} \right) \right. \right. \\
&\quad \left. \left. - \frac{k_+^2}{2} \ln \left(\frac{\frac{k_+^2 ((x - x')^2 + (f(x) - f(x'))^2)}{4}}{4 \sin^2 \left(\frac{x - x'}{2} \right)} \right) \right] \right) \frac{1 + f'(x)f'(x')}{\sqrt{1 + f'(x)^2}} \\
&= \left(\left(\frac{i}{8} - \frac{C}{4\pi} + \frac{1}{8\pi} \right) (k_-^2 - k_+^2) - \frac{1}{4\pi} \left[k_-^2 \ln \left(\frac{k^-}{2} \sqrt{1 + f'(x)^2} \right) - k_+^2 \ln \left(\frac{k^+}{2} \sqrt{1 + f'(x)^2} \right) \right] \right) \\
&\quad \times \sqrt{1 + f'(x)^2}, \tag{4.B.36}
\end{aligned}$$

where C is the Euler's constant given by (4.A.3), and Σ_1 is the function given by (4.A.7), defined in Appendix 4.A. Once the asymptotic expressions for the kernels K_r^1 , and K_r^2 (given by (4.B.34), and (4.B.36), respectively) have been computed, it is straightforward to calculate the value of K_r when $x = x'$ as

$$K_r(x, x; 0) = K_r^1(x, x; 0) + K_r^2(x, x; 0) = \left(\left(\frac{i}{8} - \frac{C}{4\pi} + \frac{1}{8\pi} \right) (k_-^2 - k_+^2) \right. \\ \left. - \frac{1}{4\pi} \left[k_-^2 \ln \left(\frac{k_-}{2} \sqrt{1 + f'(x)^2} \right) - k_+^2 \ln \left(\frac{k_+}{2} \sqrt{1 + f'(x)^2} \right) \right] \right) \sqrt{1 + f'(x)^2}.$$

If any value of shift is considered, that is, if $J > 0$, the kernel K^1 is given by (4.B.25), and the expressions for K_s^1 , and K_r^1 , are given by (4.B.27) and (4.B.29) respectively. Since the singularities appearing in the Hankel function $H_2^{(1)}$ at the origin appear only when $l = 0$, to deal with them is necessary to split the sum in two parts: $l = 0$, and $l > 0$. In this case, the values of the smooth kernel K_r^1 , when x coincides with x' , can be computed as

$$K_r^1(x, x; J) = \lim_{x' \rightarrow x} K_r^1(x, x'; J) = \lim_{x' \rightarrow x} \left[K^1(x, x'; J) - K_s^1(x, x'; J) \ln \left(4 \sin^2 \left(\frac{x - x'}{2} \right) \right) \right] \\ = \frac{i}{4} \lim_{x' \rightarrow x} \left(\sum_{l=1}^J (-1)^l \binom{J}{l} \left[k_-^2 H_2^{(1)} \left(k_- \sqrt{(x - x')^2 + (f(x) - f(x') - lh^-)^2} \right) \right. \right. \\ \times \chi(x, x'; -lh^-) \tilde{\chi}(x', x; -lh^-) - k_+^2 H_2^{(1)} \left(k_+ \sqrt{(x - x')^2 + (f(x) - f(x') + lh^+)^2} \right) \\ \times \chi(x, x'; lh^+) \tilde{\chi}(x', x; lh^+) \left. \right] \sqrt{1 + f'(x')^2} \left. \right) \\ = -\frac{i}{4} \sum_{l=1}^J (-1)^l \binom{J}{l} \frac{\left[k_-^2 H_2^{(1)}(-k_- lh^-) - k_+^2 H_2^{(1)}(k_+ lh^+) \right]}{\sqrt{1 + f'(x)^2}}.$$

On the other hand, if $J > 0$ the kernel K^2 is given by (4.B.26), and the expressions for K_s^2 , and K_r^2 , are given by (4.B.28) and (4.B.30) respectively. As in the case of the kernel K_r^1 , to deal with the singularities appearing in the Hankel function $H_1^{(1)}$ at the origin, it is necessary to deal separately with $l = 0$, and with $l > 0$. Then, the values of the smooth kernel K_r^2 at $x = x'$ are computed as

$$\begin{aligned}
K_r^2(x, x; J) &= \lim_{x' \rightarrow x} K_r^2(x, x'; J) = \lim_{x' \rightarrow x} \left(K^2(x, x'; J) - K_s^2(x, x'; J) \ln \left(4 \sin^2 \left(\frac{x - x'}{2} \right) \right) \right) \\
&= \left(\left(\frac{i}{8} - \frac{C}{4\pi} + \frac{1}{8\pi} \right) (k_-^2 - k_+^2) - \frac{1}{4\pi} \left[k_-^2 \ln \left(\frac{k^-}{2} \sqrt{1 + f'(x)^2} \right) \right. \right. \\
&\quad \left. \left. - k_+^2 \ln \left(\frac{k^+}{2} \sqrt{1 + f'(x)^2} \right) \right] \right) \sqrt{1 + f'(x)^2} \\
&\quad + \frac{i}{4} \lim_{x' \rightarrow x} \sum_{l=1}^J (-1)^l \binom{J}{l} \left[k^- \frac{H_1^{(1)} \left(k^- \sqrt{(x - x')^2 + (f(x) - f(x') - lh^-)^2} \right)}{\sqrt{(x - x')^2 + (f(x) - f(x') - lh^-)^2}} \right. \\
&\quad \left. - k^+ \frac{H_1^{(1)} \left(k^+ \sqrt{(x - x')^2 + (f(x) - f(x') + lh^+)^2} \right)}{\sqrt{(x - x')^2 + (f(x) - f(x') + lh^+)^2}} \right] \frac{1 + f'(x) f'(x')}{\sqrt{1 + f'(x)^2}} \\
&= \left(\left(\frac{i}{8} - \frac{C}{4\pi} + \frac{1}{8\pi} \right) (k_-^2 - k_+^2) - \frac{1}{4\pi} \left[k_-^2 \ln \left(\frac{k^-}{2} \sqrt{1 + f'(x)^2} \right) \right. \right. \\
&\quad \left. \left. - k_+^2 \ln \left(\frac{k^+}{2} \sqrt{1 + f'(x)^2} \right) \right] + \frac{i}{4} \sum_{l=1}^J (-1)^l \binom{J}{l} \left[k^- \frac{H_1^{(1)} (-k^- lh^-)}{-lh^-} \right. \right. \\
&\quad \left. \left. - k^+ \frac{H_1^{(1)} (k^+ lh^+)}{lh^+} \right] \right) \sqrt{1 + f'(x)^2},
\end{aligned}$$

where C is the Euler's constant given by (4.A.3).

4.C Perfectly Matched Layers

When the boundary in the transmission problem is a sinusoidal grating, it is not possible to compute an analytical solution of the problem. To compare the solution obtained with the proposed method, a finite element method (FEM) together with the use of a Perfectly Matched Layer technique (PML) have been considered. Some details about how the PMLs have been used, can be found below.

4.C.1 Statement of the quasi-periodic problem

Firstly, the original quasi-periodic problem stated in $\Omega^\# = \Omega_+^\# \cup \Omega_-^\#$ is written in terms of a unique unknown field U , such that

$$U = \begin{cases} U_+ & \text{in } \Omega_+^\#, \\ U_- & \text{in } \Omega_-^\#. \end{cases}$$

Taking into account an analogous definition for the wave number k , defined by

$$k = \begin{cases} k^+ & \text{in } \Omega_+^\#, \\ k^- & \text{in } \Omega_-^\#, \end{cases}$$

the quasi-periodic problem (4.31)-(4.36), (4.38), and (4.40) can be written as follows: Given a quasi-periodic length L , and a constant factor α , find a quasi-periodic function U , such that it holds

$$\begin{aligned} \Delta U + k^2 U &= 0 && \text{in } \Omega^\#, \\ U(x + L, y) &= U(x, y)e^{i\alpha L}, && \text{with } (x, y) \in \Omega^\#, \\ &\& \text{radiation conditions} & \text{at } |y| \rightarrow +\infty. \end{aligned}$$

The radiation conditions are used to ensure that no waves are coming from $y \rightarrow -\infty$, and that an incident plane wave $U^{\text{inc}}(x, y) = e^{i(\alpha^+ x - \beta^+ y)}$ with $(\alpha^+)^2 + (\beta^+)^2 = (k^+)^2$, is impinging the coupling boundary $\Gamma^\#$ in the medium $\Omega_+^\#$ coming from $y \rightarrow +\infty$. With this setting in mind, the computation of the scattering field requires the use of a translation of the solution, splitting the total pressure field U in two parts: the incident pressure U^{inc} , and the scattering field U^s .

Translation of the solution

If the original unknown field U is translated with respect to the incident plane wave field, the scattering field can be defined by $\tilde{U}^s = U - U^{\text{inc}}$ in $\Omega_+^\#$. This translation of the solution does not affect the Helmholtz equation since the plane wave U^{inc} is also a solution of the Helmholtz equation in $\Omega_+^\#$. Hence, it holds

$$\Delta \tilde{U}^s + (k^+)^2 \tilde{U}^s = 0 \quad \text{in } \Omega_+^\#.$$

However, the use of the same translation in $\Omega_-^\#$ would introduce a non-null source term (right-hand side) in the Helmholtz equation, which could have a non compact support in $\Omega_-^\#$, and potentially could cause some drawbacks from a computational point of view, and difficult an adequate writing of the radiation boundary conditions at $y \rightarrow -\infty$. To avoid this kind of issues, the incident plane wave is going to be replaced by a windowed version, this is,

$$U_W^{\text{inc}}(x, y) = e^{i(\alpha^+ x - \beta^+ y)} W(y, a, b),$$

where W is the window function, such that $W(y, a, b)$ is equal to the function $S(y, a, b)$ defined in (4.6) if $a \geq y \geq b$, $W(y, a, b) = 1$ if $y > a$, and $W(y, a, b) = 0$ if $y < b$. In this manner, the plane wave expression remains unmodified in $\Omega_+^\#$, whereas it will be windowed in $\Omega_-^\#$ once it is settled that lines $y = a$ and $y = b$ does not intersect the coupling boundary $\Gamma^\#$. Consequently, using this new windowed expression for U_W^{inc} , the plane wave expression is not modified in $\Omega_+^\#$, and the associated source term f_{inc} has compact support in $\Omega_-^\#$ (located in the half-plane $y > b$).

Now, taking into account that the windowed incident field U_W^{inc} is quasi-periodic, the translated quasi-periodic problem is stated as follows: Given a quasi-periodic length L , and a constant factor α , find a quasi-periodic scattering function \tilde{U}^s , such that it holds

$$\begin{aligned} \Delta \tilde{U}^s + k^2 \tilde{U}^s &= f_{\text{inc}} \quad \text{in } \Omega^\#, \\ \tilde{U}^s(L/2, y) &= \tilde{U}^s(-L/2, y) e^{i\alpha L}, \quad \text{with } (x, y) \in \Omega^\#, \\ &\& \text{radiation conditions} \quad \text{at } |y| \rightarrow +\infty, \end{aligned}$$

where the source term f_{inc} is a quasi-periodic function with compact support (which does not intersect $\Omega_+^\#$), and given by

$$f_{\text{inc}} = -\Delta U_W^{\text{inc}} - k^{+2} U_W^{\text{inc}}.$$

Obviously, the source term f_{inc} depends on the window function W (and subsequently, on parameters a and b). However, the accuracy of the numerical results will not be affected by the selection of this parameters if they are selected adequately to avoid boundary layers associated with a small value of $a - b$. Finally, the radiation conditions of the quasi-periodic problem can be written in terms of the Rayleigh expansions described in Equations (4.38) and (4.40). However, the use of a series expansion in combination with a standard finite element discretization of the quasi-periodic problem is not very suitable for its numerical approximation, since it would involve dense matrix computations (as in the classical Dirichlet-to-Neumann series approximations [85]). Instead using that numerical methodology, an equivalent periodic problem in combination with a Perfectly Matched Layer (PML) technique will be used, and described in the following sections.

Transformation into a periodic problem

From any quasi-periodic field, an associated periodic function can be defined as follows: the periodic scattering field U_{per} related to the quasi-periodic field \tilde{U}^s holds

$$\tilde{U}^s(x, y) = U_{\text{per}}(x, y) e^{i\alpha x}.$$

Replacing this expression of \tilde{U}^s in the Helmholtz equation, a new periodic formulation is obtained: Given a periodic length L , and a constant factor α , find a periodic scattering function U_{per} , such that it holds

$$\Delta U_{\text{per}} + 2i\alpha \frac{\partial U_{\text{per}}}{\partial x} + k^2 U_{\text{per}} = f_{\text{per}} \quad \text{in } \Omega^\#, \quad (4.C.1)$$

$$U_{\text{per}}(L/2, y) = U_{\text{per}}(-L/2, y), \quad \text{with } (x, y) \in \Omega^\#, \quad (4.C.2)$$

$$\& \text{ periodic radiation conditions} \quad \text{at } |y| \rightarrow +\infty, \quad (4.C.3)$$

where $f_{\text{per}}(x, y) = f_{\text{inc}}(x, y)e^{-i\alpha x}$ is a periodic function. The last aspect of the formulation written above which should be addressed before having a complete suitable formulation for a standard numerical treatment consists in the unbounded character of the domain $\Omega^\#$. More precisely, the periodic radiation conditions will be replaced by other conditions, which will be stated in a bounded computational domain. With this purpose, the Perfectly Matched Layers technique will be used to truncate the original unbounded domain $\Omega^\#$. The PML layers mimic the radiation boundary conditions within some additional absorbing layers, which will damp the solution as soon as the waves are reaching the exterior boundary of the truncated computational domain.

Perfectly Matched Layers

The main idea to introduce the governing equation associated with the Perfectly Matched Layers consists in the use of a complex-valued stretching of variables to replace the original spatial coordinates by some new complex-valued expressions, which will ensure the absorbing behavior of the Helmholtz solution inside the PML layers. With this goal, the unbounded physical domain is truncated at boundaries $y = -l$ (at the bottom of the computational domain), and $y = l$ (at the top of the computational domain), with $l > 0$, and consequently, two PML layers will be placed on the top and bottom of this truncated physical domain, which will be again denoted by $\Omega^\#$ abusing on the notation. The bottom and top PML layers are respectively located at $(-L/2, L/2) \times (-l - \delta, -l)$, and $(-L/2, L/2) \times (l, l + \delta)$, being δ the PML thickness.

Since both top and bottom PML layers should absorb the outgoing waves generated by the reflection and transmission phenomena on the coupling interface $\Gamma^\#$ and hence, to mimic the radiation conditions at $|y| \rightarrow \infty$, given by the series expansion (4.38) and (4.40), then the complex-valued stretching of y -coordinate should ensure an exponential decay not only on the propagative waves of form $e^{i(\alpha_n^\pm x \pm \beta_n^\pm y)}$ with $\beta_n^\pm \in \mathbb{R}$ in $\Omega_\pm^\#$, but also the evanescent waves $e^{i(\alpha_n^\pm x \pm \beta_n^\pm y)}$ with $\beta_n^\pm \in \mathbb{C}$, $\text{Im}\beta_n^\pm > 0$ in $\Omega_\pm^\#$. For that purpose, following the unbounded complex-valued profile designed in [28] for free-field problems and later adapted to the quasi-periodic problems in [156], the PML complex-valued variable $\hat{y}(y)$ is defined by

$$\hat{y}(y) = \begin{cases} y & \text{if } l \geq |y|, \\ \frac{1+i}{k} \int_l^{|y|} \frac{1}{l+\delta-s} ds & \text{if } l < |y| \leq l + \delta. \end{cases}$$

In this manner, the PML is designed such that the solution is expected to be null in the exterior top and bottom boundaries of the truncated bounded domain $\Omega_B^\# = (-L/2, L/2) \times (-l - \delta, l + \delta)$. Consequently, formally replacing the y -derivatives by \hat{y} -derivatives, the periodic problem (4.C.1)-(4.C.3) is transformed into an equivalent problem:

$$\frac{\partial}{\partial x} \left(\gamma \frac{\partial}{\partial x} U_{\text{pml}} \right) + \frac{\partial}{\partial y} \left(\frac{1}{\gamma} \frac{\partial}{\partial x} U_{\text{pml}} \right) + 2i\alpha\gamma \frac{\partial U_{\text{pml}}}{\partial x} + k^2 \gamma U_{\text{pml}} = \gamma f_{\text{per}} \quad \text{in } \Omega_B^\#, \quad (4.C.4)$$

$$U_{\text{pml}}(L/2, y) = U_{\text{pml}}(-L/2, y), \quad \text{for } y \in (-l - \delta, l + \delta), \quad (4.C.5)$$

$$U_{\text{pml}}(x, -l - \delta) = 0, \quad U_{\text{pml}}(x, l + \delta) = 0, \quad \text{for } x \in (-L/2, L/2), \quad (4.C.6)$$

where

$$\gamma(y) = \frac{d\hat{y}}{dy}(y) = \begin{cases} 1 & \text{if } l \geq |y|, \\ \frac{1+i}{k} \frac{1}{l+\delta-|y|} & \text{if } l < |y| \leq l + \delta. \end{cases}$$

Due to the unbounded character of the complex-valued stretching of variable \hat{y} is possible to show that $U_{\text{pml}} = U_{\text{per}}$ in $(-L/2, L/2) \times (-l, l)$ (see [28, 156] for a detailed discussion).

4.C.2 Variational formulation

Once the equivalent periodic problem has been stated in the unbounded domain $\Omega_B^\#$, an adequate weighted Sobolev space should be considered to write properly the associated weak problem. With this goal, the solution of the weak problem will be computed in

$$V = \left\{ v \in H_{\text{per}}^1(\Omega_B^\#) : \|v\|_V^2 = \int_{\Omega_B^\#} |\gamma| \left| \frac{\partial v}{\partial x} \right|^2 dS + \int_{\Omega_B^\#} \frac{1}{|\gamma|} \left| \frac{\partial v}{\partial y} \right|^2 dS + \int_{\Omega_B^\#} |\gamma| |v|^2 dS < \infty, \right\},$$

where $H_{\text{per}}^1(\Omega_B^\#)$ denotes the closure of the y -periodic C^∞ -functions with respect to the standard H^1 -norm. An asymptotic analysis of those functions belonging to V (see [27]) shown that $U_{\text{pml}} = 0$ on the exterior boundaries of the PML layers located at $|y| = l + \delta$, where the weight $|\gamma(y)| \rightarrow \infty$ when $|y|$ tends to $l + \delta$.

Hence, using a standard Green's formula argument, the variational problem associated to the PML formulation (4.C.4)-(4.C.6) is written as follows: Given a piecewise constant wave number k , a constant α , and a source term $f_{\text{per}} \in L^2(\Omega_B^\#)$, find $U_{\text{pml}} \in V$ such that it holds

$$\int_{\Omega_B^\#} \gamma \frac{\partial U_{\text{pml}}}{\partial x} \frac{\partial \bar{v}}{\partial x} dS + \int_{\Omega_B^\#} \frac{1}{\gamma} \frac{\partial U_{\text{pml}}}{\partial y} \frac{\partial \bar{v}}{\partial y} dS - k^2 \int_{\Omega_B^\#} \gamma U_{\text{pml}} \bar{v} dS = \int_{\Omega_B^\#} f_{\text{per}} \bar{v} dS, \quad (4.C.7)$$

for all $v \in V$. Notice that since the windowed source term f_{per} is null inside the PML layers by definition, so the factor γ in the right-hand side can be removed and consequently, it is not required to include further assumptions different to $f_{\text{per}} \in L^2(\Omega_B^\#)$.

4.C.3 Finite element discretization

Since functional space V is a subspace of $H_{\text{per}}^1(\Omega_B^\#)$, a standard finite element discretization can be utilized to compute a numerical approximation of the variational problem (4.C.7). With this aim, a triangular mesh \mathcal{T}_h has been used, which is conformal with the coupling boundary $\Gamma^\#$, and the inner boundaries of the PML layers located on $|y| = l$. The finite element solution U_h belongs to the discrete space of piecewise linear continuous functions, that is,

$$V_h = \{v \in C_{\text{per}}^0(\Omega_B^\#) : v|_T \in \mathbb{P}^1(\mathbb{C}), \forall T \in \mathcal{T}_h, v(x, l+\delta) = v(x, -l-\delta) = 0, x \in (-L/2, L/2)\},$$

where $C_{\text{per}}^0(\Omega_B^\#)$ is the space of the y -periodic continuous functions (with period L). Consequently, the discrete problem is written as follows: Given a piecewise constant wave number k , a constant α , and a source term $f_{\text{per}} \in L^2(\Omega_B^\#)$, find $U_h \in V_h$ such that it holds

$$\int_{\Omega_B^\#} \gamma \frac{\partial U_h}{\partial x} \frac{\partial \bar{v}_h}{\partial x} dS + \int_{\Omega_B^\#} \frac{1}{\gamma} \frac{\partial U_h}{\partial y} \frac{\partial \bar{v}_h}{\partial y} dS - k^2 \int_{\Omega_B^\#} \gamma U_h \bar{v}_h dS = \int_{\Omega_B^\#} f_{\text{per}} \bar{v}_h dS,$$

for all $v_h \in V_h$. To deal with the numerical integration of those integrals involving the singular weight γ , a quadrature rule with 12 points (see [170]) has been used to ensure an exact integration on sixth-order polynomials, which also avoids the evaluation of the integrands at the quadrature nodes placed on the exterior boundaries of the PML layers (where γ is singular). Finally, all the numerical results showed in the sections above used the PML setting $\delta = 1$, $l = 12$ and the windowed function $W(y, a, b)$ has been considered with parameters $a = -7$, $b = -10$.

Part III

Characterization of complex systems using time-dependent problems

Chapter 5

Characterization of porous materials using alpha cabins

Contents

5.1	Introduction	221
5.2	Methodology based on modal computations	222
5.2.1	Displacement formulation with rigid walls	222
5.2.2	Displacement formulation with absorbing boundaries	226
5.2.3	Displacement formulation with absorbing boundaries and porous sample	230
5.2.4	Finite element discretization	233
5.3	Methodology based on a full time-dependent discretization	237
5.3.1	Finite element discretization	239
5.4	Computation of the absorption values in an alpha cabin	241
5.4.1	Computation of the reverberation time	241
5.4.2	Computation of the absorption value	243
5.4.3	Computation of decay rates	244
5.5	Numerical results	245
5.5.1	Two-dimensional simulations	245
5.5.2	Three-dimensional simulation	251
5.6	Conclusions	254

5.1 Introduction

In the automotive industry, the effect of sound-absorbing or soundproofing materials is highly relevant. The more widespread procedure to measure the absorption coefficient of a material is the Kundt's tube, following the standard ISO 10534-2 [1]. This methodology allows us to compute the absorption coefficient at normal incidence, but this is not a realistic scenario in automotive acoustics because, in general, noise arrives from every direction. Although it is possible to compute the absorption coefficient at diffuse field by using impedance tube data [119], the best-known technique to compute the absorption coefficient at diffuse field is the reverberation room method [15, 109, 132, 166, 167]. The sound absorption coefficient of a porous material in the automotive industry is often computed in an alpha cabin [18, 130, 145], which is a small-size reverberation room where the frequency range and the sample size is adapted to the requirements of the automotive acoustics.

Although a standard for computing the absorption coefficient in an alpha cabin is not available, there exist different measurement setups for computing it in reverberation rooms, such as the described in the ISO 354:2003 standard [2] or the ASTM C423-09 standard [50]. The absorption coefficient in a reverberation room is determined by measuring the change in the reverberation time due to the placement of a sample of the material in the cabin. There exist several expressions showing the relation between the reverberation time in a room, and the sound absorption of a sample located in this room [66], such as the Sabine [160], Eyring [74], or Millington [127] formulas. Then, the absorption coefficient of a porous sample can be easily computed by measuring the reverberation time in the room with the material under study, and after, the reverberation time in the empty room. Applying one of the above-mentioned formulas, it is easy to compute the absorption coefficient of the porous sample.

The main goal of this chapter consists of the detailed description of numerical procedures to compute the absorption value at diffuse field associated with porous or fibrous materials measured in an alpha cabin. Through this chapter, different approaches to compute the absorption coefficient of a porous material in an alpha cabin, have been studied. In Section 5.2, an analysis of different mathematical models that govern the behavior of the sound field in the cabin is shown. The source and spectral problems have been described, and their variational and matrix formulations are discussed. Moreover, a numerical methodology to solve a time-dependent problem based on the computation of the decay modes of the cabin is described. Since this numerical approach does not allow us to obtain accurate results, a new numerical methodology based on full time-dependent discretization is described in Section 5.3. In Section 5.4, the different existing approaches to compute the absorption values in a reverberation room are shown, discussing the advantages and disadvantages of each one to compute the reverberation time and the absorption value in an alpha cabin. Section 5.5 is devoted to performing simulations in two-dimensional and three-dimensional domains. In Section 5.5.1, a simple rectangular domain has been considered, and some manufactured experimental data have been used to validate the methodology. Then, a real-world fibrous material has been used to illustrate that it has been possible to obtain numerical results

qualitatively similar to those reported by the experimental data. In Section 5.5.2, some three-dimensional simulations have been performed with a real fibrous material, considering as experimental data the absorption coefficient of the material measured in the alpha cabin. Finally, in Section 5.6, some remarks about the obtained results and the proposed methodology are given.

5.2 Methodology based on modal computations

To compute the absorption coefficient in an alpha cabin, it is essential to describe the behavior of the sound field inside the cabin. In this section, different mathematical models are analyzed to choose the most suitable one, which governs the behavior of the sound field in an alpha cabin. Problems are described considering a generic domain Ω . The variational formulation of each problem is described, and the time-dependent problems are solved by using a modal approximation.

5.2.1 Displacement formulation with rigid walls

First, all the boundaries in the domain are supposed rigid. Let us consider Ω the fluid domain (air in this case). This domain has two disjoint boundaries, that is, $\Omega = \Gamma_L \cup \Gamma_N$, where Γ_L is the boundary where the acoustic source is located, and Γ_N is the rest of the boundaries. Figure 5.1 shows a scheme of this domain. A rigid wall condition is imposed on Γ_N to model the behavior of the boundaries that are insensitive to the movement exerted inside the domain. Then, the source problem, written in terms of the displacement field, consists in, given $\omega > 0$, finding the complex-valued displacement field \mathbf{U} such that

$$\left\{ \begin{array}{l} -\rho_F c_F^2 \nabla(\operatorname{div} \mathbf{U}) - \omega^2 \rho_F \mathbf{U} = \mathbf{0} \quad \text{in } \Omega, \\ \mathbf{U} \cdot \mathbf{n} = 0 \quad \text{on } \Gamma_N, \\ -\rho_F c_F^2 \operatorname{div} \mathbf{U} = g \quad \text{on } \Gamma_L, \end{array} \right. \quad (5.1)$$

where ρ_F and c_F are the mass density and the sound speed of the air, respectively, g is the pressure applied on the boundary where the acoustic source is located, \mathbf{v} is the unit normal vector to the interface Γ_L pointing inwards Ω , and \mathbf{n} is the unit normal vector to the interface Γ_N pointing outwards Ω . From the time-harmonic assumption, the time-dependent displacement field is given by

$$\mathbf{u}(\mathbf{p}, t) = \operatorname{Re}(\mathbf{U}(\mathbf{p}) e^{i\omega t}),$$

where recall that now \mathbf{u} depends on the time variable t , but also the spatial position variable \mathbf{p} . Associated with the source problem (5.1), it is straightforward to write a linear spectral problem (in terms of $\lambda = \omega^2$), where the eigenvalues (resonances) and eigenfunctions (modes) can be computed. In this case, the spectral problem (with real-valued unknown fields) consists in finding a sequence of eigenpairs $(\lambda_k, \mathbf{U}^k)$, $\mathbf{U}^k \neq \mathbf{0}$, with $k \in \mathbb{N}$, and $\lambda_k > 0$

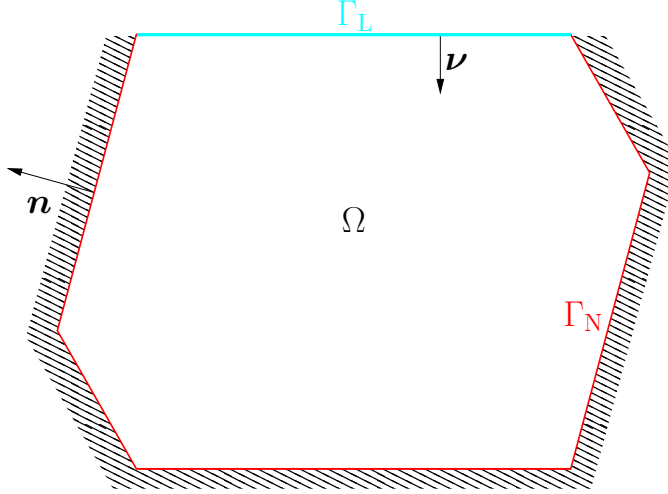


Figure 5.1: Scheme of a fluid domain (Ω), with one piston-like wall (Γ_L) highlighted in cyan, and rigid boundaries (Γ_N) highlighted in red.

such that

$$\begin{cases} -\rho_F c_F^2 \nabla(\operatorname{div} \mathbf{U}^k) - \lambda_k \rho_F \mathbf{U}^k = \mathbf{0} & \text{in } \Omega, \\ \mathbf{U}^k \cdot \mathbf{n} = 0 & \text{on } \Gamma_N, \\ -\rho_F c_F^2 \operatorname{div} \mathbf{U}^k = 0 & \text{on } \Gamma_L. \end{cases} \quad (5.2)$$

Variational formulation

Although the model with rigid boundaries is not suitable for reproducing the reverberation times in an alpha cabin, for the sake of completeness, the variational formulation of the source problem is included in this chapter. The variational formulation of the real-valued problem (5.1) is described as follows:

Given $\omega > 0$, and $g \in H^{-1/2}(\Gamma_L)$, find $\mathbf{U} \in \mathbf{H}_{\Gamma_N}(\operatorname{div}, \Omega)$, satisfying

$$\int_{\Omega} \rho_F c_F^2 \operatorname{div} \mathbf{U} \operatorname{div} \mathbf{W} dV - \omega^2 \int_{\Omega} \rho_F \mathbf{U} \cdot \mathbf{W} dV = \int_{\Gamma_L} g \mathbf{W} \cdot \mathbf{n} dS, \quad (5.3)$$

for all $\mathbf{W} \in \mathbf{H}_{\Gamma_N}(\operatorname{div}, \Omega)$, being

$$\mathbf{H}(\operatorname{div}, \Omega) = \left\{ \mathbf{W} \in (\operatorname{L}^2(\Omega))^2 : \operatorname{div} \mathbf{W} \in \operatorname{L}^2(\Omega) \right\}, \quad (5.4)$$

$$\mathbf{H}_{\Gamma_N}(\operatorname{div}, \Omega) = \left\{ \mathbf{W} \in \mathbf{H}(\operatorname{div}, \Omega) : \mathbf{W} \cdot \mathbf{n} = 0 \text{ on } \Gamma_N \right\}, \quad (5.5)$$

and $\operatorname{L}^2(\Omega)$ the space of measurable functions whose root mean square is finite. Moreover, if γ is the trace operator $\gamma : \operatorname{H}^1(\Omega) \rightarrow \operatorname{L}^2(\partial\Omega)$, it can be defined

$$\operatorname{H}^{1/2}(\partial\Omega) = \{W \in \operatorname{L}^2(\partial\Omega) : \exists V \in \operatorname{H}^1(\Omega) \text{ with } V = \gamma(W)\},$$

and $H^{-1/2}(\partial\Omega)$ its dual space, where

$$H^1(\Omega) = \{W \in L^2(\Omega) : \nabla W \in (L^2(\Omega))^2\}.$$

The variational formulation of the spectral problem (5.2) is given by:

Find a sequence of eigenpairs $(\lambda_k, \mathbf{U}^k)$, $\mathbf{U}^k \neq \mathbf{0}$, with $k \in \mathbb{N}$, $\lambda_k > 0$ and $\mathbf{U}^k \in \mathbf{H}_{\Gamma_N}(\text{div}, \Omega)$ such that

$$\int_{\Omega} \rho_F c_F^2 \operatorname{div} \mathbf{U}^k \operatorname{div} \mathbf{W}^k dV = \lambda_k \int_{\Omega} \rho_F \mathbf{U}^k \cdot \mathbf{W}^k dV, \quad (5.6)$$

for all $\mathbf{W}^k \in \mathbf{H}_{\Gamma_N}(\text{div}, \Omega)$.

The classical Fredholm's alternative theorem guarantees the existence and uniqueness of a solution of the above weak problem (see, for instance, [38]).

Computation of the time-dependent solution by a modal approximation

The calculation of the approximated solution of time-dependent problems requires to deal with spatial and time discretizations. Any time-marching scheme has implicitly errors coming from the dissipation and the dispersion phenomena, inherited from the discretization of the time derivatives. To avoid these kinds of errors and reproduce accurate solutions, even at middle-frequency regimes, a modal approximation has been used to represent the solution of the time-dependent problem.

Firstly, the time-dependent system of equations which governs the displacement field \mathbf{u} in the domain Ω with rigid boundaries, in the interval $[0, T]$, is given as follows:

$$\left\{ \begin{array}{lcl} \rho_F \ddot{\mathbf{u}} - \rho_F c_F^2 \nabla(\operatorname{div} \mathbf{u}) & = & \mathbf{0} \quad \text{in } \Omega \times [0, T], \\ \mathbf{u} \cdot \mathbf{n} & = & 0 \quad \text{on } \Gamma_N \times [0, T], \\ -\rho_F c_F^2 \operatorname{div} \mathbf{u} & = & 0 \quad \text{on } \Gamma_L \times [0, T], \\ \mathbf{u}(\cdot, 0) & = & \mathbf{u}_0 \quad \text{in } \Omega, \\ \dot{\mathbf{u}}(\cdot, 0) & = & \mathbf{v}_0 \quad \text{in } \Omega, \end{array} \right. \quad (5.7)$$

where $\dot{\mathbf{u}} = \frac{\partial}{\partial t} \mathbf{u}$, $\ddot{\mathbf{u}} = \frac{\partial^2}{\partial t^2} \mathbf{u}$, and \mathbf{u}_0 and \mathbf{v}_0 are the displacement and the velocity field at the initial state. Since the field values of this initial state are generated by the action of the acoustic source, both fields are given by

$$\mathbf{u}_0(\mathbf{p}) = \operatorname{Re}(\mathbf{U}(\mathbf{p})e^{i\omega t})|_{t=0}, \quad \mathbf{v}_0(\mathbf{p}) = \frac{\partial}{\partial t} \operatorname{Re}(\mathbf{U}(\mathbf{p})e^{i\omega t})|_{t=0}, \quad (5.8)$$

where \mathbf{U} is the complex-valued displacement field solution of (5.1). The system of equations written above is the time-dependent version of that one introduced in (5.1) under the time-harmonic assumption and considering that the acoustic source is not active. Due to this relation between both problems, it is straightforward to combine a modal expansion (based on the eigenvalues of the spectral problem (5.2)), to obtain an accurate approximation of the solution of the time-dependent problem.

Since the set of eigenmodes $\{\mathbf{U}^k\}_{k \in \mathbb{N}}$ is a Hilbert basis in $L^2(\Omega)$ [89], hence any solution of the model problem (5.1) can be accurately approximated by a finite (truncated) series of N modes, this is,

$$\tilde{\mathbf{U}}(\mathbf{p}) = \sum_{k=1}^N \tilde{u}_k \mathbf{U}^k(\mathbf{p}).$$

Since $\{\mathbf{U}^k\}_{k=1}^N$ is an orthonormal basis with respect to the $L^2(\Omega)$ -inner product, it is easy to show that the projection of \mathbf{U} in the discrete modal basis $\{\mathbf{U}^k\}_{k=1}^N$ is given by $\tilde{u}_k = \langle \mathbf{U}, \mathbf{U}^k \rangle$, where $\langle \cdot, \cdot \rangle$ denotes the $L^2(\Omega)$ -inner product. Hence, the mode expansion results

$$\tilde{\mathbf{U}}(\mathbf{p}) = \sum_{k=1}^N \langle \mathbf{U}, \mathbf{U}^k \rangle \mathbf{U}^k(\mathbf{p}). \quad (5.9)$$

Now, if it is assumed a fixed time (which can be identified as the origin of the time axis $t = 0$), the displacement and the velocity field can be written in terms of the real part of (5.9), following the same statement used in (5.8), i.e., the real-valued displacement and velocity field, at the initial time $t = 0$, are given by

$$\mathbf{u}(\mathbf{p}, 0) = \operatorname{Re}(\tilde{\mathbf{U}}(\mathbf{p}) e^{i\omega t})|_{t=0} = \operatorname{Re}(\tilde{\mathbf{U}}(\mathbf{p})), \quad (5.10)$$

$$\dot{\mathbf{u}}(\mathbf{p}, 0) = \frac{\partial}{\partial t} \operatorname{Re}(\tilde{\mathbf{U}}(\mathbf{p}) e^{i\omega t})|_{t=0} = \operatorname{Re}(i\omega \tilde{\mathbf{U}}(\mathbf{p})). \quad (5.11)$$

Therefore, the time-evolution of the displacement field \mathbf{u} , in absent of volumetric or surface sources, can be written in terms of the time evolution of a modal expansion with eigenfrequencies $\pm\omega_k = \pm\sqrt{\lambda_k}$:

$$\mathbf{u}(\mathbf{p}, t) = \operatorname{Re} \left(\sum_{k=1}^N (a_k e^{i\omega_k t} + b_k e^{-i\omega_k t}) \mathbf{U}^k(\mathbf{p}) \right).$$

Once the initial conditions (5.10)-(5.11) are imposed to determine the modal coefficients a_k and b_k , inserting (5.9) in their expressions, it holds

$$\begin{aligned} \mathbf{u}(\mathbf{p}, 0) &= \operatorname{Re} \left(\sum_{k=1}^N (a_k + b_k) \mathbf{U}^k(\mathbf{p}) \right) = \operatorname{Re} \left(\sum_{k=1}^N \langle \mathbf{U}, \mathbf{U}^k \rangle \mathbf{U}^k(\mathbf{p}) \right), \\ \dot{\mathbf{u}}(\mathbf{p}, 0) &= \operatorname{Re} \left(\sum_{k=1}^N i\omega_k (a_k - b_k) \mathbf{U}^k(\mathbf{p}) \right) = \operatorname{Re} \left(i\omega \sum_{k=1}^N \langle \mathbf{U}, \mathbf{U}^k \rangle \mathbf{U}^k(\mathbf{p}) \right). \end{aligned}$$

Applying again the orthonormal character of the modal basis $\{\mathbf{U}^k\}_{k=1}^N$, and the fact that the modes are real-valued, it is obtained

$$a_k = \frac{1}{2} \left(1 + \frac{\omega}{\omega_k} \right) \langle \mathbf{U}, \mathbf{U}^k \rangle, \quad b_k = \frac{1}{2} \left(1 - \frac{\omega}{\omega_k} \right) \langle \mathbf{U}, \mathbf{U}^k \rangle,$$

and so, the time-dependent solution for the displacement field \mathbf{u} in (5.7) is given by

$$\begin{aligned}\mathbf{u}(\mathbf{p}, t) &= \operatorname{Re} \left(\sum_{k=1}^N \left(\frac{1}{2} \left(1 + \frac{\omega}{\omega_k} \right) e^{i\omega_k t} + \frac{1}{2} \left(1 - \frac{\omega}{\omega_k} \right) e^{-i\omega_k t} \right) \langle \mathbf{U}, \mathbf{U}^k \rangle \mathbf{U}^k(\mathbf{p}) \right) \\ &= \operatorname{Re} \left(\sum_{k=1}^N \left(\cos(\omega_k t) + i \frac{\omega}{\omega_k} \sin(\omega_k t) \right) \langle \mathbf{U}, \mathbf{U}^k \rangle \mathbf{U}^k(\mathbf{p}) \right).\end{aligned}\quad (5.12)$$

Since the spectral problem (5.2) has not any dissipative effect, the eigenmodes $\{\pm\omega_k\}_{k=1}^N$ are real-valued, and the magnitude of the displacement field \mathbf{u} does not decay along time. Consequently, the field displacement given by the expansion (5.12) is not adequate to reproduce reverberation times in an alpha cabin because, from a numerical point of view, an exponential decay on the intensity field is expected.

5.2.2 Displacement formulation with absorbing boundaries

Now, some boundaries are assumed almost rigid; this is, there exist some dissipation effects. In this case, the boundaries that have dissipation effects have associated a surface impedance, using the most simple model available in the scientific literature (see, for instance, [25]).

In this case, let us consider Ω the fluid domain. This domain has three disjoint boundaries, that is, $\Omega = \Gamma_L \cup \Gamma_V \cup \Gamma_N$, where Γ_L is the boundary where the acoustic source is located, Γ_V are the boundaries with dissipation, and Γ_N are the rest of faces that are considered rigid (see Figure 5.2). A rigid wall condition is imposed on Γ_N since these boundaries are supposed rigid, and an impedance condition is imposed on Γ_V to simulate the dissipation effects. Again, the source problem in terms of the displacement field consists in, given $\omega > 0$, finding the complex-valued displacement field \mathbf{U} such that

$$\left\{ \begin{array}{ll} -\rho_F c_F^2 \nabla (\operatorname{div} \mathbf{U}) - \omega^2 \rho_F \mathbf{U} &= \mathbf{0} & \text{in } \Omega, \\ \mathbf{U} \cdot \mathbf{n} &= 0 & \text{on } \Gamma_N, \\ -\rho_F c_F^2 \operatorname{div} \mathbf{U} &= g & \text{on } \Gamma_L, \\ -\rho_F c_F^2 \operatorname{div} \mathbf{U} &= (\alpha_v + i\omega\beta_v) \mathbf{U} \cdot \mathbf{m} & \text{on } \Gamma_V, \end{array} \right. \quad (5.13)$$

where g is the pressure applied on the boundary where the acoustic source is located, $\alpha_v + i\omega\beta_v$ is the surface impedance associated with the absorbing boundaries, \mathbf{v} is the unit normal vector to the interface Γ_L pointing inwards Ω , \mathbf{n} is the unit normal vector to the interface Γ_N pointing outwards Ω , and \mathbf{m} is the unit normal vector to the interface Γ_V pointing outwards Ω .

Associated with the source problem (5.13), a quadratic spectral problem can be written in terms of $\sigma = i\omega$, where the eigenvalues (resonances) and eigenfunctions (modes) can be computed. In this case, the spectral problem (with again real-valued unknown fields) consists in finding a sequence of eigenpairs (σ_k, \mathbf{U}^k) , $\mathbf{U}^k \neq \mathbf{0}$, with $k \in \mathbb{N}$, and $\operatorname{Im}(\sigma_k) > 0$,

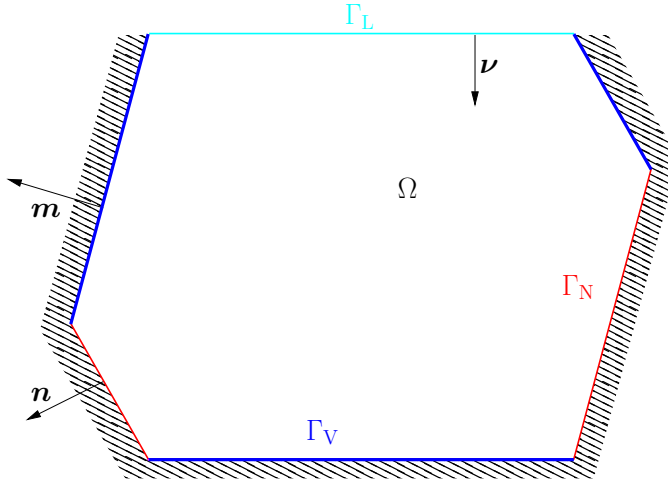


Figure 5.2: Scheme of a fluid domain (Ω), with one piston-like wall (Γ_L) highlighted in cyan, absorbing boundaries (Γ_V) highlighted in blue, and rigid walls boundaries (Γ_N) highlighted in red.

such that

$$\left\{ \begin{array}{ll} -\rho_F c_F^2 \nabla(\operatorname{div} \mathbf{U}^k) + \sigma_k^2 \rho_F \mathbf{U}^k &= \mathbf{0} & \text{in } \Omega, \\ \mathbf{U}^k \cdot \mathbf{n} &= 0 & \text{on } \Gamma_N, \\ -\rho_F c_F^2 \operatorname{div} \mathbf{U}^k &= 0 & \text{on } \Gamma_L, \\ -\rho_F c_F^2 \operatorname{div} \mathbf{U}^k &= (\alpha_v + \sigma_k \beta_v) \mathbf{U}^k \cdot \mathbf{m} & \text{on } \Gamma_V. \end{array} \right. \quad (5.14)$$

Notice that, since the spectral problem is quadratic, there exist two different alternatives to compute the eigenmodes: (a) to consider specific techniques to deal with the numerical solution of the quadratic eigenvalue problem, or (b) to introduce a new unknown $\mathbf{V}^k = \sigma_k \mathbf{U}^k$ to rewrite the quadratic problem employing a new linear spectral problem, with the double number of unknowns. If it is considered the second option, after dividing the first and third equations in (5.14) by σ_k , the formulation can be rewritten as follows:

Find a sequence of eigenpairs $(\sigma_k, (\mathbf{U}^k, \mathbf{V}^k))$, $(\mathbf{U}^k, \mathbf{V}^k) \neq (\mathbf{0}, \mathbf{0})$, with $k \in \mathbb{N}$ and $\operatorname{Im}(\sigma_k) > 0$ such that

$$\left\{ \begin{array}{ll} -\rho_F c_F^2 \nabla(\operatorname{div} \mathbf{U}^k) + \sigma_k \rho_F \mathbf{V}^k &= \mathbf{0} & \text{in } \Omega, \\ \rho_F \mathbf{V}^k &= \sigma_k \rho_F \mathbf{U}^k & \text{in } \Omega, \\ \mathbf{U}^k \cdot \mathbf{n} = 0, \mathbf{V}^k \cdot \mathbf{n} &= 0 & \text{on } \Gamma_N, \\ -\rho_F c_F^2 \operatorname{div} \mathbf{U}^k = 0, -\rho_F c_F^2 \operatorname{div} \mathbf{V}^k &= 0 & \text{on } \Gamma_L, \\ -\rho_F c_F^2 \operatorname{div} \mathbf{U}^k &= \alpha_v \mathbf{U}^k \cdot \mathbf{m} + \beta_v \mathbf{V}^k \cdot \mathbf{m} & \text{on } \Gamma_V. \end{array} \right. \quad (5.15)$$

Variational formulation

Taking into account the functional spaces defined in (5.4) and (5.5), the weak formulation of the source problem (5.13) is stated as follows:

Given $\omega > 0$, $g \in H^{-1/2}(\Gamma_L)$, and $\alpha_v, \beta_v \in \mathbb{R}$ with positive values, find $\mathbf{U} \in \mathbf{H}_{\Gamma_N}(\text{div}, \Omega)$, satisfying

$$\begin{aligned} & \int_{\Omega} \rho_F c_F^2 \operatorname{div} \mathbf{U} \operatorname{div} \mathbf{W} dV + \int_{\Gamma_V} \alpha_v \mathbf{U} \cdot \mathbf{m} \mathbf{W} \cdot \mathbf{m} dS + i\omega \int_{\Gamma_V} \beta_v \mathbf{U} \cdot \mathbf{m} \mathbf{W} \cdot \mathbf{m} dS \\ & - \omega^2 \int_{\Omega} \rho_F \mathbf{U} \cdot \mathbf{W} dV = \int_{\Gamma_L} g \mathbf{W} \cdot \mathbf{n} dS, \end{aligned} \quad (5.16)$$

for all $\mathbf{W} \in \mathbf{H}_{\Gamma_N}(\text{div}, \Omega)$.

Now, the modified spectral problem (5.15) is linear. Since the partial differential equations have real-valued coefficients, considering the functional space defined in (5.5), it is straightforward to check that the eigenmodes satisfy the following variational formulation: Given $\alpha_v, \beta_v \in \mathbb{R}$ with positive values, find a sequence of eigenpairs $(\sigma_k, (\mathbf{U}^k, \mathbf{V}^k)) \in \mathbb{C} \times \mathbf{H}_{\Gamma_N}(\text{div}, \Omega) \times \mathbf{H}_{\Gamma_N}(\text{div}, \Omega)$, $(\mathbf{U}^k, \mathbf{V}^k) \neq (\mathbf{0}, \mathbf{0})$, with $k \in \mathbb{N}$, such that

$$\begin{aligned} & - \int_{\Omega} \rho_F c_F^2 \operatorname{div} \mathbf{U}^k \operatorname{div} \mathbf{W}^k dV + \int_{\Omega} \rho_F \mathbf{V}^k \cdot \mathbf{Z}^k dV - \int_{\Gamma_V} \alpha_v \mathbf{U}^k \cdot \mathbf{m} \mathbf{W}^k \cdot \mathbf{m} dS \\ & - \int_{\Gamma_V} \beta_v \mathbf{V}^k \cdot \mathbf{m} \mathbf{W}^k \cdot \mathbf{m} dS = \sigma_k \left(\int_{\Omega} \rho_F \mathbf{V}^k \cdot \mathbf{W}^k dV + \int_{\Omega} \rho_F \mathbf{U}^k \cdot \mathbf{Z}^k dV \right), \end{aligned} \quad (5.17)$$

for all $(\mathbf{W}^k, \mathbf{Z}^k) \in \mathbf{V}$, where $\mathbf{V} = \mathbf{H}_{\Gamma_N}(\text{div}, \Omega) \times \mathbf{H}_{\Gamma_N}(\text{div}, \Omega)$.

The proof of the existence and uniqueness of the solution of the above weak problem is given in [25].

Computation of the time-dependent solution by a modal approximation

As in Section 5.2.1, to avoid errors coming from the discretization of the time derivatives, a modal approximation has been used to represent the solution of the time-dependent problem. Firstly, the time-dependent system of equations which governs the displacement field inside a domain Ω with absorbing boundaries, in the interval $[0, T]$, is given as follows:

$$\left\{ \begin{array}{ll} \rho_F \dot{\mathbf{v}} - \rho_F c_F^2 \nabla(\operatorname{div} \mathbf{u}) &= \mathbf{0} & \text{in } \Omega \times [0, T], \\ \rho_F \mathbf{v} &= \rho_F \dot{\mathbf{u}} & \text{in } \Omega \times [0, T], \\ \mathbf{u} \cdot \mathbf{n} = 0, \mathbf{v} \cdot \mathbf{n} &= 0 & \text{on } \Gamma_N \times [0, T], \\ -\rho_F c_F^2 \operatorname{div} \mathbf{u} = 0, -\rho_F c_F^2 \operatorname{div} \mathbf{v} &= 0 & \text{on } \Gamma_L \times [0, T], \\ -\rho_F c_F^2 \operatorname{div} \mathbf{u} &= \alpha_v \mathbf{u} \cdot \mathbf{m} + \beta_v \mathbf{v} \cdot \mathbf{m} & \text{on } \Gamma_V \times [0, T], \\ \mathbf{u}(\cdot, 0) &= \mathbf{u}_0 & \text{in } \Omega, \\ \dot{\mathbf{u}}(\cdot, 0) &= \mathbf{v}_0 & \text{in } \Omega, \end{array} \right. \quad (5.18)$$

where \mathbf{u}_0 and \mathbf{v}_0 are the displacement and the velocity field at the initial state. Since the field values of this initial state are generated by the action of the acoustic source, both fields are given by (5.8). Obviously, the system of equations written above is the time-dependent version of that one introduced in (5.13), under the time-harmonic assumption and considering that the source is not active. Due to this relation between both problems,

it is straightforward to combine a modal expansion (based on the eigenvalues of the spectral problem (5.15)) to obtain an accurate approximation of the solution of the time-dependent problem.

Since the spectral problem (5.15) cannot be associated with a self-adjoint compact operator, it is not straightforward to show that the eigenmodes $\{(\mathbf{U}^k, \mathbf{V}^k)\}_{k \in \mathbb{N}}$ form a Hilbert basis in $L^2(\Omega) \times L^2(\Omega)$. Notice that, this set of eigenmodes includes not only $(\sigma_k, (\mathbf{U}^k, \mathbf{V}^k))$ but also its complex-conjugate pair $(\bar{\sigma}_k, (\bar{\mathbf{U}}^k, \bar{\mathbf{V}}^k))$.

However, it will be assumed that the solution of the source model problem (5.13) can be accurately approximated by a finite (truncated) series of N modes, this is,

$$\begin{pmatrix} \hat{\mathbf{U}}(\mathbf{p}) \\ \hat{\mathbf{V}}(\mathbf{p}) \end{pmatrix} = \begin{pmatrix} \hat{\mathbf{U}}(\mathbf{p}) \\ i\omega \hat{\mathbf{U}}(\mathbf{p}) \end{pmatrix} = \sum_{k=1}^N \hat{u}_k \begin{pmatrix} \mathbf{U}^k(\mathbf{p}) \\ \mathbf{V}^k(\mathbf{p}) \end{pmatrix}. \quad (5.19)$$

In this case, it is not possible to ensure that $\{(\mathbf{U}^k, \mathbf{V}^k)\}_{k=1}^N$ is an orthogonal basis with respect to the $L^2(\Omega) \times L^2(\Omega)$ -inner product. Consequently, to compute the basis coefficients $\vec{u} = (\hat{u}_k)_{k=1}^N$, it is necessary to compute the dense matrix linear system

$$A\vec{u} = \vec{f},$$

where the matrix coefficients, and the coefficients of the right-hand side are given by

$$\begin{aligned} A_{kl} &= \langle \mathbf{U}^k, \mathbf{U}^l \rangle + \langle \mathbf{V}^k, \mathbf{V}^l \rangle = (1 + \sigma_k \bar{\sigma}_l) \langle \mathbf{U}^k, \mathbf{U}^l \rangle, \\ [\vec{f}]_k &= \langle \mathbf{U}, \mathbf{U}^k \rangle + i\omega \langle \mathbf{U}, \mathbf{V}^k \rangle = (1 + i\omega \bar{\sigma}_k) \langle \mathbf{U}, \mathbf{U}^k \rangle, \end{aligned}$$

and $[\vec{u}]_k = \hat{u}_k$ for $1 \leq k, l \leq N$. Now, if a fixed time is assumed (which can be identified as the origin of the time axis $t = 0$), the displacement and the velocity field can be written in terms of the real part of (5.19), i.e., the real-valued displacement and velocity field, at the initial time $t = 0$, are given by

$$\mathbf{u}(\mathbf{p}, 0) = \operatorname{Re}(\mathbf{U}(\mathbf{p})e^{-i\omega t})|_{t=0} = \operatorname{Re}(\mathbf{U}(\mathbf{p})), \quad (5.20)$$

$$\mathbf{v}(\mathbf{p}, 0) = \frac{\partial}{\partial t} \operatorname{Re}(\mathbf{U}(\mathbf{p})e^{-i\omega t})|_{t=0} = \operatorname{Re}(i\omega \mathbf{U}(\mathbf{p})). \quad (5.21)$$

Following the analogous assumption made for the truncated expansion in (5.19), the time-evolution of the displacement field, in absent of volumetric or surface sources, can be approximated in terms of the time evolution of a modal expansion:

$$\begin{aligned} \hat{\mathbf{u}}(\mathbf{p}, t) &= \operatorname{Re} \left(\sum_{k=1}^N \hat{u}_k e^{\sigma_k t} \mathbf{U}^k(\mathbf{p}) \right), \\ \hat{\mathbf{v}}(\mathbf{p}, t) &= \operatorname{Re} \left(\sum_{k=1}^N \hat{u}_k e^{\sigma_k t} \mathbf{V}^k(\mathbf{p}) \right) = \operatorname{Re} \left(\sum_{k=1}^N \hat{u}_k \sigma_k e^{\sigma_k t} \mathbf{U}^k(\mathbf{p}) \right). \end{aligned} \quad (5.22)$$

Due to (5.19), the initial conditions (5.20)-(5.21) are approximated by their corresponding truncated modal expansion $\hat{\mathbf{u}}(\mathbf{p}, t) = \text{Re}(\hat{\mathbf{U}}(\mathbf{p}))$ and $\hat{\mathbf{v}}(\mathbf{p}, t) = \text{Re}(\hat{\mathbf{V}}(\mathbf{p})) = \text{Re}(i\omega \hat{\mathbf{U}}(\mathbf{p}))$.

Now, since the spectral problem (5.15) takes into account the dissipative effects due to the absorbing boundaries, the eigenvalues σ_k are complex-valued, and what is essential, the real part of σ_k is negative, and hence, the magnitude of the displacement field \mathbf{u} , solution of (5.18), and its associated pressure field will decay along time.

5.2.3 Displacement formulation with absorbing boundaries and porous sample

Now, in order to compute the reverberation time in a domain with a sample of porous material, some boundaries are assumed absorbent, with an associated surface impedance, and the sample is located on another boundary. That is, let us consider Ω the fluid domain (air in this case). This domain has four disjoint boundaries, that is, $\Omega = \Gamma_L \cup \Gamma_V \cup \Gamma_I \cup \Gamma_N$ where Γ_L is the boundary where the acoustic source is located, Γ_V are the absorbing boundaries, Γ_I is the boundary where the porous sample is located, and Γ_N are the rest of faces that are considered rigid (see Figure 5.3). A rigid wall condition is imposed on Γ_N since these boundaries are supposed rigid, an impedance condition is imposed on Γ_V to simulate the dissipation effects, and in order to reproduce the absorbing behavior of the sample, an impedance condition is imposed on Γ_I . Then, the source problem can be written in terms of the displacement field as follows: Given $\omega > 0$, find the complex-valued displacement field \mathbf{U} such that:

$$\left\{ \begin{array}{ll} -\rho_F c_F^2 \nabla (\text{div } \mathbf{U}) - \omega^2 \rho_F \mathbf{U} &= \mathbf{0} & \text{in } \Omega, \\ \mathbf{U} \cdot \mathbf{n} &= 0 & \text{on } \Gamma_N, \\ -\rho_F c_F^2 \text{div } \mathbf{U} &= g & \text{on } \Gamma_L, \\ -\rho_F c_F^2 \text{div } \mathbf{U} &= (\alpha_v + i\omega\beta_v) \mathbf{U} \cdot \mathbf{m} & \text{on } \Gamma_V, \\ -\rho_F c_F^2 \text{div } \mathbf{U} &= (\alpha_s + i\omega\beta_s) \mathbf{U} \cdot \boldsymbol{\eta} & \text{on } \Gamma_I, \end{array} \right. \quad (5.23)$$

where $\alpha_v + i\omega\beta_v$ is the surface impedance associated with the absorbing boundaries, $\alpha_s + i\omega\beta_s$ is the surface impedance associated with the sample (obtained by fitting the experimental data with those computed with the impedance tube method [1]), g is the pressure applied on the boundary where the source is located, $\boldsymbol{\nu}$ is the unit normal vector to the interface Γ_L pointing inwards Ω , \mathbf{n} is the unit normal vector to the interface Γ_N pointing outwards Ω , \mathbf{m} is the unit normal vector to the interface Γ_V pointing outwards Ω and $\boldsymbol{\eta}$ is the unit normal vector to the interface Γ_I pointing inwards Ω .

Associated with the source problem (5.23), it can be written a linear eigenvalue problem: *Find a sequence of eigenpairs $(\sigma_k, (\mathbf{U}^k, \mathbf{V}^k))$, $(\mathbf{U}^k, \mathbf{V}^k) \neq (\mathbf{0}, \mathbf{0})$ with $k \in \mathbb{N}$ and $\text{Im}(\sigma_k) > 0$*

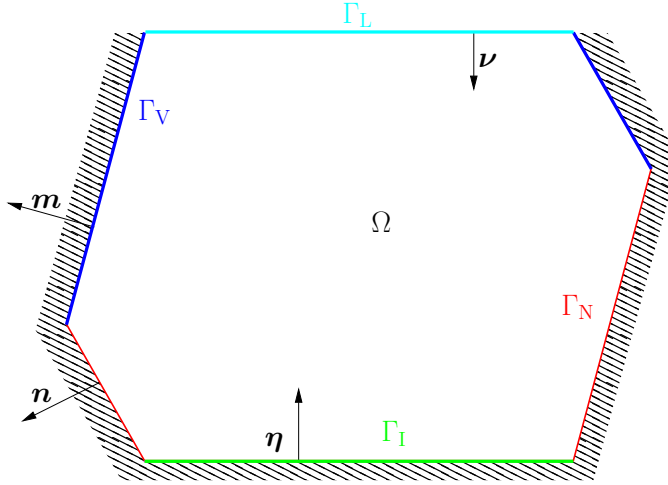


Figure 5.3: Scheme of a domain with a fluid in a cavity (Ω), with one piston-like wall (Γ_L) highlighted in cyan, absorbing boundaries (Γ_V) highlighted in blue, an absorbing sample (Γ_I) highlighted in green, and rigid boundaries (Γ_N) highlighted in red.

such that

$$\left\{ \begin{array}{ll} -\rho_F c_F^2 \nabla (\operatorname{div} \mathbf{U}^k) + \sigma_j \rho_F \mathbf{V}^k = \mathbf{0} & \text{in } \Omega, \\ \rho_F \mathbf{V}^k = \sigma_k \rho_F \mathbf{U}^k & \text{in } \Omega, \\ \mathbf{U}^k \cdot \mathbf{n} = 0, \mathbf{V}^k \cdot \mathbf{n} = 0 & \text{on } \Gamma_N, \\ -\rho_F c_F^2 \operatorname{div} \mathbf{U}^k = 0, -\rho_F c_F^2 \operatorname{div} \mathbf{V}^k = 0 & \text{on } \Gamma_L, \\ -\rho_F c_F^2 \operatorname{div} \mathbf{U}^k = \alpha_v \mathbf{U}^k \cdot \mathbf{m} + \beta_v \mathbf{V}^k \cdot \mathbf{m} & \text{on } \Gamma_V, \\ -\rho_F c_F^2 \operatorname{div} \mathbf{U}^k = \alpha_s \mathbf{U}^k \cdot \boldsymbol{\eta} + \beta_s \mathbf{V}^k \cdot \boldsymbol{\eta} & \text{on } \Gamma_I. \end{array} \right. \quad (5.24)$$

Variational formulation

The variational formulation of the source problem (5.23) is stated as follows:
Given $\omega > 0$, $g \in H^{-1/2}(\Gamma_L)$ and $\alpha_v, \beta_v, \alpha_s, \beta_s \in \mathbb{R}$ with positive values, find $\mathbf{U} \in \mathbf{H}_{\Gamma_N}(\operatorname{div}, \Omega)$, satisfying

$$\begin{aligned} & \int_{\Omega} \rho_F c_F^2 \operatorname{div} \mathbf{U} \operatorname{div} \mathbf{W} dV + \int_{\Gamma_V} \alpha_v \mathbf{U} \cdot \mathbf{m} \mathbf{W} \cdot \mathbf{m} dS + i\omega \int_{\Gamma_V} \beta_v \mathbf{U} \cdot \mathbf{m} \mathbf{W} \cdot \mathbf{m} dS \\ & + \int_{\Gamma_I} \alpha_s \mathbf{U} \cdot \boldsymbol{\eta} \mathbf{W} \cdot \boldsymbol{\eta} dS + i\omega \int_{\Gamma_I} \beta_s \mathbf{U} \cdot \boldsymbol{\eta} \mathbf{W} \cdot \boldsymbol{\eta} dS - \omega^2 \int_{\Omega} \rho_F \mathbf{U} \cdot \mathbf{W} dV = \int_{\Gamma_L} g \mathbf{W} \cdot \mathbf{n} dS, \end{aligned} \quad (5.25)$$

for all $\mathbf{W} \in \mathbf{H}_{\Gamma_N}(\operatorname{div}, \Omega)$.

Now, since the spectral problem (5.24) is linear, and the partial differential equations have real-valued coefficients, then it is straightforward to check that the eigenmodes satisfy the following variational formulation:

Given $\alpha_v, \beta_v, \alpha_s, \beta_s \in \mathbb{R}$ with positive values, find a sequence of eigenpairs $(\sigma_k, (\mathbf{U}^k, \mathbf{V}^k)) \in \mathbb{C} \times \mathbf{H}_{\Gamma_N}(\text{div}, \Omega) \times \mathbf{H}_{\Gamma_N}(\text{div}, \Omega)$, $(\mathbf{U}^k, \mathbf{V}^k) \neq (\mathbf{0}, \mathbf{0})$, with $k \in \mathbb{N}$, such that

$$\begin{aligned} & - \int_{\Omega} \rho_F c_F^2 \operatorname{div} \mathbf{U}^k \operatorname{div} \mathbf{W}^k dV + \int_{\Omega} \rho_F \mathbf{V}^k \cdot \mathbf{Z}^k dV - \int_{\Gamma_V} \alpha_v \mathbf{U}^k \cdot \mathbf{m} \mathbf{W}^k \cdot \mathbf{m} dS \\ & - \int_{\Gamma_V} \beta_v \mathbf{V}^k \cdot \mathbf{m} \mathbf{W}^k \cdot \mathbf{m} dS - \int_{\Gamma_I} \alpha_s \mathbf{U}^k \cdot \boldsymbol{\eta} \mathbf{W}^k \cdot \boldsymbol{\eta} dS - \int_{\Gamma_I} \beta_s \mathbf{V}^k \cdot \boldsymbol{\eta} \mathbf{W}^k \cdot \boldsymbol{\eta} dS \\ & = \sigma_k \left(\int_{\Omega} \rho_F \mathbf{V}^k \cdot \mathbf{W}^k dV + \int_{\Omega} \rho_F \mathbf{U}^k \cdot \mathbf{Z}^k dV \right), \end{aligned} \quad (5.26)$$

for all $(\mathbf{W}^k, \mathbf{Z}^k) \in \mathbf{V}$, where $\mathbf{V} = \mathbf{H}_{\Gamma_N}(\text{div}, \Omega) \times \mathbf{H}_{\Gamma_N}(\text{div}, \Omega)$.

The existence and uniqueness of the solution of this quadratic eigenvalue problem can be followed by applying similar arguments to those used in [25].

Computation of the time-dependent solution by a modal approximation

Firstly, the time-dependent system of equations which governs the displacement field in a domain with absorbing boundaries and an absorbing sample is given as follows:

$$\left\{ \begin{array}{rcl} \rho_F \dot{\mathbf{v}} - \rho_F c_F^2 \nabla(\operatorname{div} \mathbf{u}) & = & \mathbf{0} & \text{in } \Omega \times [0, T], \\ \rho_F \mathbf{v} & = & \rho_F \dot{\mathbf{u}} & \text{in } \Omega \times [0, T], \\ \mathbf{u} \cdot \mathbf{n} = 0, \mathbf{v} \cdot \mathbf{n} & = & 0 & \text{on } \Gamma_N \times [0, T], \\ -\rho_F c_F^2 \operatorname{div} \mathbf{u} = 0, -\rho_F c_F^2 \operatorname{div} \mathbf{v} & = & 0 & \text{on } \Gamma_L \times [0, T], \\ -\rho_F c_F^2 \operatorname{div} \mathbf{u} & = & \alpha_v \mathbf{u} \cdot \mathbf{m} + \beta_v \mathbf{v} \cdot \mathbf{m} & \text{on } \Gamma_V \times [0, T], \\ -\rho_F c_F^2 \operatorname{div} \mathbf{u} & = & \alpha_s \mathbf{u} \cdot \boldsymbol{\eta} + \beta_s \mathbf{v} \cdot \boldsymbol{\eta} & \text{on } \Gamma_I \times [0, T], \\ \mathbf{u}(\cdot, 0) & = & \mathbf{u}_0 & \text{in } \Omega, \\ \dot{\mathbf{u}}(\cdot, 0) & = & \mathbf{v}_0 & \text{in } \Omega, \end{array} \right.$$

where \mathbf{u}_0 and \mathbf{v}_0 are the displacement and the velocity field at the initial state. Since the field values of this initial state are generated by the action of the source, both fields are given by (5.8).

Following the analogous assumption made for the truncated expansion in (5.19), the time-evolution of the displacement field, in absent of volumetric or surface sources, can be approximated in terms of the time evolution of a modal expansion:

$$\begin{aligned} \hat{\mathbf{u}}(\mathbf{p}, t) &= \operatorname{Re} \left(\sum_{k=1}^N \hat{u}_k e^{\sigma_k t} \mathbf{U}^k(\mathbf{p}) \right), \\ \hat{\mathbf{v}}(\mathbf{p}, t) &= \operatorname{Re} \left(\sum_{k=1}^N \hat{u}_k e^{\sigma_k t} \mathbf{V}^k(\mathbf{p}) \right) = \operatorname{Re} \left(\sum_{k=1}^N \hat{u}_k \sigma_k e^{\sigma_k t} \mathbf{U}^k(\mathbf{p}) \right), \end{aligned}$$

where $\{(\sigma_k, (\mathbf{U}^k, \mathbf{V}^k))\}_{k=1}^N$ are the set of the eigenmodes computed in the spectral problem (5.24).

5.2.4 Finite element discretization

In this section, a finite element method is explained. This method was introduced by Raviart and Thomas [154] to solve those problems which are formulated in displacements, avoiding the spurious modes which appear in this kind of formulations (see [103] for more details). Also, the discrete and the matrix formulation of the three problems previously explained, are described.

Rigid walls

In order to approximate the fluid displacement $\mathbf{U} \in \mathbf{H}_{\Gamma_N}(\text{div}, \Omega)$ in Section 5.2.1, the lowest order Raviart-Thomas elements are used. These elements consist in vector valued functions such as, restricted to each tetrahedron, are incomplete linear polynomials of the form $\mathbf{u}_h(p_1, p_2, p_3) = (a + dp_1, b + dp_2, c + dp_3)$, $a, b, c, d \in \mathbb{C}$. Then the discrete Raviart-Thomas space is defined by

$$\begin{aligned} \mathbf{R}_h(\Omega) = \{ \mathbf{U}_h \in \mathbf{H}_{\Gamma_N}(\text{div}, \Omega) : \mathbf{U}_h|_T(p_1, p_2, p_3) &= (a + dp_1, b + dp_2, c + dp_3), \\ a, b, c, d \in \mathbb{C}, \forall T \in \mathcal{T}_h \}, \end{aligned} \quad (5.27)$$

where \mathcal{T}_h is a regular tetrahedral partition of Ω , that is, $\overline{\Omega} = \bigcup_{T \in \mathcal{T}_h} T$. These vector fields have constant normal components on each of the four faces of a tetrahedron (see Figure 5.4) which define a unique polynomial function of this type.

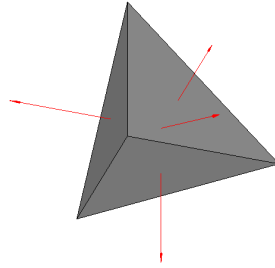


Figure 5.4: Raviart-Thomas finite element

Thus, the functional space $\mathbf{H}_{\Gamma_N}(\text{div}, \Omega)$ in (5.3) can be replaced in the discrete problem by $\mathbf{R}_h(\Omega)$. By using the finite element space (5.27), the approximation of the source problem (5.3) is defined by:

Given $\omega > 0$ and $g \in H^{-1/2}(\Gamma_L)$, find the displacement field $\mathbf{U}_h \in \mathbf{R}_h(\Omega)$, satisfying

$$\int_{\Omega} \rho_F c_F^2 \operatorname{div} \mathbf{U}_h \operatorname{div} \mathbf{W}_h \, dV - \omega^2 \int_{\Omega} \rho_F \mathbf{U}_h \cdot \mathbf{W}_h \, dV = \int_{\Gamma_L} g \mathbf{W}_h \cdot \mathbf{n} \, dS, \quad (5.28)$$

for all $\mathbf{W}_h \in \mathbf{R}_h(\Omega)$.

Let $\vec{\mathbf{U}}_h$ be the column vector of coefficients of \mathbf{U}_h in the basis associated with $\mathbf{R}_h(\Omega)$,

$$\mathbf{U}_h(\mathbf{p}) = \sum_{j=1}^N [\vec{\mathbf{U}}_h(\mathbf{p})]_j \mathbf{W}_j(\mathbf{p}).$$

So, the matrix formulation of the problem (5.28) is

$$(-\omega^2 \mathbf{M} + \mathbf{K}) \vec{\mathbf{U}}_h = \mathbf{G},$$

where the coefficients of the mass and the stiffness matrices are, respectively

$$[\mathbf{M}]_{ij} = \int_{\Omega} \rho_F \mathbf{W}_j \cdot \mathbf{W}_i dV, \quad (5.29)$$

$$[\mathbf{K}]_{ij} = \int_{\Omega} \rho_F c_F^2 \operatorname{div} \mathbf{W}_j \operatorname{div} \mathbf{W}_i dV, \quad (5.30)$$

and the coefficients of the vector \mathbf{G} are given by

$$[\mathbf{G}]_{ij} = \int_{\Gamma_L} g \mathbf{W}_i \cdot \mathbf{n} dS. \quad (5.31)$$

Now, in order to approximate the $\mathbf{U}^k \in \mathbf{H}_{\Gamma_N}(\operatorname{div}, \Omega)$ in the spectral problem (5.6), also the lowest order Raviart-Thomas elements are used, and once again, the discrete Raviart-Thomas space is defined by (5.27). Then, the approximate spectral problem is given as follows:

Find a sequence of eigenpairs $(\lambda_k, \mathbf{U}_h^k)$, $\mathbf{U}_h^k \neq \mathbf{0}$, with $k \in \mathbb{N}$ where $\lambda_k > 0$ and $\mathbf{U}_h^k \in \mathbf{R}_h$, such that

$$\int_{\Omega} \rho_F c_F^2 \operatorname{div} \mathbf{U}_h^k \operatorname{div} \mathbf{W}_h^k dV = \lambda_k \int_{\Omega} \rho_F \mathbf{U}_h^k \cdot \mathbf{W}_h^k dV, \quad (5.32)$$

for all $\mathbf{W}_h^k \in \mathbf{R}_h$.

If $\vec{\mathbf{U}}_h^k$ is the column vector of coefficients of \mathbf{U}_h^k in the basis associated with $\mathbf{R}_h(\Omega)$,

$$\mathbf{U}_h^k(\mathbf{p}) = \sum_{j=1}^N [\vec{\mathbf{U}}_h^k(\mathbf{p})]_j \mathbf{W}_j^k(\mathbf{p}),$$

the problem (5.32) can be written in matrix form as

$$\mathbf{K}^k \vec{\mathbf{U}}_h^k = \lambda_k \mathbf{M}^k \vec{\mathbf{U}}_h^k,$$

where the coefficients of the mass and the stiffness matrices are, respectively

$$[\mathbf{M}^k]_{ij} = \int_{\Omega} \rho_F \mathbf{W}_j^k \cdot \mathbf{W}_i^k dV, \quad (5.33)$$

$$[\mathbf{K}^k]_{ij} = \int_{\Omega} \rho_F c_F^2 \operatorname{div} \mathbf{W}_j^k \operatorname{div} \mathbf{W}_i^k dV. \quad (5.34)$$

Absorbing walls

To approximate the fluid displacement $\mathbf{U} \in \mathbf{H}_{\Gamma_N}(\text{div}, \Omega)$ in Section 5.2.2, the lowest order Raviart-Thomas elements are used. Thus, the functional space $\mathbf{H}_{\Gamma_N}(\text{div}, \Omega)$ can be replaced in the discrete problem by $\mathbf{R}_h(\Omega)$. By using the finite element space (5.27), the approximation of the problem (5.16) is defined by:

Given $\omega > 0$, $g \in H^{-1/2}(\Gamma_L)$, and $\alpha_v, \beta_v \in \mathbb{R}$ with positive values, find the displacement field $\mathbf{U}_h \in \mathbf{R}_h(\Omega)$, satisfying

$$\begin{aligned} & \int_{\Omega} \rho_F c_F^2 \operatorname{div} \mathbf{U}_h \operatorname{div} \mathbf{W}_h dV + \int_{\Gamma_V} \alpha_v \mathbf{U}_h \cdot \mathbf{m} \mathbf{W}_h \cdot \mathbf{m} dS + i\omega \int_{\Gamma_V} \beta_v \mathbf{U}_h \cdot \mathbf{m} \mathbf{W}_h \cdot \mathbf{m} dS \\ & - \omega^2 \int_{\Omega} \rho_F \mathbf{U}_h \cdot \mathbf{W}_h dV = \int_{\Gamma_L} g \mathbf{W}_h \cdot \mathbf{n} dS, \end{aligned} \quad (5.35)$$

for all $\mathbf{W}_h \in \mathbf{R}_h(\Omega)$.

If $\vec{\mathbf{U}}_h$ is the column vector of coefficients of \mathbf{U}_h in the basis associated with $\mathbf{R}_h(\Omega)$, the matrix formulation of the problem (5.35) is

$$(-\omega^2 \mathbf{M} + i\omega \beta_v \mathbf{C} + (\mathbf{K} + \alpha_v \mathbf{C})) \vec{\mathbf{U}}_h = \mathbf{0},$$

where the coefficients of the mass \mathbf{M} and the stiffness \mathbf{K} matrices are given by (5.29) and (5.30), respectively, the coefficients of the damping matrix are given by

$$[\mathbf{C}]_{ij} = \int_{\Gamma_V} \mathbf{W}_j \cdot \mathbf{m} \mathbf{W}_i \cdot \mathbf{m} dS, \quad (5.36)$$

and the coefficients of the vector \mathbf{G} are given by (5.31)

Now, in order to approximate the $(\mathbf{U}^k, \mathbf{V}^k) \in \mathbf{H}_{\Gamma_N}(\text{div}, \Omega) \times \mathbf{H}_{\Gamma_N}(\text{div}, \Omega)$ in the spectral problem (5.17), also the lowest order Raviart-Thomas elements are used. The discrete Raviart-Thomas space is defined by (5.27), and the approximation of the spectral problem is given as follows:

Given $\alpha_v, \beta_v \in \mathbb{R}$ with $\alpha_v, \beta_v > 0$, find a sequence of eigenpairs $(\sigma_k, (\mathbf{U}^k, \mathbf{V}^k))$, $(\mathbf{U}^k, \mathbf{V}^k) \neq (\mathbf{0}, \mathbf{0})$, with $k \in \mathbb{N}$ where $\sigma_k > 0$ and $(\mathbf{U}_h^k, \mathbf{V}_h^k) \in \mathbf{V}$, such that

$$\begin{aligned} & - \int_{\Omega} \rho_F c_F^2 \operatorname{div} \mathbf{U}_h^k \operatorname{div} \mathbf{W}_h^k dV + \int_{\Omega} \rho_F \mathbf{V}_h^k \cdot \mathbf{Z}_h^k dV - \int_{\Gamma_V} \alpha_v \mathbf{U}_h^k \cdot \mathbf{m} \mathbf{W}_h^k \cdot \mathbf{m} dS \\ & - \int_{\Gamma_V} \beta_v \mathbf{V}_h^k \cdot \mathbf{m} \mathbf{W}_h^k \cdot \mathbf{m} dS = \sigma_k \left(\int_{\Omega} \rho_F \mathbf{V}_h^k \cdot \mathbf{W}_h^k dV + \int_{\Omega} \rho_F \mathbf{U}_h^k \cdot \mathbf{Z}_h^k dV \right), \end{aligned} \quad (5.37)$$

for all $(\mathbf{W}_h^k, \mathbf{Z}_h^k) \in \mathbf{V}$, where $\mathbf{V} = \mathbf{R}_h \times \mathbf{R}_h$.

Let $\vec{\mathbf{U}}_h^k$ and $\vec{\mathbf{V}}_h^k$ be the column vectors of coefficients of \mathbf{U}_h^k and \mathbf{V}_h^k , respectively, in the

basis associated with $\mathbf{R}_h(\Omega)$,

$$\begin{aligned}\mathbf{U}_h^k(\mathbf{p}) &= \sum_{j=1}^N [\vec{\mathbf{U}}_h^k(\mathbf{p})]_j \mathbf{W}_j^k(\mathbf{p}), \\ \mathbf{V}_h^k(\mathbf{p}) &= \sum_{j=1}^N [\vec{\mathbf{V}}_h^k(\mathbf{p})]_j \mathbf{W}_j^k(\mathbf{p}).\end{aligned}$$

Then, the matrix formulation of the problem (5.37) is

$$\begin{pmatrix} -\mathbf{K}^k - \alpha_v \mathbf{C}^k & -\beta_v \mathbf{C}^k \\ 0 & \mathbf{M}^k \end{pmatrix} \begin{pmatrix} \vec{\mathbf{U}}_h^k \\ \vec{\mathbf{V}}_h^k \end{pmatrix} = \sigma_k \begin{pmatrix} 0 & \mathbf{M}^k \\ \mathbf{M}^k & 0 \end{pmatrix} \begin{pmatrix} \vec{\mathbf{U}}_h^k \\ \vec{\mathbf{V}}_h^k \end{pmatrix},$$

where the coefficients of the mass \mathbf{M}^k and the stiffness \mathbf{K}^k matrices are, respectively, (5.33) and (5.34), and the matrix \mathbf{C}^k is given by

$$[\mathbf{C}^k]_{ij} = \int_{\Gamma_V} \mathbf{W}_j^k \cdot \mathbf{m} \mathbf{W}_i^k \cdot \mathbf{m} dS. \quad (5.38)$$

Absorbing walls and porous sample

To approximate the fluid displacement $\mathbf{U} \in \mathbf{H}_{\Gamma_N}(\text{div}, \Omega)$ in Section 5.2.3, the lowest order Raviart-Thomas elements are used. Thus, the functional space $\mathbf{H}_{\Gamma_N}(\text{div}, \Omega)$ can be replaced in the discrete problem by $\mathbf{R}_h(\Omega)$. By using the finite element space (5.27), the approximation of the problem (5.25) is defined by:

Given $\omega > 0$, $g \in H^{-1/2}(\Gamma_L)$, and $\alpha_v, \beta_v, \alpha_s, \beta_s \in \mathbb{R}$ with positive values, find the displacement field $\mathbf{U}_h \in \mathbf{R}_h(\Omega)$, satisfying

$$\begin{aligned}& \int_{\Omega} \rho_F c_F^2 \operatorname{div} \mathbf{U}_h \operatorname{div} \mathbf{W}_h dV + \int_{\Gamma_V} \alpha_v \mathbf{U}_h \cdot \mathbf{m} \mathbf{W}_h \cdot \mathbf{m} dS + i\omega \int_{\Gamma_V} \beta_v \mathbf{U}_h \cdot \mathbf{m} \mathbf{W}_h \cdot \mathbf{m} dS \\ &+ \int_{\Gamma_I} \alpha_s \mathbf{U}_h \cdot \boldsymbol{\eta} \mathbf{W}_h \cdot \boldsymbol{\eta} dS + i\omega \int_{\Gamma_I} \beta_s \mathbf{U}_h \cdot \boldsymbol{\eta} \mathbf{W}_h \cdot \boldsymbol{\eta} dS - \omega^2 \int_{\Omega} \rho_F \mathbf{U}_h \cdot \mathbf{W}_h dV \\ &= \int_{\Gamma_L} g \mathbf{W}_h \cdot \mathbf{n} dS,\end{aligned} \quad (5.39)$$

for all $\mathbf{W}_h \in \mathbf{R}_h(\Omega)$.

If $\vec{\mathbf{U}}_h$ is the column vector of coefficients of \mathbf{U}_h in the basis associated with $\mathbf{R}_h(\Omega)$, the matrix formulation of the problem (5.39) is

$$(-\omega^2 \mathbf{M} + i\omega(\beta_s + \beta_v) \mathbf{C} + (\mathbf{K} + (\alpha_s + \alpha_v) \mathbf{C})) \vec{\mathbf{U}}_h = \mathbf{G},$$

where the coefficients of \mathbf{M} , \mathbf{C} , and \mathbf{K} are given by (5.29), (5.36), and (5.30), respectively, and the coefficients of the vector \mathbf{G} are given by (5.31).

Now, in order to approximate the $(\mathbf{U}^k, \mathbf{V}^k) \in \mathbf{H}_{\Gamma_N}(\text{div}, \Omega) \times \mathbf{H}_{\Gamma_N}(\text{div}, \Omega)$ in the spectral problem (5.26), also the lowest order Raviart-Thomas elements are used. The discrete Raviart-Thomas space is defined by (5.27), and the approximation of the spectral problem is given as follows:

Given $\alpha_v, \beta_v, \alpha_s, \beta_s \in \mathbb{R}$ with positive values, find a sequence of eigenpairs $(\sigma_k, (\mathbf{U}^k, \mathbf{V}^k))$, $(\mathbf{U}^k, \mathbf{V}^k) \neq (\mathbf{0}, \mathbf{0})$, with $k \in \mathbb{N}$ where $\sigma_k > 0$ and $(\mathbf{U}_h^k, \mathbf{V}_h^k) \in \mathbf{V}$, such that

$$\begin{aligned} & - \int_{\Omega} \rho_F c_F^2 \operatorname{div} \mathbf{U}_h^k \operatorname{div} \mathbf{W}_h^k dV + \int_{\Omega} \rho_F \mathbf{V}_h^k \cdot \mathbf{Z}_h^k dV - \int_{\Gamma_V} \alpha_v \mathbf{U}_h^k \cdot \mathbf{m} \mathbf{W}_h^k \cdot \mathbf{m} dS \\ & - \int_{\Gamma_V} \beta_v \mathbf{V}_h^k \cdot \mathbf{m} \mathbf{W}_h^k \cdot \mathbf{m} dS - \int_{\Gamma_I} \alpha_s \mathbf{U}_h^k \cdot \boldsymbol{\eta} \mathbf{W}_h^k \cdot \boldsymbol{\eta} dS - \int_{\Gamma_I} \beta_s \mathbf{V}_h^k \cdot \boldsymbol{\eta} \mathbf{W}_h^k \cdot \boldsymbol{\eta} dS \\ & = \sigma_k \left(\int_{\Omega} \rho_F \mathbf{V}_h^k \cdot \mathbf{W}_h^k dV + \int_{\Omega} \rho_F \mathbf{U}_h^k \cdot \mathbf{Z}_h^k dV \right), \end{aligned} \quad (5.40)$$

for all $(\mathbf{W}_h^k, \mathbf{Z}_h^k) \in \mathbf{V}$, where $\mathbf{V} = \mathbf{R}_h \times \mathbf{R}_h$.

Let $\vec{\mathbf{U}}_h^k$ and $\vec{\mathbf{V}}_h^k$ be the column vectors of coefficients of \mathbf{U}_h^k and \mathbf{V}_h^k , respectively, in the basis associated with $\mathbf{S}_h(\Omega)$, the matrix formulation of the problem (5.40) is

$$\begin{pmatrix} -\mathbf{K}^k - \alpha_v \mathbf{C}^k - \alpha_s \mathbf{B}^k & -\beta_v \mathbf{C}^k - \beta_s \mathbf{B}^k \\ 0 & \mathbf{M}^k \end{pmatrix} \begin{pmatrix} \vec{\mathbf{U}}_h^k \\ \vec{\mathbf{V}}_h^k \end{pmatrix} = \sigma_k \begin{pmatrix} 0 & \mathbf{M}^k \\ \mathbf{M}^k & 0 \end{pmatrix} \begin{pmatrix} \vec{\mathbf{U}}_h^k \\ \vec{\mathbf{V}}_h^k \end{pmatrix},$$

where the coefficients of \mathbf{M}^k , \mathbf{K}^k , and \mathbf{C}^k are, respectively, (5.33), (5.34), and (5.38), and the matrix \mathbf{B}^k is given by

$$[\mathbf{B}^k]_{ij} = \int_{\Gamma_I} \mathbf{W}_j^k \cdot \mathbf{m} \mathbf{W}_i^k \cdot \mathbf{m} dS.$$

5.3 Methodology based on a full time-dependent discretization

In this section, the mathematical models and the algorithmic procedure to compute the reverberation times with a full time-dependent approach is described in detail. This approach follows the American standard ASTM C423-09 [50] to compute the decay rates and the reverberation times associated with the alpha cabin. Although there exist another differences between both the standard ASTM C423-09 and the ISO 354 (see [31] for more details), the main one is that with the ISO it is necessary to compute the sound pressure level for a longer period of time (until the sound pressure level has decreased by 60 dB) and with the American one, it is necessary to compute the sound pressure level only over some time measurement bands. Hence, the American standard is a local procedure while the ISO one is based in a global methodology. Let us consider Ω the fluid domain. This domain has three disjoint boundaries, that is $\Omega = \Gamma_L \cup \Gamma_I \cup \Gamma_N$, where Γ_L is the acoustic source, Γ_I is the place where the porous sample is located, and Γ_N are the rest of faces (see Figure 5.5 for more details).

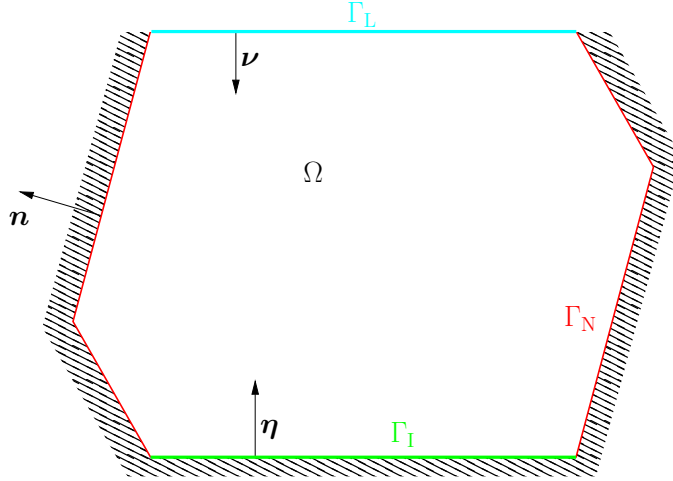


Figure 5.5: Scheme of a domain with a fluid in a cavity (Ω), with one piston-like wall (Γ_L) highlighted in cyan, an absorbing sample (Γ_I) highlighted in green, and rigid walls boundaries (Γ_N) highlighted in red.

The first step to compute the reverberation time is turned the source on, until time-harmonic state is reached. For this reason, it is necessary to solve a time-harmonic problem where a rigid wall condition is imposed on Γ_N , a pressure is imposed on the source Γ_L , and, on the place where the sample is located, Γ_I , a surface impedance condition is considered. Then, the source problem and the spectral problem are the same that are defined in Section 5.2.2 but instead of having the impedance condition on Γ_V , this condition is imposed on Γ_I . Then, the source problem consists in, given $\omega > 0$, finding the complex-valued displacement field \mathbf{U} such that

$$\left\{ \begin{array}{ll} -\rho_F c_F^2 \nabla(\operatorname{div} \mathbf{U}) - \omega^2 \rho_F \mathbf{U} = \mathbf{0} & \text{in } \Omega, \\ \mathbf{U} \cdot \mathbf{n} = 0 & \text{on } \Gamma_N, \\ -\rho_F c_F^2 \operatorname{div} \mathbf{U} = g & \text{on } \Gamma_L, \\ -\rho_F c_F^2 \operatorname{div} \mathbf{U} = (\alpha_s + i\omega\beta_s) \mathbf{U} \cdot \mathbf{m} & \text{on } \Gamma_I, \end{array} \right. \quad (5.41)$$

where g is the pressure applied on the active surface of the loudspeakers, $\alpha_s + i\omega\beta_s$ is the surface impedance associated with the sample, ν is the unit normal vector to the interface Γ_L pointing inwards Ω , \mathbf{n} is the unit normal vector to the interface Γ_N pointing outwards Ω , and \mathbf{m} is the unit normal vector to the interface Γ_I pointing outwards Ω .

In the same way, the spectral problem can be written as follows:

Find a sequence of eigenpairs $(\sigma_k, (\mathbf{U}^k, \mathbf{V}^k))$, $(\mathbf{U}^k, \mathbf{V}^k) \neq (\mathbf{0}, \mathbf{0})$, with $k \in \mathbb{N}$ and $\operatorname{Im}(\sigma_k) > 0$ such that

$$\left\{ \begin{array}{ll} -\rho_F c_F^2 \nabla(\operatorname{div} \mathbf{U}^k) + \sigma_k \rho_F \mathbf{V}^k = \mathbf{0} & \text{in } \Omega, \\ \rho_F \mathbf{V}^k = \sigma_k \rho_F \mathbf{U}^k & \text{in } \Omega, \\ \mathbf{U}^k \cdot \mathbf{n} = 0, \mathbf{V}^k \cdot \mathbf{n} = 0 & \text{on } \Gamma_N, \\ -\rho_F c_F^2 \operatorname{div} \mathbf{U}^k = 0, -\rho_F c_F^2 \operatorname{div} \mathbf{V}^k = 0 & \text{on } \Gamma_L, \\ -\rho_F c_F^2 \operatorname{div} \mathbf{U}^k = \alpha_s \mathbf{U}^k \cdot \mathbf{m} + \beta_s \mathbf{V}^k \cdot \mathbf{m} & \text{on } \Gamma_I. \end{array} \right. \quad (5.42)$$

Once the time-harmonic state has been reached, the acoustic source is turned off, the sound pressure level will decrease, and the reverberation time could be computed by measuring the decay rate at each frequency. With this purpose, it is necessary to state the time-dependent problem, which governs the displacement field inside the alpha cabin. In order to study the time evolution once the acoustic source is turned off, it is necessary to solve in the time interval $[0, T]$ the same time-dependent problem given in Section 5.2.2, where Γ_V is substituted by Γ_I . Then, (5.18) results

$$\left\{ \begin{array}{ll} -\rho_F c_F^2 \nabla(\operatorname{div} \mathbf{u}) + \rho_F \ddot{\mathbf{u}} = \mathbf{0} & \text{in } \Omega \times [0, T], \\ \mathbf{u} \cdot \mathbf{n} = 0 & \text{on } \Gamma_N \times [0, T], \\ -\rho_F c_F^2 \operatorname{div} \mathbf{u} = 0 & \text{on } \Gamma_L \times [0, T], \\ -\rho_F c_F^2 \operatorname{div} \mathbf{u} = \alpha_s \mathbf{u} \cdot \boldsymbol{\eta} + \beta_s \dot{\mathbf{u}} \cdot \boldsymbol{\eta} & \text{on } \Gamma_I \times [0, T], \\ \mathbf{u}(\mathbf{p}, 0) = \mathbf{u}_0 & \text{in } \Omega, \\ \dot{\mathbf{u}}(\mathbf{p}, 0) = \mathbf{v}_0 & \text{in } \Omega, \end{array} \right. \quad (5.43)$$

where $\dot{\mathbf{u}} = \frac{\partial}{\partial t} \mathbf{u}$, $\ddot{\mathbf{u}} = \frac{\partial^2}{\partial t^2} \mathbf{u}$, and \mathbf{u}_0 and \mathbf{v}_0 are the initial conditions for the displacement and velocity (computed from the time-harmonic source problem), this is, if \mathbf{U} is the solution of the time-harmonic source problem,

$$\begin{aligned} \mathbf{u}_0(\mathbf{p}) &= \operatorname{Re}(\mathbf{U}(\mathbf{p})e^{i\omega t})|_{t=0} = \operatorname{Re}(\mathbf{U}(\mathbf{p})), \\ \mathbf{v}_0(\mathbf{p}) &= \frac{\partial}{\partial t} \operatorname{Re}(\mathbf{U}(\mathbf{p})e^{i\omega t})|_{t=0} = \operatorname{Re}(i\omega \mathbf{U}(\mathbf{p})e^{i\omega t})|_{t=0} = \omega \operatorname{Im}(\mathbf{U}(\mathbf{p})). \end{aligned}$$

Variational formulation

The variational formulation of the source problem (5.42) and the spectral problem (5.41) are given in (5.16) and (5.17), respectively, but instead of having the integral on Γ_V , the integral is on Γ_I , and α_v and β_v are substituted by α_s and β_s . Moreover, the variational formulation of this time-dependent problem can be written as follows:

Given \mathbf{u}_0 and $\mathbf{v}_0 \in \mathbf{H}_{\Gamma_N}(\operatorname{div}, \Omega)$, $\alpha_s, \beta_s \in \mathbb{R}$ with positive values, find $\mathbf{u} \in C^1([0, T], \mathbf{H}_{\Gamma_N}(\operatorname{div}, \Omega)) \cap C^2((0, T), \mathbf{H}_{\Gamma_N}(\operatorname{div}, \Omega))$, $\mathbf{u}(\cdot, 0) = \mathbf{u}_0$, $\dot{\mathbf{u}}(\cdot, 0) = \mathbf{v}_0$, and satisfying

$$\int_{\Omega} \rho_F c_F^2 \operatorname{div} \mathbf{u} \operatorname{div} \mathbf{w} dV + \int_{\Omega} \rho_F \ddot{\mathbf{u}} \cdot \mathbf{w} dV + \int_{\Gamma_I} \alpha_s \mathbf{u} \cdot \boldsymbol{\eta} \mathbf{w} \cdot \boldsymbol{\eta} dS + \int_{\Gamma_I} \beta_s \dot{\mathbf{u}} \cdot \mathbf{n} \mathbf{w} \cdot \boldsymbol{\eta} dS = 0,$$

for all $\mathbf{w} \in \mathbf{H}_{\Gamma_N}(\operatorname{div}, \Omega)$.

5.3.1 Finite element discretization

As it has been explained before, the approximation of (5.16) and (5.17) are given by (5.35) and (5.37), with the changes mentioned before. Moreover, to approximate the fluid displacements $\mathbf{u} \in \mathbf{H}_{\Gamma_N}(\operatorname{div}, \Omega)$ the lowest order Raviart-Thomas elements are used. By using the discrete Raviart-Thomas space defined in (5.27), the functional space $\mathbf{H}_{\Gamma_N}(\operatorname{div}, \Omega)$

can be replaced by $\mathbf{R}_h(\Omega)$. Considering the associated interpolant operator \mathcal{I}_h (see [82] for further details), the approximation of the time-dependent problem (5.43) can be defined as follows:

Given \mathbf{u}_0 and $\mathbf{v}_0 \in \mathbf{H}_{\Gamma_N}(\text{div}, \Omega)$, $\alpha_s, \beta_s \in \mathbb{R}$ with positive values, find $\mathbf{u}_h \in \mathcal{C}^1([0, T], \mathbf{R}_h(\Omega)) \cap \mathcal{C}^2((0, T), \mathbf{R}_h(\Omega))$, $\mathbf{u}_h(\cdot, 0) = \mathcal{I}_h \mathbf{u}_0$, $\dot{\mathbf{u}}_h(\cdot, 0) = \mathcal{I}_h \mathbf{v}_0$, and satisfying

$$\int_{\Omega} \rho_F c_F^2 \operatorname{div} \mathbf{u}_h \operatorname{div} \mathbf{w}_h \, dV + \int_{\Omega} \rho_F \ddot{\mathbf{u}}_h \cdot \mathbf{w}_h \, dV + \int_{\Gamma_I} \alpha_s \mathbf{u}_h \cdot \boldsymbol{\eta} \mathbf{w}_h \cdot \boldsymbol{\eta} \, dS + \int_{\Gamma_I} \beta_s \dot{\mathbf{u}}_h \cdot \mathbf{n} \mathbf{w}_h \cdot \boldsymbol{\eta} \, dS = 0, \quad (5.44)$$

for all $\mathbf{w}_h \in \mathbf{R}_h(\Omega)$.

Let $\vec{\mathbf{U}}_h$ be the column vector of coefficients of \mathbf{U}_h in the basis associated with $\mathbf{R}_h(\Omega)$,

$$\mathbf{u}_h(\mathbf{p}, t) = \sum_{j=1}^N [\vec{\mathbf{U}}_h(t)]_j \mathbf{w}_j(\mathbf{p}).$$

Then, the matrix formulation of the problem (5.44) is

$$\ddot{\mathbf{M}} \vec{\mathbf{U}}_h + \beta_s \mathbf{C} \dot{\vec{\mathbf{U}}}_h + (\mathbf{K} + \alpha_s \mathbf{C}) \vec{\mathbf{U}}_h = \vec{\mathbf{0}},$$

where the coefficients of the mass, damping and stiffness matrices are, respectively

$$\begin{aligned} [\mathbf{M}]_{ij} &= \int_{\Omega} \rho_F \mathbf{w}_j \cdot \mathbf{w}_i \, dV, \\ [\mathbf{C}]_{ij} &= \int_{\Gamma_I} \mathbf{w}_j \cdot \mathbf{n} \mathbf{w}_i \cdot \mathbf{n} \, dS, \\ [\mathbf{K}]_{ij} &= \int_{\Omega} \rho_F c_F^2 \operatorname{div} \mathbf{w}_j \operatorname{div} \mathbf{w}_i \, dV. \end{aligned}$$

Numerical scheme

Once a suitable finite element discretization has been introduced for the variational formulation stated above, a time-marching scheme must be chosen to discretize the time-dependent problem. Since this problem is second-order in time (acceleration is arising in the inertial term), a Newmark scheme is used [16]. This scheme is an unconditionally stable second order method. The system of linear differential equations of second order is

$$\ddot{\mathbf{M}} \vec{\mathbf{U}} + \mathbf{C} \dot{\vec{\mathbf{U}}} + \mathbf{K} \vec{\mathbf{U}} = \mathbf{R},$$

where \mathbf{M} , \mathbf{C} , and \mathbf{K} are the mass, damping and stiffness matrices, respectively, and \mathbf{R} is the vector of externally applied loads. With this time-marching scheme, displacement and velocity field are approximated by the following expressions:

$$\begin{aligned} \dot{\vec{\mathbf{U}}}^{t+\Delta t} &= \dot{\vec{\mathbf{U}}}^t + [(1 - \delta) \ddot{\vec{\mathbf{U}}}^t + \delta \ddot{\vec{\mathbf{U}}}^{t+\Delta t}] \Delta t, \\ \vec{\mathbf{U}}^{t+\Delta t} &= \vec{\mathbf{U}}_t + \dot{\vec{\mathbf{U}}}^t \Delta t + [(1/2 - \alpha) \ddot{\vec{\mathbf{U}}}^t + \alpha \ddot{\vec{\mathbf{U}}}^{t+\Delta t}] \Delta t^2, \end{aligned}$$

where $\Delta t = T/n$ is the time step, being n the number of time steps used in the entire numerical simulation, and α and δ are parameters that can be determined to obtain integration accuracy and stability. Throughout the present chapter $\alpha = 1/4$ and $\delta = 1/2$ to reach second-order accuracy. Solving (5.43) by using the Newmark's scheme at each time t , from time 0 to time T , a sequence of approximated displacement fields are obtained, this is, $\vec{\mathbf{U}}^0, \vec{\mathbf{U}}^{\Delta t}, \vec{\mathbf{U}}^{2\Delta t}, \dots, \vec{\mathbf{U}}^T$. Associated with this displacement fields, it is straightforward to compute their respective approximations of the pressure field $\pi(\mathbf{p}, t)$ at different time steps, given by

$$\pi(\mathbf{p}, j\Delta t) = -\rho_F c_F^2 \operatorname{div} \mathbf{U}^{j\Delta t}(\mathbf{p}) \quad \text{for } j = 0, \dots, n.$$

Notice that other time-marching schemes are also utilized to discretize the time-dependent problem. More precisely, the explicit Noh-Bathe second-order scheme (see [137] for further details) has been used. Since the numerical results are similar from those obtained with the Newmark scheme, and the computational cost is much larger than the implicit scheme (since the Noh-Bathe suffers from a restrictive CFL stability condition), the numerical results obtained with this time discretization have not been included in this chapter.

5.4 Computation of the absorption values in an alpha cabin

To quantify the absorption coefficient of a porous sample in an alpha cabin, the reverberation time associated with the empty room and with the room with sample are computed. Once the different mathematical models which govern the alpha cabin have been explained, and the time-dependent problem has been solved, two different strategies to compute the reverberation time, and two expressions to compute the absorption coefficient in the cabin are described.

5.4.1 Computation of the reverberation time

Let $\{\mathbf{p}_m\}_{m=1}^M$ be a set of fixed spatial points, used to measure the pressure field. The sound pressure level (SPL measured in decibels [dB]) at these points is given by

$$\text{SPL}(t) = 20 \log_{10} \left(\frac{1}{M} \sum_{m=1}^M \frac{|\pi(\mathbf{p}_m, t)|}{\pi_{\text{ref}}} \right),$$

where $\pi_{\text{ref}} = 2 \times 10^{-5}$ Pa. Following the international norm ISO 354:2003 [2], the reverberation time of a closed room (in this case, an alpha cabin) is the time t_{rev} which satisfies

$$\text{SPL}(t_{\text{rev}}) = \text{SPL}(0) - 60 \text{ dB}, \quad (5.45)$$

i.e, it is the time in seconds, that would be required for the sound pressure level to decrease by 60 dB after the acoustic source has stopped. In fact, factors can be written from the

displacement field using the mode expansion (5.22):

$$\pi(\mathbf{p}, t) = -\rho_F c_F^2 \operatorname{div} \mathbf{u}(\mathbf{p}, t) = -\rho_F c_F^2 \operatorname{Re} \left(\sum_{j=1}^N \tilde{u}_j e^{\sigma_j t} \operatorname{div} \mathbf{U}^j(\mathbf{p}) \right), \quad (5.46)$$

and consequently,

$$\text{SPL}(t) = 20 \log_{10} \left(\frac{\rho_F c_F^2}{M \pi_{\text{ref}}} \sum_{m=1}^M \left| \operatorname{Re} \left(\sum_{j=1}^N \tilde{u}_j e^{\sigma_j t} \operatorname{div} \mathbf{U}^j(\mathbf{p}_m) \right) \right| \right). \quad (5.47)$$

The right-hand side in (5.45) is straightforward computed, since $\mathbf{u}(\mathbf{p}, 0) = \operatorname{Re}(\mathbf{U}(\mathbf{p}))$. In this case,

$$\text{SPL}(0) = 20 \log_{10} \left(\frac{\rho_F c_F^2}{M \pi_{\text{ref}}} \sum_{m=1}^M |\operatorname{Re}(\operatorname{div} \mathbf{U}(\mathbf{p}_m))| \right). \quad (5.48)$$

Since the evaluation of the pressure field at points $\{\mathbf{p}_m\}_{m=1}^M$ is straightforward from the evaluation of the mode expansion, the computation of the reverberation time is immediately computed by solving the non-linear equation inserting (5.47) and (5.48) in (5.45), and using the truncated modal expansion (5.22) to approximate the SPL level.

Fitting wall impedance in terms of experimental reverberation times The experimental reverberation time in the alpha cabin is obtained following these steps. In the following procedure, it is assumed ideally that each measurement can be performed independently for a fixed set of frequency values $\{\omega_n\}_{n=1}^N$:

- (A) One of the loudspeakers is turned on (exciting the alpha cabin at a fixed frequency value ω_n with $1 \leq n \leq N$), and $\text{SPL}_{n,k}(t)$ for $k = 1$ is measured from the pressure values at the microphone locations $\{\mathbf{p}_m\}_{m=1}^M$. Then, this loudspeaker is turned off, and another one is turned on. The procedure is repeated for each one of the L loudspeakers obtaining $\text{SPL}_{n,k}(t)$ for $k = 1, \dots, L$.
- (B) By using all the $\text{SPL}_{n,k}(t)$ measured for $k = 1, \dots, L$, the averaged SPL_n can be computed as follows:

$$\text{SPL}_n(t) = \frac{1}{L} \sum_{k=1}^L \text{SPL}_{n,k}(t) = \frac{1}{L} \sum_{k=1}^L \left(20 \log_{10} \left(\frac{1}{M} \sum_{m=1}^M \frac{|\pi_{n,k}(\mathbf{p}_m, t)|}{\pi_{\text{ref}}} \right) \right), \quad (5.49)$$

where $\pi_{n,k}$ is the pressure field measured when the loudspeaker k is turned on (working at a fixed frequency ω_n) and the rest ones is turned off.

- (C) Finally, the experimental reverberation time $t_{\text{rev}}(\omega_n)$ is computed solving (5.45), where $\text{SPL}(t_{\text{rev}}(\omega_n))$ has been computed by means of the averaged SPL_n values (5.49).

The analogous procedure has been also utilized to compute the numerical approximation of the reverberation time $\hat{t}_{\text{rev}}(\omega_n, \alpha_v, \beta_v)$, but in this numerical version of the procedure, the pressure field $\pi_k(x_m, t)$ has been approximated by the pressure field associated with the truncated modal expansion of the displacement field (see (5.46)).

Now, in order to find the values of α_v and β_v associated with the vertical walls of the alpha cabin, the experimental values of the reverberation time in the empty cabin have been used. The fitting problem is stated as follows:

Find the values $\alpha_v^ \geq 0$ and $\beta_v^* > 0$, such that minimize the difference between the experimental and the numerical reverberation times, i.e.,*

$$(\alpha_v^*, \beta_v^*) = \arg \min_{\alpha_v \geq 0, \beta_v > 0} \frac{\sum_{n=1}^N |t_{\text{rev}}(\omega_n) - \hat{t}_{\text{rev}}(\omega_n, \alpha_v, \beta_v)|^2}{\sum_{n=1}^N |t_{\text{rev}}(\omega_n)|^2}.$$

Remark 5.4.1. *Although in real-world materials both coefficients α_v and β_v actually depend on ω , in many cases, the impedance can be approximated by using a viscoelastic Kelvin-Voigt model [163], that is, neither α_v nor β_v have an arbitrary dependence of ω (see Section 1.3.4 in Chapter 1). The parameters α_v and β_v are associated with the elastic and the viscous contribution of the walls.*

5.4.2 Computation of the absorption value

Once it has been explained how to compute the reverberation time in the cabin with the porous sample and in the empty cabin, the absorption coefficient of a porous material in an alpha cabin can be defined by using, for example, Sabine formula, following the American standard ASTM C423-09 [50] or the international norm ISO 354:2003 [2].

Sabine formula

Following Sabine formula [160], the absorption coefficient of the sample is given by

$$\alpha = \frac{6 \ln(10)L}{c_F} \left(\frac{1}{t_{\text{rev}}} - \frac{1}{t_{\text{empty}}} \right), \quad (5.50)$$

where c_F is the air sound speed, L is the typical length of the cabin (space between two consecutive reflections), and t_{rev} and t_{empty} are respectively the time required to reduce in 60 dB the sound pressure level at some spatial point locations with and without absorbing specimen. The typical length of the cabin is given by

$$L = \begin{cases} V/S & \text{at normal incidence,} \\ 4V/S & \text{at diffuse field,} \end{cases} \quad (5.51)$$

where V is the total volume of the alpha cabin and S is the surface occupied by the absorbing test specimen. Notice that the floor of the alpha cabin is assumed rigid.

Millington formula

Alternatively, instead of computing the absorption coefficient using the simpler Sabine formula, it can be computed with the classical Millington formula [127], which is more robust for absorption values close to zero (see [68] for more details)

$$\ln(1 - \alpha) = \frac{6 \ln(10)L}{c_F} \left(\frac{1}{t_{\text{rev}}} - \frac{1}{t_{\text{empty}}} \right), \quad (5.52)$$

where c_F is the air sound speed, L is the typical length of the cabin given by (5.51), and t_{rev} and t_{empty} are respectively the time required to reduce in 60 dB the sound pressure level at some spatial point locations with and without absorbing specimen. Again, the floor of the alpha cabin is assumed rigid.

Remark 5.4.2. *The numerical results obtained with this numerical methodology are far from being accurate. In fact, very low absorption values are reported, which are not comparable with the experimental measurements. The origin of this lack of accuracy in the numerical results has been identified, and it has been related to two main causes: (a) the computation of the eigenmodes of the cabin is not reliable, since for a fixed range of frequency values, it cannot be ensured that all the eigenmodes have been taking into account in the modal expansion; and (b) the computation of SPL values associated with the numerical evaluation of the pressure field at a given time value could lead to unrealistic reverberation time values, which does not take into account the global decay of the pressure field.*

To overcome these two main drawbacks, a new numerical methodology has been considered, replacing the modal expansion by a full time-dependent discretization, and using the ASTM approach to compute the decay rates. Consequently, the reverberation times are based on local average of the pressures values in different time windows.

5.4.3 Computation of decay rates

Once the time-dependent problem is solved at each discretization time step $t_j = j\Delta t$, as it is proposed by the ASTM standard [50], local averages of the sound pressure level are computed in time windows of δt length. The set of averages of the sound pressure level $\{L_{\text{eq}}(0), L_{\text{eq}}(1), \dots, L_{\text{eq}}(M_d)\}$ are computed as follows:

$$L_{\text{eq}}(m) = \frac{1}{M} \sum_{j=1}^M \left(10 \log_{10} \int_{m\delta t}^{(m+1)\delta t} \frac{|\pi(\mathbf{p}_j, t)|^2}{\pi_{\text{ref}}^2} dt \right), \quad \text{for } m = 0, \dots, M_d - 1, \quad (5.53)$$

where M is the number of microphones, $\pi_{\text{ref}} = 2 \times 10^{-5}$ Pa is the reference pressure, and δt is the time windowing length. Since the pressure field is only approximated at the time steps $j\Delta t$, the time integral involved in the local averages is approximated by means of a composite Simpson's rule with time step Δt .

As it is recommended by the ASTM standard, the decay rate is the absolute value of the slope of the linear, first order regression on the average sound pressure level values, which is computed by using the following expression:

$$d_{\text{rev}} = \frac{6}{M_d(M_d^2 - 1)\delta t} \left[(M_d + 1) \sum_{i=0}^{M_d-1} L_{\text{eq}}(i) - 2 \sum_{i=0}^{M_d-1} i L_{\text{eq}}(i) \right],$$

being M_d the number of computed L_{eq} . Once the decay rate associated with each reverberation time is computed, the reverberation time can be computed as $t_{\text{rev}} = 60/d_{\text{rev}}$.

Additionally, two other numerical alternatives have been considered for computing the decay rates associated with the time evolution of the pressure field: the first one consists in the computation of the linear regression of the sound pressure level at every time step $t_j = j\Delta t$, without taking into account the local averages described above; the second one consists in the computation of the linear regression of the root-mean-square of the pressure field in the whole alpha cabin at every time step, not restricting the pressure values only to the microphone positions (as it has been considered in the other two strategies). These strategies, together with those previously described, are used in the numerical results.

5.5 Numerical results

In this section some numerical results are shown to illustrate the methodology to compute the absorption coefficient in an alpha cabin. Some simulations in two-dimensional and three-dimensional domains are performed, and the geometry used in each case is described.

5.5.1 Two-dimensional simulations

First of all, some two-dimensional simulations are performed. This section includes the description of the used geometry and the numerical results with two different datasets: manufactured data to validate the code, and experimental data of a real-world fibrous material provided by the same company that has been mentioned in Chapter 1.

Geometry

For the two-dimensional simulations, a rectangular domain $\Omega = [0, 0] \times [1, 0.75]$ is considered, with an absorbing wall (Γ_I), a piston-like wall (Γ_L), and two rigid walls (Γ_N). There are six microphones located within Ω in the positions $\mathbf{p}_i = (0.1 \times (1 + i), 0.1)$ with $i = 1, \dots, 6$. A scheme of this domain is shown in Figure 5.6.

Manufactured data

In the first two-dimensional simulation, a manufactured material is considered. The experimental data are the frequency response of the absorption coefficient at diffuse field of this material. To compute this coefficient by using the methodology described in this

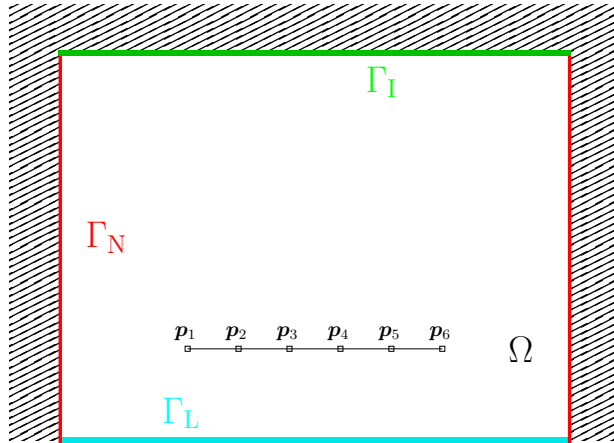


Figure 5.6: Fluid in a rectangular domain Ω , where $\Omega = [0, 0] \times [1, 0.75]$, with one absorbing wall (Γ_I) highlighted in green, one piston-like wall (Γ_L) highlighted in cyan, and two rigid walls (Γ_N) highlighted in red. The six microphones are located in p_1, \dots, p_6 .

chapter, the time-harmonic problem (5.41) and the time-dependent problem (5.43) should be solved. Thus, the time evolution of the pressure field inside the domain can be obtained, the reverberation time can be computed, and the absorption coefficient of the material can be obtained.

To solve the problems previously mentioned, it is necessary to know the surface impedance of the absorbing material under study. In this case, a material with a surface impedance smaller than the air is considered, that is, it is chosen $Z(\omega) = \alpha_s + i\omega\beta_s$ with $\alpha_s = 0 \text{ Ns/m}^3$ and $\beta_s = 206.21 \text{ Ns/m}^3$. Considering these values, the time-harmonic problem (5.41) is solved, and its solution is used as initial condition for the time-dependent problem (5.43). The considered frequency range is from 400 to 1000 Hz in third-octave (400, 500, 630, 800, and 1000 Hz). Then, the pressure field at the points where the microphones are located can be measured, and the sound pressure level can be computed at each angular frequency given. To calculate the reverberation time, the two strategies described in this chapter are followed: to use the sound pressure level (SPL) values or the L_{eq} -averages. The left plot of Figure 5.7 shows the values of the SPL obtained using (5.49), with a blue line, the values of the SPL computed using the root-mean-square (L_2 -norm) of the pressure field instead of the pointwise evaluation of the pressure field at the microphone locations, with a red line, the regression line calculated globally by using the SPL data at every time step, with a cyan line, and the regression line computed globally by using the L_2 -norm of the pressure field, with a yellow line. The right plot of Figure 5.7 shows the values of the SPL obtained using (5.49), with a blue line, and the regression lines computed considering the values of L_{eq} -averages obtained with the expression (5.53), in some windowing time intervals, with a magenta line. The dashed black line in both plots represents the point where the initial SPL has decreased by 60 dB. As it can be observed in the right plot in Figure 5.7, only

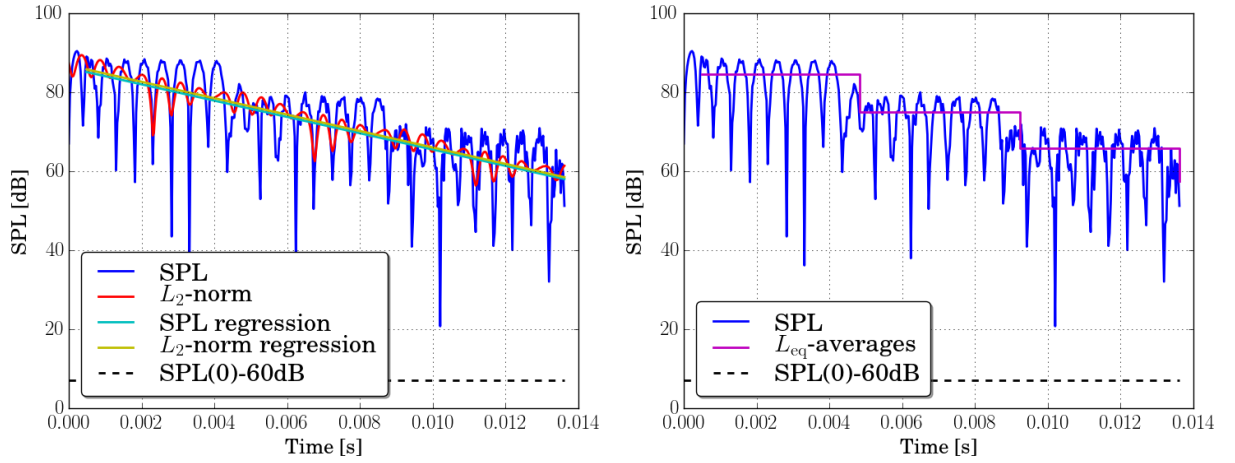


Figure 5.7: Sound pressure level at 1000 Hz of a manufactured material, computed by considering the impedance surface $Z(\omega) = i\omega\beta_s + \alpha_s$, with $\alpha_s = 0 \text{ Ns/m}^3$ and $\beta_s = 206.21 \text{ Ns/m}^3$. Left: values of the SPL computed using (5.49) (blue line), and those obtained by using the L_2 -norm of the pressure field (red line), regression line calculated globally by using the SPL data at every time step (cyan line), and regression line computed globally by using the L_2 -norm of the pressure field (yellow line). Right: values of the SPL computed by using (5.49) (blue line), and regression lines obtained from the values of L_{eq} calculated with the expression (5.53), where the windowing time interval has length $\delta t = 0.00439 \text{ s}$ (magenta line). The dashed black line in both plots represents the point where the initial sound pressure level has decreased by 60 dB.

four values of L_{eq} are used, the windowing time interval has length $\delta t = 0.00439 \text{ s}$, and the final time is $T = 0.014 \text{ s}$. As it can be observed in the left plot in Figure 5.7, a larger time interval is necessary to achieve that the initial SPL decreases 60 dB, that is, the time evolution problem should be studied at least until the solid blue line crosses the dashed black line, leading to an increase in the computational cost. As it has been explained previously, the absorption values may be obtained using the SPL, or the values of L_{eq} -averages. In Figure 5.8, the absorption values at diffuse field and at normal incidence calculated using Sabine formula (5.50) and the Millington formula (5.52) are shown. In the left plot, the absorption values are obtained from the values of SPL, and in the right plot, the absorption values are computed from the values of L_{eq} -averages. The numerical results are compared with the experimental data.

As it can be observed in both plots of Figure 5.8, Sabine formula overestimates the absorption coefficient while Millington formula obtains values closer to the experimental ones. In fact, under normal assumptions, absorption values are predicted accurately by using Millington formula, with relative errors $\varepsilon_{\text{SPL}} = 10.77\%$ and $\varepsilon_{L_{\text{eq}}} = 1.55\%$. As it has been explained before, the error obtained with the L_{eq} -averages is smaller than the obtained by considering the SPL values.

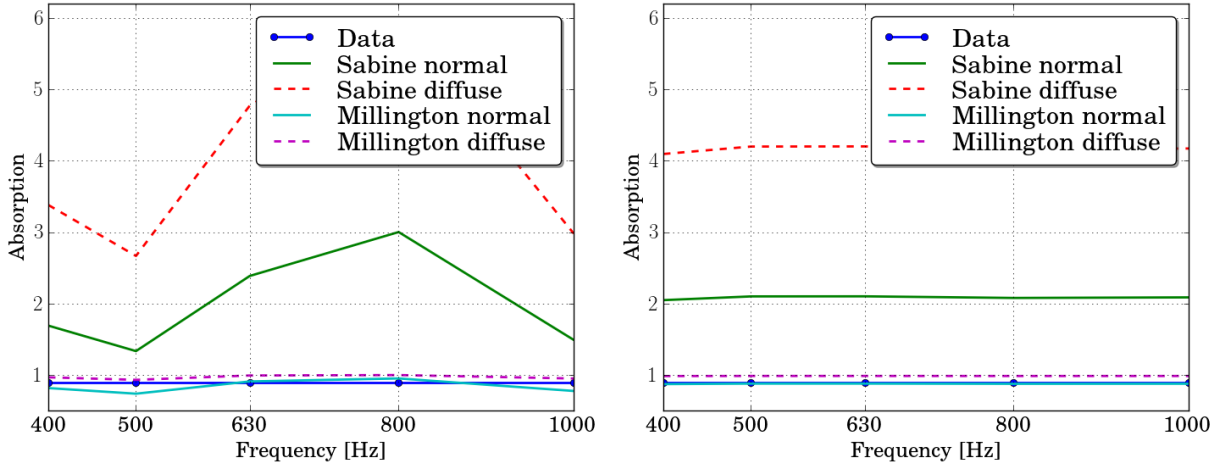


Figure 5.8: Absorption coefficient values of a manufactured material with impedance surface $Z(\omega) = i\omega\beta_s + \alpha_s$, where $\alpha_s = 0 \text{ Ns/m}^3$ and $\beta_s = 206.21 \text{ Ns/m}^3$, computed by using the Sabine formula (5.50) and the Millington formula (5.52), at normal incidence (solid lines) and diffuse field (dashed lines). The absorption values have been obtained by using the values of SPL (left plot) and the values of L_{eq} (right plot).

Simulation with a fibrous sample

In this two-dimensional simulation a material made from polypropylene fibers with thickness $h = 20 \text{ mm}$ is considered. This material is the sample 3 characterized in Section 1.7.1 in Chapter 1. As in the manufactured case, to solve the time-harmonic problem (5.41) and the time-dependent one (5.43), it is necessary to compute the values of the surface impedance associated with the material, $Z(\omega) = \alpha_s + i\omega\beta_s$, for each angular frequency ω . This sample is a fibrous material, and, as it has been described in Chapter 1, it may be modeled following a Miki model. Then, by using the fitting problem (1.16) with $M = 1$, the obtained optimal values are $\phi = 0.83$, $\sigma = 2.29 \times 10^4 \text{ Nm}^{-4}\text{s}$, $\alpha_\infty = 1.02$, and $M'' = 0.95$, and the relative error is $\varepsilon = 4.05\%$ (see Section 1.7.1 in Chapter 1 for more details about the fitting of this material). With these optimal values, the surface impedance Z_s of the material at each angular frequency ω_j may be computed (recall that if the porous material is modeled following a fluid-equivalent model, $Z_s(\omega_j) = Z(\omega_j) \coth(ik(\omega_j)h)$, where Z , k , and h are the characteristic impedance, the wave number, and the thickness of the material). Then, the fitting problem consists in finding $\alpha_s^* > 0$ and $\beta_s^* > 0$ such as

$$(\alpha_s^*, \beta_s^*) = \arg \min_{\alpha_s > 0, \beta_s > 0} \left(\frac{\sum_{j=1}^n |Z_s(\omega_j) - Z_{\text{anl}}(\omega_j, \alpha_s, \beta_s)|^2}{\sum_{j=1}^n |Z_s(\omega_j)|^2} \right), \quad (5.54)$$

where $Z_{\text{anl}}(\omega_j, \alpha_s, \beta_s) = \alpha_s + i\omega_j\beta_s$ is the computed surface impedance. The fitting problem (5.54) has been solved by using a least-square method with initial guess $(\alpha_s^0, \beta_s^0) = (100, 10)$, the obtained optimal values are $\alpha_s = 6622970.608 \text{ Ns/m}^3$ and $\beta_s = 293.047 \text{ Ns/m}^3$, and the relative error in the fitting is $\varepsilon = 1.74\%$. Figure 5.9 shows the fitting results. Left

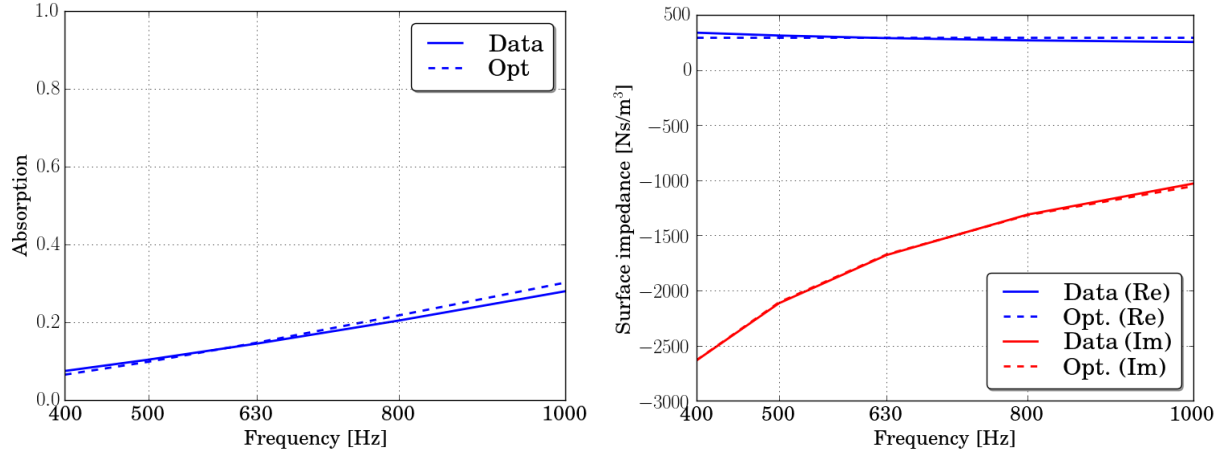


Figure 5.9: Left: Absorption coefficient of a material made from PP fibers (sample 3 of Chapter 1). The solid line represents the experimental values and the dashed line the optimized ones. The material is modeled by using the Miki model, and the optimal values of the fitting problem (1.16) are $\phi = 0.83$, $\sigma = 2.29 \times 10^4 \text{ Nm}^{-4}\text{s}$, $\alpha_\infty = 1.02$, and $M'' = 0.95$ (see Chapter 1 for more details). Right: Real (red lines) and imaginary (blue lines) parts of the fitting of the input surface impedance of the fibrous material. Solid lines represent the experimental data and the dashed lines correspond with the values computed considering the optimal values of the fitting problem (5.54), $\alpha_s = 6622970.608 \text{ Ns/m}^3$ and $\beta_s = 293.047 \text{ Ns/m}^3$.

plot shows the comparison between the experimental absorption coefficient (solid line) and the computed one with the optimal values stated above (dashed line). Right plot shows the real and the imaginary parts of the experimental values of the input surface impedance of the fibrous material (solid lines) and the computed ones with the values of α_s and β_s obtained above.

By using the values of α_s and β_s obtained with the fitting problem (5.54), the time-harmonic problem (5.41) can be solved and its solution can be used as initial condition for the time-dependent problem (5.43). Then, the pressure at the points where the microphones are located can be measured, and the SPL can be computed at each angular frequency. As it has been described through this chapter, to measure the reverberation time two different strategies may be considered: to use the SPL values or to use the L_{eq} -averages. As in the previous example, the frequency range considered is from 400 to 1000 Hz in third-octave (400, 500, 630, 800, and 1000 Hz). The left plot of Figure 5.10 shows the values of the SPL computed by using (5.49), with a blue line, the values of the SPL obtained by using the root-mean-square (L_2 -norm) of the pressure field instead of the pointwise evaluation of the

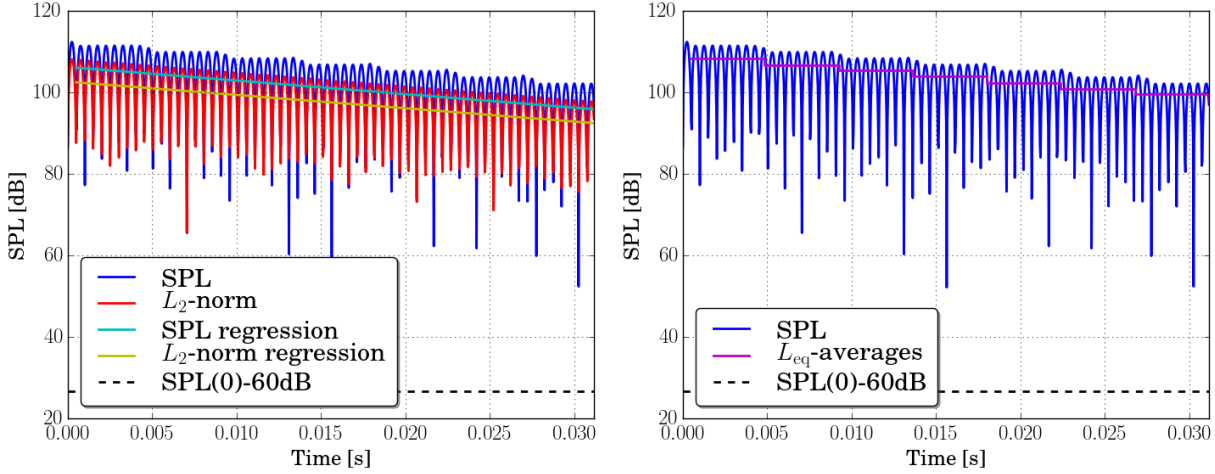


Figure 5.10: Sound pressure level at 1000 Hz of a material made from polypropylene fibers with thickness $h = 20$ mm (sample 3 of the Chapter 1). The surface impedance values are $Z(\omega) = \alpha_s + i\omega\beta_s$, with $\alpha_s = 6622970.608 \text{ Ns/m}^3$ and $\beta_s = 293.047 \text{ Ns/m}^3$. Left: values of the SPL computed by using (5.49) (blue line), values of the SPL obtained using the L_2 -norm of the pressure field (red line), regression line calculated globally using the SPL data at every time step (cyan line), and regression line computed globally using the L_2 -norm of the pressure field (yellow line). Right: values of the SPL computed considering (5.49) (blue line) and regression lines computed by using the values of L_{eq} -averages calculated with the expression (5.53) in some windowing time intervals (magenta line). The dashed black line in both plots represents the point where the initial sound pressure level has decreased by 60 dB.

pressure field at the microphone locations, with a red line, the regression line computed globally by using the SPL data at every time step, with a cyan line, and the regression line calculated globally using the L_2 -norm of the pressure field, with a yellow line. The right plot of Figure 5.10 shows the values of the SPL obtained using (5.49), with a blue line, and the regression lines calculated by using the values of L_{eq} -averages computed with the expression (5.53), in some windowing time intervals, with a magenta line. The dashed black line in both plots represents the point where the initial sound pressure level has decreased by 60 dB. In the right plot of Figure 5.10, it can be observed that only eight values of L_{eq} are used. The time interval has length $\delta t = 0.00439 \text{ s}$ as in the previous example, since both simulations use the same mesh, and the final time is $T = 0.030 \text{ s}$. The left plot shows that this amount of seconds is not enough to compute the reverberation time from the SPL values what leads to an increase in the computational time and thereby an increase in the computational cost.

Now, the absorption values have been computed. In Figure 5.11 the absorption values obtained using the Sabine expression (5.50) and the Millington expression (5.52) are shown. In both plots, the absorption values are computed at normal incidence, i.e., by using the typical length $L = V/S$ (5.51), and the results are compared with the experimental data

from the Kundt's tube and at diffuse field, i.e., by using the typical length $L = 2V/S$ (5.51), and the results are compared with the experimental data from the alpha cabin. In the left plot, the absorption values are computed by using the values of SPL, and in the right plot, the absorption values are obtained by using the values of L_{eq} .

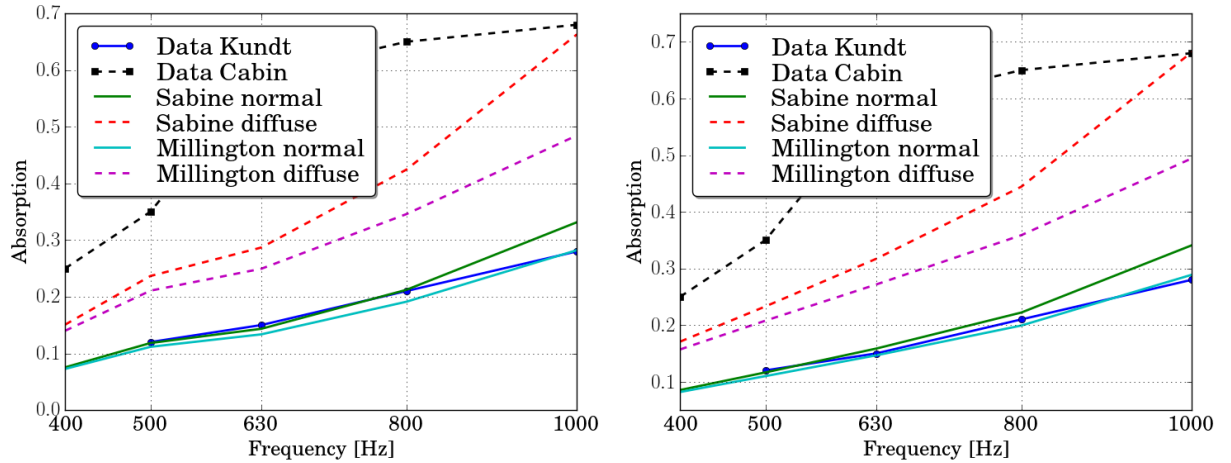


Figure 5.11: Absorption coefficient values of a real fibrous material with impedance surface $Z(\omega) = i\omega\beta_s + \alpha_s$, where $\alpha_s = 6622970.608 \text{ Ns/m}^3$ and $\beta_s = 293.047 \text{ Ns/m}^3$, computed by using the Sabine formula (5.50) and the Millington formula (5.52), at normal incidence and at diffuse field. The absorption values have been obtained by using the values of SPL (left plot) and the values of L_{eq} -averages (right plot). The values computed at normal incidence are compared with the experimental data measured in the Kundt's tube, and the values computed at diffuse field are compared with the experimental data measured in the alpha cabin.

As it can be observed in both plots of Figure 5.11, at normal incidence, Sabine formula overestimates the absorption coefficient while Millington formula predicts the absorption values accurately with relative errors $\varepsilon_{SPL} = 11.57\%$ and $\varepsilon_{L_{eq}} = 4.39\%$. This behavior of Sabine formula is well-known (in fact, [91] shows that Millington formula gives more accurate results than Sabine one). Moreover, taking into account that in a well-designed alpha cabin, the sound field approximates a diffuse field, the absorption coefficients measured in the alpha cabin should be consistent with the values computed in the Kundt's tube [143]. As can be observed in Figure 5.11 at diffuse field, both Sabine and Millington formulas underestimate the absorption coefficient, although both have the same trend as those computed at normal incidence, what shows that the proposed methodology is coherent with the literature.

5.5.2 Three-dimensional simulation

In this section, a three-dimensional simulation in the alpha cabin has been performed. This section includes the description of the geometry of the alpha cabin under consideration,

and the numerical results using as experimental data the absorption coefficient of a real-world fibrous material provided by the same company that it is mentioned in Chapter 1, measured in an alpha cabin.

Geometry

In Figure 5.12, the geometry of the alpha cabin used to measure the experimental data is shown. This alpha cabin has two non-parallel walls, a volume of 4.5 m^3 , and the internal

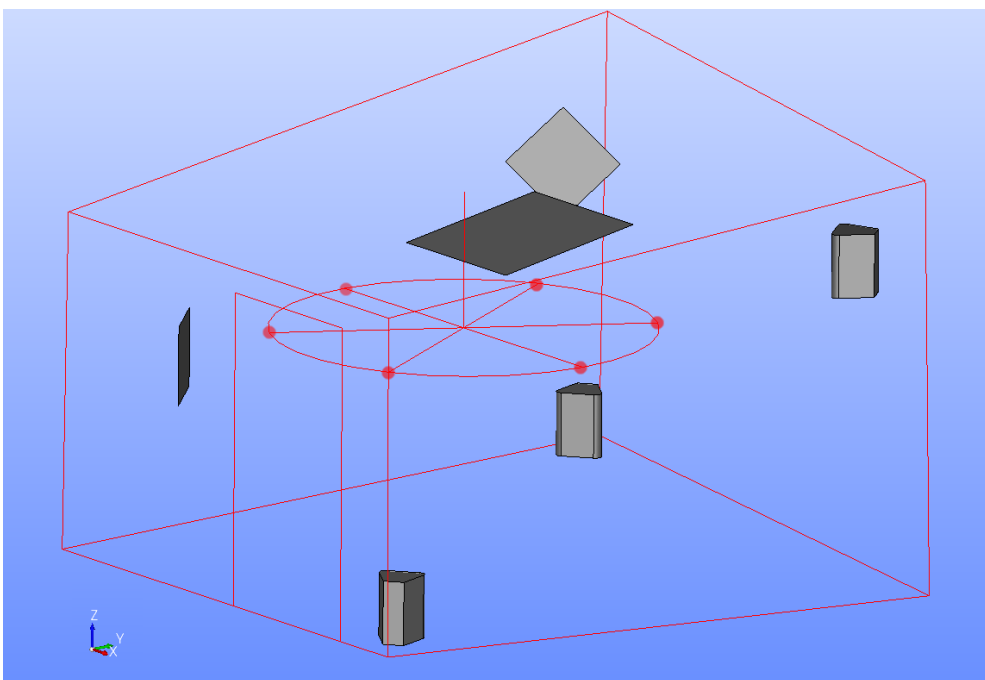


Figure 5.12: Geometry of the alpha cabin. The six microphones are located at the red points.

area is 17 m^2 . This cabin is smaller than the standard one [6], what could lead us to obtain not accurate enough experimental measurements because these dimensions could not ensure the diffusivity of the field inside the cabin. There are three loudspeakers, two on the bottom and one on the top of the cabin, six microphones, located at the red points of the Figure 5.12, and three rectangular diffusers used to achieve a satisfactory diffusion of the field inside the cabin.

In order to perform the numerical simulations, some simplifications in the cabin are considered, such as to replace the loudspeakers by hexahedrons, not to consider the double walls of the cabin, or to eliminate the sample holder, placing the sample on the floor (see Figure 5.13 to check the simplifications). It is supposed that the hexahedrons have an active face whose movement is like a piston, and the rest of them are non active faces.

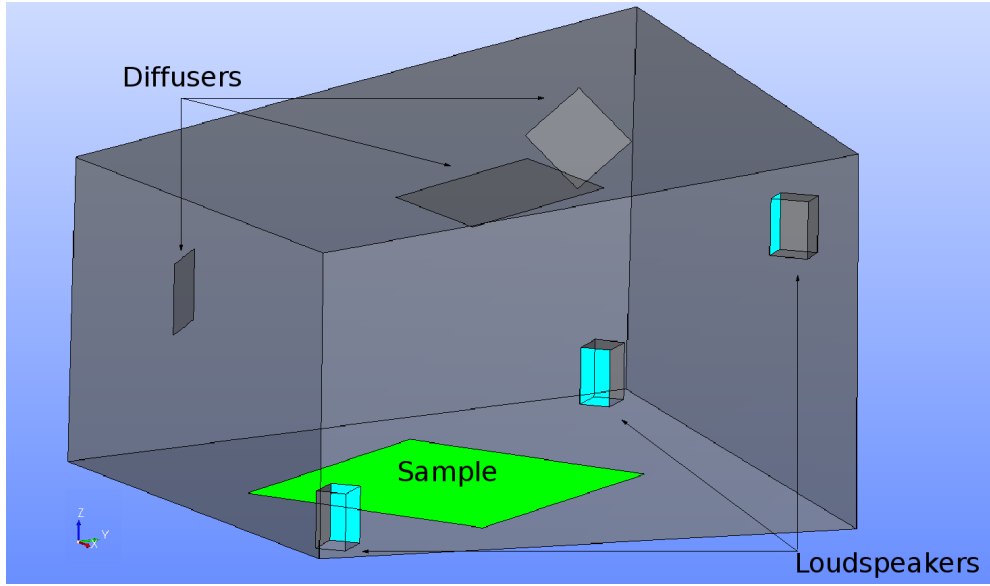


Figure 5.13: Simplified geometry of the alpha cabin used in the numerical simulations.

Simulation with a fibrous sample

The sample under consideration is the same one than in the 2D simulation (see Section 5.5.1): a material made from polypropylene fibers. Once again, in order to solve the time-harmonic problem (5.41) and the time-dependent problem (5.43), it has been considered that the surface impedance values of the material are $Z(\omega) = \alpha_s + i\omega\beta_s$, with $\alpha_s = 6622970.608 \text{ Ns/m}^3$ and $\beta_s = 293.047 \text{ Ns/m}^3$, computed as it has been explained in Section 5.5.1. By using these values, the sound pressure level can be computed at each angular frequency, and the reverberation time may be calculated by using the SPL values, or considering the L_{eq} -averages.

The left plot of the Figure 5.14 shows the values of the SPL obtained using (5.49), with a blue line, the values of the SPL using the root-mean-square (L_2 -norm) values of the pressure field instead of the pressure field computed pointwise at the microphone locations, with a red line, the regression line calculated globally by using the SPL data at every time step, with a cyan line, and the regression line computed globally by using the L_2 -norm of the pressure field, with a yellow line. The right plot of the Figure 5.14 shows the values of the SPL obtained using (5.49), with a blue line, and the regression lines computed considering the values of L_{eq} obtained with the expression (5.53), in some windowing time intervals, with a magenta line. Once again, the dashed black line represents the point where the initial sound pressure level has decreased 60 dB. In this example, only six values of L_{eq} are used, the windowing time interval has length $\delta t = 0.0004 \text{ s}$, and the final time is $T = 0.020 \text{ s}$.

Once the SPL has been calculated, the absorption values may be computed. In the left plot in Figure 5.15, the absorption values computed by using the SPL values, and in the right plot, those obtained with the values of L_{eq} are shown by using the Sabine expression (5.50), and the Millington one (5.52). These values are computed at diffuse field, i.e., by using

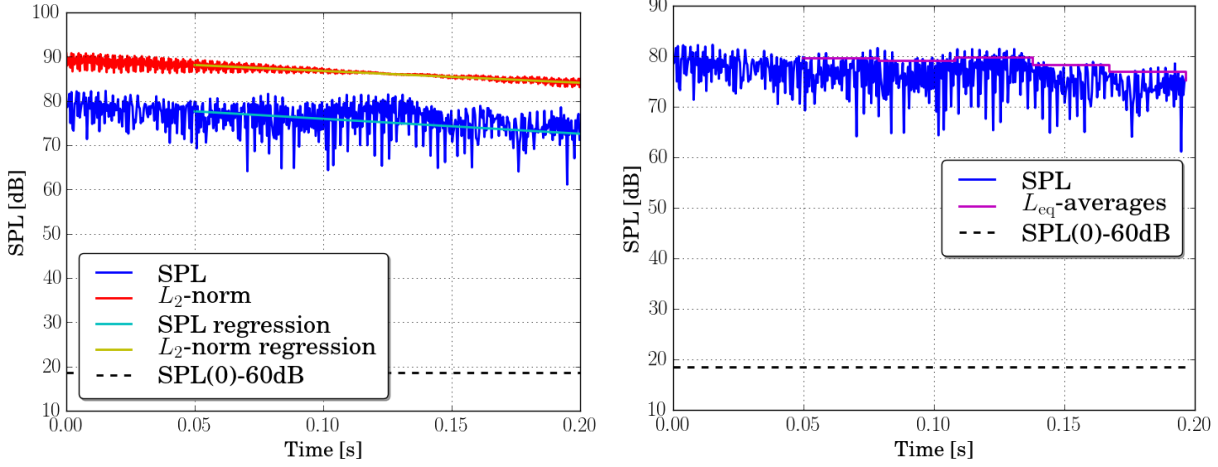


Figure 5.14: Sound pressure level at 1000 Hz, computed by using the impedance coefficients $\alpha_s = 6622970.608 \text{ Ns/m}^3$ and $\beta_s = 293.047 \text{ Ns/m}^3$. Left: values of the SPL obtained with the expression (5.49) (blue line), values computed by using the L_2 -norm of the pressure field (red line), the regression lines calculated globally by using the SPL data at every time step (cyan line), and regression line computed globally obtained by using the L_2 -norm of the pressure field (yellow line). Right: values of the SPL computed considering the expression (5.49) (blue line), and regression lines obtained from the values of L_{eq} calculated with the expression (5.53), where the windowing time interval has length $\delta t = 0.0004 \text{ s}$ (magenta line). The dashed black line represents the point where the initial SPL has decreased by 60 dB.

the typical length $L = 4V/S$ (5.51), and the numerical results are compared with the experimental data measured in the alpha cabin. As in the 2D simulations, Millington formula gives more accurate results than Sabine one, and both Sabine and Millington diffuse predictions are consistent with the Kundt's tube measurements what, once again, validate the proposed methodology.

5.6 Conclusions

In this chapter, a methodology to compute the absorption coefficient of porous materials at diffuse field in an alpha cabin has been proposed. This methodology is based on the standard ASTM C423-09 [50] to calculate the sound pressure level decay within the cabin. First of all, a discussion about the model which governs the behavior of the cabin is shown. Once the model is chosen, the time evolution of the pressure field in the cabin is studied. The time-dependent problem has been tackled in two different ways: with a methodology based on modal computations, and with a methodology based on a full time-dependent discretization, concluding than the second approach is the most suitable for describing the problem under consideration. Since to measure the absorption coefficient in the cabin

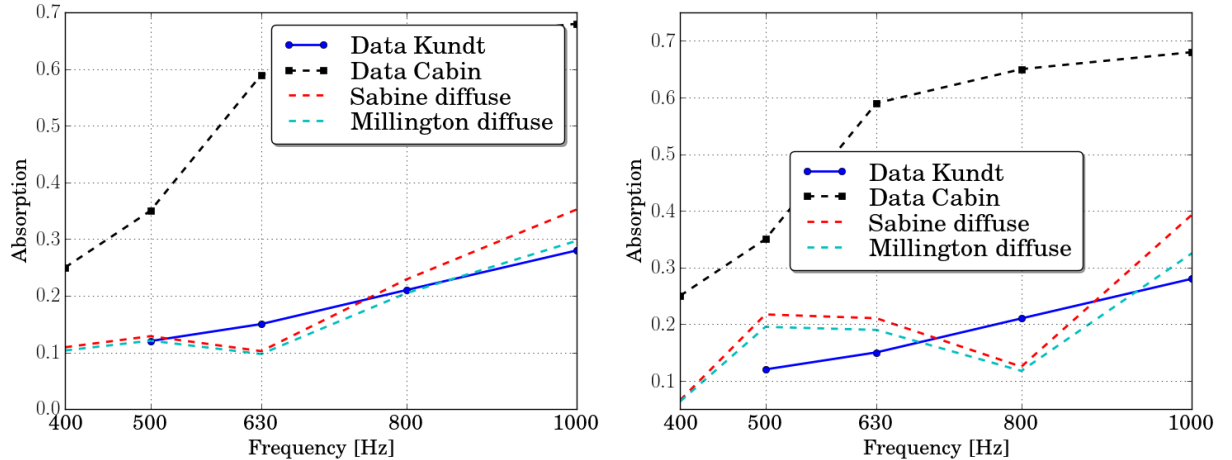


Figure 5.15: Absorption coefficient values of a real fibrous material with impedance surface $Z(\omega) = i\omega\beta_s + \alpha_s$, where $\alpha_s = 6622970.608 \text{ Ns/m}^3$ and $\beta_s = 293.047 \text{ Ns/m}^3$, computed by using the Sabine formula (5.50) and the Millington formula (5.52) at diffuse field compared with the experimental data measured in the alpha cabin. The absorption values have been obtained by using the values of SPL (left plot) and the values of L_{eq} (right plot).

it is necessary to measure the changes in the values of the reverberation time due to the placement of the sample in the cabin, a time-dependent problem is solved, the reverberation time is measured, and the absorption coefficient at diffuse field is calculated by using Sabine formula [160], or Millington one [127].

To illustrate the methodology, some numerical results in two-dimensional and three-dimensional domains have been performed. To validate the method, some two-dimensional simulations have been done, using manufactured data, and showing a good agreement between the computed results and the experimental ones. As is well-known [91], the Millington formula is more accurate than the Sabine one. Also, some two-dimensional simulations have been performed with a fibrous material. In this case, the numerical results at normal incidence are consistent with the experimental data measured in the Kundt's tube. However, it does not happen the same with the results at oblique incidence. These results are quite different with the experimental data measured in the alpha cabin. Following [143], the absorption values measured in the tube and the cabin should be consistent. This does not happen with the experimental data, but with the computed data do. Something similar is shown with the three-dimensional simulations: the computed data show good agreement with the Kundt's tube data but not with the alpha cabin. Since the Kundt's tube values are reliable, this leads us to think about the trustworthiness of the experimental data. This bad agreement could be caused by several reasons: the cabin used in this chapter is smaller than the standard one, and maybe this does not allow us to have a diffuse field, some building defects of the cabin (in [92], there are more details about all situations where a diffuse field can be expected or not). But, as it has been described in [65], often appear many discrepancies between the absorption values of a sample obtained from different laboratories,

or even from the same one due to the difficulties to reproduce the same conditions in the cabin, especially at low frequencies so the bad agreements could happen due to the lack of reproducibility of this kind of rooms.

Chapter 6

Characterization of viscoelastic materials using impact excitations

Contents

6.1	Introduction	259
6.2	Experimental determination of the dynamic stiffness using the standard ISO 9052-1	259
6.3	Design of the hierarchy of models	261
6.4	Modal decomposition of compressional solutions of a viscoelastic model	261
6.5	Full time-dependent one- and three-dimensional viscoelastic model	263
6.5.1	Strong formulation	264
6.5.2	Variational formulation	265
6.5.3	Finite element discretization	266
6.6	Full time-dependent three-dimensional poroelastic model	268
6.6.1	Strong formulation	269
6.6.2	Variational formulation	270
6.7	Inverse problem to determine the elastic coefficients	274
6.8	Numerical results	275
6.8.1	Code validation	275
6.8.2	Viscoelastic sample	281
6.9	Conclusions	283

6.1 Introduction

Floating floors have been widely studied to improve the impact sound insulation in buildings [57, 99, 104, 133, 165]. There is a wide range of materials used as underlayers, such as mineral and glass wools, polyurethane or polyethylene foams, synthetic fibers, or recycling materials as carpet waste, wood waste, or tire recycling [8, 158, 165]. The dynamic stiffness of these materials is fundamental not only to quantify the reduction of noise propagation but also to predict the reduction of the impact of the sound pressure level of a material. The dynamic stiffness per unit area can be measured using different measurement excitation methods, such as impact hammer, white noise, ESS signal, or MLS signal [87].

The standard ISO 9052-1 [3] is used to determine the dynamic stiffness of elastic materials used under floating floors, which is one of the parameters used to determine the acoustic insulation of these floors. However, such value is not directly related to the elastic coefficients typically used in the Hooke's linear model, such as the Young modulus, the Poisson coefficient, or the loss factor. Hence, an additional numerical or experimental procedure is required to determine from a quantitative point of view those material coefficients. In the present work, a numerical methodology based on a hierarchical modeling approach (introduced in [49]) is proposed, using only those experimental data obtained from the standard ISO 9052-1 framework. Consequently, the purpose of this chapter is focused on the computation of some elastic coefficients of viscoelastic and poroelastic materials by using a hierarchy of models.

The work described in this chapter is a collaboration with Jesús Carbajo, Pedro Poveda, and Jaime Ramis from the Department of Physics, System Engineering and Signal Theory of the University of Alicante, and the available experimental data are provided by the research group to which they belong. This chapter is organized as follows: Section 6.2 describes the methodology to compute the dynamic stiffness of a solid material following the standard ISO 9052-1 [3]. The design of the hierarchy of models is described in Section 6.3. Then, the different models used in the present chapter are discussed: the mode decomposition used for the compressional waves of a viscoelastic model is introduced in Section 6.4, the time-dependent one- and three-dimensional viscoelastic models are introduced in Section 6.5, and the full three-dimensional poroelastic model is described in detail in Section 6.6, respectively, including the variational formulation of the problem, and the finite element discretization. Section 6.8 presents some numerical results to validate the code as well as some simulations with viscoelastic samples. Finally, Section 6.9 summarizes the main conclusions of this chapter.

6.2 Experimental determination of the dynamic stiffness using the standard ISO 9052-1

Definition 6.2.1. *In a linear static regime, the static stiffness per surface unit s' associated with an elastic material supporting a compressional motion is the ratio between the applied*

force, and the responsive displacement due to this force, this is, it is given by

$$s' = \frac{F/S}{\Delta d},$$

where F is the force perpendicular to the sample, S is the surface of the sample, and Δd is the dynamic change in the thickness of the elastic material.

However, the determination of the apparent dynamic stiffness per surface unit of a test sample is made by a dynamic resonance method, in which the resonance frequency of the fundamental vertical vibration is measured in a mass-spring system, where the mass is the load plate, and the sample of the elastic material being tested is acting as spring (with or without damping effects).

To perform this experimental test, the elastic sample is placed between the base and the load plate. The load plate is made of steel, and has dimensions (200 ± 3) mm \times (200 ± 3) mm. Both the base and the load plate must be rigid enough to avoid bending waves within the frequency range of interest. The excitation is made following the setting shown in Figure 6.1. The total load on the test sample is 8 kg. Excitation and measurement devices must be applied in such a way that only vertical oscillations occur.

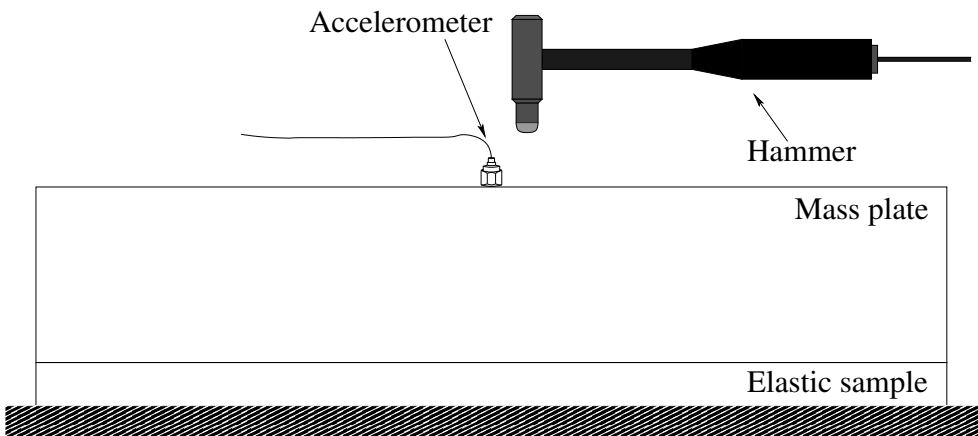


Figure 6.1: Setup used to measure the dynamic stiffness of an elastic sample following the standard ISO 9052-1 [3].

In order to obtain the resonance frequency, the acceleration of the plate is measured by means of an accelerometer, located in the center of the plate, and the plate is struck by a hammer equipped with an accelerometer in an area around the accelerometer, in order to avoid undesirable effects. Hence, from the measured input time series (force due to the hammer) and output time series (acceleration on the top surface of the steel plate), a standard spectral procedure can identify the most relevant frequency contained in such time series, which will be read as the resonance frequency.

Definition 6.2.2. *The apparent dynamic stiffness of the sample per surface unit, s'_r is defined by*

$$s'_r = 2\pi m'_t \omega_r,$$

where m'_t is the total mass per surface unit used during the test, and ω_r is the experimental resonance angular frequency.

Typically, if the material is assumed porous, and it has a high airflow resistivity, then $s' = s'_r$.

6.3 Design of the hierarchy of models

The definition of a hierarchy of models involves different assumptions, from the most simplistic ones to those where the most sophisticated details are taking into account in the model. Hence, the levels of accuracy at each item of the hierarchy are ruled mainly by the assumptions made at each model. In this proposed approach, the differences among the mathematical models are based on different used constitutive laws (viscoelastic and poroelastic models), the one- and three-dimensional configurations, and neglecting or not the shear modes, which possibly are contributed to the solution of the model. In summary, size different mathematical assumption settings are used in the hierarchical modeling approach. Table 6.1 summarizes the items of the proposed modeling approach, where the model number indicates the order in the hierarchy of models.

Model	Description
Model ₀	Time-dependent 0-dimensional mass-spring model
Model ₁	Uni-modal compressional solution of a viscoelastic model
Model ₂	Multi-modal compressional expansion of a viscoelastic model
Model ₃	Time-dependent 1-dimensional viscoelastic model
Model ₄	Time-dependent 3-dimensional viscoelastic model
Model ₅	Time-dependent 3-dimensional poroelastic model

Table 6.1: Model number and description of each item in the hierarchical modeling approach.

The first level in the hierarchy, namely Model₀ has been already described in Section 6.2, since it is the model used for the computations included in the standard ISO 9052-1. The mode decomposition used for the compressional waves of a viscoelastic model (involved in Model₁ and Model₂) is introduced in Section 6.4, the time-dependent one- and three-dimensional viscoelastic model (Model₃ and Model₄) are introduced in Section 6.5, and the full three-dimensional poroelastic model (Model₅) is described in detail in Section 6.6.

6.4 Modal decomposition of compressional solutions of a viscoelastic model

Since the geometry of the experimental setting can be read as a simple Cartesian product of intervals, a classical separation of variables procedure can be used to compute the com-

pressional modes in the perpendicular direction to the planar contact surfaces of the steel plate and the elastic sample. With this purpose, it is assumed that the contact interfaces between the rigid wall, the elastic sample and the steel plate are placed on

$$\begin{aligned}\Gamma_L &= \{(x, y, z) \in \mathbb{R}^3 : (x, y) \in (0, L)^2, z = 0\}, \\ \Gamma_C &= \{(x, y, z) \in \mathbb{R}^3 : (x, y) \in (0, L)^2, z = d\}, \\ \Gamma_N &= \{(x, y, z) \in \mathbb{R}^3 : (x, y) \in (0, L)^2, z = d + L\}.\end{aligned}$$

If a linear elastic regime is also supposed for the time-harmonic compressional vibrations of the steel plate and the elastic sample, the coupled conditions written as follows:

$$\begin{aligned}\Sigma_E(\mathbf{U}^E)\mathbf{n} &= 0 && \text{on } \Gamma_L, \\ \mathbf{U}^E \cdot \mathbf{n} &= \mathbf{U}^V \cdot \mathbf{n} && \text{on } \Gamma_C, \\ \Sigma_E(\mathbf{U}^E)\mathbf{n} \cdot \mathbf{n} &= \Sigma_V(\mathbf{U}^V)\mathbf{n} \cdot \mathbf{n} && \text{on } \Gamma_C, \\ \mathbf{U}^V \cdot \mathbf{n} &= 0 && \text{on } \Gamma_N,\end{aligned}$$

where $\Sigma_E(\mathbf{U}^E)$ and $\Sigma_V(\mathbf{U}^V)$ are the time-harmonic stress tensor in the steel plate and in the viscoelastic solid, respectively with \mathbf{U}^E and \mathbf{U}^V the displacement fields in the steel plate and in the viscoelastic solid, respectively.

Now, it is assumed that the excitation forces on the top surface of the steel plate can be read as a uniform (and so constant) force acting only on compression. In this case, the displacement fields are given by

$$\begin{aligned}\mathbf{U}^E &= (A_1 e^{ik_E z} + A_2 e^{-ik_E z}) \mathbf{e}_3, \\ \mathbf{U}^V &= (B_1 e^{ik_V z} + B_2 e^{-ik_V z}) \mathbf{e}_3.\end{aligned}$$

Hence, to compute the resonance frequencies of the mechanical coupled system, it is required to find the non-trivial solutions of the following linear system:

$$\left\{ \begin{array}{lcl} ik_E(2\mu_E + \lambda_E)A_1 - ik_E(2\mu_E + \lambda_E)A_2 & = 0, \\ e^{ik_E d}A_1 + e^{-ik_E d}A_2 - e^{ik_V d}B_1 - e^{-ik_V d}B_2 & = 0, \\ ik_E(2\mu_E + \lambda_E)e^{ik_E d}A_1 - ik_E(2\mu_E + \lambda_E)e^{-ik_E d}A_2 \\ -ik_V(2\mu_V + \lambda_V)e^{ik_V d}B_1 + ik_V(2\mu_V + \lambda_V)e^{-ik_V d}B_2 & = 0, \\ e^{ik_V(d+L)}B_1 + e^{-ik_V(d+L)}B_2 & = 0. \end{array} \right.$$

Taking into account $k_E = \frac{\omega}{c_E}$, $k_V = \frac{\omega}{c_V}$, $c_E = \sqrt{\frac{2\mu_E + \lambda_E}{\rho_E}}$ and $c_V = \sqrt{\frac{2\mu_V + \lambda_V}{\rho_V}}$, the matrix description of the above linear system is given by

$$\begin{pmatrix} \omega c_E \rho_E & -\omega c_E \rho_E & 0 & 0 \\ e^{i \frac{\omega}{c_E} d} & e^{-i \frac{\omega}{c_E} d} & -e^{i \frac{\omega}{c_V} d} & -e^{-i \frac{\omega}{c_V} d} \\ \omega c_E \rho_E e^{i \frac{\omega}{c_E} d} & -\omega c_E \rho_E e^{-i \frac{\omega}{c_E} d} & -\omega c_V \rho_V e^{i \frac{\omega}{c_V} d} & \omega c_V \rho_V e^{-i \frac{\omega}{c_V} d} \\ 0 & 0 & e^{i \frac{\omega}{c_V} (d+L)} & +e^{-i \frac{\omega}{c_V} (d+L)} \end{pmatrix} \begin{pmatrix} A_1 \\ A_2 \\ B_1 \\ B_2 \end{pmatrix} = \begin{pmatrix} 0 \\ 0 \\ 0 \\ 0 \end{pmatrix},$$

and straightforward (but tedious) calculations show that the above matrix is singular if ω is a solution of the following non-linear dispersion relation:

$$\begin{aligned} 4\omega^2 Z_E \left[-Z_V \cos\left(\frac{\omega}{c_E} d\right) \cos\left(\frac{\omega}{c_V} L\right) + Z_E \sin\left(\frac{\omega}{c_E} d\right) \sin\left(\frac{\omega}{c_V} L\right) \right] &= 0 \\ \Leftrightarrow \tan\left(\frac{\omega}{c_E} d\right) \tan\left(\frac{\omega}{c_V} L\right) &= \frac{Z_V}{Z_E}. \end{aligned} \quad (6.1)$$

If the set of solutions of the dispersion relation (compressional resonance frequencies) is denoted by $\{\omega_n\}_{n \in \mathbb{N}}$, a multimodal expansion of the compressional solutions of this coupled problem can be expressed by

$$\begin{aligned} \mathbf{U}^E(z) &= \sum_{n \in \mathbb{N}} (A_1^n e^{ik_E^n z} + A_2^n e^{-ik_E^n z}) \mathbf{e}_3, \\ \mathbf{U}^V(z) &= \sum_{n \in \mathbb{N}} (B_1^n e^{ik_V^n z} + B_2^n e^{-ik_V^n z}) \mathbf{e}_3, \end{aligned}$$

where $k_E^n = \frac{\omega_n}{c_E}$, $k_V^n = \frac{\omega_n}{c_V}$. Consequently, under this framework, the time-dependent compressional solutions can be written as

$$\begin{aligned} \mathbf{u}^E(z, t) &= \sum_{n \in \mathbb{N}} (A_1^n e^{ik_E^n z} + A_2^n e^{-ik_E^n z}) e^{-i\omega_n t} \mathbf{e}_3, \\ \mathbf{u}^V(z, t) &= \sum_{n \in \mathbb{N}} (B_1^n e^{ik_V^n z} + B_2^n e^{-ik_V^n z}) e^{-i\omega_n t} \mathbf{e}_3. \end{aligned}$$

In the case of Model₁, only the first term of the series is taking into account, which corresponds to the lowest resonance frequency ω_0 (with the smallest magnitude). If Model₂ is used, the series is truncated to considering only a finite number N of terms (being N typically a low integer value).

6.5 Full time-dependent one- and three-dimensional viscoelastic model

In this section, a viscoelastic material is considered. To find an approximated solution of this coupled problem, a discretization based on a finite element method has been utilized. In order to write the strong differential form, both models, the steel plate one and the viscoelastic solid layer, have been written in terms of the displacement field. Both one- and three-dimensional problems admit the same finite element procedure. The only difference consists in the differential operators (being only simple ordinary differential operators in the first Cartesian coordinate in the one-dimensional problem), and the computational domains (which will be intervals with lengths determined by the thickness of the steel plate and the damping sample). Having these differences in mind, and for the sake of the simplicity

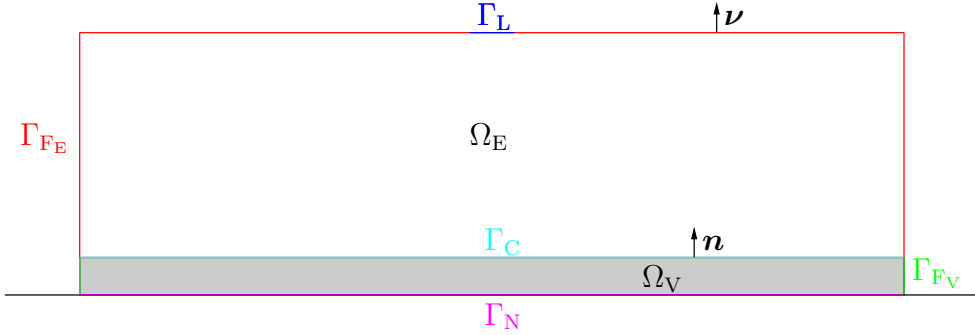


Figure 6.2: Geometric scheme of the coupled problem with all the domains and boundaries involved. The viscoelastic solid is highlighted in gray.

in the exposition, the detailed description of the method will be introduced in the three-dimensional case. Let Ω_E and Ω_V be the domains occupied by the elastic plate and the viscoelastic solid, respectively (see Figure 6.2). The domain Ω_V has 3 disjoint boundaries, $\partial\Omega_V = \Gamma_N \cup \Gamma_{F_V} \cup \Gamma_C$, being Γ_N the boundary where a rigid wall condition is imposed, Γ_{F_V} the free boundary, and Γ_C the contact between the viscoelastic solid and the elastic plate. The domain Ω_E has 3 disjoint boundaries, $\partial\Omega_E = \Gamma_L \cup \Gamma_{F_E} \cup \Gamma_C$, being Γ_L the boundary where the load is imposed, and Γ_{F_E} the free boundary. In this section, \mathbf{n} is the unit normal vector to $\Gamma_C \cup \Gamma_N \cup \Gamma_{F_V}$ outwards the viscoelastic solid, and $\boldsymbol{\nu}$ is the unit normal vector to $\Gamma_{F_E} \cup \Gamma_L$ outwards the elastic plate.

6.5.1 Strong formulation

The time-dependent problem can be described by the following coupled system of partial differential equations:

$$\rho_V \ddot{\mathbf{u}}^V - \operatorname{div}(\sigma'_V(\mathbf{u}^V)) - \operatorname{div}(\sigma''_V(\dot{\mathbf{u}}^V)) = \mathbf{0} \quad \text{in } \Omega_V \times [0, T], \quad (6.2)$$

$$\rho_E \ddot{\mathbf{u}}^E - \operatorname{div}(\sigma_E(\mathbf{u}^E)) = \mathbf{0} \quad \text{in } \Omega_E \times [0, T], \quad (6.3)$$

$$\mathbf{u}^V = \mathbf{0} \quad \text{on } \Gamma_N \times [0, T], \quad (6.4)$$

$$\sigma'_V(\mathbf{u}^V) \cdot \mathbf{n} + \sigma''_V(\dot{\mathbf{u}}^V) \cdot \mathbf{n} = 0 \quad \text{on } \Gamma_{F_V} \times [0, T], \quad (6.5)$$

$$\mathbf{u}^V \cdot \mathbf{n} = \mathbf{u}^E \cdot \mathbf{n} \quad \text{on } \Gamma_C \times [0, T], \quad (6.6)$$

$$(\sigma'_V(\mathbf{u}^V)\mathbf{n} + \sigma''_V(\dot{\mathbf{u}}^V)\mathbf{n}) \cdot \mathbf{n} = \sigma_E(\mathbf{u}^E)\mathbf{n} \cdot \mathbf{n} \quad \text{on } \Gamma_C \times [0, T], \quad (6.7)$$

$$\sigma_E(\mathbf{u}^E) \cdot \boldsymbol{\nu} = 0 \quad \text{on } \Gamma_{F_E} \times [0, T], \quad (6.8)$$

$$\sigma_E(\mathbf{u}^E) \cdot \boldsymbol{\nu} = f(t)\delta_{x_0}(x) \quad \text{on } \Gamma_L \times [0, T], \quad (6.9)$$

$$\mathbf{u}^V(\cdot, 0) = \mathbf{u}_0^V, \quad \dot{\mathbf{u}}^V(\cdot, 0) = \mathbf{v}_0^V \quad \text{in } \Omega_V, \quad (6.10)$$

$$\mathbf{u}^E(\cdot, 0) = \mathbf{u}_0^E, \quad \dot{\mathbf{u}}^E(\cdot, 0) = \mathbf{v}_0^E \quad \text{in } \Omega_E, \quad (6.11)$$

where \mathbf{u}^V , ρ_V , and σ_V are the displacement field, the mass density, and the stress tensor of the viscoelastic solid, and \mathbf{u}^E , ρ_E , and σ_E are the displacement field, the mass density, and

the stress tensor of the elastic plate, respectively, $\dot{\mathbf{u}} = \frac{\partial \mathbf{u}}{\partial t}$, and $\ddot{\mathbf{u}} = \frac{\partial^2 \mathbf{u}}{\partial t^2}$, and \mathbf{u}_0^V and \mathbf{v}_0^V are the initial conditions for the displacement and the velocity in the viscoelastic solid, and \mathbf{u}_0^E and \mathbf{v}_0^E are the initial conditions for the displacement and the velocity in the elastic plate, compute from the time-harmonic source problem.

6.5.2 Variational formulation

To write a weak formulation of the coupled problem (6.2)-(6.11), appropriate functional spaces are introduced. Let $\mathbf{H} = \mathbf{L}^2(\Omega_V) \times \mathbf{L}^2(\Omega_E)$ and $\mathbf{V} = \{(\mathbf{w}^V, \mathbf{w}^E) \in \mathbf{H}_{\Gamma_N}^1(\Omega_V) \times \mathbf{H}^1(\Omega_E) : \mathbf{w}^V \cdot \mathbf{n}|_{\Gamma_C} = \mathbf{w}^E \cdot \mathbf{n}|_{\Gamma_C}\}$, being

$$\mathbf{H}_{\Gamma_N}^1(\Omega_V) = \{\mathbf{w}^V \in (H^1(\Omega_V))^2 : \mathbf{w}^V \cdot \mathbf{n}|_{\Gamma_N} = 0\}.$$

If the equation (6.2) is multiplied by a test function \mathbf{w}^V , which vanishes on Γ_N , and this result is integrated in Ω_V ,

$$\int_{\Omega_V} \rho_V \ddot{\mathbf{u}}^V \cdot \mathbf{w}^V dV - \int_{\Omega_V} \operatorname{div}(\sigma'_V(\mathbf{u}^V)) \mathbf{w}^V dV - \int_{\Omega_V} \operatorname{div}(\sigma''_V(\dot{\mathbf{u}}^V)) \mathbf{w}^V dV = 0.$$

Using a Green's formula (see [24]), it holds

$$\begin{aligned} & \int_{\Omega_V} \rho_V \ddot{\mathbf{u}}^V \cdot \mathbf{w}^V dV + \int_{\Omega_V} \sigma'_V(\mathbf{u}^V) \cdot \nabla \mathbf{w}^V dV + \int_{\Omega_V} \sigma''_V(\dot{\mathbf{u}}^V) \cdot \nabla \mathbf{w}^V dV \\ &= \int_{\partial\Omega_V} [\sigma'_V(\mathbf{u}^V) \cdot \mathbf{n} \mathbf{w}^V + \sigma''_V(\dot{\mathbf{u}}^V) \cdot \mathbf{n} \mathbf{w}^V] dS. \end{aligned}$$

Taking into account (6.5),

$$\begin{aligned} & \int_{\Omega_V} \rho_V \ddot{\mathbf{u}}^V \cdot \mathbf{w}^V dV + \int_{\Omega_V} \sigma'_V(\mathbf{u}^V) \cdot \nabla \mathbf{w}^V dV + \int_{\Omega_V} \sigma''_V(\dot{\mathbf{u}}^V) \cdot \nabla \mathbf{w}^V dV \\ &= \int_{\Gamma_C} [\sigma'_V(\mathbf{u}^V) \cdot \mathbf{n} \cdot \mathbf{w}^V + \sigma''_V(\dot{\mathbf{u}}^V) \cdot \mathbf{n} \cdot \mathbf{w}^V] dS. \end{aligned} \tag{6.12}$$

If the equation (6.3) is multiplied by a test function \mathbf{w}^E , and this result is integrated in Ω_E ,

$$\int_{\Omega_E} \rho_E \ddot{\mathbf{u}}^E \cdot \mathbf{w}^E dV - \int_{\Omega_E} \operatorname{div}(\sigma_E(\mathbf{u}^E)) \mathbf{w}^E dV = 0.$$

Using a Green's formula (see [24]), it holds

$$\int_{\Omega_E} \rho_E \ddot{\mathbf{u}}^E \cdot \mathbf{w}^E dV + \int_{\Omega_E} \sigma_E(\mathbf{u}^E) \cdot \nabla \mathbf{w}^E dV = \int_{\partial\Omega_E} \sigma_E(\mathbf{u}^E) \cdot \boldsymbol{\nu} \mathbf{w}^E dS.$$

Taking into account (6.8) and (6.9),

$$\int_{\Omega_E} \rho_E \ddot{\mathbf{u}}^E \cdot \mathbf{w}^E dV + \int_{\Omega_E} \sigma_E(\mathbf{u}^E) \cdot \nabla \mathbf{w}^E dV = \int_{\Gamma_C} \sigma_E(\mathbf{u}^E) \cdot \boldsymbol{\nu} \mathbf{w}^E dS + \int_{\Gamma_L} f(t) \delta_{x_0}(x) \mathbf{w}^E dS. \quad (6.13)$$

Adding (6.12) and (6.13),

$$\begin{aligned} & \int_{\Omega_V} \rho_V \ddot{\mathbf{u}}^V \cdot \mathbf{w}^V dV + \int_{\Omega_V} \sigma'_V(\mathbf{u}^V) \cdot \nabla \mathbf{w}^V dV + \int_{\Omega_V} \sigma''_V(\dot{\mathbf{u}}^V) \cdot \nabla \mathbf{w}^V dV + \int_{\Omega_E} \rho_E \ddot{\mathbf{u}}^E \cdot \mathbf{w}^E dV \\ & + \int_{\Omega_E} \sigma_E(\mathbf{u}^E) \cdot \nabla \mathbf{w}^E dV = \int_{\Gamma_C} [\sigma'_V(\mathbf{u}^V) \cdot \mathbf{n} \cdot \mathbf{w}^V + \sigma''_V(\dot{\mathbf{u}}^V) \cdot \mathbf{n} \cdot \mathbf{w}^V] dS \\ & + \int_{\Gamma_C} \sigma_E(\mathbf{u}^E) \cdot \boldsymbol{\nu} \mathbf{w}^E dS + \int_{\Gamma_L} f(t) \delta_{x_0}(x) \mathbf{w}^E dS, \end{aligned}$$

and considering (6.7),

$$\begin{aligned} & \int_{\Omega_V} \rho_V \ddot{\mathbf{u}}^V \cdot \mathbf{w}^V dV + \int_{\Omega_V} \sigma'_V(\mathbf{u}^V) \cdot \nabla \mathbf{w}^V dV + \int_{\Omega_V} \sigma''_V(\dot{\mathbf{u}}^V) \cdot \nabla \mathbf{w}^V dV \\ & + \int_{\Omega_E} \rho_E \ddot{\mathbf{u}}^E \cdot \mathbf{w}^E dV + \int_{\Omega_E} \sigma_E(\mathbf{u}^E) \cdot \nabla \mathbf{w}^E dV = \int_{\Gamma_L} f(t) \delta_{x_0}(x) \mathbf{w}^E dS. \end{aligned}$$

Then, the variational formulation of the problem obtained taking into account the functional spaces described above is:

Given an imposed load $f(t) \in C^0(0, T)$, and fixed initial conditions, find $(\mathbf{u}^V, \mathbf{u}^E) \in C^1([0, T]; \mathbf{V}) \cap C^2([0, T]; \mathbf{H})$ satisfying

$$\begin{aligned} & \int_{\Omega_V} \rho_V \ddot{\mathbf{u}}^V \cdot \mathbf{w}^V dV + \int_{\Omega_E} \rho_E \ddot{\mathbf{u}}^E \cdot \mathbf{w}^E dV + \int_{\Omega_V} \sigma''_V(\dot{\mathbf{u}}^V) \cdot \nabla \mathbf{w}^V dV + \int_{\Omega_V} \sigma'_V(\mathbf{u}^V) \cdot \nabla \mathbf{w}^V dV \\ & + \int_{\Omega_E} \sigma_E(\mathbf{u}^E) \cdot \nabla \mathbf{w}^E dV = \int_{\Gamma_L} f(t) \delta_{x_0}(x) \mathbf{w}^E dS, \quad \forall (\mathbf{w}^V, \mathbf{w}^E) \in \mathbf{V}. \end{aligned} \quad (6.14)$$

6.5.3 Finite element discretization

Since the displacement field in the plate, and in the viscoelastic solid belong to the same kind of functional space, $\mathbf{H}_{\Gamma_N}^1(\Omega_V)$ and $\mathbf{H}^1(\Omega_E)$, respectively, the same type of finite elements should be used for each of them to discretize the variational problem (6.14). Let \mathcal{T}_h be a regular tetrahedral partition of $\Omega_V \cup \Omega_E$, such that Ω_V or Ω_E contain completely every tetrahedron. $\mathcal{P}_1(T)$ denotes the space of polynomials of degree 1 on $T \in \mathcal{T}_h$. On each

tetrahedron $T \in \mathcal{T}_h$, the discretization nodes are the vertices of the tetrahedron. Then, the displacement field in the plate and the viscoelastic solid are approximated by means of Lagrangian \mathcal{P}_1 elements and hence belonging respectively to the discrete spaces

$$\begin{aligned}\mathbf{L}_{h,\Gamma_N}(\Omega_V) &= \{\mathbf{w}_h^V \in \mathbf{H}_{\Gamma_N}^1(\Omega_V) : \mathbf{w}_h^V|_T \in \mathcal{P}_1(T)^2 \ \forall T \in \mathcal{T}_h, T \subset \Omega_V\}, \\ \mathbf{L}_h(\Omega_E) &= \{\mathbf{w}_h^E \in \mathbf{H}^1(\Omega_E) : \mathbf{w}_h^E|_T \in \mathcal{P}_1(T)^2 \ \forall T \in \mathcal{T}_h, T \subset \Omega_E\}.\end{aligned}$$

Since both discrete spaces, $\mathbf{L}_{h,\Gamma_N}(\Omega_V)$ and $\mathbf{L}_h(\Omega_E)$, are finite-dimensional (with dimensions N_V and N_E , respectively), a functional basis for each space can be introduced, this is, $\mathbf{L}_{h,\Gamma_N}(\Omega_V) = \langle \mathbf{w}_1^V, \mathbf{w}_2^V, \dots, \mathbf{w}_{N_V}^V \rangle$ and $\mathbf{L}_h(\Omega_E) = \langle \mathbf{w}_1^E, \mathbf{w}_2^E, \dots, \mathbf{w}_{N_E}^E \rangle$. Thus, the functional space \mathbf{V} can be replaced in the discrete problem by

$$\mathbf{V}_h = \{(\mathbf{w}_h^V, \mathbf{w}_h^E) \in \mathbf{V} : (\mathbf{w}_h^V, \mathbf{w}_h^E) \in \mathbf{L}_{h,\Gamma_N}(\Omega_V) \times \mathbf{L}_h(\Omega_E)\}.$$

Now, it is possible to write the discrete approximation of the variational problem:

Given an imposed load $f(t) \in \mathcal{C}^0(0, T)$, and fixed initial conditions, find $(\mathbf{u}_h^V, \mathbf{u}_h^E) \in \mathcal{C}^1([0, T]; \mathbf{V}_h) \cap \mathcal{C}^2([0, T]; \mathbf{V}_h)$ satisfying

$$\begin{aligned}&\int_{\Omega_V} \rho_V \ddot{\mathbf{u}}_h^V \cdot \mathbf{w}_h^V dV + \int_{\Omega_V} \sigma'_V(\mathbf{u}_h^V) \cdot \nabla \mathbf{w}_h^V dV + \int_{\Omega_V} \sigma''_V(\dot{\mathbf{u}}_h^V) \cdot \nabla \mathbf{w}_h^V dV + \int_{\Omega_E} \rho_E \ddot{\mathbf{u}}_h^E \cdot \mathbf{w}_h^E dV \\ &+ \int_{\Omega_E} \sigma_E(\mathbf{u}_h^E) \cdot \nabla \mathbf{w}_h^E dV = \int_{\Gamma_L} f(t) \delta_{x_0}(x) \mathbf{w}_h^E dS, \quad \forall (\mathbf{w}_h^V, \mathbf{w}_h^E) \in \mathbf{V}_h.\end{aligned}\tag{6.15}$$

Matrix formulation

Let $\vec{\mathbf{U}}_h^V$ the column vector of components of \mathbf{u}_h^V in the finite element basis associated with $\mathbf{L}_{h,\Gamma_N}(\Omega_V)$, this is,

$$\mathbf{u}_h^V(\mathbf{p}, t) = \sum_{j=1}^{N_V} [\vec{\mathbf{U}}_h^V(t)]_j \mathbf{w}_j^V(\mathbf{p}),$$

and $\vec{\mathbf{U}}_h^E$ the column vector of components of \mathbf{u}_h^E in the finite element basis associated with $\mathbf{L}_h(\Omega_E)$ and so,

$$\mathbf{u}_h^E(\mathbf{p}, t) = \sum_{j=1}^{N_E} [\vec{\mathbf{U}}_h^E(t)]_j \mathbf{w}_j^E(\mathbf{p}).$$

The matrix formulation of the problem (6.15) is

$$\begin{pmatrix} \mathbf{M}^V & 0 \\ 0 & \mathbf{M}^E \end{pmatrix} \begin{pmatrix} \ddot{\vec{\mathbf{U}}}^V_h \\ \ddot{\vec{\mathbf{U}}}^E_h \end{pmatrix} + \begin{pmatrix} \mathbf{C}^V & 0 \\ 0 & 0 \end{pmatrix} \begin{pmatrix} \dot{\vec{\mathbf{U}}}^V_h \\ \dot{\vec{\mathbf{U}}}^E_h \end{pmatrix} + \begin{pmatrix} \mathbf{K}^V & 0 \\ 0 & \mathbf{K}^E \end{pmatrix} \begin{pmatrix} \vec{\mathbf{U}}^V_h \\ \vec{\mathbf{U}}^E_h \end{pmatrix} = \begin{pmatrix} 0 \\ \mathbf{G}^E \end{pmatrix},$$

where the coefficients of the mass, damping and stiffness matrices are, respectively

$$\begin{aligned} [\mathbf{M}^V]_{ij} &= \int_{\Omega_V} \rho_V \ddot{\mathbf{w}}_j^V \cdot \mathbf{w}_j^V dV, & [\mathbf{M}^E]_{ij} &= \int_{\Omega_E} \rho_E \ddot{\mathbf{w}}_j^E \cdot \mathbf{w}_j^E dV, \\ [\mathbf{C}^V]_{ij} &= \int_{\Omega_V} \sigma''_V(\mathbf{w}_j^V) \cdot \nabla \mathbf{w}_j^V dV, & [\mathbf{K}^V]_{ij} &= \int_{\Omega_V} \sigma'_V(\mathbf{w}_j^V) \cdot \nabla \mathbf{w}_j^V dV, \\ [\mathbf{K}^E]_{ij} &= \int_{\Omega_E} \sigma_E(\mathbf{w}_j^E) \cdot \nabla \mathbf{w}_j^E dV, & [\mathbf{G}^E]_{ij} &= \int_{\Gamma_L} f(t) \delta_{x_0}(x) \mathbf{w}_j^E dS. \end{aligned}$$

The time-dependent system of differential equations has been solved using a second-order unconditional Newmark method (see [16] for further details).

6.6 Full time-dependent three-dimensional poroelastic model

In this section, the sample under consideration is a poroelastic material which is modeled by using the Biot model [29, 30]. In order to find an approximated solution of this coupled problem, a discretization based on a finite element method has been considered. To write the strong differential form, the steel plate model has been written in terms of the displacement field. The poroelastic solid model has been written in terms of the displacement field in the porous frame, and in terms of the pressure field in the fluid. Let Ω_E and Ω_P be the domains occupied by the elastic plate and the poroelastic solid, respectively (see Figure 6.3). The domain Ω_P has 3 disjoint boundaries, $\partial\Omega_P = \Gamma_N \cup \Gamma_{F_P} \cup \Gamma_C$, being Γ_N the boundary

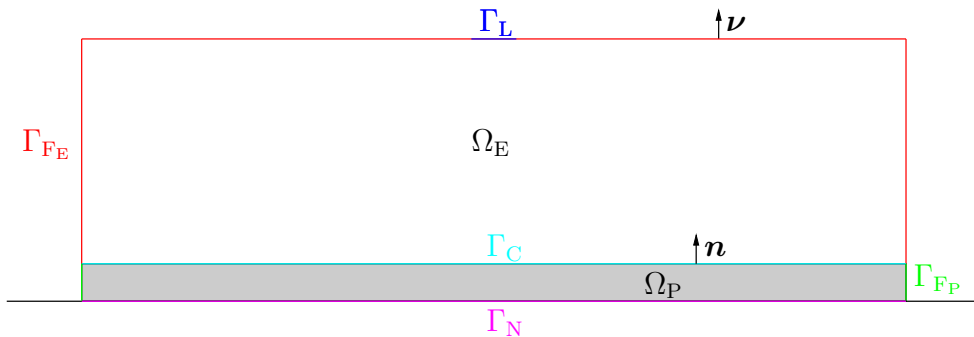


Figure 6.3: Geometric scheme of the coupled problem with all the domains and boundaries involved. The poroelastic solid is highlighted in gray.

where a rigid wall condition is imposed, Γ_{F_P} the free boundary, and Γ_C the contact between the poroelastic solid and the elastic plate. The domain Ω_E has 3 disjoint boundaries, $\partial\Omega_E = \Gamma_L \cup \Gamma_{F_E} \cup \Gamma_C$, being Γ_L the boundary where the load is imposed, and Γ_{F_E} the free boundary. In this section, \mathbf{n} is the unit normal vector to $\Gamma_C \cup \Gamma_N \cup \Gamma_{F_P}$ pointing outwards the poroelastic solid, and $\boldsymbol{\nu}$ is the unit normal vector to $\Gamma_{F_E} \cup \Gamma_L$ outwards the elastic plate.

6.6.1 Strong formulation

The time-dependent poroelastic problem [7] to solve is described by the following set of coupled governing equations:

$$\rho_P \ddot{\mathbf{u}}^S - \operatorname{div}(\tilde{\sigma}'_P(\mathbf{u}^S)) - \operatorname{div}(\tilde{\sigma}''_P(\dot{\mathbf{u}}^S)) = \tilde{\gamma} \operatorname{grad}(\pi_P) \quad \text{in } \Omega_P \times [0, T], \quad (6.16)$$

$$-\Delta \pi_P + \frac{\tilde{\rho}_{22}}{\tilde{R}} \ddot{\pi}_P - \frac{\tilde{\rho}_{22}}{\phi^2} \tilde{\gamma} \operatorname{div}(\dot{\mathbf{u}}^S) = 0 \quad \text{in } \Omega_P \times [0, T], \quad (6.17)$$

$$\rho_E \ddot{\mathbf{u}}^E - \operatorname{div}(\sigma_E(\mathbf{u}^E)) = \mathbf{0} \quad \text{in } \Omega_E \times [0, T], \quad (6.18)$$

$$\mathbf{u}^S = \mathbf{0}, \quad \mathbf{u}^F \cdot \mathbf{n} - \mathbf{u}^S \cdot \mathbf{n} = 0 \quad \text{on } \Gamma_N \times [0, T], \quad (6.19)$$

$$\sigma'_t(\mathbf{u}^S) \cdot \mathbf{n} + \sigma''_t(\dot{\mathbf{u}}^S) \cdot \mathbf{n} = 0 \quad \text{on } \Gamma_{F_P} \times [0, T], \quad (6.20)$$

$$\pi_P = 0 \quad \text{on } \Gamma_{F_P} \times [0, T], \quad (6.21)$$

$$\sigma'_t(\mathbf{u}^S) \cdot \mathbf{n} + \sigma''_t(\dot{\mathbf{u}}^S) \cdot \mathbf{n} = \sigma_E(\mathbf{u}^E) \cdot \mathbf{n} \quad \text{on } \Gamma_C \times [0, T], \quad (6.22)$$

$$\mathbf{u}^F \cdot \mathbf{n} - \mathbf{u}^S \cdot \mathbf{n} = 0, \quad \mathbf{u}^S = \mathbf{u}^E \quad \text{on } \Gamma_C \times [0, T], \quad (6.23)$$

$$\sigma_E(\mathbf{u}^E) \cdot \boldsymbol{\nu} = 0 \quad \text{on } \Gamma_{F_E} \times [0, T], \quad (6.24)$$

$$\sigma_E(\mathbf{u}^E) \cdot \boldsymbol{\nu} = f(t) \delta_{x_0}(x) \quad \text{on } \Gamma_L \times [0, T], \quad (6.25)$$

$$\mathbf{u}^S(\cdot, 0) = \mathbf{u}_0^S, \quad \dot{\mathbf{u}}^S(\cdot, 0) = \mathbf{v}_0^S \quad \text{in } \Omega_P, \quad (6.26)$$

$$\mathbf{u}^F(\cdot, 0) = \mathbf{u}_0^F, \quad \dot{\mathbf{u}}^F(\cdot, 0) = \mathbf{v}_0^F \quad \text{in } \Omega_P, \quad (6.27)$$

$$\pi_P(\cdot, 0) = \pi_0^P \quad \text{in } \Omega_P, \quad (6.28)$$

$$\mathbf{u}^E(\cdot, 0) = \mathbf{u}_0^E, \quad \dot{\mathbf{u}}^E(\cdot, 0) = \mathbf{v}_0^E \quad \text{in } \Omega_E, \quad (6.29)$$

where $\tilde{\rho}_{11}$, $\tilde{\rho}_{12}$ and $\tilde{\rho}_{22}$ are coefficients related to the geometry of the frame that can be written as

$$\tilde{\rho}_{11} = \rho_1 + \rho_a - i\sigma\phi^2 \frac{G(\omega)}{\omega},$$

$$\tilde{\rho}_{12} = -\rho_a + i\sigma\phi^2 \frac{G(\omega)}{\omega},$$

$$\tilde{\rho}_{22} = \phi\rho_1 + \rho_a - i\sigma\phi^2 \frac{G(\omega)}{\omega},$$

being ϕ the porosity, σ the airflow resistivity, $G(\omega)$ the frequency-dependent function related to the chosen porous model, ρ_a the inertial coupling term related to the tortuosity α_∞ following the expression $\rho_a = \phi\rho_0(\alpha_\infty - 1)$,

$$\tilde{\gamma} = \phi \left(\frac{\tilde{\rho}_{12}}{\tilde{\rho}_{22}} - \frac{\tilde{Q}}{\tilde{R}} \right), \quad (6.30)$$

with \tilde{R} , \tilde{P} and \tilde{Q} are the elastic coefficients, given by

$$\begin{aligned}\tilde{P} &= \frac{(1-\pi)(1-\phi - \frac{K_b}{K_s})K_s + \frac{K_s}{K_f}K_b}{1-\phi - \frac{K_b}{K_s} + \phi\frac{K_s}{K_f}} + \frac{4}{3}N, \\ \tilde{Q} &= \frac{(1-\phi - \frac{K_b}{K_s})\phi K_s}{1-\phi - \frac{K_b}{K_s} + \phi\frac{K_s}{K_f}}, \\ \tilde{R} &= \frac{\phi^2 K_s}{1-\phi - \frac{K_b}{K_s} + \phi\frac{K_s}{K_f}},\end{aligned}\quad (6.31)$$

where K_b , K_f and K_s are the bulk modulus of the frame at constant pressure in air, the bulk modulus of the air, and of the elastic solid from which the frame is made, respectively, and N is the shear modulus of the material. Since the air does not contribute to the shear restoring force, N is also the shear modulus of the frame. When K_s is infinite (if the frame is made of a not compressible material) (6.31) can be simplified and results

$$\begin{aligned}\tilde{P} &= K_b + \frac{(1-\phi)^2}{\phi}K_f + \frac{4}{3}N, \\ \tilde{Q} &= (1-\phi)K_f, \\ \tilde{R} &= \phi K_f.\end{aligned}$$

This supposition can be used for most of the sound-absorbing porous materials. The bulk modulus K_b is given by

$$K_b = \frac{2N(\nu+1)}{3(1-2\nu)},$$

where ν is the Poisson coefficient of the frame.

6.6.2 Variational formulation

To write a weak formulation of the coupled problem, appropriate functional spaces are introduced. Let $\mathbf{H} = \mathbf{L}^2(\Omega_P) \times \mathbf{L}^2(\Omega_P) \times \mathbf{L}^2(\Omega_E)$, and $\mathbf{V} = \{(\mathbf{w}^S, q, \mathbf{w}^E) \in \mathbf{H}_{\Gamma_N}^1(\Omega_P) \times H_{\Gamma_{F_P}}^1(\Omega_P) \times \mathbf{H}^1(\Omega_E) : \mathbf{w}^S|_{\Gamma_C} = \mathbf{w}^E|_{\Gamma_C}\}$, where

$$\begin{aligned}\mathbf{H}_{\Gamma_N}^1(\Omega_P) &= \{\mathbf{w} \in (\mathbf{H}^1(\Omega_P))^2 : \mathbf{w} \cdot \mathbf{n}|_{\Gamma_N} = 0\}, \\ H_{\Gamma_{F_P}}^1(\Omega_F) &= \{q \in H^1(\Omega_F) : q|_{\Gamma_{F_P}} = 0\}.\end{aligned}$$

To obtain the variational formulation of the solid part, if the equation (6.16) is multiplied by a test function \mathbf{w}^S , which vanishes on Γ_N , and this result is integrated in Ω_P , it results

$$\int_{\Omega_P} \rho_P \ddot{\mathbf{u}}^S \cdot \mathbf{w}^S dV - \int_{\Omega_P} \operatorname{div}(\tilde{\sigma}'_P(\mathbf{u}^S)) \mathbf{w}^S dV - \int_{\Omega_P} \operatorname{div}(\tilde{\sigma}''_P(\dot{\mathbf{u}}^S)) \mathbf{w}^S dV - \int_{\Omega_P} \tilde{\gamma} \nabla \pi_P \mathbf{w}^S dV = \mathbf{0}.$$

Using a Green's formula (see [24]), it holds

$$\begin{aligned} & \int_{\Omega_P} \rho_P \ddot{\mathbf{u}}^S \cdot \mathbf{w}^S dV + \int_{\Omega_P} \tilde{\sigma}'_P(\mathbf{u}^S) \cdot \nabla \mathbf{w}^S dV + \int_{\Omega_P} \tilde{\sigma}''_P(\dot{\mathbf{u}}^S) \cdot \nabla \mathbf{w}^S dV - \int_{\Omega_P} \tilde{\gamma} \nabla \pi_P \mathbf{w}^S dV \\ &= \int_{\partial\Omega_P} \tilde{\sigma}'_P(\mathbf{u}^S) \cdot \mathbf{n} \mathbf{w}^S dS + \int_{\partial\Omega_P} \tilde{\sigma}''_P(\dot{\mathbf{u}}^S) \cdot \mathbf{n} \mathbf{w}^S dS. \end{aligned}$$

Considering $\sigma_t(\mathbf{u}^S, \pi_P) = \tilde{\sigma}_P(\mathbf{u}^S) - \phi \left(1 + \frac{\tilde{Q}}{\tilde{R}}\right) \pi_P I$

$$\begin{aligned} & \int_{\Omega_P} \rho_P \ddot{\mathbf{u}}^S \cdot \mathbf{w}^S dV + \int_{\Omega_P} \tilde{\sigma}'_P(\mathbf{u}^S) \cdot \nabla \mathbf{w}^S dV + \int_{\Omega_P} \tilde{\sigma}''_P(\dot{\mathbf{u}}^S) \cdot \nabla \mathbf{w}^S dV - \int_{\Omega_P} \tilde{\gamma} \nabla \pi_P \mathbf{w}^S dV \\ &= \int_{\partial\Omega_P} \sigma'_t(\mathbf{u}^S) \cdot \mathbf{n} \mathbf{w}^S dS + \int_{\partial\Omega_P} \sigma''_t(\dot{\mathbf{u}}^S) \cdot \mathbf{n} \mathbf{w}^S dS + \int_{\partial\Omega_P} \phi \left(1 + \frac{\tilde{Q}}{\tilde{R}}\right) \pi_P \mathbf{w}^S \cdot \mathbf{n} dS, \end{aligned}$$

and taking into account (6.20) and (6.21),

$$\begin{aligned} & \int_{\Omega_P} \rho_P \ddot{\mathbf{u}}^S \cdot \mathbf{w}^S dV + \int_{\Omega_P} \tilde{\sigma}'_P(\mathbf{u}^S) \cdot \nabla \mathbf{w}^S dV + \int_{\Omega_P} \tilde{\sigma}''_P(\dot{\mathbf{u}}^S) \cdot \nabla \mathbf{w}^S dV - \int_{\Omega_P} \tilde{\gamma} \nabla \pi_P \mathbf{w}^S dV \\ &= \int_{\Gamma_C} [\sigma'_t(\mathbf{u}^S) \cdot \mathbf{n} \cdot \mathbf{w}^S + \sigma''_t(\dot{\mathbf{u}}^S) \cdot \mathbf{n} \cdot \mathbf{w}^S] dS + \int_{\Gamma_C} \phi \left(1 + \frac{\tilde{Q}}{\tilde{R}}\right) \pi_P \mathbf{w}^S \cdot \mathbf{n} dS. \quad (6.32) \end{aligned}$$

To obtain the variational formulation of the fluid part, multiplying the equation (6.17) by $\frac{\phi^2}{\tilde{\rho}_{22}}$ results

$$-\frac{\phi^2}{\tilde{\rho}_{22}} \Delta \pi_P + \frac{\phi^2}{\tilde{R}} \ddot{\pi}_P - \tilde{\gamma} \operatorname{div}(\ddot{\mathbf{u}}^S) = 0. \quad (6.33)$$

Multiplying the equation (6.33) by a test function q , which vanishes on Γ_{F_P} , and this result is integrated in Ω_P ,

$$-\int_{\Omega_P} \frac{\phi^2}{\tilde{\rho}_{22}} \Delta \pi_P q dV + \int_{\Omega_P} \frac{\phi^2}{\tilde{R}} \ddot{\pi}_P q dV - \int_{\Omega_P} \tilde{\gamma} \nabla \cdot \ddot{\mathbf{u}}^S q dV = 0.$$

Using a Green's formula (see [24]), it holds

$$\begin{aligned} & \int_{\Omega_P} \frac{\phi^2}{\tilde{\rho}_{22}} \nabla \pi_P \cdot \nabla q dV + \int_{\Omega_P} \frac{\phi^2}{\tilde{R}} \ddot{\pi}_P q dV + \int_{\Omega_P} \tilde{\gamma} \ddot{\mathbf{u}}^S \cdot \nabla q dV = \int_{\partial\Omega_P} \frac{\phi^2}{\tilde{\rho}_{22}} \frac{\partial \pi_P}{\partial \mathbf{n}} q dS \\ &+ \int_{\partial\Omega_P} \tilde{\gamma} \ddot{\mathbf{u}}^S \cdot \mathbf{n} q dS. \end{aligned}$$

It is possible to write the time-harmonic displacement field of the fluid phase in terms of the pressure in the pores, and in the terms of the displacement vector of the solid phase, that is,

$$\mathbf{U}^F = \frac{\phi}{\omega^2 \tilde{\rho}_{22}} \operatorname{grad} \pi_P + \frac{\tilde{\rho}_{12}}{\tilde{\rho}_{22}} \mathbf{U}^S,$$

and in the time domain

$$-\ddot{\mathbf{u}}^F = \frac{\phi}{\tilde{\rho}_{22}} \operatorname{grad} \pi_P - \frac{\tilde{\rho}_{12}}{\tilde{\rho}_{22}} \ddot{\mathbf{u}}^S. \quad (6.34)$$

Considering (6.30) and (6.34), it is possible to rewrite the boundary integral as

$$\frac{\phi^2}{\tilde{\rho}_{22}} \frac{\partial \pi_P}{\partial \mathbf{n}} + \tilde{\gamma} \ddot{\mathbf{u}}^S \cdot \mathbf{n} = -\phi \left(\ddot{\mathbf{u}}^F \cdot \mathbf{n} + \frac{\tilde{Q}}{\tilde{R}} \ddot{\mathbf{u}}^S \cdot \mathbf{n} \right) = -\phi (\ddot{\mathbf{u}}^F \cdot \mathbf{n} - \ddot{\mathbf{u}}^S \cdot \mathbf{n}) - \phi \left(1 + \frac{\tilde{Q}}{\tilde{R}} \right) \ddot{\mathbf{u}}^S \cdot \mathbf{n}, \quad (6.35)$$

and then

$$\begin{aligned} \int_{\Omega_P} \frac{\phi^2}{\tilde{\rho}_{22}} \nabla \pi_P \cdot \nabla q dV + \int_{\Omega_P} \frac{\phi^2}{\tilde{R}} \ddot{\pi}_P q dV + \int_{\Omega_P} \tilde{\gamma} \ddot{\mathbf{u}}^S \cdot \nabla q dV &= - \int_{\partial \Omega_P} \phi (\ddot{\mathbf{u}}^F \cdot \mathbf{n} - \ddot{\mathbf{u}}^S \cdot \mathbf{n}) q dS \\ &- \int_{\partial \Omega_P} \phi \left(1 + \frac{\tilde{Q}}{\tilde{R}} \right) \ddot{\mathbf{u}}^S \cdot \mathbf{n} q dS. \end{aligned}$$

Taking into account the first coupling condition in (6.19),

$$\begin{aligned} \int_{\Omega_P} \frac{\phi^2}{\tilde{\rho}_{22}} \nabla \pi_P \cdot \nabla q dV + \int_{\Omega_P} \frac{\phi^2}{\tilde{R}} \ddot{\pi}_P q dV + \int_{\Omega_P} \tilde{\gamma} \ddot{\mathbf{u}}^S \cdot \nabla q dV &= - \int_{\Gamma_C} \phi (\ddot{\mathbf{u}}^F \cdot \mathbf{n} - \ddot{\mathbf{u}}^S \cdot \mathbf{n}) q dS \\ &- \int_{\Gamma_C} \phi \left(1 + \frac{\tilde{Q}}{\tilde{R}} \right) \ddot{\mathbf{u}}^S \cdot \mathbf{n} q dS, \end{aligned}$$

and considering the coupling conditions,

$$\begin{aligned} \int_{\Omega_P} \frac{\phi^2}{\tilde{\rho}_{22}} \nabla \pi_P \cdot \nabla q dV + \int_{\Omega_P} \frac{\phi^2}{\tilde{R}} \ddot{\pi}_P q dV + \int_{\Omega_P} \tilde{\gamma} \ddot{\mathbf{u}}^S \cdot \nabla q dV \\ = - \int_{\Gamma_C} \phi \left(1 + \frac{\tilde{Q}}{\tilde{R}} \right) \ddot{\mathbf{u}}^S \cdot \mathbf{n} q dS. \end{aligned} \quad (6.36)$$

If the equation (6.18) is multiplied by a test function \mathbf{w}^E , and this result is integrated in Ω_E ,

$$\int_{\Omega_E} \rho_E \ddot{\mathbf{u}}^E \cdot \mathbf{w}^E dV - \int_{\Omega_E} \operatorname{div}(\sigma_E(\mathbf{u}^E)) \mathbf{w}^E dV = \mathbf{0}.$$

Using a Green's formula (see [24]), it holds

$$\int_{\Omega_E} \rho_E \ddot{\mathbf{u}}^E \cdot \mathbf{w}^E dV + \int_{\Omega_E} \sigma_E(\mathbf{u}^E) \cdot \nabla \mathbf{w}^E dV = \int_{\partial \Omega_E} \sigma_E(\mathbf{u}^E) \cdot \boldsymbol{\nu} \mathbf{w}^E dS.$$

Taking into account (6.24) and (6.25),

$$\begin{aligned} \int_{\Omega_E} \rho_E \ddot{\mathbf{u}}^E \cdot \mathbf{w}^E dV + \int_{\Omega_E} \sigma_E(\mathbf{u}^E) \cdot \nabla \mathbf{w}^E dV &= \int_{\Gamma_C} \sigma_E(\mathbf{u}^E) \cdot \boldsymbol{\nu} \mathbf{w}^E dS \\ &+ \int_{\Gamma_L} f(t) \delta_{x_0}(x) \mathbf{w}^E dS, \end{aligned} \quad (6.37)$$

and adding (6.32), (6.36) and (6.37),

$$\begin{aligned}
& \int_{\Omega_P} \rho_P \ddot{\mathbf{u}}^S \cdot \mathbf{w}^S dV + \int_{\Omega_P} \tilde{\sigma}'_P(\mathbf{u}^S) \cdot \nabla \mathbf{w}^S dV + \int_{\Omega_P} \tilde{\sigma}''_P(\dot{\mathbf{u}}^S) \cdot \nabla \mathbf{w}^S dV - \int_{\Omega_P} \tilde{\gamma} \nabla \pi_P \mathbf{w}^S dV \\
& + \int_{\Omega_P} \frac{\phi^2}{\tilde{\rho}_{22}} \nabla \pi_P \cdot \nabla q dV + \int_{\Omega_P} \frac{\phi^2}{\tilde{R}} \ddot{\pi}_P q dV + \int_{\Omega_P} \tilde{\gamma} \ddot{\mathbf{u}}^S \cdot \nabla q dV + \int_{\Omega_E} \rho_E \ddot{\mathbf{u}}^E \cdot \mathbf{w}^E dV \\
& + \int_{\Omega_E} \sigma_E(\mathbf{u}^E) \cdot \nabla \mathbf{w}^E dV = \int_{\Gamma_C} [\sigma'_t(\mathbf{u}^S) \cdot \mathbf{n} \cdot \mathbf{w}^S + \sigma''_t(\dot{\mathbf{u}}^S) \cdot \mathbf{n} \cdot \mathbf{w}^S] dS \\
& + \int_{\Gamma_C} \phi \left(1 + \frac{\tilde{Q}}{\tilde{R}} \right) \pi_P \mathbf{w}^S \cdot \mathbf{n} dS - \int_{\Gamma_C} \phi \left(1 + \frac{\tilde{Q}}{\tilde{R}} \right) \ddot{\mathbf{u}}^S \cdot \mathbf{n} q dS - \int_{\Gamma_C} \sigma_E(\mathbf{u}^E) \cdot \mathbf{n} \mathbf{w}^E dS \\
& + \int_{\Gamma_L} f(t) \delta_{x_0}(x) \mathbf{w}^E dS. \tag{6.38}
\end{aligned}$$

Since the most part of porous materials used in acoustics verify that the bulk modulus of the porous material is negligible compared to the bulk modulus of the material from which the skeleton is made (see [10] for more details), $K_b/K_s \ll 1$. Then by using the definitions of the elastic coefficients (6.31),

$$\phi \left(1 + \frac{\tilde{Q}}{\tilde{R}} \right) = 1 - \frac{K_b}{K_s} \cong 1. \tag{6.39}$$

Taking into account (6.22) and (6.39), (6.38) results

$$\begin{aligned}
& \int_{\Omega_P} \rho_P \ddot{\mathbf{u}}^S \cdot \mathbf{w}^S dV + \int_{\Omega_P} \tilde{\sigma}'_P(\mathbf{u}^S) \cdot \nabla \mathbf{w}^S dV + \int_{\Omega_P} \tilde{\sigma}''_P(\dot{\mathbf{u}}^S) \cdot \nabla \mathbf{w}^S dV - \int_{\Omega_P} \tilde{\gamma} \nabla \pi_P \mathbf{w}^S dV \\
& + \int_{\Omega_P} \frac{\phi^2}{\tilde{\rho}_{22}} \nabla \pi_P \cdot \nabla q dV + \int_{\Omega_P} \frac{\phi^2}{\tilde{R}} \ddot{\pi}_P q dV + \int_{\Omega_P} \tilde{\gamma} \ddot{\mathbf{u}}^S \cdot \nabla q dV + \int_{\Omega_E} \rho_E \ddot{\mathbf{u}}^E \cdot \mathbf{w}^E dV \\
& + \int_{\Omega_E} \sigma_E(\mathbf{u}^E) \cdot \nabla \mathbf{w}^E dV = \int_{\Gamma_C} \pi_P \mathbf{w}^S \cdot \mathbf{n} dS - \int_{\Gamma_C} \ddot{\mathbf{u}}^S \cdot \mathbf{n} q dS + \int_{\Gamma_L} f(t) \delta_{x_0}(x) \mathbf{w}^E dS.
\end{aligned}$$

Then, the variational formulation of the problem obtained taking into account the functional spaces described above is:

Given an imposed load $f(t) \in C^0(0, T)$, and fixed initial conditions, find $(\mathbf{u}^S, \pi_P, \mathbf{u}^E) \in C^1([0, T]; \mathbf{V}) \cap C^2([0, T]; \mathbf{H})$ satisfying

$$\begin{aligned}
& \int_{\Omega_P} \rho_P \ddot{\mathbf{u}}^S \cdot \mathbf{w}^S dV + \int_{\Omega_P} \tilde{\gamma} \ddot{\mathbf{u}}^S \cdot \nabla q dV + \int_{\Omega_P} \frac{\phi^2}{\tilde{R}} \ddot{\pi}_P q dV + \int_{\Omega_E} \rho_E \ddot{\mathbf{u}}^E \cdot \mathbf{w}^E dV \\
& + \int_{\Omega_P} \tilde{\sigma}''_P(\dot{\mathbf{u}}^S) \cdot \nabla \mathbf{w}^S dV + \int_{\Omega_P} \tilde{\sigma}'_P(\mathbf{u}^S) \cdot \nabla \mathbf{w}^S dV - \int_{\Omega_P} \tilde{\gamma} \nabla \pi_P \mathbf{w}^S dV \\
& + \int_{\Omega_P} \frac{\phi^2}{\tilde{\rho}_{22}} \nabla \pi_P \cdot \nabla q dV + \int_{\Omega_E} \sigma_E(\mathbf{u}^E) \cdot \nabla \mathbf{w}^E dV = - \int_{\Gamma_C} \ddot{\mathbf{u}}^S \cdot \mathbf{n} q dS \\
& + \int_{\Gamma_C} \pi_P \mathbf{w}^S \cdot \mathbf{n} dS + \int_{\Gamma_L} f(t) \delta_{x_0}(x) \mathbf{w}^E dS, \quad \forall (\mathbf{w}^S, q, \mathbf{w}^E) \in \mathbf{V}.
\end{aligned}$$

6.7 Inverse problem to determine the elastic coefficients

From an experimental point of view, both the force imposed by the hammer at the impact point, and the acceleration at one point on the top surface of the steel plate are the only available information. With this kind of databases in mind, it is straightforward to design a least-square problem where the mechanical properties of the elastic part of the solid material, this is, the Young modulus E and the loss factor η , can be computed as the solution of the following inverse problem: given the force $f^{\text{exp}}(t)$, and the normal acceleration $a^{\text{exp}}(t)$ measured at point \mathbf{p} on the top steel surface Γ_L , both in the time interval $[0, T]$, find the values E^* and η^* such that

$$(E^*, \eta^*) = \arg \min_{E>0, \eta>0} \frac{\|a^{\text{exp}}(t) - \ddot{\mathbf{u}}^E(\mathbf{p}, t) \cdot \mathbf{n}\|_{L^2(0,T)}^2}{\|a^{\text{exp}}(t)\|_{L^2(0,T)}^2}, \quad (6.40)$$

where \mathbf{u}^E is the displacement field of the steel plate computed for a given pair of values (E, η) with any of the models of the hierarchy, Model _{n} with $n = 0, \dots, 5$. Typically, the numerical solution of this optimization problem involves a high computational cost using a full three-dimensional model, since it is required to solve the direct problem a large number of times. However, taking into account the hierarchy of models, it is possible to reduce this computational cost, using in an ordered manner the simplest models to estimate roughly the optimal values (E^*, η^*) , and then in a subsequent step, refine such computation using a reduced number of solutions of any of the full models.

However, to mimic the experimental procedure described by the standard ISO 9052-1 (see more details in Section 6.2), instead of comparing directly the time series measured by the accelerometer, a fitting procedure is used to compute the main resonance frequency, and the damping decay of the measured signal. With this purpose, let consider an arbitrary time-dependent signal $a(t)$ defined in the time interval $[0, T]$, the main frequency ω_a , and a damping decay α_a associated with the signal $a(t)$, given by $(\omega_a, \alpha_a) = \Pi(a(t))$, where ω_a and α_a are part of the parametric solution of the following least-square problem:

$$(\omega_a, \alpha_a, A_a, \phi_a) = \arg \min_{\substack{A>0, \omega>0 \\ \alpha>0, 0 \leq \phi < 2\pi}} \frac{\|a(t) - Ae^{-\alpha t} \cos(\omega t + \phi)\|_{L^2(0,T)}}{\|a(t)\|_{L^2(0,T)}}.$$

Consequently, using the fitting operator Π , the inverse problem (6.40) is replaced by an analogous one where operator Π is involved, this is,

$$(E^*, \eta^*) = \arg \min_{E>0, \eta>0} \frac{\|\Pi(a^{\text{exp}}(t)) - \Pi(\ddot{\mathbf{u}}^E(\mathbf{p}, t) \cdot \mathbf{n})\|_{L^2(0,T)}^2}{\|\Pi(a^{\text{exp}}(t))\|_{L^2(0,T)}^2}.$$

The above optimization problem is used in all the numerical results presented in the section below.

6.8 Numerical results

In this section, numerical simulations are performed to illustrate the proposed methodology. First of all, some numerical results with manufactured data are shown to validate the code. Then, numerical simulations considering a viscoelastic sample are performed.

6.8.1 Code validation

Firstly, to validate the hierarchy of models, some manufactured data have been considered, not only for cross-testing the coherent behavior of every model in the hierarchy, but also to illustrate numerically the uniqueness of the solution of the inverse problem stated in the section above. In what follows, the manufactured data have been obtained by running the time-dependent one-dimensional viscoelastic element (Model₃), and they have been compared with Model₁ and Model₄. In both cases, the output results are pretty similar and, for the sake of simplicity in the exposition, only the numerical results related to Model₄ are shown.

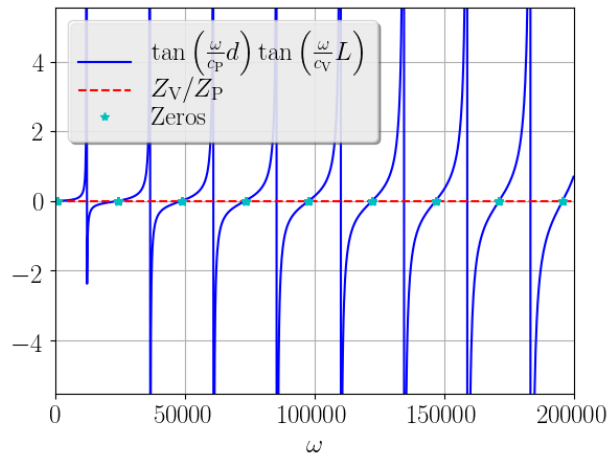


Figure 6.4: Left- and right-hand side of the dispersion equation (6.1) used to identify their zeros using a convenient initial guess, which is plotted with respect to the frequency values.

Notice that, in the case of using Model₁, the nonlinear dispersion relation (6.1) must be solved numerically to obtain the first zero (with the smallest magnitude). If the damping is not considered, i.e. $\eta = 0$ and $E \in \mathbb{R}$, Figure 6.4 shows the location of the zeros of this dispersion relation as the cutoff points of left- and right-hand side of the dispersion equation.

Two different materials have been considered to build the manufactured database. For the viscoelastic material A, the sample thickness is 3 mm, $E = 10^5$ Pa, $\eta = 1.6 \times 10^{-2}$, $\nu = 0.47$, and $\rho = 1.1 \times 10^3$ kg/m³. In the case of the second material, the viscoelastic material B has the same thickness, and the elastic properties $E = 10^5$ Pa, $\eta = 1.6 \times 10^{-5}$,

$\nu = 0.47$, and $\rho = 1.1 \times 10^3 \text{ kg/m}^3$. So, the only difference relies on the value of the loss factor η . To generate the manufactured data, the time series which governs the force of the hammer acting on the center of the top surface of the steel plate is given by a smooth function (shown in Figure 6.5).

Figure 6.6 shows the values of acceleration for the two sets of manufactured data (viscoelastic material A in left plot, and viscoelastic material B in right one), created with Model₃.

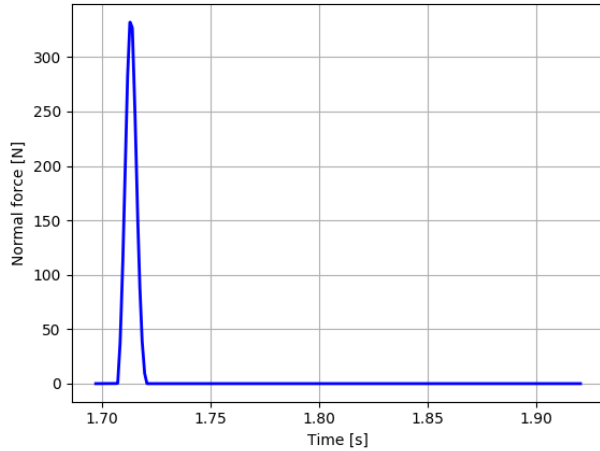


Figure 6.5: Time-dependent force response, which is exerted by the hammer on the center of the top surface of the steel plate.

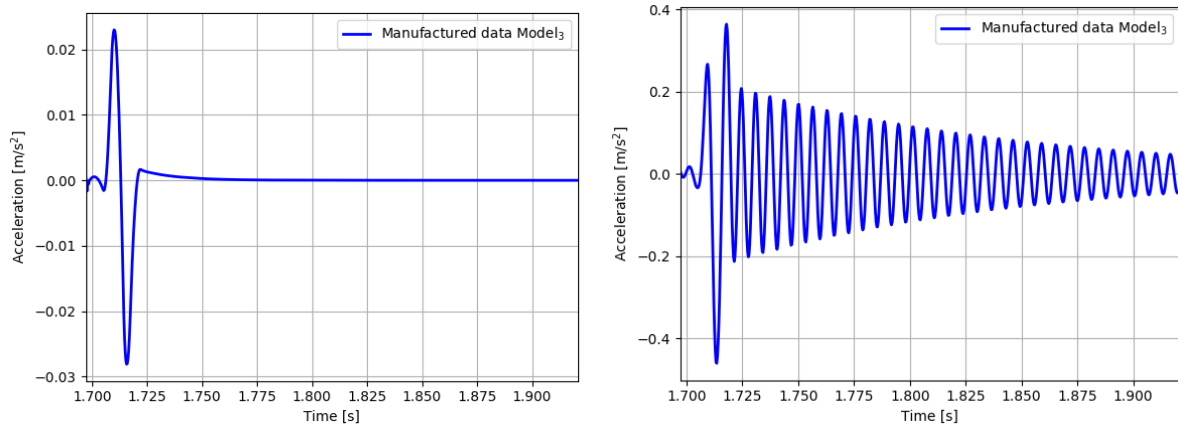


Figure 6.6: Acceleration values for the referenced manufactured data created with Model₃. Left: viscoelastic material A. Right: viscoelastic material B.

To illustrate numerically that the optimization problem has an unique local minimum (and hence global minimum), the cost function has been evaluated in a grid of values sweeping a large variety of pairs (E, η) . Figure 6.7 shows the cost function of the minimization

problem, this is, the relative errors between the manufactured data, and the computed ones with Model₃, in the left plot for the viscoelastic material A, and in the right plot for the viscoelastic material B.

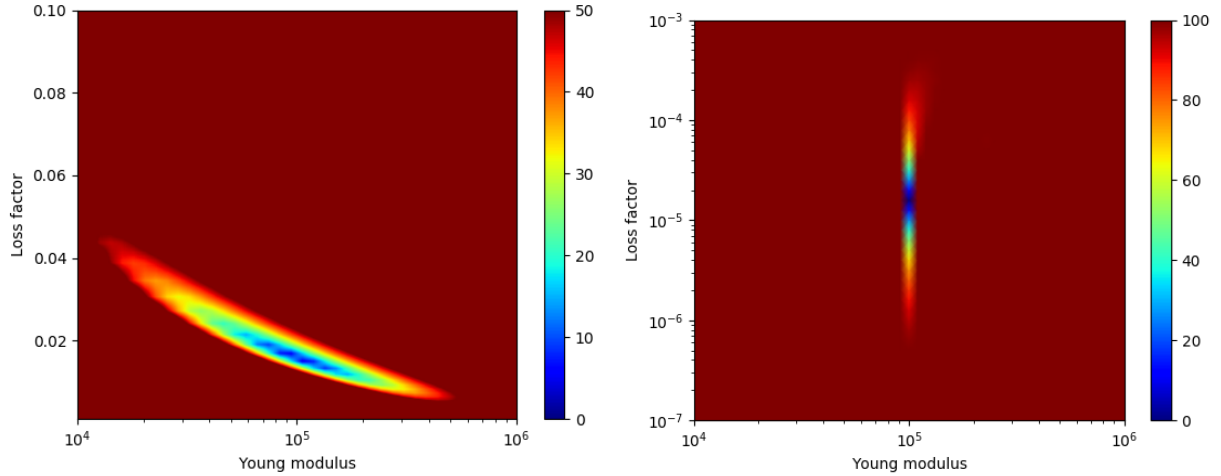


Figure 6.7: Relative errors in terms of the Young modulus, and the loss factor for the manufactured data created with Model₃. Left: viscoelastic material A. Right: viscoelastic material B.

Figure 6.8 shows the comparison between the acceleration values for the manufactured data, created with Model₃ and the numerical results computed by using the full one-dimensional model. Left plot shows the results for the viscoelastic material A, and right plot for the material B. If the fitting is performed by using the Model₃, and a standard least-square procedure, the elastic coefficients recovered by the numerical solution of the inverse problem for the material A are $E = 1.199 \times 10^5$, and $\eta = 1.463 \times 10^{-2}$, whereas in the case of the material B, it has been obtained $E = 1.0 \times 10^5$, and $\eta = 1.602 \times 10^{-5}$. From this comparison, it is clear the weak dependence of the least-square fitting with respect to the Young modulus values and the accurate prediction of the loss factor in both materials.

Figures 6.9 and 6.10 show the comparison between the acceleration values for the manufactured data, created with Model₃, and the numerical results computed by using the full three-dimensional model for the materials A and B, respectively. In left plots, the computed results are not post-processed, and in right ones, the computed results are smoothed. The results computed with the three-dimensional model have been smoothed to compare the data avoiding the oscillations due to the time step discretization. If the fitting is performed by using the Model₄, and a standard least-square procedure, the elastic coefficients recovered by the numerical solution of the inverse problem for the material A are $E = 1.083 \times 10^5$, and $\eta = 1.538 \times 10^{-2}$, whereas in the case of the material B, it has been obtained $E = 1 \times 10^5$, and $\eta = 3.210 \times 10^{-5}$. As it can be observed in Figure 6.10, when the material has a small loss factor, the three-dimensional model underestimates the computed values.

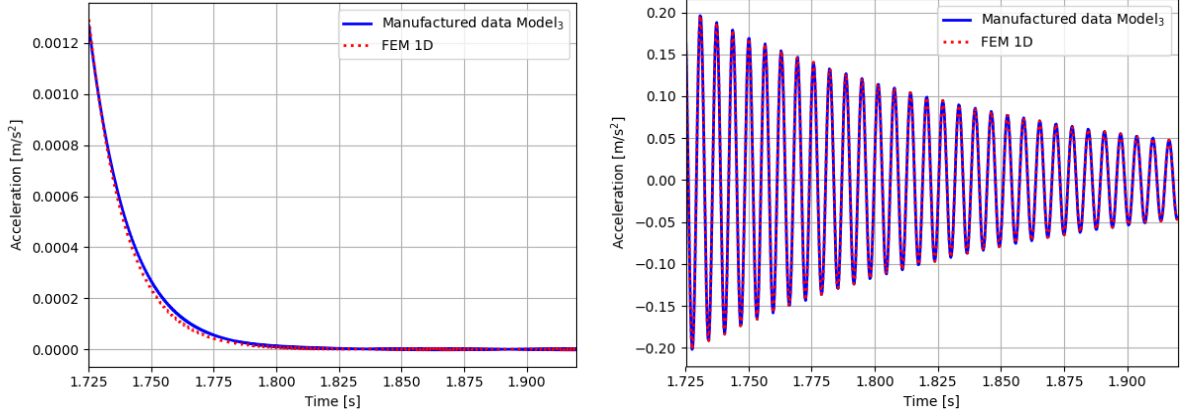


Figure 6.8: Referenced manufactured data created with Model₃ (solid blue lines), and those values computed by using the one-dimensional model (dashed red lines). Left: viscoelastic material A. Right: viscoelastic material B.

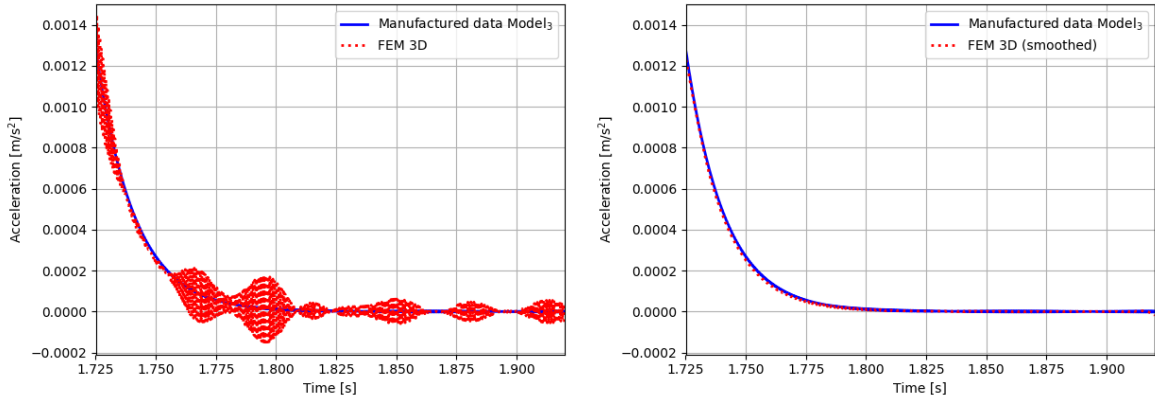


Figure 6.9: Referenced manufactured data created with Model₃ (solid blue lines), and those values computed by using the full three-dimensional model (dashed red lines) for the viscoelastic material A. Left: results without post-processing. Right: smoothed results.

Now, the same two viscoelastic materials, A and B, have been considered, but in this case, the manufactured data have been created with Model₄. Figure 6.11 shows the acceleration values for these two sets of manufactured data.

Following the same procedure as with Model₃, to illustrate numerically that the optimization problem has an unique local minimum, the cost function has been evaluated in a grid of values sweeping a large variety of pairs (E, η) . Figure 6.12 shows the relative errors between the manufactured data, and the computed ones with Model₄, in the left plot for the viscoelastic material A, and in the right plot for the viscoelastic material B.

Figures 6.13 and 6.14 show the comparison between the acceleration values for the manufactured data created with Model₄, and the numerical results computed by using the one-dimensional model for the viscoelastic materials A and B, respectively. Left plots show the computed results without post-processing, and right plots show the smoothed results.

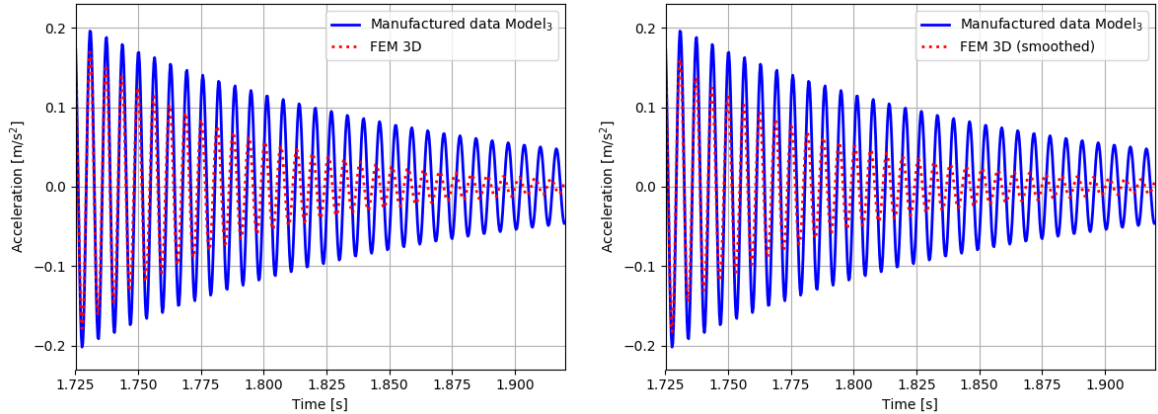


Figure 6.10: Referenced manufactured data created with Model₃ (solid blue lines), and those values computed by using the full three-dimensional model (dashed red lines) for the viscoelastic material B. Left: results without post-processing. Right: smoothed results.

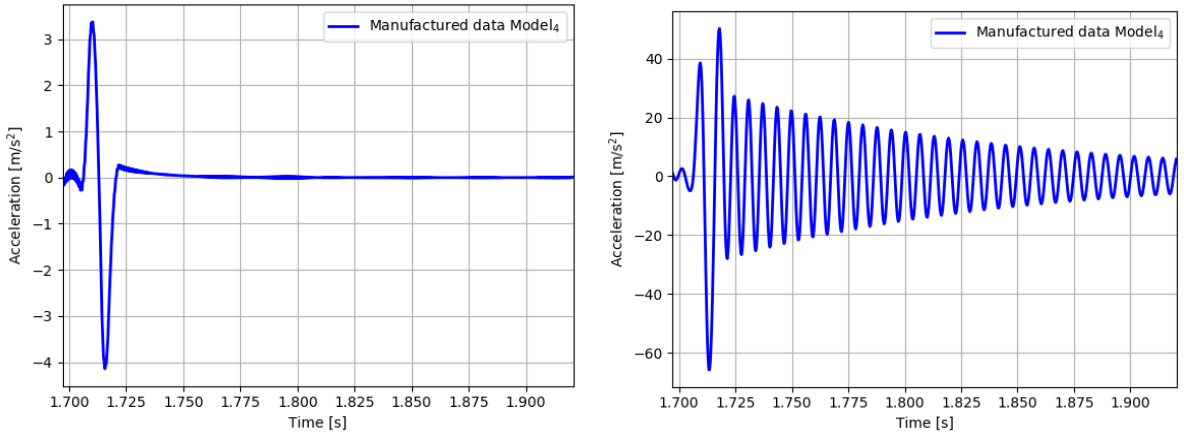


Figure 6.11: Acceleration values for the referenced manufactured data created with Model₄. Left: viscoelastic material A. Right: viscoelastic material B.

As it can be observed, in this case, since the spurious oscillations in the computed data do not appear, the smoothed data do not show better results than the original ones. If the fitting is performed by using the Model₄, and a standard least-square procedure, the elastic coefficients recovered by the numerical solution of the inverse problem for the material A are $E = 1.359 \times 10^5$, and $\eta = 1.375 \times 10^{-2}$, whereas in the case of the material B, it has been obtained $E = 1.023 \times 10^5$, and $\eta = 1.509 \times 10^{-5}$.

Figures 6.15 and 6.16 show the comparison between the acceleration values for the manufactured data created with Model₄, and the numerical results computed by using the full three-dimensional model for the materials A and B, respectively. In left plots, the computed results are not post-processed, and in right ones, the computed results are smoothed. As before, the computed results have been smoothed to avoid the spurious

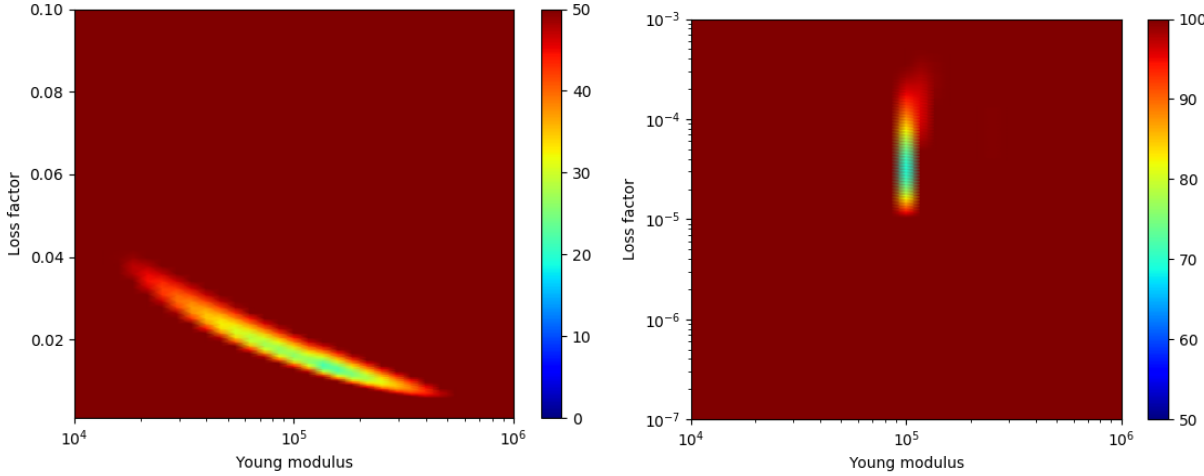


Figure 6.12: Relative errors in terms of the Young modulus, and the loss factor for the manufactured data created with Model₄. Left: viscoelastic material A. Right: viscoelastic material B.

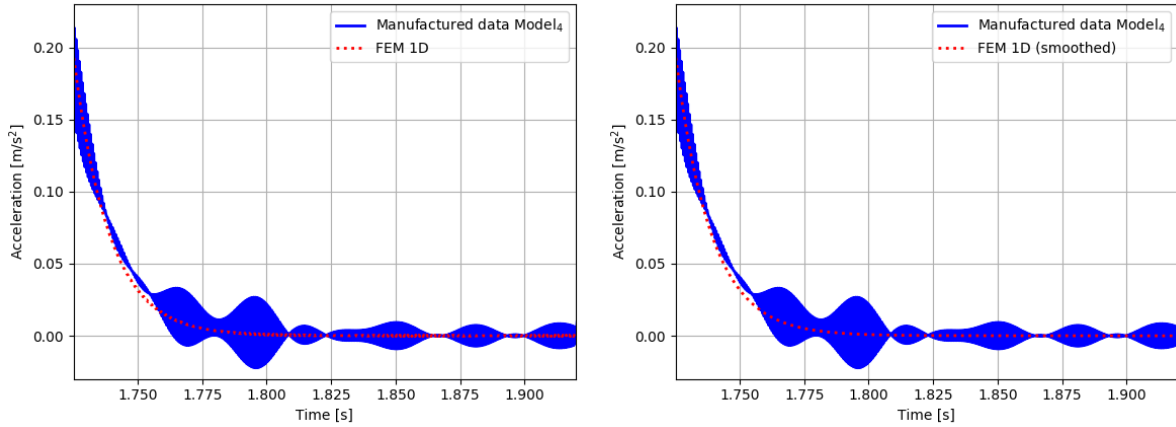


Figure 6.13: Referenced manufactured data created with Model₄ (solid blue lines), and those values computed by using the one-dimensional model (dashed red lines) for the viscoelastic material A. Left: results without post-processing, right: smoothed results.

oscillations due to the time step discretization. If the fitting is performed by using the Model₄, and a standard least-square procedure, the elastic coefficients recovered by the numerical solution of the inverse problem for the material A are $E = 1.15 \times 10^5$, and $\eta = 1.497 \times 10^{-2}$, whereas in the case of the material B, it has been obtained $E = 10^5$, and $\eta = 1.6 \times 10^{-5}$.

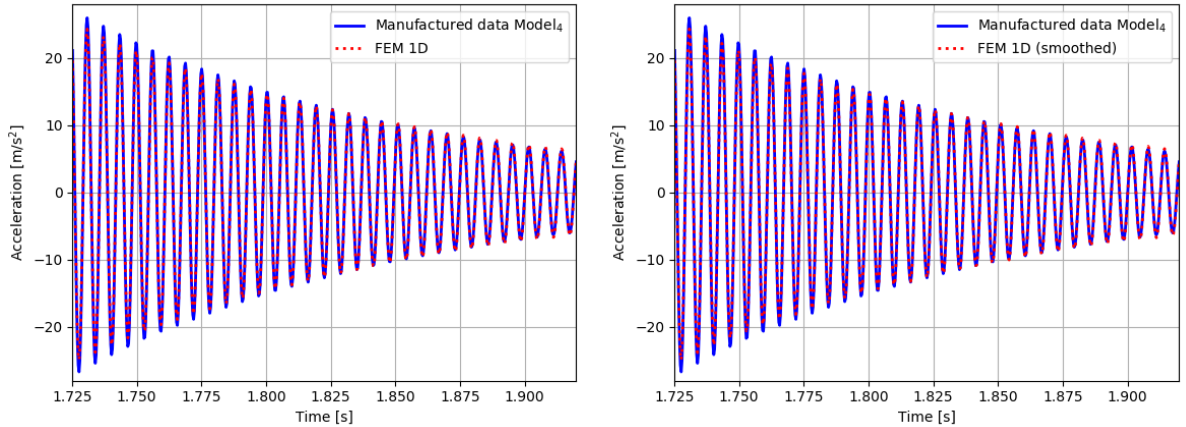


Figure 6.14: Referenced manufactured data created with Model₄ (solid blue lines), and those values computed by using the one-dimensional model (dashed red lines) for the viscoelastic material B. Left: results without post-processing, right: smoothed results.

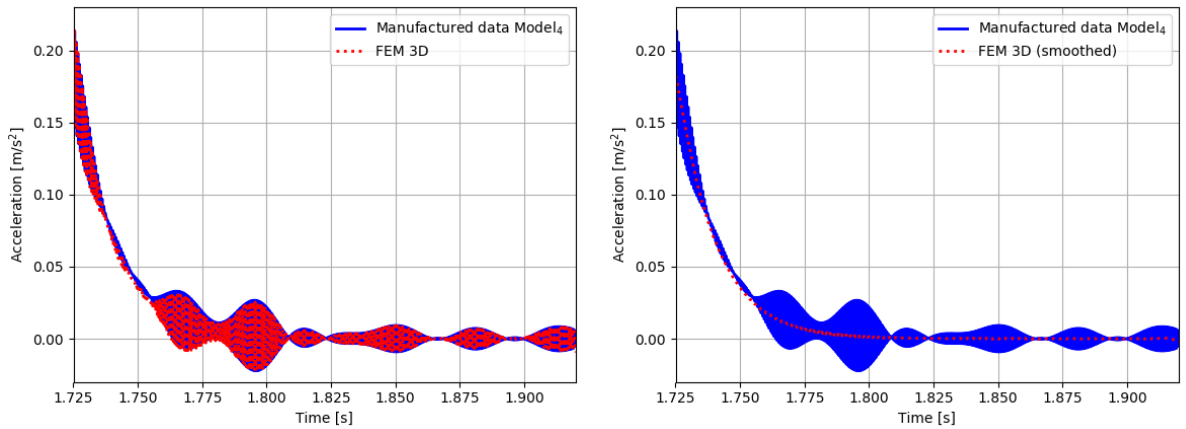


Figure 6.15: Referenced manufactured data created with Model₄ (solid blue lines), and those values computed by using the full three-dimensional model (dashed red lines) for the viscoelastic material A. Left: results without post-processing, right: smoothed results.

6.8.2 Viscoelastic sample

Now, a viscoelastic material of thickness 3 mm has been considered. Figure 6.17 shows the sample of viscoelastic material used in the experimental measurements in left plot, and in right plot, the time-dependent force exerted by the hammer on the center of the top surface of the steel plate. Figure 6.18 shows, in the left plot, the values of acceleration for the viscoelastic material under consideration. To illustrate the difficulties appearing in the optimization problem, the cost function has been evaluated in a grid of values sweeping a large amount of pairs (E, ν). In the right plot of Figure 6.18, the relative errors between the available experimental data, and the computed ones are shown. Figure 6.19 shows the

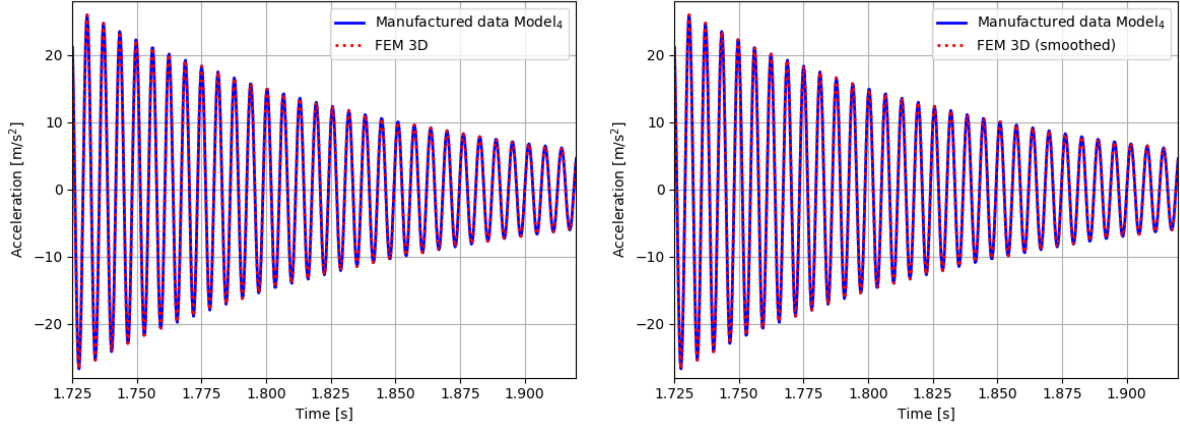


Figure 6.16: Referenced manufactured data created with Model_4 (solid blue lines), and those values computed by using the full three-dimensional model (dashed red lines) for the viscoelastic material B. Left: results without post-processing, right: smoothed results.

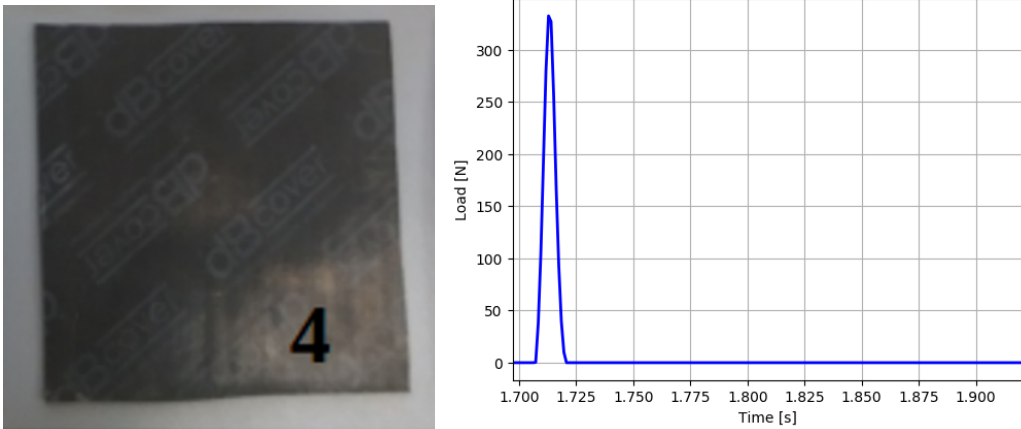


Figure 6.17: Left: Viscoelastic material (Sample 4) whose results are shown in this work. Right: Time-dependent force response exerted by the hammer on the center of the top surface of the steel plate.

comparison between the values of acceleration for the Sample 4, and the numerical results computed by using the one-dimensional model, in left plot, and the full three-dimensional model, in right plot. As it can be observed in Figure 6.19, it does not appear major differences between both simulations.

The results obtained with the manufactured data and with the viscoelastic sample allow us to conclude that the use of a more complex model, such as the three-dimensional one, does not provide better results. It could be considered that the force applied by the hammer acts only perpendicularly to the sample and that other modes of excitation do not appear.

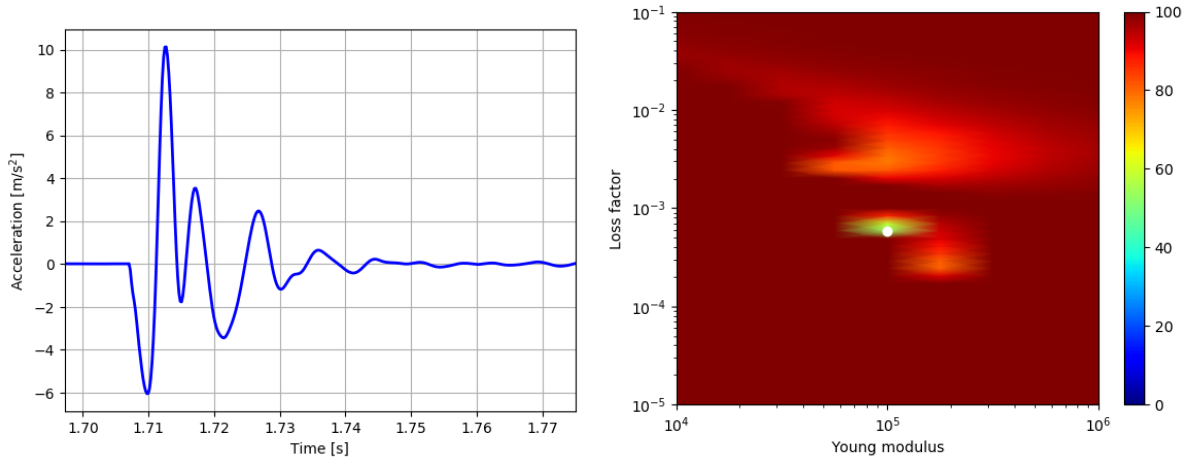


Figure 6.18: Left: Acceleration values for the viscoelastic material considered. Right: Relative errors in terms of the Young modulus and the loss factor for the Sample 4.

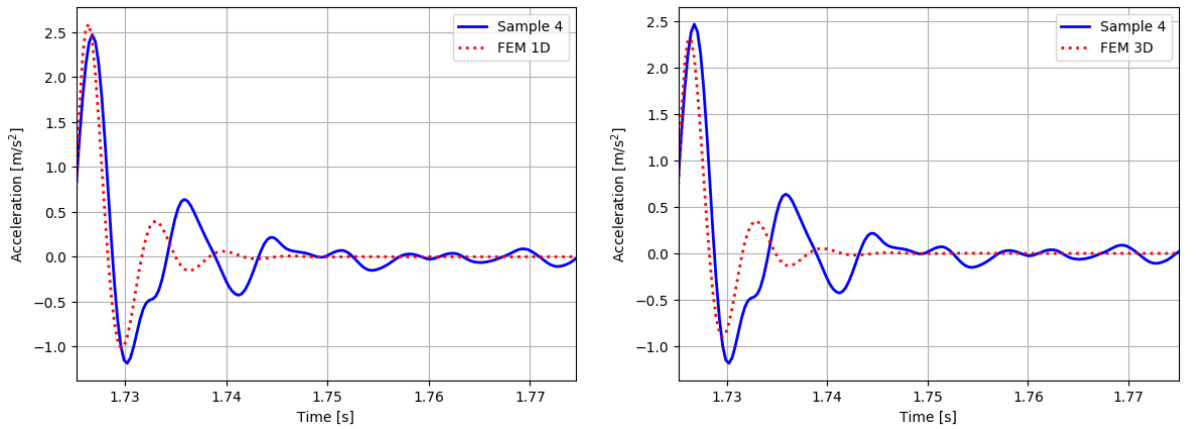


Figure 6.19: Available experimental data for the Sample 4 (solid blue lines), and the computed ones by using the Finite Element method (dashed red lines). Left: values computed by using the one-dimensional model. Right: values computed by using the three-dimensional model.

6.9 Conclusions

The standard ISO 9052-1 provides a framework to determine the dynamic stiffness of a given solid material experimentally under a pointwise excitation. However, that setting does not provide any direct estimation to compute its elastic coefficients at linear regime, such as the elastic modulus and the loss factor. The present work presents a novel hierarchical modeling procedure to compute these elastic coefficients numerically using only a reduced experimental database under the standard ISO 9052-1. In this novel approach, to define the hierarchy of models, analytical models, compressional modal decomposition techniques,

one-dimensional models, and full three-dimensional models are involved. These models have been considered for viscoelastic and poroelastic materials. Numerical simulations with manufactured data have been performed to validate the proposed methodology, showing a good agreement even with the simplest models. Moreover, some preliminary results with a real viscoelastic sample are shown. In both cases, the results show that it is not necessary to use a three-dimensional model to get more accurate results. Some numerical results with different damping materials used for sound insulation in industrial applications are being performed to improve the existing results.

Further research

To conclude this work, a brief resume of the research lines that can be followed in the future is given. First of all, open problems derived from the work made in the thesis are explained. These problems are being solved, or will be solved in the coming months. Moreover, some open research lines that are challenging and could be really interesting are described.

Concerning the problem of acoustic characterization of viscoelastic materials, two different research lines can be followed:

- The first one, related to the resolution of the highly oscillatory integrals appearing in Chapter 3. A wide range of applications in acoustics and electromagnetism needs of computing definite integrals involving highly oscillatory kernels. These integrals can be written as the product of two functions: a smooth and non-oscillatory function, and an oscillatory kernel which satisfies a p -th order ordinary differential equation whose coefficients are smooth functions depending on a large parameter. There exists a variety of numerical methods to deal with this kind of oscillatory kernels, such as Filon-type methods, Levin-type methods, or steepest descent methods [72]. Among these methods, the classical Levin method and the moment-free Filon method can approximate the highly oscillatory integral by solving an associated ordinary differential equation by a collocation method, involving only a reduced number of collocation points (mainly the endpoints of the integration interval), and also considering a limited value for their multiplicities [142]. However, assuming bounded coefficients in the integration interval is the main drawback of these methods. Consequently, these methods cannot be applied to the integration of oscillatory kernels, such as the Bessel and Airy functions within integration intervals, including $x = 0$. To overcome such limitation, some authors have designed novel methods that compute this kind of integrals by using a Filon-type method [180] but restricted to some specific oscillatory kernels.

The proposed future research line consists of developing an efficient generalized Levin-type method to deal with any kind of exotic oscillatory kernels, even in the case of coefficients present asymptotes in the integration interval. This technique should be mainly based on rewriting the differential equation and an extension of the classical Levin method. Hence, with an adequate selection of the multiplicity of the collocation points, the method should achieve the same accuracy as the classical Levin method.

- In Chapter 4, a fast convergent integral equation method to solve a transmission problem is introduced. This method achieves a fast convergence far away from Wood anomaly frequencies. The proposed method is based on the use of quasi-periodic Green functions in combination with a smooth-windowing technique. The future research is devoted to solving the same problem at certain “Rayleigh-Wood anomalous frequencies”, at which the classical Green function ceases to exist [39]. Since in many cases, the integral operators involved in the integral formulation of the problems are not invertible at Wood anomalies, a finite number of Rayleigh modes in the spectral expansion of the shifted quasi-periodic Green function G_J^q presents difficulties because their denominators tend to zero as a Wood anomaly is approached. If these terms are excluded from the infinite sum, then the convergence of G_J^q is achieved. Following a similar argument to [39], a modification of G_J^q is necessary to add these lost Rayleigh modes.

Once the transmission problem with two media in contact in a periodic setting is solved, achieving superalgebraically convergence at all frequencies, even at and around Wood anomalies, several open problems appear, such as to consider the shear effects on the viscoelastic material, to study a multilayer material, or consider a non-planar directivity pattern for the acoustic source.

Related to the acoustic characterization of materials by using their dynamic stiffness, two different lines can be followed. The code has been validated, but the results with the real data for a viscoelastic material do not show good agreement with the experimental measurements. It is necessary to make some adjustments, such as filter the signal or reduce the time interval, to achieve better results. Moreover, some simulations with other kinds of materials will be performed, such as cork, porous materials with vegetable origin, or poroelastic materials.

In connection with the use of the data-driven approach described in this dissertation, this methodology has been used to characterize rigid porous materials and viscoelastic materials. It is interesting to apply it to other kinds of porous materials, such as double porosity materials [35, 141], whose parametric models have more intrinsic parameters than those shown in Chapter 1. Also, to characterize viscoelastic materials because when a parametric model is used, both the elastic and the porous intrinsic parameters are considered, increasing the computational cost of the fitting problem.

In this document, different setups have been used to measure the experimental data. For this reason, the data-driven approach has been adapted to each experimental setup. A very challenging open problem is to use the proposed methodology to characterize a viscoelastic material reproducing other experimental setups, such as the used in the Oberst Beam method [71, 139, 178].

Resumen en castellano

La caracterización acústica de materiales juega un papel muy importante en un gran número de aplicaciones industriales. La preocupación por el confort acústico en los medios de transporte ha aumentado en los últimos años: la reducción del ruido emitido por los motores de los aviones o el control de las vibraciones de un vehículo son problemas muy estudiados en la actualidad. Utilizar una combinación adecuada de materiales para mejorar el confort acústico es un gran desafío en las industrias automovilística y aeroespacial. Del mismo modo, el uso de nuevos materiales, como las fibras naturales o recicladas, que tienen un menor impacto medioambiental, se ha hecho cada vez más popular en la industria.

Conocer las propiedades intrínsecas de un material puede suponer una gran ventaja, especialmente en la etapa de diseño de sistemas de control del ruido, porque permite describir de una forma precisa el comportamiento acústico del material. Esto supone un mejor aprovechamiento de los materiales existentes, o incluso el uso de otros nuevos, durante la etapa de diseño, provocando una reducción tanto de los costes como del tiempo de producción. El conocimiento de las propiedades acústicas de un material es una tarea cada vez más ardua. Por un lado, el incesante desarrollo de nuevos materiales, algunos de ellos formados por una mezcla de materiales conocidos pero con propiedades diferentes entre sí, o incluso de materiales de reciclaje, hace difícil encontrar las propiedades intrínsecas del material resultante. Por otro lado, existen materiales con propiedades desconocidas, que forman parte de dispositivos de control de ruido y que, debido a sus características o a su naturaleza, no pueden ser estudiados cuando el material se considera de forma individual, y es necesario estudiar sus propiedades cuando dicho material forma parte de un sistema más complejo.

El objetivo principal de esta tesis es dar algunas herramientas novedosas que nos permitan caracterizar acústicamente tanto materiales de una sola capa como materiales compuestos de varias capas. En la literatura existe una gran variedad de modelos paramétricos para caracterizar, de forma precisa, una capa de gran parte de los materiales existentes. Para conseguir una caracterización adecuada, es fundamental la elección correcta del modelo paramétrico porque cuanto más apropiado sea el modelo, más precisa será su respuesta mecánica, en comparación con los datos experimentales. Habitualmente, la metodología utilizada con los modelos paramétricos es la siguiente: se fija la ley constitutiva dependiente de la frecuencia, y después se ajustan las medidas experimentales disponibles con la respuesta mecánica del modelo elegido. De ese modo, se pueden estimar aquellos parámetros del modelo que son desconocidos. Esta metodología de modelización sufre de la incer-

tidumbre epistémica de una selección inadecuada del modelo. En esta tesis se considera un enfoque basado en datos, evitando la necesidad de elegir una ley constitutiva para la optimización. El problema de ajuste consiste en minimizar la distancia entre un conjunto de datos experimentales disponibles y los valores obtenidos de la respuesta mecánica del modelo. Por lo tanto, la modelización matemática de los materiales y la elección de sus leyes constitutivas dependientes de la frecuencia se basan únicamente en las mediciones experimentales disponibles, y no en la imposición de una dependencia funcional de los parámetros intrínsecos en términos de la frecuencia. Esta metodología basada en datos requiere la solución numérica de un problema inverso para cada frecuencia de interés.

Este documento se divide en tres partes bien diferenciadas, con un hilo conductor: la caracterización acústica de materiales monocapa o multicapa utilizados en la industria considerando un novedoso enfoque no paramétrico. Cabe destacar que todas las simulaciones numéricas mostradas a lo largo de este documento se han realizado utilizando escenarios reales y con la colaboración de distintos grupos de investigación o empresas. La primera parte de esta tesis está dedicada a la caracterización de materiales porosos y fibrosos. Los datos experimentales disponibles son valores de absorción en incidencia normal, medidos en un tubo de Kundt. En la segunda parte, el material objeto de estudio es un sólido viscoelástico, y los datos experimentales disponibles son la reducción del eco, la pérdida por inserción y el coeficiente de disipación de potencia, a frecuencias ultrasónicas. Finalmente, la última parte de la tesis muestra la caracterización de sistemas complejos, que involucran materiales porosos y sólidos viscoelásticos, en marcos dependientes del tiempo. Las medidas disponibles para los materiales porosos son valores del coeficiente de absorción en campo difuso medidos en una cabina alfa, y las de los sólidos viscoelásticos provienen de un método de excitación y son valores de rigidez dinámica. A continuación se presenta un resumen de cada parte y de cada capítulo.

Parte I: Caracterización de materiales porosos en el tubo de Kundt. Esta primera parte se centra en el estudio del comportamiento acústico de materiales porosos y fibrosos de una y de varias capas, utilizados en la industria automovilística, en el dominio de la frecuencia. La predicción de las propiedades acústicas de estos materiales es de gran interés para una amplia gama de aplicaciones industriales. Sin embargo, el constante desarrollo de estos materiales hace necesario el uso de nuevas técnicas para describir su comportamiento acústico. Desde un punto de vista clásico, los materiales porosos se pueden modelar mediante el uso de modelos paramétricos. Sin embargo, el modelo elegido podría no ser adecuado para un material en particular. Por esta razón, se propone un nuevo enfoque no paramétrico. El objetivo principal de esta parte es comparar el enfoque paramétrico y la metodología no paramétrica, señalando las diferencias entre ambos. Esta primera parte está organizada de la siguiente manera:

- **Capítulo 1: Caracterización paramétrica de materiales porosos multicapa.** Desde un punto de vista macroscópico, los materiales porosos pueden ser modelados utilizando un modelo paramétrico clásico, como el modelo de fluido equivalente. Por esta razón, a lo largo del capítulo, se ha realizado una revisión detallada de los distintos modelos paramétricos de fluido equivalente, atendiendo a sus parámetros

intrínsecos. Puesto que los datos experimentales disponibles son de materiales con una y con varias capas, se ha realizado un estudio de varios problemas de propagación acústica en medios multicapa con distintas configuraciones, especificando las diferentes condiciones de acople utilizadas entre los medios (condiciones de contacto, pared rígida o condiciones de radiación) y las cantidades acústicas más relevantes (coeficiente de absorción o impedancia de superficie de un medio). Por último, se muestran resultados numéricos obtenidos utilizando un ajuste con un modelo paramétrico, para ilustrar en qué situaciones es útil un enfoque paramétrico, y los puntos débiles de esta metodología, en los que un enfoque no paramétrico puede no solo mejorar los resultados del ajuste paramétrico sino también solucionar las dificultades que aparecen cuando se utiliza dicho ajuste.

- **Capítulo 2: Enfoque no paramétrico de fluido equivalente para la caracterización acústica de materiales porosos rígidos.** Para evitar la incertidumbre epistémica cuando el modelo paramétrico elegido para caracterizar un material poroso rígido no es el adecuado, en este capítulo se considera un enfoque basado en datos, evitando la elección de una ley constitutiva dependiente de la frecuencia para el ajuste. Teniendo en cuenta los datos experimentales disponibles y sin considerar ninguna dependencia funcional de los parámetros, se resuelve numéricamente un problema inverso para cada frecuencia de interés. En este capítulo, se definen las cantidades acústicas utilizadas para caracterizar los materiales porosos y se describe el montaje utilizado para medir los datos experimentales. Dicho montaje describe la metodología desarrollada por Utsuno [171] para caracterizar materiales de una capa, por lo que se ha utilizado para validar los resultados obtenidos con la metodología propuesta. Se explica detalladamente el problema inverso utilizado, se estudia si el problema está bien o mal planteado y se examinan cuatro estrategias diferentes utilizadas para elegir las incógnitas en el problema inverso. Cada una de ellas supera las limitaciones de la estrategia anterior. Los resultados numéricos muestran que la metodología propuesta es útil en una configuración de una sola capa de material poroso, comparando los resultados con los obtenidos con el método de Utsuno, y que puede ampliarse a una configuración de dos capas de materiales porosos, en la que no pueden aplicarse otras metodologías, mostrando una buena concordancia cuando se comparan los resultados numéricos con los datos experimentales.

El trabajo descrito en este capítulo es una colaboración con Jesús Carbajo y Jaime Ramis del Departamento de Física, Ingeniería de Sistemas y Teoría de la Señal de la Universidad de Alicante, y parte de los resultados presentados en este capítulo se encuentran publicados en [54].

Parte II: Caracterización de materiales viscoelásticos en acústica submarina La segunda parte de este documento está dedicada al estudio del comportamiento acústico de un material viscoelástico a frecuencias ultrasónicas en acústica submarina. El material es una capa de polímero que tiene un comportamiento viscoelástico a frecuencias ultrasónicas. Los datos experimentales disponibles son la reducción de eco (ER), la pérdida por inserción

(IL) y el coeficiente de disipación de potencia (FPD), medidas dentro de un tanque de agua. Esta segunda parte tiene dos objetivos principales. El primero es caracterizar el material viscoelástico considerando que tiene superficie plana, utilizando un enfoque basado en datos. En este primer caso, se ha estudiado un problema de propagación acústica donde se han tenido en cuenta dos fuentes acústicas diferentes: una onda plana que incide en el material con un ángulo de incidencia oblicuo, y una fuente acústica con un patrón de directividad no plano. El segundo objetivo de esta parte es caracterizar el material viscoelástico teniendo en cuenta su superficie periódica y no plana. Para ello, se utiliza un método de ecuaciones integrales para resolver un problema de transmisión entre dos medios, considerando una interfaz de acople periódica entre ellos. A continuación se explica la organización de esta segunda parte:

- **Capítulo 3: Caracterización no paramétrica de materiales viscoelásticos.**

En este capítulo, se ha caracterizado una capa de material polimérico debajo del agua, a frecuencias ultrasónicas. Aunque el material original tiene una superficie no plana, se considera como primera simplificación que su superficie es plana. En primer lugar, se describen los modelos matemáticos de los medios involucrados en el multicapa: fluido compresible disipativo y sólido viscoelástico. Despues se describe el problema acoplado que se está considerando, y las cantidades acústicas de interés (coeficientes de reflexión y de transmisión, ER, IL y FPD). Se han descrito dos problemas de propagación de ondas: cuando la fuente es una onda plana que incide en el material con incidencia oblicua, y cuando la fuente acústica es un array paramétrico, con un patrón de directividad no plano. Puesto que la metodología utilizada para la caracterización es un enfoque basado en datos, se resuelve numéricamente un problema inverso para cada frecuencia de interés. A lo largo del capítulo, se muestran diferentes leyes constitutivas que se han considerado sobre las incógnitas del problema inverso (considerar que el módulo de Young es una función lineal de la frecuencia, que está gobernado por una función arbitraria suave y dependiente de la frecuencia, o considerar unas nuevas variables que dependen del número de onda del material y de su espesor), mostrando las dificultades derivadas de cada una de ellas y cómo pueden superarse. Se ha demostrado que el problema está mal planteado y se ha realizado una validación de la metodología propuesta, utilizando datos manufacturados. Para ilustrar la robustez de la metodología utilizada con respecto al iterante inicial elegido para resolver el problema de optimización, se ha considerado una variedad de iterantes iniciales en una cuadrícula alrededor del valor exacto. Se han realizado curvas de ajuste para las cantidades de interés, ER, IL y FPD, para mostrar la variabilidad de las respuestas en frecuencia al variar el iterante inicial. Finalmente, se muestran resultados numéricos con un material real para ilustrar la eficacia del método propuesto.

- **Capítulo 4: Simulación numérica de materiales con geometrías no planas.**

Se considera el mismo sólido viscoelástico que en el capítulo anterior, pero, en este caso, su superficie es periódica y no plana. Dado que el problema de transmisión entre dos medios, con una superficie periódica no plana y considerando que la fuente tiene

un patrón de directividad no plano presenta muchas dificultades, se han hecho varias simplificaciones (la fuente acústica considerada es una onda plana que incide con un ángulo de incidencia oblicuo y se han despreciado los posibles efectos de cizallamiento, suponiendo que el material solamente puede deformarse por tensiones mecánicas de tensión/compresión). A lo largo de este capítulo se propone un método de ecuaciones integrales para resolver este problema. El problema que aparece en dicho método es que no converge para todas las frecuencias. Para lograr que el método propuesto tenga una convergencia rápida, se ha usado una función de Green cuasi-periódica desplazada y una técnica de ventaneo. A lo largo del capítulo y en aras de la completitud, se han descrito dos problemas diferentes. El primer problema es la dispersión de ondas acústicas por una superficie periódica con frontera libre. Para resolver este problema se han utilizando representaciones de simple y de doble capa. En ambos casos se ha detallado el desarrollo del método integral, explicando el problema de convergencia que aparece en los núcleos integrales. Puesto que estos núcleos involucran funciones de Hankel y de Bessel, aparecen singularidades logarítmicas que hay que tratar de forma separada, dividiendo dichos núcleos en una parte suave y una parte que contiene la singularidad. Además, se definen reglas de cuadratura para aproximar todas las integrales que aparecen en el método. El segundo problema a estudiar, es el problema de transmisión por una interfaz de acople periódica entre dos medios. Al igual que en el caso anterior, se han utilizado potenciales de simple y de doble capa en las formulaciones integrales. En este caso, además de aparecer los núcleos que aparecían en el primer problema, aparecen núcleos hipersingulares. Dichos núcleos también tienen singularidades logarítmicas que son resueltas separando la integral en dos integrales (una con un núcleo suave y otra que contiene la parte logarítmica), que son aproximadas con las reglas de cuadratura descritas anteriormente. Al final del capítulo se muestran los resultados numéricos. Para validar la metodología, se han comparado los resultados con los obtenidos utilizando el método de elementos finitos con una malla grosera, mostrando que los errores son varios órdenes menores. Además, se calculan las eficiencias para mostrar el rápido orden de convergencia del método.

El trabajo descrito en este capítulo es una colaboración con el profesor Oscar P. Bruno del California Institute of Technology, realizado durante una estancia predoctoral de 14 semanas.

Parte III: Caracterización de sistemas complejos utilizando problemas dependientes del tiempo. La última parte de la tesis muestra la caracterización de sistemas complejos en los que intervienen diferentes tipos de materiales, como materiales porosos rígidos, sólidos viscoelásticos o materiales poroelásticos, utilizando problemas dependientes del tiempo. Los datos experimentales disponibles proceden de dos configuraciones diferentes: los coeficientes de absorción en campo difuso, medidos en una cabina alfa, y la rigidez dinámica, medida mediante un método de excitación. En primer lugar, se propone una metodología para calcular el coeficiente de absorción en campo difuso de un material

poroso en una cabina alfa. En segundo lugar, se explica un nuevo método basado en un enfoque de modelización jerárquica para calcular la rigidez dinámica de un sólido viscoelástico o poroelástico. Esta tercera parte se organiza de la siguiente manera:

- **Capítulo 5: Caracterización de materiales porosos utilizando cabinas alfa.**

Aunque el coeficiente de absorción en campo difuso de un material puede ser calculado a partir de el coeficiente de absorción medido en el tubo de Kundt, la técnica más común para calcularlo es el utilizar una cámara reverberante. En la industria automovilística el coeficiente de absorción de un material se suele medir en una cabina alfa que es una cámara reverberante donde el rango de frecuencia y el tamaño de la muestra está adaptado a los requerimientos de la acústica automovilística. Puesto que no existe un standard sobre cómo medir el coeficiente de absorción en la cabina, en este capítulo se propone una modificación de la técnica utilizada en la cámara reverberante. El objetivo principal es adaptar la metodología disponible a las dimensiones de la cabina alfa para conseguir medir el campo difuso. Por esta razón, se hacen diferentes supuestos sobre el comportamiento del sonido dentro de la cabina. Para medir el coeficiente de absorción, es necesario medir el tiempo de reverberación en la cabina con la muestra y sin la muestra. Por tanto, se considera una discretización dependiente del tiempo para calcular el tiempo de reverberación en la cabina, y se dan dos expresiones diferentes para obtener el coeficiente de absorción en campo difuso a partir de dicho tiempo de reverberación (fórmulas de Sabine y Millington). Por último, se muestran resultados numéricos en dominios bidimensionales y tridimensionales para ilustrar la eficacia del método propuesto.

- **Capítulo 6: Modelado jerárquico para determinar las propiedades mecánicas de un material elástico utilizando su rigidez dinámica.**

La rigidez dinámica de un material elástico es muy importante para cuantificar la reducción de la propagación del ruido. Por esta razón, esta cantidad puede ser utilizada para determinar el aislamiento acústico producido por este tipo de materiales. El propósito de este capítulo consiste en obtener los coeficientes elásticos del material, utilizando una metodología numérica basada en un modelado jerárquico, y considerando únicamente los datos experimentales disponibles. La definición de la jerarquía de modelos se hace considerando desde los modelos más simples hasta aquellos en los que se tienen en cuenta los detalles más sofisticados y sus niveles de precisión se basan en las suposiciones hechas en cada nivel. En este enfoque, las diferencias entre los modelos matemáticos se basan en la elección de un modelo unidimensional o tridimensional y en el uso o no de los modos de cizallamiento que posiblemente estén contribuyendo a la solución. Se proponen diferentes modelos para describir el comportamiento de los materiales viscoelásticos y poroelásticos, y se considera una discretización dependiente del tiempo para resolver el problema. Se presentan algunos resultados numéricos con datos manufacturados para validar el código, además de algunos resultados preliminares con un material real.

El trabajo descrito en este capítulo es una colaboración con Jesús Carbajo, Pedro

Poveda y Jaime Ramis del Departamento de Física, Ingeniería de Sistemas y Teoría de la Señal de la Universidad de Alicante.

La última parte de este documento está dedicada a proponer algunas líneas de investigación futuras, algunas de las cuales están comenzando a desarrollarse, y otras son problemas abiertos que, debido a su relevancia, podrían estudiarse en un futuro.

Fundings

This work has been partially supported by

- the Xunta de Galicia project ED431C2018/33, “Axudas do programa de consolidación e estructuración de unidades de investigación competitivas”.
- the MINECO project MTM2016-76497-R, “Modelos matemáticos y simulación numérica para retos en finanzas cuantitativas, medioambiente, biotecnología y eficiencia industrial”.
- the Xunta de Galicia project CN2012/130, “Axudas do programa de consolidación e estructuración de unidades de investigación competitivas”.
- the Technological Institute for Industrial Mathematics project ITMATI-OT-07/2016, “Investigación en materiales poliméricos para la protección térmica y acústica”.

Furthermore, the last part of the thesis was made in an stage in California Institute of Technology (United States of America) founded by the grant INDITEX-UDC 2018.

Bibliography

- [1] ISO 10534-2:1998. Determination of sound absorption coefficient and impedance in impedance tubes. Part 2: Transfer-function method. International. Technical report, International Standard Organization, Geneva, Switzerland, 1998.
- [2] ISO 354:2003(E). Acoustics - Measurement of sound absorption in a reverberation room. Technical report, International Standard Organization, Geneva, Switzerland, 2003.
- [3] ISO 9052-1:1989. Determination of dynamic stiffness. Part 1: Materials used under floating floors in dwellings. Technical report, International Standard Organization, Geneva, Switzerland, 1989.
- [4] M. Abramowitz and I. A. Stegun. *Handbook of Mathematical Functions with Formulas, Graphs, and Mathematical Tables*. Dover, 10 edition, 1972.
- [5] Precision Acoustic. Aptflex SF5048 data sheet. <http://acoustics.co.uk/products/acoustic-absorbers-syntactic-foams/anechoic-absorbers/apltile-sf5048>. [Online; Last accessed: 25th September 2019].
- [6] T. Ahlersmeyer. 9-Advanced experimental techniques in vehicle noise and vibration refinement. In X. Wang, editor, *Vehicle Noise and Vibration Refinement*, pages 189–216. Woodhead Publishing, 2010.
- [7] J. F. Allard and N. Atalla. *Propagation of Sound in Porous Media: Modeling Sound Absorbing Materials*. John Wiley & Sons, 2nd edition, 2009.
- [8] J. P. Arenas, J. L. Castaño, L. Troncoso, and M. L. Auad. Thermoplastic polyurethane/laponite nanocomposite for reducing impact sound in a floating floor. *Applied Acoustics*, 155:401–406, 2019.
- [9] T. Arens, S. Chandler-Wilde, and J. DeSanto. On integral equation and least squares methods for scattering by diffraction gratings. *Communications in Computational Physics*, 1:1010–1042, 2006.
- [10] N. Atalla, R. Panneton, and P. Debergue. A mixed displacement-pressure formulation for poroelastic materials. *Journal of the Acoustical Society of America*, 3(104):1444–1452, 1998.

- [11] K. Attenborough. Acoustical characteristics of porous materials. *Physics Reports*, 82(3):179–227, 1982.
- [12] K. Attenborough. Acoustical impedance models for outdoor ground surfaces. *Journal of Sound and Vibration*, 99(4):521–544, 1985.
- [13] K. Attenborough, K. M. Li, and K. V. Horoshenkov. *Predicting Outdoor Sound*. Taylor & Francis, 2006.
- [14] R. L. Bagley and P. J. Torvik. On the fractional calculus model of viscoelastic behavior. *Journal of Rheology*, 30(1):133–155, 1986.
- [15] C. G. Balachandran. Random sound field in reverberation chambers. *Journal of the Acoustical Society of America*, 31(10):1319–1321, 1959.
- [16] K. J. Bathe. *Finite Element Procedures*. Prentice Hall, 1996.
- [17] G. A. Beamish, G. Hayman, and S. P. Robinson. The provision of standards for underwater acoustics at simulated ocean conditions by use of the NPL acoustic pressure vessel. NPL report, 2001.
- [18] F. X. Bécot, C. Locqueteau, and J. Ródenas. Predicting alpha cabin sound absorption in an industrial context. volume 253, page 46484658. Institute of Noise Control Engineering, 2016.
- [19] T. Bein, J. Bös, D. Mayer, and T. Melz. 10-Advanced materials and technologies for reducing Noise, Vibration and Harshness (NVH) in automobiles. In Jason Rowe, editor, *Advanced Materials in Automotive Engineering*, pages 254–298. Woodhead Publishing, 2012.
- [20] V. A. Belogol'skii, S. S. Sekoyan, L. M. Samorukova, S. R. Stefanov, and V. I. Levtssov. Pressure dependence of the sound velocity in distilled water. *Measurement Techniques*, 42(4):406–413, 1999.
- [21] L. L. Beranek and I. L. Vér. *Noise and Vibration Control Engineering: Principles and Applications*. A Wiley Interscience publication. Wiley, 1992.
- [22] U. Berardi and G. Iannace. Acoustic characterization of natural fibers for sound absorption applications. *Building and Environment*, 94:840–852, 2015.
- [23] L. Bergmann. *Der Ultraschall*. S. Hirzel, Stuttgart, 6th edition, 1954.
- [24] A. Bermúdez. *Continuum Termomechanics*. Birkhauser, 2004.
- [25] A. Bermúdez, R. G. Durán, R. Rodríguez, and J. Solomín. Finite element analysis of a quadratic eigenvalue problem arising in dissipative acoustics. *SIAM Journal on Numerical Analysis*, 38(1):267–291, 2001.

- [26] A. Bermúdez, J. L. Ferrín, and A. Prieto. A finite element solution of acoustic propagation in rigid porous media. *International Journal for Numerical Methods in Engineering*, 62(10):1295–1314, 2005.
- [27] A. Bermúdez, L. Hervella-Nieto, A. Prieto, and R. Rodríguez. An exact bounded perfectly matched layer for time-harmonic scattering problems. *SIAM Journal on Scientific Computing*, 30:312–338, 2007.
- [28] A. Bermúdez, L. Hervella-Nieto, A. Prieto, and R. Rodríguez. An optimal perfectly matched layer with unbounded absorbing function for time-harmonic acoustic scattering problems. *Journal of Computational Physics*, 223(2):469–488, 2007.
- [29] M. A. Biot. Theory of propagation of elastic waves in a fluid-saturated porous solid. I. Low-frequency range. *Journal of the Acoustical Society of America*, 28(2):168–178, 1956.
- [30] M. A. Biot. Theory of propagation of elastic waves in a fluid-saturated porous solid. II. Higher frequency range. *Journal of the Acoustical Society of America*, 28(2):179–191, 1956.
- [31] M. S. Bischel, K. P. Roy, and J. V. Greenslade. Comparison of ASTM and ISO sound absorption test methods. *Journal of the Acoustical Society of America*, 123(5):3189–3189, 2008.
- [32] D. T. Blackstock. *Fundamentals of Physical Acoustics*. John Wiley & Sons, 2000.
- [33] P. Bonfiglio and F. Pompoli. Inversion problems for determining physical parameters of porous materials: Overview and comparison between different methods. *Acta Acustica united with Acustica*, 99:341–351, 2013.
- [34] B. Botterman, G. C. H. Doudart de la Grée, M. C. J. Hornikx, Q. L. Yu, and H. J. H. Brouwers. Modelling and optimization of the sound absorption of wood-wool cement boards. *Applied Acoustics*, 129:144–154, 2018.
- [35] C. Boutin, P. Royer, and J. L. Auriault. Acoustic absorption of porous surfacing with dual porosity. *International Journal of Solids and Structures*, 35:4709–4737, 1998.
- [36] A. W. Bowman and A. Azzalini. *Applied Smoothing Techniques for Data Analysis: the Kernel Approach with S-Plus Illustrations*, volume 18. OUP Oxford, 1997.
- [37] L. M. Brekhovskikh. *Waves In Layered Media*, volume 16 of *Applied Mathematics and Mechanics*. Academic Press, 2nd edition, 1980.
- [38] H. Brézis, P. G. Ciarlet, and J. L. Lions. *Analyse Fonctionnelle: Théorie et Applications*. Collection Mathématiques Appliquées pour la Maîtrise. Dunod, 1999.

- [39] O. P. Bruno and B. Delourme. Rapidly convergent two-dimensional quasi-periodic Green function throughout the spectrum - including Wood anomalies. *Journal of Computational Physics*, 262:262–290, 2014.
- [40] O. P. Bruno and A. G. Fernandez-Lado. Rapidly convergent quasi-periodic Green functions for scattering by arrays of cylinders-including Wood anomalies. *Proceedings of the Royal Society A: Mathematical, Physical and Engineering Sciences*, 473(2199):20160802, 2017.
- [41] O. P. Bruno, E. Garza, and C. Pérez-Arancibia. Windowed Green function method for nonuniform open-waveguide problems. *IEEE Transactions on Antennas and Propagation*, 65(9):4684–4692, 2017.
- [42] O. P. Bruno and M. C. Haslam. Efficient high-order evaluation of scattering by periodic surfaces: deep gratings, high frequencies, and glancing incidences. *Journal of the Optical Society of America A*, 26(3):658–668, 2009.
- [43] O. P. Bruno and M. C. Haslam. Efficient high-order evaluation of scattering by periodic surfaces: vector-parametric gratings and geometric singularities. *Waves in Random and Complex Media*, 20(4):530–550, 2010.
- [44] O. P. Bruno and F. Reitich. Solution of a boundary value problem for the Helmholtz equation via variation of the boundary into the domain. *Proceedings of the Royal Society of Edinburgh: Section A Mathematics*, 122(3-4):317–340, 1992.
- [45] O. P. Bruno and F. Reitich. Numerical solution of diffraction problems: a method of variation of boundaries. *Journal of the Optical Society of America*, 10(6):1168–1175, 1993.
- [46] O. P. Bruno and F. Reitich. Numerical solution of diffraction problems: a method of variation of boundaries. II. Finitely conducting gratings, Padé approximants, and singularities. *Journal of the Optical Society of America*, 10(11):2307–2316, 1993.
- [47] O. P. Bruno, S. P. Shipman, C. Turc, and S. Venakides. Superalgebraically convergent smoothly windowed lattice sums for doubly periodic Green functions in three-dimensional space. *Proceedings of the Royal Society A: Mathematical, Physical and Engineering Science*, 472:20160255, 2016.
- [48] O. P. Bruno, S. P. Shipman, C. Turc, and S. Venakides. Three-dimensional quasi-periodic shifted Green function throughout the spectrum, including Wood anomalies. *Proceedings of the Royal Society A: Mathematical, Physical and Engineering Sciences*, 473(2207):20170242, 2017.
- [49] M. L. Bucalem and K. J. Bathe. *The Mechanics of Solids and Structures-Hierarchical Modeling and the Finite Element Solution*. Springer Science & Business Media, 2011.

- [50] ASTM C423-09a. Standard test method for sound absorption and sound absorption coefficients by the reverberation room method. Technical report, American Society for Testing Materials, United States, 2009.
- [51] C. J. Cameron, P. Wennhage, and P. Göransson. Prediction of NVH behaviour of trimmed body components in the frequency range 100-500Hz. *Applied Acoustics*, 71(8):708–721, 2010.
- [52] F. Capolino, D. R. Wilton, and W. A. Johnson. Efficient computation of the 3D Greens function for the Helmholtz operator for a linear array of point sources using the Ewald method. *Journal of Computational Physics*, 223:250–261, 2007.
- [53] J. Carbajo, A. Prieto, J. Ramis, and L. Río-Martín. Data-driven characterization of porous materials by using frequency-dependent measurements. In *Tecniacústica 2017: 48º Congreso Español de Acústica; Encuentro Ibérico de Acústica; European Symposium on Underwater Acoustics Applications; European Symposium on Sustainable Building Acoustics: A Coruña 3-6 Octubre 2017*, pages 739–746. Sociedad Española de Acústica, 2017.
- [54] J. Carbajo, A. Prieto, J. Ramis, and L. Río-Martín. A non-parametric fluid-equivalent approach for the acoustic characterization of rigid porous materials. *Applied Mathematical Modelling*, 76:330–347, 2019.
- [55] Y. Champoux and J. F. Allard. Dynamic tortuosity and bulk modulus in air-saturated porous media. *Journal of Applied Physics*, 70:1975–1979, 1991.
- [56] J. Y. Chen. Reducing noise in automotive interiors. *Textile Advances in the Automotive Industry*, pages 198–228, 2008.
- [57] T. Cho. Experimental and numerical analysis of floating floor resonance and its effect on impact sound transmission. *Journal of Sound and Vibration*, 332(25):6552–6561, 2013.
- [58] R. M. Christensen. *Theory of Viscoelasticity*. Dover Civil and Mechanical Engineering. Dover Publications, 2nd edition, 2013.
- [59] T. F. Coleman and Y. Li. An interior, trust region approach for nonlinear minimization subject to bounds. 6:418–445, 1996.
- [60] T. F. Colleman and Y. Li. On the convergence of interior-reflective Newton methods for nonlinear minimization subject to bounds. *Mathematical Programming*, 67(2):189–224, 1994.
- [61] T. F. Colleman and Y. Li. A reflective Newton method for minimizing a quadratic function subject to bounds on some of the variables. *SIAM Journal on Optimization*, 6:418–445, 1996.

- [62] R. E. Collin. *Field Theory of Guided Waves*. IEEE Press, 1991.
- [63] D. L. Colton. *Partial Differential Equations: an Introduction*. Dover books on mathematics. Dover Publications, 2004.
- [64] S. Conti, S. Müller, and M. Ortiz. Data-driven problems in elasticity. *Archive for Rational Mechanics and Analysis*, 229(1):79–123, 2018.
- [65] A. Cops, J. Vanhaecht, and K. Leppens. Sound absorption in a reverberation room: Causes of discrepancies on measurement results. *Applied Acoustics*, 46(3):215–232, 1995.
- [66] T. Cox and P. D’Antonio. *Acoustic Absorbers and Diffusers. Theory, Design and Application*. Spon Press, 3rd edition, 2016.
- [67] A. Cuevas, M. Febrero, and R. Fraiman. Robust estimation and classification for functional data via projection-based depth notions. *Computational Statistics*, 22(3):481–496, 2007.
- [68] S. M. Dance and B. M. Shield. Modelling of sound fields in enclosed spaces with absorbent room surfaces. Part I: performance spaces. *Applied Acoustics*, 58(1):1–18, 1999.
- [69] M. A. Delany and E. N. Bazley. Acoustic properties of fibrous absorbent materials. *Applied Acoustics*, 3:105–116, 1970.
- [70] O. Doutres, Y. Salissou, N . Atalla, and R. Panneton. Evaluation of the acoustic and non-acoustic properties of sound absorbing materials using a three-microphone impedance tube. *Journal of the Acoustical Society of America*, 71(6):506–509, 2010.
- [71] ASTM E756-98. Standard test method for measuring vibration-damping properties of materials. Technical report, American Society For Testing and Materials, 2010.
- [72] B. Engquist, A. Fokas, E. Hairer, and A. Iserles. *Highly Oscillatory Problems*. London Mathematical Society Lecture Note Series, 366. Cambridge University Press, 2009.
- [73] R. M. Errico. What is an adjoint model? *Bulletin of the American Meteorological Society*, 78(11):2577–2592, 1997.
- [74] C. F. Eyring. Reverberation time in ‘dead’ rooms. *Journal of the Acoustical Society of America*, 1(2):217–241, 1930.
- [75] F. Fahy. *Foundations of Engineering Acoustics*. Academic Press, 2001.
- [76] F. J. Fahy. *Sound and Structural Vibration. Radiation, Transmission and Response*. Academic Press, 1987.

- [77] M. Febrero-Bande and M. O. de la Fuente. Statistical computing in functional data analysis: The R package fda.usc. *Journal of Statistical Software*, 51(i04), 2012.
- [78] Z. E. A. Fellah, C. Depollier, S. Berger, W. Lauriks, P. Trompette, and J. Y. Chapelon. Determination of transport parameters in air-saturated porous materials via reflected ultrasonic waves. *Journal of the Acoustical Society of America*, 114(5):2561–2569, 2003.
- [79] Z. E. A. Fellah, F.G. Mitri, M. Fellah, E. Ogam, and C. Depollier. Ultrasonic characterization of porous absorbing materials: Inverse problem. *Journal of Sound and Vibration*, 302(4-5):746–759, 2007.
- [80] J. D. Ferry. *Viscoelastic Properties of Polymers*. Wiley, 1980.
- [81] W. Flügge. *Viscoelasticity*. A Blaisdell Book in Solid Mechanics. Blaisdell Publishing Company, 1967.
- [82] G. Gatica. Raviart-Thomas spaces. In *A Simple Introduction to the Mixed Finite Element Method. Theory and Applications*, chapter 3, pages 61–91. Springer, 2014.
- [83] A. Geslain, J. P. Groby, O. Dazel, S. Mahasaranon, K. V. Horoshenkov, and A. Khan. An application of the Peano series expansion to predict sound propagation in materials with continuous pore stratification. *Journal of the Acoustical Society of America*, 132(1):208–215, 2012.
- [84] M. B. Giles and N. A. Pierce. An introduction to the adjoint approach to design. *Flow, Turbulence and Combustion*, 65(3):393–415, 2000.
- [85] D. Givoli. *Numerical Methods for Problems in Infinite Domains*, volume 33. Elsevier, 2013.
- [86] D. González, F. Chinesta, and E. Cueto. Consistent data-driven computational mechanics. *AIP Conference Proceedings*, 1960(1):090005, 2018.
- [87] P. Guidorzi, L. Barbaresi, and M. Garai. Measuring the dynamic stiffness of resilient materials using ESS and MLS signals. *Applied Acoustics*, 138:92–100, 2018.
- [88] M. E. Gurtin and E. Sternberg. On the linear theory of viscoelasticity. *Archive for Rational Mechanics and Analysis*, 11(1):291–356, 1962.
- [89] D. Habault. *Fluid-Structure Interactions in Acoustics*. CISM International Centre for Mechanical Sciences. Springer Vienna, 2014.
- [90] C. Hazard and E. Lunéville. An improved multimodal approach for non-uniform acoustic waveguides. *IMA Journal of Applied Mathematics*, 73(4):668–690, 2008.

- [91] M. Hodgson. Experimental evaluation of the accuracy of the Sabine and Eyring theories in the case of non-low surface absorption. *Journal of the Acoustical Society of America*, 94(2):835–40, 1993.
- [92] M. Hodgson. When is diffuse field theory applicable? *Applied Acoustics*, 49(3):197–207, 1996.
- [93] K. V. Horoshenkov. A review of acoustical methods for porous material characterisation. *International Journal of Acoustics and Vibration*, 22(1):92–103, 2017.
- [94] D. Huet. *Décomposition Spectrale et Opérateurs*. Le Mathématicien. Presses Universitaires de France, 1976.
- [95] V. F. Humphrey and H. O. Berkay. The transmission coefficient of a panel measured with a parametric source. *Journal of Sound and Vibration*, 101(1):85–106, 1985.
- [96] F. Ihlenburg. *Finite Element Analysis of Acoustic Scattering*, volume 132. Springer, 2006.
- [97] International Association for the Properties of Water and Steam, IAPWS R6-95. Revised release on the IAPWS formulation 1995 for the thermodynamic properties of ordinary water substance for general and scientific use. In *Proceedings of the 15th International Association for the Properties of Water and Steam*, 2018.
- [98] V. G. Jayakumari, R. K. Shamsudeen, R. Ramesh, and T. Mukundan. Modeling and validation of polyurethane based passive underwater acoustic absorber. *Journal of the Acoustical Society of America*, 130(2):724–730, 2011.
- [99] J. Y. Jeon, J. Jeong, M. Vorländer, and R. Thaden. Evaluation of floor impact sound insulation in reinforced concrete buildings. *Acta Acustica united with Acustica*, 90:313–318, 2004.
- [100] D. L. Johnson, J. Koplik, and R. Dashen. Theory of dynamic permeability and tortuosity in fluid-saturated porous media. *Journal of Fluid Mechanics*, 176:379–402, 1987.
- [101] P. Junglas. Implementing the IAPWS-95 standard in MATLAB. In *Proceedings of the 15th International Conference on the Properties of Water and Steam*, 2008.
- [102] R. Keshavarz and A. Ohadi. A new analytical approach for the modeling of sound propagation in a stratified medium. *Applied Mathematical Modelling*, 50:237–256, 2017.
- [103] L. Kiefling and G. C. Feng. Fluid-structure finite element vibrational analysis. *AIAA Journal*, 14(2):199–203, 1976.

- [104] S. Y. Kim and D. H. Lee. Identification of fractional-derivative-model parameters of viscoelastic materials from measured FRFs. *Journal of Sound and Vibration*, 324:570–586, 2009.
- [105] T. Kirchdoerfer and M. Ortiz. Data-driven computational mechanics. *Computer Methods in Applied Mechanics and Engineering*, 304:81–101, 2016.
- [106] A. Kirsch. Diffraction by periodic structures. In L. Päivärinta and E. Somersalo, editors, *Inverse Problems in Mathematical Physics*, pages 87–102, Berlin, Heidelberg, 1993. Springer Berlin Heidelberg.
- [107] R. Kress. *Linear Integral Equations*. Applied Mathematical Sciences. Springer New York, 3rd edition, 2013.
- [108] R. Kussmaul. Ein numerisches Verfahren zur Lösung des Neumannschen Außenraumproblems für die Helmholtzsche Schwingungsgleichung. *Computing*, 4:246–273, 1969.
- [109] H. Kuttruff. *Room Acoustics*. Spon Press, 5th edition, 2009.
- [110] D. Lafarge. *Propagation du Son dans les Matériaux Poreux à Structure Rigide Saturés par un Fluide Viscothermique-Définition de Panamètres Géométriques, Analogie Électromagnétique, Temps de Relaxation et “Théorie Universeile”*. PhD thesis, Université du Main, 1993.
- [111] D. Lafarge, P. Lemarinier, J. F. Allard, and V. Tarnow. Dynamic compressibility of air in porous structures at audible frequencies. *Journal of the Acoustical Society of America*, 102:1995–2006, 1997.
- [112] J. C. Lagarias, J. A. Reeds, M. H. Wright, and P. E. Wright. Convergence properties of the Nelder-Mead simplex method in low dimensions. *SIAM Journal on Optimization*, 9(1):112–147, 1998.
- [113] L. D. Landau and E. M. Lifshitz. *Fluid Mechanics*. Pergamon Press, 1987.
- [114] W. Larbi. Numerical modeling of sound and vibration reduction using viscoelastic materials and shunted piezoelectric patches. *Computers & Structures*, page 105822, 2017.
- [115] N. N. Lebedev and R. A. Silverman. *Special Functions and Their Applications*. Dover Books on Mathematics. Dover Publications, 1972.
- [116] C. M. Linton. The Green’s function for the two-dimensional Helmholtz equation in periodic domains. *Journal of Engineering Mathematics*, 33:377–401, 1998.
- [117] C. M. Linton. Lattice sums for the Helmholtz equation. *SIAM Review*, 52:630–674, 2010.

- [118] E. G. Loewen and E. Popov. *Diffraction Gratings and Applications*. Optical Science and Engineering. Taylor & Francis, 1997.
- [119] A. London. The determination of reverberant sound absorption coefficients from acoustic impedance measurements. *Journal of the Acoustical Society of America*, 22(2):263–269, 1950.
- [120] Mahmood-ul-Hassan. Wave scattering by soft-hard three spaced waveguide. *Applied Mathematical Modelling*, 38(17):4528–4537, 2014.
- [121] F. Mainardi. *Fractional Calculus and Waves in Linear Viscoelasticity. An introduction to Mathematical Models*. Imperial College Press, 2010.
- [122] E. Martensen. Über eine Methode zum räumlichen Neumannschen Problem mit einer Anwendung für torusartige Berandungen. *Acta Mathematica*, 109:75–135, 1963.
- [123] D. Maystre. I. Rigorous Vector Theories of Diffraction Gratings. volume 21 of *Progress in Optics*, pages 1–67. Elsevier, 1984.
- [124] M. A. Meyers and K. K. Chawla. *Mechanical Behavior of Materials*. Prentice Hall, 1999.
- [125] Y. Miki. Acoustical properties of porous materials, generalization of empirical models. *Journal of the Acoustical Society of Japan (E)*, 11:25–28, 1990.
- [126] Y. Miki. Acoustical properties of porous materials, modifications of Delany-Bazley models. *Journal of the Acoustical Society of Japan (E)*, 11:19–24, 1990.
- [127] G. Millington. A modified formula for reverberation. *Journal of the Acoustical Society of America*, 4:69–81, 1932.
- [128] J. A. Monro. *A Super-Algebraically Convergent, Windowing-Based Approach to the Evaluation of Scattering from Periodic Rough Surfaces*. PhD thesis, California Institute of Technology, 2008.
- [129] R. Morgans, C. Howard, A. Zander, C. Hansen, and D. Murphy. Derivative free optimisation in engineering acoustics. In *ICSV 2007: Proceedings of the 14th International Congress on Sound and Vibration*, volume 1, 2007.
- [130] D. H. Mueller and A. Krobjilowski. New discovery in the properties of composites reinforced with natural fibers. *Journal of Industrial Textiles*, 33(2):111–130, 2003.
- [131] J. A. Nelder and R. Mead. A simplex method for function minimization. *The Computer Journal*, 7(4):308–313, 1965.
- [132] H. Nélisse and J. Nicolas. Characterization of a diffuse field in a reverberant room. *Journal of the Acoustical Society of America*, 101(6):3517–3524, 1997.

- [133] P. A. Nelson. Vibration isolation on floating floors. *Applied Acoustics*, 15(2):97–109, 1982.
- [134] M. Nevière and E. Popov. *Light Propagation in Periodic Media: Differential Theory and Design*. Marcel Dekker, New York, 2003.
- [135] A. Nick, U. Becker, and W. Thoma. Improved acoustic behavior of interior parts of renewable resources in the automotive industry. *Journal of Polymers and the Environment*, 10:115–118, 2002.
- [136] J. Nocedal and S. Wright. *Numerical Optimization*. Springer Series in Operations Research and Financial Engineering. Springer New York, 2006.
- [137] G. Noh and K. J. Bathe. An explicit time integration scheme for the analysis of wave propagations. *Computers & Structures*, 129:178–193, 2013.
- [138] E. J. Nyström. Über Die Praktische Auflösung von Integralgleichungen mit Anwendungen auf Randwertaufgaben. *Acta Mathematica*, 54:185–204, 1930.
- [139] H. Oberst and K. Frankenfeld. Über die Dämpfung der Biegeschwingungen dünner Bleche durch fest haftende Beläge. *Acustica* 2, AB:181–194, 1952.
- [140] R. Ohayon and C. Soize. *Structural Acoustics and Vibration: Mechanical Models, Variational Formulations and Discretization*. Elsevier Science, 1997.
- [141] X. Olny and C. Boutin. Acoustic wave propagation in double porosity media. *Journal of the Acoustical Society of America*, 114:73–89, 2003.
- [142] S. Olver. *Numerical approximation of highly oscillatory integrals*. PhD thesis, University of Cambridge, 2008.
- [143] D. Olynyk and T. D. Northwood. Comparison of reverberation room and impedance tube absorption measurements. *Journal of the Acoustical Society of America*, 36(11):2171–2174, 1964.
- [144] R. Panneton. Comments on the limp frame equivalent fluid model for porous media. *Journal of the Acoustical Society of America*, 122(6):EL217–EL222, 2007.
- [145] D. V. Parikh, Y. Chen, and L. Sun. Reducing automotive interior noise with natural fiber nonwoven floor covering systems. *Textile Research Journal*, 76(11):813–820, 2006.
- [146] R. Petit, L. C. Botten, M. Cadilhac, G. H. Derrick, D. Maystre, R. C. McPhedran, M. Neviere, and P. Vincent. *Electromagnetic Theory of Gratings*. Topics in Current Physics. Springer Berlin Heidelberg, 2013.

-
- [147] S. R. Pride, F. D. Morgan, and A. F. Gangi. Drag forces of porous-medium acoustics. *Physical Review B*, 47(9):4964–4978, 1993.
 - [148] J. Prisutova, K. Horoshenkov, J. P. Groby, and B. Brouard. A method to determine the acoustic reflection and absorption coefficients of porous media by using modal dispersion in a waveguide. *Journal of the Acoustical Society of America*, 136(6):2947–2958, 2014.
 - [149] D. Rade, J. F. Deü, D. Castello, A. M. G. Lima, and L. Rouleau. *Passive Vibration Control Using Viscoelastic Materials*, pages 119–168. 2019.
 - [150] J. Ramis, J. Alba, R. del Rey, E. Escuder, and V. J. Sanchís. New absorbent material acoustic based on kenaf’s fibre. *Materiales de Construcción*, 60(299):133–143, 2010.
 - [151] J. Ramsay, J. Ramsay, and B.W. Silverman. *Functional Data Analysis*. Springer Series in Statistics. Springer, 2005.
 - [152] M. D. Rao. Recent applications of viscoelastic damping for noise control in automobiles and commercial airplanes. *Journal of Sound and Vibration*, 262(3):457–474, 2003. 2001 India-USA Symposium on Emerging Trends in Vibration and Noise Engineering.
 - [153] S. S. Rao. *Engineering Optimization: Theory and Practice*. John Wiley & Sons, 2009.
 - [154] P. A. Raviart and J. M. Thomas. *A Mixed Finite Element Method for Second Order Elliptic Problems*, volume 606, pages 292–315. Springer, 1977.
 - [155] Lord Rayleigh. III. Note on the remarkable case of diffraction spectra described by Prof. Wood. *The London, Edinburgh, and Dublin Philosophical Magazine and Journal of Science*, 14(79):60–65, 1907.
 - [156] C. Rivas, R. Rodríguez, and M. E. Solano. A perfectly matched layer for finite-element calculations of diffraction by metallic surface-relief gratings. *Wave Motion*, 78:68–82, 2018.
 - [157] V. Romero-García, E. Fuster-Garcia, J. V. Sánchez-Pérez, L. M. Garcia-Raffi, X. Blasco, J. M. Herrero, and J. Sanchis. Genetic algorithm in the optimization of the acoustic attenuation systems. In *International Work-Conference on Artificial Neural Networks*, pages 614–621. Springer, 2007.
 - [158] I. M. Rushforth, K. V. Horoshenkov, M. Miraftab, and M. J. Swift. Impact sound insulation and viscoelastic properties of underlay manufactured from recycled carpet waste. *Applied Acoustics*, 66(6):731–749, 2005.
 - [159] Y. Saad and M. H. Schultz. GMRES: A generalized minimal residual algorithm for solving nonsymmetric linear systems. *SIAM Journal on Scientific and Statistical Computing*, 7(3):856–869, 1986.

- [160] W. C. Sabine. *Collected Papers on Acoustics*. Harvard University Press, 1922.
- [161] Y. Salissou and R. Panneton. Wideband characterization of the complex wave number and characteristic impedance of sound absorbers. *Journal of the Acoustical Society of America*, 128(5):2868–2876, 2010.
- [162] Y. Salissou, R. Panneton, and O. Doutres. Complement to standard method for measuring normal incidence sound transmission loss with three microphones. *Journal of the Acoustical Society of America*, 131(3):EL216–EL222, 2012.
- [163] G. Sandberg and R. Ohayon. *Computational Aspects of Structural Acoustics and Vibration*. CISM International Centre for Mechanical Sciences. Springer Vienna, 2009.
- [164] A. Santoni, P. Bonfiglio, P. Fausti, C. Marescotti, V. Mazzanti, F. Mollica, and F. Pompoli. Improving the sound absorption performance of sustainable thermal insulation materials: Natural hemp fibres. *Applied Acoustics*, 150:279–289, 2019.
- [165] A. Schiavi, A. Pavoni Belli, M. Corallo, and F. Russo. Acoustical performance characterization of resilient materials used under floating floors in dwellings. *Acta Acustica united with Acustica*, 93:477–485, 2007.
- [166] M. R. Schroeder. Measurement of sound diffusion in reverberation chambers. *Journal of the Acoustical Society of America*, 31(11):1407–1414, 1959.
- [167] T. J. Schultz. Diffusion in reverberation rooms. *Journal of Sound Vibration*, 16:17–28, 1971.
- [168] D. R. Smart. *Fixed Point Theorems*, volume 66. Cambridge University Press, 1980.
- [169] B. H. Song and J. S. Bolton. A transfer-matrix approach for estimating the characteristic impedance and wave numbers of limp and rigid porous materials. *Journal of the Acoustical Society of America*, 107(3):1131–1152, 2000.
- [170] W. G. Strang and G. J. Fix. *An Analysis of the Finite Element Method*. Prentice-Hall series in automatic computation. Prentice-Hall, 1973.
- [171] H. Utsuno, T. Tanaka, T. Fujikawa, and A. F. Seybert. Transfer function method for measuring characteristic impedance and propagation constant of porous materials. *Journal of the Acoustical Society of America*, 86(2):637–643, 1989.
- [172] S. Valvano, C. Orlando, and A. Alaimo. Design of a noise reduction passive control system based on viscoelastic multilayered plate using PDSO. *Mechanical Systems and Signal Processing*, 123:153–173, 2019.
- [173] M. Vašina, D. C. Hughes, K. V. Horoshenkov, and L. Lapčík Jr. The acoustical properties of consolidated expanded clay granulates. *Applied Acoustics*, 67:787–796, 2006.

- [174] A. G. Voronovich. *Wave Scattering from Rough Surfaces*. Springer Series on Wave Phenomena. Springer Berlin Heidelberg, 2013.
- [175] S. Whitaker. Flow in porous media I: A theoretical derivation of Darcy's law. *Transport in porous media*, 1(1):3–25, 1986.
- [176] C. H. Wilcox. Scattering theory for diffraction gratings. *Mathematical Methods in the Applied Sciences*, 6(1):158–158, 1984.
- [177] K. Wilson. Relaxation-matched modeling of propagation through porous media, including fractal pore structure. *Journal of the Acoustical Society of America*, 94(2):1136–1145, 1993.
- [178] J. L. Wojtowicki, L. Jaouen, and R. Panneton. New approach for the measurement of damping properties of materials using the Oberst beam. *Review of Scientific Instruments*, 75(8):2569–2574, 2004.
- [179] R. W. Wood. On a remarkable case of uneven distribution of light in a diffraction grating spectrum. *Proceedings of the Physical Society of London*, 18(1):269–275, 1902.
- [180] S. Xiang and H. Wang. Fast integration of highly oscillatory integrals with exotic oscillators. *Mathematics of computation*, 79(270):829–844, 2010.
- [181] X. T. Xiong, W. X. Shi, and Y. C. Hon. A one-dimensional inverse problem in composite materials: Regularization and error estimates. *Applied Mathematical Modelling*, 39(18):5480–5494, 2015.
- [182] C. Zwicker and C. W. Kosten. *Sound Absorbing Materials*. Elsevier Publishing Company, 1949.